LEABHARLANN CHOLÁISTE NA TRÍONÓIDE, BAILE ÁTHA CLIATH | TRINITY COLLEGE LIBRARY DUBLIN
Ollscoil Átha Cliath | The University of Dublin

Terms and Conditions of Use of Digitised Theses from Trinity College Library Dublin

Copyright statement

All material supplied by Trinity College Library is protected by copyright (under the Copyright and Related Rights Act, 2000 as amended) and other relevant Intellectual Property Rights. By accessing and using a Digitised Thesis from Trinity College Library you acknowledge that all Intellectual Property Rights in any Works supplied are the sole and exclusive property of the copyright and/or other IPR holder. Specific copyright holders may not be explicitly identified. Use of materials from other sources within a thesis should not be construed as a claim over them.

A non-exclusive, non-transferable licence is hereby granted to those using or reproducing, in whole or in part, the material for valid purposes, providing the copyright owners are acknowledged using the normal conventions. Where specific permission to use material is required, this is identified and such permission must be sought from the copyright holder or agency cited.

Liability statement

By using a Digitised Thesis, I accept that Trinity College Dublin bears no legal responsibility for the accuracy, legality or comprehensiveness of materials contained within the thesis, and that Trinity College Dublin accepts no liability for indirect, consequential, or incidental, damages or losses arising from use of the thesis for whatever reason. Information located in a thesis may be subject to specific use constraints, details of which may not be explicitly described. It is the responsibility of potential and actual users to be aware of such constraints and to abide by them. By making use of material from a digitised thesis, you accept these copyright and disclaimer provisions. Where it is brought to the attention of Trinity College Library that there may be a breach of copyright or other restraint, it is the policy to withdraw or take down access to a thesis while the issue is being resolved.

Access Agreement

By using a Digitised Thesis from Trinity College Library you are bound by the following Terms & Conditions. Please read them carefully.

I have read and I understand the following statement: All material supplied via a Digitised Thesis from Trinity College Library is protected by copyright and other intellectual property rights, and duplication or sale of all or part of any of a thesis is not permitted, except that material may be duplicated by you for your research use or for educational purposes in electronic or print form providing the copyright owners are acknowledged using the normal conventions. You must obtain permission for any other use. Electronic or print copies may not be offered, whether for sale or otherwise to anyone. This copy has been supplied on the understanding that it is copyright material and that no quotation from the thesis may be published without proper acknowledgement.

Electrochemical Studies of the Oxygen Evolution Reaction at Passive Oxide Covered Ni, Co and Fe Electrodes in Aqueous Alkaline Solution

Michael Brandon

A Thesis submitted to
The University of Dublin
in application for the degree of
Doctor of Philosophy



School of Chemistry
University of Dublin
Trinity College
Dublin 2

September 2008

Thesis
8657

Declaration

This thesis is submitted by the undersigned for examination for the degree of Doctor in Philosophy at the University of Dublin. It has not been submitted as an exercise for a degree at any other university.

With the exception of the advice mentioned in the acknowledgements, the work described herein was carried out by the author alone.

I agree that the library may lend or copy this thesis freely on request

Michael Brandon

Michael Brandon

Summary

There has been an abundance of publications over the last twenty years on electrode materials proposed to be suitable catalysts for the oxygen evolution reaction (o.e.r.) in concentrated alkaline solution. Although it is generally accepted that RuO_2 is the most efficient electrocatalyst towards the reaction, its cost renders prohibitive the widespread adoption of this material for commercial applications. Amongst the more cost effective materials that have been forwarded as o.e.r. anodes are, various inter-metallic alloys (often containing significant amounts of Ni, Co or Fe), electrodeposited Ni (NiO_x) and Co (Co_3O_4) oxides, and mixed oxides, including spinels (particularly nickelites, cobaltites and ferrites) and perovskites. Many of these studies have been conducted on an essentially empirical basis with little attention devoted to the details of the o.e.r. mechanistic pathway. Yet the fact is, that there remains considerable controversy in the literature regarding the latter point, even in the case of passive oxide covered polycrystalline metallic electrodes. In view of this, the present work reports a comprehensive electrochemical study on the o.e.r. at Ni, Co and Fe electrodes in aqueous alkaline solution, with particular attention being paid to the question of whether or not the reaction proceeds via a common pathway at the anodic oxide covered surfaces of these three metals.

Steady state polarisation experiments have been used to quantify and compare the o.e.r. catalytic activity of electrodes at a given applied potential, and also yield experimental values of kinetically significant parameters, such as the Tafel slope, b, and the reaction order, m_{OH^-}, with respect to [OH^-]. Cyclic voltammetry has been applied in the characterisation of the surface electrochemistry of the various electrodes, and has been effective in revealing the impact of electrochemical ageing upon the passive oxide films that form on the polycrystalline metal surfaces. Electrochemical Impedance spectroscopy (EIS) measurements have demonstrated that the o.e.r. Tafel slopes, derived for the systems under study, by either dc or ac techniques, are truly characteristic of the kinetics of the reaction, and do not arise owing to the potential dependence of the resistivity and dielectric properties of the anodic oxide films. For the Ni and Fe electrodes, excellent agreement has been noted between the values of b measured by steady state polarisation and those derived from EIS measurements.

The problem of active surface area (as opposed to geometric area) estimation has been tacked by utilising the double layer capacitance ratio approach, as well as by adopting an experimental technique based upon the determination of the charge passed during the desorption of the o.e.r. intermediate species, which accompanies the discharge of an electrode following the interruption of steady state galvanostatic polarisation.

The electrochemical ageing of the surface oxy-hydroxide films, due to polarisation at the extreme anodic potentials associated with significant rates of oxygen evolution, proved to be a hindrance to the collection of reproducible kinetic data. To circumvent this problem it was necessary to devise electrode pre-treatment routines. The experimental data suggested that a different o.e.r. pathway prevails at Ni electrodes in comparison to Co and Fe electrodes. Appropriate reaction mechanisms were outlined – the oft proposed Krasil'shchikov pathway is not likely in either case. Some of characteristic values of b, that were observed, were postulated to arise due to the existence, under certain circumstances, of an addition energy barrier for charge migration across the oxide layers, in series with the usual barrier for electrochemical charge transfer at the electrode/solution interface. On the basis of voltammetric results we have identified this oxide barrier with the inner compact region of the passive film.

The current density values in the steady state polarisation curves for both non-pre-treated and pre-reduced electrodes have been normalised to the estimated real active surface areas. This analyses indicates that a catalytic activity series, towards oxygen evolution, of Ni > Co > Fe prevails over the practically important range of potentials associated with the lower straight-line Tafel regions of the respective polarisation curves. While the same conclusion arises for the data when it is normalised to the geometric surface area, the latter approach overestimates the degree of the catalytic inferiority of the Fe electrodes relative to the other metals.

Acknowledgements

First and foremost, I would like to extend my sincere thanks to my supervisor, Dr M.E.G. Lyons, whose advice and guidance always pointed me in the correct direction during both the practical and write-up stages of the present work.

Gratitude is also due to all those in the School of Chemistry whose assistance with day-to-day matters proved invaluable. These include the technical staff, particularly Patsy, Martin, Teresa, Fred and Eddie, the administrative staff - Corinne, Tess, Helen and Maria, and also Dr Noelle Scully.

The following colleagues, who passed through the Lyons group over the years are acknowledged as upstanding human beings and top class scientists – Johnny Colleran, Ray O'Brien, Michael Kinsella, Gar Keeley, Deirdre Kelleher, Dominic Janisch and Paulo DaSilva.

I would like to thank my parents Maura and Pat and my brother Paul for their patience and understanding, especially during the write-up phase of the project. Finally, I apologise to my friends for my neglect of our companionship during the writing of this thesis and promise to make reparations.

Table of Contents

List of Symbols i - vii

1.0 INTRODUCTION AND LITERATURE REVIEW

1.1 Review of Relevant Electrochemical Theory 1

1.1.1 Thermodynamic Concepts of Electrochemical Interfaces 1

1.1.2 Models of the Electrode-Solution Interface 8

1.1.3 The Oxide-Solution Interface 14

1.2 Electrode Kinetics 25

1.2.1 Fundamentals of Electrode Kinetic Theory 25

1.2.2 Adsorption Isotherms 35

1.2.3 Multistep Electrode Kinetics 40

1.3 Electrocatalysis 53

1.3.1 Basic Concepts of Electrocatalysis 53

1.3.2 The Hydrogen Evolution Reaction 57

1.3.3 Further Observations on Electrocatalysis 61

1.4 The Surface Electrochemistry of Ni, Fe and Co Electrodes in Aqueous Alkaline Solution 68

1.4.1 Nickel 68

1.4.2 Iron 87

1.4.3 Cobalt 97

1.5 The Oxygen Electrode 104

1.5.1 The Thermodynamics of the Oxygen Electrode 104

1.5.2 The Oxygen Reduction Reaction 108

1.5.3 General Comments on the Oxygen Evolution Reaction 112

1.5.4 Reaction Pathways for the Oxygen Evolution Reaction 115

2.0 EXPERIMENTAL METHODOLOGY AND PROCEDURE

2.1 Introduction To Experimental Methodology 135

2.1.1 Steady State Polarisation Measurements 135

2.1.2 Cyclic Voltammetry 138

2.1.3 Electrochemical Impedance Spectroscopy 139

2.1.4 Simple AC Circuit Theory 140

2.1.5 Extension of Impedance Theory to Electrochemical Systems 145

2.1.6 Practical Considerations and EIS Measurement Systems 152

2.1.7 Extracting Electrochemical Parameters From EIS Raw Data 156

2.1.8 Kramers-Kronig Transforms 164

2.1.9 Determination of Real Surface Area 166

2.2 Materials and Instrumentation 173

2.2.1 Electrochemical Cell 173

2.2.2 Working Electrodes 173

2.2.3 Reference Electrode 174

2.2.4 Auxiliary Electrode 176

2.2.5 Electrolyte Solutions 176

2.2.6 Electrode Pre-treatment 177

2.2.7 The Zahner elektrik IM6 Impedance measurement unit 178

2.2.8 The Potentiostat 179

2.2.9 Measuring Steady State Polarisation Data 179

2.2.10 Measuring Electrochemical Impedance Data 180

2.2.11 Experimental Estimation of Real Surface Areas 181

3.0 STEADY STATE POLARISATION AND VOLTAMMETRY STUDIES

3.1 Introduction 183

3.2 Nickel: Steady State Polarisation and Voltammetry Results 183

3.2.1 Bright Non-pre- treated Ni electrodes 183

3.2.2 Pre-reduced and Pre-oxidised Ni electrodes 198

3.3 Cobalt: Steady State Polarisation and Voltammetry Results 213

3.3.1 Bright Non-pre-treated Co electrodes 213

3.3.2 Pre-reduced and Pre-oxidised Co electrodes 237

3.4 Iron: Steady State Polarisation and Voltammetry Results 249

3.4.1 Bright Non-pre-treated Fe Electrodes 249

3.4.2 Pre-reduced and Aged Fe Electrodes 259

3.5 Further Discussion 282

3.5.1 Mechanistic Pathway for Oxygen Evolution at Ni Electrodes 282

3.5.2 The Variation of the Tafel Slope From ca. 40 to 46 mV dec^{-1} and an Appropriate Mechanism 290

3.5.3 The Dual Tafel Slope Polarisation Behaviour of Extremely Aged Electrodes 314

3.5.4 Concluding Remarks on the Mechanism of Oxygen Evolution on

Ni, Co and Fe Electrodes in Alkaline Solution, as Revealed by Steady State Polarisation Measurements 329

4.0 ELECTROCHEMICAL IMPEDANCE SPECTROSCOPY STUDIES

4.1 Introduction 333

4.2 EIS Studies of Oxygen Evolution on Fe Electrodes 333

4.2.1 Experimental Results and Discussion of an Appropriate Equivalent Circuit 333

4.2.2 Derivation of Tafel slopes from the Impedance Data for the Fe Electrodes 359

4.3 EIS Studies of Oxygen Evolution on Co Electrodes 362

4.4 EIS Studies of Oxygen Evolution on Ni Electrodes 373

5.0 ACTIVE SURFACE AREAS AND COMPARISON OF CATALYTIC PERFORMANCE

5.1 Introduction 388

5.2 Roughness Factors for the Ni Electrodes 388

5.3 Roughness Factors for the Co Electrodes 399

5.4 Roughness Factors for the Fe Electrodes 404

5.5 Comparison of Active Surface Area Normalised O.E.R.

Catalytic Activities 413

5.6 Relative Activities of the Anodic Oxides Formed on Ni, Co and Fe Electrodes Towards the O.E.R. in Alkaline Solution 422

6.0 CONCLUSIONS AND FUTURE WORK

6.1 Summary of Conclusions 430

6.2 Future Work 437

The number of the page on which the quantity is first introduced, and where relevant the number of the equation in which it is defined, are included in parenthesis.

α Depending on context is either the transfer coefficient (p 46) or CPE exponent (p 161, 2.1.36)

β The electron transfer symmetry factor (p 27)

β_f Symmetry factor for field assisted migration of the charge carriers in a barrier oxide film (p 293)

β_s Symmetry factor for the rate determining step of the interfacial electrochemical charge transfer reaction in dual barrier analysis (p 293)

β_t Overall symmetry factor in dual barrier analysis (p 294, 3.5.19)

Γ_i Gibbs surface excess of species i in the interface (p 4, 1.1.9)

γ The interfacial surface tension (p 4, 1.1.8) in section 1.1 – otherwise Temkin adsorption symmetry factor (p 39)

$\gamma_{\pm}$ Mean ionic activity coefficient (p 177)

δ The half jump distance of charge carriers (Mott Cabrera model) (p 293)

ε Depending on context is either, the dielectric constant of a material (p 11) or the energy level of an electron (p 310)

ε_H Dielectric constant in the compact layer (p 18)

ζ The "zeta" or electrokinetic potential (p 12)

η Overpotential (p 25, 1.2.1, also p 32, 1.2.27)

θ Depending on context $\theta = nF/RT$ (section 1.2.1) or elsewhere represents the total fractional coverage of intermediates

κ Transmission coefficient (p 26, 1.2.5 and p 310, 3.5.40)

μ_i^{α} Chemical potential of entity i in phase α (p 1, 1.1.1)

$\bar{\mu}_i^{\alpha}$ Electrochemical potential of entity i in phase α (p 2, 1.1.2)

σ Characteristic reaction length in Eyring equation (p 26, 1.2.5)

σ_s Charge due to ions in the solution phase diffuse layer (p 17)

σ_{ad} Charge of adsorbed ions in the compact layer (p 17)

σ_{sc} Charge in semiconductor space charge layer (p 17)

σ_{ss} Charge in surface states (p 17)

τ Characteristic relaxation time or "RC time constant" (p 342)

ν Kinematic viscosity (p 110)

ν_i Depending on context is either the rate of reaction *i*, or the stoichiometric number of the i^{th} step of a reaction pathway (p 45)

Φ Electric field magnitude

Φ^m The work function of a metal in contact with vacuum (p 53, 1.3.1)

$\Phi^{m(s)}$ The work function of a metal electrode in contact with an aqueous solution (p 54, 1.3.2)

ϕ Depending on context is either inner potential of a phase in vacuum (p 3, 1.1.6), or a phase angle (p 140)

ϕ_2 The potential of the diffuse layer (p 12)

$^m\Delta^s\phi$ Inner or Galvani potential difference between a metallic and a solution phase (p 3)

$\Delta\phi_d$ The potential difference between the O.H.P. and the bulk solution (p 17)

$\Delta\phi_H$ The potential difference between the compact layer and the O.H.P. (p 17)

$\Delta\phi_{ib}$ The Galvani potential difference across the inner barrier in the Damjanovic-Birss dual barrier model (p 309)

$\Delta\phi_{ob}$ The Galvani potential difference across the outer barrier in the Damjanovic-Birss dual barrier model (p 309)

$\Delta\phi_{sc}$ The potential difference between the bulk and surface of a semiconductor (p 17)

χ Surface potential of a phase in vacuum (p 3)

χ^m Electron overlap potential difference (p 53)

$^m\Delta^s\chi$ The surface potential difference between a metallic and a solution phase (p 3, 1.1.5)

ψ The outer potential of a phase in vacuum (p 2)

$^m\Delta^s\psi$ The outer or Volta potential difference between a metallic and a solution phase (p 2, 1.1.4)

ω Depending on context is either the rotational frequency (revolutions per min) in a rotating disk electrode experiment (p 110), or the angular frequency (Hz) of the sinusoidal voltage perturbation in an EIS experiment (p 140)

ω''_{max} Frequency at which Z″ has its maximum value (p 162)

A Depending on context is either the electrode/electrolyte interfacial surface area, or $1/C_{\alpha=1}$ in eqn. (2.1.36) p 161

A' Arrhenius coefficient (p 26, 1.2.4)

a The Tafel parameter, $a = -b\log i_0$ (p 425)

a.c. Alternating current

a_0 The unit cell parameter in the basal plane

a_i The activity of species i in solution

a_i^{∞} The bulk activity of the species i (p 27)

$a_i(0,t)$ The activity of species i at the electrode surface (x = 0) at time t (p 30)

b The Tafel slope (p 26, 1.2.2)

b_{diff} The differential Tafel slope (p 163, 2.1.42)

b_{EIS} Tafel slope derived from EIS measurements via equation (2.1.44)

b_{SS} Tafel slope as measured by dc steady state polarisation technique

C The magnitude of a capacitance (p 141, 2.1.6)

$\tilde{C}_{ac}$ Frequency dependent pseudo-capacitive quantity measured by EIS (p 355)

C_{cell} The equivalent series capacitance of an electrochemical cell (p 147)

C_{diff} Differential capacitance of an interface (p 7, 1.1.11)

C_{dl} The double layer capacitance (p 146)

C_{eff} Effective capacitance derived from CPE fitting parameters (p 162, 2.1.39)

C_{ps} The steady state adsorption pseudo-capacitance (p 40, 1.2.51)

$C_{\alpha=1}$ A capacitance value in the absence of frequency dispersion (p 161)

C_{ϕ} The pseudo-capacitance associated with a faradaic reaction (p 147)

CNLS Complex non-linear least squares (p 157)

CPE Constant phase element (p 161)

c_0 Crystalline inter-lamellar distance (p 74)

D Oxide film thickness

D_i The diffusion coefficient of species i

D_{ss} Density of surface states (p 18)

d_H The compact layer thickness (p 18)

E Electrode potential

EIS Electrochemical impedance spectroscopy

EQCM Electrochemical quartz crystal microbalance

E_{act} The activation energy for a chemical reaction (p 26, 1.2.4)

E_{ad} Energy level of an adsorbed water molecule (p 310)

E_F^{α} The Fermi level of a phase α (p 19)

E_N The thermodynamic Nernst potential (p 27, 1.2.7)

E_{pzc} Potential of zero charge for a given interface (p 5)

E_0 Maximum amplitude of a sinusoidally varying potential (p140)

E^0 Standard potential for a redox couple (p 27)

$\dot{\boldsymbol{E}}$ Voltage phasor (p 140, 2.1.5, see also Fig. 2.1.1)

e Elementary charge, 1.60218×10^{-19} C

F The Faraday constant, 96,485.31 C mol^{-1}

F.R.A. Frequency response analyser (p 154)

f Frequency in Hz

$f(\varepsilon)$ The Fermi function for electron states in a metal (p 310)

f_r Electrode roughness factor (p 167)

ΔG_0^* The free energy of activation at E_N (p 27)

ΔG_f^* The free energy of activation in the forward direction (p 28, 1.2.9)

ΔG_r^* The free energy of activation in the reverse direction (p 28, 1.2.8)

g Dipole potential difference caused by an aqueous layer (p 54)

ΔH^{0*} Standard enthalpy change of activation

$\Delta H_f'^0$ Standard enthalpy change of formation

h The Planck constant, 6.626×10^{-34} J s

I_D Disk current in a RRDE experiment (p 110)

I_R Ring current in a RRDE experiment (p 110)

I_0 Maximum amplitude of an a.c. current density (p 140)

$\dot{\boldsymbol{I}}$ Current phasor (p 140, 2.1.5, see also Fig. 2.1.1)

I.H.P. The inner Helmholtz plane (p 9)

ΔI Potentiostat current tolerance (p 180, 2.2.4)

i Current density

i_0 Exchange current density (p 30, 1.2.20)

i_{appl} Applied galvanostatic polarisation current density in roughness factor estimation experiments (p 388)

i_s Current density due to the interfacial electrochemical reaction in dual barrier analysis (p 295)

K Integral capacitance of an interface (p 7, 1.1.13)

K_B The Boltzmann constant, 1.38065×10^{-23} J K^{-1}

K_S Solubility constant (p 84)

K_w The ionic product of water, 1.008×10^{-14} at 25°C (p 84)

k Chemical rate constant (p 26, 1.2.4)

k^0 Standard electrochemical rate constant (p 29, 1.2.13)

k' Electrochemical rate constant (p 29)

L_D The Debye length (p 18, 1.1.17)

M Molar concentration (mol dm^{-3})

m Molal concentration (mol Kg^{-1})

m_e Electron rest mass (9.109×10^{-31} Kg)

m_i The reaction order with respect to the species i (p 49)

N Depending on context is either the ring collector efficiency in a RRDE experiment (p 110), or the number of cycles of the applied wave over which integration is performed in sine wave correlation (p 154)

$N(\varepsilon)$ The distribution function of electron energy levels, ε, at the I.H.P. (p 310)

N.H.E. The normal hydrogen electrode

n_i Concentration of species i

n Number of moles of electrons transferred according to the balanced equation for an electrochemical reaction

O.H.P. The outer Helmholtz plane (p 9)

$P(t)$ Sinusoidal perturbation signal in sine wave correlation (p 154, 2.1.31)

p.s.d. Phase sensitive detector (p 152)

p.z.c. Potential of zero charge (p 5)

p_{O_2} The partial pressure of gaseous oxygen (p 105)

Q Active charge capacity determined by integration of a voltammetric peak

Q_{dec} The total charge passed in the course of a current decay process (p 171)

q The magnitude of the charge residing on the plates of a capacitor (p 141)

q_m Surface charge density on a metal

q_1 Charge passed during the deposition of a monolayer of adsorbed intermediate (p 40)

R The magnitude of a resistance

RDS Rate determining step

R.H.E. Reversible hydrogen electrode

RRDE Rotating ring disk electrode

R_{cell} Equivalent series resistance of an electrochemical cell (p 147)

R_{ct} The charge transfer resistance (p 148)

R_{far} The total Faradaic resistance of the working electrode (p 163)

R_p The polarisation resistance (p 151)

R_s The series resistance (p 147)

R_Ω The uncompensated electrolyte solution resistance (p 138, 2.1.1)

r_i The rate of change of the free energy of adsorption of species i at a total fractional coverage θ (p 51, 1.2.94)

S.C.E. Saturated calomel electrode

SECM Scanning electrochemical microscopy

$S(\varepsilon)$ The density of electron states in a metal (p 310)

$S(t)$ Measured a.c. current signal in sine wave correlation (p 154, 2.1.32)

ΔS^{0*} Standard entropy change of activation

T Absolute temperature

TGA Thermogravimetric analysis

$V(x)$ Magnitude of energy barrier experienced by a tunnelling electron at a distance x from the metal/oxide interface (p 311, 3.5.42)

V_f The potential affecting the charge migration process across the barrier oxide layer in the dual barrier model (p 293)

V_{fb} The flat band potential of a semiconductor (p 19)

V_{Sch} The Schottky barrier height in a semiconductor (p 19)

V_s The potential affecting the electrochemical charge transfer barrier at the electrode/solution interface in the dual barrier model (p 293)

W Electron tunnelling probability (p 310)

w_i The Christiansen parameter for the i^{th} step of a multi-step reaction pathway (p 41, 1.2.53, 1.2.54)

XPS X-ray photoelectron spectroscopy

X_C The capacitive reactance (p 141)

$\mathbf{Z}$ The impedance (vector quantity) (p 142, 2.1.11)

Z' Real component of impedance (p 142)

Z'' Imaginary component of impedance (p 142)

Z_{CPE} Impedance of a capacitive process displaying frequency dispersion (p 161, 2.1.36)

Z_f The generalised Faradaic impedance (p 146)

Z_W The Warburg impedance (p 148, 2.1.20)

z_i Whole number of fundamental charges on the species i (p 2)

CHAPTER 1

INTRODUCTION AND LITERATURE REVIEW

1.1 Review of Relevant Electrochemical Theory

In view of the fact that this thesis deals with the surface electrochemistry of transition metal electrodes in aqueous solution, it is considered pertinent to begin with a brief review of concepts of electrochemical interfacial structure and electron transfer kinetics. Later in the chapter, consideration is given to the present state of knowledge in the field, particularly regarding the anodic oxygen evolution reaction in alkaline solution.

1.1.1 Thermodynamic Concepts of Electrochemical Interfaces

An interface region refers to that region, in the vicinity of the boundary between two chemically distinct phases, in which the properties of the region differ from either of the bulk phases. The electrified interface between a solid electrode and an electrolyte solution is often, generally, called *the electrical double layer* and consists of a spatially varying distribution of ions, electrons, solvent molecules and possibly other species. The properties of the double layer depend on whether the material of the solid electrode is a metal, a semiconductor or an insulator. Metal – solution and oxide – solution interfaces, are those of most relevance to this work and their properties will be reviewed in Sections 1.1.2 and 1.1.3. Presently however, an outline is presented of the thermodynamics of electrified interfaces.

In the theory of chemical thermodynamics, the *chemical potential* or partial molar free energy, μ_i^{α}, of entity i in phase α, on which there is no surface charge or potential, is given by

$$\mu_i^{\alpha} = -(\partial G^{\alpha}/\partial n_i)_{T,P,n_{j\neq i}} \quad , \tag{1.1.1}$$

where n_i is the number of moles of species i in phase α. μ_i^{α} arises from chemical forces, essentially due to electron interaction with the nuclei of the constituent atoms of the phase. If however, phase α is assumed to have a potential ϕ^{α} and an

excess surface charge, and entity i is assumed to possess a charge of z_iF per mole, it is necessary to define an electrochemical potential, $\overline{\mu}_i^{\alpha}$, of entity i in phase α, as

$$\overline{\mu}_i^{\alpha} = \mu_i^{\alpha} + z_i F \phi^{\alpha} \tag{1.1.2}$$

The second term on the right hand side of equation (1.1.2) is the electrical interaction energy between the entity i, and the electrical charge density that resides on the surface of phase α. The condition for electrochemical equilibrium of entity i between two phases α and β is therefore:

$$\overline{\mu}_i^{\alpha} = \overline{\mu}_i^{\beta} \tag{1.1.3}$$

A tangible example of such an entity might be a metal ion M^{z+} in equilibrium with an electrode of the same metal (one phase) and an aqueous solution (the other phase) of a salt of that metal.

It is useful at this point to introduce the concept of polarisable and nonpolarisable interfaces. At an *ideal nonpolarisable interface*, electrons pass very easily across the interface and equilibrium is achieved rapidly. If an external potential is applied across the interface, more electrons may cross the interface, but they continue to do so at a fast rate, and so, there is no build-up of excess charge at the interface. For an *ideal polarisable interface*, electron transfer across the interface is difficult. When an external potential is applied, there is a build-up of charge at the interface, since the electrons cannot cross. When an excess surface charge density develops on an electrode, it is said to be polarised.

Electrochemical measurements usually involve the determination of the current, i, – potential, E, relation for a given electrode process. It is therefore important to understand the exact meaning of the measured or applied potential, since several different electrode potentials are defined. The *outer potential* ψ, for a phase with an excess surface charge in vacuum is defined as the electrostatic work required to bring a +1 test charge from infinity to a point "just outside" the phase[1]. The term "just outside" refers to a region of quasi-constancy of potential, which has been estimated to be 10^{-5} to 10^{-3} cm from the electrode surface for a metallic electrode of 1 cm diameter[2]. The outer or *Volta potential difference* ${}^{m}\Delta^{s}\psi$, between a metal and solution phase, might then be though of in terms of the difference of the outer potentials for

each of the phases in contact with vacuum, where the excess charge on the metallic and solution phases is equal in magnitude, but opposite in sign:

$$^{m}\Delta^{s}\psi = \psi^{m} - \psi^{s} \tag{1.1.4}$$

Both the outer potential of a single phase in vacuum and the Volta potential difference between two phases can be determined experimentally. The outer potential arises due to electrostatic forces and becomes zero if the excess charge on the phase is zero. In the case where there is no excess charge on a phase in vacuum, the test charge will not experience an electrostatic force as it is brought from infinity toward to the phase. In fact interactive forces only commence when the test charge passes through the first layer of ions on the surface, in the case of a metal, or through a layer of dipoles oriented orthogonally to the surface for a solution phase[2]. The potential difference that exists across the surface of a phase with no excess surface charge, in vacuum, is known as the *surface potential* χ. Hypothetically, the *surface potential difference* $^{m}\Delta^{s}\chi$, between a metal and a solution phase, could then be defined as the difference in the surfaces potentials of each of these phases:

$$^{m}\Delta^{s}\chi = \chi^{m} - \chi^{s} \tag{1.1.5}$$

The surface potential difference cannot be measured experimentally[1,2,3]. The *inner potential* ϕ of a phase in vacuum is then given by:

$$\phi = \psi + \chi \tag{1.1.6}$$

The question then arises, as to which potential is measured in a conventional electrochemical experiment? Bockris[1,2] quotes the measured potential difference V_{meas}, between a metallic test electrode of metal m, and a metallic reference electrode of metal m_{ref}, in a solution s, where the net current in the external circuit is zero, as being,

$$V_{meas} = (^{m}\Delta^{s}\phi - \mu_{e}^{m}/nF) - (^{mref}\Delta^{s}\phi - \mu_{e}^{mref}/nF) = V_{m} - V_{ref} \quad , \tag{1.1.7}$$

where μ_e^m, μ_e^{mref}, are the chemical potentials of an electron in the metals m and m_{ref} respectively. In this case the potential of the electrochemical cell is the difference of two quantities each of the form ${}^m\Delta^s\phi - \mu_e^m / nF$. Therefore, one might think of the test electrode as having a potential of $V_m = {}^m\Delta^s\phi - \mu_e^m / nF$. Bockris[2] comments that while there is a popular association of the *inner or Galvani potential difference* ${}^m\Delta^s\phi$ by itself, with the term "electrode potential", equation (1.1.7) 'binds us to associate the phase with a Galvani potential difference between the electronic and ionic conductor, from which has been subtracted the chemical potential of the electron in the metal'. If the reference potential, i.e. the second bracketed term on the right hand side of equation (1.1.7) is denoted as zero on an arbitrary scale, then the potential of the test electrode as measured by a conventional electrochemical experiment is given by ${}^m\Delta^s\phi - \mu_e^m / nF$, and has the significance assigned to it by Bockris in the quotation above.

Much of the experimental investigation which has led to modern models of the metallic electrode/solution interface, involve electrocapillary studies on the interface between mercury electrodes and various electrolyte solutions. Such experiments involve measurement of the interfacial surface tension γ with applied potential as a function of the concentration of a given electrolyte. Mercury, as a metallic liquid provided the idea electrode material for such studies, since the interfacial tension of a liquid-liquid interface is much easier to measure compared to that of a solid-liquid interface.

The thermodynamic basis of the electrocapillary method lies in the so-called electrocapillary equation,

$$d\gamma = -q_m dE - \frac{q_m}{z_j F} d\mu_j - \sum \Gamma_i d\mu_i \ , \qquad (1.1.8)$$

where, q_m is the surface charge density on the metal, and E is the applied potential. Γ_i is the called the Gibbs surface excess and is defined as,

$$\Gamma_i = \int_0^\infty c_i(x)dx \ , \qquad (1.1.9)$$

where $c_i(x)$ is the excess concentration of species i in the interface compared to the bulk solution. It should be noted that the subscript j in equation (1.1.8) represents an ionic species that crosses the interface with ease, while species i passes across the interface with difficulty. For fixed solution composition $d\mu_i = 0$, $d\mu_j = 0$, and the electrocapillary equation reduces to the *Lippmann equation*:

$$\left(\frac{d\gamma}{dE}\right)_{T,P,\mu_I} = -q_m, \tag{1.1.10}$$

Electrocapillary measurements are usually reported as plots of γ against E^4 – see Figure 1.1.1.

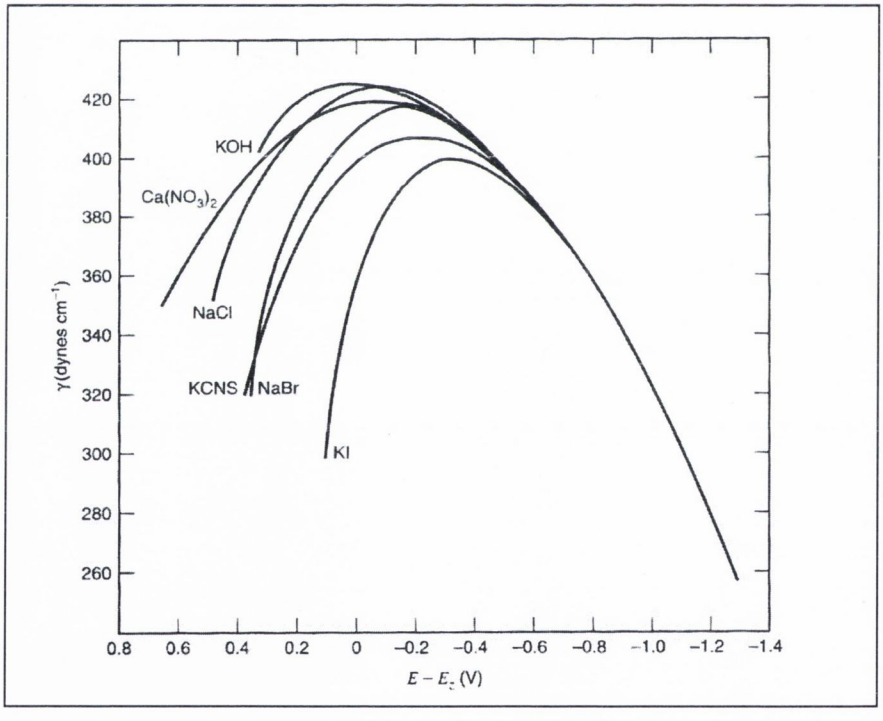


Figure 1.1.1 *Electrocapillary curves for mercury in contact with aqueous solutions of different electrolytes at 18°C. The potential is plotted with respect to the p.z.c. for NaF. Reproduced from Ref. 4.*

It is obvious from Figure 1.1.1, that electrocapillary curves pass through a maximum, corresponding to the potential at which $(d\gamma/dE)_{T,P,\mu_I} = 0$. This potential is known as the *potential of zero charge* (p.z.c.). To explain the general shapes of the curves in Figure 1.1.1 it is necessary to consider adsorption effects at an electrode-solution interface. At the start of this section the concept of the electrical double layer was

introduced. Models of the structure of the double layer will be considered later – at present consideration is given to the reason for its formation.

The double layer is established at an interface, due to a difference in the chemical potential of an electron between the two phases. The resulting free energy difference causes a flow of charge to occur in order to equalise the chemical potential at the interface. In turn, a separation of charge is produced. The flow of charge continues until the thermodynamic driving force for this process, is cancelled by the electrostatic forces of the separation of charge. *Non-specific adsorption* refers to the process of build-up of ions on the solution side of the interface, that is governed by long range electrostatic forces[5]. Apart from the magnitude of the charge on such ions, and possibly their radii, the chemical identity of such species is unimportant with regard to their adsorption characteristics – hence their 'non-specificity'. In aqueous solution non-specifically adsorbed ions tend to be solvated. On the other hand, *specifically adsorbed* species are bound to the electrode by short range forces[5] and therefore the chemical identity of the adsorbate is significant. These short range forces are quantum mechanical in origin, and are not fully understood, with computer simulation latterly being applied to the problem of their elucidation[6].

The decrease in interfacial tension at potentials both above and below the p.z.c., is attributed to increasing mutual repulsion between adsorbed ions, which occurs as a consequence of increased adsorption, as the potential graduates away from the p.z.c. The differences in the cathodic and anodic behaviour of the electrocapilary curves in figure 1.1.1, points towards the occurrence, under different conditions, of both specific and non-specific adsorption at the mercury surface. For potentials less than the p.z.c., the decline in surface tension is the same regardless of the electrolyte composition. This is indicative of non-specific adsorption, since the characteristics of the process are independent of the ions present in solution. On the other hand, at potentials more positive than the p.z.c., the curves diverge rapidly. Clearly the behaviour of the system in this region of potential depends specifically on the identity of the ions in solution. The deviations in the electrocapillary curves occur at positive potentials where, anions must be in excess on the solution side of the interface. The occurrence of specific adsorption of anions at these potentials rationalises this behaviour.

The separation of charge at the interface gives it the property of an electrical capacitor. Unlike a simple parallel plate capacitor, there is generally not a direct linear

relationship between the charge and potential for this capacitor. Instead a *differential capacitance* C_{diff} is defined by differentiating the Lippmann equation with respect to potential,

$$C_{diff} = \left(\frac{\partial q_m}{\partial E}\right)_{T,P,\mu_i} = -\left(\frac{\partial^2 \gamma}{\partial E^2}\right) \qquad (1.1.11)$$

For mercury-solution interfaces the differential capacitance can be plotted as a function of potential simply by differentiating the electrocapillary curve. In the case of solid electrodes C_{diff} can be measured using electrochemical impedance spectroscopy. Indeed integration of equation (1.1.11) with respect to potential at constant composition suggests a method of applying Gibbsian thermodynamics to solid electrodes, where the difficulty is the measurement of γ without setting up a stress (which is not allowed for in the theory) in the solution phase[1]. Integration of equation (1.1.11) yields[7],

$$\gamma = \gamma_1 - \int_{E_1}^{E}\int \frac{\partial^2 \gamma}{\partial E^2} dE dE \quad , \qquad (1.1.12)$$

where E_1 and γ_1 are integration constants. This implies that it is necessary to determine the surface tension at one potential in order to derive the $\gamma(E)$ curve. This may be difficult to do in practice and consequently much of the experimental data for solid-solution interfaces has been obtained[1] using spectroscopic methods, radiotracer methods, friction measurements, and more recently, atomic force microscopy[8].

An *integral capacitance K*, which *is* analogous to an ordinary parallel plate capacitor, may also be defined,

$$K = \frac{q_m}{E - E_{pzc}} \quad , \qquad (1.1.13)$$

where E_{pzc} is the potential of zero charge. The differential and integral capacitances are related as follows:

$$C_{diff} = K + (E - E_{pzc})\frac{dK}{dE} \tag{1.1.14}$$

It is clear that $C_{diff} = K$ at the p.z.c.

The Gibbs surface excess of component i in solution is given by the following expression[2],

$$\Gamma_i = \frac{-1}{2RT}\left(\frac{\partial\gamma}{\partial \ln a_i}\right)_{E,\mu j \neq i} \tag{1.1.15}$$

where a_i is the activity of i in solution. Equation (1.1.15) predicts that a plot of surface tension against the log of solution component concentration will have a slope given by Γ_i. Non-specific adsorption does not occur at the p.z.c., and thus the value of Γ_i at the p.z.c. is regarded as a measure of the relative amount of specific adsorption of species i.

1.1.2 Models of the Electrode-Solution Interface

In section 1.1.1, it was observed that a separation of charge occurs at the interface between two phases, and that the interfacial region is often referred to as the electrical double layer. The term 'double layer' has its origins in the first model of a metal solution interface due to Helmholtz[9,10], in the nineteenth century. Helmholtz proposed that the excess charge on the surface of the metallic electrode was exactly counterbalanced by a sheet of equal and opposite charge that resided at the solution side of the interface. The model envisaged discontinuities in the potential at the surface of the electrode, and at the electrical centre of the counterbalancing charge in solution, with these two points being joined by a linear potential gradient. This situation corresponds to that of a parallel plate capacitor, implying that the differential capacitance should be a constant, independent of potential and solution concentration. As was observed in section 1.1.1, experimental data shows that the differential capacitance varies with potential and ion concentration in a very definite manner –

consequently a more sophisticated model is required. The next level of sophistication was added to the model by the work of Gouy[11] in 1910, and, independently by Chapman[12] in 1913. This model proposed a *diffuse layer*, where there is no special layer of ions or water molecules at the solution side of the interface, but rather a distribution of excess charge, diminishing with increasing distance from the electrode surface. The thickness of the diffuse layer region depends on applied potential and ion concentration. Again the potential energy function is assumed to have constant values in the electrode up to the surface, and also in the bulk solution – these points now being joined with a curve. While the Gouy-Chapman model predicts a $C_{diff}(E)$ function that resembles experimental data for some systems at low concentration and at potentials close to the p.z.c., significant divergence was observed otherwise[5].

The major problem with the Gouy-Chapman model was that it envisaged the ions as being point charges[2,5]. This meant that at high polarisation, the separation between the metallic and solution charge zones decreases towards zero. In reality ions cannot approach the electrode surface any closer than the ionic radius at the very least – hence one might envisage a plane of closest approach for the centres of the ions at some finite distance from the electrode surface. This was the approach adopted by Stern[13] in 1924. Stern basically added the earlier models of Helmholtz and Gouy-Chapman together, postulating that, while there is a layer of excess charge close to the electrode surface, some of the charge required to compensate the excess charge on the metal occupies a diffuse layer that stretches out into solution. Stern further proposed that the ions closest to the electrode (i.e. those accounted for by the Helmholtz element of the model), can be further separated into two layers. This idea was expanded by Grahame[4], and proposes an *inner Helmholtz plane* (IHP) which is the locus of the electrical centres of specifically adsorbed ions (usually anions), and an *outer Helmholtz plane* (OHP) which passes through the electrical centres of electrostatically bound, non-specifically adsorbed ions, that are separated from the electrode surface by their solvation sheaths. The Gouy-Chapman-Stern-Grahame (GCSG) type model gives predictions that, broadly speaking, account for the gross features of the behaviour in real syatems[5]. Discrepancies still exist however – the successes and shortcomings of the GCSG model can be roughly illustrated by considering the data in Figure 1.1.2.

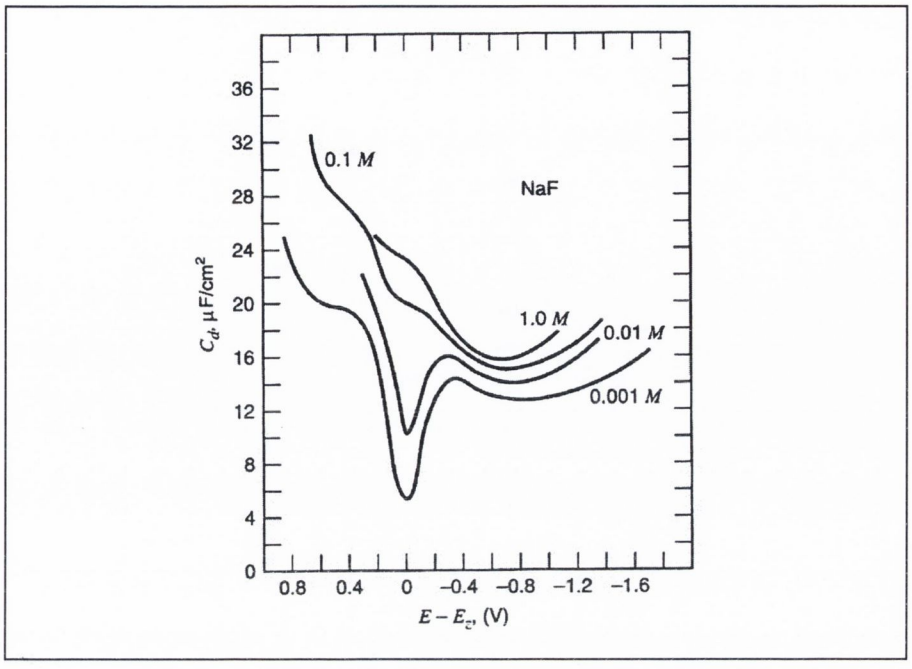


Figure 1.1.2 *Differential capacitance vs. potential for NaF solutions in contact with mercury at 25°C. Reproduced from Ref. 4.*

Firstly, it must be commented that the GCSG model is most successful at lower electrolyte concentration – therefore consideration is given to the 0.001 and 0.01 M curves in this discussion. Without going into much detail, it has been shown[5] that the capacitance minimum observed in the vicinity of the p.z.c. is well predicted by the diffuse layer aspect of the model, whereas the Helmholtz inner layers model the approximately constant capacitance region observed at potentials between circa. –0.4 and –1.2 V. The diminishing applicability of the GCSG model with increasing concentration, can be largely explained by the fact that the diffuse layer element of the model is based upon the Debye-Hückel theory of activity in electrolytes in its zeroth order approximation[2]. This approximation neglects the finite size of ions and can only be accurately applied up to about 0.001 M for 1:1 electrolytes[1]. In simple terms, the problem is that at concentrations greater than 0.001M, the average distance between ions is greater than the diffuse layer thickness. Bockris[1] comments that diffuse layer theory is often applied to solutions with concentrations of 100 – 1000 times greater than its applicability, and that quantities calculated by its use under such conditions must be treated with caution.

While, the limitations of the diffuse layer theory explain the diminishment of the capacitance minima, with increasing ion concentration, they do not explain the observation of capacitance maxima, as for example in the 1.0 M plot in Figure 1.1.2.

This behaviour was accounted for, in a model developed in the early 1960s, by Bockris, Devanathan and Müller - the BDM model[14]. This model was based on the realisation that the dipolar properties of water would result in an oriented layer of water molecules on the electrode surface, which would affect the interfacial potential. Generally speaking, it is the interaction of these water molecules, specifically adsorbed ions, and the metal surface that give rise to the observed capacitance maxima in differential capacitance vs. potential plots. The BDM model still forms the backbone of modern metal electrode-solution interface theory and its various aspects are considered pictorially in Figure 1.1.3.

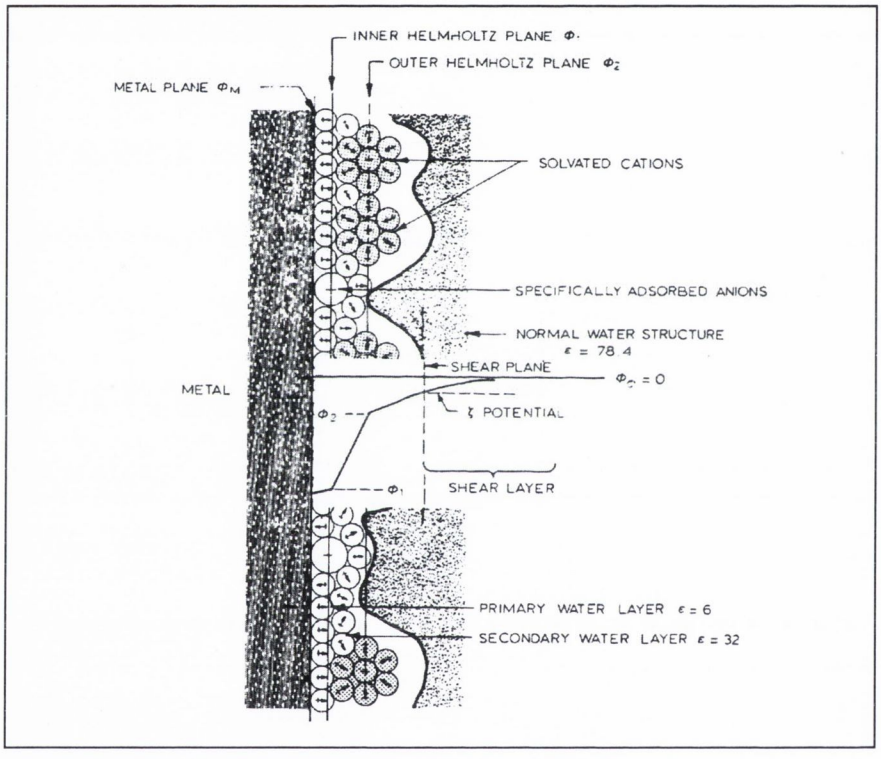


Figure 1.1.3 *Schematic representation of the BDM model at a metal solution interface. Reproduced from Ref. 15*

As with the diffuse layer model, the simple BDM model is applicable only for dilute solutions. Obviously, the issues mentioned previously, regarding the Debye length in more concentrated electrolytes, still pertain to the diffuse layer element of the BDM model. The BDM model accounts for the dielectric properties of the interface in dilute aqueous solutions by assigning dielectric constants, ε, of approximately 6, and 32 to the inner and outer Helmholtz layers respectively, and 78.4 to the bulk[15]. However, the degree of dielectric saturation, and the structure of the dielectric in the compact layer will vary with solution concentration and electrode polarisation[1, 5]. Other effects

that lead to decreasing applicability of the BDM model, with increasing solution concentration include, ion-ion pairing in the double layer, and strong non-specific interactions of the ions with the electrode surface charge[5].

Since it appears in Figure 1.1.3, it is appropriate to define the zeta (ζ) potential. The *zeta* or *electrokinetic potential* [16] is the potential at the shear plane between two charged phases, when one of the phases is moved tangentially to the other. Contrary to the arbitrary positioning of the shear plane in Figure 1.1.3, it is often set equal to the OHP, and it can be assumed that $\zeta = \phi_2$, the potential of the diffuse layer, an approximation that is valid at low potentials.

Much of the effort over the past forty years in improving the correlation between the BDM model and experiment, has focused on the nature of the solvent in the inner layers[1,17]. For charged electrodes, electrostatic considerations suggest that, as the potential is swept from negative to positive, compact layer water molecules change their orientation so that the oxygen becomes closer to the electrode, with the hydrogens tilting away[18]. Watts-Tobin and Mott[19,20] proposed a two state model which envisages the existence of two orientations of solvent dipoles adjacent to an electrode surface. One orientation is denoted "spin up" and the dipole points away from the electrode surface – in the "spin down" orientation the dipole points toward the surface. The occupation numbers of each state are related by Boltzmann statistics and a mathematical development leads to an expression for the potential drop across the inner compact layer as a function of electrode surface charge density. Modern theories have however abandoned the idea that water (in any case) dipoles can only take up two discrete orientations[6]. Fawcett[21] suggested a three state model, with the third state corresponding to a dipole oriented parallel to the electrode surface. This model was found to be most applicable to non-aqueous solvents[17].

A different take on the three state theory was proposed by Bockris and Habib[22], who suggested that at the p.z.c. for Hg in contact with an aqueous solution, the situation is best represented by a layer consisting of approximately two-thirds water dimers (two water molecules associated by hydrogen bonding) and one third unassociated water molecules. The "spin up" and "spin down" dipoles from the "free" water molecules constitute two of the phases, while the dimers constitute the other.

A four state model was proposed by Damaskin and Frumkin[23], which envisages the formation of clusters of solvent molecules. Solvent molecules can exist in the compact layer as either clusters or free molecules – both types of species are allowed to have

up or down orientations, however it is proposed that the effective dipole moment of the clusters are smaller than that of the free molecules. At the p.z.c., more of the solvent molecules are clustered than free, however charging the electrode causes field induced destruction of the clusters. This in turn leads to increased polarisation of the double layer and accounts for the rising parts observed in experimental $C_{diff}(E)$ curves. Bockris and Khan[1] have however questioned the ability, of a "clumsy cluster" consisting of several solvent molecules, to turn about its axis and take up two positions.

Another aspect of the metal-solution interface, that has attracted the attention of theoretical chemists, is the shape of the potential-distance function at the interface. In the original BDM model, the potential is assumed to undergo a sharp change at the metal surface - see Figure 1.1.3. Trasatti[24] noted that, the capacity of the inner compact layer at the p.z.c., for low atomic number metals in aqueous solution, increases with their electronic densities. This was interpreted in terms of an increase of the electronic polarisability of the metal surface with the increasing electron density associated with increasing atomic number. This behaviour was modelled by the application of the so-called *jellium model* to metal-solution interfaces by Badiali et al[25] and Schmickler[26]. This model, which was developed in the early 1970s[27], had been applied to the theory of metal surfaces in vacuum. It envisaged the metal as consisting of a skeleton of positively charged metal ions represented by a constant background charge density, that drops abruptly to zero at the surface. The valence electrons are represented as being an inhomogeneous electron gas, and it was shown, using low energy helium atom scattering experiments[28] that a "tail of quasi-free electrons spilled out of the ionic skeleton of the metal"[17]. In the mathematical modelling[17], the averaged electronic charge density n, is calculated as a function of distance z from the edge of the ionic skeleton – see Figure 1.1.4. The curve in Figure 1.1.4 suggests that the potential-distance relationship is continuous through the metal surface, effectively 'blurring the line' at the electrode solution interface. The potential reaches a constant value just inside the metal, at a distance from the surface, typically of the order of 1Å, called the Thomas-Fermi length[1]. It is also noteworthy, that where there is an excess negative surface charge, σ, the centre of mass of the excess charge moves further outside the metal – see dashed curve in Figure 1.1.4.

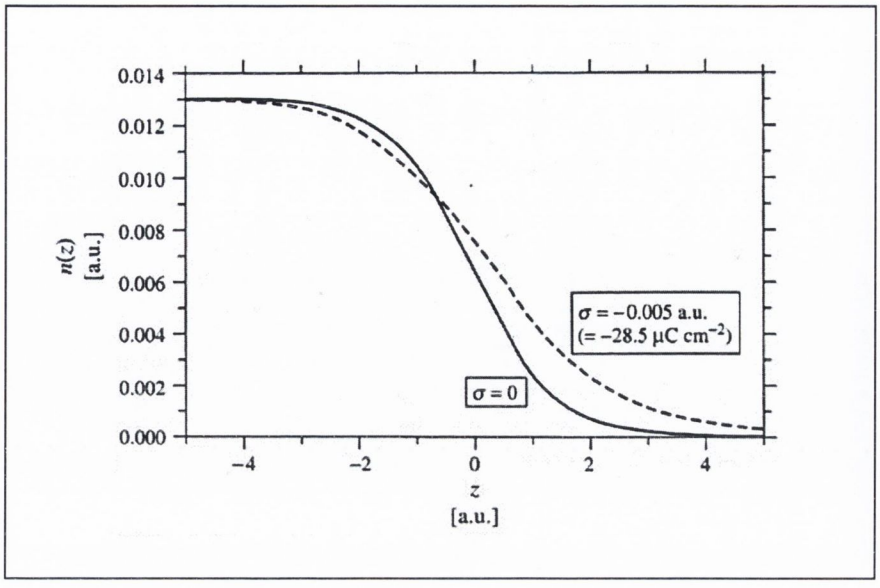


Figure 1.1.4 *The surface electronic density profiles calculated for a neutral and negatively charged jellium, based upon the bulk electron density of Hg. Reproduced from Ref. 17.*

1.1.3 The Oxide-Solution Interface

The models and concepts discussed in the previous section (1.1.2) refer to metal-solution interfaces. The main thrust of the present work is towards the anodic oxygen evolution reaction on transition metal electrodes – in section 1.5, it will be seen that this reaction occurs on an oxide film atop the metal surface. This may alter the nature of the model appropriate for the electrode-solution interface, relative to those discussed in section 1.1.2.

In contrast to metallic electrodes which are classified as conductors, most metal oxides are ionic crystals that are either insulators or semiconductors depending of the magnitude of their band gap[29]. In simplistic terms, during the formation of ionic metal oxides, crystal field splitting raises the energy levels of the electrons in the frontier orbitals of the metal ions to form an antibonding conduction band, while lowering the energies of the frontier orbital electrons in the oxide ions to form a bonding valance band. In the case of Al_2O_3, the frontier 3s and 3p orbitals of an Al atom form the conduction band by donating electrons, while the frontier 2p orbitals of an O atom accepts two electrons from the aforementioned Al orbitals to form the valence bond. Al_2O_3 has a band gap of approximately 7 eV, making it an insulator[29].

On the other hand, in the case of transition metal oxides the d band often appears in an

otherwise broad band gap, and has the effect of reducing the band gap[29]. In section 1.4.2, it is considered, that the oxide film on a polycrystalline Fe electrode in aqueous alkaline solution at the onset potential of oxygen evolution, may contain either or both Fe_2O_3 and Fe_3O_4. In the case of α-Fe_2O_3 there are two valance bands, one consists of a hybridisation of the Fe^{3+} 3d bonding orbital and the O^{2-} 2p antibonding orbital, and the other is a band consisting of O^{2-} 2p bonding orbitals[30]. The conduction band is formed from the frontier Fe^{3+} 2p antibonding orbitals. A band gap of 2.2 eV exists between the hybridized valance band and the conduction band – this is the direct band gap for α-Fe_2O_3. Furthermore an indirect band gap with a magnitude of approximately 3.5 eV exists between the conduction band and the other valance band. In general materials with a band gap of under ~ 4 eV are classified as semiconductors[29], and therefore crystalline α-Fe_2O_3 is a semiconductor. In the case of Fe_3O_4, the hybridised valance band contains unoccupied energy levels, making this material electronically conductive[30]. A discussion of the nature of the (oxy) hydroxide films that form at anodic potentials on polycrystalline Fe, Co, and Ni electrodes in alkaline solution is presented later in this chapter – for now it is worth commenting that these oxide phases can be hydrous, non-stoichiometric and vary in their degree of crystallinity, so that the electronic conductivity properties of an 'ideal' crystal of a metal oxide cannot be assumed to be the same as that of a film of the same oxide formed anodically on an electrode surface. It is possible to measure the conductivity of a given oxide phase – for the case of the nickel oxides in alkaline solution, photoelectrochemical measurements[31] indicate that the Ni(II) species (probably β-$Ni(OH)_2$) is a p-type semiconductor with an estimated band gap of about 3.7 eV, whereas the Ni(III) species (probably β-NiOOH) is an n-type semiconductor with an estimated band gap of approximately 1.75 eV.

In real semiconductor materials, the overall conductivity is determined not only by the band gap between valance and conduction bands, but also by lattice defects, impurities and surface effects. For metal oxides, the presence of interstitial metal ions or oxygen vacancies introduce electron donor levels into the band gap, while the presence of metal vacancies introduces acceptor levels. Impurities will also introduce either acceptor or donor levels to the band gap, depending on the nature of the impurity. The p-type conductivity of β-$Ni(OH)_2$ has been attributed to the presence of Ni ion vacancies in the lattice, which introduce electron acceptor levels above the valance band edge[29].

The bulk three-dimensional energy bands and band gap levels, discussed previously, do not account for the entire conductivity of a semiconductor. Two-dimensional surface states must also be considered, and these can be further sub-classified[29] as, (a) surface dangling states or (b) surface ion induced states. *Surface dangling states* arise due to the dangling bonds of surface atoms on covalently bonded semiconductors. These dangling bond surface states may act as either donor or acceptor levels, however thermodynamics dictates that a large proportion of them will combine with a neighbouring dangling bond in order to reduce the surface energy. This process leads to the formation of bonding (donor) levels above the valence band edge and antibonding (acceptor) levels below the conduction band edge in the energy level diagram.

The surface ion induced state (or Tamm state) arises in compound ionic semiconductors due to the potential difference between the surface lattice potential and the bulk lattice potential. The surface anion induced donor is found above the valance band edge, while the surface cation induced acceptor is found below the conduction band edge. It is pointed out by Sato[29], that many transition metal oxides may be classified as partially ionic and partially covalent, and thus their surfaces may contain both dangling bond and surface ion induced states. While the aforementioned surface states are intrinsic properties of a semiconductor, there are also extrinsic surface states caused by adsorbed particles that depend upon the environment to which the surface is exposed[1, 29]. Surface state concentration varies between factors of 10^{-6} to 10^{-1} of surface atom concentration[29] (depending on factors such as the semiconductor in question, the environment at the surface and surface roughness), and therefore can be very significant in determining the interfacial properties of a metal oxide-solution interface.

Significant work on semiconductor electrochemistry began in the 1950s when pure Si and Ge became commercially available. Early reviews on the topic include those due to Gerischer[32] and Ahmed[33] while, more recent reviews have been provided by Memming[34], Lewis [35], and Nozik and Memming[36]. There are also a number of useful books devoted largely to the topic[37, 38].

As was discussed in section 1.1.2, the charge, on a metallic electrode at the interface with a solution, is concentrated on the electrode surface. In the case of a semiconductor electrode, with a small concentration of surface states, the charge on the electrode is spread out over a three-dimensional diffuse *space charge layer* in the

solid phase, in an analogous manner to the existence of the ionic diffuse layer in solution near an electrode surface. In fact, in real metals, such a space charge layer also exists, but its depth tends to be of the order of 1 Å, as opposed to ~ 1000 Å in a lightly doped semiconductor (10^{15} cm^{-3}) [1]. In the presence of surface states and adsorbed ions, the semiconductor-solution interface can be represented as a three-layer model, as depicted in Figure 1.1.5. The interfacial charge consists of, σ_{sc}, the charge in the semiconductor space charge layer, σ_{ss}, the charge in the surface states, σ_{ad}, the charge due to adsorbed ions in the compact layer, and σ_s, the charge due to ionic species in the solution phase diffuse layer. The total Galvani potential difference, $\Delta\phi$, across the interfacial region is given by,

$$\Delta\phi = \Delta\phi_d + \Delta\phi_H + \Delta\phi_{sc} \quad , \tag{1.1.16}$$

where, $\Delta\phi_d$ is the potential difference between the O.H.P. and the bulk solution, $\Delta\phi_H$ is the potential difference between the compact layer and the O.H.P., and $\Delta\phi_{sc}$ is the potential difference between the bulk of the semiconductor and its surface.

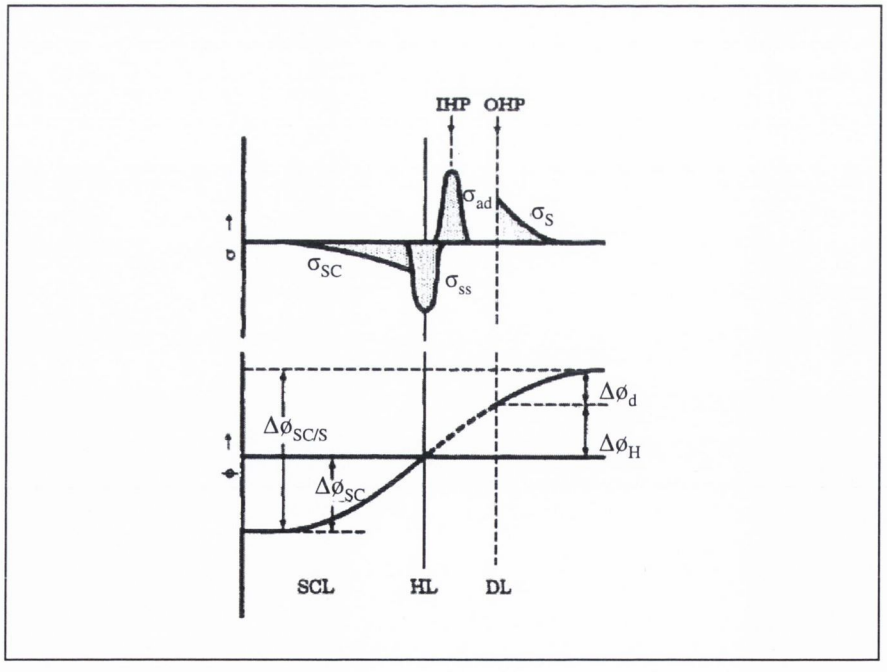


Figure 1.1.5 *A schematic representation of the interfacial charge and potential profiles for a semiconductor-solution interface, in the presence of surface states and absorbed ions. See the text for more details Reproduced from Ref. 39.*

The thickness of the space charge layer, and the diffuse layer, depend on the concentrations of mobile charge carriers n_i in the semiconductor and the ionic solution respectively – the *Debye length*, L_D, can be used as an estimate of their respective thicknesses[39], where L_D is given by:

$$L_D = \sqrt{\frac{\varepsilon kT}{e^2 \sum n_i z_i^2}} \tag{1.1.17}$$

It is clear from equation (1.1.17), that the thickness of both the space charge layer and the diffuse layer are inversely proportional to the sum of the segmental charge densities in the relevant material, where it is assumed that these dispersions of charge can be represented in terms of a number of segments i of constant charge carrier density n_i.

It can be shown[40, 41], to a first approximation, that the distribution of the electrode potential across the compact Helmholtz layer and the space charge layer, is given by,

$$\frac{\delta\Delta\phi_H}{\delta\Delta\phi_{sc}} = \frac{ed_H\sigma_{ss}}{K_B T\varepsilon_H} \tag{1.1.18}$$

where, d_H is the compact layer thickness, and ε_H is the dielectric constant in the compact layer. Elementary calculations show that $\delta\Delta\phi_H / \delta\Delta\phi_{sc} \cong 1$ at a density, D_{ss}, of surface states of about 10^{13} cm^{-1}, which is approximately 1% of the surface atoms of semiconductors. At a surface state density above 1% of surface atom density, $\delta\Delta\phi_H / \delta\Delta\phi_{sc} > 1$, and therefore, almost all of the change in electrode potential difference occurs across the compact layer. In this situation, the interfacial structure is quite similar to that of the metal-solution interface, and the semiconductor electrode is said to be *quasi-metallic*. In the case of quasi-metallisation of a semiconductor solution interface, the compact Helmholtz layer effectively extends into the solid - state semiconductor, due to the presence of the surface states. Bockris and Otagawa[42,43], using electrochemical impedance measurements to determine interfacial capacitance, found that the oxygen reduction reaction (o.r.r.) on the perovskite material $Nd_{0.9}Sr_{0.1}CoO_3$ in alkaline solution, occurs in a region of potential where the material has the properties of a p-type semiconductor. However, with increasing anodic potential, it was found that significant metallisation occurred, so that the

oxygen evolution reaction occurred on a much more conductive substrate, than did the o.r.r. The metallisation was attributed to the inducement of surface states by the adsorption of OH^- ions, with increasing positive potential.

To further advance the discussion of the semiconductor-solution interface, it is necessary to consider how exactly this interface is formed. In section 1.1.1, the build-up of the metal-solution interface, was discussed in terms of the development of a separation of charge, owing to a flow of electrons from one phase to the other, in order to equalise the chemical potential of an electron in both phases at the interface. The Fermi level, E_F^α, of a phase α, can be identified with the electrochemical potential $\overline{\mu}_e^\alpha$, of an electron in phase α, which was already introduced in equation (1.1.2), so that:

$$E_F^\alpha = \overline{\mu}_e^\alpha = \mu_e^\alpha - e\phi^\alpha \tag{1.1.19}$$

Using the Fermi level terminology, a flow of charge occurs, when two phases are brought together, in order to equalise the Fermi levels of the phases at the interface. At a metal-solution interface, all the charge on the metal resides on the surface and there is no potential gradient between the bulk and the region of the metal adjacent to the interface. As a result of this, the band energies in the interfacial region and the bulk are the same. In the case of a semiconductor, excess charge is distributed in a space charge region. When a semiconductor electrode is brought into contact with a solution, the process of equalisation of the Fermi levels of the phases must still occur at the interface, however the electric field due to the space charge region affects the electrochemical potential of electrons in this region, with the result that the band energies vary in proportion to the charge density at all points between the surface and the bulk. This leads to the effective *bending of bands*, from the electrode surface, across the space charge region to its other extreme (i.e. the bulk), where the band structure becomes "flat" again. The degree of this bending, expressed in volts, is called the *Schottky barrier height* V_{Sch}. In an n-type semiconductor, in contact with an electrolyte solution, the bands are bent downward in energy, and a Schottky barrier, V_{Sch}, exists between the semiconductor surface and its bulk. Application of a negative bias in this situation will increase the energy of electrons in the semiconductor, the bands will move upwards in energy, and V_{Sch} will be reduced. At a certain bias, termed the *flat band potential*, V_{fb}, there will no longer be any band bending and the

band structure will be flat. It has been found[1], owing to the presence of surface OH groups (a phenomena that will be discussed shortly), that, for many metal oxide semiconductors V_{fb} varies with electrolyte solution pH, according to the following Nernstian expression due to Hoffman-Perez and Gerischer[44],

$$V_H = \text{constant} - (2.3RT/F)\text{pH} \quad , \tag{1.1.20}$$

where, V_H is the potential drop across the Helmholtz compact layer.

In analyses of the semiconductor-solution interface, such as that which lead to the derivation of the expression for the potential profile across the space charge layer and the compact layer in equation (1.1.18), it is found that under the range of typical experimental conditions, the potential drop across the diffuse layer in solution may be neglected so that to a good approximation, $\Delta\phi \cong \Delta\phi_H + \Delta\phi_{sc}$ (cf. equation (1.1.16)). In the case where the entire change of potential at a semiconductor-solution interface occurs across the space charge layer, the semiconductor is said to be *band edge pinned*. Band edge pinning occurs when the Fermi level at the interface is located in the band gap, away from the band edge levels and surface state levels. When the electrode is band edge pinned, applying a bias (either negative or positive) doesn't alter the interfacial charge, and thus there is no change in potential across the compact Helmholtz layer, with all the change in electrode potential occurring in the space charge layer.

If, on the other hand, the Fermi level at the interface is equal to a surface state of high density, or the conduction or valance band edge level, the semiconductor electrode is said to be *Fermi level pinned*. When a bias is applied to a Fermi-level pinned semiconductor-solution interface, all the change in electrode potential appears across the compact layer, with the potential of the space charge layer remaining unchanged. It is Fermi level pinning that causes the metallisation of semiconductor-solution interfaces, that was considered above. Of course, if a potential sweep is applied to a semiconductor-solution interface, the system will make transitions between band edge, and Fermi level, pinning, as is illustrated schematically in Figure 1.1.6.

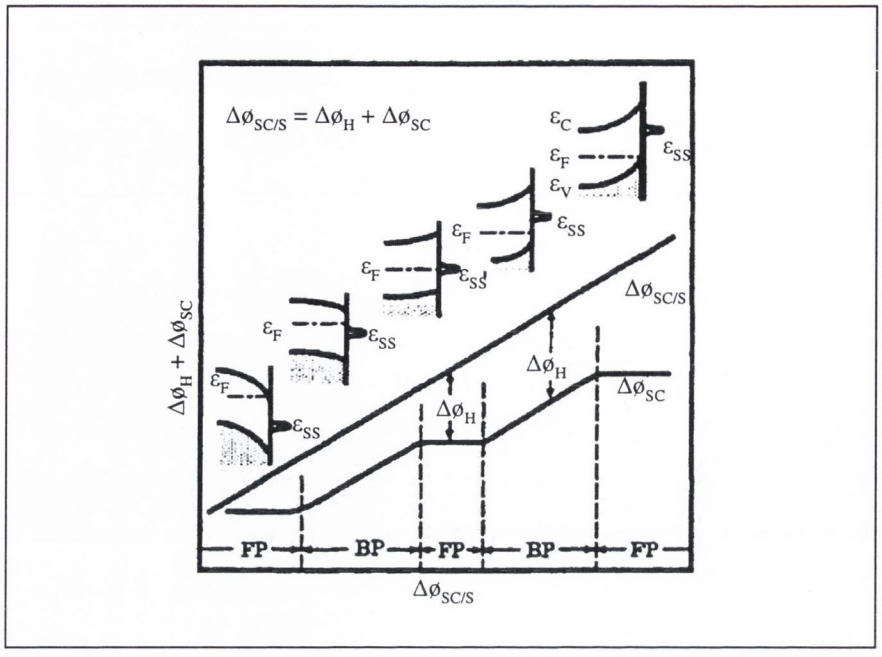


Figure 1.1.6 *Potential across an interface of semiconductor electrode distributed to the space charge layer, $\Delta\phi_{sc}$, and to the compact layer, $\Delta\phi_H$, as a function of total potential, $\Delta\phi_{sc/s}$, over a wide range of electrode potential: BP = band edge level pinning; FP = Fermi level pinning. Reproduced from Ref. 45.*

Consider, for example, the situation in the second sector from the left in Figure 1.1.6. Here, the electrode is band edge pinned, and applying an increasingly positive interfacial potential sweep, serves to lower the energy of the electrons in the bands, thus reducing the degree of band bending. The applied bias only affects the potential across the space charge layer. As the bias is increased further, the Fermi level at the interface becomes equal to the energy of the surface state (middle region of Figure 1.1.6). The Fermi level is then pinned at this surface state, until the surface state has become fully charged or discharged by accepting electrons from, or donating electrons to, the solution phase species. This charge transfer alters the potential across the compact layer, while the potential across the space charge region remains invariant in this situation. When the surface state is fully charged or discharged, the electrode again becomes band edge pinned, with increasing potential. In this way it can be seen how a semiconductor electrode can pass into, and out of, regions of quasi-metallisation, with changing applied potential.

Another significant difference between the oxide-solution and metal-solution interface, which has been alluded to previously, is that, for the former type with aqueous solution, there is an additional reversible double layer within the compact

layer due to the transfer of H^+ and OH^- ions across the interface, owing to a number of adsorption and dissociation reactions. The concentration of adsorbed H^+ and OH^- ions on the oxide surface varies with pH, leading to a dependence of the potential across the compact layer with pH.

On a polycrystalline metal oxide surface, O^{n-} and M^{m+} charge centres develop (where M is the metal involved), since the charge of surface ions is not fully compensated by the charge of adjacent ions, as is the case in the bulk. When the metal oxide is in contact with an aqueous phase, water molecules react with the charge centres, releasing H^+ and OH^- ions. This brings about the formation of hydroxyl groups on the surface, and it is accepted[33, 46, 47], that many oxide (and indeed semiconductor in general) surfaces undergo hydroxylation in aqueous solution, forming two types of hydroxyl groups – the *acid* –OH(a) and *base* –OH(b) types. The most widely accepted model for the formation of these Brønsted acid/base groups is the so-called *one-site/two*-pK model which is depicted in Figure 1.1.7.

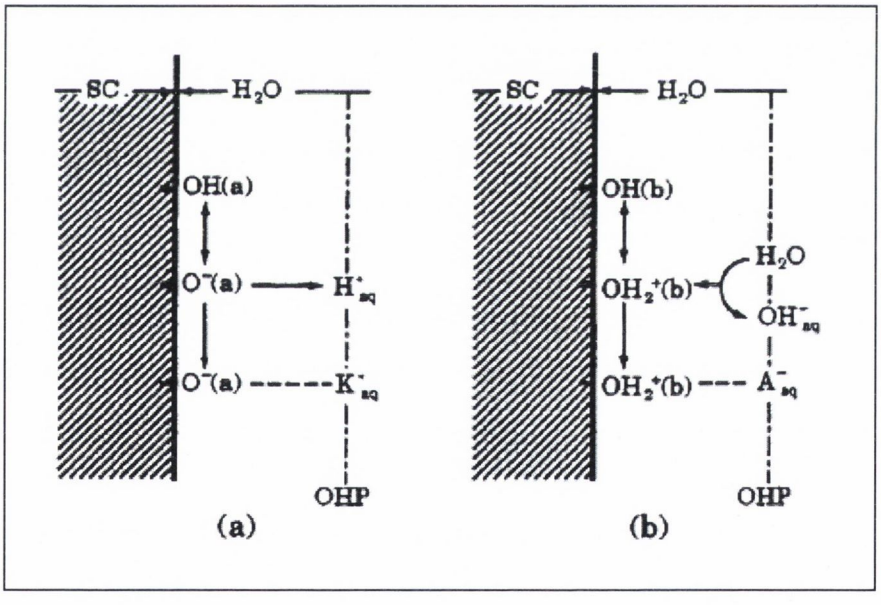


Figure 1.1.7 *The one-site/two-pK model for the dissociation of hydroxyl groups at oxide-solution interfaces. (a) Dissociation of acid type group. (b) Dissociation of the base type group. K_{aq}^+ represents a hydrated cation, while A_{aq}^- represents a hydrated anion. Reproduced from Ref. 48.*

This is a "one-site" model, because, in theory, the adsorbed OH species is the same in either the acid or base case, before ionisation occurs. The hydroxylation of metal oxide surfaces is of much interest in the field of colloidal chemistry and there does exist some other models to explain the acid/base behaviour of metal oxides in aqueous solution. The simplest of these is the *one-site/one* pK model[49], which proposes the

existence of one type of surface hydroxyl group, in which the oxygen has a charge equal to –1/2. These hydroxyl groups are in equilibrium with the conjugated acid group MOH_2, which has an oxygen charge of +1/2:

$$M - OH^{1/2-} + H^+ \overset{K}{\longleftrightarrow} M - OH_2^{1/2+} \qquad (1.1.21)$$

In more recent years, more complex, multi-site models have started to appear in the colloidal chemistry literature[50, 51] to describe the properties of amphoteric oxides.

As illustrated in Figure 1.1.7, non-specific adsorption of hydrated cations or anions, will occur at the acid and base surface groups respectively, to form *interfacial ion pairs*,

$$\text{-OH(a)} + K_{aq}^+ \leftrightarrows \text{-O}^-\text{(a)}\cdot K^+ + H_{aq}^+ \quad , \qquad (1.1.22)$$

$$\text{-OH(b)} + H_2O + A_{aq}^- \leftrightarrows -OH_2^+\text{(b)}\cdot A_{aq}^- + OH_{aq}^- \quad , \qquad (1.1.23)$$

where, K_{aq}^+ represents a hydrated cation, while A_{aq}^- represents a hydrated anion. It is the processes in equations (1.1.22) and (1.1.23) that lead to the formation of the reversible double layer at an oxide electrode in aqueous solution. Specific adsorption is also possible, where the acid or base site is covalently bonded to a dehydrated ion, to form a so-called *interfacial complex*[52].

For an oxide-solution interface it is necessary to define a *point of zero charge*, as opposed to the potential of zero charge defined for a metal-solution interface. The point of zero charge for an oxide-solution interface (rather confusingly also commonly abbreviated as the p.z.c.), in the absence of other potential determining ions, is defined[16] as the pH at which the surface excesses of H^+ and OH^- ions on the oxide surface are equal. The surface charge density, σ_{ox}, is related to the Gibbs surface excesses of H^+ and OH^- ions by the following expression,

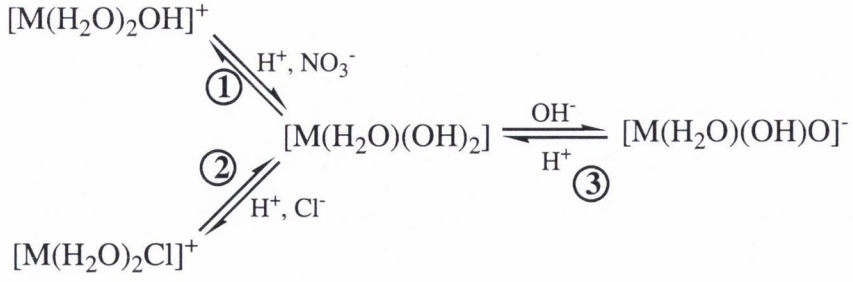
$$\sigma_{ox} = F(\Gamma_{H+} - \Gamma_{OH-}) \quad , \qquad (1.1.24)$$

clearly, when $\Gamma_{H+} = \Gamma_{OH-}$, $\sigma_{ox} = 0$.

It has long been recognised[53], that the low conductivity of oxides, makes it difficult to experimentally probe the oxide-solution interface, using the interfacial capacitive measurement methods that have been applied to the metal-solution interface. In a

recent review[54] on metal oxide surfaces and their interactions with aqueous solutions, it has been commented that "structural hypotheses concerning the electrical double layer are just beginning to be tested directly for metal oxide-aqueous solution interfaces now that appropriate measurement tools are becoming available". This review proceeds to outline details of AFM, second harmonic generation, and X-ray standing wave measurements. Notwithstanding this, the conventional wisdom regarding metal oxide-solution interfaces is principally based on experimental data derived from pH titrations and microelectrophoretic studies of various oxides in electrolytic suspensions[55].

In the acid-base titration method, the amount of acid or base consumed in the titration is related to the amounts of acid or base bound to the surface of the oxide suspension (the surface area of which has previously been determined using, for example, B.E.T. methods) plus that bound to form various aquo complexes. The interpretation of titration results can be complicated, by the fact that metal oxides are known to adsorb H^+ and OH^- ions in two steps, which occur on very different timescales[33]. The primary equilibrium process, which is that depicted in Figure 1.1.7 is thought to be complete within (at the most) minutes. The secondary process is believed to involve dissolution of the oxide, leading to such processes as complex formation and adsorption of dissolved complexes. These complex secondary processes may continue for days or even weeks. Fresh samples of oxide and solution are often utilised for each data point, in an attempt to experimentally isolate the effects of the primary process. A mechanism[33] for the development of surface charge due to the primary equilibrium process over a wide pH range in a pH titration is presented in equation (1.1.25),



(1.1.25)

The species, [-$M(H_2O)(OH)_2$], at the centre of the scheme in equation (1.1.25) is a neutral surface aquo-complex – such species are envisaged to be adsorbed on the oxide surface at the p.z.c., leading to an effective surface charge density of zero. Most oxides acquire a positive surface charge in solutions of pH, below the p.z.c. of the

oxide. In some cases the magnitude of the positive charge density has been experimentally observed, to depend only upon the H^+ ion concentration (or more correctly the H_3O^+ activity), and to be largely independent of anion concentration. This situation can be rationalised in terms of process 1 in equation (1.1.25) – a proton is added to the neutral surface complex, however the hydroxyl group remains intact. Ahmed[56] observed this type of behaviour for Al_2O_3 in solutions containing NO_3^-, ClO_4^- and Cl^-. In contrast, scenario 2 in equation (1.1.25) involves, not only the protonation of the neutral surface complex, but also the replacement of the hydroxyl group by an anion. In this case, in addition to solution pH, the concentration of anions will be significant in determining the acquired surface charge density. Behaviour of this type has been experimentally observed[56] for ZrO_2 in solutions containing ClO_4^- and Cl^-. As indicated by process 3 in equation (1.1.25), when the solution pH exceeds the p.z.c. of a given metal oxide, it is generally observed that the oxide surface acquires an excess negative charge density.

1.2 Electrode Kinetics

A brief review is now presented of the concepts of electrode kinetic theory most relevant to the present work. There exist many comprehensive reviews of electrochemical kinetics[60-64] and therefore the purpose of the present treatment is merely to identify and discuss the aspects of the theory that will be utilised in the analysis of the experimental data presented later.

1.2.1 Fundamentals of Electrode Kinetic Theory

Electrochemical kinetics may be regarded as a branch of heterogeneous reaction kinetics, however electrode reactions differ from ordinary heterogeneous chemical reactions, in that at least one step of the overall process involves the transfer of charge. The beginning of quantitative phenomenological electrode kinetics can be traced back to 1905, when Tafel[65], observed an exponential relationship between the shift of electrode potential, η, from its equilibrium value E_N, and the rate of reaction as manifested by the electrode current density i,

$$\eta = a + b \log i \quad , \tag{1.2.1}$$

where, a is a temperature dependent constant. The parameter b is known as the *Tafel slope* and for the case of a simple single step one-electron transfer it is defined as follows,

$$b = \frac{RT}{\beta F} \quad , \tag{1.2.2}$$

β is a constant known as the *symmetry factor*. Rearranging equation (1.2.1) achieves:

$$i = A\exp\left[\frac{-\beta\eta F}{RT}\right] \tag{1.2.3}$$

If equation (1.2.3) is compared to the Arrhenius equation of chemical kinetics,

$$k = A'\exp\left[\frac{-E_{act}}{RT}\right] \quad , \tag{1.2.4}$$

where, k is the reaction rate constant, and E_{act} is the activation energy, it is clear that $\beta\eta F$ must be related to the energy of activation of an electrode reaction. The theoretical Eyring equation,

$$k = \kappa\left\{\frac{K_B T}{h}\right\}\sigma\exp\left[\frac{\Delta S^{0*}}{R}\right]\exp\left[\frac{-\Delta H^{0*}}{RT}\right] \quad , \tag{1.2.5}$$

links *transition state theory, TST*, to experiment in regular chemical kinetics. The κ parameter in equation (1.2.5) is a constant known as the transmission coefficient, σ is a reaction length of the order of a molecular diameter, while ΔS^{0*} and ΔH^{0*} are the standard entropy and enthalpy changes of the activation process, respectively. The $(K_B T/h)\sigma$ term is related to the upper limit set on a heterogeneous rate constant by the vibrations of the transition state. The pre-exponential and first exponential term in equation (1.2.5) can be associated with the experimentally measurable Arrhenius coefficient A' in equation (1.2.4), while the second exponential term in the Eyring equation is linked to the activation energy E_{act}, which can also be measured by

experiment. Since the parallels between equations (1.2.3) and (1.2.4) have been highlighted, it is apparent that transition state theory can also be adapted to account for electrode kinetic behaviour.

The analysis is most simple and transparent for a single step electron transfer reaction occurring at the electrode-solution interface, which might be represented as,

$$O + e^- \leftrightarrows R \qquad (1.2.6)$$

where, the forward reaction has the rate constant k'_f and the reverse process has rate constant k'_r, where the $'$ superscript denotes an electrochemical as opposed to a chemical rate constant. It is assumed that the reaction is charge transfer controlled. The thermodynamic equilibrium for reaction (1.2.6) is characterised by the *Nernst equation*, which in this case may be written as,

$$E_N = E^0 - \frac{RT}{nF} \ln \frac{a_R^\infty}{a_O^\infty} \quad , \qquad (1.2.7)$$

where, E^0 is the standard potential for the redox couple, n is the number of electrons transferred in the balanced equation (one in this case), a_O^∞ , a_R^∞ are the bulk activities of the species O and R respectively, and E_N is the thermodynamic Nernst potential, which is determined for a given system by the ratio a_R^∞ / a_O^∞ . At E_N, the forward and reverse free energies of activation are ΔG_{0f}^* and ΔG_{0r}^*, respectively – see Figure 1.2.1. If the potential is changed from E_N to a new value E, the energy of an electron at the electrode surface changes by an amount $-F(E - E_N)$. In the case of a positive potential change, the free energy curve for the forward reaction is lowered by an amount $-F(E - E_N)$, and so the potential barrier for the reverse reaction, ΔG_r^*, becomes less than its equilibrium value ΔG_{0r}^*, by a quantity of magnitude $\beta F(E - E_N)$. The parameter β ($0 \leq \beta \leq 1$), is known as the *symmetry factor*, and, as can be appreciated even from the simple schematic in Figure 1.2.1, its value will depend on the relative shapes of the free energy functions at the point of intersection, although it is usually found to be ~ ½.

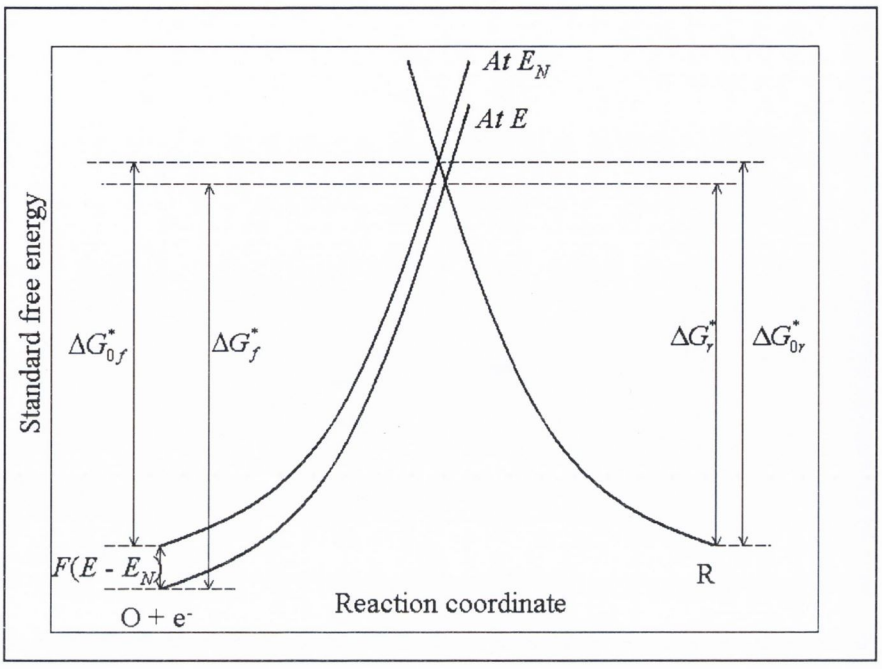


Figure 1.2.1 *Schematic representation of the effects of a potential change on the free energies of activation for oxidation and reduction.*

The free energy of activation of the reverse reaction at the potential E is therefore related to its value at equilibrium, as follows:

$$\Delta G_r^* = \Delta G_{0r}^* - \beta F(E - E_N) \tag{1.2.8}$$

In contrast, applying a positive change in potential, serves to increase the free energy of activation for the forward reaction, as can be appreciated from Figure 1.2.1:

$$\Delta G_f^* = \Delta G_{0f}^* + (1-\beta)F(E - E_N) \tag{1.2.9}$$

Since $\Delta G^{0*} = \Delta H^{0*} - T\Delta S^{0*}$, the Eyring equation (1.2.5), can be written as:

$$k = \kappa\left\{\frac{K_B T}{h}\right\}\sigma \exp\left[\frac{-\Delta G^{0*}}{RT}\right] \tag{1.2.10}$$

The rates, v, of the forward and reverse reactions are

$$v_f = k'_f a_O^{\infty} = \frac{i_{cathodic}}{nFA} \quad , \tag{1.2.11}$$

$$v_r = k'_r a_R^{\infty} = \frac{i_{anodic}}{nFA} \quad , \tag{1.2.12}$$

where, A is the active surface area of the electrode. At the thermodynamic Nernst potential for any $a_R^{\infty} / a_O^{\infty}$ ratio, the system is in equilibrium, and so $v_f = v_r$. In the special case where the $a_R^{\infty} / a_O^{\infty}$ ratio is equal to unity, $E_N = E^{\emptyset}$, and so for this particular situation $k'_f = k'_r = k^{\emptyset}$, where $k^{\emptyset}$ is the *standard rate constant* for the electrochemical system. If the pre-exponential term in equation (1.2.10) is denoted as Z, then k'_0 is defined as

$$k'^{0} = Z \exp\left(-\Delta G_0^* / RT\right) \tag{1.2.13}$$

It follows from equation (1.2.13), that in the case where $a_O^{\infty} = a_R^{\infty}$, the equilibrium energy barrier must be symmetrical, since $\Delta G_{0f}^* = \Delta G_{0r}^* = \Delta G^{0*}$. The rate constant at any other potential E can now be written in terms of $k^{\emptyset}$,

$$k'_f = k'^{0} \exp\left[-(1-\beta)\theta(E - E_N)\right], \tag{1.2.14}$$

$$k'_r = k'^{0} \exp\left[\beta\theta(E - E_N)\right], \tag{1.2.15}$$

where, $\theta = nF / RT$. These expressions apply regardless of the value of the $a_R^{\infty} / a_O^{\infty}$ ratio, because the symmetry factor takes account of the more general situation where $E_N \neq E^{\emptyset}$. As an example, it can be shown that if the system in the case where $a_O^{\infty} = a_R^{\infty}$ is treated by a simple harmonic oscillator approximation, the free energy curves can be assumed to be identical parabolas, and the symmetry factor is given by[64]:

$$\beta = \frac{1}{2} + \frac{nF(E - E^0)}{16\Delta G^{0*}} \tag{1.2.16}$$

The symmetry factor is thus a potential dependent quantity, however its apparent independence of potential (as for example, was empirically observed by Tafel[65]) is due to the fact that the second term on the right hand side is often small in comparison to the first term. This is the case where E - E^0 is small, or ΔG^{0*} is large (i.e. for slow reactions). In case where $a_O^\infty \neq a_R^\infty$, the energy barrier at the equilibrium potential E_N ($E_N \neq E^0$ in this case) is no longer symmetrical, however if E_N - E^0 is not too large, β in this situation can be approximated as:

$$\beta \cong \frac{1}{2} + \frac{nF(E-(E_N - E^0))}{16\Delta G^{0*}} \qquad (1.2.17)$$

The above example illustrates how the symmetry factor effectively facilitates the extension of the use of k^0 from the situation where $a_O^\infty = a_R^\infty$, to the more general situation as exemplified by equations (1.2.14) and (1.2.15) where $a_O^\infty \neq a_R^\infty$ and $E_N \neq E^0$.

The net electrode current density i is the difference between the anodic and cathodic currents –

$$i = i_{anodic} - i_{cathodic} = nF[k_r' a_R(0,t) - k_f' a_O(0,t)] \qquad (1.2.18)$$

Inserting the expressions for k'_f and k'_r from equations (1.2.14) and (1.2.15) into equation (1.2.18) yields,

$$i = Fk'^0[a_R(0,t)\exp\beta\theta(E-E_N) - a_O(0,t)\exp-(1-\beta)\theta(E-E_N)] \qquad (1.2.19)$$

where, $a_O(0,t)$ and $a_R(0,t)$, refer respectively to the activities of species O and R at the electrode surface (x = 0) at time t. Equation (1.2.19) is the current-potential characteristic for the general electrochemical system of equation (1.2.6). In the general situation, where $a_O^\infty \neq a_R^\infty$, the Nernst equation (1.2.7) predicts, that at equilibrium (i = 0), the electrode potential will differ from the standard potential for the couple by an amount $E_N - E^0$. Furthermore, at equilibrium there is no activity gradient between the bulk solution and the electrode surface and so, $a_O(0,t) = a_O^\infty$ and

$a_R(0,t) = a_R^{\infty}$. The net current density, i, is zero at equilibrium, because $i_{anodic} = i_{cathodic}$; this particular value of current density is called the *exchange current density* i_0, and from equation (1.2.19) can be written as:

$$i_0 = Fk'^0 a_R^{\infty} \exp\beta\theta(E_N - E^0) = Fk'^0 a_O^{\infty} \exp(1-\beta)\theta(E_N - E^0) \qquad (1.2.20)$$

Taking the Nernst equation (1.2.7), raising each side to the power of $-(1-\beta)$, and rearranging achieves:

$$e^{-(1-\beta)\theta(E_N - E^0)} = \left(\frac{a_O^{\infty}}{a_R^{\infty}}\right)^{-(1-\beta)} \qquad (1.2.21)$$

Substituting equation (1.2.21) into equation (1.2.20) yields the following useful expression,

$$i_0 = Fk'^0 a_R^{\infty\,(1-\beta)} a_O^{\infty\,\beta}, \qquad (1.2.22)$$

which, shows that the exchange current density is directly proportional to the standard electrochemical rate constant k^0. In practice the i_0 value is often quoted in the literature as a measure of the kinetics of a given electrochemical process. Dividing equation (1.2.19) by equation (1.2.22) yields the following expression:

$$\frac{i}{i_0} = \frac{a_R(0,t)}{a_R^{\infty}} e^{\beta\theta(E-E_N)} \left(\frac{a_R^{\infty}}{a_O^{\infty}}\right)^{\beta} - \frac{a_O(0,t)}{a_O^{\infty}} e^{-(1-\beta)\theta(E-E_N)} \left(\frac{a_R^{\infty}}{a_O^{\infty}}\right)^{-(1-\beta)} \qquad (1.2.23)$$

The $\left(a_R^{\infty} / a_O^{\infty}\right)^{\beta}$ and $\left(a_R^{\infty} / a_O^{\infty}\right)^{-(1-\beta)}$ terms can be evaluated from the Nernst equation in an analogous manner to the derivation of equation (1.2.21) – it can be shown[63] that substituting the resulting expressions into equation (1.2.23) yields the following,

$$i = i_0 \left[\frac{a_R(0,t)}{a_R^{\infty}} e^{\beta\theta\eta} - \frac{a_O(0,t)}{a_O^{\infty}} e^{-(1-\beta)\theta\eta} \right], \qquad (1.2.24)$$

where, the *overpotential* η is defined as $\eta = E - E_N$. Equation (1.2.24) predicts that, upon sweeping the potential away from E_N, the magnitude of the current will increase rapidly in the region adjacent to E_N going in either direction, because the exponential terms dominate at lower values of η, and the electrochemical system is charge transfer controlled. At extreme values of η in either direction the $i(\eta)$ function levels off, because the $a_R(0,t)/a_R^{\infty}$ and $a_O(0,t)/a_O^{\infty}$ terms now dominate and the system is mass transfer controlled. The mechanistic analyses presented in the present work are based upon observing the $i(\eta)$ behaviour in the charge transfer controlled region, where mass transfer effects can be neglected, and so equation (1.2.24) may be approximated in this region as:

$$i = i_0\left[e^{\beta\theta\eta} - e^{-(1-\beta)\theta\eta}\right] \tag{1.2.25}$$

Equation (1.2.25) is the form of the current-overpotential relation that is most commonly encountered, and is called the *Butler-Volmer* equation since it was first derived analytically based upon the work of Butler[67] and Volmer[68] in the 1920s.

At larger overpotentials in the charge transfer controlled region (typically η > 120 mV) one of the exponential terms in equation (1.2.25), depending on whether the polarisation is cathodic or anodic, becomes negligible with respect to the other. At high anodic polarisation, the conditions under which the oxygen evolution reaction prevails, equation (1.2.25) reduces to:

$$i = i_0 \exp[\beta\theta\eta] \tag{1.2.26}$$

Rearranging equation (1.2.26) yields,

$$\eta = \frac{RT}{\beta F}\ln i - \frac{RT}{\beta F}\ln i_0 = \frac{2.303RT}{\beta F}\log i - \frac{2.303RT}{\beta F}\log i_0 \tag{1.2.27}$$

for the case of a single step one electron transfer electrochemical reaction at large η. It is apparent that equation (1.2.27) has the same form as equation (1.2.1) (i.e. $\eta = a + b\log i$), where:

$$a = -\frac{2.303RT}{\beta F}\log i_0, \qquad b = \frac{2.303RT}{\beta F} \tag{1.2.28}$$

The theoretical model derived in the 1920s (although not using transition state theory[61] as shown here – TST wasn't developed at that stage) therefore predicts Tafel's empirical relation from 1905. Graphs of log*i* vs. η are referred to as *Tafel plots*, while, as previously mentioned, the parameter *b* is called the Tafel slope. It will be seen later, that the Tafel slope provides a very useful criterion in comparing experimental $i(\eta)$ data for an electrochemical process, with the theoretical predictions of various possible mechanisms. Furthermore the parameter *a* can be obtained from the intercept of a Tafel slope with the log*i* axis at η = 0, yielding a value of the exchange current density i_0 for the process characterised by that Tafel slope.

At this stage a few further comments are in order regarding the significance of the symmetry factor β, which was considered in passing in equations (1.2.16) and (1.2.17). If the intersection region of the free energy curves for the forward and reverse reactions of equation (1.2.6) is considered to be locally linear, then it can be represented in terms of the schematic presented in Figure 1.2.2.

By simple trigonometry, the following relations are obviously true:

$$\tan\theta = \frac{(1-\beta)F\eta}{d} \tag{1.2.29}$$

$$\tan\phi = \frac{\beta F\eta}{d} \tag{1.2.30}$$

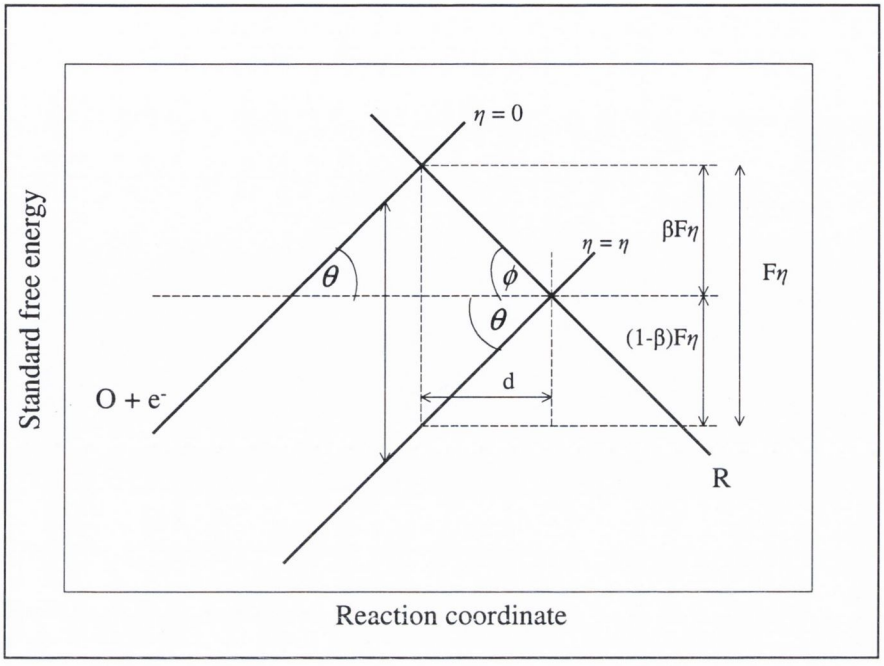


Figure 1.2.2 *Schematic representation of the relationship between the symmetry factor and the angles of intersection of the free energy curves. Details of the meanings of the various symbols are provided in the text.*

Solving for β from equations (1.2.29) and (1.2.30) yields:

$$\beta = \frac{\tan\phi}{\tan\phi + \tan\theta} \tag{1.2.31}$$

If $\theta = \phi$, the activation energy barrier is symmetrical (which as previously discussed is the situation that prevails when the system is at equilibrium on open circuit, and $a_O^\infty = a_R^\infty$), and β= 1/2. Linearity in free energy curves is unlikely over an extended range of reaction coordinate, and thus θ and ϕ should change as the shape of the intersection alters with applied potential. This would have the knock-on effect of causing deviations of β from ½ with increasing η. However in the majority of experiments, β appears to be a constant ~ ½ [63], because the range of measurable kinetics very often corresponds to free energy changes that are only a few percentage[63] of the activation energy, and therefore the curvature of the profiles effectively appear quasi-linear owing to the small accessible range. Essentially β dictates what fraction of electrical energy present at an electrochemical interface is available to alter the activation energy of a Faradaic process. It is evident from the schematic in Figure 1.2.2, that β can be represented in terms of the *changes* in

the free energy of activation ΔG_0^*, and free energies of reaction, $\Delta G_f, \Delta G_r$ of the forward and reverse reactions, where these changes are induced by a change in η (or indeed a_R^∞ / a_O^∞):

$$\beta = \frac{\delta \Delta G_r}{\delta \Delta G_0^*} = 1 - \frac{\delta \Delta G_f}{\delta \Delta G_0^*} \tag{1.2.32}$$

1.2.2 Adsorption Isotherms

The foregoing discussion on electrode kinetics considered the effects of applied overpotential and electrolyte concentration on the rates of electrochemical reactions. Another factor, not mentioned thus far, that often has a significant influence on electrochemical kinetics is the extent of electrode surface coverage, by adsorbed reaction intermediates or products. In the context of the adsorption of the species *i* on an electrode surface, an *adsorption isotherm* gives the relationship between the amount, a_i^A, of *i* adsorbed per unit area of the electrode, the activity, a_i^B, of *i* in the bulk electrolyte solution and the electrode potential. The isotherm is obtained, by recalling from section 1.1.1, that for a system in equilibrium, the electrochemical potential of species *i* is equal in the adsorbed and bulk solution states – i.e., $\overline{\mu}_i^A = \overline{\mu}_i^B$. The standard electrochemical potentials, $\overline{\mu}_i^{O,A}$, $\overline{\mu}_i^{O,B}$, of species *i* in the adsorbed and bulk states are then related as follows:

$$\overline{\mu}_i^{0,A} + RT \ln a_i^A = \overline{\mu}_i^{0,B} + RT \ln a_i^B \tag{1.2.33}$$

The standard free energy of adsorption, $\Delta G_i'^0$, of species *i* must be the difference between the standard electrochemical potentials of that species in the adsorbed and bulk states, i.e.:

$$\Delta G_i'^0 = \overline{\mu}_i^{0,A} - \overline{\mu}_i^{0,B} \tag{1.2.34}$$

From equation (1.2.33), $\overline{\mu}_i^{0,A} - \overline{\mu}_i^{0,B} = RT\left(\ln a_i^B - \ln a_i^A\right)$ - substituting this into equation (1.2.34) and rearranging yields,

$$a_i^A = a_i^B \exp(-\Delta G_i'^0 / RT) = K_i a_i^B \quad , \tag{1.2.35}$$

where,

$$K_i = \exp(-\Delta G_i'^0 / RT) \tag{1.2.36}$$

Equation (1.2.35) is the general form of the adsorption isotherm for species i – the exact form will depend on the model of adsorption that is adopted for a particular situation.

To examine the most commonly utilised adsorption isotherms in electrochemistry, consider the following simple proposed mechanism for the anodic oxygen evolution reaction (o.e.r.) in aqueous solution:

$$M + OH^- \leftrightarrows MOH + e^- \tag{1.2.37, I}$$

$$MOH + OH^- \leftrightarrows MO + H_2O + e^- \tag{1.2.37, II}$$

$$MO + MO \leftrightarrows 2M + O_2 \tag{1.2.37, III}$$

This mechanism was proposed by Bockris[69], and is often called the *electrochemical oxide path* for the o.e.r. The electrochemical kinetics of multi-step electrode reactions will be considered in the next section, for the moment it is noted that M may be the metal of the electrode or a film of the metallic oxide. MOH and MO are adsorbed intermediate species. The rate constants for the first two steps are denoted k'_I and k'_{II}, while k'_{-I} and k'_{-II} are the rate constants for the reverse of these steps. If $k'_{II} << k'_I, k'_{-I}, k'_{II}$ then it can be assumed that the rate of (1.2.37, II) will determine the rate of the overall process, and that the coverage of the intermediate MO, will be negligible compared to that of MOH. The rate v_I (with units of mol $cm^{-2}s^{-1}$) of the forward reaction of (1.2.27, I) at an overpotential η is given by,

$$v_I = k_I'^0 a_{OH} (1-\theta) \exp(\beta \eta F / RT) \quad , \tag{1.2.38}$$

where, θ is the fractional coverage of the electrode surface by adsorbed MOH, while a_{OH} is the activity of OH^- in the electrolyte solution. The rate of the reverse of (1.2.27, I) is:

$$v_{-I} = k'^{0}_{-I}\theta \exp(-(1-\beta)\eta F / RT) \qquad (1.2.39)$$

In the situation where $k'_{II} << k'_{I}, k'_{-II}$ it can be assumed that $v_I = v_{-I}$ (more will be said on such an assumption in the next section). Equating equations (1.2.38) and (1.2.39), and solving for θ yields,

$$\theta = \frac{Ka_{OH}e^{\eta F / RT}}{1 + Ka_{OH}e^{\eta F / RT}} \quad , \qquad (1.2.40)$$

where, $K = k'^{0}_{I} / k'^{0}_{-I} = \exp(-\Delta G^{\emptyset}/RT)$ – cf. equation (1.2.36). Equation (1.2.40) is a simple electrochemical adsorption isotherm, which, since K is a constant, assumes that $\Delta G^{\emptyset}$ is independent of θ. Rearranging equation (1.2.40) achieves:

$$\frac{\theta}{1-\theta} = Ka_{OH} \exp(\eta F / RT) \qquad (1.2.41)$$

$$= Ka_{OH} \exp(\eta F / RT)$$

When written in the form of equation (1.2.41), it is obvious that the isotherm just derived is in fact an electrochemical form of the well known *Langmuir adsorption isotherm*, with its characteristic relation between $\theta/1-\theta$ and the activity of the adsorbed species in solution. The Langmuir isotherm is based upon the following assumptions – (a) there are no interactions between the adsorbed species on the electrode surface, (b) adsorption occurs at every adsorption site with an equal probability – i.e. the electrode surface is completely homogeneous, (c) the coverage of adsorbed species increases linearly with its increasing bulk activity (i.e. - $\Delta G^{\emptyset}$ is independent of θ), forming a complete monolayer in the limit of high bulk activity, after which no further adsorption occurs. In reality none of these assumptions is likely to be realistic, although it is often found[70], that kinetic analyses based upon the Langmuir isotherm accurately predict experimental behaviour in situations where the intermediate coverage is likely to be very small ($\theta \rightarrow 0$) or nearly complete ($\theta \rightarrow 1$). This occurs because isotherms which assume, that $\Delta G^{\emptyset}$ is dependent on coverage reduce to the Langmuir isotherm at the extremes of coverage.

Clearly, a more realistic adsorption isotherm would require the apparent free energy of adsorption, $\Delta G'^{0}_{\theta}$ at a given coverage θ, to depend on that value of θ. If $\Delta G'^{0}_{\theta}$ is assumed to be a linear function of θ, one might write,

$$\Delta G_{\theta}^{\prime 0} = \Delta G_{0}^{\prime 0} + r\theta \qquad (1.2.42)$$

where, $\Delta G_{0}^{\prime 0}$ is the standard free energy of adsorption of a bare surface. The parameter r (units $Jmol^{-1}$) is a constant, independent of θ, which takes values of $r > 0$ in the case of repulsive interactions between adsorbed species and $r < 0$ for attractive mutual interactions of these species. A relation of the form of equation (1.2.42) was, first used to devise an electrochemical adsorption isotherm by Frumkin[71] in 1925, however Temkin[72] proposed a modification of this isotherm in 1941, that is based on a more realistic physical model than the original Frumkin isotherm. Temkin envisaged the electrode surface as being subdivided into a large number of small patches *ds*, with the Langmuir isotherm applicable on each, but with the value of the standard free energy of adsorption increasing progressively by small amounts from one patch to the other. The isotherm is obtained by the following expression,

$$\theta = \int_{0}^{1} \frac{K_r(s)a}{1+K_r(s)a} ds \quad , \qquad (1.2.43)$$

where, the integration is performed over the entire surface area of the electrode from $s = 0$ to $s = 1$. The equilibrium constant K_r is a function of s and can be written as,

$$K_r(s) = K\exp(-rs/RT), \qquad (1.2.44)$$

where K retains the significance of equation (1.2.36). Performing the integration of equation (1.2.43) yields,

$$\theta = \frac{1}{g}\ln\left[\frac{1+Ka}{1+Ka\exp(-g)}\right], \qquad (1.2.45)$$

where, $g = r/RT$. At intermediate activities (and hence intermediate fractional coverages), where a is sufficiently low to satisfy $Ka\exp(-g) << 1$, yet large enough for $Ka >> 1$, equation (1.2.45) can be approximated as,

$$\theta = \frac{1}{g}\ln(Ka), \tag{1.2.46}$$

which, is often referred to as the *logarithmic isotherm.* Temkin[72] showed that the same isotherm (equation (1.2.45)) is obtained if the difference between $\Delta G'^{0}_{\theta}$ and $\Delta G'^{0}_{0}$ is assumed to be due to lateral interactions between the adsorbed species or to be due to a dipole potential induced by these species.

Referring back to the example of the electrochemical oxide mechanism for the o.e.r. (equation (1.2.37)). If the same assumptions about equation (1.2.37) being rate determining are adopted as previously, then the analogues, under adsorption conditions defined by equation (1.2.42), of equations (1.2.38) and (1.2.39) for the forward and reverse rates of equation (1.2.37, I) are:

$$v_I = k'^{0}_{I} a_{OH} (1-\theta)\exp(\beta\eta F / RT)\exp(-\gamma r\theta / RT) \tag{1.2.47}$$

$$v_{-I} = k'^{0}_{-I}\theta\exp(-(1-\beta)\eta F / RT)\exp((1-\gamma)r\theta / RT) \tag{1.2.48}$$

The γ parameter is a symmetry factor, where $0 < \gamma < 1$, and $\gamma = 1-\beta$. As before, it is assumed that since $k'_{II} << k'_{I}, k'_{-I}$ it is admissible to equate v_I with v_{-I}, yielding:

$$\frac{\theta}{1-\theta} = Ka_{OH}\exp(\eta F / RT)\exp(-r\theta / RT) \tag{1.2.49}$$

The $\theta/1-\theta$ term will be approximately equal to unity if $0.2 < \theta < 0.8$, i.e. at intermediate fractional coverage of MOH, and under these conditions equation (1.2.49) reduces to:

$$r\theta = RT\ln K + RT\ln a_{OH} + \eta F \tag{1.2.50}$$

This relation is obviously equivalent to the logarithmic isotherm (equation (1.2.46)) with the addition of the ηF term, which accounts for the effect of an applied overpotential, η, on the adsorption behaviour.

The process of the electro-adsorption of intermediates gives rise to a so-called

pseudo-capacitance. Conway[73] comments that "formally, pseudo-capacitance of an electrode is recognised when the accepted or delivered charge, q, is Faradaic and is a function of the potential E. Then there is a derivative dq/dE, which is a capacitive quantity and can be measured as such, except that the charge originates from a Faradaic electron transfer process, involving a potential dependent change of oxidation state." This pseudo-capacitance therefore contrasts with the double-layer capacitance that was discussed in sections 1.1.1 and 1.1.2 since, the later involves mainly non-Faradaic accumulation of charge difference across an interface that is electrostatic rather than electrochemical in origin[73]. The pseudo-capacity, C_{ps}, associated with electro-adsorption is given by,

$$C_{ps} = \frac{dq}{d\eta} = q_1 \frac{d\theta}{d\eta} \quad , \tag{1.2.51}$$

where, q is the charge which is related to the fractional surface coverage θ by the expression $q = q_1\theta$. The term q_1, is therefore the total charge required for the deposition of a monolayer of the adsorbed intermediate. In principle this means that if C_{ps} is accessible over a range of η, then θ, or changes of θ, as a function of η can be evaluated by integration of $(C_{ps}/q)d\eta$. Substituting the expression for the Temkin isotherm (equation (1.2.50)) into equation (1.2.51) yields, at constant temperature and solution activity:

$$C_{ps} = \frac{q_1 F}{r} = \frac{q_1 F}{gRT} \tag{1.2.52}$$

Equation (1.2.52) implies that there should be a constant pseudo-capacitance associated with adsorption under a Temkin isotherm, over the range of potential at which the isotherm is operative.

1.2.3 Multistep Electrode Kinetics

The discussion of electrochemical kinetics in section 1.2.1 was restricted to the simple case of a one-electron transfer, which occurs in one step, as exemplified by reaction (1.2.6). In practice it is found that most electrochemical reactions consist of a number of consecutive steps – although it is usually assumed that only one electron

may be transferred in any given step. A number of methods for the treatment of multistep electrode kinetics were proposed in the 1950s[69, 74]. These methods have in common, the assumption that the rate constant of a single step is significantly smaller than that of any other step in the consecutive mechanism, and may therefore be considered as rate determining. As a guideline, it has been commented[75] that the free energy of activation of a proposed *rate determining step* (rds) should be ≥ ca. 10 KJ mole^{-1} greater than that of any other step in the overall scheme.

One approach, championed by Bockris in an early seminal paper[69] on proposed kinetic reaction mechanisms for the oxygen evolution reaction (o.e.r.) in aqueous solution is based upon a mathematical analysis first performed by Christiansen[76] for a multistep reaction mechanism occurring at a velocity v in the steady state. In this approach, it is assumed that for a series of consecutive electrochemical reactions, the concentration of reactants in the initial state of the reaction (i.e. OH^- ions in the o.e.r.) remains constant throughout the reaction. Furthermore it is assumed that steps before the rds are effectively in equilibrium. The net velocity of the ith non-rate controlling step is; $v = v_i - v_{-i}$. Likewise the net velocity of the jth step which is assumed to be the rds, is given by $v = v_j - v_{-j}$. However, since $v_i > v_j$ and $v_{-i} >> v_{-j}$, one can write $v_i \approx v_{-i}$. The Christiansen approach[76] is based on the identification of a set of parameters w_i. If the over-all reaction has a forward velocity v, then,

$$v = w_1 - w_{-1}c_{X(1)}, \tag{1.2.53}$$

where $w_1 = k'_1 c_1$, k'_1 is the electrochemical rate constant for the forward direction of the first step, c_1 is the concentration of the known entity in the initial state (e.g. OH^- in the o.e.r.), while $c_{X(1)}$ is the concentration of the radical X_1 produced in the first stage of the reaction. For the second step of the reaction sequence one can write,

$$v = w_2 c_{X(1)} - w_{-2}c_{X(2)}, \tag{1.2.54}$$

where X_2 is the entity produced by the forward direction of the second step. Following this logic, equations similar in form to equation (1.2.54) can be written for each of the consecutive reactions, yielding n simultaneous equations in v and $(n-1)w$'s. Christiansen[76] gave the general solution to such a set of simultaneous equations for the over-all rate of the forward reaction under steady-state conditions as:

$$\frac{1}{v} = \frac{1}{w_1} + \frac{w_{-1}}{w_1 w_2} + \frac{w_{-1} w_{-2}}{w_1 w_2 w_3} + \ldots + \frac{w_{-1} w_{-2} \cdots w_{-(n-1)}}{w_1 w_2 w_3 \cdots w_n} \qquad (1.2.55)$$

Correspondingly, the over-all rate of the back reaction is

$$\frac{1}{v} = \frac{1}{w_{-n}} + \frac{w_n}{w_{-n} w_{-(n-1)}} + \ldots + \frac{w_n w_{n-1} \cdots w_2}{w_{-n} w_{-(n-1)} \cdots w_{-1}} \qquad (1.2.56)$$

These general solutions will clearly contain a number of rate constants and as commented by Bockris[69] – "If simple conditions can be found for which this expression (equation (1.2.55)) reduces to one containing only one rate constant, that of the i^{th} reaction in the forward direction, then such conditions are those giving rise to rate control of the entire reaction by that step". One of the o.e.r. mechanisms analysed by Bockris is the electrochemical oxide path, which has already been introduced to the present work in equations (1.2.37, I – III).The overall equation for the o.e.r. in aqueous solution is:

$$4OH^- \rightarrow O_2 + 2H_2O + 4e^- \qquad (1.2.57)$$

As an illustration of the workings of the Bockris steady-state approach, consideration is now given to the electrochemical oxide path, with the second step (1.2.37, II) assumed to be the rds. Using the principles outlined in sections 1.2.1 and 1.2.2 for single step electron transfer reactions it is a trivial task to write the rate equations for the various steps of reaction (1.2.37) – the forward and reverse rate equations are quoted for steps I and II below:

$$v_I = k_I'^0 (1 - \theta_{MOH}) c_{OH} \exp(\beta \eta F / RT) \qquad (1.2.58)$$

$$v_{-I} = k_{-I}'^0 c_{MOH} \exp(-(1 - \beta) \eta F / RT) \qquad (1.2.59)$$

$$v_{II} = k_{II}'^0 c_{OH} c_{MOH} \exp(\beta \eta F / RT) \qquad (1.2.60)$$

$$v_{-II} = k'^{0}_{-II} c_{MO} \exp(-(1-\beta)\eta F / RT) \tag{1.2.61}$$

Once the rate equations have been deduced, it is possible to write out the Christiansen w terms. To do this it is necessary to obtain the expression for $v = v_I - v_{-I}$,

$$v_I - v_{II} = k'^{0}_{I} c_{OH} e^{\beta\eta F / RT} - (k'^{0}_{I} k^{1} c_{OH} e^{\beta\eta F / RT} - k'^{0}_{-I} e^{-(1-\beta)\eta F / RT}) c_{MOH} \tag{1.2.62}$$

where, $\theta_{MOH} = k^{1} c_{MOH}$. Comparing equation (1.2.62) with equation (1.2.53), it is easy to identify w_I and w_{-I} as:

$$w_I = k'^{0}_{I} c_{OH} e^{\beta\eta F / RT} \tag{1.2.63}$$

$$w_{-I} = k'^{0}_{I} k^{1} c_{OH} e^{\beta\eta F / RT} - k'^{0}_{-I} e^{-(1-\beta)\eta F / RT} \tag{1.2.64}$$

The w_{II}, w_{-II}, and w_{III}, w_{-III} parameters can be obtained from $v = v_{II} - v_{-II}$, and $v = v_{III} - v_{-III}$ respectively, in an analogous manner to the determination of w_I, w_{-I}. It can be shown[69] that w_{II}, w_{-II}, w_{III}, and w_{-III} are given by the following expressions:

$$w_{II} = k'^{0}_{II} c_{OH} \exp(\beta\eta F / RT) \tag{1.2.65}$$

$$w_{-II} = k'^{0}_{-II} \exp(-(1-\beta)\eta F / RT) \tag{1.2.66}$$

$$w_{III} = k^{0}_{III} c_{MO} \tag{1.2.67}$$

$$w_{-III} = k^{0}_{-III} \tag{1.2.68}$$

Applying the general solution of equation (1.2.55), setting $\beta = ½$, and assuming that since step II is the rds, $k'_{II} \rightarrow k'_{-II} \rightarrow 0$, achieves the following expression for the overall forward rate v:

$$v = \frac{k'^{0}_{I} k'^{0}_{II} c_{OH}{}^{2} e^{\eta F / 2RT}}{k'^{0}_{-I} e^{-\eta F / 2RT} + k'^{0}_{I} k^{1} c_{OH} e^{\eta F / 2RT}} \tag{1.2.69}$$

Recall that any step *i*, before the rds is assumed to be in effective equilibrium, allowing the following expression to be written for step I:

$$v_I \approx v_{-I}, \therefore k_I'^0 c_{OH} e^{\eta F/2RT} - k_I'^0 k^1 c_{MOH} c_{OH} e^{\eta F/2RT} \approx k_{-I}'^0 c_{MOH} e^{-\eta F/2RT} \tag{1.2.70}$$

Under conditions where a low coverage Langmuir isotherm is operative, $\theta = k^I c_{MOH} \rightarrow 0$, and equation (1.2.70) will approximately reduce to,

$$k_I'^0 c_{OH} e^{\eta F/2RT} \approx k_{-I}'^0 c_{MOH} e^{-\eta F/2RT} \tag{1.2.71}$$

since $k_I'^0 k^1 c_{MOH} c_{OH} e^{\eta F/2RT} << k_I'^0 c_{OH} e^{\eta F/2RT} \approx k_{-I}'^0 c_{MOH} e^{-\eta F/2RT}$ under these conditions. This further implies that the second term in the sum in the denominator of equation (1.2.69) will be negligible compared to the first term, under conditions of very low MOH coverage. In this case equation (1.2.69) reduces to,

$$v = K_I k_{II}'^0 c_{OH}{}^2 e^{3\eta F/2RT} \tag{1.2.72}$$

where, $K_I = k_I'^0 / k_{-I}'^0$. Since two electrons effectively pass to the external circuit each time the rds occurs (one from step I and one from step II), the current density *i* due to the over-all process is given by:

$$i = 2Fv = 2FK_I k_{II}'^0 c_{OH}{}^2 e^{3\eta F/2RT} \tag{1.2.73}$$

The predicted Tafel slope, for the reaction mechanism (1.2.37), with step II rate controlling, under low coverage Langmuir adsorption conditions, is therefore,

$$b = \frac{d\eta}{d\log i} = 2.303\frac{2RT}{3F} \tag{1.2.74}$$

which has a value of 39.44 mV dec^{-1} at 25°C. At sufficiently high values of η, the first term in the denominator of equation (1.2.69) becomes negligible compared to the

second term, and the equation reduces to:

$$v = \frac{k_{II}'^{0}}{k^{1}} c_{OH} e^{\eta F / 2RT} \tag{1.2.75}$$

The corresponding current density is,

$$i = \frac{2F}{k^{1}} k_{II}'^{0} c_{OH} e^{\eta F / 2RT} \quad , \tag{1.2.76}$$

which, leads to a Tafel slope of:

$$b = \frac{d\eta}{d \log i} = 2.303 \frac{2RT}{F} \tag{1.2.77}$$

This corresponds to a value of 118.33 mV dec^{-1} at 25°C. In the publication[69] in which he outlined the method of analysis of multistep electrochemical reaction mechanisms described above, Bockris considered four other potential schemes for the o.e.r. In general he found that the overall rate of reaction depended on the rate constant of the rds and the product of the equilibrium constants of the preceding steps.

Parsons[74] adopted a different approach to the problem of mutistep electrode kinetics. He utilised the hypothesis of *pseudo-equilibrium*, which holds that a step or number of steps preceding the rds can effectively be considered to be in equilibrium if their rate is much greater than that of the rds. The condition for a step j to be in pseudo-equilibrium is that $i_j \approx 0$. This in turn implies that the forward i_j and reverse i_{-j} rates are approximately equal - $i_j \approx i_{-j}$. Applying the pseudo-equilibrium approximation, Parsons obtained the following expression for the overall reaction current density,

$$i = i_0 \left\{ \exp\left[\left(\frac{n_s}{\nu_r} + n_r \beta \right) \frac{\eta F}{RT} \right] - \exp\left[-\left(\frac{n_\Sigma - n_s}{\nu_r} - n_r \beta \right) \frac{\eta F}{RT} \right] \right\} \tag{1.2.78}$$

where, n_r is the number of electrons transferred in the rds respectively, while n_Σ denotes the total number of electrons transferred in the overall reaction. The ν parameter is known as *the stoichiometric number* and is defined as the number of

times the rds occurs for one act of the overall reaction. There seems to be some confusion over the meaning of the parameter n_s. For example, in Bockris and Khan's textbook[75], n_s is rather imprecisely defined as "the number of electrons passing before the rds". A more precise definition is provided by Damjanovic et al.[77], who define n_i as the number of electrons transferred in a single pre-rds step i, and v_i as the stoichiometric number of step i. The n_s parameter is then defined as follows:

$$n_s = \sum_{i=1}^{r-1} v_i n_i \tag{1.2.79}$$

It is obvious that equation (1.2.78) is a version of the Butler-Volmer reaction, and may be written (cf. equation (1.2.25)) as:

$$i = i_0 \left\{ \exp\left[\vec{\alpha} \frac{\eta F}{RT} \right] - \exp\left[-\bar{\alpha} \frac{\eta F}{RT} \right] \right\} \tag{1.2.80}$$

where

$$\vec{\alpha} = \frac{n_s}{v} + n_r \beta \tag{1.2.81}$$

$$\bar{\alpha} = \frac{n_\Sigma - n_s}{v} - n_r \beta \tag{1.2.82}$$

The quantities $\vec{\alpha}$ and $\bar{\alpha}$ are the *transfer coefficients* for the forward and reverse directions of the overall reaction. While they might be considered as multistep reaction analogues of the symmetry factor β, an examination of equations (1.2.81) and (1.2.82) indicates that they are fundamentally different quantities. The symmetry factor arises from the activation of vibrational states and the energy required to break bonds (see section 1.2.1). The physical basis of the transfer coefficient still incorporates these factors, since α is expressed in terms of β, however α is also associated with the stoichiometry of the reaction (through v) and the succession of steps in the overall reaction (through n_Σ, n_r and n_s). It has been seen (section 1.2.1) that β can generally be taken to be ½ - equations (1.2.81) and (1.2.82) imply that this isn't the case for α. In fact the value of the transfer coefficients determine the Tafel slope b ($=d\eta/d\log i$) of a multistep reaction and can be diagnostic of a particular

reaction mechanism.

Recall that a value of b = 2.303(2*RT*/3*F*) was found for the Tafel slope of reaction (1.2.37) (the electrochemical oxide path) using the Bockris-Christiansen method when step II was the rds, and the fractional coverage of the intermediate MOH tended towards zero. Since $b = d\eta / d\log i = 2.303RT / \bar{\alpha}F = 2.303(2RT/3F)$, $\bar{\alpha}$ clearly has a value of 3/2 in this case. However, in the case where step I is taken to be rate determining, the Bockris-Christiansen approach predicts[69] that b = 2.303(2RT/F) and thus $\bar{\alpha}$ = ½. If each step in a proposed mechanism, has a unique associated value of α, in the case where that step is consider to be rate determining, then it is, in principle possible to experimentally identify the actual rds, by deriving the value of α from the measured Tafel slope. It is however often found, that under certain conditions different steps may have identical associated values of α, and therefore further criteria are required to identify the operative rds.

To check for consistency between the outcome of the Bockris-Christiansen approach and the predictions of the Parsons analysis, consider again reaction (1.2.37), with step II rate controlling. In this situation, $n_s = n_I \nu_I$ = (1)(2) = 2, ν= 2, n_r = 1, and β is again assumed to be ½. Applying equation (1.2.81), $\bar{\alpha}$ = 2/2 + 1(1/2) = 3/2. Now $b = 2.303RT / \bar{\alpha}F = 2.303(2RT/3F)$, which is consistent with the prediction of the Bockris-Christiansen method for the case where step II is the rds, and a low coverage Langmuir isotherm applies to the adsorbed MOH intermediate.

Parsons[74] also pointed out that, if the anodic and cathodic Tafel slopes (b_a and b_c respectively) are obtained from polarisation measurements, the stoichiometric number ν can be determined experimentally using the following expression:

$$\nu = 1 \Big/ \left[\frac{2.303RT}{n_\Sigma F} \left(\frac{1}{b_a} - \frac{1}{b_c} \right) \right] \qquad (1.2.83)$$

Equation (1.2.83) only applies if the activated complex in the rate determining reactions is the same for both the oxidation and reduction processes.

The two methods outlined above provide for a link between experimentally determined Tafel slopes and proposed reaction mechanisms. Although useful, they are limited in their applicability by the fact that they are based upon the Langmuir adsorption isotherm. The Parsons approach for example, predicts the value of α under low intermediate coverage Langmuir conditions at low overpotentials. As has been

previously considered (section 1.2.2) a different isotherm (e.g. the Temkin isotherm) may be more appropriate under certain conditions. Furthermore, the Bockris and especially the Parsons method, are rather opaque to developing an intuitive understanding, of the relative influence of the steps before and including the rds in determining the overall reaction kinetics. Therefore a more general analytical approach is often applied in multi-step kinetic mechanistic analysis, and will also be used in the present work. To illustrate the principles of this method, consideration will again be given the electrochemical oxide path for the o.e.r. (equation (1.2.37)), with rate determining step II. The quantitative predictions of this mechanism will be derived, firstly under Langmuir adsorption conditions, and then using the Temkin isotherm.

The initial part of the analysis of this problem under Langmuir adsorption conditions has already been tackled in section (1.2.2). With step II rate determining, the pseudo-equilibrium approximation was applied to step I, and expressions for the forward and reverse rates of this first step (v_I and v_{-I}) were derived in equations (1.2.38) and (1.2.39). It was assumed that the coverage of the intermediate MO was negligible compared to that of MOH. The rates v_I and v_{-I} were then equated, and an expression for the fractional coverage θ_{MOH} of the adsorbed hydroxyl species was obtained in equation (1.2.40), which was shown to be a form of the electrochemical Langmuir isotherm -

$$\theta_{MOH} = \frac{Kc_{OH}e^{\eta F/RT}}{1+Kc_{OH}e^{\eta F/RT}} \quad , \tag{1.2.40}$$

where, $K = k_I'^{0}/k_{-I}'^{0} = \exp(-\Delta G^{0}/RT)$. The $Kc_{OH}e^{\eta F/RT}$ term can be written as $c_{OH}\exp\left[\left(-\Delta G'^{0}+\eta F\right)/RT\right]$. At lower values of η, the $\Delta G'^{0}$ term will dominate the exponent, which will therefore be a significant negative quantity, and thus, in this overpotential range $Kc_{OH}e^{\eta F/RT} << 1$ and equation (1.2.40) reduces to:

$$\theta_{MOH} = Kc_{OH}\exp(\eta F/RT) \tag{1.2.84}$$

Since $\theta_{MOH} = Kc_{OH}e^{\eta F/RT} << 1$, it is clear that at low overpotentials, the Langmuir isotherm is operative in its low coverage mode. The rate equation for reaction (1.2.37,

II) may be written as,

$$v_{II} = k'^{0}_{II}\theta_{MOH}c_{OH}\exp(\beta\eta F/RT) \tag{1.2.85}$$

Substituting for θ_{MOH} from equation (1.2.84) into equation (1.2.85) and writing the rate in terms of i yields:

$$i = 2Fv_{II} = 2FKk'^{0}_{II}c_{OH}^{2}\exp((1+\beta)\eta F/RT) \tag{1.2.86}$$

Taking natural logarithms achieves:

$$\ln i = \ln 2FKk'^{0}_{II} + 2\ln c_{OH} + (1+\beta)\eta F/RT \tag{1.2.87}$$

Setting β = ½, leads to values for the Tafel slope, b, and *the reaction order with respect to OH⁻ ion concentration*, m_{OH}, of:

$$b = \left(\frac{\partial\eta}{d\log i}\right)_{C_{OH}} = 2.303\frac{2RT}{3F} \tag{1.2.88}$$

$$m_{OH} = \left(\frac{\partial\ln i}{d\ln c_{OH}}\right)_{\eta} = 2 \tag{1.2.89}$$

Clearly, the value of b as calculated by the above analysis, is the same as the value yielded by the Parsons approach, and by the Bockris-Christiansen method at $\theta_{MOH}\rightarrow 0$. Electrochemical reaction orders are analogous to the reaction orders of regular chemical kinetics. They provided an extra diagnostic criterion for the elucidation of electrochemical reaction mechanisms. To be consistent with a particular mechanism, experimental polarisation data should not only match the Tafel slope predicted for that mechanism over a range of overpotentials, but should also match the predicted reaction order for the mechanism, when a plot of log i against log c (or more correctly log a) at a given value of η is constructed from polarisation data collected from electrolytes of different concentration.

At high overpotentials, the $Kc_{OH}e^{\eta F/RT}$ term in equation (1.2.40)

becomes >> 1, and therefore θ_{MOH} approaches unity. In the limit of $\theta_{MOH} \rightarrow 1$, equation (1.2.85) reduces to, $v_{II} = k'^{0}_{II} c_{OH} (\beta\eta F / RT)$ and thus the overall current becomes:

$$i = 2Fk'^{0}_{II} c_{OH} \exp(\beta\eta F / RT) \tag{1.2.90}$$

Again taking natural logarithms,

$$\ln i = \ln 2Fk'^{0}_{II} + \ln c_{OH} + \beta\eta F / RT \tag{1.2.91}$$

As before β = ½, and so b and m_{OH}, have the following values:

$$b = \left(\frac{\partial \eta}{d \log i} \right)_{C_{OH}} = 2.303 \frac{2RT}{F} \tag{1.2.92}$$

$$m_{OH} = \left(\frac{\partial \ln i}{d \ln c_{OH}} \right)_{\eta} = 1 \tag{1.2.93}$$

This value of Tafel slope is again consistent with that predicted by the Bockris-Christiansen method at high η.

In the discussion of the Temkin isotherm in section 1.2.2, the variation of $\Delta G'^{0}_{0}$ with the fractional coverage of intermediates θ, was proposed to take the form, $\Delta G'^{0}_{\theta} = \Delta G'^{0}_{0} + r\theta$ - see equation (1.2.4). The parameter r was attributed to the effects of lateral interactions between adsorbed species, where $r > 0$ in the case of repulsive interactions, and $r < 0$ for attractive interactions of these species. A somewhat different approach to the r parameter, which helps to make more transparent, the application of the Temkin isotherm to kinetic mechanistic analysis, was adopted by Damjanovic et al.[77] in an important work on the o.e.r. These workers based their analysis of coverage effects due to adsorbed intermediates, on the principle that a decrease in the free energy of adsorption of an intermediate species that is a product of a given step, results in an increase in the free energy of activation for that step. In contrast, a decrease in the free energy of adsorption of an intermediate species, which

is a reactant in a particular step, will cause a decrease in the free energy of activation for the step. In terms of this model the free energy of adsorption of a given species *i*, depends on the total coverage θ[77, 78] of all adsorbed reaction intermediate species on the electrode surface according to,

$$\Delta G'^{0}_{\theta} = \Delta G'^{0}_{0} - r_i\theta \quad , \tag{1.2.94}$$

since it is the sites remaining beyond the overall fractional coverage that determine, through the respective *r* values, the energy of adsorption that *i* will experience when adsorbed under such conditions. The term r_i in equation (1.2.94) is clearly the rate of change of the free energy of adsorption of species *i* with the total coverage. The approach outlined above is useful in the analysis of the situation where there may be two or more adsorbed intermediate species present simultaneously on an electrode surface. The standard example that has been used so far, of the electrochemical oxide path for the o.e.r.,(equation 1.2.37), is an example of such a situation – the intermediate species MOH is formed in step I, and then is a reactant in step II, where another adsorbed intermediate, MO, is produced. Again, consideration will be given to the prediction of the kinetic parameters arising from this reaction path, with step II as rds, except this time under Temkin conditions with the assumptions discussed above operative.

The forward and reverse rates of step I are,

$$v_I = k'^{0}_{I} c_{OH} (1-\theta_{MOH}) \exp(\beta\eta F / RT) \exp(-\gamma r_{MOH}\theta / RT) \quad , \tag{1.2.95}$$

$$v_{-I} = k'^{0}_{-I} \theta_{MOH} \exp(-(1-\beta)\eta F / RT) \exp((1-\gamma) r_{MOH}\theta) / RT) \tag{1.2.96}$$

where, γ is, as before (section 1.2.2.) a symmetry factor, $0 < \gamma < 1$, and $\gamma = 1 - \beta$. The overall rate of reaction is limited by the rate determining second step:

$$v_{II} = k'^{0}_{II} c_{OH} \theta_{MOH} \exp(\beta\eta F / RT) \exp\{(1-\gamma) r_{MOH}\theta - \gamma r_{MO}\theta) / RT\} \tag{1.2.97}$$

With some rearrangement of the second exponential term, and setting $\gamma = \beta = ½$, the following expression is obtained:

$$v_{II} = k_{II}'^{0} c_{OH} \theta_{MOH} \exp(\eta F / 2RT) \exp\{(r_{MOH}\theta - \tfrac{1}{2} r_{MOH}\theta - \tfrac{1}{2} r_{MO}\theta) / RT\} \quad (1.2.98)$$

The values of the r parameters depend on the nature of the adsorbed species, however in the case of MOH and MO the r values can reasonably be expected to be very similar, since both species involve bonding by oxygen atoms to the substrate M. Setting $r_{MO} = r_{MOH} = r$, and expressing the rate in terms of current density, equation (1.2.98) reduces to:

$$i_{II} = 2Fk_{II}'^{0} c_{OH} \theta_{MOH} \exp(\eta F / 2RT) \quad (1.2.99)$$

This expression differs from equation (1.2.90), for the current density of the overall reaction with step II rate determining under high coverage Langmuir conditions at high η, only by the pre-exponential factor of θ_{MOH}. Kinetic analysis of the electrochemical oxide path (equation (1.2.37)) with step II as rds under Temkin adsorption conditions (i.e. $0.2 \leq \theta \leq 0.8$), therefore predicts the same values of b = $2.303 \times 2RT/F$, and $m_{OH} = 1$, that prevail under the Langmuir isotherm with $\theta \rightarrow 1$. It is however noteworthy, that a Tafel slope of $b = 2.303 \times 2RT/3F$, and reaction order of $m_{OH} = 2$, as were found for the electrochemical oxide path (step II as rds), under low coverage Langmuir adsorption conditions at low values of η (see equations (1.2.88) and (1.2.89)) cannot be obtained from the kinetic analysis where the free-energy of activation is dependent on the fractional coverage of intermediates, i.e. under Temkin adsorption conditions. This leads to the important general conclusion that identical reaction mechanisms may lead to different predicted kinetic parameters under a formal kinetic analysis, depending on which model of adsorption is adopted.

1.3 Electrocatalysis

1.3.1 Basic Concepts of Electrocatalysis.

Although the term *electrocatalysis* was introduced as recently as 1963 by Grubb[79], in relation to the anodic and cathodic reactions in fuel cells, the phenomena that fall into the field of electrocatalysis have been under study since at least the 1920s. Having coined the term, Grubb[80], provided a general definition of electrocatalysis, as referring to the catalytic influence of electrode material upon an electrochemical reaction under standard conditions. There exist many reviews of electrocatalysis, both as sections in more general textbooks[81, 82, 83] and as dedicated works of varying length and detail[84, 85, 86].

Perhaps the first phenomenological interpretation of, what later became known as electrocatalysis, was provided by Horiuti and Polanyi[87] in a classic study on the hydrogen evolution reaction (h.e.r.). They envisaged that the potential energy of a proton moving towards the electrode will have a maximum at the intersection of the potential energy curve of the proton in solution and that of a H atom adsorbed on the electrode surface. A good catalyst material for the h.e.r. is therefore, one for which this maximum will be relatively small. Nowadays it is well known, that both the electronic and geometric properties of an electrode material, play an important role in electrocatalysis. Many of the transition metals, their alloys, and their oxides are good electrocatalysts for the o.e.r., the oxygen reduction reaction (o.r.r.) and the oxidation of small organic molecules (e.g. CH_3OH and CO). Some of the pertinent electronic factors with regard to the electrocatalytic ability of a given transition metal (or its oxides) are its *work function* Φ, and the percentage d-band character of the metal.

At this stage a few comments are in order regarding the meaning of the term "work function" in relation to electrodes in contact with electrolyte solution. In solid-state physics or chemistry, the work function of a metal Φ^m is defined as the work required to move, to infinity an electron from the Fermi level of a metal in contact with a vacuum[88]. Therefore Φ^m might be written as[89],

$$\Phi^m = -\mu_e^m + F\chi^m \qquad (1.3.1)$$

where, μ_e^m is the chemical potential of an electron in the electrode and χ^m is known as the electron overlap potential difference. The former quantity is a bulk property of the electrode material, whereas the latter (and thus Φ^m) is dependent on the crystal face concerned. A more relevant definition of the work function for an electrode in contact with an aqueous solution is[90],

$$\Phi^{m(s)} = -\mu_e^m + Fg^m - Fg^s, \tag{1.3.2}$$

where, g refers to the dipole potential difference caused by the aqueous layer.

In ordinary heterogeneous catalysis, the catalytic properties of different substrates towards a particular reaction, are often compared by determining the standard rate constant k^0 for the reaction on each of the substrates. Since $i_0 = (n/\nu)Fk'^0 a_i$, the exchange current density for an electrochemical reaction at an electrode of a particular material, is often used as a convenient measure of the electrocatalytic activity of the material towards the reaction in question. There are however a number of drawbacks with this practice. Bockris and Khan[81] have pointed out that a comparison of i_0 values takes no account of the influence of the transfer coefficient α, which from the point of view of energy lost in overpotential has a significance comparable to that of i_0. The importance of this point is discussed in detail by Bockris and Otagawa[43] in relation to the o.e.r. at perovskite electrodes. Therefore another means of quantifying electrocatalysis is to compare current density values i at a particular overpotential η or vice-versa. This approach also allows the comparison of electrocatalysts at typical operating current densities found in practical applications such as alkaline water electrolysers and fuel cells.

Consider the general anodic multistep electrode process in equation (1.3.3),

$$\mathrm{R} \rightarrow \mathrm{T} + \mathrm{e}^- \rightarrow \mathrm{O}, \tag{1.3.3}$$

where, T is a reaction intermediate species, and it is considered that its formation is the rds. If the process occurs at an electrode which catalyses the reaction, then if T is adsorbed on the surface, the formation of T will occur with a lower Gibbs free energy of activation than it would otherwise. If potential energies curves are envisaged analogous to those in Figure 1.2.1 (section 1.2.1), the adsorption of T, brings about a

vertical lowering of its Gibbs energy curve. The rate of reaction can then be represented as

$$i = FAk'^{0} c_R \exp\left[\frac{\alpha F \eta}{RT}\right] \exp\left[-\frac{\alpha \Delta G_T'^{0}}{RT}\right], \tag{1.3.4}$$

if it assumed that $\theta_T \rightarrow 0$. As previously mentioned, a common approach to comparing the electrocatalytic properties of different electrodes, is to observe the current density for each electrode at a given value of η. Therefore, when comparing different electrode materials, the sole variable in equation (1.3.4) is the Gibbs free energy of adsorption of species T, $\Delta G_{ads}'^{0}$. In that case, for different materials at constant η:

$$\ln i \propto -\Delta G_{ads}'^{0} \tag{1.3.5}$$

Equation (1.3.5) predicts that the rate of the electrode reaction increases as $\Delta G_{ads}'^{0}$ changes from positive values (very weak adsorption) to negative (very strong adsorption). However, as $\Delta G_{ads}'^{0}$ becomes more negative the fractional coverage θ_T of the intermediate T increases, so when comparing the electrocatalytic activities of different electrodes, the assumption that $\theta_T \rightarrow 0$ cannot be utilised. Equation (1.3.4) will therefore have to be rewritten as:

$$i = FAk'^{0}(1-\theta_T) c_R \exp\left[\frac{\alpha F \eta}{RT}\right] \exp\left[-\frac{\alpha \Delta G_T'^{0}}{RT}\right] \tag{1.3.6}$$

In the case where θ_T can be described by the Langmuir isotherm, the $(1-\theta_T)$ term, to a first approximation, decreases more rapidly with decreasing $\Delta G_{ads}'^{0}$, than the corresponding rate of increase of the second exponential term. This implies that:

$$\ln i \propto \Delta G_{ads}'^{0} \tag{1.3.7}$$

Clearly equations (1.3.5) and (1.3.7) predict opposing behaviour – the observed behaviour will be a combination of the two factors and thus at a given value of $\Delta G'^{0}_{ads}$, the current density will be determined by whichever factor produces the slowest rate[91]. If ln i is plotted against $\Delta G'^{0}_{ads}$ (which of course depends on the electrode material) for a range of $\Delta G'^{0}_{ads}$ from negative to positive values, it is therefore expected that a so-called *volcano plot* will arise – see Figure 1.3.1.

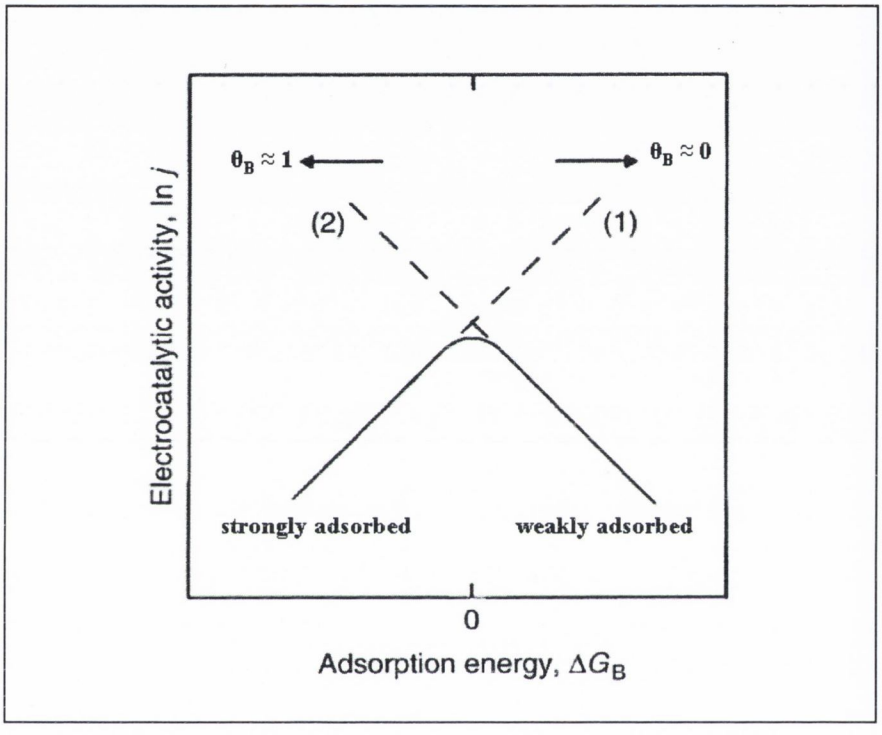


Figure 1.3.1 *Sketch of the form of an ideal volcano curve in electrocatalysis, where the adsorption of T is the rds. Adapted from Ref. 91.*

The maximum electrocatalytic effect occurs at the apex of the volcano curve, where $\Delta G'^{0}_{ads} = 0$. Physically, this means that the strength of the bonds formed with the surface is equal to that of the bonds broken to form the intermediate T. Branch (2) in Figure 1.3.1 is related to the behaviour predicted by equation (1.3.5) – the electrocatalytic ability increases as $\Delta G'^{0}_{ads}$ decreases. Branch (1) is associated to the behaviour predicted by equation (1.3.7) – as $\Delta G'^{0}_{ads}$ becomes more negative there is a hindrance effect due to the increasing coverage of species T. This increase in coverage arises because of an increase in the free energy required for the desorption of T to form the product O, owing to the increasing substrate-T bond strength with

decreasing $\Delta G'^{0}_{ads}$. Volcano curves are a graphical manifestation of the qualitative *Sabatier principle*, which is well known in the field of heterogeneous catalysis[83, 91]. This principle states that reactants should be moderately adsorbed on the catalyst surface, and that very weak or very strong adsorption leads to low catalytic activity. Had a logarithmic isotherm such as the Temkin isotherm been admitted, in equations (1.3.4) and (1.3.6) the opposing effects of decreasing activation energy for adsorption, and surface "blockage" would be less extreme, and values of ln*i* would be predicted to show less variation with $\Delta G'^{0}_{ads}$, thus broadening and lowering the height of the "volcano".

1.3.2 The Hydrogen Evolution Reaction

Although the present work is principally concerned with the anodic oxygen evolution reaction, it is worth devoting some attention to the cathodic hydrogen evolution reaction (h.e.r.), since, as pointed out by Bockris and Khan[81] it "acts as the archetype for the study of electrochemical reactions, for it involves simple versions of features which are met in nearly all of them". Furthermore, it is the cathodic reaction that occurs at the counter-electrode in aqueous solution while oxygen evolution proceeds at the working anode. Widespread interest in the h.e.r. followed upon a 1928 publication by Bowden and Rideal[92] and has continued more or less unabated ever since. Up to date reviews of the topic have been provided by Breiter[93] and Lasia[94]. To this day, there is still no common agreement amongst workers on the exact details of the h.e.r. on various substrates in either acidic or alkaline solutions[94, 95], with contradictory data often being published. Lasia[94] comments that much of these problems are due to the difficulty of preparation of clean electrodes and solutions (especially in alkaline media) and/or to the difficulty of decoupling the contributions of surface roughness and intrinsic electrocatalytic properties to the overall kinetics of the h.e.r. on a given electrode. As will be discussed later, these remarks might equally well apply to the o.e.r.

What is universally agreed, is that the h.e.r. proceeds in two elementary steps, with only one reaction intermediate involved. The first step is known as the *Volmer step*, and comprises of a displacement of water molecules, with the adsorption of hydrogen atoms onto the electrode surface:

$$H_3O^+ + M + e^- \rightarrow MH_{ads} + H_2O \quad (1.3.8, a)$$

$$H_2O + M + e^- \rightarrow MH_{ads} + OH^- \quad (1.3.8, b)$$

Equation (1.3.8, a) refers to the reaction in acidic solution, while equation (1.3.8, b) refers to alkaline solution – M refers to an active site on the electrode (usually a metal) surface. There are two possibilities for the next step, which brings about the detachment of molecular hydrogen from the surface. This can occur by chemical desorption via the following reaction, known as the *Tafel step*, which is identical in acidic or alkaline solution:

$$MH_{ads} + MH_{ads} \rightarrow H_2 + 2M \quad (1.3.9)$$

Alternatively the desorption process may consist of a second discharge of H_3O^+ (in the case of acidic electrolyte) or H_2O (when the solution is alkaline), which occurs on top of the adsorbed H produced by the Volmer step:

$$MH_{ads} + H_3O^+ + e^- \rightarrow M + H_2 \quad (1.3.10, a)$$

$$MH_{ads} + H_2O + e^- \rightarrow M + H_2 + OH^- \quad (1.3.10, b)$$

The reaction in equation (1.3.10) is known as the *Heyrovsky step*, where (1.3.10, a) refers to the situation in acid and (1.3.10, b) refers to the process in base.

Either step in each pathway may be the rds. The combination of the Volmer and Tafel steps (V-T) is often called the *catalytic path*[81]. In the catalytic path, if reaction (1.3.8) is assumed to be rate-determining, the fractional coverage of adsorbed hydrogen θ_H will be small, since it will be consumed in the chemical recombination step (1.3.9) as soon as it arrives on the surface. This situation is known as the *Volmer mechanism.* On the other hand if the chemical recombination step is rate-determining, θ_H will be larger than in the Volmer mechanism – this case is known as the *Tafel mechanism.* If the overall reaction proceeds via step (1.3.8) followed by step (1.3.10), the situation is often denoted as the *electrochemical desorption path*[81] or abbreviated as the V-H path. For the electrochemical desorption path, the Volmer step may again be rate determining, or alternatively the Heyrovsky step may limit the kinetics. The latter case is referred to as the *Heyrovsky* mechanism and if it is operative, it can be expected that $\theta_H \rightarrow 0$. If a kinetic analysis is performed, based upon the psuedo-

equilibrium approximation, with the assumption of a Langmuir adsorption isotherm, it can be shown[82, 93, 96] that the mechanistic parameters listed in Table 1.3.1 are obtained.

		$\theta_H \rightarrow 0$		$\theta_H \rightarrow 1$	
Path	**RDS**	***b*** ($\partial\eta/\partial\ln i$)	***m*** $\left(\partial \ln i/\partial \ln c_{H3O^+}\right)_\eta$	***b*** ($\partial\eta/\partial\ln i$)	***m*** $\left(\partial \ln i/\partial \ln c_{H3O^+}\right)_\eta$
V-T	1.3.8	-2RT/F	1		
V-T	1.3.9	-RT/2F	2	∞	0
V-H	1.3.8	-2RT/F	1		
V-H	1.3.10	-2RT/3F	2	-2RT/F	1

Table 1.3.1 *Tafel slopes, b, and reaction orders, m, predicted by a formal kinetic analysis of possible reaction paths for the hydrogen evolution reaction, under the assumption of a Langmuir adsorption isotherm.*

The analysis that yields these parameters is analogous to that outlined in section (1.2.3) in relation to the electrochemical oxide path (equation (1.2.37)) for the o.e.r. Indeed, it is noteworthy, that the values of $|b|$ and m, obtained for the V-H path with the Heyrovsky step as rds, are identical to those obtained for the electrochemical oxide path with rate determining step II under Langmuir adsorption conditions – see equations (1.2.88 – 89) and (1.2.92 - 93). This is not surprising, since in the analysis that leads to the directly aforementioned equations, the coverage of MO in step (1.2.37, II) is considered to be negligible. Under these conditions the electrochemical oxide path for the o.e.r. is the anodic equivalent of the Heyrovsky mechanism, since both mechanisms consist of an electrochemical step involving the adsorption of the significant reaction intermediate, followed by a rate determining electrochemical removal of that intermediate. Hence the formal mathematical kinetic analyses of these two situations under the pseudo-equilibrium principle are very similar.

In 1946, Bockris[97] pointed out that there exists a linear relation between the exchange current density, i_0, for the h.e.r., and the work function, Φ, of the electrode metal. He noted that for the so-called "soft" s-p metals (eg. Hg, Pb, Sn) in acidic solution, i_0 decreased with an increase in work function. On the contrary, transition metals display increased i_0 values with an increase in work function. This idea was further

developed by Conway and Bockris in 1957[98], when they observed the opposite correlation between i_0 and the metal-hydrogen bond (M-H) strength – i.e. for the s-p metals the rate of the h.e.r. at the reversible potential increases exponentially with increasing M-H bond strength, while it decreases exponentially with this bond strength in the case of transition metals. Trasatti[99] plotted the logarithm of the exchange current densities for the h.e.r. on different metals in acidic solution, against the metal-hydrogen bond strength. This yielded a volcano-like relation, as is depicted in Figure 1.3.2.

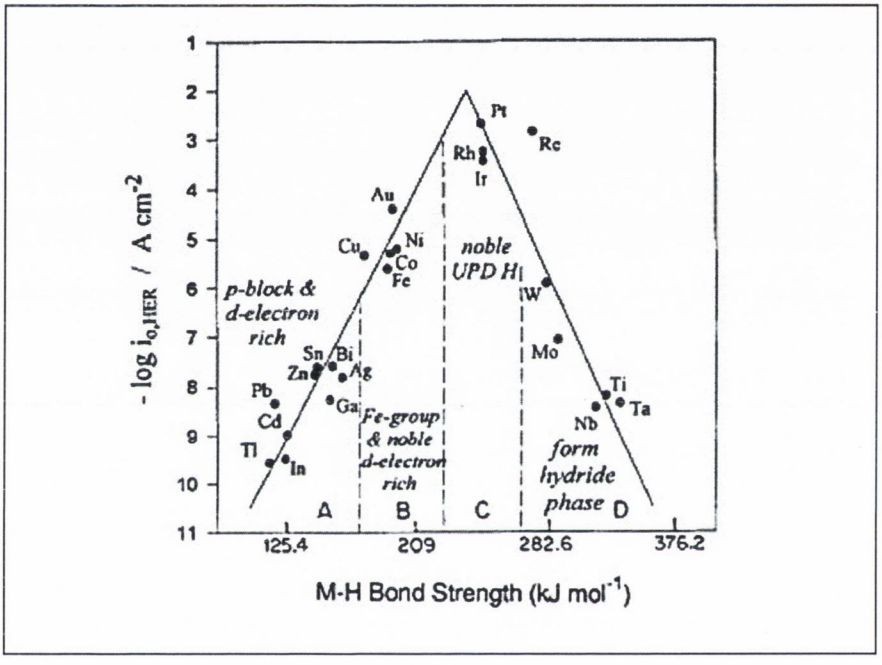


Figure 1.3.2 *Volcano plot of log i_0 versus M-H bond strength for the h.e.r. on different metals in acid. Reproduced from Ref. 100.*

By consideration of the volcano plot for the h.e.r., and experimental kinetic data (e.g. Tafel slopes), Conway and Bockris[101] concluded, that in general, the rds, for the h.e.r. in acidic solution on metals on the low M-H energy side of the volcano plot, is the Volmer step. On the other hand, for the strong M-H bond energy side, the rds is often a desorption step (i.e. either the Tafel or Heyrovsky step). This arises, since on the left hand branch of the volcano, adsorption of H is difficult (although increasingly easy moving from the extreme left to the centre) and is therefore the rds, while on the right hand branch removal of H_{ads} is difficult and hence rate-determining. Trasatti[91] cautions against, the general interpretation of volcano plots in this manner. He points out that such an interpretation understands a change in mechanism or rds between the two branches, which is not always the case. A volcano relation arises, even if the

same rds prevails across the entire range of electrode-adsorbed species bond strengths, as has been discussed in section 1.3.1, adjacent to equations (1.3.4) – (1.3.7). Indeed, it has been pointed out[102] that exchange current densities for different metals should only be compared in a volcano curve type analysis, if the mechanism (as indicated for example by the Tafel slope) is the same on each of the metals, which isn't the case for the h.e.r.

The aforementioned issue of changing rds or mechanism, is only one of several difficulties commonly met in the field of comparative electrocatalysis, that arise on examining the volcano plot for the h.e.r. as presented in Figure 1.3.2. Other problems, inherent in constructing the volcano curve for the h.e.r., include the fact that the data utilised were obtained by different workers, often under quite differing experimental conditions, and the fact that the state of the electrode surface is different for different metals. In region D of Figure 1.3.2, it can be seen that the metals W, Mo, Nb, Ti, and Ta all form stable hydrides in acidic solution. In these cases the hydride-H_{ads} bond strength is more relevant than the M-H bond strength. Furthermore *underpotential deposited* (upd) H occupies most of the available metal sites on Pt, Rh and Ir electrode surfaces as the potential approaches the hydrogen reversible value – see region C in Figure 1.3.2. Only weakly adsorbed, *overpotential deposited* (opd) H partakes in the gas evolution reaction, but the adsorption energies used in constructing the volcano plot are those of the upd process. Conway and Jerkiewicz[100] have discussed the effect of upd adsorbed H on the volcano plot positions of Pt, Rh and Ir. In view of the fact that the aforementioned (and several other – see ref 94) difficulties arise, when comparing the catalytic activities of different metals for the h.e.r., which is, after all the simplest of electrocatalytic processes, similar complexities can be envisaged in the theoretical electrocatalytic comparison of different substrates for more sophisticated reactions (e.g. the o.e.r.).

1.3.3 Further Observations on Electrocatalysis

In section (1.3.1) it was shown, how in general, the variation of the standard Gibbs free energy of adsorption of a given reaction intermediate on different metal electrodes, will lead to a "volcano plot", if a theory of electrocatalysis due to activated chemisorption is admitted. It has been shown that approximate volcano relations do exist for the h.e.r. on metals[99], the o.e.r. on transition metal oxides[103] and the o.r.r. on

macrocycles[104]. In practice, the available experimental data are enthalpies, rather than Gibbs energies, and thus in the case of the h.e.r., it is the variation in the standard enthalpy of adsorption $\Delta H'^{0}_{ads}$ that is responsible for the change in catalytic activity with electrode material. Indeed it is often the enthalpy of a particular process that is correlated with activity in comparative electrocatalytic studies. For example Bockris and Otagawa[43] show a linear dependence between o.e.r. reaction rate, and both the standard enthalpy of formation $\Delta H'^{0}_{f}$ of hydroxide $M(OH)_3$, and the enthalpy change for the transition from lower to higher valent oxide $\Delta H'^{0}_{t}$, in the case of electrodes consisting of the perovskite materials $La_{1-x}Sr_xMO_3$ (M = Ni, Co, Fe, Mn, Cr) in 1M NaOH.

Trasatti[103] also correlated catalytic activity towards the o.e.r. on various transition metal oxides in acidic solution, with the enthalpy change for the transition from lower to higher valent oxide. The same author has subsequently pointed out[91] that the real difficulty from a theoretical viewpoint is the identification of the properties of materials that govern the magnitudes of these enthalpies and comments that "a true theory of electrocatalysis will not be available until activity can be calculated a priori from some known properties of the materials". Referring again to the h.e.r. on various metals in acidic solution, he concludes that any quantity that is conceptually linked to the heat of adsorption (e.g. the work function Φ which was the original bulk property to be correlated with i_0 for the h.e.r.[97]) can provide reasonable correlation, but this doesn't imply that it is this quantity that is the primary factor dictating the electrocatalytic activity of the material. Thus in the absence of a "true theory" of electrocatalysis, all that can be done is to attempt to identify a phenomenological dependence of catalytic activity, based on correlations with appropriate physiochemical parameters.

It has been pointed out[82], that while metals, alloys, semiconductors (particularly oxides) and complexes have all been shown to exhibit catalytic properties, almost invariably these catalysts are based on transition metals. The success of transition metals as catalysts, lies in the fact that they possess unpaired d-electrons, and unfilled d-orbitals that are available to form bonds with would-be adsorbed species. The enthalpy of adsorption will, of course, depend on the number of unpaired d-electrons and on their energy levels. It has long been known in heterogeneous gas phase catalysis[105] by transition metals, that a correlation exists between reaction rate and d-

band character (or d-vacancies). The more unpaired electrons that a transition metal has in its d-band, the lower the percentage of d-band character it is said to possess. For a reaction with a rate-determining adsorption step, the best catalyst would be expected to be one with a low-percentage d-band character, while the converse would be true if the rds involves the desorption of a reaction intermediate. Clearly the percentage d-band character, the number of d-band vacancies, or simply the number of d-electrons, fall into the category of material properties conceptually linked to the heat of adsorption, as discussed previously. Correlations have been shown between electrocatalytic activity and d-band vacancies for the o.r.r. on various metals and alloys[106], and for the o.e.r. on various perovskite materials[43].

Thus-far the discussion of electrocatalysis has focussed principally on the electronic parameters that might affect the catalytic activity of a given electrode material. Geometric properties such as crystal structure, inter-atomic distance, grain size, concentration of defects and defect type can also have a profound effect on electrocatalytic activity. A dependence of catalytic activity on crystal face orientation and inter-atomic distance has been shown, for example by Marković et al.[107] for the h.e.r. on Pt in 0.05 M H_2SO_4. These workers found that the activity decreased in the sequence Pt(110) > Pt(100) > Pt(111) – i.e. the Pt(111) crystal plane which has the highest density of Pt atoms is the least active for the h.e.r. Trasatti[108] noted that the same anode material, thermally prepared at different decomposition temperatures and lengths of time, displayed differences in i_0 values and Tafel slopes. These observations were attributed to the influence of the preparation regime on features such as the crystallite size, the surface area, and the number of defect sites. Crystallite or particle size can have a significant effect on the electrocatalytic activity of a material, since, as noted by Appleby[109], the specific surface area, and the relative distribution of catalytic sites between crystal faces, edges and corners, can depend on the physical dimensions of crystallites or particles.

A common approach in the optimisation of electrocatalysts, is the empirical search for so-called synergetic effects. This is essentially based on the idea that if two materials, one on the right-hand side ($\Delta H_{ads}^{'0} > 0$) and the other on the left hand side ($\Delta H_{ads}^{'0} < 0$) of a volcano plot of ln i vs. $\Delta H_{ads}^{'0}$, are mixed together, a material with the ideal intermediate bond strength, $\Delta H_{ads}^{'0} \approx 0$, should result. Approaches to obtaining synergetic electrocatalytic effects include, the alloying of metals, the production of

mixed metal oxides, and the sub-monolayer deposition of one material on another. Trasatti[91] points out, that the expectation of obtaining a material with enhanced electrocatalytic properties from a synergetic approach is based on the assumption of a linear dependence of $\Delta H'^{0}_{ads}$ on composition, which is in turn based upon a further assumption that upon mixing the two materials an intimate atomic mixture is obtained. In general neither of these assumptions might hold in a particular case. Economics often drives the search for alloys or intermetallic compounds displaying synergetic effects. Referring to the volcano plot in Figure 1.3.2, it is clear that the best cathode materials for the h.e.r. are the noble metals Pt, Rh or Ru. On an industrial scale (e.g. for use in commercial alkaline water electrolysers) the high cost of these metals renders their use inexpedient. It has been found[110] that alloying the much cheaper metals Ni and Mo (which are located on opposite sides of the volcano plot) leads to an active electrocatalyst towards the h.e.r., with the activity dependant on the exact composition of the alloy, and the method and conditions of alloying[94].

An elegant demonstration of synergetic electrocatalytic effects has been provided by Mukerjee et al.[106] for the o.r.r. on Pt-Ru alloys of various relative composition. Their data is presented in Figure 1.3.3, with the catalytic activity being correlated to the number of d-band vacancies. It is obvious that each of the Pt-Ru alloys have activities that lie between those of the pure metals. It will be seen later, that much of the more recent published work on the o.e.r. has focussed on the search for synergetic catalytic effects.

As mentioned in section 1.3.1, the electrocatalytic activity of an electrode material towards a particular reaction is routinely quoted as either the exchange current density i_0, or the current density value i at a particular overpotential η. A major problem inherent in this approach is that the electrode real surface area is rarely known, and so i_0 or $i(\eta)$ is expressed per geometric surface area. When comparing catalytic activities on this basis, it is impossible to differentiate between the effects of intrinsic catalytic activity and apparent catalytic activity due to large real surface area. A comparison of the electrocatalytic activity of different materials based on current density, should not be performed, unless a meaningful attempt has been made to determine the real surface area of the electrode materials, and to normalise the current density values accordingly. The question of real surface area measurement for the electrodes in the present work is discussed in Chapters 2 and 5.

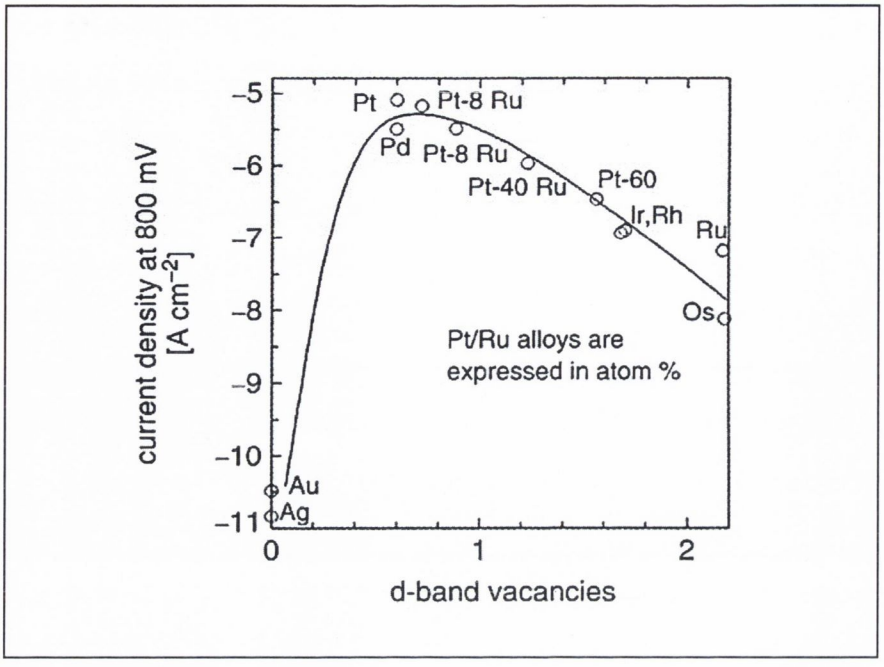


Figure 1.3.3 *Volcano plot for the o.r.r. versus d-orbital vacancies. The electrolyte is 85% H_3PO_4 and the measurements were performed at 25°C. Reproduced from Ref. 106*

Heretofore, the treatment of the topic of electrocatalysis, has focussed exclusively on the activated chemisorption model. As has been discussed, it is envisaged that adsorption of a reaction intermediate on the electrode surface, reduces the Gibbs free energy of activation for a reaction, by providing increased stability to the intermediate. Perusal of the previously cited reviews on electrocatalysis[81-86], and indeed the literature on the topic in general, will leave the reader in no doubt that the activated chemisorption model is almost universally applied in the explanation of electrocatalytic phenomena. Alternative theories, based on the participation of metastable active surface sites, in heterogeneous catalysis, have existed since the work of Taylor[111] in the 1920, however they have never received widespread attention, especially in electrocatalysis. A model, which has relevance to electrocatalysis by transition metal electrodes, is the so-called *Incipient Hydrous Oxide/Adatom Mediator* (IHOAM) model due to Burke[112-114].

The development of the IHOAM model arose from the observation that, the potential for the onset of electrocatalyis of a soluble solution phase species at a given metal electrode, often coincides with that for hydrous mutilayer oxide reduction on that metal[112]. Further impetus was given to this model by the observation of Haruta et al.[115] that, oxide-supported gold nanoparticles possess high catalytic activity for processes such as CO oxidation, even thought gold, as a very weak chemisorber, has

historically been regarded as a poor electrocatalyst. The IHOAM model is based on the hypothesis of two limiting types of surface states – low energy equilibrated metal surfaces (EMS) and high energy metastable metal surfaces (MMS). The catalytic metal surface consists of a layer of EMS atoms in their equilibrium positions at the lattice surface, and also a small coverage of low coordination MMS species, which might exist either as individual ad-atoms or small clusters of atoms. These MMS species will be highly disordered and difficult to generate reproducibly. In addition, owing to their low lattice stabilisation energies, they are expected to be more electropositive than atoms in the bulk. The IHOAM model envisages that these metastable active species and their oxidation products can act as redox mediators in electrocatalytic processes.

Burke and co-workers[112-114] have sought to demonstrate the existence of MMS species, by "activating" metal surfaces using either extreme cathodic polarisation or thermal pre-treatment. Such a surface should have a larger than normal (although still much lower than the concentration of EMS atoms) concentration of MMS species and is said to be *superactive* [113, 116]. Indeed such a surface effectively traps some of the energy used in its creation in the form of the MMS states. A key feature of such activated surfaces for several metals is that hydrous (β) metal oxide species are observed at potentials in the double layer region, well below the potentials associated with conventional monolayer (α) oxide formation. Such species exist in small concentrations on the metal surface, but as reviewed by Burke et al.[113], have been detected on gold, silver and copper electrodes in alkaline solution using Surface Enhanced Raman Spectroscopy (SERS).

Put simply, it is envisaged under the IHOAM model, that upon reduction of a multi-layer oxide film on a metal electrode, cathodic peaks observed in the double-layer region are due to the formation of MMS states of the metal. At high surface concentration much of these MMS states rapidly decay to EMS states and thus it is often observed that the aforementioned double layer cathodic peaks don't have (or have very muted) anodic counterparts. Nonetheless it is assumed that a small concentration of MMS states won't decay to the EMS form. These MMS states and their oxidation products (β metal oxide species) as discussed above are hypothesised to act as redox mediators for the oxidation and reduction of solution phase species. Experimental evidence for this is provided by the fact that the observed potentials for

the oxidation and reduction of dissolved species very often coincide with the potentials of the cathodic reduction peaks referred to previously.

Much of the recent work by Burke and his group in this area, has focussed on Au[112, 114], Ag[114], Cu[113, 114], and Pt[113, 114] – however in the context of the present work it is noteworthy that they considered, some years ago, the behaviour of Ni[117], Co[118] and Fe[118] in alkaline solution, with respect to the IHOAM model. Catalytic activity (although often not dramatic in terms of current density) towards the oxidation or reduction of solution phase species at a Co electrode was noted at potentials corresponding to the formation of various Co oxide and oxyhydroxide species. At potentials just below 0 V (vs. R.H.E.) solution species such as dimethylamine borane (DMAB) and hypophosphite $H_2PO_2^-$(aq) were oxidised. It was noted that these species are of anionic character and thus it was proposed[118] that their oxidation at this potential was mediated by the presence of a cationic Co(I) surface species – possibly existing in the form $[Co(H_2O)_n]_{ads}^+$. Electrostatic forces between the cationic surface mediator and the anionic solution species were envisaged as triggering the oxidation process. On the other hand, uncharged solution species such as hydrazine were oxidised at somewhat higher potentials, just above 0 V (vs. R.H.E.). These redox processes were attributed to the presence of an anionic Co(II) hydrous oxide mediator species at this potential range. Further electrocatalytic activity towards solution phase species was observed in the potential region of the Co(II) → Co(III) surface oxidation process.

In comparison to Co, it was found[118] that Fe was a very poor electrocatalyst towards the oxidation or reduction of soluble species. This was attributed to the absence of an Fe(I) interfacial mediator species and the fact that the initial oxidation of Fe in base takes place in a potential region of high hydrogen coverage, which would tend to "smother" any Fe MMS species. Ni[117] displayed very similar electrocatalytic activity to Co towards the same solution phase species. Again the anionic species such as $H_2PO_2^-$ were observed to be oxidised at potentials below 0 V (vs. R.H.E.) – the reaction assumed to be mediated by a cationic Ni(I) hydrous oxide species. The oxidation of neutral species such as hydrazine commenced just above 0 V (vs. R.H.E.); in this case a Ni(II) hydrous oxide species was envisaged as the redox mediator. The electrocatalytic metastable surface species concept has recently been extended to the analysis of the h.e.r. on metastable metal oxide electrodes such as ruthenium dioxide cathodes[119]. Its potential applicability to the o.e.r., is a subject that

has not been broached, probably because proving the existence of hydrous oxide mediator states, at the surface of phase oxides at high anodic potentials would be experimentally difficult. Nonetheless, it is worth bearing in mind, that alternative theories to the activated chemisorption model of electrocatalysis, have been shown to be feasible for the electrode materials utilised in the present work, albeit at lower potentials than those studied here.

1.4 The Surface Electrochemistry of Ni, Fe and Co Electrodes in Aqueous Alkaline Solution.

It is well established, that at the anodic potentials at which the o.e.r. occurs in aqueous solution, metal electrodes are covered by hydrous oxide films. In order to understand the o.e.r., it is essential to understand the nature of the substrate on which it occurs, with respect to such factors, as the oxidation state of the metal sites in the oxide film, and the morphology and degree of hydration of that film. In the following review, it will be seen, that over the past forty years, cyclic voltammetry has been the principal electrochemical technique that has been used to characterise anodic oxide films on metallic electrodes. Other techniques that have been usefully applied, include electrochemical quartz crystal microbalance (EQCM) studies, electrochemical impedance spectroscopy, rotating ring disk electrode studies, ellipsometry, X-Ray diffraction, and spectroscopic techniques; in particular Raman spectroscopy.

1.4.1 Nickel

It is probably fair to say that the redox switching behaviour of nickel hydroxides and oxyhydroxides is one of the most studied systems in all of electrochemistry. This arises for several reasons relating to the practical utilisation of nickel and nickel oxide electrodes in several technologically important areas. Nickel hydroxides have long been used as the active material in the positive electrodes of several alkaline batteries

– e.g. the commercially important nickel-cadmium battery. In addition to this, their high corrosion resistance and relative inexpensiveness (as compared to materials such as RuO_2 and IrO_2) has lead to Ni and some of its alloys becoming the materials of choice for use in commercial alkaline electrolysis[120]. Despite the widespread practical application of nickel and nickel hydroxide electrodes, progress in understanding the nature of the redox reactions of these materials in aqueous solution has been slow, owing to the complexity of these reactions and their variability with respect to factors such as the electrode preparation and electrode history. As commented by McBreen [121] in his review on the electrochemistry of nickel hydroxides; "Items which are normally trivial exercises for most battery electrodes, such as the determination of the open circuit potential, the overall reaction, and the oxidation state of the charged material, have required much effort and ingenuity". A point which must be bourn in mind during the following review, is that, although the present work is concerned with nickel oxide and hydroxide films grown electrochemically by anodic polarisation, much of the potentially useful data that has been obtained over the years, relates to nickel hydroxides that have been electrodeposited on various substrates, or indeed (in the case of XRD measurements) to crystalline precipitates of nickel hydroxide. The physical and chemical properties of these materials have been found to depend on the details of their preparation, and therefore one must attach a degree of caution in generalising the applicability of data obtained on nickel hydroxide prepared by a particular technique.

In this review of the surface electrochemistry of polycrystalline Ni in aqueous alkaline solutions, it has been decided to reproduce a typical cyclic voltammogram from the literature, for the purpose of discussion and reference. This approach will also be followed in the reviews of the surface electrochemistry of Co and Fe electrodes. In each case the reference voltammogram should be compared with those reported in the present work, which will be presented in later chapters. A typical CV, from the literature[122], of a polycrystalline Ni electrode in 1.0 M KOH solution is presented in Figure 1.4.1.

The CV reproduced in Figure 1.4.1. was chosen for inclusion here, since it was recorded using a similar electrolyte, similar sweep rate, and the same reference

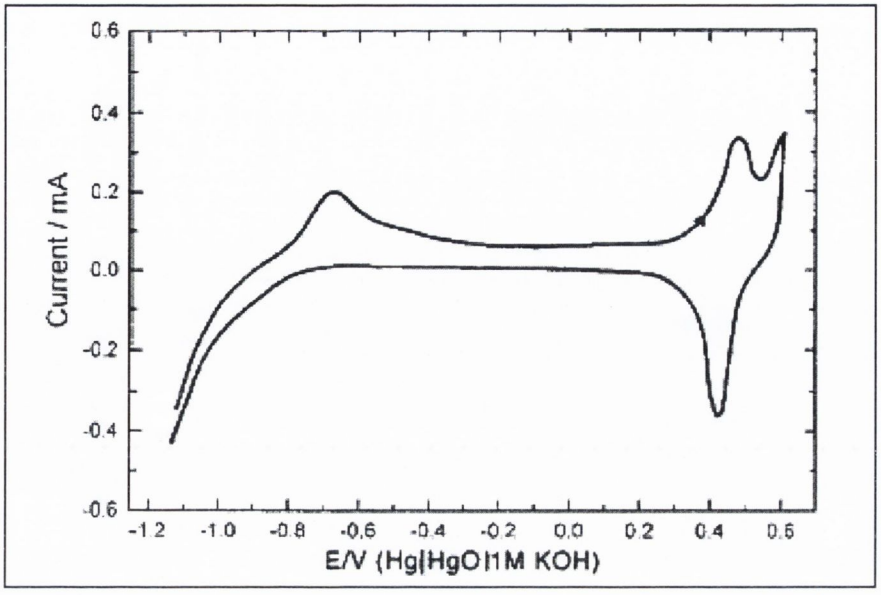


Figure 1.4.1 *A typical CV of a polycrystalline Ni electrode in 1 M KOH at 25°C. The sweep rate was 50 mV s^{-1}. Reproduced from Ref. 122.*

electrode as were utilised in the present work. Similar CVs are presented in many works in the literature – random examples include publications due to Burke et al.[123, 124], Visscher and Barendrecht[125], de Souza et al.[126] and Simpraga and Conway[127] to name but only a few.

It is almost universally agreed that the lower anodic peak observed at –0.8 to -0.6 V in Figure 1.4.1 is principally associated with the oxidation of metallic Ni(0) to Ni(II) species. There has been historically, some disagreement about the nature of the Ni(II) oxide species formed at this potential with, for example, Makrides[128] proposing the production of NiO and $Ni(OH)_2$, while Okuyama[129] proposed that the oxide film in this potential region was non-stiochiometric, consisting of NiO and Ni_3O_4. More recently the complex nature of the film even at these low potentials has been emphasised. Based on the variation of the peak potential with pH in alkaline solution, Burke and Twomey[123] proposed that both oxidation and hydrolysis processes were operative in this potential region, leading to the formation of a somewhat anodic species, tentatively assigned the formula (for the purpose of rationalisation) of $Ni(OH)_{2.4}^{0.4-}$.

When the anodic limit of the potential sweep was maintained well below the upper redox peaks Burke and Twomey[123] observed a pH invariant cathodic peak at potentials of the order of 0.3V lower than the anodic peak. In view of this they

concluded that with the change in sweep direction the initially produced anodic hydrous species alters to a more anhydrous form, e.g. NiO, so that the reduction peak would be due to the process $NiO + H_2O + 2e^- \rightarrow Ni + 2OH^-$. In essence their proposal is that, due to post electrochemical place exchange reactions, the anionic oxide becomes neutral before being reduced back to Ni metal. They also point out that the lower oxidation peak appears to be superimposed on a background current that is probably due to a combination of adsorbed hydrogen oxidation, and formation of a layer of OH_{ads} species. In an ellipsometric study, de Souza et al.[126] found that the first layer of oxide formed in the vicinity of the lower anodic peak consists of NiO, however this becomes covered with a thick film of $Ni(OH)_2$ upon further increase of potential. A further significant observation of Burke and Twomey[123] was that the magnitude and position of the lower anodic peak didn't alter much upon repetitive cycling. This lead them to the important conclusion that it is the inner oxide layer that is reduced at significant cathodic potentials and thus even on cycling, the lower anodic peak is associated with oxidation of Ni metal to Ni(II) at the metal/porous hydrous oxide interface. Seghiouer et al.[122] observed that a bright polycrystalline Ni electrode, displayed an open-circuit potential of ca. –0.4 V (vs. Hg/HgO 1M KOH), and thus concluded, in agreement with several earlier works (e.g. ref 130, 131), that the formation of Ni(II) oxide species occurs immediately upon the immersion of Ni in aqueous alkaline solution.

The upper anodic peak observed at approximately 0.45 → 0.55 V in Figure 1.4.1 is associated with the oxidation of Ni(II) ($Ni(OH)_2$) to Ni(III) (NiOOH) species. The rising part of the profile, anodic to this peak is due to the onset of the o.e.r. Therefore the state of the electrode surface, at potential values just below that at which the o.e.r. becomes the dominant process, is largely dictated by the redox process occurring at the upper anodic peak. The magnitude of the area under the anodic peak and under its cathodic counterpart increase on repetitive cycling[122, 123], and so it is the Ni(II) → Ni(III) transition that is associated with the development of a charge storage film on nickel hydroxide electrodes in alkaline solution. Hence it is the $Ni(OH)_2$/ NiOOH redox system that is of interest in the battery applications of nickel and nickel hydroxide electrodes. It is often observed that upon, ageing or repetitive cycling of a Ni electrode in alkaline solution, the upper cathodic response will split into a doublet[123], or will display a shoulder adjacent to the main peak at lower potentials[122, 132] – see Figure 1.4.2. These observations hint towards the great complexity inherent

in the redox switching behaviour of $Ni(OH)_2$ films in alkaline solution, referred to in the introduction to this section.

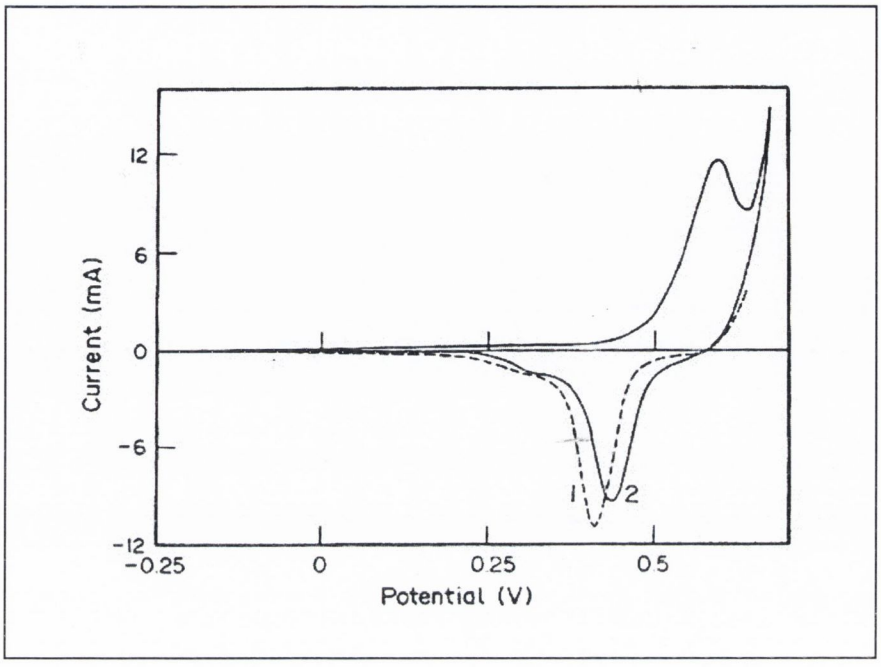


Figure 1.4.2 *CV of an aged polycrystalline Ni electrode in 2 M NaOH . The sweep rate was 100 mV s^{-1} .The dashed trace is for the first cycle whereas the continuous trace is described as being recorded after a "relatively large" number of sweeps. Reproduced from Ref. 132.*

A major advance in the understanding of the Ni(II) → Ni(III) transition was made by Bode et al.[133] in 1966. These workers rationalised the redox switching behaviour of nickel hydroxide films in terms of four phases. Thus the discharged $Ni(OH)_2$ material could exist as a hydrous phase denoted as α-$Ni(OH)_2$ or as a largely anhydrous phase denoted as β-$Ni(OH)_2$. Oxidation of β-$Ni(OH)_2$ is envisaged to yield a phase referred to as β-NiOOH, whereas oxidation of α-$Ni(OH)_2$ yields γ-NiOOH. The Bode scheme is presented in Figure 1.4.3 in its traditional cyclical formation, and also in a useful graphical format reproduced from a recent review paper[134]. From these diagrams it can be seen that upon ageing (especially in more concentrated alkali solution) the α-$Ni(OH)_2$ can dehydrate and recrystallise as β-$Ni(OH)_2$. Furthermore, upon overcharge, β-NiOOH can convert to γ-NiOOH. The non-stiochiometric nature of both the discharged and charged material is indicated by the average oxidation states of Ni in each phase as indicated in Figure 1.4.3. Bode et al.[133] envisaged that the oxidation of α-$Ni(OH)_2$ to γ-NiOOH, would occur at a lower potential than the redox transition

between the two β phases, a point that has been experimentally verified - e.g. ref. 135. Indeed in his review of nickel hydroxides, Mc Breen[121] states that "all subsequent work has in general validated" the broad conclusions of the Bode model.

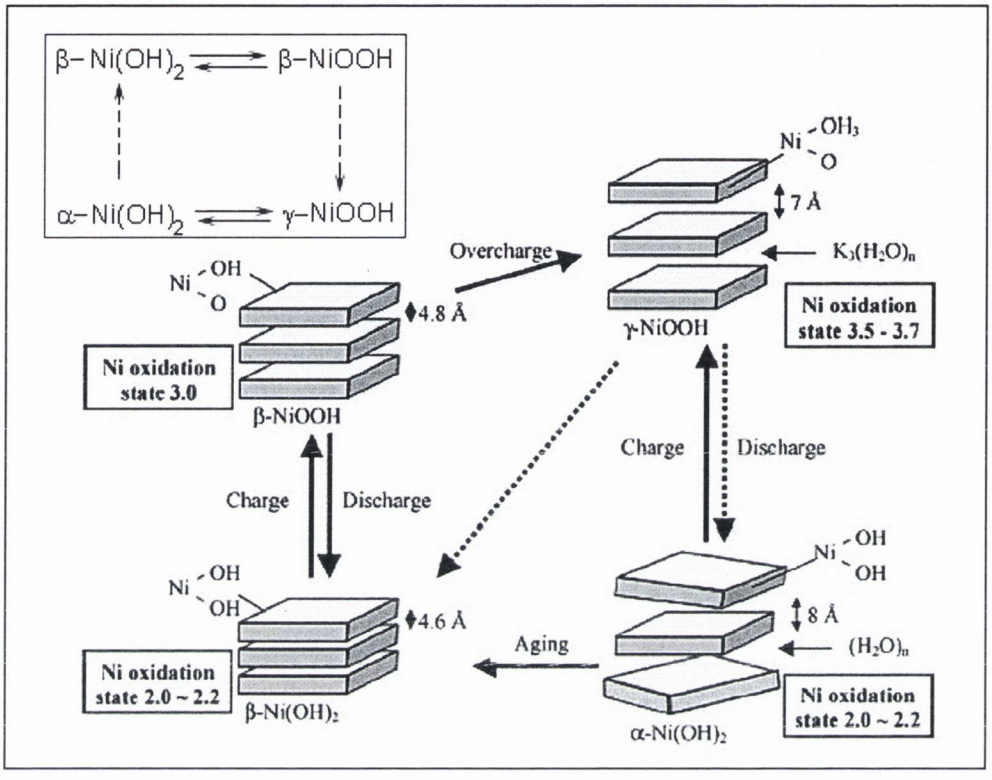


Figure 1.4.3 *Graphical representation of the Bode scheme for the $Ni(OH)_2$ →NiOOH redox transformation in alkaline solution. Reproduced from Ref. 134. Inset – More traditional representation of the Bode scheme.*

While there is general acceptance for the principles of the Bode model, it is important to understand that it is inappropriate to think about the formation of a compound or phase with a definite stoichiometry, during the complex $Ni(OH)_2$ to NiOOH transformation. Instead, the four phases of the Bode scheme should be considered as the limiting divalent and trivalent materials - the actual composition of the oxide at a given potential depending on a range of factors including, its history, method of preparation, degree of hydration, concentration of defects etc. Nonetheless it is instructive to briefly review what is known of the nature and structures of the four limiting model phases.

The definitive crystallographic work on β-$Ni(OH)_2$ was performed by Greaves and Thomas[136]. These workers conducted powder neutron and X-ray diffraction studies on both a well crystallised deuterated $Ni(OD)_2$ sample pre-treated by a hydrothermal

method, and also a high surface area $Ni(OH)_2$ sample that was precipitated from a $NiSO_4$ solution upon the addition of KOH. They found that well crystallised β-$Ni(OD)_2$ adopts a brucite-type structure with layers of $Ni(OD)_2$ (the basal planes) perfectly stacked along the c-axis – see Figure 1.4.4. The $Ni(OD)_2$ layers consist of a hexagonal planar arrangement of Ni^{2+}-oxygen octahedra. As commented by McBreen[121] the nickel ions are all in the (0001) plane and are surrounded by six hydroxyl groups, each of which is alternatively above and below this plane. The brucite structure of β-$Ni(OH)_2$ is isomorphous with the divalent hydroxides of Ca, Mg, Cd, and significantly in the context of the present work, Fe and Co[121]. For the well crystallised $Ni(OD)_2$, the unit cell parameter in the basal plane, a_0, was found to be 3.126 Å, the inter-lamellar distance, c_0, was determined as 4.593 Å, while 0.973 Å was reported for the O-H bond length. The less well crystallised material precipitated from the sulphate solution, yielded the following values for these parameters; a_0 = 3.119 Å, c_0 = 4.686 Å and O-H bond length = 1.08 Å. On the basis of this data Greaves and Thomas[136] concluded that the structure of the high surface area as-precipitated β-$Ni(OH)_2$ is similar to the well crystallised material, but has a much greater amount of defects related to a high concentration of surface OH^- groups. Significantly, it was noted that the well crystallised material displayed much lower electrochemical activity than the defective as-precipitated species.

Greaves and Thomas[136] also applied infrared spectroscopy to the study of the two aforementioned materials. They observed a broad absorption band in the region of 1630 cm^{-1} in the spectrum for the high surface area material, which was absent from the spectrum of the well crystallised hydroxide. They attributed this to the presence of a small amount of absorbed water in the more defective material. This hypothesis is consistent with the increase in the O-H bond length and c_0 parameter for the defective material, in comparison with the more crystallised material, as was detailed above.

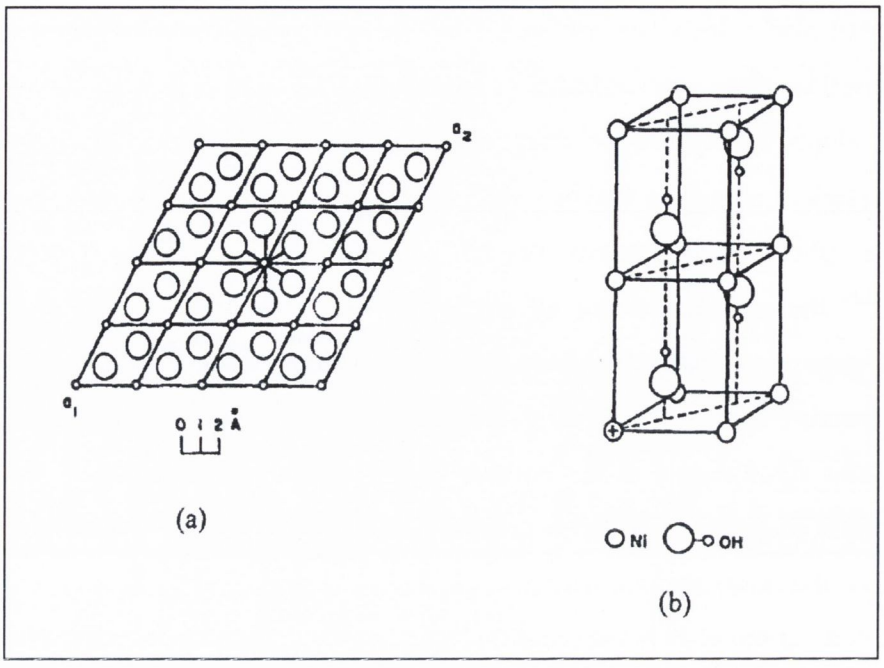


Figure 1.4.4 *The brucite structure of β-Ni(OH)$_2$. (a) The hexagonal brucite layer – alternate O atoms are above and below the plane of the Ni atoms. (b) The stacking of the planes showing the orientation of the O-H bonds. Reproduced from Ref. 121.*

In his review on nickel hydroxides, McBreen[121] reports that other workers using XRD, IR, Raman spectroscopy, and Thermogravimetric analysis (TGA) have arrived at conclusions similar to those of Greaves and Thomas[136]. In summary the discharge product on the β cycle in nickel hydroxide battery materials is similar, but not identical to well crystallised β-Ni(OH)$_2$. Its defect structure permits water adsorption and facilitates enhanced electrochemical activity. Following this analysis it is probably reasonable to assume that anodically generated β-Ni(OH)$_2$ will also be defective and contain some absorbed water, despite being formally described as the anhydrous form of the hydroxide.

Typical XRD spectra[137] for both α-Ni(OH)$_2$ and β-Ni(OH)$_2$ are reproduced in Figure 1.4.5. The α-Ni(OH)$_2$ was prepared[138] by the cathodic electrodeposition of a film of the oxide onto a Pt plate in a solution of 0.1 M Ni(NO$_3$)$_2$. The film was removed from the plate, washed, dried in a desiccator, and ground into powder form for the XRD measurement. The β-Ni(OH)$_2$ material was prepared according to the Bode scheme by ageing a sample of the α powder in a 6 M KOH solution at 70°C for 45 minutes.

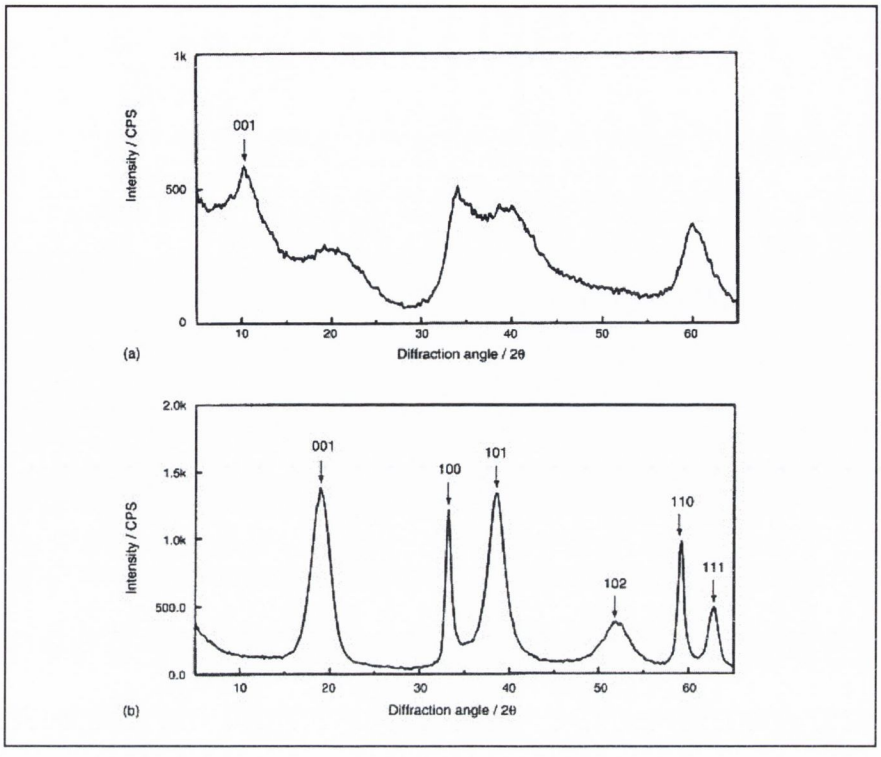


Figure 1.4.5 *XRD patterns of (a) α-Ni(OH)$_2$ and (b) β-Ni(OH)$_2$. See text for more details. Reproduced from Ref. 137.*

Comparison of the diffraction patterns in Figure 1.4.5 indicates that the α phase is significantly more amorphous than the β phase, which displays crystallographic peaks with superior resolution and intensity. This data corroborates older XRD work by Le Bihan and Figlarz[138]. These workers demonstrated that the principal difference between the α-Ni(OH)$_2$ and β-Ni(OH)$_2$ phases arises in the stacking of the planes along the c axis. They reported an inter-lamellar distance of ca. 8 Å and envisaged that the brucite like layers are misoriented with respect to each other. Furthermore they proposed that the expansion of the c-axis spacing, relative to that characteristic of the β phase, is due to the presence of water molecules and anionic species in the van der Waals gap, leading to the formation of a turbostratic phase. They further contended that the water molecules separating the brucite planes are hydrogen bonded to the Ni-OH groups in these planes. These hydrogen bonded interlamellar H_2O molecules are often referred to as *intercalated water*[121] as distinct from adsorbed surface water. TGA measurements performed by Mani and deNeufville[139] found that the surface adsorbed water is removed at temperatures between 50° and 90°C, while the intercalated water is removed at higher temperatures up to 180°C.

In his nickel hydroxide review[121], McBreen, has compared Raman spectroscopy results, obtained by various workers, on α-$Ni(OH)_2$ prepared by different means, including chemical precipitation, cathodic deposition and electrochemical reduction of γ-NiOOH. He concluded that there were differences in these spectra, both in the lattice modes and the O-H stretching modes, depending on the preparation method. Interestingly, in terms of the present work, he proposes that the shifts in the lattice modes for the reduced γ-NiOOH, may be due to the material having an oxidation state greater than Ni(II) (c.f. the graphical scheme in Figure 1.4.3).

From the point of view of electronic conductivity, it has been found using photoelectrochemical measurements, that $Ni(OH)_2$ is a rather poor electronic conductor[31,140]. It displays p-type conductivity with an estimated band-gap of ca. 3.7 eV[31].

It is difficult to make accurate determinations of the structures of the β-NiOOH and γ-NiOOH since they are amorphous materials[121], however it is generally accepted that they do display greater structural organisation than α-$Ni(OH)_2$[134]. In the case of β-NiOOH it is thought that the brucite structure is more or less maintained upon oxidation of β-$Ni(OH)_2$. The unit cell parameters change from a_0 = 3.126 Å and c_0 = 4.605 Å for β-$Ni(OH)_2$ to a_0 = 2.82 Å and c_0 = 4.85 Å for β-NiOOH[121]. Clearly this indicates an expansion along the c-axis, but a contraction in the in-plane Ni distance[141] on the oxidation of β-$Ni(OH)_2$ to β-NiOOH. It has long been appreciated[135, 142] that β-NiOOH obtained from the electrochemical oxidation of β-$Ni(OH)_2$ displays a Ni oxidation state of 2.7-2.8 rather than the expected value of 3.0, again pointing to the non-stoichiometric nature of the various phases envisaged by the Bode scheme. Despite this it is often pointed out (e.g. refs., 135, 145) that anodically prepared NiOOH will rarely be free from some amount of Ni in the +IV oxidation state. Kober[143, 144] reported the replacement of a sharp infrared band at 3644 cm^{-1}, attributed to hydroxyl groups in the brucite structure (see Figure 1.4.4), by a more diffuse band at 3450cm^{-1} upon oxidation of β-$Ni(OH)_2$. The later band indicates, that upon the removal of half the protons from the unit cell, hydrogen bonding occurs between the remaining protons and the O atoms in the brucite structure, thus rationalising the observed changes in a_0 and c_0. Having reviewed much literature in this area McBreen[121] comments that "β-NiOOH probably has some adsorbed and absorbed water" but there is a lack of relevant data (e.g. TGA data) available on this question.

From the point of view of electronic conductivity, the previously cited photoelectrochemical work of Carpenter et al.[31] and Madou et al.[140] indicates that β-NiOOH is a much better conductor than its reduced form – it displays n-type conductivity with an estimated band-gap of ca. 1.75 eV[31]. This enhanced conductivity relative to $Ni(OH)_2$ and also the γ form of NiOOH (which contains more Ni^{4+} - this forms an oxide of lower conductivity[146, 147]) is probably one of the reasons that that β-NiOOH is sometimes referred to as "the right type of oxide"[147] for the catalysis of the o.e.r.

As indicated by the Bode scheme (Figure 1.4.3) γ-NiOOH is obtained by the oxidation of the turbostratic α-$Ni(OH)_2$ phase, or by the overcharge of β-NiOOH in concentrated alkaline solution. In comparison to the disorganised α-$Ni(OH)_2$ precursor with its misoriented layers, γ-NiOOH has a much more organised layer structure with a c_0 value of 7.2 Å[121]. Having compared XRD data for the various phases in the Bode scheme, McBreen[121] comments that the diffraction patterns for γ-NiOOH have more and much sharper lines than those for either α-$Ni(OH)_2$ or β-NiOOH. The increase in the inter-lammelar distance upon overcharge of β-NiOOH is attributed[121, 141] to the incorporation of water solvated alkali ions in the van der Waals gap. Sac-Epee et al.[141] used high resolution electron microscopy (HREM) to view, along the c-axis, both well crystallised β-$Ni(OH)_2$, and γ-NiOOH obtained from the overcharge of the former. They found that the β phase demonstrated well stacked parallel planes with a regular interlammelar distance of 4.6 Å. In contrast the γ-NiOOH layers were found to be strongly exfoliated, rendering interlayer distance measurement difficult (they report an average value of 7 Å). These authors summed up their findings with the following elegant description – "the solid-state process associated with the β(II) → γ(III) oxidation reaction involves strains along the c axis which are relieved by the exfoliation of the NiO_2 sheets along the c axis".

From the results of a series of charging and discharging experiments on various forms of $Ni(OH)_2$, Barnard et. al.[135] concluded that the γ-NiOOH phase has a higher Ni oxidation state of 3.3 – 3.67, compared to the oxidation state of β-NiOOH (2.7 – 3.0), owing to the presence of a relatively greater amount of Ni^{4+} charge centres. Indeed, Aleshkevich et al.[148] estimated that less energy would be required to remove a proton from a hydroxyl group bonded to a Ni^{3+} ion, than from one bonded to a Ni^{2+} ion. On the basis of this they predicted that kinetic factors would favour the oxidation of Ni(II) to Ni(IV). This is an important point, since as commented by Briggs[145], it

means that anodically prepared NiOOH will rarely be free from Ni(IV). Barnard et al.[135] took this concept a step further when they proposed that the required Ni oxidation state of 3.67 in their γ phase material could best be rationalised in terms of an empirical formula achieved by using a mixture of Ni^{2+} and Ni^{4+} cations rather than Ni^{3+} and Ni^{4+} cations. Noting that the oxidation of α-$Ni(OH)_2$ to the γ phase occurs at a lower potential than the oxidation of β-NiOOH to this phase, these authors commented that it "is easier to rationalise the development of the co-existing phases in the α-$Ni(OH)_2$/ γ-phase system in terms of only one high valent species".

Experimental determination of the equilibrium potential for the $Ni(OH)_2 \rightarrow$ NiOOH redox process is not a trivial matter[121, 135] and thus some consideration will presently be devoted to this problem. In general it can be difficult to reconcile theoretical thermodynamic reversible potentials for the various corrosion processes involved in the formation of anodic oxide films on metal electrodes, with experimentally observed potentials (e.g. as measured by cyclic voltammetry, potential decay or galvanostatic charging curves) for these processes. As was recently commented by Liu et al.[149] there is often disagreement between measured potentials and the thermodynamic potentials predicted in the Pourbaix atlas[150]. Liu et al.[149] comment that these discrepancies are not surprising since the behaviour of electrochemically formed thin films is rarely identical to that of well defined phases of bulk oxides, and that furthermore, these films are generally hydrous in nature, containing structural water, which has a significant bearing on the thermodynamic potentials exhibited. Many of the issues regarding the experimental determination of the equilibrium potential for the $Ni(OH)_2 \rightarrow$ NiOOH redox transition are therefore also applicable to the electrolytically formed oxide films on Fe and Co.

McBreen[121] asserts, that, owing to the complexity of the redox reactions of the nickel hydroxide anode, a revised pH-potential phase diagram, devised by Silverman[151] is more appropriate than Pourbaix's original effort[150]. According to Silvermans' work[151], the calculated $Ni(OH)_2$/NiOOH reversible potential is 0.41V vs. Hg/HgO. An immediate problem, that is obvious when one thinks about attempting to experimentally measure this value, is that the α-$Ni(OH)_2$/γ and β-$Ni(OH)_2$/β –NiOOH transitions will have different reversible potentials. Early attempts to measure the $Ni(OH)_2$/NiOOH reversible potential yielded inconsistent and conflicting results[135]. These measurements were performed before the "breakthrough" of the Bode scheme in 1966 and so were hindered by a lack of understanding regarding the different

phases of the charged and discharged forms of nickel hydroxide. Another important realisation, regarding the use of simple open circuit potential decay measurements to determine the reversible potential, was made by Conway and Bourgault[152]. These workers realised that the $Ni(OH)_2$/NiOOH reversible potential lay above the reversible oxygen potential, and thus that potential decay measurements yielded a mixed potential. In view of this, they developed an extrapolation technique[152-154] that enabled the removal of the influence of the o.e.r. from the analysis of experimental potential decay data. Significantly, in the context of the present work, Conway and Bourgault, found that the oxygen evolution partial reaction is rate-controlling in the self discharge of the nickel oxide electrode, and they utilised this fact to obtain fundamental data related to the o.e.r. from the potential decay curves[153, 154].

From the point of view of the Ni^{2+}/Ni^{3+} reversible potential, Conway et al.[155] obtained a value of 0.424 V (vs. Hg/HgO 1M KOH) – this work was published in 1962, several years before Bode's work[133] indicated that, two different reversible potentials are possible, depending on whether the nickel hydroxide electrode is operating on the α-γ or β-β cycle. Barnard et al.[135, 156] tackled this problem in the 1980s using a modification of the measurement and data treatment procedures of Conway et al.[152-55]. These workers (Barnard et al.) prepared what they classified as "activated" and "deactivated" β-$Ni(OH)_2$ electrodes, and also "activated" and "deactivated" α-$Ni(OH)_2$ electrodes. The recorded open circuit potentials depended on which type of electrode was examined, however in general the recorded values were 0.44 – 0.47 V (vs.Hg/HgO) for the β-β transition, and 0.39 – 0.44 V (vs. Hg/HgO) for the α-γ transition[135]. In cyclic voltammetry experiments[135] on the β-β couple the oxidation peak potential was 0.5 V, while the reduction peak potential was 0.37 V (both vs. Hg/HgO). The corresponding values for the α-γ couple were 0.43 V for the oxidation peak and 0.34 V for the reduction peak.

Little variation of the reversible potential for the β-β transition was observed with changing KOH concentrations over a range of solution concentrations from 0.01 M to 7.1 M[135, 156]. On the other hand the reversible potential for the "activated" α-γ couple was observed to fall from ~ 0.423 V to ~ 0.340 V with increasing concentration over the same concentration range, whereas the reversible potential dropped from ~ 0.443 V to ~ 0.356 V as the KOH concentration was varied from 1.0 M to 10.4 M [135, 156]. Significantly, it was found[156] that the variation of reversible potential with OH^-

activity was reduced upon ageing of the α-$Ni(OH)_2$ material, as the later was converted to β-$Ni(OH)_2$.

It is generally believed that the $Ni(OH)_2 \rightarrow NiOOH$ reaction is a solid-state topochemical type reaction that does not involve soluble intermediates[121]. Transmission electron microscope (TEM)[141] images of micro-scale particles of a pristine β-$Ni(OH)_2$ phase, showed that upon oxidation to the γ phase, the global size and shape of the particles are retained, strongly suggesting a solid state mechanism. As was discussed previously, the IR studies of Kober[143, 144] suggest that protons are removed from the brucite lattice upon oxidation of $Ni(OH)_2$. In recent times EQCM has been applied by several groups of workers seeking to elucidate details of the $Ni(OH)_2 \rightarrow NiOOH$ redox transition, work that has been reviewed by Wehrens-Dijksma and Notten[134]. On the basis of their examination of the various EQCM work performed the latter authors state that "during oxidation of $Ni(OH)_2$ more mass is transferred than can be accounted for by a simple H^+ extraction as suggested by the chemical equation, $Ni(OH)_2 + OH^- \rightarrow NiOOH + H_2O + e^-$. Because electro-neutrality has to be maintained, this will be accompanied by the incorporation or release of either positive or negative ions from the solution, possibly accompanied by H_2O". A variety of redox models have been proposed to describe the mass changes that take place during the oxidation of $Ni(OH)_2$. Wehrens-Dijksma and Notten[134] have divided these models into two categories – H^+ transport models or OH^- transport models.

In the various H^+ transport models that have been proposed, it is generally agreed[134] that the oxidation of $Ni(OH)_2$ takes place in two steps – insertion of cations, and deprotonation. Bernard et al.[157] have proposed a model where, initially non-hydrated $Ni(OH)_2$ (i.e. the β phase) incorporates alkali cations and different amounts of water molecules upon oxidation, depending on the alkali cation present in solution (i.e. Li^+, Na^+, K^+, Rb^+, Cs^+). In the case of initially hydrated $Ni(OH)_2$, Cheek and O'Grady[158] have proposed a model, where as oxidation proceeds with cation incorporation, different amounts of water are expelled from the lattice, again depending on which alkali cation is present in solution.

The application of OH^- transport models, follow a proposal by Feuilade and Jacoud[159]on the basis of radio isotope measurements, that the transport of hydroxide rather than that of protons is predominant in $Ni(OH)_2$ films. Wehrens-Dijksma and Notten[134] summarise a number of these OH^- transport models in their review. Again all the models seem to agree that as oxidation proceeds, alkali metal cations are

incorporated into the oxide structure. There is disagreement between the various models on whether the mass change with oxidation should depend on the cation size, with some models proposing that it is cation independent, since relatively more H_2O will be incorporated into the oxide along with the lighter cations.

A number of modifications to the Bode scheme (Figure 1.4.3) have been proposed. The scheme depicted in Figure 1.4.6 is due to Sac-Epee et al[141, 160]. The leftmost transition in this scheme can be represented as γ-NiOOH$\leftrightarrow$ $\beta_{ex\gamma}$-Ni(OH)$_2$.

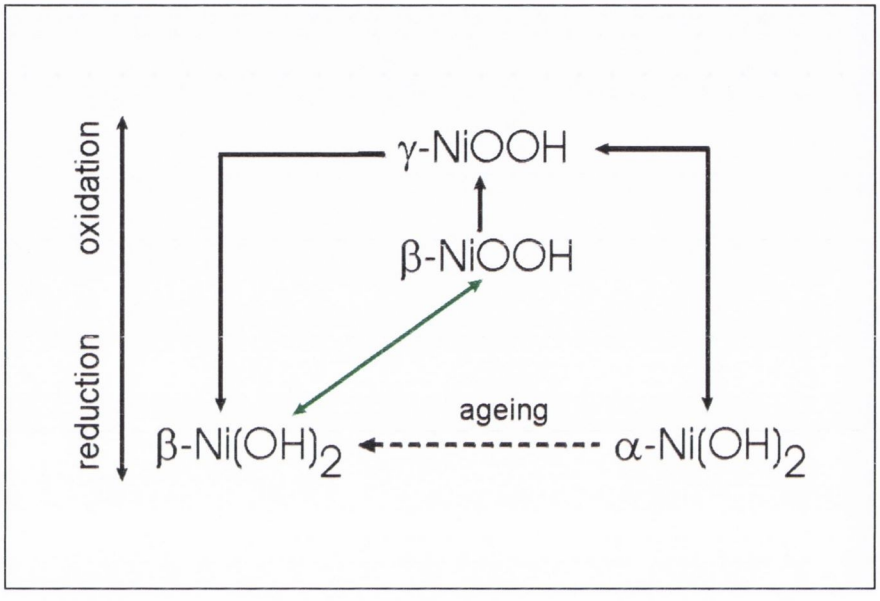


Figure 1.4.6 *The Ni(II)→Ni(III) redox transition scheme envisaged by Sac-Epee et al. See text for more details.*

The species $\beta_{ex\gamma}$-Ni(OH)$_2$ was first isolated by Sac-Epee et al.[141, 160], with TEM measurements showing that this phase retained the textural features of its precursor γ(III) phase and therefore was different from the original β(II) phase. In addition these workers showed that the new $\beta_{ex\gamma}$- Ni(OH)$_2$ phase directly transformed to the γ(III) phase without having to go through the β-NiOOH phase as in the Bode sheme, i.e. the following reaction occurs directly - $\beta_{ex\gamma}$-Ni(OH)$_2\rightarrow$ γ-NiOOH + H^+ +e^-. They point out that the γ-NiOOH$\leftrightarrow$ $\beta_{ex\gamma}$-Ni(OH)$_2$ cycle is a non-thermodynamically reversible process facilitated by defects, and it is possible that material locked in this cycle will remain in this reaction scheme for structural reasons, rather than following the thermodynamically predicted route (i.e. the Bode route).

Another approach has been detailed by Cornilsen and co workers[161], following their proposal, based upon Raman spectroscopy data[162, 163], that the four electrochemically active materials (at least in their cathodically deposited forms) of the Bode scheme, actually share a common nonclose-packed structure with ...ABBCCA...stacking. These workers assert[161] that this nonclose-packed structure should properly be called the γ structure and comment that it contrasts with close-packed β structure which is "electrochemically unstable under normal cycling conditions". They propose that the conventional β structure will be obtained on ageing of the "active mass" in concentrated alkaline solution. Their proposals can be summarised in the modified Bode scheme of Figure 1.4.7.

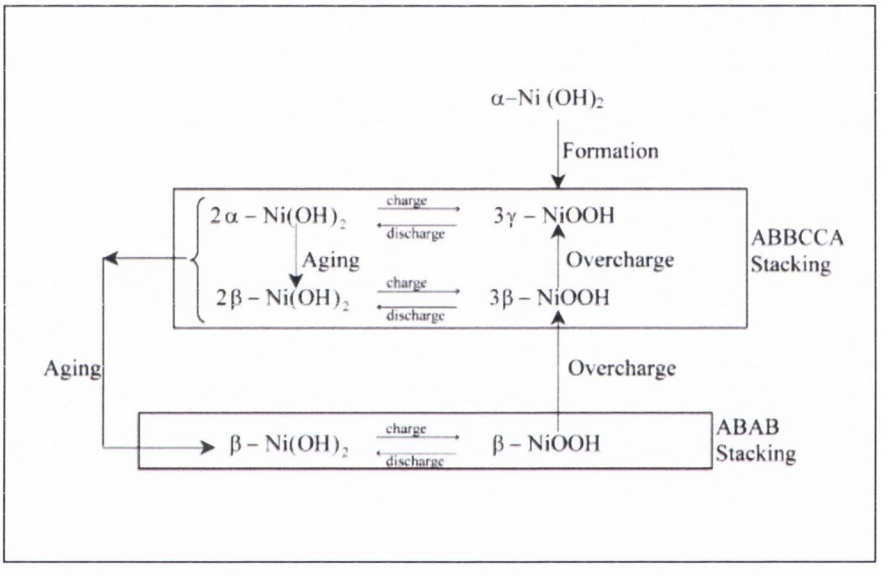


Figure 1.4.7 *The Ni(II)→Ni(III) redox transition scheme envisaged by Cornilsen et al. See text for more details. Reproduced from ref. 161.*

Since the cycles denoted as 2α-3γ and 2β-3β involve non-close-packed materials, Cornilsen et al.[161], point out that there is no phase transition involved in going from one cycle the other. They have developed a *point defect model*[162, 163] to predict the properties of these non-stoichiometric materials, and point out that the difference between the 2α-3γ and 2β-3β cycles arises in the level of Ni vacancies, with materials in the 2α-3γ cycle having 25% Ni vacancies, while those in the 2β-3β cycle have 11% Ni vacancy defects. In their point defect model the Ni vacancies may be occupied by protons, alkali ions or may be left vacant. Varying the defect parameters can explain phenomena, such as the oxidation state of 3.67 observed by Barnard et al.[135], and can

be used to quantitatively explain mass and charge capacity changes in coupled CV and EQCM experiments[161].

As was previously noted in the discussion of the lower anodic/cathodic peak couple in the CV of polycrystalline Ni in alkaline solution (Figure 1.4.1), it was postulated[123], on the basis of the variation of the anodic peak potential with pH, that the initially formed hydroxide species in this potential range is anionic in nature. In fact the peak potential decreased linearly from 0.35 V (vs. RHE) at pH 9 to ca. 0.3 V (vs. RHE) at pH 13.1, giving a mean potential/pH shift of around – 13mV/pH unit[123]. This negative potential/pH shift was rationalised in terms of the oxidised product having an overall negative charge of about 0.4 (i.e. $Ni(OH)_{2.4}^{0.4-}$) relative to the neutral reduced Ni metal, based on a two electron transfer. This is but one example of a so-called *super-Nernstian shift*, a phenomenon, that is often encountered in peak potential/pH studies on electrochemically generated hydrous oxide films, as reviewed by Burke and Lyons[164].

Consider a metal oxide/hydroxide electrode system described by the general equation:

$$MO_n + nH_2O + 2ne^- \leftrightarrows M + 2nOH^- \qquad (1.4.1)$$

The solubility constant, K_S, for the hydroxide is defined by reference to the equation,

$$M(OH)_n \leftrightarrows M^{n+} + nOH^-, \qquad (1.4.2)$$

and is given by:

$$K_S = a_{M^{n+}} a_{OH-}^n \qquad (1.4.3)$$

Rearranging for the metal ion activity achieves,

$$a_{M^{n+}} = \frac{K_S}{a_{OH-}^n} = \frac{K_S a_{H_3O+}^n}{K_w^n}, \qquad (1.4.4)$$

where, K_w $(= a_{H_3O+}.a_{OH-})$ is the ionic product of water. The Nernst equation for the redox process, $M^{n+} + ne^- \leftrightarrows M$, can be written as:

$$E = E^0 - \frac{RT}{nF} \ln \frac{a_M}{a_{M^{n+}}} \tag{1.4.5}$$

Substituting for $a_{M^{n+}}$ from equation (1.4.4) and following the usual convention that $a_M = 1$ yields the following expression:

$$E = E^0 + \frac{RT}{nF} \ln \frac{K_S . a^n_{H_3O+}}{K^n_w} \tag{1.4.6}$$

Equation (1.4.6) can be re-written as:

$$E = E^0 + \frac{RT}{nF} \ln \frac{K_S}{K^n_w} - \frac{2.303RT}{F} pH \tag{1.4.7}$$

The potential variation with pH, for the redox transition $M^{n+} + ne^- \leftrightarrows M$, at 25°C is then given by:

$$\frac{\partial E}{\partial pH} = -\frac{2.303RT}{F} = -0.059 \text{ V} \tag{1.4.8}$$

According to equation (1.4.8), the potential for an ideal oxide electrode system in aqueous solution at 25°C, decreases with increasing pH by ca. 59 mV/pH unit, with respect to a pH independent reference electrode such as the N.H.E. or the saturated calomel electrode (S.C.E.). Such a shift in potential with pH, is referred to as a *Nernstian shift*, since it is predicted by the Nernst equation. It should be noted that if the reference electrode is pH dependent, such as the reversible hydrogen electrode (R.H.E.) or the Hg/HgO electrode, no potential pH shift will be observed, since the potential of this type of electrode also alters by ca. 59 mV per unit change in pH at 25°C.

As previously mentioned Burke and Lyons[164] have discussed super-Nernstain shifts that have been observed for various hydrous oxide systems – in these cases the potential/pH shift differs from the expected 0.059V/pH unit at 25°C. The

mathematical treatment of this situation is beyond the scope of the present review, but suffice to say, the phenomena have been qualitatively summarised[164] as discussed presently. Thus, a zero potential shift (with respect to a pH dependent reference electrode) implies that both the reactants and the product possess the same net charge. A positive potential shift with pH, is indicative of an oxidised state that is more positive than the reduced state, whereas the converse is true in the case of an observed negative potential/pH shift.

Burke and Twomey[124] observed a decrease in peak potential of approximately ½(2.303 RT/F) V/pH unit for an upper cathodic peak in the CVs of a multicycled Ni anode. This was a peak that they attributed to the reduction of the γ phase to α-$Ni(OH)_2$. Another cathodic peak at slightly lower potential was assigned to the β-NiOOH → β-$Ni(OH)_2$ reduction[124] – this peak potential was found to be invariant with pH. The authors hypothesised that the pH invariant peak was indicative of an Ni(III)→ Ni(II) transition in an inner anhydrous region of the oxide film, consisting of β material. On the other hand the reduction process associated with the pH dependent peak was rationalised in terms of the following equation:

$$[Ni(OH)_{3.5} \bullet nH_2O]^{0.5-} \bullet (Na^+)_{0.5} + e^- \leftrightarrows Ni(OH)_2 \bullet n\,H_2O + 0.5Na^+ + 1.5OH^- \qquad (1.4.9)$$

Just like the assignment of the formula $Ni(OH)_{2.4}^{0.4-}$ to the species formed at the first anodic peak as discussed above, equation (1.4.9) represents an attempt to rationalise, in the simplest possible terms, a complex reaction, and the authors didn't necessarily claim that the reduction process follows the exact equation outlined. It was envisaged[124] that reaction (1.4.9) occurs in an outer, dispersed hydrous region of the oxide layer, and thus super-Nernstian shifts might be regarded as being associated with the development of such hydrous films. Similar potential/pH shift behaviour was observed, for example with hydrous iridium oxide systems[165], and also with electro-generated iron oxyhydroxide films, as will be discussed later. It must be said that the model of an outer-dispersed oxide layer with a redox shift represented along the lines of reaction (1.4.9) is consistent with the Raman based observations of Cornilsen et al.[161-163], that the nickel hydroxide film, upon cycling, consists of a non-close packed structure that doesn't conform to any of the model phases in the Bode scheme. The assignment by Burke and Twomey[124] of the structure on the left hand side of equation

(1.4.9) to the charged form of the hydroxide, is consistent with the view of Barnard et al.[135, 155] that the notion of a Ni(III) based γ phase (i.e. γ-NiOOH) is incompatible with the results of charge/discharge experiments.

Recall from section 1.1.3 that the amphotheric nature of metal oxides in aqueous solution was discussed in terms of the formation of acidic -OH(a) and basic -OH(b) surface hydroxyl species. The interaction of such an acidic species with a hydrated potassium cation, in the case of immersion of the oxide in KOH solution was considered as follows; $-OH(a) + K_{aq}^{+} \leftrightarrows -O^{-}(a)\cdot K^{+} + H_{aq}^{+}$. Burke and co-workers[124, 164] have proposed that the acidic character of hydrous oxides is involved in the formation of anionic oxidation products commenting[124] that "anion formation may be regarded in various ways, e.g. loss of protons from coordinated water molecules, adsorption of hydroxide ions or hydroxyl complex formation".

1.4.2 Iron

Two typical characteristic CVs, reproduced from the literature, of a bright iron electrode in 1.0 M NaOH solution are depicted in Figure 1.4.8. The relation of the potential scales of these CVs to the (Hg/HgO, 1M NaOH) reference scale are indicated in the caption, since the latter is the reference electrode utilised in the present work. The electrochemistry of iron, especially in acidic and neutral electrolyte solutions, has received much attention, owing to its fundamental importance in understanding the mechanism of steel corrosion and the formation of corrosion resistant passive films[168]. Passivation is a phenomenon whereby a metal substantially resists corrosion in an environment where thermodynamically there is a large free energy decrease associated with the passage from the metallic state to corrosion products. A review of the corrosion, dissolution and passivation of iron in various aqueous media has been presented by Bockris and Khan[169]. Of interest in the present work is the nature of the anodic oxyhydroxide film formed on Fe in alkaline solutions, since the o.e.r. will occur on the surface of such a film.

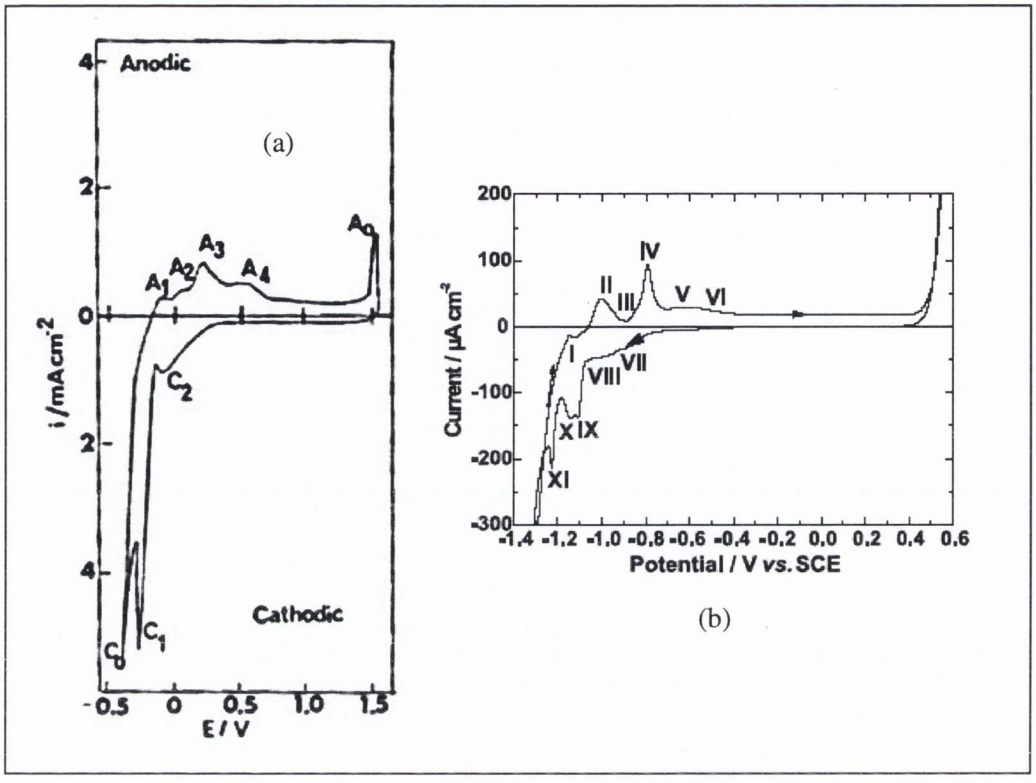


Figure 1.4.8 *Two examples of "typical" CVs of a bright polycrystalline Fe electode in 1M NaOH, reproduced from the literature. (a) Scan rate 40 mV s^{-1}- reproduced from ref. 166. Potentials in this CV were recorded relative to the RHE, E(Hg/HgO,1M) ≈ E(RHE)-0.926V. (b)Slow scan rate of 0.5 mV s^{-1} – reproduced from ref. 167. Potentials in this CV were recorded relative to the SCE, E(Hg/HgO,1M) ≈ E(SCE)+0.143V. Both CVs were recorded at 25°C.*

Upon repetitive potential cycling, between the onset potentials for the h.e.r. and the o.e.r., (features C_0 and A_0 respectively, in Figure 1.4.8 (a)), a hydrous oxide film is formed (at least for electrolyte solutions with a pH of ~ 13-14), with only peaks A3 and C2 observed to be enhanced[166]. Indeed, while the other anodic peaks show a zero shift in peak potential with respect to a pH dependent reference electrode over a range of solution pH (~7-14), the complementary peaks A3 and C2 display a super Nerstian shift of the order of ½(2.303 RT/F) V/pH unit[166]. As was discussed in connection with nickel hydroxide, such super Nernstian shifts are often a characteristic of hydrous oxide films. There have been numerous proposals on the mechanism of the formation of the passive oxide film on Fe in alkaline solution. There is general agreement[166-174] that peak A2 (or II in Figure 1.4.8 (b)) is due to the formation of ferrous (Fe^{2+}) species, while several workers[166, 170-173] have attributed peaks A3 and A4 (IV and V in Fig. 1.4.8 (b)) to the formation of ferric (Fe^{3+}) species. It has been pointed out[170], and indeed is obvious from comparing the two voltammograms in Figure 1.4.8, that the

exact profile obtained for Fe in cyclic voltammetry experiments depends on the nature of the potential perturbation applied. In the current short review, further consideration will be given to two of the possible mechanisms that have a stronger correlation with experimental data.

The first of these is due to Burke and Lyons[166] who recorded the CV depicted in Figure 1.4.8 (a). Their scheme proposes that peak A1 is most probably due to the formation of a layer of adsorbed hydroxyl species

$$Fe + OH^- \rightarrow FeOH(ads.) + 2e^- \quad (1.4.10)$$

in combination with a displacement of adsorbed hydrogen:

$$FeH(ads.) \rightarrow Fe + H^+ + e^- \quad (1.4.11)$$

The peak denoted as A2 is related to the formation of ferrous species:

$$FeOH(ads.) + OH^- \rightarrow Fe(OH)_2 + e^- \quad (1.4.12)$$

$$FeOH(ads.) + OH^- \rightarrow FeO + H_2O + e^- \quad (1.4.13)$$

In agreement with other workers[170-174], Burke and Lyons[166] propose that peak A3 is associated with the formation of ferric species, however they postulate, based on the aforementioned super Nerstian shift of A3's peak potential, that the operative reaction is not the formation of species such as Fe_2O_3 or FeOOH in a compact well defined phase, but rather a Fe(II)/Fe(III) transition in a dispersed hydrous oxide phase. Such a phase is envisaged to result from the hydration of the outer region of the Fe(II) oxides formed in equations (1.4.12) and (1.4.13). The decrease in the peak potential of A3 (and indeed its complimentary cathodic peak C2) with increasing pH points to the formation of an anionic hydrous oxyhydroxide species. A Nernstian analysis of the observed potential/pH shift has concluded that the redox process that gives rise to peak A3 could be represented as,

$$[Fe_2(OH)_6 \cdot 3H_2O]^{2-} + 3OH^- \rightarrow [Fe_2(OH)_9]^{3-} + 3H_2O + 2e^- \quad (1.4.14)$$

or alternatively, by analogy to the Ni(II) →Ni(III) hydrous oxide transition of equation (1.4.9) as:

$$[Fe(OH)_{3.5} \bullet nH_2O]^{0.5-} \bullet (Na^+)_{0.5} + e^- \leftrightarrows Fe(OH)_2 \bullet n\,H_2O + 0.5Na^+ + 1.5OH^- \quad (1.4.15)$$

Peak A4 is also related to an Fe(II)/Fe(III) redox transition – however at this potential it is the inner more amorphous region of the Fe(II) species that is oxidised in the region of the film close to the metal surface. Possibly oxidation products are largely anhydrous phases of Fe_2O_3, Fe_3O_4 or FeOOH.

Owing to the fact that the cathodic peak C2 displays a similar super-Nernstian shift to peak A3, Burke and Lyons[166] have attributed it to the reduction of the Fe(III) species in the outer hydrous region of the film. As for the cathodic peak C1, these authors attribute it to the reduction of the inner compact layer according to the following equation:

$$FeO.FeOOH + H_2O + 3e^- \rightarrow Fe + FeO_2^{2-} + H_2O + OH^- \quad (1.4.16)$$

A useful aspect of this reaction is that the charge capacity of peak C1 (which can be calculated by integration of the peak between appropriate limits) can be used to estimate the extent of the compact layer growth.

Due to the change in the CV profile with cycling, it is reasonable to assume that there will be differences between the oxide layer formed during the first anodic sweep, and those formed in successive cycles. Indeed the reaction sequences outlined above, represent the simplest possible rationalisation of the oxidation of the bright iron surface. As noted previously, repetitive potential cycling between limits that have been optimised[166], results in the formation of a thick yellowish brown hydrous oxide layer. This arises, since in general[166, 168, 174], slightly more oxide is formed on a given anodic sweep, than is reduced on the corresponding cathodic sweep. Over a number of cycles, the excess oxide will tend to accumulate leading to thickening of the hydrous oxide structure.

Burke and co-workers[175] have proposed a dual layer structure for the passive oxide films formed on certain metals including Ni and Ir – see Figure 1.4.9. This model proposes the existence of an inner amorphous compact anhydrous layer of general

formula MO_X, where M is a metallic species. Beyond the compact layer, the oxide becomes dispersed, polymeric and hydrous and gel-like in nature, and is assigned the general formula $MO_a(OH)_b(OH_2)_c$.

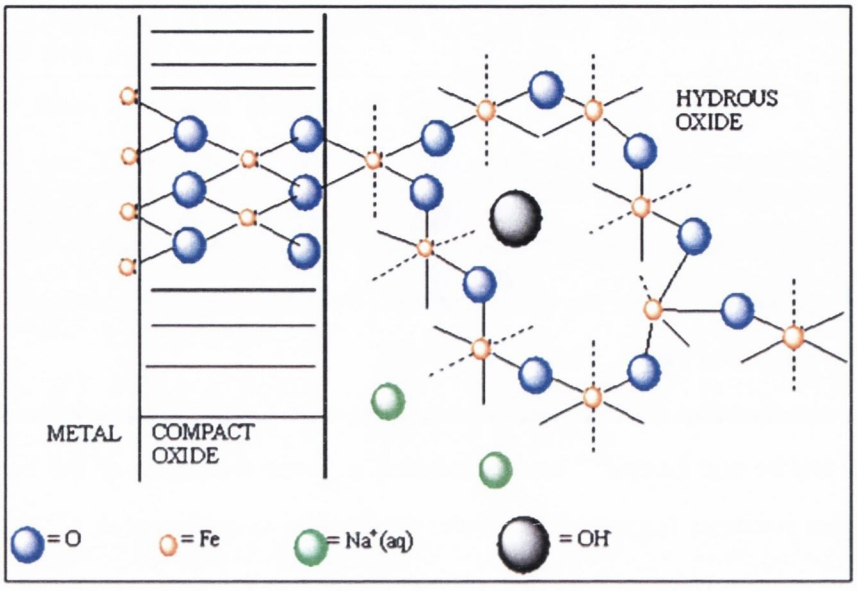


Figure 1.4.9 *Schematic of the dual layer structure proposed for the hydrous oxyhydroxide formed on Ni and Fe electrodes under potential cycling in aqueous alkaline solution.*

From a structural point of view, ions in the inner compact amorphous layer are proposed to be held rigidly in a network of polar covalent bonds, while the outer oxide layer consists of a much more open crystalline matrix, through which ionic species can readily diffuse. The discussion, by Burke and Lyons[166], of the structure of the oxyhydroxide layer formed on Fe in alkaline solution, indicates that the model depicted in Figure 1.4.9 is also appropriate in this case. Based on their experimental observations these workers propose that the passivating species is the anhydrous material of the compact inner layer. The concept of the hydrous oxide existing in a dispersed polymeric form, is supported by the fact that Fe oxyhydroxide films of various thickness, demonstrate[166] a charge capacity dependence on sweep rate that is in line with Laviron's well known theory[176] for redox polymer electrodes. In-situ Mossbauer spectroscopic studies[177] also support the notion of the passive film on Fe existing in a hydrous, polymeric, gel-like form.

A final observation by Burke and Lyons[166], that is of interest in the present work, is that prolonged anodising of a multicycled iron electrode in the oxygen evolution region, seems to remove the much of the hydrous oxide film. They attributed this observation to soluble ferrate (FeO_4^{2-}) formation under these extreme conditions.

The other possible reaction mechanism to be discussed here, arises as a result of a recent multi-technique study[167] of the oxide film on polycrystalline Fe in 1 M NaOH. These workers have applied cyclic voltammetry, electrochemical impedance spectroscopy, rotating ring disk electrode studies, EQCM and in-situ Raman spectroscopy to the problem of the elucidation of the chemical composition and structure on the anodic film on Fe. The first cycle of the voltammogram recorded in the aforementioned study is reproduced here as Figure 1.4.8 (b). This CV, though largely similar, exhibits more fine structure peaks than that due to Burke and Lyons (Figure 1.4.8 (a)) – this may well be attributable to the very slow scan rate at which it was recorded (0.5 mV s^{-1}). Before discussing the peak assignment of Joiret et al.[167], some of their more interesting experimental results are remarked upon.

In order to obtain sufficiently well resolved Raman spectra, these workers had to cycle the electrode potential for 2 hours at 10 mV s^{-1}. The major result of the in-situ Raman study was that magnetite Fe_3O_4 (as characterised by a peak at 670 cm^{-1} in the Raman spectra) was detected over the full potential range examined on both the anodic and subsequent cathodic sweep. In the anodic sweep, at the potential of peak VI, a Raman peak corresponding to the presence of α-FeOOH was observed in addition to the Fe_3O_4 peak. At potentials more anodic to peak VI, the magnetite signal progressively decreased, while a peak corresponding to γ-Fe_2O_3 and/or its hydrated form γ-FeOOH was observed. The presence of magnetite on the reverse scan was observed, even at potentials as low as –0.90 V (vs. S.C.E.).

Some of the ring disk electrode results of Joiret et al. are reproduced in Figure 1.4.10. Tiny amounts of Fe^{2+} species were detected by the vitreous carbon ring in the vicinity of peaks I – III , while peaks in the Fe^{3+} ring current were observed at the potentials of peaks II, III and V. The authors comment that only a small part of the disk current is used in the formation of soluble species (especially in the case of Fe^{2+} species). These results largely corroborate the data of older ring disk studies[178, 179] on Fe electrodes in alkaline media, and strongly suggest that the redox transformations of the iron oxyhydroxide film are largely topotactic solid state processes, in an analogous manner to those of the nickel hydroxide electrode, as discussed previously.

Also of interest in probing the ingress and egress of solution phase species and water from the anodic film, are the EQCM results obtained by these workers. For these measurements they electrodeposited iron on a gold EQCM electrode, and then

subjected it to a heat treatment in an attempt to eliminate absorbed hydrogen. Their EQCM results for the first three cycles are reproduced in Figure 1.4.11.

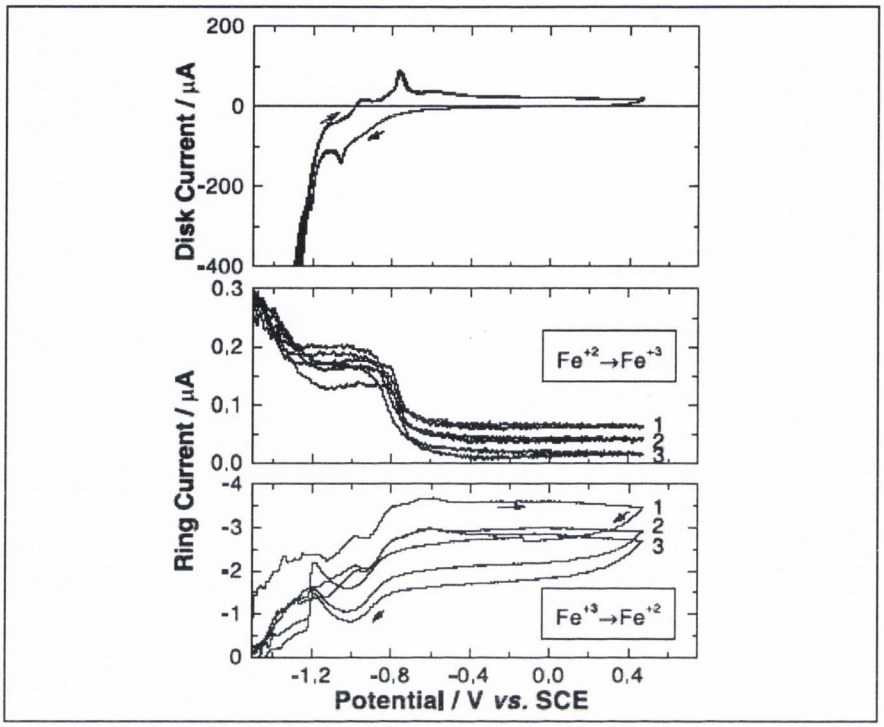


Figure 1.4.10 *RRDE experiments. Iron disk (ø=5mm) and glassy carbon ring (øin = 5.1 mm, øext = 7 mm). Collection efficiency = 0.463. Scan rate = 1mV s^{-1}. The labels in the figure correspond respectively to the 1st, 2nd and 3rd cycles of disk potential sweep. The ring potential for collection of Fe^{3+} was –1.13 V, and that for Fe^{2+} was +0.125 V vs S.C.E. Reproduced from ref. 167.*

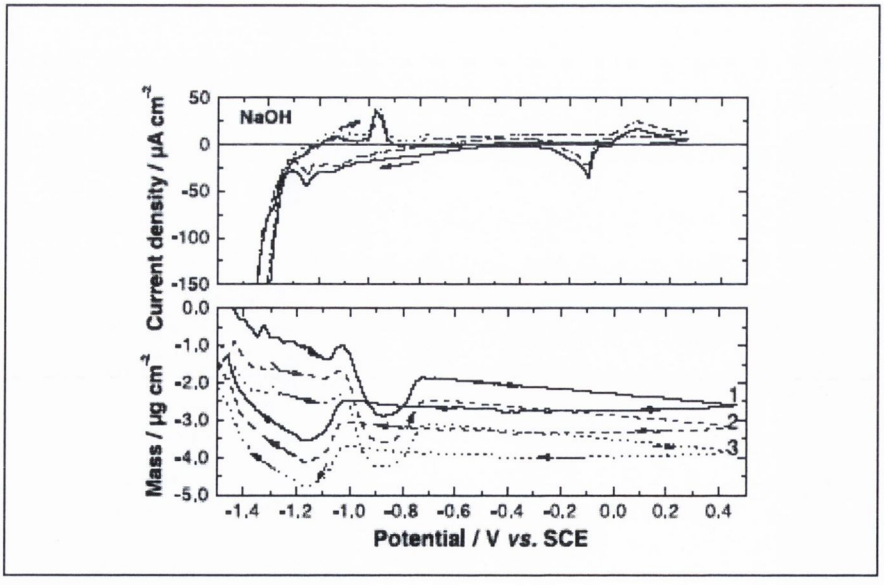


Figure 1.4.11 *EQCM measurements performed on Fe electrodeposited on a gold electrode in 1M NaOH. The sweep rate was 1mV s^{-1}. The labels in the figure correspond respectively to the 1st, 2nd and 3rd cycles of electrode potential sweep. Reproduced from ref. 167.*

According to Joiret et al.[167] the significant features of the voltmassograms of Figure 1.4.11 are as follows. Firstly it is noteworthy that there is a significant mass loss from cycle to cycle. On the anodic sweep, the electrode mass decreases initially, until the observation of a slight peak in the region of –1.0 V (vs. S.C.E.). The authors (perhaps dubiously!) claim that this verifies the existence of their proposed peak III (see Figure 1.4.8 (b)) which they comment "is often difficult to visualise" on voltammograms. The mass clearly decreases significantly before the onset of peak IV (the hydrous oxide A3 peak in the scheme of Burke and Lyons), before increasing until the potential region of peak V. This mass increase is attributed[167] to the insertion of cations and water molecules into the film – the authors point out that similar behaviour is often observed in the oxidation of redox conducting polymers. They associate the gradual decrease in electrode mass at potentials anodic to peak V with the expulsion of water molecules from the oxide film. On the cathodic sweep, the decrease in film mass between –1.0 V and –1.2 V (vs. S.C.E.) would seem to corroborate the ideas of Burke and Lyons[166], that the reduction process in this potential region is the reduction of a hydrous oxide species. The increase in electrode mass at potentials cathodic to this is attributed by Joiret et al.[167] to the insertion of hydrated cations, necessary to maintain electro-neutrality, as the Fe^{2+} are reduced to Fe^{0}, and also to the onset of the h.e.r.

A final matter of note, is the appearance of an anodic peak in the CV of Figure 1.4.11 at ca. 0.1 V, and a corresponding cathodic peak at ca. –0.1 V. Referring to the Pourbaix diagram for Fe[150], and the literature on ferrate production in alkaline media, the authors[167] attribute these peaks to an Fe^{3+}/Fe^{6+} redox transition, and claim to have observed similar peaks in voltammetric studies on a mild steel specimen in alkaline solution.

Considering their experimental data and a charge balance analysis based upon Gaussian deconvolution of the voltammetry peaks, Joiret et al.[167] propose the following mechanism for the formation of the oxyhydroxide film on polycrystalline iron in 1M NaOH. In agreement with Burke and Lyons[166], peak I in their CV (Figure 1.4.8 (b)) is attributed to the reduction of adsorbed hydrogen on the Fe surface. There is partial agreement with Burke and Lyons, for the assignment of peaks II and III, which are envisaged to be due to the formation of ferrous species – however Joiret and co-workers propose that these species are formed by the direction oxidation of Fe^{0} (see equations (1.4.17) and (1.4.18) below) whereas Burke and Lyons (probably

more reasonably in concentrated alkaline solution) proposed the oxidation of $FeOH_{ads}$ (equations (1.4.12 & .13)) –

$$Fe + 3H_2O \rightarrow FeO + 2H_3O^+ + 2e^- \quad (1.4.17)$$

$$Fe + 4H_2O \rightarrow Fe(OH)_2 + 2H_3O^+ + 2e^- \quad (1.4.18)$$

An interesting suggestion by Joiret et al., that has resonance with the ideas of Burke and co-workers regarding the existence of EMS and MMS states (see section 1.3.3), is that peak III (if it actually exists) is due to the oxidation of Fe^0 species in a different energy state to those oxidised at peak II. These workers however suggest that the two different Fe^0 energy states might arise from (a) species near the oxide surface and (b) species dispersed in the oxide interstices. They assign the cathodic peaks X and XI to the reduction of the species formed in reactions (1.4.17) and (1.4.18).

The major difference between the mechanism of Burke and Lyons and that due to Joiret et al. arises in the assignment, by the latter of peak IV (A3 in the scheme of the former authors) to the formation of magnetite, which they observed in their Raman analysis, by the following reactions:

$$3Fe(OH)_2 + 2OH^- \rightarrow Fe_3O_4 + 4H_2O + 2e^- \quad (1.4.19)$$

$$3FeO + 2OH^- \rightarrow Fe_3O_4 + H_2O + 2e^- \quad (1.4.20)$$

The cathodic peak IX is then related to the reduction of this magnetite. It must be said that Joiret et al.[167] are far from unique in their proposal of magnetite formation during oxide film growth on Fe in alkaline media. For example McDonald and Owen[180] attributed the second anodic peak in the voltammogram of Fe in 1.0 M LiOH, to the reaction denoted as (1.4.19) in the present work. Amaral et al.[174] on the basis of an involved peak de-convolution procedure and subsequent charge balance calculations in tandem with the thermodynamic predictions of the Pourbaix atlas[150], also envisaged the formation of magnetite at the second anodic peak. Some further direct experimental evidence for the formation of magnetite in iron oyhydroxide films comes from the work of Fierro et al.[181], who applied in-situ Mossbauer spectroscopy to the study of $Fe(OH)_2$ dispersed on carbon in alkaline solution, and found that the

oxidation of this material yielded either, an ensemble of small magnetite particles of different sizes, or a mixture of superparamagnetic and bulk-like magnetite crystals, depending on the exact details of the potential sweep utilised.

Continuing with the peak assignments of Joiret et al.[167], they attribute, on the basis of their Raman data, anodic peaks V and VI to the formation of the ferric species, α-FeOOH and γ-Fe_2O_3, respectively:

$$Fe_3O_4 + OH^- + H_2O \rightarrow 3\alpha\text{-}FeOOH + e^- \quad (1.4.21)$$

$$2Fe_3O_4 + 2OH^- \rightarrow 3\gamma\text{-}Fe_2O_3 + H_2O + 2e^- \quad (1.4.22)$$

The cathodic peak VII is then associated with the reduction of the γ-Fe_2O_3 material, whereas peak VIII is due to reduction of α-FeOOH. Joiret et al. use their EIS results to lend further support to their reaction mechanism. This EIS data shows that the oxyhydroxide film is more conducting at potentials in the vicinity of peaks IV and V as compared to the potential region anodic to peak VI. It is claimed that this decrease in conductivity is due to the oxidation of magnetite, a good electronic conductor, to α-FeOOH and γ-Fe_2O_3, which are poor electronic conductors. Despite the differences in peak assignments Joiret et al.[167] ultimately agree with Burke and Lyons[166] on the structure of the oxyhydroxide film. The former authors conclude that the film consists of a magnetite based inner region, (which endows the oxide with its passivity), while the outer region is a three dimensional structure, the exact composition of which depends on the electrode potential.

In view of the foregoing discussion it is obvious that significant differences in opinion still exist in the literature regarding the chemical composition of the passive layer formed on a polycrystalline iron electrode in alkaline solution. There is, however, general consensus that the outer region of the film, even that formed on the first anodic sweep, is hydrous in nature, while a more compact inner region provides corrosion resistance to the metal. From the point of view of the nature of the surface oxide at the potentials just below that for the onset of significant oxygen evolution, there is general agreement that the outer film, across which much of the potential drop between electrode and solution would be expected to appear, consists predominantly of poor electron conductors such as α-FeOOH and γ-Fe_2O_3.

1.4.3 Cobalt

As with Ni and Fe, a brief review is presented on the electrochemistry of polycrystalline Co in aqueous alkaline solution, with the intention of gaining a conceptual understanding of the oxide surface that facilitates the o.e.r. at high anodic potentials. Cobalt hydroxides were also studied by Bode et al.[133] as part of the seminal work that lead to the development of the Bode scheme of Figure 1.4.3, that has already been discussed in relation to the nickel hydroxide electrode. In an analogous manner to the situation for divalent nickel hydroxides, there exists both hydrous α-$Co(OH)_2$ and the largely anhydrous β-$Co(OH)_2$[133, 145, 182]. The structures of these materials are closely related to the corresponding phases in the nickel system. Again the β(II) phase has a brucite-like, lamellar structure, with the basal plane consisting of edge sharing CoO_6 octahedra[145, 182]. This phase is pink in colour and displays a c_0 distance of 4.65 Å[182]. The α(II) phase contains excess H_2O and has an approximate composition range of $Co(OH)_2 \cdot 0.9\text{-}1.4\ H_2O$[145]. It is blue in colour, has a turbostratic structure, with a mean inter-lamellar distance of 8.4 Å[182].

Benson et al.[183], cathodically deposited blue α-$Co(OH)_2$ on Pt, and observed its oxidation behaviour in an alkaline medium. Chemical oxidation by air yielded, after some time, a brown CoOOH phase, which was found to be very resistant to oxidation beyond a formal Co charge of 2.14. This material has been studied by several workers, has been found to display a c_0 parameter of 4.40 Å, and is denoted as β-CoOOH[182]. On anodic polarisation[183], the α-$Co(OH)_2$ was readily oxidised to a phase, that exhibited an average Co oxidation state of 3.3. The inter-lamellar distance of this phase is 6.80 Å[182] and it has been recognised[145] as the Co analogue of the γ-NiOOH phase discussed in section 1.4.1.

Cyclic voltammograms of polycrystalline Co in 1 M KOH, typical of those observed in the literature, are depicted in Figure 1.4.12. Before discussing the assignment of the peaks in this CV, some experimental results on the system, as obtained by both electrochemical and other means are reviewed.

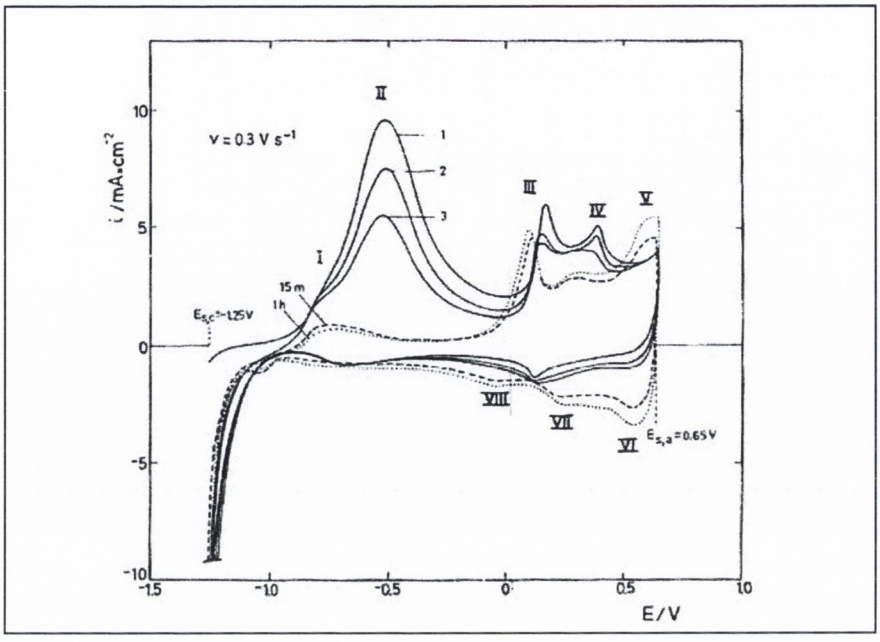


Figure 1.4.12 *Cyclic Voltammograms of a polycrystalline Co electrode in 1M KOH at 25°C vs. Hg/HgO 1M KOH. The sweep rate was 300mV s^{-1}. The first three sweeps and those recorded after both 15 min and 1 hr of cycling are shown. Reproduced from ref. 184.*

In ring disk electrode studies, Behl and Toni[185] observed small but significant amounts of dissolved Co^{2+} species, the concentration of which reached a maximum at potentials just below those corresponding to peak II in Figure 1.4.12. The amount of dissolved Co^{2+} increased with increasing KOH concentration. No soluble Co^{3+} or Co^{4+} species were observed. This data was corroborated, and added to, by a combined rotating ring disk electrode (RRDE), scanning electrochemical microscopy (SECM) study carried out more recently by Erts et al.[186]. In their ring disk electrode experiments, they observed that ~ 3% soluble species were collected in 1M NaOH in the same potential region as Behl and Toni[185] made their soluble species observation. No soluble species were detected at the ring in 0.1 M NaOH[186]. According to Erts and co-workers[186], SECM offers a more accurate method of quantification of concentrations of soluble species since "the tip electrode can be located close to the surface and more short lived species can be detected". In 1.0 M NaOH in the potential region of peak II, they observed that a "much larger fraction of the reaction proceeds through the dissolution/ precipitation path than revealed from RRDE". The disparity between the SECM results and the RRDE data was explained in terms of a rapid precipitation of the soluble Co^{2+} species, with the result that much of the soluble species couldn't escape to the bulk solution and register a ring current. In 0.1 M

NaOH no soluble species were detected by SECM[186], indicating a solid-state oxidation mechanism, in the less concentrated solution.

Ellipsometry measurements have been carried out on electrochemically generated passive films on Co in alkaline solution [187, 188]. The most general conclusion of these studies was that cobalt forms two types of passive layers in alkaline solution. The first is formed at lower potentials, has a pH dependent thickness, and consists of $Co(OH)_2$ and CoO. A second passive layer is formed outside the Co(II) layer at potentials above ca. 0 V (vs. Hg/HgO) and is envisaged to consist of Co(III) and possibly Co(IV) species. X-ray photoelectron spectroscopy (XPS) measurements by Foelske et al.[189] on polycrystalline Co in 0.1 M NaOH, also emphasises the concept of a twin layer type passive film. Below the potential region corresponding to peak III in Figure 1.4.12, the passive layer is described as being a $Co(OH)_2$ film, which can grow to 40 nm thickness, depending on time and potential. Significantly, the authors claim that no CoO was detected, at least in the early stages of passivation. At potentials anodic to peak III the outer layers of the film are said to be dominated by Co(III) species, with the XPS measurements identifying Co_3O_4 and CoOOH. In an XPS investigation of a thick hydrous oxyhydroxide layer formed by multi-cycling a polycrystalline Co electrode in 0.5 M NaOH over a potential range of 650 mV up to just below significant oxygen evolution, the dominant species identified was Co_3O_4[190]. In agreement with the XPS data of Foelske et al.[189], an IR study[191] could identify only the presence $Co(OH)_2$ and not CoO in the lower potential region.

Mössbauer spectroscopy studies performed in the 1970s[192] also indicated that α-$Co(OH)_2$ is the primary hydroxide species in the lower potential region. These studies involved analysis of emission spectra of the ^{57}Fe isotope derived from ^{57}Co isotopes that been plated on natural Co, which was then subjected to anodic polarisation. Perhaps the most significant conclusion of this Mössbauer work was that, at high anodic potentials, the outer surface of a CoOOH film is oxidised to a Co(IV) state.

A very interesting series of papers were published by Šimpraga and Conway, in which voltammetry studies were conducted on polycrystalline Co[190], Fe[193] and Ni[127] in alkaline media at temperatures down to 240 K. The aim of these experiments was to determine whether reversible formation of 2-D arrays of adsorbed OH or O species at sub-monolayer coverage, could be observed at low temperatures, at which re-construction of such 2-D layers into 3-D phase oxide by place exchange is thermally inhibited. It is known[194] in the cases of Pt, Rh, Ru, Ir, Pd, and Au that the initial stages

of formation of anodic oxide films involves the quasi-reversible deposition of sub-monolayer extents of OH or O species. Further formation of the oxide film to monolayer coverage and beyond is highly irreversible due to the occurrence of place exchange processes. Although Šimpraga and Conway[190, 193, 127] noted that sub-monolayer coverage of $Co(OH)_2$, $Fe(OH)_2$ and α-$Ni(OH)_2$ could be achieved on the respective metals, in 0.5 M NaOH in a mixture of 80 mol% CH_3OH + 20 mol% H_2O at ca. 260 K, the formation and reduction processes remained completely irreversible, suggesting a nucleation and growth mechanism, rather than the 2-D surface process observed at the other metals mentioned above. Liu et al.[194], showed that the formation and reduction of the oxide film on Co in 0.5 M NaOH, progresses from the aforementioned irreversible behaviour during early potential cycles, to largely reversible behaviour upon the formation of a thick hydrous oxide with extensive cycling. Two "mirror image" reversible redox peaks, with peak potentials of ca. 525 mV and 225 mV (vs. Hg/HgO) were observed to become increasingly well resolved from about the 600^{th} voltammetric cycle (at 20 mV s^{-1}) through to the 2885^{th} cycle. It was found that the amount of anodic charge reversibly accessible in the 2885^{th} cycle, was only 3% of the total accumulated charge over the course of the film growth. This lead the authors to conclude that, for this thick hydrous oxide film, it is only a surface region layer that displays accessible redox activity.

Regarding the interpretation of the various peaks in the CV of initially bright Co in alkaline solution (see Figure 1.4.12), there appears to be fairly good general agreement between the various authors who have tackled this problem[184, 185, 190, 194-196]. The approach adopted in most of the aforementioned works is based on that of Behl and Toni[185] who compared the observed peak potentials with thermodynamic data. Thus, peak I (Fig 1.4.12) is attributed to the formation of adsorbed OH species on the electrode surface:

$$Co + OH^- \leftrightarrows CoOH_{ads} + e^- \qquad (1.4.23)$$

The major peak II, is attributed to a combination of the formation of a passivating film of $Co(OH)_2$ and/or CoO,

$$Co + 2OH^- \leftrightarrows Co(OH)_2 + 2e^- , \qquad (1.4.24)$$

$$Co + 2OH^- \leftrightarrows CoO + H_2O + 2e^- , \quad (1.4.25)$$

and on the basis of the ring disk electrode, and SECM measurements previously mentioned, a dissolution process forming the slightly soluble[196] Co(II) species $CoO{\cdot}OH^-$:

$$Co + 2OH^- \rightarrow CoO{\cdot}OH^-(aq) + H^+ + 2e^- \quad (1.4.26)$$

With repetitive potential cycling (Fig 1.4.12), it is obvious that the magnitude of peak II decreases, while the peak potential shifts to more negative values. While the charge associated with peak II is observed to decrease over the first three cycles, the magnitude of the corresponding broad cathodic peak at ca. –0.6 → -0.85 V (Hg/HgO) is observed to remain approximately invariant. Šimpraga[190] noted that the ratio of the charges associated with this set of corresponding anodic and cathodic peaks in 0.5M NaOH at 298 K, became unity after ca.15 cycles in the potential range of approximately –1.125 to -0.325 V (vs. Hg/HgO). Similar observations were made by other workers[194-196]. This behaviour has been attributed to the stabilisation of the developing anodic film with respect to the dissolution process of equation (1.2.26), so that after a number of cycles the anodic peak in the potential region of –0.6 to –0.8 V (Hg/HgO) should be almost entirely due to a solid state process. While the formation of a passivating CoO film according to equation (1.2.25), is proposed by several authors[184, 185, 190, 195, 196], it is noteworthy that, as mentioned above, more recent IR[191] and XPS[189] studies have discounted the formation of this particular Co(II) species, at least under certain conditions.

The rather poorly distinguished peaks III and IV are attributed to the oxidation of Co(II) species to Co(III) species. It is obvious that the voltammetric profile in this region changes significantly with cycling, tending eventually to the type of reversible behaviour observed by Liu et al.[194] and described above. On the first voltammetric sweep, thermodynamic data[185] indicates that the oxidation of Co(II) species should begin in the region of –0.4 V (vs. Hg/HgO, 1M KOH), with Co_3O_4 being the initial oxidation product. Gomez Meier et al.[184] envisage this process in terms of the oxidation of an inner CoO layer to Co_3O_4 according to,

$$3CoO_{inner} + H_2O \leftrightarrows Co_3O_4 + 2H^+ + 2e^- , \quad (1.4.27)$$

while Burke et al.[118] commented that an illustrative rationalisation of the process could be provided by the reaction:

$$3Co(OH)_2 + 2OH^- \leftrightarrows Co_3O_4 + 4H_2O + 2e^- \quad (1.4.28)$$

As regards the actual peaks denoted III and IV in Figure 1.4.12, Burke and co-workers[196] commented that "in view of the large background currents in the anodic sweep, in the region above about 0.6 V(vs. R.H.E. ≈ - 0.325 V vs. Hg/HgO IM), that a hydrous Co(II) film is gradually converted to such Co(III) containing species as Co_3O_4, Co_2O_3 and CoOOH". They point out that, the situation is further complicated by a number of other factors, such as the existence (according to Benson et al.[183]) of three forms of CoOOH, i.e. CoOOH(I), CoOOH(II) and $CoHO_2$. These authors add, that hydration effects will tend to render inaccurate, the assignment, on the basis of thermodynamic data, of closely spaced peaks to specific Co(II)→Co(III) transitions. Gomez Meier et al.[184] also allude to the complex hydrous nature of the anodic oxide formed on Co in alkaline solution. These authors view the oxide growth process in terms of the formation of "sandwich-type" structures, with a $Co/CoO/Co(OH)_2$ "sandwich" formed at lower potentials. They then envisage the oxidation of a hydrous form of this "sandwich" to form a new hydrated "sandwich" structure at more positive potentials (peak III), according to the process,

$$[Co(CoO)(Co(OH)_2)\cdot xH_2O] \rightarrow [Co(CoO)(CoOOH\cdot x'H_2O)] + H^+ + x''H_2O + e^- \quad (1.4.29)$$

where, x"= x'+x. The nature of the "sandwich" will further change with increasing potential, with the CoO component being oxidised to Co_3O_4. According to this viewpoint, peak IV will then correspond to a process along the lines of:

$$[Co(Co_3O_4\cdot CoOOH)] + 2\,H_2O \rightarrow [Co\,(CoOOH)_4] + H^+ + e^- \quad (1.4.30)$$

On the basis of a perceived correlation between their voltammetric peak data and the predictions of thermodynamics, Gomez Meier et al.[184], conclude that, in the formation of the anodic film on Co, "the electrochemical reactions involve fast proton transfers,

and that the advance in the degree of oxidation of the metal is accompanied by a deprotonation and change in the water content at different parts of the complex electrochemical interface".

While Burke et al.[196] and Gomez Meier et al.[184] may disagree on the validity of using thermodynamic predictions to assign exact processes to given anodic peaks, there is agreement between these authors, and indeed others[190, 194] that peak V is due to a surface Co(III) to Co(IV) oxidation. Burke et al.[196] attribute an electrochromic effect observed in this potential region to this Co(III) → Co(IV) transition, a process that they represent as:

$$CoOOH\ (orange) + OH^- \leftrightarrows CoO_2\ (dark\ brown) + H_2O + e^- \qquad (1.4.31)$$

The charge associated with peak V increases on cycling, indeed cathodic peak VI corresponding to the reduction of Co(IV) species is virtually absent on the first cycle – peaks V and VI only become well defined at appreciable film thickness. This observation in tandem with the conclusions of Liu et al.[194], that the accessible reversible charge in a thick Co oxyhydroxide film resides adjacent to the surface, indicates very strongly that the oxidation of Co(III) to Co(IV) species is predominantly a surface process, occurring at the interface between a hydrous oxide layer and the solution phase. In the context of the present work, this formation of surface Co(IV) species is likely to be quite significant, occurring as it does at potentials immediately below those associated with a significant oxygen evolution current. Regarding the relatively small charge associated with the Co(III) ⇆ Co(IV) transition during the initial potential cycles, Burke et al.[196] comment that the initial film is possibly "of such a compact nature that the increase in oxygen coordination necessary to produce CoO_2 does not occur readily or, alternatively, the layer may not be of a porous hydrated structure".

The relatively small amounts of charge associated with the cathodic peaks in Figure 1.4.12 during the early potential cycles, indicates that the initially formed passivating film is not easily reduced. Peak VIII and the broad ill-defined cathodic peak at potentials between approximately –0.4 and –0.8 V (vs Hg/HgO, 1M KCl) are generally attributed to the reduction of Co(III) species[118, 184, 185, 190, 194-196]. Although it is not particularly apparent in Figure 1.4.12, probably owing to the relatively fast scan rate at which these CVs were recorded, most workers[118, 190, 194, 196] have observed a

reasonably well-defined peak at ca. –1.0 V (vs. Hg/HgO, 1M). This peak is associated with the reduction of Co(II) species. As previously described, Liu et al.[194], have attributed the increasing reversibility achieved with increasing film thickness, to redox processes in the vicinity of the hydrous oxide surface. The contrast between this behaviour and the irreversibility noted during the earlier stages of film formation, reinforces the concept of the initially formed oxide (or inner regions of a thick film) being difficult to reduce.

1.5 The Oxygen Electrode

The electrochemical reduction of oxygen to water, and its evolution from water, have received much research attention, owing to the importance of these reactions in practical applications and also due to their intrinsic complexity. Oxygen reduction is the normal cathodic reaction in electrochemical energy conversion and thus optimising this reaction is the key to achieving maximum fuel oxidation in fuel cell systems. The oxygen reduction reaction (o.r.r.) is also of interest in metal-air batteries, and in corrosion studies since it serves as the counter electrode reaction in many corrosion systems. The oxygen evolution reaction (o.e.r.) is commercially important in alkaline water electrolysis, and as a counter electrode reaction for electrowinning. While one would seek to reduce the operational overpotential for the o.e.r. in an electrolysis cell, the optimisation of certain other processes calls for the inhibition of the o.e.r. For example, oxygen evolution is a competing anodic process for oxidative synthesis reactions such as chlorine production, while the o.e.r. can be detrimental to the operation of secondary alkaline batteries, owing to the so-called "self discharge" process.

The present review will commence with a treatment of some of the thermodynamic aspects of the oxygen electrode, before moving on to a brief description of the o.r.r. Finally, a detailed literature review of the oxygen evolution reaction and associated issues will be presented.

1.5.1 The Thermodynamics of the Oxygen Electrode

The thermodynamics of the oxygen electrode reaction has been discussed in detail by Hoare[197], Tarasevich et al.[198], and more recently in a succinct form by Lasia[94]. The following treatment is based upon the aforementioned works. Thus, the oxygen

electrode reactions in both aqueous acidic (pH 0) and alkaline (pH 14) solutions at 25°C are represented by equations (1.5.1) and (1.5.2) respectively:

$$O_2 + 4H^+ + 4e^- \leftrightarrows 2H_2O \qquad E^0 = 1.229 \text{ V (vs. N.H.E.)} \qquad (1.5.1)$$

$$O_2 + 2H_2O + 4e^- \leftrightarrows 4OH^- \qquad E^0 = 0.401 \text{ V (vs. N.H.E.)} \qquad (1.5.2)$$

The values of the standard potentials as quoted above have been calculated, from the best available literature values for the Gibbs free energy of formation of the various products and reactants in reactions (1.5.1) and (1.5.2) respectively. The Nernst equation for reactions (1.5.1) and (1.5.2) can be written, respectively as,

$$E = E^0 + \frac{RT}{4F}\ln p_{O_2} + \frac{RT}{F}\ln a_{H^+} - \frac{RT}{2F}\ln a_{H_2O} \qquad (1.5.3)$$

$$E = E^0 + \frac{RT}{4F}\ln p_{O_2} + \frac{RT}{F}\ln a_{OH^-} - \frac{RT}{2F}\ln a_{H_2O} \qquad (1.5.4)$$

where p_{O_2} denotes the partial pressure of gaseous oxygen. Examining equations (1.5.3) and (1.5.4), it is obvious that the oxygen electrode exhibits a shift in reversible potential E, with H_3O^+ or OH^- activity of RT/F per pH unit ($\approx$ 59 mV/pH unit).

Experimental determination of the thermodynamic rest potential for the oxygen electrode has proved to be very difficult, owing to the irreversibility of the electrode reaction, even on noble metal electrodes, at which, i_0 is typically of the order of 10^{-10} A cm^{-2} at 25°C[199]. This is in stark contrast to the situation for the hydrogen electrode reaction – $H^+ + e^- \leftrightarrows \frac{1}{2} H_2$. The reversible potential for this reaction is easily achievable in acidic solution with a fixed H_2 gas pressure, leading to the choice of the N.H.E. as the standard reference potential scale in aqueous electrochemistry. The essential difficulty in establishing the reversible potential arises from the low exchange current value – thus even very low concentrations of depolarising impurities will offset the oxygen reaction. Tarasevich et al.[198] have commented that even with very carefully prepared systems, the observed reversible potential at a Pt electrode in acidic solution with oxygen partial pressure of 1 atm. at 25°C rarely exceeds 1.1 V vs. N.H.E. What is actually observed is a so-called *mixed potential* which is the net result

of the simultaneous occurrence of two or more steady state electrode reactions. This situation is depicted schematically for the oxygen electrode in acidic solution in Figure 1.5.1.

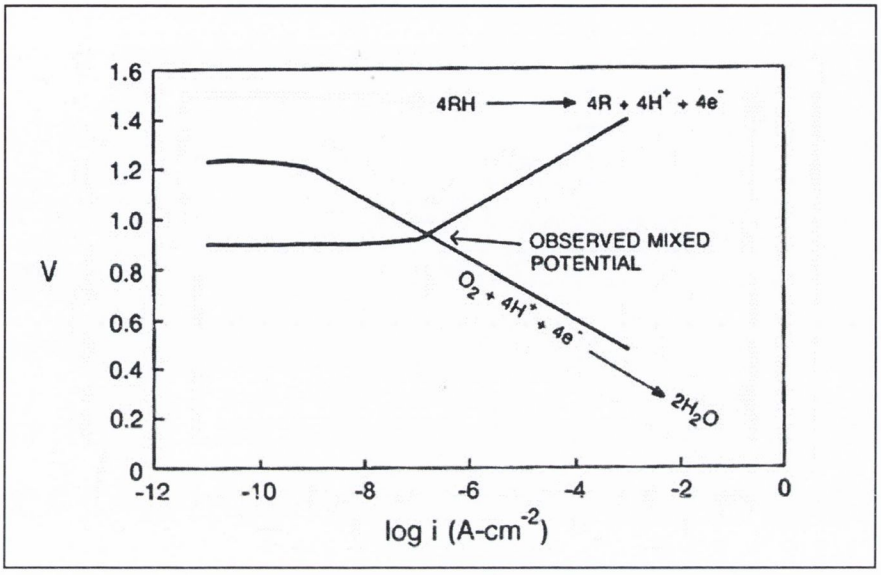


Figure 1.5.1 *Schematic representation of the experimental observation of a mixed potential, for a Pt electrode in acidic solution in the presence of O_2 and an anodically oxidisable impurity RH. Reproduced from ref. 199.*

Considering the model presented in Figure 1.5.1, the observed cathodic shift in open circuit potential from the thermodynamic reversible potential, would have to be caused by some anodic electrode reaction, providing a current of ~ 10^{-7} A cm^{-2}, to balance the oxygen reduction current at the open circuit potential. Several theories have been advanced as to the nature of the possible depolarising reactions. Wroblowa et al.[200] considering the case of the oxygen reduction reaction at an oxide free Pt electrode in contact with an acidic solution containing O_2, proposed that the observed open circuit potential might arise from a mixed potential between the oxygen reduction reaction and an anodic reaction involving impurities. These authors listed a number of potential anodic reactions, including the following

$$Pt + 2H_2O \leftrightarrows Pt(OH)_2 + 2H^+ + 2e^- \qquad E^0 = 0.98 \text{ V (vs. N.H.E.)} \qquad (1.5.5)$$

$$Pt + H_2O \leftrightarrows PtO + 2H^+ + 2e^- \qquad E^0 = 0.88 \text{ V (vs. N.H.E.)} \qquad (1.5.6)$$

$$H_2O_2 \leftrightarrows O_2 + 2H^+ + 2e^- \qquad E^0 = 0.68 \text{ V (vs. N.H.E.)} \qquad (1.5.7)$$

Bockris and Oldfield[201] emphasised the possible role of reaction (1.5.7) in determining the observed open circuit potential, while Giner[202] also suggested a mixed potential based on the O_2/H_2O_2 couple and the Pt/chemisorbed O_2 couple. In his book on the electrochemistry of oxygen, Hoare[197] is dismissive of the concept of peroxide species governing the mixed potential. His counter proposal is that the O_2/H_2O couple and a Pt/PtO couple (PtO refers to a layer of adsorbed oxygen atoms on the Pt surface) contribute to the observed open circuit potential.

The reversible oxygen potential was, first experimentally observed by Bockris and Huq[203] in 1956. These workers noted the Tafel plot for the o.e.r. deviated from the theoretical linear relation at progressively lower current densities as increasingly severe cathodic electrolysis was used to purify the electrolyte solution. To ultimately attain the reversible potential, they found that it was necessary to follow the cathodic electrolysis by an anodic purification electrolytic procedure. Strong experimental verification that the observed potential, was indeed the reversible oxygen potential, was provided by the fact that the measured potential conformed to the p_{O2} dependence predicted by equation (1.5.3).

The extreme irreversibility of the oxygen evolution and reduction processes, means that practical experimental kinetic studies on the respective reactions must be conducted at widely separated potentials. As a result of this, it is inevitable that the electrode surface differs considerably at the experimental potential windows of the reduction and evolution reactions, and hence the anodic and cathodic processes are not complementary. It has, for example, been known since the 1960s[197] that while the o.r.r may proceed on both oxide-covered and bare electrode surfaces, the o.e.r. will always occur on a phase oxide surface. Therefore the principle of microscopic reversibility cannot be applied to mechanistic analysis based on current-potential data, and hence, such data can only provide information up to the rate-determining step. Earlier studies of the o.r.r. and o.e.r. used the experimentally determined value of the stoichiometric number v (see equation (1.2.83, section 1.2.3), calculated from the measured values of the cathodic and anodic Tafel slopes (b_c and b_a respectively), as a criterion in matching experimental data to a proposed reaction mechanism. However, Parsons' analysis[74], which yielded the relation between v and b_c and b_a, insisted upon a common transition state for both anodic and cathodic reactions, a situation that is unlikely to prevail for the oxygen electrode reactions, owing to differences in the

nature of the catalytic surfaces on which they occur. The dubiousness inherent in using the value of v, as determined from equation (1.2.83), as a criterion in mechanistic determinations for the o.r.r. and o.e.r., was well established by the time of Hoare's 1968 book[197].

1.5.2 The Oxygen Reduction Reaction

It has been commented by Bockris and Khan[199], that "were one to choose a single electrode reaction having the greatest breadth of practical relevance, it would certainly have to be the oxygen reduction reaction (o.r.r.)". Owing to its range of practical applications (see the introduction to section 1.5) the o.r.r. has been extensively studied, and therefore there exists numerous reviews on the topic that have appeared over the years, including those due to Hoare[3], Tarasevich et al.[198], Damjanovic[204], Kinoshita[146], Bockris and Khan[199], and Gattrell and MacDougall[205] to name but a few. Although the kinetics and mechanism of the o.r.r. are dependent on the electrocatalytic electrode material and the nature of the electrolyte solution, it is accepted that the overall process in aqueous solution proceeds via one of two overall pathways. The first of these is the *direct four electron pathway*, also referred to as the *parallel pathway*[205], and it can be represented by equations (1.5.8) and (1.5.9) for acidic and alkaline solutions respectively:

$$O_2 + 4H^+ + 4e^- \leftrightarrows 2H_2O \qquad E^0 = 1.229 \text{ V (vs. N.H.E.)} \qquad (1.5.8)$$

$$O_2 + 2H_2O + 4e^- \leftrightarrows 4OH^- \qquad E^0 = 0.401 \text{ V (vs. N.H.E.)} \qquad (1.5.9)$$

The E^0 values quoted, refer to the N.H.E., with electrolyte solutions of pH 0 for reaction (1.5.8) and pH 14 for reaction (1.5.9), and with all species in their standard states at 25°C.

The alternative pathway is the *peroxide* or *series* path. This starts with a two electron reduction process, represented by equations (1.5.10) and (1.5.11) for acidic and alkaline electrolytes respectively:

$$O_2 + 2H^+ + 2e^- \leftrightarrows H_2O_2 \qquad E^0 = 0.67 \text{ V (vs. N.H.E.)} \qquad (1.5.10)$$

$$O_2 + H_2O + 2e^- \leftrightarrows HO_2^- + OH^- \qquad E^0 = -0.065 \text{ V (vs. N.H.E.)} \qquad (1.5.11)$$

These steps may be followed by the chemical decomposition of the peroxide species, according to equations (1.5.12) for acidic solutions and (1.5.13) for basic solutions:

$$2H_2O_2 \rightarrow 2H_2O + O_2 \qquad (1.5.12)$$

$$2HO_2^- \rightarrow 2OH^- + O_2 \qquad (1.5.13)$$

Alternatively, the peroxide species formed by reactions (1.5.10) and (1.5.11), may be electrochemically reduced, as represented by equations (1.5.14) and (1.5.15) respectively:

$$H_2O_2 + 2H^+ + 2e^- \leftrightarrows 2H_2O \qquad E^0 = 1.77 \text{ V (vs. N.H.E.)} \qquad (1.5.14)$$

$$HO_2^- + H_2O + 2e^- \leftrightarrows 3OH^- \qquad E^0 = 0.867 \text{ V (vs. N.H.E.)} \qquad (1.5.15)$$

As will be discussed below, the four electron pathway, consists of a number of intermediate steps, which may or may not involve an adsorbed peroxide intermediate species – however this direct pathway will not lead to solution phase peroxide. In contrast peroxide will exist as a solution phase species in the series path. This suggests that the rotating ring disk electrode studies, on the o.r.r. at a given electrode in a particular electrolyte, should allow the determination of whether the reaction proceeds via the two electron or four electron reduction. If a ring current due to dissolved peroxide is observed then it can be concluded that the two electron path is operative, whereas no peroxide ring current would be expected for the four electron path. A problem arises with such an analysis, in the case of the series mechanism, where the electrochemical reduction of peroxide according to reactions (1.5.14) or (1.5.15), occurs at a much greater rate than the chemical decomposition of reactions (1.5.12) or (1.5.13). In this case the peroxide ring current would be very small and the analyst might be lead to the mistaken conclusion of a direct four electron pathway.

An approach towards circumventing this problem was initially proposed by Damjanovic et al.[206] in the 1960s, and has been described by Bockris and Khan[199] as a "development of special note" in the study of the o.r.r. Damjanovic et al.[206] proposed

the simple alternative pathways model depicted in Figure 1.5.2. The scheme depicted in the figure, distinguishes between the peroxide mechanism via the steps characterised by rate constants k_2 and k_3, and the direct mechanism, with its earlier breaking of the O-O bond, characterised by rate constant k_1. Considering the steady state rate equations, these workers derived the following expression for the relation between the ratio of the disk current to the ring current I_D/I_R and the RRDE rotation rate ω,

$$\frac{I_D}{(I_R/N)} = \left(\frac{4k_1}{2k_2} + 1\right) + \left(\frac{4k_1}{2k_2} + 2\right) k'\omega^{-1/2} \qquad (1.5.16)$$

where, N is the ring collector efficiency and $k' = 1.61D^{-2/3}\nu^{1/6}k_3$ (D is the diffusion coefficient of peroxide and ν is the kinematic viscosity).

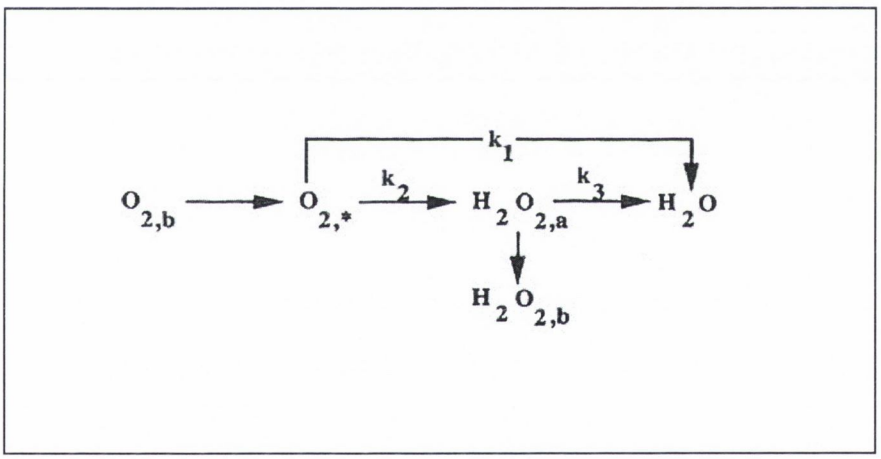


Figure 1.5.2 *Model for oxygen reduction in aqueous electrolytes as proposed by Damjanovic et al.[206]. Key: a – adsorbed on electrode surface, * - in vicinity of electrode surface, b – in bulk solution. Reproduced from ref. 146.*

By fitting the experimental I_D/I_R (ω) data to equation (1.5.16) it should be possible to determine the k_1/k_2 ratio, and thereby (recalling that for parallel reaction steps the faster one will predominate), ascertain whether the o.r.r. proceeds via the four electron, or two electron route. Equation (1.5.16) is based on the assumption that the rate of release of the soluble peroxide species from the disk is governed by mass transport, which results in its dependence on rotation rate. This might not necessarily be the case, and in addition the simple model of Damjaniovic et al.[206] is not

sufficiently general[205] in that it doesn't include processes such as peroxide decomposition, and adsorption and desorption of reactants and products. This has limited its application to real systems, although it is reported[146] that the conclusions from Pt RRDE studies of oxygen reduction in aqueous solutions of H_2SO_4, H_3PO_4, $HClO_4$ and KOH have been shown to be consistent with the model of Damjaniovic et al.[206]. More sophisticated modifications of the original model of Damjanovic et al. have been proposed by Wroblowa et al.[207], Appleby and Savy[208] and Anastasijevic et al.[209] amongst others. The model of Anastasijevic et al.[209] is depicted in Figure 1.5.3, and serves to show the potentially complex nature of the oxygen reduction reaction.

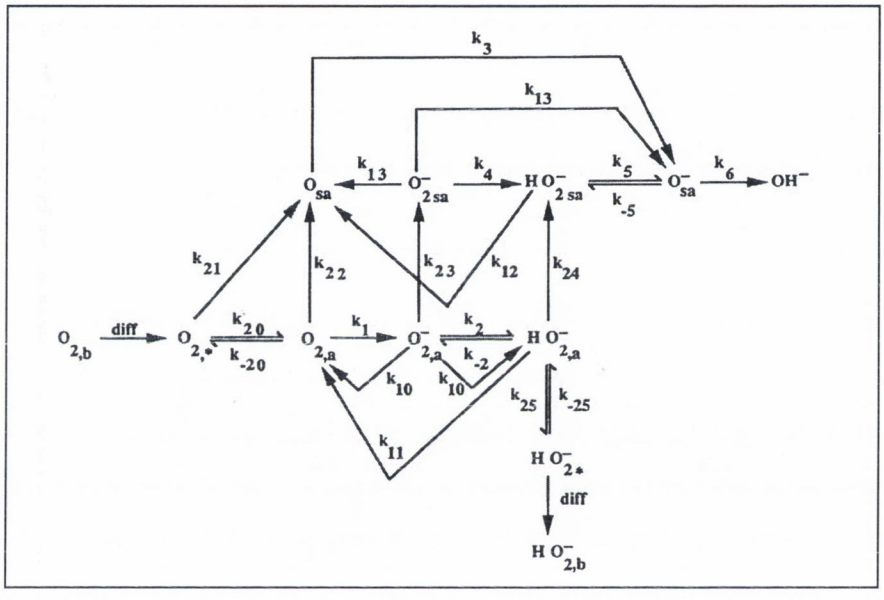


Figure 1.5.3 *Model for oxygen reduction in aqueous alkaline solution proposed by Anastasijevic et al. [209]. Key: a – adsorbed on electrode surface, * - in vicinity of electrode surface, b – in bulk solution, sa – strongly adsorbed, wa – weakly adsorbed. Reproduced from ref. 146.*

The operative pathway for the o.r.r. depends strongly on the nature of the electrode surface. It would be reasonable to expect that materials that interact strongly with oxygen could bring about the dissociation of the O-O bond, thus readily facilitating the four electron mechanism. On the other hand, the two electron reduction to peroxide is more likely for electrode materials that have weak interaction with oxygen. It has been observed[146, 205] that the direct four electron reduction is the most likely mechanism on the following substrates; the noble metals Pt, Pd, Ag, Pt alloys, perovskites, some transition metal macrocycles, metallic iron in neutral solution, and the gold (100) surface in alkaline solution. The peroxide mechanism is generally

observed[146, 205] for graphite and other carbon materials, gold (except the particular example mentioned above), mercury, most oxide covered metals including Ni and Co, mercury, most transition metal oxides e.g. NiO, and the passive film on iron in neutral solution. Platinum and its alloys generally display the greatest electrocatalytic activity towards the o.r.r., and are found in the vicinity of the 'apex' of volcano plots, correlating o.r.r. activity against various physicochemical parameters - e.g. see Figure 1.3.3 section 1.3.3.

There exists in the literature several comprehensive summaries of step-wise reaction mechanisms. The first of these was due to Damjanovic et al.[77] who listed 14 mechanistic schemes along with their theoretical Tafel slopes (calculated on the basis of Langmuir adsorption conditions) and stoichiometric numbers. Gnanamuthu and Petrocelli[210] listed 16 reaction schemes (the 14 listed in reference 77 plus 2 more) and indicated if a particular step was a candidate for RDS in either acid or alkaline solution, based upon the experimental data known for Pt and Au at the time. The most comprehensive and informative list of o.r.r. mechanisms is that due to Pillai and Bockris[70]. This summary quotes 17 mechanisms, along with the predicted Tafel slopes, and reaction orders with respect to both oxygen partial pressure and H_3O^+ or OH^- concentration, in the case of any given step in any mechanism being the RDS. The theoretical mechanistic parameters are quoted for both Langmuir type ($\theta \rightarrow 0$ and $\theta \rightarrow 1$ cases) and Temkin type adsorption of the reaction intermediates. Obviously, the reverse of any listed o.r.r. mechanism provides a potential o.e.r. mechanism, but as was discussed in section 1.5.1, it cannot in general be assumed, that if a particular oxygen reduction mechanism applies to a given system, that the reverse of the same mechanism is operative for oxygen evolution from that system.

1.5.3 General Comments on the Oxygen Evolution Reaction

Since, the principle focus of the present work is on the o.e.r., at polycrystalline Ni, Co and Fe electrodes in aqueous alkaline solution, a detailed review is now presented on the literature in this area. Although discussion of the nature of the reaction on the three aforementioned metals will receive priority in this review, many potentially relevant experimental observations have been made on other electrodes and in acidic solution, and some of these will also be included.

Amongst the numerous reviews on various aspects of the o.e.r., are those courtesy of Hoare[197], Damjanovic[211], Horiuti[212], Appleby[213], Trasatti and Lodi[214], Burke[215], Lyons[168], Bockris and Khan[199], Kinoshita[146], and Gattrell and MacDougall[205]. These works have been consulted in the compilation of the present review, in addition to the primary literature that will be cited.

Modern studies of the oxygen evolution reaction can be traced back to the important 1956 work of Bockris and Huq[203], which has already been discussed in section 1.5.1 in relation to the experimental observation of the oxygen electrode thermodynamic reversible potential, at Pt in rigorously purified H_2SO_4 solution. Work on the o.e.r. has been focused on gaining an understanding of the reaction mechanism, and on the development of anode materials that display stability and high catalytic activity towards the reaction. The driving forces behind this work include the need to improve the operational efficiency of alkaline water electrolysers, as well as the intrinsic scientific interest in the o.e.r. from the point of view of developing a better understanding of electrocatalysis in general.

A consideration, that must be ever present in any study of oxygen evolution anodes, is that oxide growth is a parallel electrochemical process that always accompanies the o.e.r., be it on initially oxide free metallic electrodes or on metal oxide electrodes. Thus, the possible impact of oxide growth and the influence of the oxide surface must always be bourn in mind when dealing with the o.e.r. This matter will be discussed in tandem with kinetic and electrocatalytic considerations throughout this review. At the outset it is noted[146] that, in general, oxygen evolution on noble metal anodes (e.g. Pt, Ir, Rh, Ru) occurs at potentials where relatively thin oxide films are present. On base metals, such as those of interest in the present work, the oxide layers are likely to be significantly thicker. The work of Šimpraga and Conway[127, 190, 193] as was discussed in section 1.4.3 is worth recalling in this regard.

In general it has been found[146] that anodes composed of bulk metal oxides such as RuO_2, IrO_2, NiO and perovskites have superior electrocatalytic activity towards the o.e.r. relative to metallic electrodes. Briefly, addressing the question as to what general factors, dictate whether a material is a useful o.e.r. electrocatalyst or not, Ruetschi and Delahay[216] proposed that the electrocatalytic activity of metallic electrodes decreased with an increase in metal-OH bond strength. Tseung and Jasem[217] performed a review of the properties of twenty metal oxides in order to provide "guidelines for the choice of semiconducting oxides as oxygen evolving

electrodes". The properties they considered were; the equilibrium potential of the metal/metal oxide or lower metal oxide/higher metal oxide couples, the conductivity, the corrosion resistance at pH 14, and the oxygen reduction performance. They found that it was difficult to get an oxide that fulfilled all of their criteria, but perhaps significantly in the context of the present work, they concluded that the most suitable candidate couples were Co_2O_3/CoO_2, Ni_2O_3/NiO_2, and 'lower' Co_2NiO_4/Co_2NiO_4. The later material, a spinel type oxide, was found to be preferable to the former two, owing to its superior electrical conductivity. While bulk RuO_2 had suitable electrical, and catalytic properties, its poor corrosion resistance in concentrated alkaline solution was highlighted by Tseung and Jasem[217], although they did note that when coated on Ti it would prove more stable with respect to corrosion. Miles et al.[218] observed the following trend in electrocatalytic activity of metal oxides towards the o.e.r. in alkaline solution Ru >Ir~Pt~Rh~Pd~Ni~Os>>Co>>Fe. Poor activities were observed on V, Cr, Mo, W, Mn, and Re oxide electrodes. The metal oxides were thermally prepared by electrodepositing from the appropriate metal chloride, and the electrocatalytic activity was measured in 30wt% KOH solutions at 80°C.

Indeed it is accepted nowadays[146, 214] that ruthenium oxide (RuO_x) is the best electrocatalyst towards the o.e.r., especially in acidic solution where it is less prone to corrosion than in alkaline electrolyte. One of the factors contributing to its success as an o.e.r. electrocatalyst is its high electronic conductivity. Bulk samples of RuO_x display a metallic-like conductivity[146] (2×10^4 - 3×10^4 $\Omega^{-1}cm^{-1}$ at room temperature), in comparison to most other metal oxides, which, as was discussed in chapter 1, are generally semiconductors or insulators. RuO_2 electrodes are generally prepared[214] by the thermal decomposition of $RuCl_3$, which is applied as a thin coating on a metallic substrate (generally Ti). Such electrodes are often called dimensionally stable anodes or DSAs. In contrast to the thermally prepared oxide, the anodic oxide film that forms on a metallic Ru electrode is a poor electrocatalyst towards the o.e.r. in alkaline solution[219]. Burke and Whelan[219] proposed that the poor electrocatalytic activity of the anodic oxide, arose, owing to a high rate of dissolution at positive potentials, with appreciable oxygen evolution currents only being observed at an overpotential of ca. 1.0 V. These workers envisaged that the anodically generated oxide layer was amorphous and hydrous in its outer region and contained a high defect concentration. The cations in the oxide film therefore exhibit a higher coordination number relative to those in the thermally prepared oxide, in which cation-cation bonding via oxygen

bridging, is relatively stronger. The higher coordination number of the cations in the anodic film would allow them to pass easily into solution upon oxidation. IrO_2 also displays a low overpotential for oxygen evolution, however it is prone to corrosion in both acidic[146] and especially in alkaline[218] media.

The high corrosion resistance and relatively low cost of Ni and its alloys have lead to these metals becoming the most utilised anode materials for alkaline water electrolysis[146, 220]. The choice of Ni as the anode material involves something of a balancing act, in that, while it offers advantages in cost and stability relative to other electrocatalytic materials, it also suffers from the disadvantage of having a higher oxygen evolution overpotential than, for example, RuO_2. The anodic overpotential is a major factor in limiting the operational efficiency of alkaline water electrolysers[220], and thus efforts have been made to lower the value of this parameter as displayed by Ni. An approach[220] that has achieved some success in improving the efficiency of porous Ni anodes, involves impregnating the surface with $Ni(OH)_2$, which has the effect of lowering the overpotential by up to 60 mV in 30%wt KOH at 80°C.

1.5.4 Reaction Pathways for the Oxygen Evolution Reaction

It has been pointed out by Milner[221], that an enormous amount of pathways for the o.e.r. can be envisaged, if all possible reaction intermediates are taken into account. This point is easy to appreciate if one considers the o.e.r. as the reverse of the model for the o.r.r., proposed by Anastasijevic et al.[209] and depicted in Figure 1.5.3. Hoare[197] and Kinohita[146] both point out that if a number of assumptions are admitted, the number of possible pathways can be reduced to ten or eleven. A further problem inherent in attempts at kinetic mechanistic analysis, lies in the fact, that even with this reduced number of candidate mechanisms, the values of kinetic parameters (such as Tafel slopes) predicted for a given path are not unique. Hence it is often very difficult to unambiguously identify the pathway operative for a particular system, however the compilation of further experimental evidence (beyond Tafel slopes) can point the analyst in a particular direction.

An early kinetic mechanistic analysis of possible o.e.r. pathways was produced by Bockris[69] in 1956. In this work, as has been discussed at length in section 1.2.3, the Christiansen method was applied to calculate the expected values of the Tafel slope under Langmuir intermediate adsorption conditions, in the case of any given step in a

multistep mechanism being rate-determining. Five possible pathways were analysed. This analysis was advanced a step further by Conway and co-workers[78, 153, 155], who derived the predicted kinetic parameters for various pathways in the case of Temkin adsorption of intermediate species. Damjanovic et al.[77], listed 14 possible o.e.r. pathways giving the predicted Tafel slope value at both limitingly low and high adsorbed intermediate coverage, in the event of any given step in any one of the pathways being the RDS. Reproduced here as Table 1.5.1 is a more succinct summary of the diagnostic criteria of proposed paths for the o.e.r., that was originally provided by Bockris and Otagawa[42]. These authors describe the five particular mechanisms listed in Table 1.5.1 as being "the paths most often considered in oxygen evolution studies".

		Langmuir				Temkin				
		$\partial V/\partial \ln i$		$(\partial \ln i/\partial \ln C_{OH^-})_{V,\zeta}$[c]		$\partial V/\partial \ln i$				
rate-determining step	ν[b]	$\theta \to 0$	$\theta \to 1$	$\theta \to 0$	$\theta \to 1$	NA[d]	A[e]	NA[d]	A[e]	condition[f]
(I) Bockris's Oxide Path										
1. $M + OH^- \to MOH + e^-$	4	$2RT/F$		1						
2. $2MOH \to MO + M + H_2O$	2	$RT/2F$	∞	2	0	$2RT/F$		0.5		$r_{OH} \sim r_O$
						RT/F		1		$r_{OH} >> r_O$
3. $2MO \to 2M + O_2$	1	$RT/4F$	∞	4	0	$RT/2F$	RT/F	2	1	$K_3 \sim 1$
						$RT/4F$	$RT/3F$	2	1	$K_3 << 1$
(II) Bockris's Electrochemical Path										
1. $M + OH^- \to MOH + e^-$	2	$2RT/F$		1						
2. $MOH + OH^- \to MO + H_2O + e^-$	2	$2RT/3F$	$2RT/F$	2	1	$2RT/F$		1		$r_{OH} \sim r_O$
						RT/F		1.5		$r_{OH} >> r_O$
3. $2MO \to 2M + O_2$	1	$RT/4F$	∞	4	0	$RT/2F$	RT/F	2	1	$K_3 \sim 1$
						$RT/4F$	$RT/3F$	4	3	$K_3 << 1$
(III) Krasil'shchikov's Path										
1. $M + OH^- \to MOH + e^-$	2	$2RT/F$		1						
2. $MOH + OH^- \to MO + H_2O$	2	RT/F	∞	2	1	∞		1		$r_{OH} \sim r_O$
						$2RT/F$		1.5		$r_{OH} >> r_O$
3. $Mo^- \to MO + e^-$	2	$2RT/3F$	$2RT/F$	2	0	$2RT/F$		0		$K_2 \sim 1$
						$2RT/F$		1		$K_2 << 1$
4. $2MO \to 2M + O_2$	1	$RT/4F$	∞	4	0	$RT/2F$	RT/F	2	1	$K_3 \sim 1$
						$RT/4F$	$RT/3F$	2	1	$K_3 << 1$
(IV) O'Grady's Path										
1. $M^z + OH^- \to M^zOH + e^-$	2	$2RT/F$		1						
2. $M^zOH \to M^{z+1}OH + e^-$	2	$2RT/3F$	$2RT/F$	1	0	$2RT/F$		0		$r_1 \sim r_2$[g]
						RT/F		0.5		$r_1 >> r_2$
3. $2M^{z+1}OH + 2OH^- \to 2M^z + H_2O + O_2$	1	$RT/4F$	∞	4	2	$RT/2F$	RT/F	4	3	$K_3 \sim 1$
						$RT/4F$	$RT/3F$	4	3	$K_3 << 1$
(V) Kobussen's Path										
1. $M + OH^- \to MOH + e^-$	1	$2RT/F$		1						
2. $MOH + OH^- \to MO + H_2O + e^-$	1	$2RT/3F$	$2RT/3F$	2	1	$2RT/F$		1		$r_{OH} \sim r_O$
						RT/F		1.5		$r_{OH} >> r_O$
3. $MO + OH^- \to MO_2H$	1	$RT/2F$	∞	3	1	∞		1		$K_2 \sim 1$
						RT/F		2		$K_2 << 1$
4. $MO_2H^- + OH^- \to MO_2^- + H_2O + e^-$	1	$2RT/5F$	$2RT/F$	4	1	$2RT/F$		1		$K_3 \sim 1$
						$2RT/F$		2		$K_3 << 1$
5. $MO_2^- \to M + O_2 + e^-$	1	$2RT/7F$	∞	4	0	RT/F	$2RT/F$	1	0.5	$K_4 \sim 1$
						$RT/2F$	$2RT/3F$	1	1.5	$K_4 << 1$

[c] Symmetry factors, i.e., β, γ, and δ, in all steps, were taken as $^1/_2$. [b] Stoichiometric number. [c] ζ is the potential difference between the cHp (outer Helmholtz plane) and the bulk of the solution (ζ potential). [d] Nonactivated desorption of O_2. [e] Activated desorption of O_2. [f] r is a coefficient determining the variation of heat of adsorption of a particular species with coverage. Unless stated, r values for each species were taken as equal. K_i is the equilibrium constant of the ith step. [g] r_1 and r_2 refer to r for M^zOH and r for $M^{z+1}OH$, respectively.

Table 1.5.1 *Diagnostic criteria of proposed paths for the oxygen evolution reaction. Reproduced from ref. 42.*

The pathway of Krasil'shchikov[221] (mechanism III in Table 1.5.1), originally proposed for the o.e.r. on Ni, or modifications thereof, is almost certainly the most commonly proposed reaction mechanism for the o.e.r. on both anodic oxide films on metallic electrodes and on thermally prepared metal oxide electrodes. Authors who rationalise their data in terms of the Krasil'shchikov mechanism, have been able to attribute changes in the slopes of steady state polarisation curves with increasing overpotential, to changes in the rate determining step within the pathway. Steps 1, 2, or 3 are usually considered to be the RDS (depending on the observed Tafel slope), and thus it can be seen, that in general, the Krasil'shchikov pathway predicts that the O-O bond of the evolved oxygen molecule will be formed after the rate-determining step. The important early work of Damjanovic, Dey, and Bockris[77], regarding the o.e.r. on Pt electrodes in both acidic and alkaline solutions, led these authors to the general conclusion, that the following modified Krasil'shchikov scheme could explain the observed experimental kinetic parameters in the alkaline case:

$$M + OH^- \leftrightarrows MOH + e^- \qquad (1.5.17, I)$$

$$MOH + OH^- \leftrightarrows MO\text{-}H\text{-}OH^- \qquad (1.5.17, II)$$

$$MO\text{-}H\text{-}OH^- \leftrightarrows MO\text{-}H\text{-}OH + e^- \qquad (1.5.17, III)$$

$$MO\text{-}H\text{-}OH \leftrightarrows MO + H_2O \qquad (1.5.17, IV)$$

$$2MO \leftrightarrows 2M + O_2 \qquad (1.5.17, V)$$

In the scheme above (as indeed in all the pathways presented in Table 1.5.1), M represents a catalytically active site on the metal oxide surface. Experimentally, Damjanovic, Dey, and Bockris had found that the anodic Tafel slope in 1 N KOH at 25°C was approximately 2.303RT/F (~60 mV dec^{-1}) at lower values of overpotential η, changing to approximately 2.303×2RT/F (~120 mV dec^{-1}) at higher η. A cathodic slope of 2.303RT/F was measured, and hence a value of ~ 1.8 was determined for the stoichiometric number v, according to equation (1.2.83). At the time of this paper, the authors placed a lot of value on v as a diagnostic criterion. There was perhaps some justification in this approach in the case of the pre-oxidised Pt electrodes that they utilised both in the determination of the o.e.r. and o.r.r. Tafel slopes, however as discussed before, the experimental value of v is rarely utilised as a diagnostic criterion in the more recent literature.

In any case Damjanovic, Dey, and Bockris proposed that the observed Tafel slope behaviour at low η could be rationalised by admitting step (1.5.17, II) as RDS, under low coverage Langmuir adsorption conditions, with step (1.5.17, I) becoming rate determining under Temkin adsorption conditions at higher overpotentials. Alternatively, they envisaged that step (1.5.17, II) could be rate determining over the entire Tafel region of potential, with the relevant adsorption isotherm for the reaction intermediates, being low coverage Langmuir at low η, changing to Temkin at higher η, in the case where the Temkin parameter $r_{MO} << r_{MOH}$. It can readily be seen that the value of v associated with either steps (1.5.17, I) or (1.5.17, II) is 2, corroborating the experimental value. The authors emphasised that this mechanistic rationalisation of the experimental data for Pt in alkaline media was somewhat tentative – for example they didn't make a proposal for the physical conditions that might correspond to $r_{MO} << r_{MOH}$. It has already been commented in section 1.2.3 that in the case of adsorbed intermediates MOH and MO, the r values are expected to be very similar, since both species involve bonding by oxygen atoms to the substrate M.

Another important issue that was considered in detail by Damjanovic, Dey, and Bockris[77] was the origin of the change in Tafel slope observed in their experimental data from steady state polarisation measurements of Pt in 1N KOH, as outlined above. Such changes in Tafel slope with increasing overpotential are often observed in polarisation measurements that characterise the kinetics of the o.e.r., and so the discussion of Damjanovic et al. has wider applicability than the specific system that they investigated. The authors considered four possible explanations for the change in Tafel slope: (a) a change in reaction pathway, (b) a change in the electrode substrate, (c)a change in the RDS within a given pathway, and (d) the influence of changing potential on the adsorption of the reaction intermediate(s). They concluded that the latter two reasons were most likely, and that it might be possible to discriminate between behaviour due to (c) or (d) by carefully examining the steady state polarisation curves. For example, they provide a rough calculation which shows that, if the heat of adsorption of an intermediate species changes by a typical value of about 10 Kcal/mole as its fractional coverage increases from $\theta = 0.1$ to $\theta = 0.9$, then the range of potential over which Temkin conditions might be expected to prevail is limited to ~ 150 mV. Observation of the limitation of one of the straight line Tafel regions to such a potential range, would point towards (d) as opposed to (c) being the reason behind the dual slope behaviour in such a case.

Hoar[222] had also observed a Tafel slope of ca. 2.303RT/F at low overpotential for the o.e.r. at Pt in alkaline solution, and furthermore had obtained an experimental stoichiometric number of approximately 2, data, which, as was mentioned above, was subsequently corroborated by Damjanovic, Dey, and Bockris[77]. Hoar's proposed path for the o.e.r. in alkaline media is presented below:

$$M + OH^- \leftrightarrows MOH + e^- \qquad (1.5.18, I)$$

$$MOH + OH^- \leftrightarrows MH_2O_2^- \qquad (1.5.18, II)$$

$$2\,MH_2O_2^- \leftrightarrows M + MO_2^{2-} + 2\,H_2O \qquad (1.5.18, III)$$

$$MO_2^{2-} \leftrightarrows M + O_2 + 2e^- \qquad (1.5.18\ IV)$$

The pathway of equation (1.5.18) predicts the values of *b* and *v*, found by Hoar, if step (1.5.18, II) is considered to be rate determining under Langmuir adsorption conditions. It is worth noting that Hoar's alkaline path is fundamentally different to the Krasil'shchikov mechanism, in that the O-O bond of the evolved O_2 molecule is formed as early as the second, and rate-determining step.

As is evident from Hoare's 1968 book[197] (which remained the standard text on oxygen electrochemistry for many years), with the exception of Ni, most of the early work on the o.e.r. was confined to precious metals. In view of the literature that he had reviewed, Hoare summarised the mechanisms that had been proposed up to that time (1968) for the o.e.r. in both alkaline and acidic solutions with the general scheme outlined below. He commented in the case of Pt that "most likely the overall mechanism of oxygen evolution is the same in acid and alkaline solutions, as pointed out by Krasil'shchikov with the rate determining step as (written for acidic electrolyte)

$$(H_2O)_{ads} \rightarrow (OH)_{ads} + H^+ + e^- \text{ "} \qquad (1.5.19, I)$$

He envisaged that this would be followed by a rapid reaction, either

$$(OH)_{ads} + (OH)_{ads} \rightarrow (O)_{ads} + H_2O \qquad (1.5.19, II)$$

or

$$(OH)_{ads} \rightarrow (O)_{ads} + H^+ + e\text{-} \qquad (1.5.19, III)$$

The final step would then be oxygen evolution,

$$(O)_{ads} + (O)_{ads} \rightarrow (O_2)_{ads} \qquad (1.5.19, IV)$$

and

$$(O_2)_{ads} \rightarrow O_2 \qquad (1.5.19, V)$$

This scheme more or less covers, both Bockris's Electrochemical Path (which will be discussed later) and the Krasil'shchikov Path. The apparent coincidence of experimental data and theoretically predicted parameters for a scheme such as that outlined in reaction (1.5.19) by Hoare, contributed to what Birss and Damjanovic[223] described in 1987 as a "widely held view", that the mechanism of the o.e.r. at Pt electrodes in alkaline solution, was well understood. Experimental data in the intervening period seemed to support the view that the Krasil'shchikov pathway was the operative mechanism in the o.e.r. at Pt in alkaline media. Iwakura et al.[224], had, in agreement with the earlier work of Damjanovic, Dey, and Bockris[77], observed a slope of ca. 60 mV dec^{-1} at low current density and a second slope of ca. 120 mV dec^{-1} at higher current density, during polarisation measurement on oxygen evolution at PtO_2 on a Ti substrate in alkaline solution. Furthermore they observed reaction orders with respect to OH^- concentration of approximately unity in both Tafel slope regions. This experimental data was rationalised in terms of the Krasil'shchikov mechanism (see Table 1.5.1) with the second step rate controlling at low current density, and the first step as RDS at higher current density.

Doubts however, were cast upon the conventional wisdom regarding the o.e.r. on Pt in alkaline solution, when the system was revisited by Damjanovic working with Birss[223]. These workers studied the o.e.r. at a range of pH values between 12 and 14. They confirmed the older results of Damjanovic et al.[77] as regards the observation of a Tafel slope of ca. 60 mV dec^{-1} at low current density and ca. 120 mV dec^{-1} at higher values of current density. However, while they found a reaction order with respect to OH^- of ca. 2 at lower current densities, a value, which can be accounted for by the Krasil'shchikov pathway, they observed a non-integral reaction order of 3/2 at higher values of current density. A Tafel slope of 2.303×2RT/F and an associated reaction order of 3/2 cannot be reconciled with the Krasil'shchikov mechanism (or indeed according to the authors any other standard o.e.r. mechanism proposed in the literature) regardless of whether the Langmuir or Temkin isotherm is admitted. Birss and Damjanovic[223] also observed that, while the rate of reaction in the 60 mV dec^{-1}

Tafel region was independent of film thickness, it decreased with increasing film thickness in the upper Tafel region.

In a follow up publication[225] (oddly part II was published before part I!) they proposed a rather complex dual barrier mechanism to explain the observed behaviour. Dual barrier models will be discussed further in relation to the results of the present investigations – for the moment it is noted that such theories envisage that only a fraction of the total potential difference across the metal/solution interface has a direct effect on the kinetics of the o.e.r. Put simply, Birss and Damjanovic proposed, that, while the magnitude of the potential drop between the I.H.P. (recall the discussion of interfacial structure in section 1.1.1) and the Pt metal varies with applied potential for a given oxide film thickness but is independent of solution pH, the potential drop across the O.H.P. remains invariant with changing potential at constant pH. In effect this means, that a given electrolyte concentration, only the potential difference across the film and the inner Helmholtz layer, affects the rate of oxygen evolution directly. They attributed the anomalous reaction order values to this effect, and showed that if the term for the potential drop across the entire interface in the kinetic equations, was replaced with a term representing the potential drop between the metal and the I.H.P. (across the oxide film), then reaction orders of unity would be obtained for both Tafel slope regions. On the basis of this model, the authors proposed a reaction pathway, which effectively amounts to a Krasil'shchikov mechanism, altered to take account of the complex nature of the electrode/solution interface. Thus, they envisaged that the Tafel slope of ca. 120 mV dec^{-1} arose from the initial discharge of an OH^- ion at the I.H.P., across the inner Helmholtz layer and the oxide film,

$$OH^-_{IHP} \rightarrow OH_{IHP} + e^- \quad , \qquad (1.5.20, I)$$

where a rapid equilibrium exists between the OH^- species at the IHP and those in the bulk solution. At lower current densities in the ca. 60 mV dec^{-1} Tafel region, they proposed that a rate determining chemical step is operative – reactions such as,

$$OH_{IHP} + 2H_2O_{IHP} \rightarrow [H_2O_2^-{}_{IHP} + H_3O^+{}_{IHP}] \qquad (1.5.20, II)$$

or,

$$OH_{IHP} + H_2O \rightarrow [O^-{}_{IHP} + H_3O^+] \qquad (1.5.20, III)$$

satisfy the observed kinetic parameters. If nothing else, the example of these studies by Birss et al., demonstrates the merits of re-examining the o.e.r. at various substrates in the context of improving and developing the overall understanding of the reaction.

The Krasil'shchikov mechanism was originally devised for the o.e.r. on Ni[221] and several studies over the years[147, 226] have concurred with its applicability to that system. Lu and Srinivasan[147] found that steady state polarisation measurements on the o.e.r. in 1N KOH at a Ni electrode, that had been pre-anodised at ca. 575 mV (vs. Hg/HgO 1N KOH) in the same solution (or rejuvenated by anodisation under these conditions) yielded a single Tafel slope region with b = ~ 40 mV dec^{-1}. On the other hand, Ni electrodes that had been pre-oxidised or rejuvenated at the higher potentials of ca. 0.875 V or ca. 1.075 V, yielded two Tafel slope regions – at lower current densities the slope was again ~ 40 mV dec^{-1}, while at higher current densities a less well defined slope of ~ 170 mV dec^{-1} was observed. The authors proposed that this kinetic data could be accounted for, by the following modified Krasil'shchikov mechanism, with step (1.5.21, III) rate determining in the low Tafel slope region of potential:

$$OH^-_{(ads)} \leftrightarrows OH_{(ads)} + e^-_{(latt)} \qquad (1.5.21, I)$$

$$OH_{(ads)} + OH^- \leftrightarrows O^-_{(ads)} + H_2O \qquad (1.5.21, II)$$

$$2\ \beta\text{-}NiOOH_{(surf)} + O^-_{(ads)} \leftrightarrows 2NiO_{2(surf)} + H_2O + e^-_{(latt)} \qquad (1.5.21, III)$$

$$2NiO_{2(surf)} + H_2O \leftrightarrows 2\ \beta\text{-}NiOOH_{(surf)} + O_{(ads)} \qquad (1.5.21, IV)$$

$$O_{(ads)} + O_{(ads)} \leftrightarrows O_2 \qquad (1.5.21, V)$$

As was mentioned in section 1.4.1, Lu and Srinivasan have proposed, based upon their experimental observations that β-NiOOH is the "right type of oxide" for the electrocatalysis of the o.e.r. They have attributed the decrease in electrocatalytic activity, which they observed upon extended anodic polarisation, to the formation of NiO_2 on the surface of the oxide film, proposing that generation of each Ni^{4+} ion on the film surface creates an inert site for oxy evolution. The authors further proposed, based upon the optical constants derived from ellipsometric measurements on the oxide films, that the "unusually high Tafel slopes of ~ 170 mV dec^{-1} observed at high η" in the case of the electrodes pre-anodised at higher potentials, arise from barrier

layer effects associated with the poor conductivity of the oxide films generated at these potentials, owing to their relatively higher Ni^{4+} content.

Modified Krasil'shchikov mechanisms have also been proposed in the rationalisation of o.e.r. kinetic data obtained on Co electrodes in alkaline solution. Burke et al.[196] performed steady state polarisation measurements in 6 M KOH at 30°C on a Co electrode, on which a hydrous oxyhydroxide layer had been grown by the potential cycling method, and also on an initially oxide free Co electrode. The potential cycling regime used in the oxide growth, involved cycling between limits of 0 and 1.2 V (vs. R.H.E.) at 33 mV s^{-1} in 6 M KOH for 30 minutes. A tafel slope of 60 mV dec^{-1} was observed for the initially oxide free electrode, while a somewhat lower slope of 52 mV dec^{-1} was recorded for the pre-cycled electrode. The polarisation curves for the two electrodes were coincident at the lowest current densities, however owing to its smaller Tafel slope, the current density achieved at the pre-cycled electrode was higher than the other electrode by a factor of 2-3 over a potential range between 1.6-1.7 V. The two polarisation curves converged at higher overpotentials. These workers proposed the following modification of the Krasil'shchikov pathway in order to explain their results:

$$OH^- \leftrightarrows OH_{ad} + e^- \qquad (1.5.22, I)$$

$$OH_{ad} + OH^- \leftrightarrows O^-_{ad} + H_2O \qquad (1.5.22, II)$$

$$Co{\cdot}O_2 + O^-_{ad} \leftrightarrows CoO_2{\cdot}O + e^- \qquad (1.5.22, III)$$

$$CoO_2{\cdot}O \leftrightarrows CoO_2 + O_{ad} \qquad (1.5.22, IV)$$

$$2O_{ad} \leftrightarrows O_2 \qquad (1.5.22, V)$$

It is noteworthy that reaction scheme (1.5.22) is similar, in the first two steps, to that proposed by Lu and Srinivasan[147] (equation (1.5.21)), for the o.e.r. on Ni in alkaline solution as discussed above. A significant difference between these two schemes arises in the respective third steps. In step (1.5.22, III) of the scheme of Lu and Srinivasan, the electrocatalytically active surface species is a Ni(III) entity, with these authors placing particular emphasis on the importance of β-NiOOH in the course of the o.e.r. on an anodised Ni electrode. On the other hand, in the scheme of Burke et al., the active surface species in the third step is a Co(IV) entity. As was discussed in section 1.4.3, there is reasonable evidence to support the existence of Co(IV) at the surface of the anodic film formed on Co in alkaline solution, at potentials immediately

preceding the onset of significant oxygen evolution. Burke et al.[196] comment that the precise composition of the unstable cobalt species involved in the o.e.r. is uncertain, but do point out that cobalt peroxide can exist as a monohydrate ($CoO_2 \cdot H_2O$), implying that the Co(IV) ion is capable of coordinating a further oxygen atom, as is envisaged in step (1.5.22, III).

In further contrast to the mechanism for the o.e.r. at Ni, as envisaged by Lu and Srinivasan[147], the experimental data of Burke et al.[196] is satisfied by admitting the second, chemical step (1.5.22, II) as the RDS, as opposed to the third electrochemical step that is rate-determining in the scheme of the former workers. Burke and co-workers were unable to provide an exact explanation for the lower Tafel slope of 52 mV dec^{-1} observed for the pre-cycled electrode – they made the tentative suggestion that for this hydrous material the rate might be determined by a combination of steps (1.5.22, II and III).

Lyons and Burke[227] performed a study on both multi-cycled and initially oxide free Fe electrodes, similar to that outlined above for Co. In this case the steady state polarisation measurements were carried out in 1 M NaOH at 25°C. The hydrous oxide film, was grown by sweeping the potential of the Fe electrode between –0.5 and 1.25 V (vs. R.H.E.) at a rate of 350 mV s^{-1} in 1 M NaOH. It was observed that the rate of oxygen evolution was enhanced by a factor of approximately ten on the multi-cycled hydrous oxide film, relative to the rate on the initially oxide free electrode. Significantly from a mechanistic viewpoint, the same Tafel slope behaviour was observed on both types of electrode, indicating a common reaction pathway despite the differences in electrocatalytic activity. At lower overpotentials the Tafel slope adopted a value of ca. 60 mV dec^{-1}, changing to ca. 120 mV dec^{-1} at higher potentials. As in the case of their study of oxygen evolution on Co, Lyons and Burke proposed a modified Krasil'shchikov pathway in the rationalisation of their experimental data. This pathway does however exhibit some differences from reaction (1.5.22) and therefore is outlined below:

$$S + OH^- \leftrightarrows SOH + e^- \qquad (1.5.23, I)$$

$$SOH + OH^- \leftrightarrows SO^- + H_2O \qquad (1.5.23, II)$$

$$SO^- + OH^- \leftrightarrows SO_2H^- + e^- \qquad (1.5.23, III)$$

$$SO_2H^- + OH^- \leftrightarrows S + O_2 + H_2O + 2e^- \qquad (1.5.23, IV)$$

An obvious difference between this pathway, and that proposed for Co in reaction (1.5.22) lies in the theoretical value of the stoichiometric number v for any given step being rate determining. For example, if any of the first three steps in reaction (1.5.23) is the RDS, the associated value of v is 1. In contrast, if any of the first three steps in reaction (1.5.22) is considered to be rate determining, then $v = 2$. Whatever about the validity of the experimental determination of v from anodic and cathodic polarisation data in the case of the oxygen electrode reaction at Pt, it is commented by Lyons and Burke[227] that "the mechanism of oxygen gas reduction on iron is most unlikely to involve the species SOH, i.e. the anodic and cathodic reactions are likely to follow considerably different pathways", thus rendering derivation of v from experimental data invalid in the case of Fe (and indeed Ni and Co). This is an illustration of the fact, alluded to earlier in section 1.5.1, that in the case of the oxygen electrode it isn't possible to obtain experimental data for steps following the RDS in oxygen evolution, by determining the Tafel slope for oxygen reduction (or indeed vice-versa). This was acknowledged by Lyons and Burke[227], who pointed out that their proposed mechanism (certainly in respect to the details of the step after the RDS) was only one of several possible sequences that could rationalise their data – a pathway analogous to reaction (1.5.22) might equally well be valid. In any case the real point is that traditional polarisation measurements cannot yield information on an o.e.r. pathway beyond the RDS.

If pathway (1.5.23) is admitted, the observed 60 mV dec^{-1}slope corresponds to step (1.5.23, II) being rate limiting, whereas the 120 mV dec^{-1}slope indicates that rate control switches to the step outlined in (1.5.23, I) at high potentials. Also of interest is the identity of the catalytic species S at the oxide surface. Owing to the high potentials and high pH involved, Lyons and Burke[227] have proposed that it might well be a ferrate FeO_4^{2-} entity. This is a point worth bearing in mind, in the context of the voltammetry peaks observed by Joiret et al.[167] and attributed to Fe^{3+}/Fe^{6+} redox transition as was discussed in section 1.4.2.

As previously mentioned the Krasil'shchikov pathway, is the mechanism most often invoked to explain experimental o.e.r. data. Miles et al.[218] proposed that the polarisation data that they collected for the o.e.r. on oxides of various metals in 30wt% KOH solutions at 80°C could be rationalised by the Krasil'shchikov mechanism for all the oxides. However the RDS differed depending on the exact material. Thus, it was proposed that the initial discharge step was rate limiting in the

case of the oxides of Co and Fe. The chemical second step was envisaged to be the RDS for the oxides of Ru, Rh, Pd, Ni and Os. Finally, the authors attributed rate limitation in the cases of the oxides of Pt and Ir to the third step of the Krasil'shchikov path.

Gottesfeld and Srinivasan[228] observed a Tafel slope of ca. 50 mV dec^{-1} for the o.e.r. on a thick hydrous layer of iridium oxide grown by potential multi-cycling on a metallic Ir electrode in 0.5 M H_2SO_4. They interpreted this data in terms of a rate determining second step of a Krasil'shchikov mechanism. Consultation of Table 1.5.1 indicates that the predicted slope in this case should be 2.303 RT/F (or ~ 60 mV dec^{-1} at 25°C). It could be suggested that the experimental slope of Gottesfeld and Srinivasan, might equally well be interpreted in terms of a rate determining third step (expected Tafel slope = ~ 40 mV dec^{-1} at 25°C), which would correspond to the prediction of Miles et al.[218] for iridium oxide as discussed above.

The o.e.r. has also been proposed to proceed via a Krasil'shchikov pathway in the case of certain perovskite materials in 1 M KOH at 25°C. Matsumoto et al.[229] observed Tafel slopes of 65 mV dec^{-1} for $La_{1-x}Sr_xCoO_3$ electrodes, both for the case of x = 0.2 and 0.4. In each case the reaction order with respect to OH^- activity was observed to be of the order of 1.8. Such data ties in very nicely with the proposal of an operative Krasil'shchikov pathway, with the chemical second step determining the overall reaction flux under limitingly low coverage of the reaction intermediate(s). A subsequent study[230] by the same authors on the o.e.r. at a wider range of perovskite materials was also indicative of oxygen evolution via the Krasil'shchikov mechanism, with the rate determining step dependent on oxide stoichiometry.

Some randomly selected, more recent publications that have interpreted o.e.r. polarisation data in terms of the Krasil'shchikov mechanism are those due to Wu et al.[231], Wang et al.[232] and Zhang et al.[233]. Wu et al.[231] studied the electrocatalytic activity of a Co and Ni mixed oxide electrode, towards the o.e.r. in alkaline media. They considered materials with five different Co^{2+}/Ni^{2+} mole ratios and found that polarisation measurements on all the electrodes yielded two well defined Tafel regions. At low overpotentials the Tafel slopes ranged from 40 mV dec^{-1} to 48 mV dec^{-1}, while at higher overpotentials the slopes lay between 110 and 120 mV dec^{-1}. The reaction orders with respect to OH^- concentration were ca. 2 in the lower Tafel region and ca. 1 in the upper Tafel region. On the basis of these observations, the authors proposed the classical Krasil'shchikov mechanism (as presented in Table

1.5.1) to be operative for oxygen evolution on their anodes. Wang et al.[232] examined the o.e.r. at two nickel hydroxide electrodes, one of which was modified by electroless Co coating. A Tafel slope of 61 mV dec^{-1}, was noted for the modified electrode in an electrolyte consisting of 6 M KOH and 0.6 M LiOH, leading to the conclusion that the Krasil'shchikov mechanism with a rate determining second step was consistent with the experimental data.

The foregoing examples demonstrate that the kinetic predictions of the Krasil'shchikov mechanism have been found to be consistent with experimental data obtained for the o.e.r. on many different substrates in both alkaline and acidic media. There is a danger that this mechanism has become such an institution in this area of study, that researchers are inclined to interpret experimental kinetic data that falls anywhere close to its predicted kinetic parameters, as strong proof of the applicability of the Krasil'shchikov mechanism to the particular system under study. As an example of this Zhang et al.[233] (although this phenomenon isn't limited to these workers, especially in the more recent literature) begin a communication regarding the effect of various amounts of Co on the catalytic activity of nickel hydroxide towards the o.e.r., by stating (citing Hoare's forty year old book[197]) that the Krasil'shchikov mechanism is the generally accepted pathway for the reaction on the nickel anode. They then proceed to interpret their data (a Tafel slope of 56.4 mV dec^{-1} at low η, changing to 143 mV dec^{-1} at higher η for the unmodified nickel hydroxide electrode) as being consistent with the Krasil'shchikov mechanism, which might be regarded as a somewhat dubious assertion.

Indeed much attention has been devoted to the Krasil'shchikov pathway in the present review – therefore the focus will now switch to some of the alternative mechanisms that have been proposed over the years. Damjanovic et al.[234] studied the kinetics of the o.e.r. at Rh, and Ir electrodes in both acidic and alkaline media. For Rh they observed a Tafel slope of 42 mV dec^{-1} at low overpotentials and a slope of 115 mV dec^{-1} at higher potentials in 1N NaOH. In the case of the Ir anode in the same solution a Tafel slope of 40 mV dec^{-1} characterised the polarisation behaviour at low η, changing to 120 mV dec^{-1} at higher values of η. This data was rationalised in terms of Bockris's Electrochemical Oxide Path (see Table 1.5.1). At low overpotential it was envisaged that the second step (an electron transfer but not the primary discharge of OH^- on the electrocatalytic site) was rate determining. At higher values of η, it was proposed that the initial discharge step becomes the RDS.

This mechanism was also adopted by Sato and Okamoto[235], who performed a study on the o.e.r. at the Ni anode in alkaline media. These workers observed a Tafel slope of 48 mV dec^{-1} at low current densities. The steady state polarisation curve adopted the properties of a limiting current (e.g. its position was highly dependent on the rate of solution stirring) at potentials anodic to the aforementioned Tafel region. At still higher current densities, a second straight line region was observed in the polarisation curve with a slope of ca. 100 mV dec^{-1}. The authors proposed that a rate limiting adsorbed species-ion discharge step (step 2 in the Electrochemical oxide path) was compatible with the polarisation data at lower current densities. Sato and Okamoto noted that the upper Tafel region appeared at the same overpotential in both alkaline and acidic media, and hence interpreted this behaviour as being indicative of a rate determining discharge of H_2O at these high current densities. Therefore the operative RDS in this region of the polarisation curve is the first step of the Electrochemical Oxide pathway, represented as $M + H_2O \leftrightarrows MOH + H^+ + e^-$.

Rasiyah and Tseung[236, 237] conducted an interesting study into oxygen evolution at $NiCo_2O_4$ electrodes in alkaline media. These authors re-emphasised the earlier conclusions of Tseung and Jasem[217] that for oxygen evolution on metal or metal oxide electrodes, the potential of the metal/metal oxide or the lower metal oxide/higher metal oxide couple must be achieved before gas evolution will occur. In the first part of the study[236] the nature of the oxide at the potential corresponding to the onset of significant oxygen evolution, and at potentials below this, was studied in 5M KOH at 25°C. A cyclic voltammogram recorded at 110 mV s^{-1} showed the presence of two anodic peaks at potentials before the onset of a significant o.e.r. current, with a corresponding broad reduction peak (possibly with a shoulder) on the cathodic sweep. The authors commented that it was therefore unclear from voltammetry, whether the current passed was due to one or more oxides.

They claim to have solved this problem using potential step chronocoulometry. By pulsing the potential from rest to various potentials in the potential region of interest, and then evaluating the charge passed with time as the system relaxed, the authors claim to have identified three distinct regions of current-potential behaviour. The first of these, extending from ca. 1.27 – 1.33 V (vs. N.H.E.), they attributed to the oxidation of Co^{2+} species to Co^{3+}. The second region (1.33 – 1.43 V) was envisaged to be due to the oxidation of Ni^{2+} species to Ni^{3+}. Finally, they attributed the third region, which extended from ca. 1.43 V up to the potential of significant gas

evolution, to either the oxidation of all Co^{3+} species to Co^{4+}, or alternatively to the oxidation of all trivalent, tetrahedrally coordinated ions M^{3+} to M^{4+}, stating that the latter suggestion "may hold greater weight". These proposals arose from the author's earlier work, which showed that their $NiCo_2O_4$ material had the spinel structure $Co_{0.9}^{2+}Co_{0.1}^{3+}(Ni_{0.9}^{2+}Ni_{0.1}^{3+}Co^{3+})O_{3.2}^{2-}O_{0.8}^{-}$, where the ions in parentheses have tetrahedral coordination and those outside have octahedral coordination. They also observed that the total charge passed to form higher oxides was 9.7% of the maximum charge that would be passed if all cations in the $NiCo_2O_4$ material were oxidised to the +4 state, thus concluding that the formation of the higher oxides was limited to the surface of the $NiCo_2O_4$ particles. In conclusion they made the significant comment that the onset of oxygen evolution "coincides with the formation of a higher valent oxide in a concerted reaction".

Rasiyah and Tseung concentrated on determining the mechanistic pathway for the o.e.r. on their $NiCo_2O_4$ electrodes in the second part[237] of the study. Galvanostatic steady state polarisation curves were recorded for the o.e.r. at various concentrations of KOH solution at 25°C. At electrolyte concentrations $\geq$ 1.2 molar, two Tafel slope regions were observed. At lower current densities the Tafel slope had a value of ~ 40 mV dec^{-1}, changing to a value of approximately ~ 120 mV dec^{-1} at higher current densities. The Bockris Electrochemical Oxide path was proposed as the mechanism at higher current densities, where M in the scheme (see Table 1.5.1 (II)) is initially envisaged to be a divalent Ni or Co ion. This divalent species will be oxidised to a trivalent ion in the first step. In the subsequent step it is further oxidised to a tetravalent ion, as was observed in the first part of the study[236]. This second electron transfer step was proposed to be rate determining under a limitingly high fractional coverage of MOH ($\theta \rightarrow 1$).

Consulting the predicted Tafel parameters in Table 1.5.1, it would then appear that a logical explanation for the mechanism at lower current density, would be to assume the same pathway with the same RDS, except under the condition where $\theta_{MOH} \rightarrow 0$. The authors point out however that in this potential region, according to the stoichiometric formula $Co_{0.9}^{2+}Co_{0.1}^{3+}(Ni_{0.9}^{2+}Ni_{0.1}^{3+}Co^{3+})O_{3.2}^{2-}O_{0.8}^{-}$, 2/5 of the cationic reaction sites are trivalent. If M in the Electrochemical Oxide path was assumed to be trivalent, step 2 of the mechanism would produce a pentavalent species, which runs contrary to the observations of the first part of the study[236]. Bearing this in mind the

authors made the following novel prediction regarding the o.e.r. pathway at lower overpotentials:

$$T + OH^- \leftrightarrows TOH + e^- \quad (1.5.24, I)$$

$$TOH + OH^- \leftrightarrows TO^- + H_2O \quad (1.5.24, II)$$

$$TO^- + M \leftrightarrows T\text{-}O\text{-}M + e^- \quad (1.5.24, III)$$

$$2T\text{-}O\text{-}M + OH^- \leftrightarrows 2T + 2M + O_2 \quad (1.5.24, IV)$$

In path (1.5.24) T is a trivalent site, while M may be a divalent or trivalent site. The T-O-M site involves a bridge-bonded oxygen. Since the formal kinetic mechanistic analysis of this scheme is equivalent to that of the Krasil'shchikov pathway, the low η slope of ca. 2.303×2RT/3F can be rationalised by admitting step (1.5.24, III) as the RDS under low coverage Langmuir conditions.

Significantly, in the context of the present study a similar mechanism was proposed, for the oxygen evolution reaction on a Co anode in alkaline media, by Willems, Kobussen and co-workers[238]. The scheme envisaged by these workers takes the following form:

$$CoO + OH^- \leftrightarrows CoOOH + e^- \quad (1.5.25, I)$$

$$CoOOH + OH^- \leftrightarrows CoO_2^- + H_2O \quad (1.5.25, II)$$

$$CoO_2^- \leftrightarrows CoO_2 + e^- \quad (1.5.25, III)$$

$$CoO_2 \leftrightarrows CoO + O_{ad} \quad (1.5.25, IV)$$

$$2O_{ad} \rightarrow O_2 \quad (1.5.25, V)$$

The analogy between pathway (1.2.25) (which again is formally a Krasil'shchikov (type mechanism) and the pathway of Rasiyah and Tseung (1.5.24) can be appreciated when one considers the charge state of the Co species in each step. In step (1.5.25, I) a Co(II) species is oxidised to Co(III). The second step in the mechanism consists of the formation of an unstable surface entity via a proton transfer step. The importance of proton transfer with solution phase species at the electrocatalytic oxide surface, in tandem with electron transfer has also been emphasised by Bockris and Otagawa[42] in their studies on the o.e.r. at perovskite surfaces in alkaline media. The unstable Co(III) surface species is discharged in step (1.5.25, III) to form a more stable Co(IV) surface species – recall from section 1.4.3, that significant evidence exists for the

stabilisation of Co(IV) species at the surface of anodic Co oxides in concentrated alkaline solution at very positive potentials. Pathway (1.5.25) emphasises that the oxygen evolution process on anodic oxide films cannot really be decoupled from the processes that occur in the formation and oxidation of the film. This is why a significant review of the nature of the anodic oxides formed on Ni, Co and Fe electrodes in alkaline solution, was undertaken in section 1.4. The oxygen evolution reaction cannot be understood without an appreciation of the surface chemistry of the substrate.

One of the few existing studies to consider together, the nature of the o.e.r. on Ni, Co, and Fe anodes was performed by Scarr[239]. The author observed Tafel slopes of approximately 46 mV dec^{-1} (~ 2.303×4RT/5F) for the o.e.r. on Ni, Co and Fe electrodes in 1M KOH at room temperature. He noted that a conventional kinetic analysis (assuming Langmuir adsorption conditions) of any of the standard proposed o.e.r. mechanisms, could not yield a prediction of a Tafel slope of 2.303×4RT/5F, regardless of which step was considered to be the RDS. A perusal of Table 1.5.1 will show that this is also the case if the Temkin adsorption isotherm is adopted. To explain his experimental data, Scarr proposed the following reaction pathway:

$$M + OH^- \leftrightarrows MOH + e^- \qquad (1.5.26, I)$$

$$MOH + OH^- \leftrightarrows MH_2O_2^- \qquad (1.5.26, II)$$

$$MH_2O_2^- \leftrightarrows MH_2O_2 + e^- \qquad (1.5.26, III)$$

$$MH_2O_2 + OH^- \leftrightarrows MHO_2^- + H_2O \qquad (1.5.26, IV)$$

$$MHO_2^- \leftrightarrows MHO_2 + e^- \qquad (1.5.26, V)$$

$$MHO_2 + OH^- \rightarrow M + O_2 + H_2O + e^- \qquad (1.5.26, VI)$$

Of immediate note is the fact that the first two steps of this mechanism are common with the alkaline path of Hoar (pathway (1.5.18)) as discussed previously. An adsorbed peroxide species is formed in the second step, meaning that the O-O bond of the O_2 molecule to be evolved, is formed earlier in these pathways than in the Krasil'shchikov case.

The kinetic analysis of scheme (1.5.26) is based on a dual barrier approach originally proposed by Gnanamuthu and Petrocelli[210] for the o.r.r., that considers the effect of the potential gradient on the reaction intermediates as a consequence of their position in the interfacial region. This means that adsorbed intermediates, which are involved

in charge transfer with either the electrode or the bulk solution alone, are acted upon only by that portion of the potential associated with the particular interfacial region. The adsorbed intermediates reside at the inner Helmholtz plane, which was assumed by the author to mark the half way point in the potential gradient, therefore the fraction of the total potential applicable to either region is one half. Scarr quotes the following expression for the Tafel slope b of a given mechanism step,

$$b = \frac{\nu}{\Sigma_i Z_i f_i + (1-\alpha) Z_r f_r} \cdot \rho \qquad (1.5.27)$$

where ν is the stoichiometric number, ρ = 2.303RT/F, α is the cathodic transfer coefficient, Z_i is the number of charges transferred in a given step prior to the rate determining step, f_i is the fraction of the total potential difference which is effective in the i^{th} charge transfer, while Z_r and f_r have similar meanings for the RDS. Equation (1.5.27) arises from an expression derived by Gnanamuthu and Petrocelli[210] for this dual barrier theory, based upon equation (1.2.83) from Parsons' original analysis of the kinetics of multistep electrochemical mechanisms (see section 1.2.3).

Applying equation (1.5.27) to scheme (1.5.26), if the first step is the RDS, ν = 1, α = ½ (as is conventional in this type of kinetic analysis), Z_r = 1 and f_r = 1 (since the charge is transferred between the electrode surface and the bulk solution). Inserting these values into (1.5.27), b = 2RT/F is achieved, which means that if (1.5.26, I) were the r.d.s. a slope of ~ 120 mV dec^{-1} would be expected at 25°C. Working out b for step (1.5.26, II); ν = 1, α = ½ and as before, Z_i = 1, f_i = 1 (one term in the sum since there is only one step prior to r.d.s.), Z_r = 1, and f_r = ½ since in this case the charge transfer occurs only between the bulk solution and the adsorbed intermediates. Inserting these values in equation (1.5.27), yields a predicted value for the Tafel slope of b = 4RT/5F. It transpires that this is the only step in pathway (1.5.26), which yields this value of b upon analysis by equation (1.5.27). Thus Scarr[239] concluded that the o.e.r. polarisation data that he obtained on Ni, Co and Fe anodes in alkaline solution, could be satisfactorily explained by pathway (1.5.26), with the chemical second step in which the O-O is formed as the RDS.

It should be commented at this stage that, if equation (1.5.27) is applied to either the Krasil'shchikov mechanism, as presented in Table 1.5.1, or Hoar's alkaline path (1.5.18), a value of 4RT/5F will also be predicted for the Tafel slope. Scarr[239]

discriminated against these pathways on the basis that they involve the species MO^- or MO^{2-}. This arose from the fact that he had also observed a Tafel slope of ca. 46 mV dec^{-1} at low overpotentials on a Pt electrode in 1 M KOH. On the basis of this, he proposed that the o.e.r. proceeded via a common mechanism on Ni, Co, Fe and Pt in alkaline solution. However, he believed that PtO, PtO^-, or PtO^{2-}, could not be an intermediate species in the o.e.r. at Pt, on the basis of his interpretation of results obtained some years previously by Rozental and Vesolovskii[240]. Using O^{18} tracer techniques these workers had shown that O atoms that formed part of the anodic oxide layer on Pt, did not get evolved as gaseous oxygen under o.e.r. conditions. Scarr commented that "oxygen adsorbed at these potentials is known to have the stoichiometry PtO, and if it is in fact not identical to the species MO, then the two should be equivalent through an exchange process". On this basis and in view of the conclusions of Rozental and Vesolovskii, Scarr ruled out the involvement of MO^- or MO^{2-} species in the o.e.r., and thereby also ruled out the Krasil'shchikov mechanism and the Hoar alkaline mechanism. It must be said, that the question of whether oxygen atoms from an anodic oxide layer, can partake in the o.e.r. remains contentious, and therefore Scarr's argument remains unproven.

A more recent proposal regarding the formation of the O-O bond as an adsorbed peroxide entity, in the second step of an o.e.r. pathway has come from Bockris and Otagawa[42, 43] in an attempt to rationalise the o.e.r. behaviour on a range of thermally prepared perovskite materials $La_{1-x}A'_xMO_3$ (A' = Sr, K, Ca, Ce, Th, M = Cr, Mn, Fe, Co, Ni) in alkaline solution. The pathway that the authors proposed is as follows,

$$M^z + OH^- \leftrightarrows M^z\text{-}OH + e^- \qquad (1.5.28, I)$$

$$M^z\text{-}OH + OH^- \leftrightarrows M^z\text{-} \text{-}H_2O_2 + e^- \qquad (1.5.28, II)$$

$$(H_2O_2)_{phys} + OH^- \leftrightarrows (HO_2^-)_{phys} + H_2O \qquad (1.5.28, III)$$

$$(H_2O_2)_{phys} + (HO_2^-)_{phys} \leftrightarrows O_2 + H_2O + OH^- \qquad (1.5.28, IV)$$

where, M^z is a transition metal ion with the valence state z+ at the surface of a perovskite. In pathway (1.5.28) the hydrogen peroxide species is envisaged to be physisorbed. Bockris and Otagawa correlated the activity of the perovskite materials towards the o.e.r. with the M-OH bond strength, and concluded that the breaking of an M-OH bond is rate determining for the process. Thus, although the experimentally derived kinetic parameters could be accounted for, by either, the Bockris

electrochemical oxide path, or O'Grady's path (see Table 1.5.1), these mechanisms were ruled out on the basis that the relevant rate determining steps contained M-OH or M-O species, both as reactants and products, thus making it difficult to reconcile such steps with the proposed inverse dependence of rate on M-OH bond strength. This problem is solved by admitting step (1.5.28, II) as the RDS, since, a chemical M-O bond is only involved on one side of this step. Thus the weaker the M^z-OH bond, the greater the rate of the overall reaction, in agreement with the authors' hypothesis regarding the correlation of o.e.r. electrocatalytic activity with M-OH bond strength. Observed changes in Tafel slopes and reaction orders, both for different transition metals M, and at different overpotentials within the polarisation curve of a given perovskite were successfully explained in terms of changes of M-OH coverage, rather than changes in the RDS[42, 43]. A mechanism similar to (1.5.28), has been postulated by Singh and co-workers for Co_3O_4 and $NiCo_2O_4$ electrodes[241-243].

The final, possible o.e.r. pathway to be commented upon here, is that due to O'Grady et al.[244], presented in Table 1.5.1 as mechanism (IV). This mechanism was formulated to explain o.e.r. polarisation data obtained on RuO_2 electrodes in alkaline solution. O'Grady and co-workers observed a Tafel slope of ca. 40 mV dec^{-1}, with an associated reaction order with respect to OH^- concentration of ca. 1. In a similar manner to Rasiyah and Tseung[236, 237], these authors emphasise the importance of oxide redox transitions in the course of the o.e.r. In the initial OH^- discharge step a surface oxide lattice ion of valance Z is oxidised to a higher valance state, with a partial transfer of electron charge from the OH^- to the metal, and the consequent formation of a $(MOH)^z$ surface complex. Oxidation of the M^z ion to $M^{z+1}OH$ is completed in the second step. Oxygen evolution occurs by the recombination of two of the higher valence $M^{z+1}OH$ species, with the regeneration of the original M^z sites. In the original scheme of O'Grady et al.[244] it was envisaged that the M^z site corresponded to a Ru^{4+} ion. The authors rationalised their experimental data by proposing that the second step was rate determining, with low coverage Langmuir adsorption prevailing. A similar mechanism was proposed by O'Sullivan and Burke[245] for oxygen evolution on thick hydrous Rh oxides formed by repetitive potential cycling in 1 M NaOH solution.

Chapter 1 References

1 Bockris, J.O'M., Khan, S.U.M., "Surface Electrochemistry – A Molecular Level Approach", Plenum Press, New York, 1993, chapter 2.

2 Bockris, J.O'M., Reddy, A.K.N., "Modern Electrochemistry", Plenum Press, New York, 1970, chapter 7.

3 Hoare, J.P., "The Electrochemistry of Oxygen", Interscience, New York, 1968, chapter 1.

4 Grahame, D.C., *Chem. Rev.*, **1947**, *41*, 441.

5 Bard, A.J., Faulkner, L.R., "Electrochemical Methods-Fundamentals and Applications", J. Wiley & Sons, 2001, chapter 13.

6 Schmickler, W., in "Encyclopedia of Electrochemistry, Volume 1 – Thermodynamics and Electrified Interfaces", Bard, A.J., Stratmann, M., Eds., Gileadi, E., Urbakh, M., Vol, Eds., Wiley-VCH, Weinheim, 2002, section 2.2.

7 Greef, R., Peat, R., Peter, L.M., Robinson, J., "Instrumental Methods in Electrochemistry", Ellis, Chichester, 1985, chapter 5.

8 Butt, H-J. , in "Encyclopedia of Electrochemistry, Volume 1 – Thermodynamics and Electrified Interfaces", Bard, A.J., Stratmann, M., Ed., Gileadi, E., Urbakh, M., Vol, Ed., Wiley-VCH, Weinheim, 2002, chapter2.

9 von Helmholtz, H.L.F., *Ann. Physik.*, **1853**, *89*, 211.

10 von Helmholtz, H.L.F., *Ann. Physik.*, **1879**, *7*, 337.

11 Gouy, G., *J. Phys. Radium.*, **1910**, *9*, 457.

12 Chapman, D.L., *Phil. Mag.*, **1913**, *25*, 475.

13 Stern, O., *Z. Elektrochem.*, **1924**, *30*, 508.

14 Bockris, J.O'M, Devanathan, M.A.V., Müller, K., *Proc. Roy. Soc.*, **1963**, *A274*, 55.

15 Hansen, W.N., *J. Electroanal. Chem.*, **1983**, *150*, 133.

16 Everett, D.H., Ed., "Definitions, Terminology and Symbols in Colloid and Surface Science", Part 1, (Appendix to the "IUPAC Manual of Symbols and Terminology for Physiochemical Quantities and Units"), Butterworths, London 1972.

17 Kornyshev, A.A, Spohr, E., Vorotyntsev., M.A., in "Encyclopedia of Electrochemistry, Volume 1 – Thermodynamics and Electrified Interfaces", Bard, A.J., Stratmann, M., Ed., Gileadi, E., Urbakh, M., Vol, Ed., Wiley-VCH, Weinheim, 2002, section 2.1.

18 Toney, M. F.; Howard, J. N.; Richer, J.; Borges, G. L.; Gordon,J. G.; Melroy, O. R.; Wiesler, D. G.; Yee, D.; Sorensen, L. B. ,*Nature* **1994**, *368*, 444.

19 Watts-Tobin, R.G., *Philos. Mag.*, **1961**, *6*, 133.

20 Mott, N.F., Watts-Tobin, R.G., *Electrochimica Acta.*, **1961**, *4*, 79.

21 Fawcett, W.R., *J. Phys. Chem.*, **1978**, *82*, 1385.

22 Bockris, J.O'M., Habib, M.A., *J. Electroanal. Chem.*, **1976**, *68*, 367.

23 Damaskin, B.B., Frumkin, A.N., *Electrochimica Acta.*, **1974**, *19*, 173.

24 Trasatti, S., *J. Electroanal. Chem.*, **1981**, *123*, 2031.

25 Badiali, J.P., Rosinberg, M.L., Goodisman, J., *J. Electroanal. Chem.*, **1983**, *143*, 73.

26 Schmickler, W., *J. Electroanal. Chem.*, **1983**, *150*, 19.

27 Lang, N.D., Kohn, W., *Phys. Rev. B.,* **1970**, *1*, 4555.

28 Harris, J., Liebsch, A., *Vacuum,* **1983**, *33*, 655.

29 Sato, N., "Electrochemistry at Metal and Semiconductor Electrodes", Elsevier, 1998, chapter 2.

30 Anderson, M., Kennedy, J.H., in "Semiconductor Electrodes, Studies in Physical and Theoretical Chemistry 55", Finklea, H.O., Ed., Elsevier, 1988, p. 147.

31 Carpenter, M.K., Corrigan, D.A., *Abstract No. 490 of papers presented at the Atlanta Meeting of the Electrochem. Soc.,* May 15-20, **1988**, p. 700.

32 Gerischer, H., in "Physical Chemistry – An Advanced Treatise, Vol. IXA", Eyring, H., Henderson, D., Jost, W., Ed., Academic Press, New York, 1970, chapter 5.

33 Ahmed, S.M., in "Oxides and Oxide Films, Vol. 1", Vijh, A.K., Ed., Marcel Dekker, New York, 1977, p. 341.

34 Memming, R., in "Comprehensive Treatise of Electrochemistry, Vol. 7", Conway, B.E., Bockris, J.O'M., Yeager, E., Khan, S.U.M., White, R.E., Eds., Plenum Press, New York, 1983, p. 529.

35 Lewis, N.S., *Annu. Rev. Phys. Chem.*, **1991**, *42*, 543.

36 Nozik, A.J., Memming, R., *J. Phys. Chem.*, **1996**, *100*, 13061.

37 Finkler, H.D., Ed., "Semiconductor Electrodes", Elsevier, New York, 1987.

38 Sato, N., "Electrochemistry at Metal and Semiconductor Electrodes", Elsevier, 1998.

39 Sato, N., "Electrochemistry at Metal and Semiconductor Electrodes", Elsevier, 1998, chapter 5.

40 Green, M., in "Modern Aspects of Electrochemistry, Vol. 2", Bockris, J.O'M., Ed., Butterworths, London, 1959, p. 343.

41 Myamlin, V.A., Pleskov, Y.V., "Electrochemistry of Semiconductors", Plenum Press, New York, 1967.

42 Bockris, J.O'M., Otagawa,T., *J. Phys. Chem.*, **1983**, *87*, 2960.

43 Bockris, J.O'M., Otagawa,T., *J. Electrochem. Soc.*, **1984**, *131*, 290.

44 Hoffman-Perez, M., Gerischer, H., *Z. Elektrochem.*, **1961**, *65*, 771.

45 Sato, N., *Corrosion,* **1989**, *45*, 354.

46 Boem, H.P., *Disc. Faraday Soc.*, **1971**, *62*, 264.

47 Nieuwenhuys, B.E., Ponec, V., van Koten, G., van Leeuwen, P.W.N.M., van Santen, R.A. in, "Studies in Surface Science and Catalysis: vol. 79.Catalysis", Moulijn, J.A., van Leeuwen, P.W.N.M., van Santen, R.A., Eds., Elsevier, Amsterdam; 1993. p. 143– 149. Chapter 4.

48 Tamura, H., Furuichi, R., *Bunseki Kagaku,* **1991**, *40*, 635.

49 Van Riemsdijk, W.H., Bolt, G.H., Koopal, L.K., Blaakmeer, J., *J. Colloid Interface. Sci.*, **1986**, *109*, 219.

50 Hiemstra, T., Van Riemsdijk, W.H., *J. Colloid Interface. Sci.,* **1996**, *179*, 488.

51 Hiemstra, T., Van Riemsdijk, W.H., *J. Colloid Interface. Sc.i*, **1999**, *210*, 182.

52 Stumm, W., "Chemistry of the Solid-Water Interface", John Wiley & Sons, New York, (1992).

53 Carr, J.P., Hampson, N.A., Taylor, R., *J. Electroanal. Chem.,* **1970**, *27*, 109.

54 Brown Jr., G.E., Henrich, V.E., Casey, W.H., Clark, D.L., Eggleston, C., Felmy, A., et al., *Chem. Rev.*, **1999**, *99*, 77.

55 Bourikas, K., Kordulis, C., Vakros, J., Lycourghiotis, A., *Adv. Colloid Interface. Sci.,* **2004**, *110*, 97.

56 Ahmed, S.M., *J. Phys. Chem.*, **1969**, *73*, 3546.

57 Furlong, D.N., Yates, D.E., Healy, T.W., in "Electrodes of Conductive Metallic Oxides. Part B", Trasatti, S., Ed., Elsevier, Amsterdam, 1981, p. 367.

58 James, R.O., Leckie, J.O., Davis, J.A., *J. Colloid Interface. Sc.i*, **1978**, *65*, 331.

59 Yates, D.E., Levine, S., Healy, T.W., *J. Chem. Soc., Faraday Trans.* **1974**, *70*, 1807.

60 Bockris, J.O'M., in "Modern Aspects of Electrochemistry, Vol. 1", Bockris, J.O'M., Ed., Butterworths, London, 1954, chapter 4.

61 Vetter, K.J., "Electrochemical Kinetics, Theoretical and Experimental Aspects", Academic Press, London, 1967.

62 Bockris, J.O'M., Reddy, A.K.N., "Modern Electrochemistry", Plenum Press, New York, 1970, chapters 8 & 9.

63 Bard, A.J., Faulkner, L.R., "Electrochemical Methods-Fundamentals and Applications", J. Wiley & Sons, 2001, chapter 3.

64 Greef, R., Peat, R., Peter, L.M., Robinson, J., "Instrumental Methods in Electrochemistry", Ellis, Chichester, 1985, chapter 3.

65 Tafel, J., *Z. Physik. Chem*,, **1905**, *50A*, 641.

66 Bard, A.J., Faulkner, L.R., "Electrochemical Methods-Fundamentals and Applications", J. Wiley & Sons, 2001, section 2.1.6.

67 Butler, J.A.V., *Trans. Faraday Soc.*, **1924**, *19*, 729.

68 Erdey-Gruz, T., Volmer, M., *Z. Physik. Chem.,* **1930**, *150A*, 203.

69 Bockris, J. O'M. , *J. Chem. Phys.*, **1956,** *24*, 817.

70 Pillai, K.C., Bockris, J.O'M., *J. Electrochem. Soc.*, **1984**, *131*, 568.

71 Frumkin, A.N., *Z. Phys. Chem.,* **1925**, *116*, 466.

72 Temkin, M., *Zh. Fiz. Khim.*, **1941**, *15*, 296.

73 Conway, B.E., in "Impedance Spectroscopy – Theory, Experiment, and Applications", 2nd Edition, Barsoukov, E., Macdonald, J.R., Ed., J. Wiley & Sons, 2005, section 4.5.

74 Parsons, R., *Trans. Faraday Soc.,* **1951**, *47*, 1332.

75 Bockris, J.O'M., Khan, S.U.M., "Surface Electrochemistry – A Molecular Level Approach", Plenum Press, New York, 1993, section 3.5.

76 Christiansen, C.A., *Z. Physik. Chem*,, **1936**, *B33*, 145; **1937**, *B37*, 374.

77 Damjanovic, A., Dey, A., Bockris, J.O'M., *Electrochimica. Acta.,* **1966**, *11*, 791.

78 Conway, B.E., Gileadi, E., *Trans. Faraday Soc.*, **1962**, *58*, 2493.

79 Grubb, W.T., *17th Annual Power Sources Conference,* Atlantic City, 1963.

80 Grubb, W.T., *Nature*, **1963**, *198*, 883.

81 Bockris, J.O'M., Khan, S.U.M., "Surface Electrochemistry – A Molecular Level Approach", Plenum Press, New York, 1993, section 3.21 – 3.23.

82 Greef, R., Peat, R., Peter, L.M., Robinson, J., "Instrumental Methods in Electrochemistry", Ellis, Chichester, 1985, chapter 7.

83 Katsaounis, A., Brosada, S., Vayenas, C.G., in "Encyclopedia of Electrochemistry, Volume 5 – Electrochemical Engineering", Bard, A.J., Stratmann, M., Eds., Macdonald, D.D., Schmuki, P., Vol, Eds., Wiley-VCH, Weinheim, 2007, chapter2.

84 Vielstich, W., Lamm, A., Gasteiger, H.A., Eds., "Handbook of Fuel Cells, Fundamentals Technology and Applications, Vol 2, Electrocatalysis", John Wiley and Sons, Chichester, 2003.

85 Lipkowski, J., Ross, P.N., Eds., "Electrocatalysis", John Wiley and Sons-VCH, New York, 1998.

86 Pletcher, D., *J. Appl. Electrochem.*, **1984**, *14*, 403.

87 Horiuti, I., Polanyi, M., *Acta Physiochimica URSS*, **1935**, *2*, 505, *Trans. Faraday Soc.*, **1934**, *30*, 1164.

88 Krishtalik, L.I., in "Comprehensive Treatise of Electrochemistry, Vol. 7", Conway, B.E., Bockris, J.O'M., Yeager, E., Khan, S.U.M., White, R.E., Eds., Plenum Press, New York, 1983, p. 87.

89 Parsons, R., in "Modern Aspects of Electrochemistry, Vol. 1", Bockris, J.O'M., Ed., Butterworths, London, 1954.

90 Bockris, J.O'M., Khan, S.U.M., "Surface Electrochemistry – A Molecular Level Approach", Plenum Press, New York, 1993, section 3.14.

91 Trasatti, S., in "Handbook of Fuel Cells, Fundamentals Technology and Applications, Vol 2, Electrocatalysis", Vielstich, W., Lamm, A., Gasteiger, H.A., Eds., John Wiley and Sons, Chichester, 2003, chapter 10.

92 Bowden, F.P., Rideal, E., *Proc. Roy. Soc.*, **1928**, *A120*, 59.

93 Breiter, M.W., in "Handbook of Fuel Cells, Fundamentals Technology and Applications, Vol 2, Electrocatalysis", Vielstich, W., Lamm, A., Gasteiger, H.A., Eds., John Wiley and Sons, Chichester, 2003, chapter 25.

94 Lasia, A., in "Handbook of Fuel Cells, Fundamentals Technology and Applications, Vol 2, Electrocatalysis", Vielstich, W., Lamm, A., Gasteiger, H.A., Eds., John Wiley and Sons, Chichester, 2003, chapter 29.

95 Krstajic, N., Popovic, M., Grgur, B., Vojnovic, M., Sepa, D., *J. Electroanal. Chem.*, **2001**, *512*, 16.

96 Bockris, J.O'M., Koch, D.F.A., *J. Phys. Chem.*, **1961**, *65*, 1941.

97 Bockris, J. O'M., *Nature*, **1946,** *158*, 584.

98 Conway, B.E., Bockris, J. O'M. , *J. Chem. Phys.*, **1957,** *26*, 532.

99 Trasatti, S., *J. Electroanal. Chem.*, **1972**, *39*, 163.

100 Conway, B.E., Jerkiewicz, G., *Electrochimica. Acta.*, **2000**, *45*, 4075.

101 Conway, B.E., Bockris, J. O'M. , *Can. J. Chem.*, **1957,** *33*, 1124.

102 Petrii, O.A., Tsirlina, G.A., *Electrochimica. Acta.*, **1994**, *39*, 1739.

103 Trasatti, S., *J. Electroanal. Chem.*, **1980**, *111*, 125.

104 Zagal, J.H., *Coord. Chem. Rev.*, **1992**, *119*, 89.

105 Bond, G.C., "Catalysis by Metals", Academic Press, New York, 1962.

106 Mukerjee, S., Srinivasan, S., Soriaga, M.P., McBreen, J., *J. Electrochem. Soc.*, **1995**, *142*, 1409.

107 Marković, N.M., Grugur, B.N., Ross, P.N., *J. Phys. Chem.*, **1997**, *101*, 5405.

108 Trasatti, S., *Electrochimica. Acta.*, **1984**, *29*, 1503.

109 Appleby, A.J., *Catal. Rev.*, **1970**, *4*, 221.

110 Jakšić, M.M., *Int. J. Hydrogen Energy*, **1986**, *11*, 519.

111 Taylor, H.S., *Proc. Roy. Soc. Lond. A.*, **1925**, *108*, 105.

112 Burke, L.D., *Gold Bull.*, **2004**, *37*, 125.

113 Burke, L.D., Collins, J.A., Horgan, M.A., Hurley, L.M., O'Mullane, A.P., *Electrochimica. Acta.*, **2000**, *45*, 4127.

114 Burke, L.D., Kinsella, L.M., O'Connell, A.M., *Russ. J. Electrochem.*, **2004**, *40*, 1105.

115 Haruta, M., Yamada, N., Kobayashi, T., Iijima, S., *J. Catal.*, **1989**, *115*, 301.

116 Burke, L.D., Hurley, L.M., Murphy, M.A., *J. Solid State Electrochem.* , **1999**, *4*, 34.

117 Burke, L.D., Lee, B.H., *J. Electrochem. Soc.*, **1991**, *138*, 2496.

118 Burke, L.D., Murphy, M.M., *J. Electrochem. Soc.*, **1991**, *138*, 88.

119 Burke, L.D., Naser, N.S., *J. Appl. Electrochem.*, **2005**, *35*, 931.

120 Hall, D.E., *J. Electrochem. Soc.*, **1983**, *130*, 317.

121 McBreen, J., in "Handbook of Battery Materials", Besenhard, J.O., Ed., Wiley-VCH, Weinheim, 1999.

122 Seghiouer, A., Chevalet, J., Barhoun, A., Lantelme, F., *J. Electroanal. Chem.*, **1998**, *442*, 113.

123 Burke, L.D., Twomey, T.A.M., *J. Electroanal. Chem.*, **1984**, *162*, 101.

124 Burke, L.D., Twomey, T.A.M., *J. Electroanal. Chem.*, **1984**, *167*, 285.

125 Visscher, W., Barendrecht, E., *J. Appl. Electrochem.*, **1980**, *10*, 269.

126 de Souza, L.M.M., Kong, F.P., McLarnon, F.R., Muller, R.H., *Electrochimica. Acta.*, **1997**, *42*, 1253.

127 Šimpraga, R., Conway, B.E., *J. Electroanal. Chem.*, **1990**, *280*, 341.

128 Makrides, A.C., *J. Electrochem. Soc.*, **1966**, *113*, 1158.

129 Okuyama, M., Haruyama, S., *Corros. Sci.*, **1974**, *14*, 1.

130 Wolf, J.F., Yeh, L-S. R., Damjanovic, A., *Electrochimica. Acta.*, **1981**, *26*, 409.

131 Weininger, J.L., Breiter, M.W., *J. Electrochem. Soc.*, **1963**, *110*, 484.

132 Gennero De Chialvo, M.R., Chialvo, A.C., *Electrochimica. Acta.*, **1988**, *33*, 825.

133 Bode, H., Dehmelt, K., Witte, J., *Electrochimica. Acta.*, **1966**, *11*, 1079.

134 Wehrens-Dijksma, M., Notten, P.H.L., *Electrochimica. Acta.*, **2006**, *51*, 3609.

135 Barnard, R., Randell, C.F., Tye, F.L., *J. Appl. Electrochem.*, **1980**, *10*, 109.

136 Greaves, C., Thomas, M.A., *Acta Cryst.*, **1986**, *B42*, 51.

137 Kim, M.S., Hwang, T.S., Kim, K.B., *J. Electrochem. Soc.*, **1997**, *144*, 1537.

138 Le Bihan, S., Figlarz, M., *J. Cryst. Growth*, **1972**, *13/14*, 458.

139 Mani, B., deNeufville, J.P., *J. Electrochem. Soc.*, **1988**, *135*, 801.

140 Madou, M.J., McKubre, M.C.H., *J. Electrochem. Soc.*, **1983**, *130*, 1056.

141 Sac-Epee, N., Palacin, M.R., Delahaye-Vidal, A., Chabre, Y., Tarascon, J-M., *J. Electrochem. Soc.*, **1998**, *145*, 1434.

142 Milner, P.C., Thomas, U.B., in "Advances in Electrochemistry and Electrochemical Engineering, Vol 5", Tobias, C.W., ed., Interscience, New York, 1967, chapter 1.

143 Kober, F.P., *J. Electrochem. Soc.*, **1965**, *112*, 1064.

144 Kober, F.P., *J. Electrochem. Soc.*, **1967**, *114*, 215.

145 Briggs, G.W.D., in "Electrochemistry - Vol 4, Specialist Periodical Reports", The Chemical Society, London, 1974, chapter 3.

146 Kinoshita, K., "Electrochemical Oxygen Technology", Wiley-Interscience, New York, 1992, chapter 2.

147 Lu, P.W.T., Srinivasan, S., *J. Electrochem. Soc.*, **1978**, *125*, 1416.

148 Aleshkevich, S.A., Golovchenko, E.I., Morozov, V.P., Sagoyan, L.N., *Soviet Electrochem.*, **1968,** *4*, 530, 1117.

149 Liu, T.-C., Pell, W.G., Conway, B.E.., *Electrochimica. Acta.*, **1999**, *44*, 2829.

150 Pourbaix, M., "Atlas of Electrochemical Equilibrium in Aqueous Solutions", Pergamon Press, London, 1965.

151 Silverman, D.C., *Corrosion*, **1981**, *37*, 546.

152 Bourgault, P.L., Conway, B.E., *Can. J. Chem.*, **1960**, *38*, 1557.

153 Bourgault, P.L., Conway, B.E., *Can. J. Chem.*, **1962**, *40*, 1690.

154 Conway, B.E., Bourgault, P.L., *Trans. Faraday Soc.*, **1962**, *58*, 593.

155 Conway, B.E., Gileadi, E., *Can. J. Chem.*, **1962**, *40*, 1933.

156 Barnard, R., Randell, C.F., Tye, F.L., *J. Electroanal. Chem.*, **1981**, *119*, 17.

157 Bernard, P., Gabrielli, C., Keddam, M., Takenouti, H., Leonardi, J., Blanchard, P., *Electrochimica. Acta.*, **1991**, *36*, 743.

158 Cheek, G.T., O'Grady, W.E., *J. Electroanal. Chem.*, **1997**, *421*, 173.

159 Feuillade, G., Jacoud, R., *Electrochimica. Acta.*, **1969**, *14*, 1297.

160 Sac-Epee, N., Palacin, M.R., Beaudoin, B., Delahaye-Vidal, A., Jamin, T., Chabre, Y., Tarascon, J-M., *J. Electrochem. Soc.*, **1997**, *144*, 3896.

161 Srinivasan, V., Cornilsen, B.C., Weidner, J.W., *J. Solid State Electrochem.*, **2005**, *9*, 61.

162 Cornilsen, B.C., Karjala, P.J., Loyselle, P.L., *J Power Sources*, **1988**, *22*, 351.

163 Cornilsen, B.C., Shan, X., Loyselle, P.L., *J Power Sources*, **1990**, *29*, 453.

164 Burke, L.D., Lyons, M.E.G., in "Modern Aspects of Electrochemistry, Vol. 18", White, R.E., Bockris, J.O'M., Conway, B.E., Ed., Plenum Press, New York, 1986, p169.

165 Burke, L.D., Whelan, D.P., *J. Electroanal. Chem.*, **1984**, *162*, 121.

166 Burke, L.D., Lyons, M.E.G., *J. Electroanal. Chem.*, **1986**, *198*, 347.

167 Joiret, S., Keddam, M., Novoa, X.R., Perez, M.C., Rangel, C., Takenouti, H., *Cement & Concrete Composites*, **2002**, *24*, 7.

168 Lyons, M.E.G., Ph.D. Thesis, University College, Cork, 1983.

169 Bockris, J.O'M., Khan, S.U.M., "Surface Electrochemistry – A Molecular Level Approach", Plenum Press, New York, 1993, chapter 8.

170 Guzman, R.S.S., Vilche, J.R., Arvia, A.J., *Electrochimica. Acta.*, **1979**, *24*, 395.

171 Juanto, S., Guzman, R.S.S., Zerbino, J.O., Vilche, J.R., Arvia, A.J., *Electrochimica. Acta.*, **1991**, *36*, 1143.

172 Flis, J., Oranowska, H., Szklarska-Smialowska, Z., *Corros. Sci.*, **1990**, *30*, 1085.

173 MacDonald, D.D., Roberts, B., *Electrochimica. Acta.*, **1978**, *23*, 557.

174 Amaral, S.T., Martini, E.M.A., Muller, I.L, *Corros. Sci.*, **2001**, *43*, 853.

175 Burke, L.D., Casey, M.I., Cunnane, V.J., Murphy, O.J., Twomey, T.A.M. *J. Electroanal. Chem.*, **1985**, *189*, 353.

176 Laviron, E. *J. Electroanal. Chem.*, **1980**, *112*, 1.

177 O'Grady, W.E., Bockris, J.O'M., *Surf. Sci.*, **1973**, *38*, 249.

178 Armstrong, R.D., Baurhoo, I., *J. Electroanal. Chem.*, **1972**, *34*, 41.

179 Amaral, S.T., Muller, I.L., *Corros. Sci.*, **1999**, *41*, 759.

180 MacDonald, D.D., Owen, D., *J. Electrochem. Soc.*, **1973**, *120*, 317.

181 Fierro, C., Carbonio, R.E., Scherson, D., Yeager, E.B., *J. Phys. Chem.*, **1987**, *91*, 6579.

182 Butel, M., Gautier, L., Delmas, C., *Solid State Ionics*, **1999**, *122*, 271.

183 Benson, P., Briggs, G.W.D., Wynne-Jones, W.F.K., *Electrochimica. Acta.*, **1964**, *9*, 275.

184 Gomez Meier, H., Vilche, J.R., Arvia, A.J., *J. Electroanal. Chem.*, **1982**, *138*, 367.

185 Behl, W.K., Toni, J.E., *J. Electroanal. Chem.*, **1971**, *31*, 63.

186 Erts, D., Ahlberg, E., Asbjörnsson, J., Olin, H., Prikulis, J., *J. Appl. Phys.*, **1998**, *A 66*, S477.

187 Ohtsuka, T., Sato, N., *J. Electroanal. Chem.*, **1983**, *147*, 167.

188 Heusler, K.E., in "Passivity of Metals", Frankenthal, R.P., Kruger, J., Eds., Electrochemical Soc. Inc. Princeton, New Jersey, 1978, p. 771.

189 Foelske, A., Strehblow, H.-H., *Surf. Interf. Anal.*, **2002**, *34*, 125.

190 Šimpraga, R.P., *J. Electroanal. Chem.*, **1993**, *355*, 79.

191 Bewick, A., Gutierrez, C., Larramora, G., *J. Electroanal. Chem.*, **1992**, *333*, 165.

192 Simmons, G.W., in "Passivity of Metals", Frankenthal, R.P., Kruger, J., Eds., Electrochemical Soc. Inc. Princeton, New Jersey, 1978, p. 899.

193 Šimpraga, R., Conway, B.E., *J. Electroanal. Chem.*, **1991**, *313*, 161.

194 Liu, T.-C., Pell, W.G., Conway, B.E., *Electrochimica. Acta.*, **1999**, *44*, 2829.

195 Gomez Meier, H., Vilche, J.R., Arvia, A.J., *J. Electroanal. Chem.*, **1982**, *134*, 251.

196 Burke, L.D., Lyons, M.E.G., Murphy, O.J., *J. Electroanal. Chem.*, **1982**, *132*, 247.

197 Hoare, J.P., "The Electrochemistry of Oxygen", Interscience, New York, 1968, chapter 2.

198 Tarasevich, M.R., Sadkowski, A., Yeager, E., in "Comprehensive Treatise of Electrochemistry, Vol. 7", Conway, B.E., Bockris, J.O'M., Yeager, E., Khan, S.U.M., White, R.E., Eds., Plenum Press, New York, 1983, p 301.

199 Bockris, J.O'M., Khan, S.U.M., "Surface Electrochemistry – A Molecular Level Approach", Plenum Press, New York, 1993, section 3.23.

200 Wroblowa, H., Rao, M.L.B., Damjanovic, A., Bockris, J.O'M., *J. Electroanal. Chem.*, **1967**, *15*, 139.

201 Bockris, J.O'M., Oldfield, L.E., *Trans. Faraday Soc.*, **1955**, *51*, 249.

202 Giner, J.Z., *Z. Electrochem.*, **1959**, *63*, 386.

203 Bockris, J.O'M. Huq, A.K.M.S., *Proc. Roy. Soc.*, **1956**, *273A*, 1733.

204 Damjanovic, A., in "Electrochemistry in Transition" Murphy, O.J., Srinivasan, S., Conway, B.E., Eds., Plenum Press, New York, 1992, p107.

205 Gattrell, M., MacDougall, B., in "Handbook of Fuel Cells, Fundamentals Technology and Applications, Vol 2, Electrocatalysis", Vielstich, W., Lamm, A., Gasteiger, H.A., Eds., John Wiley and Sons, Chichester, 2003, chapter 30.

206 Damjanovic, A., Genshaw, M.A., Bockris, J.O'M., *J. Chem. Phys.*, **1966**, *45*, 4057.

207 Wroblowa, H.S., Pan, Y.C., Razumney, G., *J. Electroanal. Chem.*, **1976**, *69*, 195.

208 Appleby, A.J., Savy, M., *J. Electroanal. Chem.*, **1978**, *92*, 15.

209 Anastasijevic', N.A., Vesovic, V., Adzic', R.R., *J. Electroanal. Chem.*, **1987**, *229*, 305 & 317.

210 Gnanamuthu, D.S., Petrocelli, J.V., *J. Electrochem. Soc.*, **1967**, *114*, 1036.

211 Damjanovic, A., in "Modern Aspects of Electrochemistry, Vol. 5", Bockris, J.O'M., Conway, B.E., Eds., Plenum Press, New York, 1969, p369.

212 Horiuti, J. in "Physical Chemistry, An Advanced Treatise, Vol. IXB", Eyring, H., Ed., Academic Press, New York, 1970, p 543.

213 Appleby, A.J., in "Modern Aspects of Electrochemistry, Vol. 9", Bockris, J.O'M., Conway, B.E., Eds., Plenum Press, New York, 1973, p369.

214 Trasatti, S., Lodi, G., in "Electrodes of Conductive Metallic Oxides, Part B", Trasatti, S., Ed., Elsevier, New York, p 521.

215 Burke, L.D., in "Electrodes of Conductive Metallic Oxides, Part A", Trasatti, S., Ed., Elsevier, New York, p 141.

216 Ruetschi, P., Delahay, P., *J. Chem. Phys.*, **1955**, *23*, 556.

217 Tseung, A.C.C., Jasem, S., *Electrochimica. Acta.*, **1977**, *22*, 31.

218 Miles, M.H., Huang, Y.H., Srinivasan, S., *J. Electrochem. Soc.*, **1978**, *125*, 1931.

219 Burke, L.D., Whelan, D.P., *J. Electroanal. Chem.*, **1979**, *103*, 179.

220 Hall, D.E., *J. Electrochem. Soc.*, **1983**, *130*, 317.

221 Krasil'shchikov, A.I., *Zh. Fiz. Khim.*, **1963**, *37*, 531.

222 Hoar, T.P., *Proc. 8th Meeting CITCE,* Madrid 1956, Butterworths, London, 1958, p. 439.

223 Birss, V.I., Damjanovic, A., *J. Electrochem. Soc.*, **1987**, *134*, 113.

224 Iwakura, C., Fukuda, K., Tamura, H., *Electrochimica. Acta.*, **1976**, *21*, 501.

225 Birss, V.I., Damjanovic, A., Hudson, P.G., *J. Electrochem. Soc.*, **1986**, *133*, 1621.

226 Ferreira, A.C., Gonzalez, E.R., Ticianelli, E.A., Avaca, L.A., Matvienko, B., *J. Appl. Electrochem.*, **1988**, *18*, 894.

227 Lyons, M.E.G., Burke, L.D., *J. Electroanal. Chem.*, **1984**, *170*, 377.

228 Gottesfeld, S., Srinivasan, S., *J. Electroanal. Chem.*, **1978**, *86*, 89.

229 Matsumoto, Y., Manabe, H., Sato, E., *J. Electrochem. Soc.*, **1980**, *127*, 811.

230 Matsumoto, Y., Yamada, S., Nishida, T., Sato, E., *J. Electrochem. Soc.*, **1980**, *127*, 2360.

231 Wu, G., Li, N., Zhou, D-R., Mitsuo, K., Xu, B-Q., *J. Solid State Chem.*, **2004**, *177*, 3682.

232 Wang, X., Luo, H., Yang, H., Sebastian, P.J., Gamboa, S.A., *Int. J. Hydrogen Energy*, **2004**, *29*, 967.

233 Zhang, Y., Coa, X., Yuan, H., Zhang, W., Zhou, Z., *Int. J. Hydrogen Energy*, **1999**, *24*, 529.

234 Damjanovic, A., Dey, A., Bockris, J.O'M., *J. Electrochem. Soc.*, **1966**, *113*, 739.

235 Sato, N., Okamoto, G., *Electrochimica. Acta.*, **1965**, *10*, 495.

236 Rasiyah, P., Tseung, A.C.C., Hibbert, D.D., *J. Electrochem. Soc.*, **1982**, *129*, 1724.

237 Rasiyah, P., Tseung, A.C.C., *J. Electrochem. Soc.*, **1983**, *130*, 2384.

238 Willems, H., Kobussen, A.G.C., De Wit, J.H.W., and Broers, G.H.J., *J. Electroanal. Chem.*, **1984**, *170*, 227.

239 Scarr, R.F., *J. Electrochem .Soc.*, **1969**, *116*, 1526.

240 Rozental', K.I., Vesolovskii, V.F., *Doklady Akad. Nauk, SSSR*, **1956**, *111*, 637.

241 Singh, R.N., Hamadani, M., Koenig, J.-F., Poillerat, G., Gautier, J.L., Chartier, P., *J. Appl. Electrochem*, **1990**, *20*, 442.

242 Singh, R.N., Koenig, J.-F., Poillerat, G., Chartier, P., *J. Electrochem. Soc.*, **1990**, *137*, 1408.

243 Tiwari, S.K., Samuel, S., Singh, R.N., Poillerat, G., Koenig, J.-F., Chartier, P., *Int. J. Hydrogen Energy*, **1994**, *20*, 9.

244 O'Grady, W., Iwakura, C., Huang, J., Yeager, E., in "Proceedings of the Symposium on Electrocatalysis", Breiter, M.W., ed., The Electrochemical Society Inc., Pennington, NJ, 1974, p286.

245 O'Sullivan, E.J.M., Burke, L.D., *J. Electrochem. Soc.*, **1990**, *137*, 466.

CHAPTER 2

EXPERIMENTAL METHODOLOGY AND PROCEDURE

2.1 Introduction To Experimental Methodology

In this chapter consideration is given to the experimental techniques applied in the current work. In section 2.1, treatment is given to the theoretical basis behind the utilised methods, and the nature of the data that can be obtained from such measurements. Descriptions of the practical application of these experimental techniques, and of the materials used, are reserved for section 2.2.

In the background description of the experimental methodology in section 2.1, the emphasis is placed on the more complex techniques such as *Electrochemical Impedance Spectroscopy* (EIS), and on the theory behind the less often used experimental approaches such as the transient measurements applied here to probe real electrode surface areas. Cyclic Voltammetry (CV) is nowadays so universally utilised, and well understood by virtually all electrochemists, that a detailed discussion of this technique is considered superfluous in the present work. Instead, a short summary of its application to the systems under study is presented in section 2.1.2.

2.1.1 Steady State Polarisation Measurements

The principal means by which kinetic data was experimentally obtained in the present work, was through the use of steady state polarisation measurements. In such measurements the potential of the working electrode (relative to the reference electrode) is set at a constant potential and the current density is observed as a function of time, until a constant current density is observed over a period of time. When such a constant current density is obtained it is assumed that the electrochemical system is at a *steady state*. In practice, in the present work, a potential step function was applied to the working electrode within the Tafel slope potential region. Upon attaining a new potential value, E, the working electrode was allowed to remain at that potential until a consistent value of current density i was obtained. The potentiostat control software adjudged a steady-state to be achieved, when the variation of i with time t over a certain time period, fell below a user defined limit – for more on this, see section 2.2. When a steady-state current was achieved, this value was recorded to disk by the digitally controlled potentiostat, and the potential was

stepped to its next defined value, where the procedure was repeated. When steady state current densities are recorded at a number of different potentials, it is possible to plot the logarithm of i against E. The slope, $b = dE/d\log i$, obtained from such a plot is of course the Tafel slope, that was discussed in section 1.2.1. Since a Tafel slope obtained in the manner described above, refers to a steady state situation, the multi-step kinetic analyses of section 1.2.3 based upon the principal of pseudo-equilibrium can be applied to compare the values of b predicted by various theoretical mechanisms, to the value of b so measured. Recall from section 1.2.3 that the Tafel slope b is related to the kinetically significant transfer coefficient α as follows; $b = d\eta / d\log i = 2.303RT / \bar{\alpha}F = 2.303(2RT/3F)$.

The method of potentiostatic measurement of steady state polarisation data, as described above, became feasible after the introduction, in 1941 by Hickling[1] of an electronic feedback technique for maintaining a given electrode potential. Prior to this development steady state polarisation curves had to be recorded by galvanostatically setting a series of constant current densities, and recording the potential vs. time relation. Such an approach was adopted by Bowden and Rideal[2] in their early seminal work on the h.e.r., that was referred to in section 1.3.1. Indeed, if one reviews the literature on the o.e.r. (see for example Hoare's 1968[3] review on progress on the o.e.r. up to that time), they will find that until relatively recently (the 1980s), steady state polarisation curves were generally recorded galvanostatically as opposed to potentiostatically. In theory, the same data set should be obtained, whichever approach is adopted, although as commented by Bockris and Khan[4]- "conceptually, the potential step method is the better of the two methods for obtaining steady-state data because the rate depends exponentially on potential".

A significant issue that arises in the collection of steady-state polarisation data, is the question as to whether an apparent, time invariant constant current density, actually constitutes a steady state of the system, and indeed what is the meaning of the "steady state" of an electrochemical system? The possibility of continued oxide growth on an oxygen evolution electrode during the course of significant gas evolution, makes these questions particularly relevant in the case of steady state measurements that attempt to characterise the kinetics of the o.e.r. As a relevant example from the literature, Lu and Srinivasan[5] studied the effects of the growth of Ni oxide that occurs in parallel to the o.e.r. on Ni anodes in alkaline solution. Over the course of a 20 hour polarisation, in 1

N KOH at 1.8 V (vs R.H.E.) the recorded current density on a pre-anodised Ni electrode dropped continuously from ca. 80 mA cm^{-2} to ca. 14 mA cm^{-2}. Therefore a steady current value was never observed over this period. Ellipsometric measurements showed that the thickness of oxide film increased from 190 Å to 690 Å, over the same time period. The variation in measured optical constants indicated that the film became an increasingly poor electronic conductor with increasing polarisation time at 1.8 V. Therefore, the authors, quite reasonably, concluded that the continuously decreasing current density was as a result of the growth of an oxide film that became increasingly less conductive with time, owing to the conversion of Ni^{3+} ions to Ni^{4+} ions. Thus, the failure to obtain a constant current was a manifestation of electrochemical processes in the oxide film and not of the kinetics of the o.e.r.

The experience from the literature indicates that a *kinetically significant* steady state current should be achieved within a time scale of minutes from stepping the potential to a new value, depending, of course, on the particular system under investigation, and the size of the potential steps. In a publication, that has been reviewed in section 1.5.4, Burke et al.[6] performed steady state polarisation measurements on the o.e.r. at a Co electrode in 6.0 M NaOH. These workers increased the applied potential in steps of 50 mV, and found that a satisfactorily steady current was obtained after 10 minutes. In the present work, potential steps of 5 mV have been utilised in steady state polarisation measurements and steady currents (see section 2.2) have been observed and recorded after periods of 1 – 2 minutes following perturbation of the system. The requirement of shorter times to observe a satisfactorily steady current in the present work relative to the work of Burke et al., is presumably related to the smaller magnitude of the potential steps utilised.

It is generally possible to distinguish between the relaxation of an electrochemical system to a kinetically significant steady state (in o.e.r. studies at any rate), and the effects of a process relating to oxide growth/transformation, by examining a plot of current against time following the application of a potential step. The latter process tends to be defined by a much longer characteristic time scale, and the initial relaxation of current to a kinetically significant value will occur on an obviously shorter time scale, effectively 'superimposed' on the current characteristic of the longer process.

Another factor that must be taken into account, when conducting steady state polarisation measurements with the aim of determining kinetic parameters such as the

Tafel slope, is that of the uncompensated solution resistance, R_Ω. As is discussed in section 2.1.4, in relation to the Randles equivalent circuit representation of an electrochemical interface, R_Ω will always be present in series with the so called *series resistance* R_s of the electrode (the significance of this will be discussed in section 2.14) when a potential is applied to an electrode. Therefore, if a potential E_{app} applied to the working electrode, causes a current i to flow across the electrochemical interface, these parameters are related as follows:

$$E_{app} = i(R_\Omega + R_s) \tag{2.1.1}$$

A fraction of the potential, given by iR_Ω is dissipated by the solution resistance, and thus the effective potential E_{eff} applied to the electrode is given by iR_s. Thus, the kinetically significant polarisation data is $i(E_{eff})$ as opposed to $i(E_{app})$. The value of E_{eff} that causes a current i to flow is given by,

$$E_{eff} = E_{app} - iR_\Omega \tag{2.1.2}$$

To obtain kinetically significant steady state polarisation data, it is necessary to perform the correction outlined in equation (2.1.2) for each value of E_{app}. Therefore it is necessary to obtain the value of the solution resistance. A common method for measuring this parameter is the so-called *current interruption* technique[7]. In the present work however, electrochemical impedance spectroscopy, is utilised to determine R_Ω. The uncompensated solution resistance is obtained from the high frequency intercept of a Nyquist plot with the Z' as described in detail in section 2.1.4. Impedance scans to determine R_Ω are conducted at potentials in the so-called *double layer* region of a particular electrochemical system, away from potentials at which Faradaic processes occur with significant current densities.

2.1.2 Cyclic Voltammetry

As mentioned at the start of the chapter, it is not proposed to undertake a thorough discussion of cyclic voltammetry in this work, for two principal reasons. Firstly, the technique is so ubiquitous in modern electrochemistry, and its principals and applications have therefore been thoroughly discussed in most of the standard general

electrochemistry tests[8, 9, 10]. Secondly, since cyclic voltammetry is a potentiodynamic technique, it has limited application to the determination of the steady state kinetic behaviour of the oxygen evolution reaction. The technique is therefore principally applied to qualitative analysis of the surface electrochemistry of the polycrystalline Ni, Co and Fe oxygen evolution anodes, studied in the present work. Detailed discussions of the voltammetric profiles of these metals in alkaline solution have been presented in section 1.4. Cyclic voltammetry has been used in our work, to characterise the state of electrodes prior to steady state polarisation measurements, with the purpose of ensuring that data obtained in the latter experiments relates to a reproducible oxide surface. As well as serving this use, some of the CVs so-obtained have yielded potentially valuable information on the relationship between the oxide surface and the activity of the anode towards the o.e.r., as will be discussed in Chapter 3.

2.1.3 Electrochemical Impedance Spectroscopy

Traditional methods of electrochemical measurement, involving the imposition of potential sweeps or steps to an electrode, cannot fully characterise the electrochemical reaction at an electrode-electrolyte interface. While undoubtedly useful, these methods are based upon the analysis of currents that contain both Faradaic and non-Faradaic components. On the other hand *electrochemical impedance spectroscopy* (EIS) provides a method by which these components can be uncoupled through the analysis of the measured impedance of an electrochemical cell as a function of frequency. The basic approach is to perturb the system with an alternating potential signal of small magnitude and observe its response to the perturbation at steady state[11]. In practice, the frequency of the alternating potential is swept over a large range (10^{-4} to 10^{6} Hz is routinely possible nowadays[11]), and the response of the system is monitored via its impedance. Impedance can be defined[12] as a complex resistance encountered when a current flows through a circuit consisting of resistors and/or capacitors and/or inductors. Consideration will now be given to the concept of electrical impedance and its application to the study of electrochemical interfaces.

2.1.4 Simple AC Circuit Theory

In order to understand the principles of EIS, knowledge of fundamental alternating current (a.c.) theory is required. A sinusoidal voltage may be represented as

$$E = E_0 \sin(\omega t) \tag{2.1.3}$$

where E_0 is the maximum amplitude of the signal, and ω is the angular frequency ($\omega=2\pi f$ where f is the conventional frequency in Hz). The relationship between the voltage E and the current i is of interest in a.c. circuit analysis. In general the current will also be sinusoidal and have the same frequency ω as the voltage. However i and E will usually differ in amplitude and phase. Therefore, if the voltage E, from equation (2.1.3), is applied across the terminals of an a.c. circuit, the current flowing in the circuit can be represented as

$$i = I_0 \sin(\omega t + \phi) \tag{2.1.4}$$

where I_0 is the maximum amplitude of the current. The voltage E and current i can conveniently thought of as a rotating vector quantities (known as *phasors*) $\dot{\boldsymbol{E}}$ and $\dot{\boldsymbol{I}}$, as depicted in Figure 2.1.2. The maximum amplitude of a quantity represented by a phasor is given by the length of the phasor, whereas the instantaneous value is given by the projection on the 0 axis in the diagram. In Figure 2.1.2, it can be seen that the current and voltage phasors ($\dot{\boldsymbol{I}}$ and $\dot{\boldsymbol{E}}$ respectively) are separated by a *phase angle, ϕ*. If the voltage phasor is taken as the reference then the current is said to lag the voltage by a phase angle of ϕ, which in this case will have a negative sign.

If a sinusoidal voltage $\dot{\boldsymbol{E}}$ is applied across a pure resistance, R, then Ohm's law applies and the resulting current $\dot{\boldsymbol{I}}$ is given by the expression:

$$\dot{\mathbf{I}} = \frac{\dot{\mathbf{E}}}{R} \quad . \tag{2.1.5}$$

It is evident that the phase angle ϕ is zero in this case.

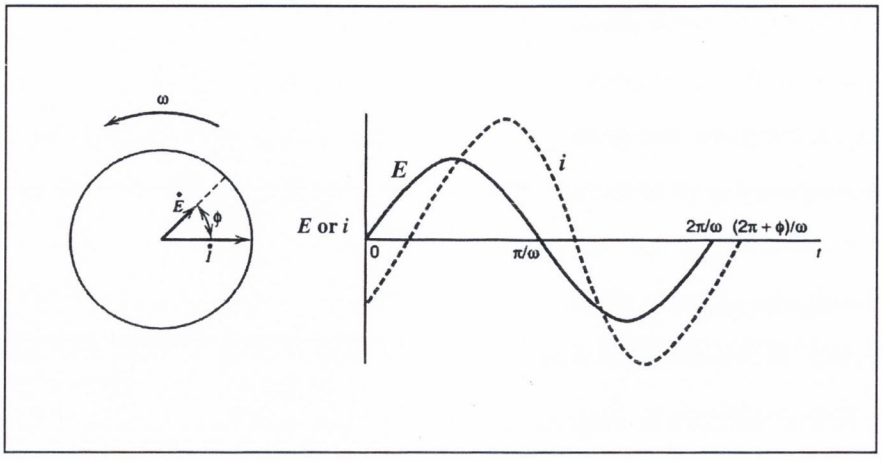


Figure 2.1.1 *Composite phasor diagram showing voltage and current phasors separated by a phase angle ϕ. Reproduced from Ref. 11.*

The capacitance C across a parallel plate capacitor is the constant of proportionality between the applied potential E and the charge q residing on the plates:

$$q = CE \quad . \tag{2.1.6}$$

An expression for current i is obtained by differentiating equation (2.1.6),

$$i = \frac{dq}{dt} = C\frac{dE}{dt} \tag{2.1.7}$$

which, from the definition of E in (2.1.3), yields

$$i = \omega C \Delta E \cos(\omega t) \quad . \tag{2.1.8}$$

It is common practice to define a quantity X_C, called the *capacitive reactance*, where $X_c = 1/\omega C$, so that equation (2.1.8) can be rewritten (in phasor notation) as

$$i = \frac{E}{X_C}\sin\left(\omega t + \frac{\pi}{2}\right) \quad . \tag{2.1.9}$$

In this situation the phase angle is $\pi/2$ and the current is said to lead the voltage.

It is apparent that the phasor relationship, represented by equation (2.1.9) has expanded to planar space relative to that in equation (2.1.5). This can be utilised, for mathematical convenience, to represent the phasors in terms of complex numbers. In complex notation, magnitudes along the ordinate axis are said to be *imaginary* and are multiplied by $j = \sqrt{-1}$. On the other hand components along the abscissa are assigned as *real*. The common practice in circuit analysis[11] is to plot the current phasor along the abscissa, in which case the relationship in equation (2.1.9) can be written in complex notation as

$$\dot{\mathbf{E}} = -jX_C\dot{\mathbf{I}} \quad . \tag{2.1.10}$$

Clearly, (2.1.10) is similar in form to Ohm's law (2.1.5) with the complex quantity $-jX_C$ replacing the resistance R. A dimensional analysis shows that X_C must have units of ohms, however, unlike R its magnitude is frequency dependent.

For a resistor and capacitor in series (RC series circuit), the sum of the voltage drops across each element must equal the total applied voltage $\dot{\mathbf{E}}$, so that

$$\begin{aligned} \dot{\mathbf{E}} &= \dot{\mathbf{E}}_R + \dot{\mathbf{E}}_C \\ \dot{\mathbf{E}} &= \dot{\mathbf{I}}(R - jX_C) \\ \dot{\mathbf{E}} &= \dot{\mathbf{I}}\mathbf{Z} \end{aligned} \tag{2.1.11}$$

where the vector quantity $\mathbf{Z} = R - iX_C$ is called the *impedance*. It is evident that $\mathbf{Z}$, has both a real component defined by $Z' = R$, and an imaginary part given by $Z'' = -X_C = -1/\omega C$. The current – voltage behaviour of an RC series circuit can be graphically represented on an Argand plane, as in Figure 2.1.2.

It is apparent from the Argand diagram in Figure 2.1.2 that the current will no longer be either in phase or 90^0 out of phase with the voltage. The phase angle is now frequency dependent and is obtained by the following expression:

$$\tan\phi = \frac{X_C}{R} = \frac{1}{\omega RC} \tag{2.1.12}$$

The magnitude $|Z|$ of the impedance, is given by

$$|Z| = \sqrt{Z'^2 + Z''^2} = \sqrt{R^2 + X_C^2} \tag{2.1.13}$$

It must be remarked, that although impedance is treated mathematically, as having "real" and "imaginary" components, both components are physically measurable quantities, since practical EIS equipment measures both the magnitude and phase angle of the impedance.

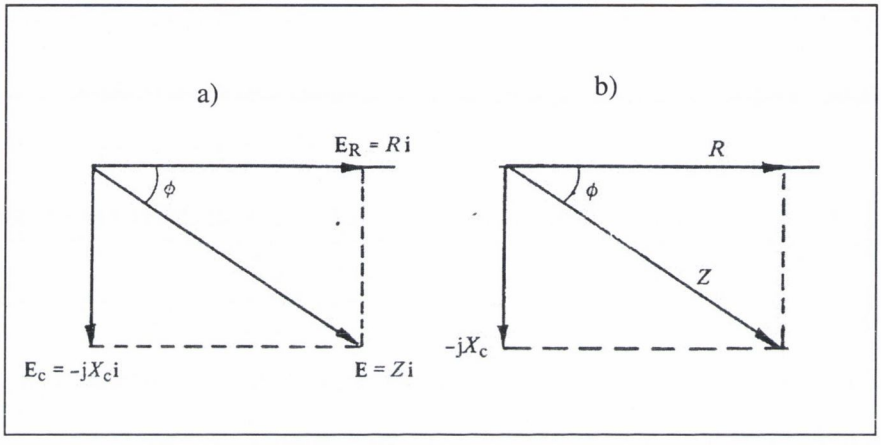


Figure 2.1.2 *a)Phasor diagram for an RC series circuit, showing the potential* **E** *as the resolution of the resistive and capacitive components Ri and* jX_C *i. b)An Argand diagram showing the same relationship in terms of impedances. Adapted from Ref. 13.*

The foregoing analysis can be extended to circuits of greater complexity by noting that impedances combine with rules analogous to those of resistors in simple circuit analysis. In the case of impedances in series, the overall impedance is the sum of the individual values. For a parallel arrangement, the reciprocal of the overall impedance is the sum of the reciprocals of the individual values. It should be clear, that vector algebra is required when dealing with impedance combinations, as opposed to the scalar operations involved when combining simple resistance values.

When impedance spectra are presented on an Argand plane, with the Z′ data plotted on the abscissa and the Z″ values plotted on the ordinate, the resultant diagram is termed a *Nyquist plot*. The Nyquist plots for some simple RC circuits are presented in Figure 2.1.3. From Figure 2.1.3 it can be seen that an RC parallel combination yields a semicircle in a Nyquist plot. This semicircle is said to be characteristic of a single *RC time constant*. EIS plots often contain several such semicircles, corresponding to

separate processes occurring on different timescales. It is common practice to plot the negative of Z″ on the y axis in a Nyquist diagram, since this ensures, for graphical convenience, that semicircles characteristic of RC loops appear in the first quadrant.

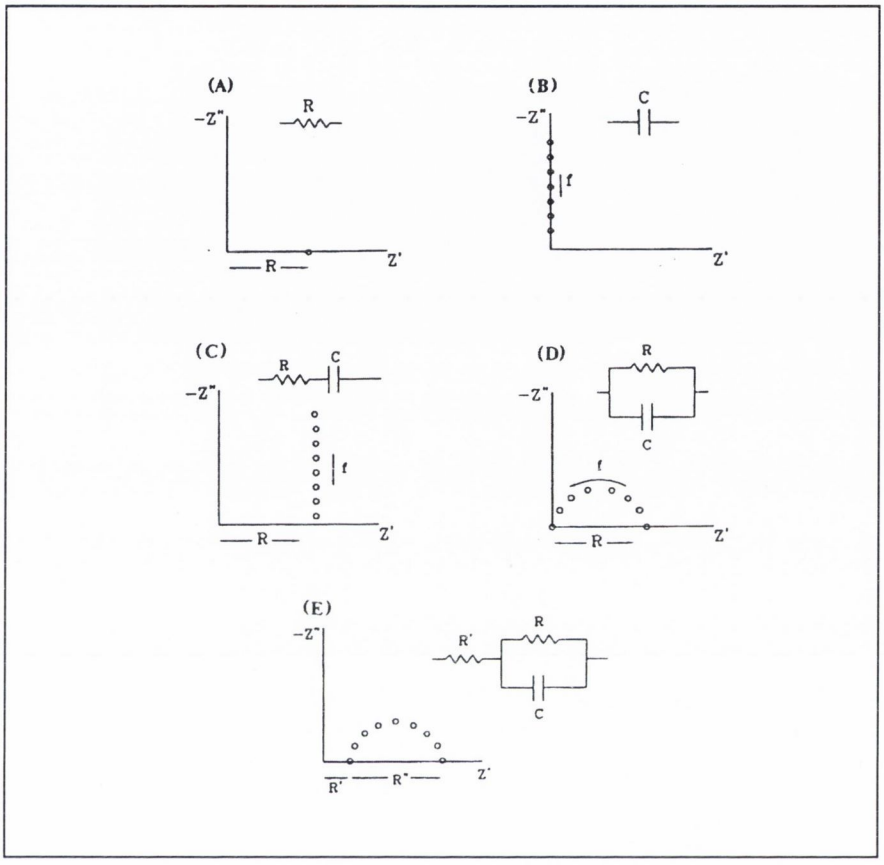


Figure 2.1.3. *Some simple circuits and their associated Nyquist plots.*

Impedance data may also be presented in the form of a *Bode plot*. In such a plot, both $\log|Z|$ and ϕ are plotted against log ω. According to equation (2.1.5) a pure resistance is frequency independent, yielding a slope of zero on the $\log|Z|$ against log ω plot, with a phase angle of 0°. For a pure capacitance, $|Z|$ is inversely proportional to ω, since $Z'' = -X_C = -1/\omega C$. Hence the $\log|Z|$ against log ω plot has a slope of –1, while equation (2.1.9) predicts a phase angle of -90°. In Figure 2.1.4, a Bode plot for a simple parallel RC circuit with one time constant is presented. In this diagram it is evident that the resistive behaviour dominates at lower frequencies, with the capacitive response becoming more important at values of log frequency above 3 to 4. For more complicated circuits, it may not be so easy to attribute the impedance response at a given frequency to a single circuit element.

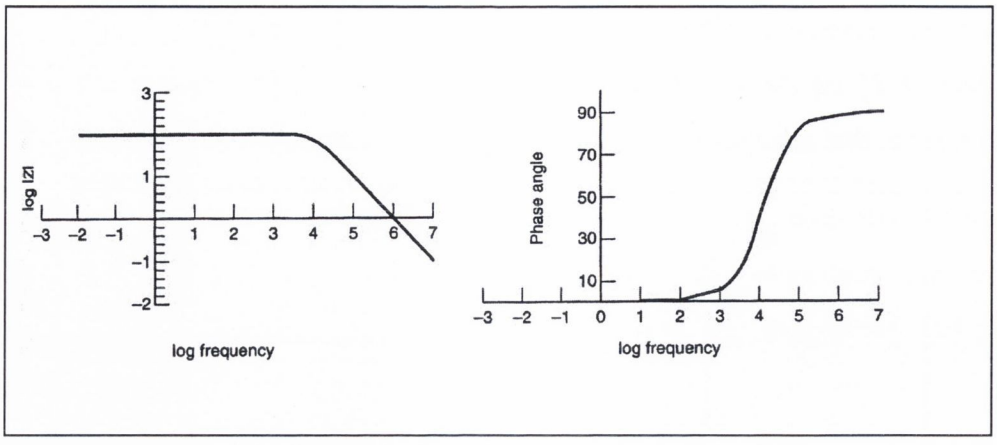


Figure 2.1.4 *Bode representations of a single time constant, parallel RC circuit with R = 100 Ω and C = 1 μF. Reproduced from Ref. 11.*

In the present work, both Bode and Nyquist representations are used. While the Nyquist diagram divides the impedance response into its resistive and capacitive components, it does have the shortcoming of not explicitly specifying the frequency of a given point. Furthermore, the high frequency data become bunched together towards the $\omega \rightarrow \infty$ intercept on the Z' axis[14]. Bode diagrams, while not splitting **Z** into its components, provide frequency information and plot the impedance data with equal weight at all frequencies along the length of the diagram.

2.1.5 Extension of Impedance Theory to Electrochemical Systems

The simplest and therefore most developed a.c. theories are *linear* theories. From a practical viewpoint a linear system is one that responds to a potential perturbation of frequency ω, with a current exclusively of the same frequency ω. Furthermore, if the magnitude of the input voltage to a linear system is increased, the magnitude of the current response will increase by the same proportion.

Since the Butler-Volmer equation (section 1.2.1) describes the current response to an applied potential for an electrochemical system, it is obvious that electrochemical systems are not linear. This problem can be circumvented by noting that an electrochemical system will behave in a pseudo-linear manner, if the magnitude of the exciting a.c. potential signal is kept small, since the linear approximation to the Butler-Volmer equation is applicable under such circumstances. In practice it is

recommended that the peak to peak amplitude of the applied voltage should not exceed 10 mV [12, 13].

An *equivalent circuit* is a circuit constructed from conventional circuit elements that seeks to simulate the impedance response of a real electrochemical cell. One of the simplest equivalent circuits is the *Randles equivalent circuit* as depicted in Figure 2.1.5. The total current in this circuit is the sum of the double layer charging current, which flows across the capacitive element C_{dl}, and the current due to any faradaic process occurring at the electrode, which flows through the generalised impedance element Z_f. The resistive element R_Ω represents the uncompensated solution resistance. Owing to their physical (as opposed to electrochemical) origins, it is to be expected that the double layer capacitance and the solution resistance will be largely independent of applied frequency, and therefore it is justifiable to represent them by conventional capacitive and resistive elements respectively. On the other hand the faradaic current will in general show frequency dispersion, since it is related to the kinetics and mass transport behaviour of the reaction. It therefore requires a more complicated representation in the Randles circuit, in the form of Z_f.

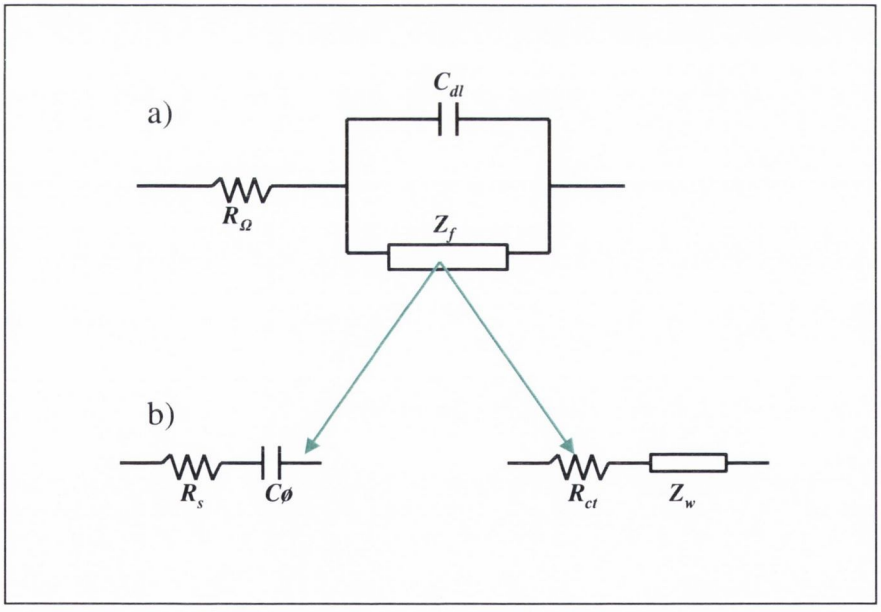


Figure 2.1.5 *a) The most general form of the Randles equivalent circuit. b) Alternative representations of Z_f in terms of R_s and C_ϕ or R_{ct} and Z_w.*

To further progress the application of the Randles circuit to real electrochemical systems, it is necessary to elucidate the nature of Z_f. For the following discussion, consideration is given to the simple redox reaction

$$O + ne^- \leftrightarrows R \quad , \tag{2.1.14}$$

occurring at its equilibrium potential E_0, where O is the soluble oxidised species and R is the soluble reduced species. The o.e.r. is clearly more complex than the general reaction in Equation (2.1.14), however it will be seen that many of the principles developed for the simple system are also applicable to the impedance behaviour of more elaborate redox reactions.

The earliest electrochemical impedance experiments were conducted by varying an unknown series resistance R_{cell} and capacitance C_{cell} on one arm of a Wheatstone bridge arrangement, to balance the impedance response of an electrochemical cell on the other arm, at a given applied a.c. frequency[11, 13, 15]. R_{cell} measured in such an experiment, where the electrochemical reaction can be represented by equation (2.1.14), contains contributions from both the resistance due to the faradaic process and R_Ω. Likewise, C_{cell} is due to both the capacitance of the faradaic process at the applied a.c. frequency and C_{dl}. It will be shown that it is possible to separate the faradaic components of the overall cell impedance from C_{dl} and R_Ω, by considering the frequency dependencies of R_{cell} and C_{cell}, but for the moment it is assumed that this is indeed possible. Under such circumstances it is therefore possible to represent Z_f, at a given frequency, in terms of a *series resistance,* R_s and a *pseudocapacitance,* C_ϕ, - see figure 2.1.5 b). It can be shown[11], that if a sinusoidal current of magnitude I is passed through the R_s and C_ϕ series, then the rate of change of the magnitude of the potential across the series is given by:

$$\frac{dE}{dt} = (R_s I\omega)\cos\omega t + \left(\frac{I}{C_\phi}\right)\sin\omega t \tag{2.1.15}$$

The potential $E(t)$ of the system in equation (2.1.14) as a function of time, depends on the cell current $i(t)$ and the concentrations $C_O(0, t)$ *and* $C_R(0, t)$ of the oxidised reduced species respectively at the working electrode. This coupled diffusion and electrochemical problem can be solved[11], yielding,

$$\frac{dE}{dt} = \left(R_{ct} + \frac{\sigma}{\omega^{1/2}} \right) I\omega \cos \omega t + I\sigma\omega^{1/2} \sin \omega t \qquad (2.1.16)$$

where, R_{ct} is known as the *charge transfer resistance*, and σ is a term that depends on the diffusional characteristics of the system. By equating the coefficients of the sine and cosine terms in the electrical (2.1.15) and chemical (2.1.16) equations, R_s and C_ϕ are identified as:

$$R_s = R_{ct} + \sigma / \omega^{1/2} \qquad (2.1.17)$$

$$C_\phi = \frac{1}{\sigma\omega^{1/2}} \qquad (2.1.18)$$

It can be shown that, for planar diffusion[13],

$$R_{ct} = \frac{RT}{nFi_0} \qquad (2.1.19)$$

This inverse proportionality between R_{ct} and the exchange current density i_0, indicates that R_{ct} is characteristic of the charge transfer kinetics of the electrochemical reaction.

The faradaic impedance of the cell Z_f, as measured by determining the unknown series resistance R_s and capacitance C_ϕ is given by the following expression,

$$Z_f = R_s - 1/j\omega C_\phi = R_{ct} + \left(\sigma/\omega^{1/2} - \sigma/j\omega^{1/2} \right), \qquad (2.1.20)$$

where the term in brackets represents the *Warburg impedance* Z_W, which can be regarded as a frequency dependent resistance. It follows that the Z_f element in the Randles circuit might be represented as a series combination of R_{ct} and Z_W as an alternative to the R_s and C_ϕ series - see Figure 2.1.5 b). The Warburg impedance is a function of σ, which is, as previously noted related to mass transport effects - Z_W therefore characterises the mass transfer properties of the electrochemical system. The magnitude of Z_W is calculated as follows,

$$|Z_W| = \sqrt{\left(\sigma/\omega^{1/2}\right)^2 + \left(-\sigma/\omega^{1/2}\right)^2} = (2/\omega)^{1/2}\sigma \qquad (2.1.21)$$

Since the magnitudes of the real and imaginary parts of Z_W are equal, it is characterised by a phase angle of - 45°, independent of frequency.

It was previously commented, that in a real EIS experiment, the total cell impedance is measured as a resistance value R_{cell} and a capacitance value C_{cell} in series, and that it is possible to extract the contributions of C_{dl} and R_Ω from the total impedance, yielding the faradaic impedance. This extraction can be performed graphically, by considering the Nyquist plot obtained from the measurement of the cell impedance for a given electrochemical system. In Figure 2.1.3, theoretical Nyquist plots were presented for various simple circuits, and using the rules for the addition of impedance elements, it is, likewise, possible to derive[11] (rather complicated) expression for the real, Z′, and imaginary, Z″, parts of the impedance of the Randles circuit as functions of C_{dl}, R_Ω, R_{ct}, σ and ω. If Z″ is plotted against Z′ over a range of frequencies the theoretical complex plane plot is obtained for the Randles circuit – see Figure 2.1.6. Owing to the complexity of the expressions for Z′ and Z″, it is most convenient to examine the limiting forms of these expressions at high and low values of ω.

At high frequencies, $\omega \rightarrow \infty$, and equation (2.1.20) predicts that diffusion (via the Warburg impedance) becomes negligible compared to the charge transfer kinetics. The system is therefore under kinetic control, and the limiting expressions for Z′ and Z″ are:

$$Z' = R_\Omega + \frac{R_{ct}}{1+\omega^2 C_{dl}^2 R_{ct}^2} \qquad (2.1.22)$$

$$Z'' = \frac{\omega C_{dl} R_{ct}^2}{1+\omega^2 C_{dl}^2 R_{ct}^2} \qquad (2.1.23)$$

Elimination of ω from this pair of equations gives:

$$\left(Z' - R_{\Omega} - \frac{R_{ct}}{2}\right)^2 + Z''^2 = \left(\frac{R_{ct}}{2}\right)^2 \qquad (2.1.24)$$

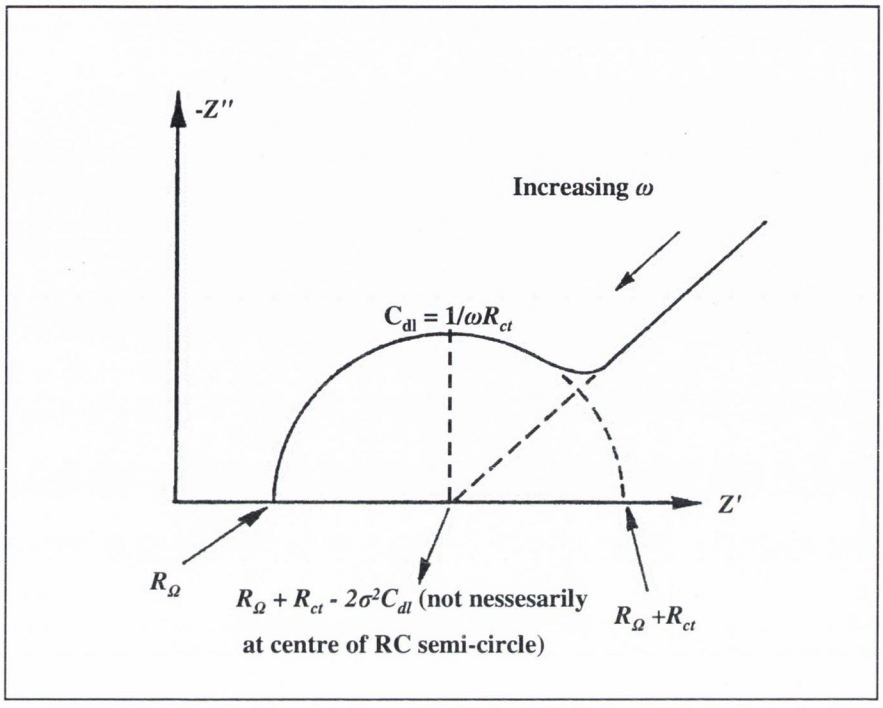


Figure 2.1.6 *Theoretical form of the Nyquist plot for the Randles equivalent circuit, depicted in Figure 2.1.5. Adapted from Ref. 13.*

This is the equation of a circle centred on $Z' = R_{\Omega} + R_{ct}/2$ and $Z''= 0$, with a radius of $R_{ct}/2$. The Nyquist plot representation of the high frequency response of the Randles circuit is therefore the semicircular trace in Figure 2.1.6. It is evident that the values of R_{Ω} and R_{ct} may be gleaned from this plot by considering the intersections of the semicircle with the Z' axis. It can further be shown[13], that C_{dl} may be calculated from the maximum of Z'' in the semicircular region, where $1/\omega C_{dl} = R_{ct}$. The semicircle obtained in the high frequency, kinetic control regime for the Randles circuit is characteristic of the parallel arrangement of R_{ct} and C_{dl}. Real electrochemical systems may be represented by equivalent circuits with more that one RC parallel combination. In such circumstances the Nyquist plot will contain a semicircle for each parallel RC loop.

As $\omega \rightarrow 0$, the real and imaginary components of the impedance are given by:

$$Z' = R_{\Omega} + R_{ct} + \sigma\omega^{-1/2} \qquad (2.1.25)$$

$$Z'' = \sigma\omega^{-1/2} + 2\sigma^2 C_{dl} \tag{2.1.26}$$

Again, eliminating ω between equations (2.1.25) and (2.1.26), the following expression for the imaginary part of the impedance is obtained:

$$Z'' = Z' - R_\Omega - R_{ct} + 2\sigma^2 C_{dl} \tag{2.1.27}$$

In a conventional Nyquist plot of $-Z''$ against Z', this equation is that of a straight line of unit slope with a Z' axis intercept of $R_\Omega + R_{ct} - 2\sigma^2 C_{dl}$, as shown in the low frequency region of Figure 2.1.6. It can be seen from equations (2.1.25) and (2.1.26), that the frequency dependence of the impedance in the low frequency regime, arises entirely from the Warburg terms. Hence it may be concluded that the linear, unit slope Z'' against Z' frequency region is characteristic of a diffusion controlled process.

The foregoing discussion is applicable only to the simple redox reaction in equation (2.1.14), occurring at its equilibrium potential, as modelled by the Randles equivalent circuit. Nonetheless many of the principles developed above are applicable to the analysis of the impedance response of the o.e.r. , as will be seen in chapter 4. A few comments are in order at this stage, regarding the extension of the theory from the simple case of equation (2.1.14) to the o.e.r. As was considered in chapter 1, the measurable region of linearity in the *log i* vs. *E* characteristic for the o.e.r. occurs in the order of hundreds of millivolts anodic to the E^0 for the process. For the case of impedance measurements performed in this straight line Tafel region, the resistive element in parallel to C_{dl}, will not merely be R_{ct} (as defined by equation (2.1.19)), but is in fact the polarisation resistance R_p [12]. The polarisation resistance is the resistance to current flow, when the electrochemical process is forced away from its equilibrium potential E^0, by the application of an overpotential η to the system. R_p is a function of the applied potential and it becomes equal to R_{ct} at η =0. It is important to note that there is no simple relation between R_p and i_0, so it is not possible to calculate i_0 for the o.e.r. by determining the resistance in parallel to C_{dl} , at some potential in the linear *log i* vs. *E* regime. In chapter 1 it was seen that the o.e.r. at transition metal anodes is a highly irreversible process with quoted literature values of i_0 typically of the order of $10^{-10} - 10^{-8}$ A cm^{-2}. This means that at potentials corresponding to the linear part of

the *log i* vs. *E* characteristic, the o.e.r. is controlled by interfacial electron transfer kinetics, and one would not expect to see, in a Nyquist plot, the Warburg behaviour characteristic of diffusion control. In practice this turns out to be the case – see chapter 4.

2.1.6 Practical Considerations and EIS Measurement Systems

Significant care must be taken in the design of cells for EIS measurements. Since the amplitude of the a.c. exciting signal must be small, environmental electrical noise and pickup at mains frequency can be issues. It is therefore desirable that the cell be electrically isolated in a Faraday cage and that shielded BNC cables of the shortest possible length be used to connect the cell to the control/measurement equipment. Of particular importance in impedance measurements, is that the working and counter electrodes should be symmetrically oriented[13], to provide a very uniform current distribution in the cell. A measured impedance will include, not only the impedance of the working electrode, but also that of the counter electrode as well as the resistance of the electrolyte between them. As was shown in section 2.1.5, the uncompensated solution resistance can readily be separated from the rest of the impedance response by graphical methods. In practice the counter electrode impedance should be made negligibly small by using a counter electrode of much greater surface area than that of the working electrode.

The earliest electrochemical impedance measurements were performed using Wheatstone bridge type set-ups. The cell was placed in the unknown arm, and the bridge was balanced by varying a series resistance and capacitance in the opposite arm. The balancing procedure would have to be repeated for each required frequency, and the experimentalist could calculate the real and imaginary components of the impedance, since $Z' = R$ and $Z'' = -X_C = -1/\omega C$. Apart from being cumbersome, this method was restricted in frequency range, not being useful below about 10 Hz[13].

Later EIS equipment measured the real and imaginary parts of the impedance, by determining the a.c. part of the cell current, rather than compensating for the series resistance and capacitance of the cell. The approach involved using an analogue *phase sensitive detector* (p.s.d). The p.s.d. takes a potential, $e_i = E\sin(\omega_i t + \phi)$, proportional to the a.c. cell current as its input, where ω_i is the angular frequency of the a.c.

potential e_{appl} applied to the cell by the potentiostat, $E = I_{cell}R_s$, where I_{cell} is the amplitude of the a.c. cell current (R_s is a resistance in series with the counter electrode), and ϕ is the phase shift of the cell current relative to the applied potential. The detector takes a square wave potential e_{ref} as a reference, where e_{ref} is represented in terms of its Fourier components as:

$$e_{ref} = \frac{4}{\pi}\left[\sin(\omega_r t) + \frac{1}{3}\sin(3\omega_r t) + \frac{1}{5}\sin(5\omega_r t) + \ldots\right] \tag{2.1.28}$$

The reference signal e_{ref} is derived from the same source as e_{appl}, and therefore $\omega_{appl} = \omega_i = \omega_r$. The input and reference signals are passed through a multiplexing circuit, which effectively multiplies the two signals. The multiplied signal is then passed through a time averaging circuit. The detailed mathematics of these operations is considered in ref 16 (p. 143) – of interest here, is that, the final output is a d.c. voltage, $e_{out} = 2/\pi A\cos(\phi)$, the value of which is proportional to the phase angle ϕ. The magnitude of the impedance at a given frequency is given by[16]:

$$|Z| = \frac{R_s|e_{appl}|}{|e_i|} \tag{2.1.29}$$

The phase angle is determined from e_{out}, as described above, and therefore the real and imaginary parts of the impedance are readily found since,

$$Z' = |Z|\cos(\phi) \tag{2.1.30}$$

$$Z'' = |Z|\sin(\phi) \tag{2.1.31}$$

Measurement systems based on p.s.d.s have the advantage of rejecting adventitious frequencies, since the output of the time averaging circuit is zero for $\omega_i \neq \omega_r$, except for the case of odd numbered harmonics of the input frequency[16]. The main disadvantage of p.s.d. based systems is that a high amplitude noise signal can drive the circuitry into saturation[13], and therefore a high signal to noise ratio is essential. The frequency range of equipment based on analogue p.s.d.s is generally between 0.5-

10Hz and 10^5Hz[16]. Such equipment was state of the art during the 1980s and early 1990s.

In the past decade, the analogue equipment described above, has been largely superseded by digital equipment based on frequency response analysers (F.R.A.s). This equipment measures cell impedance using an approach known as *sine wave correlation*. In this procedure the measured signal *S(t)* is multiplied by two sine wave reference signals derived from the perturbation signal[11,12,16]. One of the reference signals is in phase with the perturbation, while the other is in quadrature. The perturbation signal *P(t)* can be represented as,

$$P(t) = |P|\sin(\omega t) \quad , \tag{2.1.31}$$

where, $|P|$ is the amplitude of the sine wave. The cell response is given by[16],

$$S(t) = |P|\,|Z(\omega)|\sin[\omega t + \phi(\omega)] + \sum_m A_m \sin(m\omega t - \phi_m) + M(t), \tag{2.1.32}$$

where the first term on the right hand side is the fundamental component. As discussed previously, the non-linear nature of electrochemical systems, will introduce harmonics of ω to the cell response – these are accounted for by the second term on the right side of equation (2.1.32). The contribution of random electrical noise, such as pickup from the mains, is included as the *M(t)* term. The multiplied signals are then integrated over a number, *N* of cycles of the applied wave, yielding the following expressions for the real and imaginary parts of the impedance[13, 16],

$$Z'(\omega) = \frac{1}{NT}\int_0^{NT} S(t)\sin(\omega t)dt \tag{2.1.33}$$

$$Z''(\omega) = \frac{1}{NT}\int_0^{NT} S(t)\cos(\omega t)dt \quad , \tag{2.1.34}$$

where *T* is the period of the applied sine wave. If equations (2.1.33) and (2.1.34) are substituted into equations (2.1.31) and (2.1.32), expressions can be obtained[16] for Z′ and Z″ which each consist of the sum of three integrals – one related to the

fundamental, one related to harmonics of the applied signal and the final one related to the cell response to random noise. If the noise is completely random it can be shown that the corresponding integrals in the aforementioned expressions for Z′ and Z″ are equal to zero, provided the integration is performed over infinite time. Obviously, in real measurements, integration over infinite time isn't possible, however it transpires that the signal to noise ratio is enhanced by a factor of $N^{1/2}$, where N is, as before, the number of periods of the applied wave[12]. Furthermore, it can be shown[16], that FRAs effectively reject the harmonic components of the cell response, if the integration is carried over multiples of $2\pi T$, since the relevant integrals in the overall expressions for Z′ and Z″ are identically equal to zero under these conditions.

Impedance measurements, such as those described above, utilising FRA equipment, are classified as *single sine* techniques. In single sine measurements a low amplitude sinusoidal voltage is impressed upon the cell at a given frequency. The impedance of the cell is then calculated based upon the measured a.c. current passing through the cell. This process is repeated, at typically 10 – 20 representative frequencies per decade, to characterise the cell impedance across the frequency range of interest. As is apparent from the discussion above, it is often necessary to sweep several cycles at a given frequency to obtain a satisfactory signal to noise ratio. At high frequencies this often isn't a significant problem, but at lower frequencies these sweeps require a long time. For example at 1 mHz, a single sweep takes 1000 s, and considering the need to sample a number of frequencies per decade, it becomes obvious how the required time for a measurement can build up at lower frequencies. A given system may have changed significantly during the course of a spectral measurement (even within the period of one sweep of a lower frequency), and this is the major shortcoming of single sine impedance measurements. In case of impedance investigations of the o.e.r., one has to consider, for example, the possibility of significant oxide growth during the course of a full impedance experiment.

An alternative approach to EIS experiments, which can potentially reduce measurement time, is based upon *Fast Fourier Transform* (FFT) analysis. This method is based upon the application of a multiple frequency perturbation to the cell, and the subsequent Fourier transformation of the cell response into its real and complex components. The best kind of perturbation signal is phase varying, odd harmonic pseudo-random white noise[13], which is computer synthesised in such a way,

that the amplitude of the component frequencies are equal. During a measurement, the cell response is fed to a computer FFT algorithm, the cross power spectrum is calculated, and the data is resolved into its real and imaginary components. The FFT method offers advantages when measuring time variant systems, and yields a consistent data set since all frequencies are measured simultaneously. At first glance it may therefore appear to be a superior approach to sine wave correlation, however FFT methods have some inherent problems. They are more subject to both environmental noise and distortion by harmonics[13]. This requires rigorous analogue (with the associated danger of introduction of phase shifts) and digital filtering[17], and more than likely the need to average the signal[13] over a number of applications of the perturbation, which serves to increase the total experiment time. Since all frequencies are measured simultaneously, issues with the dynamic range of the instrument often arise[17], when measuring over several decades of frequency. The impedance of a capacitive sample changes by an order of magnitude for each decade of frequency, forcing the equipment to resolve a wide range of current levels at the same time. In practice this can lead to noisy measurements at the low frequency end of the spectrum and "clipping" of the signal at the high frequency end. In considering the relative merits of the single sine vs. FFT approaches, Sayers[17], comments that the former is unsurpassed in terms of accuracy and ability to minimise noise and distortion from the cell, and that the latter is most usefully applied as a complementary measurement to the single sine technique.

2.1.7 Extracting Electrochemical Parameters From EIS Raw Data

In section 2.1.5, it was shown how simple graphical methods, can in principle be used to extract parameters such as R_{Ω}, R_{ct}, σ, C_{dl}, and C_{ϕ} from the Nyquist plot of a given electrochemical system – see Figure 2.1.6. In practice however, more than one, often overlapping, arcs are commonly observed in complex plane impedance results. Furthermore, experimental arcs rarely approximate exact semicircles very well[18]. The most commonly used method of gleaning required parameters from impedance data is based upon modelling the electrochemical system in terms of an equivalent circuit. The concept of equivalent circuits has already been introduced in section 2.1.5 in relation to the Randles equivalent circuit, which models the simple electrochemical system of equation (2.1.14). In the equivalent circuit approach, the experimental data

is fitted to a theoretically postulated circuit, using complex non-linear least squares (CNLS) algorithms, that systematically vary the values of the circuit elements until the best fit of the data to the model circuit is achieved. Equivalent circuits can in general be classified as either physical models or empirical models[19].

In physical models, each of the elements of the equivalent circuit is associated with a physical or electrochemical process in the cell. The kinetic and thermodynamic properties of a given system generally dictate which elements should be present and their values, while the connection scheme reflects the electrochemical mechanism. Physical models are constructed, based upon educated postulation (possibly with reference to complementary experimental data or the literature) regarding the physical nature of a given system. It is often found that a particular impedance spectrum can be equally well modelled by several equivalent circuits – in other words there is not a unique equivalent circuit that represents the system[14,19,20]. Hence it cannot be assumed, that an equivalent circuit, which produces a good fit to experimental data, necessarily provides an accurate model of an electrochemical system. In view of the foregoing comments, fitting data to an equivalent circuit may not satisfy the purist[20], who would seek to derive analytical expressions for the impedance response of a particular system, in the same manner as was outlined in section 2.1.5 for the simple redox reaction of equation (2.1.14). However, for complex multistep reactions, such as the o.e.r., it can be difficult to reconcile the experimental data with the theoretical impedance response, predicted by a model derived from a kinetic analysis[21,22]. Therefore the utilisation of CNLS fitting of EIS data to physical equivalent circuit models is standard practice in the literature, although the cautionary comments of this paragraph should be bourn in mind.

Empirical models are developed, simply by building up an equivalent circuit, to give the best possible match between the model's impedance and the measured impedance. Their components are not assigned to physical processes in the cell. All equivalent circuits considered in the present work are physical models, based upon a critical review of the relevant literature.

A brief treatment is now given to the theory of CNLS fitting procedures. Consider the transfer function, $f_t(\omega, \mathbf{p})$, of an equivalent circuit model, where $\mathbf{p}$ is a set of values for the various circuit elements. The experimental data consists of measurements made at a series of discrete frequencies ω_i. The function, $f_t(\omega, \mathbf{p})$ can be separated into real,

$f_t^{re}(\omega,\mathbf{p})$, and imaginary, $f_t^{im}(\omega,\mathbf{p})$, components, which correspond to Z_t' and Z_t''. The CNLS fitting algorithm varies the values of the parameters **p**, in order to minimise the sum of squares function[18],

$$S_{sq} = \sum_{i=1}^{k} \left\{ w_i'[f_{ei}' - f_t'(\omega_i,\mathbf{p})]^2 + w_i''[f_{ei}'' - f_t''(\omega_i,\mathbf{p})]^2 \right\} \quad , \qquad (2.1.35)$$

where w'_i and w_i'' are weights associated with the i^{th} data point and f'_{ei} and f_{ei}'' are experimental data values.

The initial estimates, or seed values, of the parameters **p** must be made by the analyst. In general this involves examining the experimental data in the Bode plot format – the absence of explicit frequency data in Nyquist plots makes the estimation of capacitance values difficult. As an example of the method of estimating seed values, consider the Bode plot presented in Figure 2.1.7.

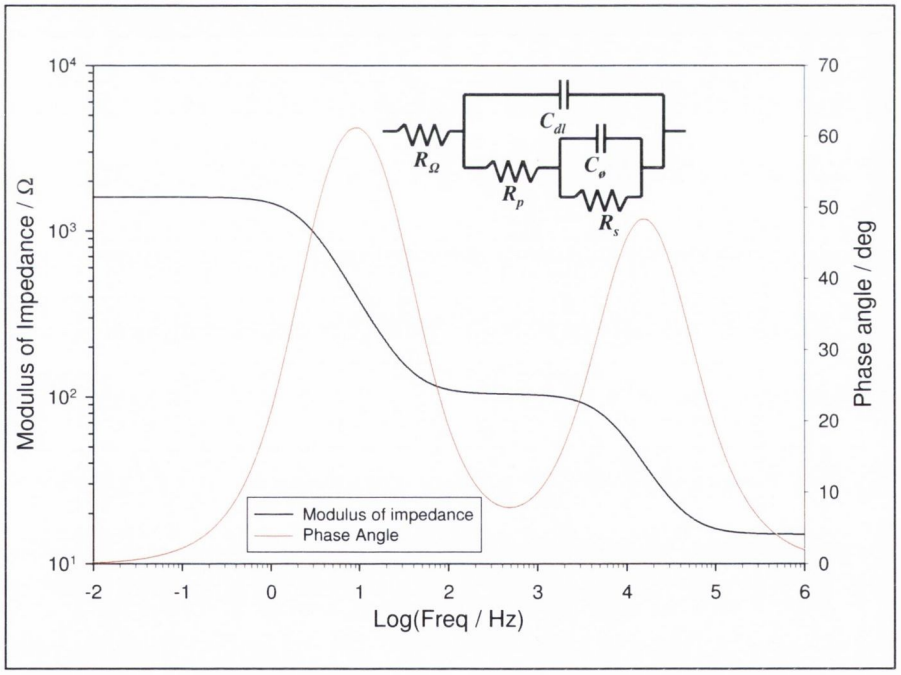


Figure 2.1.7 *Ideal Bode plot for the equivalent circuit in the inset when it is constructed from physical circuit elements. See text for more details.*

This is the theoretical impedance response calculated for the equivalent circuit in the inset, when this circuit is constructed from real physical circuit components. This equivalent circuit is often called *The Armstrong Henderson equivalent circuit*[23], and is

used to model the behaviour of a multistep reaction involving an adsorbed intermediate, such as the hydrogen evolution reaction (h.e.r.). The significance of the parameters R_Ω, R_p, and C_{dl} has been discussed previously. The pseudo-capacitive element, C_ϕ, was traditionally thought to account for the rate of adsorption or desorption of the intermediate (a more contemporary view of its significance is discussed in chapter 4), while R_s is associated with the surface concentration of the intermediate.

Referring to the Bode plot in Figure 2.1.7, a horizontal region is observed in the $|Z|$ vs. f plot at high frequencies (above 10^5 Hz), while the phase angle tends towards zero. As was considered in section 2.1.4 (see for example Figure 2.1.4), a phase of angle of zero and a constant $|Z|$ value in the corresponding frequency region, are indicative of resistive behaviour. It is, of course, not surprising that the impedance response is resistive at the highest frequencies, since the capacitive reactance, $X_C = 1/\omega C$, and tends to zero, as the frequency approaches infinity. As illustrated in Figure 2.1.6, the solution resistance, R_Ω, can be extracted from the impedance response at the highest frequencies, since its response is frequency independent, and will still be manifested in an impedance spectrum at frequencies whose corresponding temporal period τ is much less than the time constant of either of the RC loops. From the $|Z|$ vs. f plot, R_Ω appears to have a value of ~ 14 Ω, thus providing the first seed value.

At low frequencies (< 1Hz), there is also a plateau in the $|Z|$ vs. f plot, and the phase angle tends towards zero – again this is suggestive of a dominant resistive impedance. At low frequencies, $\omega \rightarrow 0$, and the capacitive reactance becomes large – however, both capacitors in the equivalent circuit are in parallel with resistors, and since impedances add in a reciprocal manner, it is the impedance of the resistors that will dominate at low frequencies, thus explaining the form of the Bode plot at these frequencies. The impedance response below ~ 1 Hz is therefore the sum of R_Ω, R_p, and R_s. The magnitude of this impedance response is ~ 1600 Ω. The impedance response also appears to be dominantly resistive in the mid-frequency region between approximately 100 and 1000 Hz, where $|Z| \approx 110$ Ω. The question arises, as to which resistor is principally responsible for this mid-frequency resistive region? Considering the structure of the equivalent circuit, it is obvious that the mid-frequency impedance plateau is due mainly to R_p, since the R_sC_ϕ loop cannot provide an impedance

response independently of the R_pC_{dl} loop, the reverse situation not being true. Hence, a reasonable estimate for R_p is: R_p = 110 Ω - R_Ω = 110 Ω - 14 Ω = 96 Ω. The low frequency resistive region is dominated by the response of R_s, and this parameter is estimated as follows; R_s = 1600 Ω- (R_Ω + R_p) = 1600 Ω- (R_Ω + R_p) = 1600 Ω - 110 Ω ≈ 1500 Ω.

What of the seed values for the capacitive elements? The decrease in $|Z|$ between 1 and 100 Hz must be mainly due to C_ϕ. In a region of frequency, where the impedance response is principally capacitive, the approximation can be made (c.f. equations (2.1.6) and (2.1.7)) that, $|Z| = 1/2\pi fC$, and thus $C = (2\pi f|Z|)^{-1}$. In Figure 2.1.7, at 10 Hz, $|Z| \approx 350\ \Omega$, and therefore $C_\phi = (2\pi \times 10 \times 350)^{-1} = 45.5\mu F$. The seed value for C_{dl} can be obtained in an analogous manner by examining Figure 2.1.7 in the frequency region between 5000 and 50,000 Hz, where the decline in $|Z|$ and increase in magnitude of the phase angle with increasing frequency, are indicative of a capacitive dominated impedance response. The actual values of the circuit elements used to generate the Bode plot in this example are: R_Ω = 15 Ω, R_p = 90 Ω, R_s = 1500 Ω, C_ϕ = 45 μF, and C_{dl} = 300 nF. It can be seen that, there is in general, excellent agreement between the estimated seed values and the actual values of the circuit elements. It must be commented, however, that it is easy to estimate the seed values in the example presented, since the Bode plot is based on a circuit constructed from ideal elements, and furthermore each element corresponds to a very clearly defined frequency region in the plot. In real analysis of EIS data, significant overlapping of the frequency regions due to each element in a postulated equivalent circuit, is often observed, making the analysis of the Bode plot and estimation of seed values for a CNLS fitting procedure more complicated than in the above example. Nonetheless, the simple example presented, illustrates the procedure and train of thought that the analyst must follow.

Another factor contributing to the fact, that real EIS data is usually more difficult to interpret than the ideal cases presented, for example, in Figures 2.1.6 and 2.1.7, is that capacitive processes in real electrochemical cells rarely conform to ideal capacitive behaviour. That is to say, that real "electrochemical capacitors" display frequency dispersion – on a Nyquist plot this is manifested as a slope of less than 90° from the Z′ axis[4] (compare with the Nyquist plot for an ideal capacitor – Figure 2.1.3(B)). In the

equivalent circuits considered in the present work, parallel RC loops are of significance. The capacitive frequency dispersion causes a depression of the ideal semicircular complex plane behaviour of a parallel RC combination (c.f. Figure 2.1.3(D)), effectively rotating it in a clockwise direction by an angle of $90°(1-\alpha)$, so that the centre of the semicircle no longer resides on the Z′ axis, but rather below it – the significance of the parameter α will be discussed presently. The deviation from ideal capacitive behaviour is often dealt with in, an empirical manner, by the introduction of the so called "*constant phase element*" (CPE), where the impedance Z_{CPE} of a capacitive process displaying frequency dispersion, is expressed as:

$$Z_{CPE} = A(j\omega)^{-\alpha} \tag{2.1.36}$$

In equation (2.1.36), $A = 1/C_{\alpha=1}$, where $C_{\alpha=1}$ is the value of the capacitance in the absence of frequency dispersion, and α is an exponent ($0.5 \leq \alpha \leq 1$ for a physically reasonable situation) equal to unity in the case of an ideal capacitor. CNLS programs generally return values for $C_{\alpha=1}$ and α, when asked to fit impedance data to a CPE.

While it isn't surprising that adsorption pseudocapacity should display frequency dispersion (it is a pseudo – capacity after all), the origin of the frequency dispersion displayed by the double layer capacitance is a controversial matter in the literature[14]. While it is generally agreed that surface roughness and inhomogeneity will cause deviation from ideal capacitive behaviour in the case of polycrystalline solid electrodes, the origin of the effect has caused much debate. Pajkossy[24] comments that the most commonly held view, first proposed by Frumkin, envisages surface roughness, leading to current density inhomogeneities on the surface, which in turn cause effects of solution bulk resistance and interfacial capacity to become mutually obscured, so that it becomes impossible to separate the real and imaginary components of the impedance. However, owing to the results of Pajkossy's own experimental work, a counter theory is forwarded[24], in which it is proposed that frequency dispersion effects in the double layer capacitance are related to the complexity of anion adsorption kinetics at roughened surfaces. Overall, whichever hypothesis is admitted, it seems to be reasonable to qualitatively associate the value of α with the degree of surface roughness, although caution must be exercised owing to the current lack of a strong physical basis for the α parameter.

While using a constant phase element, facilitates the fitting of impedance data with capacitive frequency dispersion to an equivalent circuit, a problem arises if one seeks to extract a numerical value for the effective capacitance C_{eff} using the results of a fitting procedure. As mentioned above, commercial CNLS fitting software outputs a value for $C_{\alpha=1}$, however this parameter only has the correct dimensions for a capacitance (F = Ω^{-1}s), when α =1 (i.e. in the case of an ideal capacitor) – otherwise the dimension is Ω^{-1} s^{α}. It has been pointed out[25] that the impedance of a parallel connection of a CPE and a resistor can be expressed using either of the two following equations,

$$Z(\omega) = \frac{R}{1+(j\omega C_{\alpha=1}R)^{\alpha}} \tag{2.1.37}$$

$$Z(\omega) = \frac{R}{1+(j\omega)^{\alpha} C_{\alpha=1}R} \tag{2.1.38}$$

In an analysis of this problem Jovic[26] points out that equation (2.1.38) is used "in all commercially available software for fitting impedance spectra". At the frequency, ω''_{max}, where - Z'' is at its maximum, it can be assumed that the impedance is heavily dominated by the capacitive contribution. In this situation the effective capacitive C_{eff}, which has been modelled by the CPE as represented by equation (2.1.36), and which has been fitted to the RCPE parallel loop using equation (2.1.38) may be written as:

$$Z_{CPE} = \frac{1}{j\omega''_{\max} C_{eff}} = \frac{1}{(j\omega''_{\max})^{\alpha} C_{\alpha=1}} .$$

Equating the denominators yields the following expression, first derived by Hsu and Mansfeld[17] for the correction of capacity to its real value, C_{eff}, in the case of the parallel connection of a CPE and a resistor:

$$C_{eff} = C_{\alpha=1}(\omega''_{\max})^{\alpha-1} \tag{2.1.39}$$

It is clear that C_{eff}, as defined in equation (2.1.39) has the dimension of $(\Omega^{-1} s^{\alpha})(s^{1-\alpha}) = \Omega^{-1}s$ = F, as required for a capacitance. Equation (2.1.39) implies that the required effective capacitance may be calculated using $C_{\alpha=1}$, and α, which are outputted by commercial software, and ω''_{max}. The question then arises as to how the relevant value for ω''_{max} may be derived? Jovic[26] points out equation (2.1.37) should be used in preference to equation (2.1.38) (which is used by the commercial CNLS fitting programs) because the frequency dispersion of the capacity due to the surface inhomogeneity, $j\omega C_{\alpha=1}$, is closely related to the charge transfer over the same surface, R, and these two factors are mutually dependent – i.e. the CPE shouldn't be treated as an independent parameter, as in equation (2.1.38). The imaginary magnitude of the impedance of a parallel combination of a resistance and a CPE as represented by equation (2.1.37), is given by the following expression [26,27]:

$$|Z''| = \frac{R(\omega C_{\alpha=1}R)^{\alpha}\sin\left(\frac{\alpha\pi}{2}\right)}{1+2(\omega C_{\alpha=1}R)^{\alpha}\cos\left(\frac{\alpha\pi}{2}\right)+(\omega C_{\alpha=1}R)^{2\alpha}} \qquad (2.1.40)$$

The value of ω''_{max} required for equation (2.1.39) is graphically obtained, by substituting the CNLS fit values for $C_{\alpha=1}$, R, and α into equation (2.1.40), and then plotting the magnitude of Z'' vs. ω.

Tafel slopes are normally measured directly using steady state polarisation methods, however they can also be determined using impedance measurements. Recall that at an overpotential η, where simple Tafel behaviour prevails, the current density i is related to η via the following expression,

$$i = i_0 \exp(2.303\eta/b), \qquad (2.1.41)$$

where, b is the Tafel slope ($d\eta/d \log_{10} i$). The *differential Tafel slope*, b_{diff}, at a particular value of η is given by the following expression,

$$b_{diff} = d\eta/d\log i = 2.303 i_{dc}(d\eta/di) = 2.303 i_{dc} R_{far}, \qquad (2.1.42)$$

where, i_{dc} is the current density corresponding to the applied overpotential η, and R_{far} is the total Faradaic resistance of the working electrode. R_{far} can be calculated from the CNLS fit values for the various resistors that contribute to the total Faradaic resistance in a given equivalent circuit model.

The b_{diff} parameter is an instantaneous Tafel slope at one given η – however a Tafel slope can also be derived from R_{far} values obtained over a range of potentials. The derivative of equation (2.1.41) with respect to η is given by:

$$\frac{\mathrm{d}i}{\mathrm{d}\eta} = \frac{2.303 i_0}{b} \exp(2.303\eta/b) \tag{2.1.43}$$

Taking the logarithm of equation (2.1.43), and noting that $\mathrm{d}i/\mathrm{d}\eta = 1/R_{far}$, the following expression is achieved:

$$\log\left(\frac{1}{R_{far}}\right) = \frac{\eta}{b} + \log\left(\frac{2.303 i_0}{b}\right) \tag{2.1.44}$$

Equation (2.1.44) implies that the slope of a plot of log ($1/R_{far}$) against η is equal to the inverse of the Tafel slope.

2.1.8 Kramers-Kronig Transforms.

From the discussions in the previous sections, it can be appreciated that the results of electrochemical impedance measurements are quite prone to the introduction of experimental artefacts from several sources. This problem was particularly discussed in section 2.1.6 in relation to impedance measurement equipment. Spurious data may arise from non-linearity in the measured system, random noise and system instability owing to the long timescale necessary for many EIS experiments. The *Kramers-Kronig (K-K) transforms* are a set of mathematical relations that can be obtained from the properties of continuous functions of a complex variable[13] and they serve as a useful tool in assessing the validity of experimental EIS data. The transforms may be stated as follows for the impedance of an electrochemical system[28],

$$Z'(\omega) - Z'(\infty) = \left(\frac{2}{\pi}\right)\int_0^\infty \frac{\chi Z''(\chi) - \omega Z''(\omega)}{\chi^2 - \omega^2} d\chi \quad , \tag{2.1.45}$$

$$Z'(\omega) - Z'(0) = \left(\frac{2\omega}{\pi}\right)\int_0^\infty \left[\left(\frac{\omega}{\chi}\right)Z''(\chi) - Z''(\omega)\right]\frac{1}{\chi^2 - \omega^2} d\chi \quad , \tag{2.1.46}$$

$$Z''(\omega) = -\left(\frac{2\omega}{\pi}\right)\int_0^\infty \frac{Z'(\chi) - Z'(\omega)}{\chi^2 - \omega^2} d\chi \quad , \tag{2.1.47}$$

$$\phi(\omega) = \left(\frac{2\omega}{\pi}\right)\int_0^\infty \frac{\ln|Z(\chi)|}{\chi^2 - \omega^2} d\chi \tag{2.1.48}$$

where, ω and χ are frequencies. The above equations indicate that the real component of the impedance can be calculated from the imaginary component, and vice versa, and furthermore that the phase angle can be determined from the magnitude of the impedance. Of course, it is impossible to evaluate the integrals in equations (2.1.45) to (2.1.48) over an infinite range of frequencies, however the error in performing the integration over a finite bandwidth can be minimised if the limits bound a frequency gap of six or seven decades[13]. A physical system will only be transformable under the K-K transforms if it fulfils all of the following criteria[13,28]:

1. *Causality*: The measured response must be due to the applied perturbation and not contain contributions from other sources.
2. *Linearity*: The relationship between the perturbation and the response must be linear.
3. *Stability*: The system must return to its original state upon removal of the perturbation
4. *Finiteness*: The response must be finite at all frequencies, including $\omega = 0$, and $\omega = \infty$ - it must also be continuous at all intermediate frequencies.

If impedance data are not transformable under the K-K transforms, one of more of the above conditions is not satisfied, and the relevant data should not be admitted as an accurate reflection of the electrochemical system. As discussed in sections 2.1.4 and 2.1.6 the requirement for linearity may not be achieved if the magnitude of the

perturbing signal is too large, since electrochemical systems are intrinsically non-linear. System instability during low frequency measurements due to the long time scale required, is a common cause of deviation between the measured data and the values calculated using the K-K transforms. The adsorption-desorption processes in the oxygen evolution reaction are often manifested as a low-frequency impedance response – however if reported data has not been subject to a K-K test for internal consistency, then such data must necessarily be treated with caution. While the usefulness, and indeed necessity, of checking EIS data with the K-K transforms has been appreciated for over thirty years[29], McKubre and Macdonald[16] have recently commented that "experimenters frequently report and draw conclusions from impedance data sets, that have not been subjected to the scrutiny of the K-K rules". All impedance data presented in the present work has been subjected to a K-K rule check, and not admitted if it fails – see section 2.2.10.

2.1.9 Determination of Real Surface Area

The most significant problem in comparing the electrocatalytic performance of one electrode relative to another, arises in decoupling the intrinsic catalytic properties of the electrode materials due to their surface and electronic properties, from effects arising from the relative amount of available electrochemically active surface area in each case. In view of this, numerous experimental methods have been proposed for the determination of real surface areas in electrochemistry. The IUPAC Commission on Electrochemistry provided a critical appraisal of 15 such methods (11 in-situ and 4 ex-situ) in 1991[30]. The following assertion is a direct quotation from that report - "Electrode reaction rates and most double layer parameters are extensive quantities and have to be referred to the unit area of the interface. Knowledge of the real surface area of the electrodes is therefore needed. Comparison of experimental data with theories or of experimental results for different materials and/or from different laboratories to each other is physically groundless without normalisation to unit real area of the electrode surface." In spite of this, we have noted, during the preparation of the literature review of sections 1.5.3 – 1.5.4, that the majority of publications on the o.e.r., have quoted current density values in terms of geometric surface area as opposed to real surface area. This is scarcely surprising, since the IUPAC

Commission on Electrochemistry[30] expresses fairly strong reservations about the absolute significance of the "real" surface area values yielded by most of the techniques that it evaluated. It has been commented by Bai, Gao and Conway[31] that experimentally determined real surface area values are usually found to be dependent on the nature of the method applied.

Following the definitions used in the aforementioned IUPAC report[30], the *geometric* surface area, A_g, is defined as the projection of the real surface on a plane parallel to the macroscopic visible phase boundary. If the *real* surface area is denoted as A, then, the real surface area per unit geometric surface area is called the *roughness factor* f_r, where (clearly), $f_r = A/A_g$. For polycrystalline metallic electrodes an obvious source of surface roughness is the variation in the periodicity of distribution of atoms from site to site on the electrode surface[30]. Clearly the use of abrasives and/or mechanical polishing in the preparation of smooth bright metallic electrode surfaces will also add to the heterogeneous nature of such surfaces. In the case of the oxide covered electrodes at which oxygen evolution occurs, the surface roughness will depend on the morphology of the oxide. Recall, for example, from section 1.5.4, that Lyons and Burke[32] attributed the enhanced o.e.r. catalytic activity at multicycled Fe anodes in 1.0 M NaOH, relative to initially bright Fe electrodes, to the greater surface area provided by the open dispersed hydrous oxide layer pre-formed on the former electrode type relative to that provided by the anodic oxide formed on the latter type.

The situation is further complicated by the fact, that the true surface area (e.g. that wettable by the electrolyte solution), might not necessarily correspond to the electrochemically active area for a given Faradaic process. This was demonstrated for electrodes comprised of microporous RuO_2 layers on Ti substrates. For this particular case, Burke and co-workers found that the rate of the chlorine evolution reaction[33] was essentially independent of the roughness factor, while in contrast the o.e.r. catalytic activity[34] demonstrated a marked dependence on this parameter. These observations indicate that, whereas the chlorine evolution reaction is essentially a case of two-dimensional catalysis, occurring atop the outer electrode surface, the o.e.r. can be a case of quasi-3D electrocatalysis[35] where additional "inner" active surface area is available.

Amongst the in-situ techniques considered by the IUPAC commission[30] were methods based on capacitance ratios, the underpotential deposition (upd) of monolayer hydrogen or metallic ad-layers on electrode surfaces, and the growth of oxide

monolayers on anode surfaces. Ex-situ methods evaluated included BET (Brunauer, Emmett and Teller) adsorption isotherm based techniques, mercury porosimetry, and various types of microscopy.

The monolayer upd hydrogen adsorption method is based on the premise that the one hydrogen atom is adsorbed per surface metal atom. If the spatial distribution of metal atoms can be reasonably estimated, then the charge transferred in the deposition of a monolayer of hydrogen atoms per unit real surface area can be evaluated on this basis. The density of metal atoms per unit area is well defined for a given single crystal face – in the case of polycrystalline metals, this surface density is estimated as an average of the values associated with the main low-index faces. Thus for polycrystalline Pt the accepted value[30] of the surface atomic density is 1.31×10^{15} cm^{-2}, leading to a hypothetical value of the charge, Q_H, transferred in the deposition of a monolayer of upd H of Q_H = 210 μC cm^{-2}. The experimental charge Q_{EXP} associated with the underpotential deposition process can be evaluated by the integration of the voltammetric peaks characteristic of this process. In this case the appropriate roughness factor is given by $f_r = Q_{EXP} / Q_H$. Obviously, this method is applicable only to metals that display clear upd hydrogen adsorption peaks at potentials anodic to significant hydrogen evolution. In practice this limits the utilisation of the technique principally to Pt[36] and to a lesser extent[30] Rh and Ir. Owing to the overlap of the hydrogen adsorption and oxide growth regions for Ni, Co and Fe electrodes[30], it is not possible to apply the upd hydrogen method to the evaluation of the real surface areas of the electrodes utilised in the present work.

The monolayer oxide growth technique is based on the same principal as the upd hydrogen method, except in this case the "benchmark" charge quantity is that associated with the one 1 O atom to 1 metal atom formation of an oxide monolayer on the electrode surface. If this is assumed to involve the transfer of two electrons per site, then the reference charge Q_O for polycrystalline Pt would clearly be $Q_O = 2Q_H$ = 420 μC cm^{-2}. The technique has been most successfully applied to Au electrodes[30]. We recall at this stage, the work of Šimpraga and Conway on the initial oxidation of Ni[37], Fe[38] and Co[39] electrodes in alkaline solution, as was reviewed in section 1.4.3. These workers showed that the monolayer-type adsorption of OH or O species that occurs at noble metals such as Pt, or Au, does not occur at the aforementioned base metals, even at low temperatures down to 240 K. This renders the monolayer oxide technique useless in the estimation of active surface area for the electrode materials of

the present study. In any case, even for metals that permit the estimation of real surface area values by the upd hydrogen or monolayer oxide techniques, there is no guarantee that the surface area so-derived is that which is active for a given Faradaic reaction, as highlighted by the chlorine evolution/oxygen evolution example cited above.

One of the most commonly utilised methods in electrochemistry for real surface area estimation is based upon double layer capacitance, C_{dl}, measurements. The concept of the interfacial double layer and its capacitance were discussed in section 1.1.2. The double layer capacitance should be related to the real amount of the electrode surface exposed to electrolyte, thus providing the basis of its application in real surface area measurements. In principle, if a reference value were available for the double layer capacitance per unit metallic electrode area, then the roughness factor of a given electrode could be estimated by dividing its experimentally determined C_{dl} value by this reference value. In section 1.1.2 it was noted that much of our knowledge on the nature of metallic electrode/solution interfaces is based upon experimental measurements on mercury/aqueous solution interfaces. This arises principally owing to the fact that electrocapillary measurements may be performed at the liquid metal/solution interface, however the smoothness of the liquid metal surface is also an advantage, with the real surface area tending towards the geometric surface area in a manner not possible for solid metallic electrodes. Thus the area specific double layer capacitance of a Hg electrode in aqueous solution would seem to be a suitable candidate for providing the reference value mentioned above. In practice, the standard double layer capacitance per unit area for a metallic electrode in contact with an aqueous solution is usually taken[30] to be in the range of 15 – 17 μF cm^{-2}. This value is taken from the shallow minima observed in the differential capacitance vs. $E - E_{pzc}$ curves for Hg electrodes at potentials moderately negative to the pzc – e.g. see Figure 1.1.2, section 1.1.2.

The main criticism of this method is the unrealistic assumption that the double layer capacitance is constant for all metallic electrodes in the region moderately negative to the pzc. Frumkin et al.[40] showed that the double layer capacitance at such potentials for several metals varies from ~ 16 to ~ 25 μF cm^{-2}. Furthermore, experimental measurements of C_{dl} for a given metal should be performed at potentials similarly negative to the pzc, as those at which the capacitance minimum of 15 – 17 μF cm^{-2} is noted for Hg electrodes. In many cases however (most d-block metals), the position of

the pzc is unknown[30]. In addition many solid electrodes do not present a well defined double layer potential region, as with Hg or Pt, where the electrode is ideally polarisable and unambiguous C_{dl} measurements can be conducted.

Another problem is obvious in the application of the capacitance ratio method to the determination of the real surface area of oxygen evolution anodes – namely that the o.e.r. occurs on oxide covered electrode surfaces as opposed to metallic surfaces. Bockris and Otagawa[41] applied the double layer capacitance technique to the estimation of the real surface area of perovskite oxygen evolution anodes. These authors choose a reference value of C_{dl} = 60 μF cm^{-2} on the basis that their capacitance measurements (performed by cyclic voltammetery at various scan rates over a strictly limited potential range of 0.34 – 0.39 V in 1 M NaOH) were conducted in a region near, or positive to the flatband potential, and thus that the more appropriate capacitance for reference was that of the Hg/solution interface on the positive branch – again c.f. Figure 1.1.2. In view of this approximation and the other reservations discussed above, they concluded that their experimentally derived roughness factors probably did not have an absolute significance better than ± 100%.

The capacitance ratio method was also applied by Ho and Piron[42], to provide a comparison for real surface area values determined for oxygen evolution anodes, by a transient decay method that will be discussed further below. These authors made the (probably reasonable - see section 1.2.4) assumption that the a.c. impedance response at a d.c. potential several hundred millivolts positive to the onset of significant oxygen evolution is mainly that of the charging and discharging of the C_{dl} coupled with the faradaic resistance. Following an earlier work by Frumkin[43], they adopted the value of 40 μF cm^{-2} as the double-layer capacitance for a smooth oxide covered electrode.

The transient decay method proposed by Ho and Piron[42] is based essentially on the same principle as outlined above for the upd hydrogen and monolayer oxygen methods. As previously discussed the latter two methods are inapplicable to Ni, Co and Fe electrodes because of the overlap between the hydrogen and oxygen adsorption regions (in the case of the upd hydrogen method) and due to the fact that oxide growth does not occur on these base metals via a monolayer type growth mechanism (this excludes the use of the monolayer oxygen method). Ho and Piron sought to circumvent this problem for electrodeposited Ni, Co and $Ni_{20}Co_{80}$ electrodes by attempting to measure the charge involved in the desorption of the intermediate species involved in the o.e.r. These workers galvanostatically charged the

aforementioned anodes in 5.0 M KOH to steady state current values corresponding to various points along the oxygen evolution steady state polarisation curves for the same electrodes. They held the electrode at each chosen steady state current density for 10 s and then allowed it to discharge through a large platinized platinum plate counter electrode across a 1 Ω series resistor. The potential-time decay transient was followed by a digital storage oscilloscope connected across the resistor. This transient was readily converted to an *i-t* plot.

A cathodic current was thus observed, the initial magnitude of which (i.e. at time $t = 0$ corresponding to the interruption of the steady state current) was many times larger than that of the prior anodic charging current. Obviously the total charge, Q_{dec}, passed in the course of the decay process can be evaluated by integrating the experimental *i-t* plot between $t = 0$, and the time at which the decay current becomes zero. Ho and Piron[42] monitored this current decay on a millisecond time scale. The time required for decay of the transient to zero, varied with the magnitude of the initial steady state anodic charging current, however even for the largest charging currents the process was completed in less than ca. 16 ms.

The authors postulated that the o.e.r. at their anodes occurred via the following mechanism:

$$M^{3+}.O.OH + OH^- \rightarrow M^{4+}.O.O + H_2O + 2e^- \qquad (2.1.65, I)$$

$$2M^{4+}.O.O + H_2O \rightarrow 2M^{3+}.O.OH + \tfrac{1}{2} O_2 \qquad (2.1.65, II)$$

They envisaged that upon termination of the polarisation, oxygen evolution would continue to occur, with the electrode undergoing a decrease in oxidation state, possibly by step (2.1.65, II), until its potential is the same as the o.e.r. reversible potential or some other stable value. The real surface area determination method is however, based upon the assumption that this chemical recombination mode of desorption of OH_{ads} is relatively slow in comparison to electrochemical OH_{ads} desorption via the reverse of step (2.1.65, I). The authors therefore proposed that, following the interruption of polarisation at any given current density, the majority of OH_{ads} species should undergo this 2 electron cathodic process.

Upon plotting Q_{dec} vs. log*i* for their various electrodes, Ho and Piron[42] noted that Q_{dec} increased with log*i*, for the lower values of the latter, associated with the lower Tafel slope region in the o.e.r. steady state polarisation curve for the same electrode. At

higher log*i* values, plateau regions were observed in the Q_{dec} vs. log*i* plots. The authors proposed that the relatively constant Q_{dec} values associated with this plateau region corresponded to the discharge of OH_{ads} for the situation where the fractional coverage θ of this intermediate tends towards unity. They assumed that the charge per unit area, based upon the two electron desorption of the reverse of step (2.1.65, I) could be taken as 420 $\mu C\ cm^{-2}$ – this is of course, double the accepted value of the charge required for the 1 electron deposition of a monolayer of upd H on a polycrystalline Pt surface, as was discussed earlier. On this basis Ho and Piron estimated the roughness factor for their o.e.r. anodes using the following expression:

$$f_r = \frac{Q_{dec}(plateau)}{420\mu C\,cm^{-2}} \quad , \tag{2.1.66}$$

Ho and Piron[42] found that the values of roughness factor estimated by the OH_{ads} desorption method were of the same order of magnitude as those evaluated by the double layer capacitance ratio method for the various electrodes that they examined, with the exception of the electrodeposited Co electrode. These workers applied a similar technique to derive the real surface area for the hydrogen evolution reaction at Pt and stainless steel electrodes in alkaline solution[44].

Having reviewed various methods of real surface area evaluation, it is clear that there are a rather limited number of options available for convenient in-situ determination of the roughness factor applicable to the polycrystalline Ni, Co and Fe electrodes utilised in the present work. The two options most readily available are that of the double layer capacitance ratio method, and the OH_{ads} desorption technique of Ho and Piron. Both types of experiment have been conducted as part of the present body of work. The practical considerations are dealt with in section 2.2.12, while the results are outlined and discussed in chapter 4 and particularly chapter 5. It is to be emphasised at this point that we are fully aware of the weaknesses of these two methods especially with respect to questions regarding the validity of the respective assumptions on which each are based. It is however not our aim to obtain absolute values of the true surface areas of the electrodes, but rather to obtain estimates of the roughness factors for the various anodes, in order to facilitate a more meaningful comparison of the intrinsic catalytic activities of the oxides of Ni, Co and Fe towards the oxygen evolution reaction.

2.2 Materials and Instrumentation

2.2.1 Electrochemical Cell

The classical three electrode arrangement was utilised for all the experimental work. The cell vessel was a shot glass with an approximate volume of 40 cm^3. A suitably tight fitting lid for the specifications of the shot glass was machined from Teflon®. Four suitably sized circular holes were drilled in this cell cap to facilitate the insertion of the three electrodes and also a glass tube for the purpose of degassing of solutions. Degassing of the working solution with a stream of inert nitrogen gas was conducted for approximately fifteen minutes before experimentation, and during experimentation a blanket of the gas was maintained over the solution. The primary purpose of nitrogen purging of solutions is to remove dissolved oxygen. All experiments were performed at 25 ± 1 °C. During experiments, the cell was placed in an earthed Faraday cage (as supplied by CH Instruments, Inc.), to shield against electrical noise.

2.2.2 Working Electrodes

In electrochemical experiments the working electrode is normally selected to facilitate the electron transfer reaction(s) of a redox couple in the electrolyte solution. In this study we are interested in the electrochemical reactions of the working electrode – i.e. the material of the electrode itself is under examination. Ni, Co and Fe electrodes are generally not commercially available for laboratory purposes, and therefore it was necessary to construct suitable working electrodes in the laboratory. The Ni working electrodes were prepared from a 1 mm thick polycrystalline nickel foil as supplied by Alfa Aesar (Johnson Matthey), purity 99.9945% (metals basis). The Co electrodes were prepared from either a 1 mm thick polycrystalline cobalt foil from Alfa Aesar (Johnson Matthey), purity 99.95% (metals basis), or a polycrystalline Co wire, diameter 2 mm, purity 99.9+%, as supplied by Aldrich. Iron electrodes were prepared from either a 1mm thick polycrystalline iron foil from Alfa Aesar (Johnson Matthey), purity 99.995% (metals basis), or a polycrystalline Fe wire of diameter 2 mm, purity 99.9+%, supplied by Aldrich.

In the preparation of electrodes from the foils, small sections of the metal were cut from the as-supplied foil, and filed to a size of 4 mm × 4 mm (geometric surface area = 0.16 cm^2), taking great care not to scratch the surface to be exposed as part of

the electrode. The square piece of foil was then washed with copious Millipore water®, polished thoroughly with alumina powder (as described below), degreased with acetone, and washed again with Millipore water®. A length of copper wire was attached to the backside of the foil using a conductive epoxy as supplied by Circuit Works. After several days the square of foil was sealed into a glass tube using epoxy (Araldite®). The glass tube was previously bent into a periscope shape, and the metal surface to be exposed was placed at the vertical outlet at the bottom of the tube. In sealing the foil into the tube, the entire metal was covered with epoxy. After several days, when the Araldite® had completely hardened, it was polished back with fine abrasive paper until the 0.16 cm^2 area of metal was exposed. The newly exposed metal surface was polished with alumina powder and washed with copious Millipore water® before the electrode was used for experiments.

In case of electrodes prepared from the 2mm diameter wires, an appropriate length of wire was cut, and the cross section was filed back until a flat circular surface was achieved (geometric area = 0.0314 cm^2). The piece of wire was then subjected to the cleaning regime described above, for the foils. Following this, a length of copper wire was wrapped around one end of the electrode metal wire using a pliers. Some of the Circuit Works conductive epoxy was applied to the junction between the two wires, to guarantee good ohmic contact. When this bond had matured, the wire was sealed, using Araldite®, into a regular vertical glass tube, with care taken to ensure that the circular disk of metal to be exposed was in line with the end of the tube. Again, following the hardening of the epoxy, it was polished back to expose the circular metal surface.

2.2.3 Reference Electrode.

A reference electrode provides a time invariant potential benchmark against which, potential changes of the working electrode can be monitored. The potential of the reference electrode is related to a standard potential scale, for example, to the normal hydrogen electrode (N.H.E.). The potentiostat circuitry ensures that only small currents pass through the reference electrode, to prevent it becoming polarized. The reference electrode utilised in the present work was a mercury-mercuric oxide (Hg/HgO) electrode as supplied by Radiometer Analytical (cat no. XR400). A schematic diagram of this electrode is presented in Figure 2.2.1. According to classic

work of Ives and Janz[45] the Hg/HgO electrode is uniquely well behaved among metal-metal oxide electrodes, in that it displays the expected Nernstian shift of ~ -59 mV/pH unit against a pH independent reference electrode, with increasing pH at 25°, as was discussed in section 1.4.1. These authors also recommend that the mercury-mercuric oxide electrode is the most stable and suitable commonly available reference electrode for use in alkaline solutions.

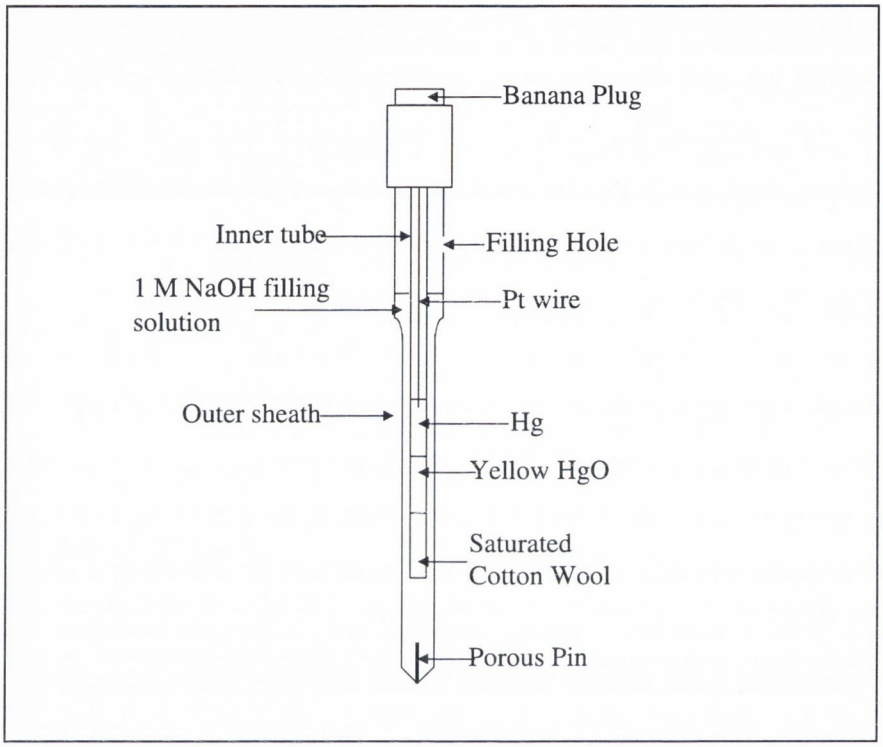


Figure 2.2.1 *Schematic diagram of the Hg/HgO reference electrode utilised in the present work.*

Silver/silver chloride electrodes, as an example, are unstable in alkaline solution, because OH^- ions that migrate into the chloride filling solution react with the silver chloride and form a silver oxide. Thus the observed reversible potential becomes a mixed potential between metallic silver and both its oxide and chloride. The equilibrium potential of the cell

$$Pt(H_2)|NaOH(aq)|HgO|Hg \qquad (2.2.1)$$

is 0.926 V at 25°C[45, 46]. Since the equilibrium oxygen electrode potential is 1.229 V vs. the RHE, it follows that $E^0_{O_2}$ is 0.303 V vs. Hg/HgO in the same solution. It is common practice (see for example refs.47, 48) in the literature on the o.e.r., to express

potential in terms of the oxygen overpotential η, when the reference electrode is a Hg/HgO electrode in the same solution as the working anode. Clearly, in this case η is related to the voltage E_{meas} measured on the Hg/HgO scale as follows:

$$\eta = E_{meas} - 0.303 \text{ V (at 25°C)} \qquad (2.2.2)$$

Electrolyte solutions of various concentrations are used in the present work, in the determination of reaction orders with respect to OH^- activity for the oxygen evolution reaction. For the sake of consistency it was elected to use Hg/HgO, 1M NaOH, as the universal reference standard in this work – therefore all voltages are quoted against this reference electrode. When used in NaOH solutions of different concentrations, the potential of the Hg/HgO electrode was checked relative to a second Hg/HgO, 1 M NaOH electode, both before and after the experiment. No significant potential drift was noted after such experiments, implying that the concentration of the NaOH in the reference electrode chamber remains effectively constant over the time scale of typical polarisation measurements (ca. 2 – 3 hours). In any case, the 1 M NaOH solution in the reference electrode was changed on a weekly basis to ensure experimental consistency.

2.2.4 Auxiliary Electrode

The purpose of the auxiliary (counter) electrode is to supply the current required by the working electrode thereby preventing the polarization of the reference electrode due to passage of excess current through that electrode. A platinum wire electrode as supplied by CH Instruments, Inc. (catalogue no. CHI 115) was employed as the counter electrode in this study.

2.2.5 Electrolyte Solutions

Aqueous solutions of sodium hydroxide (BDH AnalaR®, minimum 98% purity) were used as the electrolyte in all experiments. All solutions were made up using ultra-pure water from a Millipore® water purification system. For the accurate construction of reaction order plots (see chapter 3) it is necessary to plot the logarithm of the current density at a given potential against the logarithm of the OH^- activity a_{OH^-} as opposed

to the logarithm of the molar concentration of the OH^- ions. The ionic activity of OH^- ions in a solution of NaOH of *molality m* is given by the following expression,

$$a_{OH^-} = \gamma_{\pm} m \ , \qquad (2.2.3)$$

where, $\gamma_{\pm}$ is the *mean ionic activity coefficient* for an NaOH solution of that concentration. Mean ionic activity coefficients have been experimentally determined for many ionic solutions, and are generally quoted in terms of molality. The molalities of the various solutions utilised in this work were obtained by accurately determining the mass of a known volume of a NaOH solution of known concentration, and calculating the number of moles per Kg of the solution. Values of the mean ionic activity coefficients for NaOH solutions of different molalities at 25°C were obtained from reference 49, and the appropriate values of a_{OH^-} for each solution were calculated. These values are summarised in Table 2.2.1.

Molarity mol dm^{-3}	Molality mol Kg^{-1}	Mean activity coefficient $\gamma_{\pm}$	Ionic activity a_{OH^-}	log a_{OH^-}
0.1000	0.1000	0.7640	0.0764	-1.1169
0.2000	0.2000	0.7250	0.1450	-0.8386
0.2500	0.2500	0.7130	0.1783	-0.7490
0.5000	0.5000	0.6880	0.3440	-0.4634
1.0000	1.0100	0.6770	0.6838	-0.1651
2.0000	2.0240	0.7070	1.4310	0.1556
3.0000	3.0520	0.7850	2.3958	0.3795
5.0000	5.1920	1.1050	5.7372	0.7587

Table 2.2.1 *Values of ionic activity a_{OH^-} calculated for the various NaOH solutions utilised.*

2.2.6 Electrode Pre-treatment

Obtaining a consistent electrode substrate in order to make reproducible measurements on the kinetics of the o.e.r. at polycrystalline Ni, Co and Fe electrodes is not a trivial matter, and indeed has possibly been the greatest challenge in obtaining a meaningful set of data on these systems. Various electrolytic pre-treatment regimes have been applied to the electrodes in order to (hopefully) produce a standard electrode surface on which to study oxygen evolution. These pre-treatments will be outlined in chapter 3 in combination with the presentation of data obtained on electrodes to which they have been applied.

For the present it is noted, that upon their initial preparation as discussed in section 2.2.2, all working electrodes were polished to a mirror "bright" finish. Before and after any experiment, mechanical polishing was performed to ensure that this "bright" appearance was achieved. Polishing was performed in a slurry of 0.05 micron alumina powder in Millipore® water on a fine grit pad. Following polishing, the electrode surface was rinsed with copious Millipore® water. Any remaining polishing residue was removed with a soft tissue paper, and the electrode was again rinsed with Millipore® water before being placed in the electrolyte solution or being put in storage.

2.2.7 The Zahner elektrik IM6 Impedance measurement unit

All electrochemical data was obtained using a Zahner elektrik IM6 Impedance measurement unit. As the unit's name suggests, this device is primarily designed for the collection of electrochemical impedance data. However, the high quality electronics required for complex impedance measurements can also be readily applied to other electrochemical measurements such as cyclic voltammetry (CV), steady state polarisation measurements and open-circuit potential decay measurements. At its most fundamental the IM6 rig contains a waveform generator to produce a time varying signal, a potentiostat to apply this signal as a potential perturbation to the electrochemical cell, and a current to voltage converter to measure the resultant current flow. The output from the current to voltage converter is passed through an analog to digital converter (ADC). In turn the digital output siginal from the ADC is sent to the IM6's inbuilt microprocessor. This microprocessor is interfaced to a PC, which acts as both an input and output device via a Microsoft DOS based software suite called the Thales suite. All the experimental/control parameters are entered via the IM6/DOS interface. As the experiment is run the data is processed by the IM6 microprocessor and is then transmitted to the PC, where the appropriate Thales software enables it to be displayed in virtual real-time. This software also permits the analysis of the raw data, which can alternatively be transferred to third party spreadsheet based programs via exported text files.

The IM6 Impedance unit has a potential control range of -10⟶ + 10 V, a current range of -3⟶ + 3 A and is capable of measuring current down to picoamperes. Time variant potential or current perturbation can be applied to the working electrode

to a resolution of 10^{-4} sec per step, while a sampling rate of 10 kHz is possible. The wide range of user-specifiable parameters available on the IM6 rig relative to other commercial digital electrochemical work-stations available in our laboratory, made the IM6 the system of choice for the current work, especially in relation to the recording of steady-state polarisation.

2.2.8 The Potentiostat

The potentiostat (and indeed galvanostat) arrangement applied in this study utilises a three electrode configuration. The purposes of the three electrodes (working, reference and counter) has been discussed previously. A potentiostat is a device that controls the applied potential between the working electrode and the reference electrode. This device is based upon an electronic component called an operational amplifier (op amp). Modern op amps come in the form of an integrated circuit, often with different characteristics, depending on the application for which they are required. At the most basic level the operational amplifier circuit in a potentiostat acts as a feedback loop, controlling the potential between the working and reference electrodes, while simultaneously adjusting its output to provide a sufficient current to the counter electrode. This current sustains the electron transfer reaction at the working electrode, and thus has the effect of preventing the passage of large currents through the reference electrode – undesirable, since this could alter the potential of the latter electrode. A comprehensive discussion of how op amps are incorporated into potentiostat circuitry is provided in reference 50.

2.2.9 Measuring Steady State Polarisation Data

The philosophy behind steady state polarisation measurements was presented in section 2.1.1. This method involves stepping the voltage applied to the working electrode to a given potential, and then waiting for the current response to reach a consistent value. The steady current is then recorded digitally, and the applied voltage stepped to the next measurement potential. The IM6 rig provides a facility for recording steady state polarisation data, that enables the user to define potential step size, minimum and maximum waiting times at each potential and current tolerance at equilibrium amongst other parameters. The current tolerance is defined as:

$$\Delta I = \frac{I_n - I_{n-1}}{\Delta t} \qquad (2.2.4)$$

In the above expression I_n represents the current recorded at the time of the n^{th} sample while Δt is the time between recording of the n^{th} and $n\text{-}1^{th}$ sample. The potentiostat waits until the current fluctuation falls within the specified ΔI (or until the user defined maximum waiting period has elapsed) before stepping to the next potential. A current tolerance of 5 nA s^{-1} was used in the present work. The IM6 unit also allows the user to input a value of the uncompensated solution resistance, and it applies the appropriate correction to the outputted data.

2.2.10 Measuring Electrochemical Impedance Data

Issues pertaining to the measurement of EIS data have already been discussed in detail in section 2.1.6. In this section some brief comments are made regarding impedance measurements with the IM6 unit. The IM6 falls into the FRA based category of impedance measurement systems. It has an upper frequency limit of 8 MHz. By default measurements start at 66Hz (or some other user specified intermediate frequency value) and sweep to the required high frequency limit before sweeping back to the low frequency limit. This approach affords the operator the opportunity to evaluate whether the electrochemical system is stable or not. If the values of impedance and phase angle measured by the initial increasing frequency sweep are not retraced as the frequency is being reduced, it can be concluded that the system is not stable over this time scale. As was discussed in section 2.1.6 there is something of a "trade off" between the improvement in data quality achieved by measuring at a greater number of frequencies per decade (and averaging over a greater number of cycles at each given frequency), and the time required for the experiment. The IM6 control software attempts to address this problem by allowing the operator to specify a different number of measurement frequencies per decade and measurement cycles at each frequency in the high frequency region (> 66 Hz.) and the low frequency region (< 66 Hz).

The concept of fitting experimental impedance data to equivalent circuit models using CNLS routines was discussed in section 2.1.7. Such fitting operations are facilitated by the SIM module of the IM6 Thales software suite. A further useful feature of the

SIM software is its *Kramers-Kronig rule check* option. The Kramers-Kronig transforms and their fundamental importance in evaluating the reliability of EIS data were discussed in section 2.1.8. The Kramers-Kronig rule check option calculates the impedance of a real data set from its phase angle data, and compares these values with the measured impedance values. All impedance data presented in the current work has been subjected to this consistency check, and has been rejected if it fails the test.

2.2.11 Experimental Estimation of Real Surface Areas

Values of the double layer capacitance C_{dl} were derived from CNLS fitting of EIS spectra recorded for the various electrodes in 1.0 M NaOH at potentials within the region of significant oxygen evolution current densities. The principles of extracting values for C_{dl} from the fitting of raw impedance data to (hopefully) meaningful equivalent circuit models were discussed in section 2.1.7.

A schematic diagram is presented in Figure 2.2.2 of the basic circuitry used in the galvanostatic charging/discharging experiments aimed at true surface area evaluation by the OH_{ads} desorption method (see section 2.1.10). This circuit is a modification of that originally proposed by Ho and Piron[42, 44]. The current source was the IM6 rig operating in its galvanostatic mode. The oscilloscope was a Velleman PCS100 pc controlled digital storage oscilloscope. This measurement device is controlled by a personal computer and its settings may be altered through a Windows® interface. This interface also permits the display of the measured voltage-time characteristic in virtual real time. Each recorded decay transient was saved directly to the pc hard-disk for later analysis. A sampling frequency of 80 KHz was chosen – this corresponds to the periodic recording of voltage values at 0.0125 ms intervals following the triggering of the oscilloscope. Owing to Ohms law, the instantaneous magnitude of the decay current through the 1 Ω series resistor is obviously equal to the magnitude of the voltage across the resistor at that particular moment. Thus for a 1 Ω resistor, and a 1 Ω resistor only, the oscilloscope trace effectively maps the decay current – time transient. The 1 Ω series resistance was provided by a Levell R701 Resistance Box.

The range of values of current density to be applied to a given electrode were chosen with reference to a steady state polarisation curve recorded for the o.e.r. at that

electrode on the previous day. Values were selected corresponding to potentials from that at which significant oxygen evolution currents commenced, up to potentials several hundred mV anodic to that point. During the experiments, the electrodes were polarised for a period of 30 s at each current density, and were then immediately discharged through the series resistance by 'tripping' the relay switch. In order to estimate the experimental error associated with these experiments, they were each repeated four times - once a day, over consecutive days. The results are presented and discussed in chapter 5.

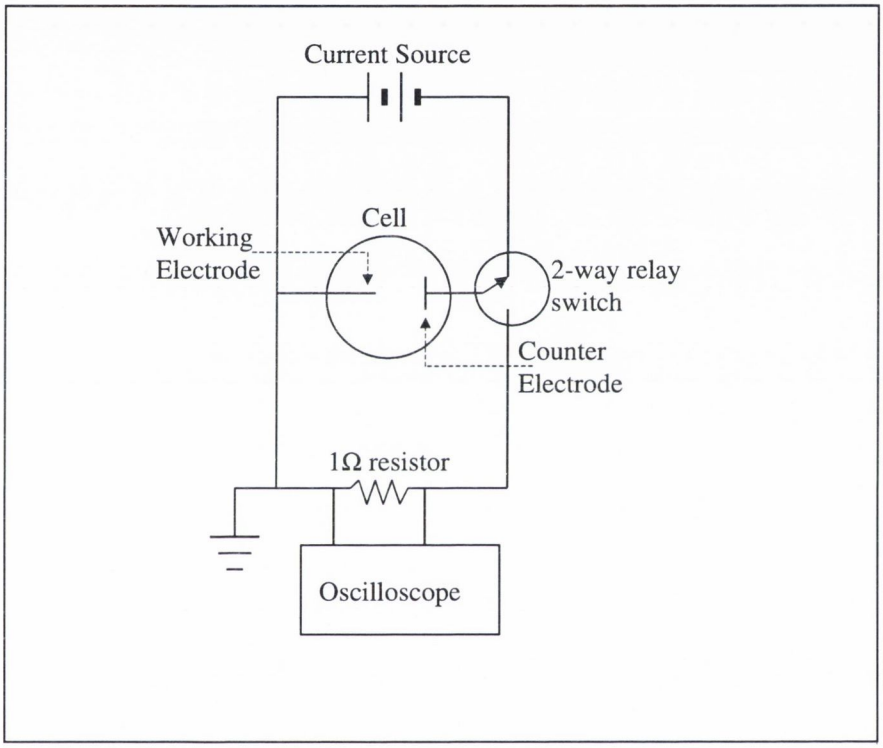


Figure 2.2.2 *Schematic diagram of the apparatus and basic circuitry used in the transient decay method of surface area estimation.*

Chapter 2 References

1 Hicking, A., *Trans. Faraday Soc.*, **1941**, *37*, 532.

2 Bowden, F.P., Rideal, E., *Proc. Roy. Soc.*, **1928**, *A120*, 59.

3 Hoare, J.P., "The Electrochemistry of Oxygen", Interscience, New York, 1968, chapters 3 & 7.

4 Bockris, J.O'M., Khan, S.U.M., "Surface Electrochemistry – A Molecular Level Approach", Plenum Press, New York, 1993, section 1.2.

5 Lu, P.W.T., Srinivasan, S., *J. Electrochem. Soc.*, **1978**, *125*, 1416.

6 Burke, L.D., Lyons, M.E.G., Murphy, O.J., *J. Electroanal. Chem.*, **1982**, *132*, 247.

7 Katsaounis, A., Brosada, S., Vayenas, C.G., in "Encyclopedia of Electrochemistry, Volume 5 – Electrochemical Engineering", Bard, A.J., Stratmann, M., Eds., Macdonald, D.D., Schmuki, P., Vol, Eds., Wiley-VCH, Weinheim, 2007, chapter2.

8 Bard, A.J., Faulkner, L.R., "Electrochemical Methods-Fundamentals and Applications", J. Wiley & Sons, 2001.

9 Greef, R., Peat, R., Peter, L.M., Robinson, J., "Instrumental Methods in Electrochemistry", Ellis, Chichester, 1985.

10 Brett, C.M.A., Brett, AM.O., "Electrochemistry- Principles, Methods and Applications", Oxford Science Publications, 1993.

11 Bard, A.J., Faulkner, L.R., "Electrochemical Methods-Fundamentals and Applications", J. Wiley & Sons, 2001, chapter 10.

12 Park, Su-Moon, Yoo, Jung-Suk, *Anal. Chem.*, **2003**, *75*, 455 A.

13 Greef, R., Peat, R., Peter, L.M., Robinson, J., "Instrumental Methods in Electrochemistry", Ellis, Chichester, 1985, chapter 8.

14 Conway, B.E., in "Impedance Spectroscopy – Theory, Experiment, and Applications", 2nd Edition, Barsoukov, E., Macdonald, J.R., Ed., J. Wiley & Sons, 2005, section 4.5.

15 Macdonald, D.D., *Electrochimica Acta.*, **2006**, *51*, 1376.

16 McKubre, M.C.H., Macdonald, D.D., in "Impedance Spectroscopy – Theory, Experiment, and Applications", 2nd Edition, Barsoukov, E., Macdonald, J.R., Eds., J. Wiley & Sons, 2005, section 3.1.

17 Sayers, B., in "Impedance Spectroscopy – Theory, Experiment, and Applications", 2nd Edition, Barsoukov, E., Macdonald, J.R., Ed., J. Wiley & Sons, 2005, section 3.2.

18 Macdonald, J.R., in "Impedance Spectroscopy – Theory, Experiment, and Applications", 2nd Edition, Barsoukov, E., Macdonald, J.R., Ed., J. Wiley & Sons, 2005, section 3.3.

19 Gamry Instruments, Application Note, "Electrochemical Impedance Spectroscopy Primer", Gamry Instruments, 2005.

20 Harrington, D.A., Conway, B.E., *Electrochimica Acta.*, **1987**, *32*, 1703.

21 Kobussen, A.G.C., *J. Electroanal. Chem.*, **1981**, *126*, 199.

22 Kobussen, A.G.C., Broers, G.H.J., *J. Electroanal. Chem.*, **1981**, *126*, 221.

23 Armstrong, R.D., Henderson, M., *J. Electroanal. Chem.*, **1972**, *39*, 81.

24 Pajkossy, T., *J. Electroanal. Chem.*, **1994**, *364*, 111.

25 Orazem, M.E., Shukla, P., Membrino, M.A., *Electrochimica Acta.*, **2002**, *47*, 2027.

26 Jovic, V.D., Gamry Instruments, Application Note, "Determination of the correct value of C_{dl} from the impedance results fitted by the commercially available software", Gamry Instruments, 2003.

27 Hsu, C.H., Mansfeld, F., *Corrosion*, **2001**, *57*, 747.

28 McKubre, M.C.H., Macdonald, D.D., in "Impedance Spectroscopy – Theory, Experiment, and Applications", 2nd Edition, Barsoukov, E., Macdonald, J.R., Eds., J. Wiley & Sons, 2005, section 4.4.

29 Van Meirhaege, R.L., Dutoit, E.C., Cardon, F., Gomes, W.P., *Electrochimica Acta.*, **1976**, *21*, 39.

30 Trasatti, S., Petrii, O.A., *Pure & Appl. Chem.*, **1991**, *63*, 711.

31 Bai, L., Gao, L., Conway, B.E., *J. Chem. Soc., Faraday Trans.*, **1993**, *89(2)*, 235.

32 Lyons, M.E.G., Burke, L.D., *J. Electroanal. Chem.*, **1984**, *170*, 377.

33 Burke, L.D., O'Neill, J.F., *J. Electroanal. Chem.*, **1979**, *101*, 341.

34 Burke, L.D., Murphy, O.J., O'Neill, J.F., Venkatesan, S., *J. Chem. Soc., Faraday Trans. 1*, **1977**, *73*, 1659.

35 Burke, L.D., O'Sullivan, E. J.M., *J. Electroanal. Chem.*, **1981**, *117*, 155.

36 Conway, B.E., Angerstein-Kozlowska, H., *Acc. Chem. Res.*, **1981**, *14*, 49.

37 Šimpraga, R., Conway, B.E., *J. Electroanal. Chem.*, **1990**, *280*, 341.

38 Šimpraga, R., Conway, B.E., *J. Electroanal. Chem.*, **1991**, *313*, 161.

39 Šimpraga, R.P., *J. Electroanal. Chem.*, **1993**, *355*, 79.

40 Frumkin, A., Damaskin, B., Grigoryev, N., Bagotskaya, I., *Electrochimica Acta.*, **1974**, *19*, 69.

41 Bockris, J.O'M., Otagawa,T., *J. Electrochem. Soc.*, **1984**, *131*, 290.

42 Ho, J.C.K., Piron, D.L., *J. Appl. Electrochem.*, **1996**, *26*, 515.

43 Frumkin, A. N., *J. Res. Inst. Catalysis* (Hokkaido Univ.), **1967**, *15*, 61.

44 Ho, J.C.K., Piron, D.L., *J. Electrochem. Soc.*, **1995**, *142*, 1144.

45 Hills, G.J., Ives, D.J.G., in "References Electrodes", Ives, D.J.G., Janz, G.J., Eds., Academic Press, New York, 1961, chapter 7.

46 Sawyer, D.T., Sobkowiak, A., Roberts, Jr., J.L., "Electrochemistry for Chemists, Second Edition", Wiley-Interscience, New York, 1995. chapter 5.

47 Willems, H., Kobussen, A.G.C., De Wit, J.H.W., and Broers, G.H.J., *J. Electroanal. Chem.*, **1984**, *170*, 227.

48 Gennero De Chialvo, M.R., Chialvo, A.C., *Electrochimica Acta*, **1990**, *35*, 437.

49 Robinson, R.A., Stokes, R.H., "Electrolyte Solutions", Butterworth & Co. Ltd., London, 1951.

50 Von Fraunhofer, J.A., Banks, C.H., "Potentiostat and its Applications, 1st Edition", Butterworth & Co. Ltd., London, 1972.

CHAPTER 3

STEADY STATE POLARISATION AND VOLTAMMETRY STUDIES

3.1 Introduction

This chapter focuses on the presentation of the results of steady state polarisation measurements on the oxygen evolution reaction on polycrystalline Ni, Co, and Fe electrodes in alkaline solution. Also included, are relevant cyclic voltammograms, that yield information on the nature of the catalytic surfaces on which the o.e.r. proceeds in these systems. The experimental data is presented in turn for the Ni, Co and Fe electrodes. A discussion of the significance of these results, particularly with respect to the determination of the operative o.e.r. mechanism(s), is then undertaken.

3.2 Nickel: Steady State Polarisation and Voltammetry Results

3.2.1 Bright Non-pre- treated Ni electrodes

In view of the widely reported (see section 1.4.1) complexity and variability of the surface electrochemistry of nickel in alkaline media (especially in connection to the inter-conversion of the various Ni(II) and Ni(III) hydroxides and oxyhydroxides, and the non-stoichiometry of the anodically generated oxide film), it was elected to begin the investigation of the o.e.r. on Ni by characterising the redox behaviour of the metal, and determining whether a stable, reproducible anode surface could be obtained on which to study the reaction. To this end, a freshly prepared polycrystalline Ni electrode was subjected to series of potential cycling experiments, over the course of a number of days, to effectively "break it in". These experiments involved placing the electrode (which had previously been vigorously polished as described in chapter 2), in 1.0 mol dm^{-3} NaOH solution, cycling its potential, four times, between –800 and 700 mV, before removing it from solution, polishing, rinsing and drying it (with soft tissue paper), and leaving for several hours before repeating the procedure. The voltammetric profiles of the first cycles of the second, fifth, and ninth series of such experiments are presented in Figure 3.2.1. The rising edge of the oxygen evolution current is obvious at the most anodic potentials in these voltammograms, especially in that of the most aged electrode (9^{th} series). Indeed, for this electrode, there is no clear separation between the redox peak associated with the oxidation of Ni(II) species to higher oxidation states and the rising current due to the o.e.r. This would seem to support the view[1] that oxygen evolution at oxide anodes is essentially a "side-reaction" associated with the decomposition of an anodically generated unstable oxide entity, in this case, possibly surface nickel species with a net charge above three.

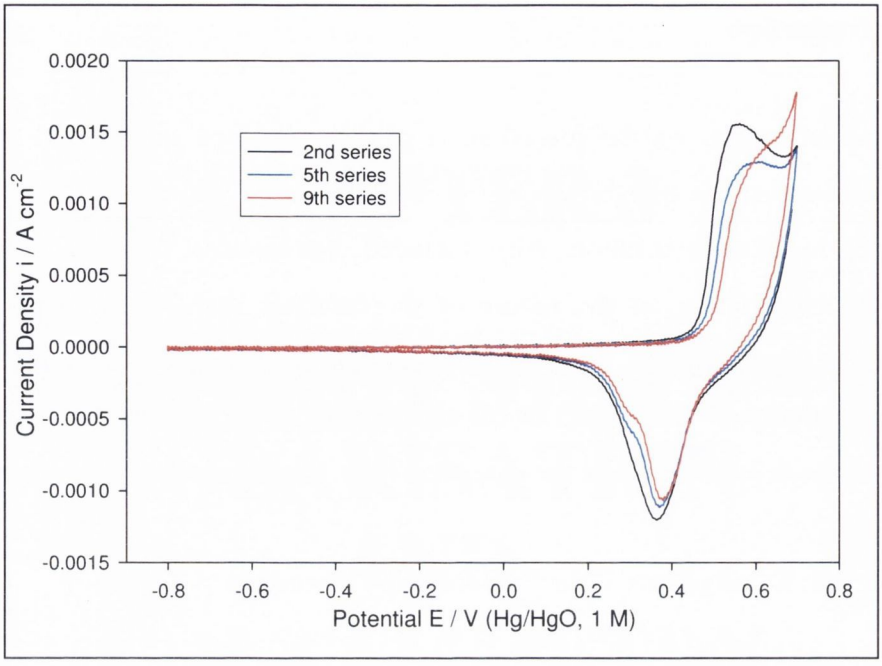


Figure 3.2.1 *CVs of the first cycle of the 2nd, 5th and 9th series of voltammetric experiments (see text above for more details) on a new polycrystalline Ni electrode in 1.0 M NaOH solution at 25°C. The sweep rate was 40 mV s-1.*

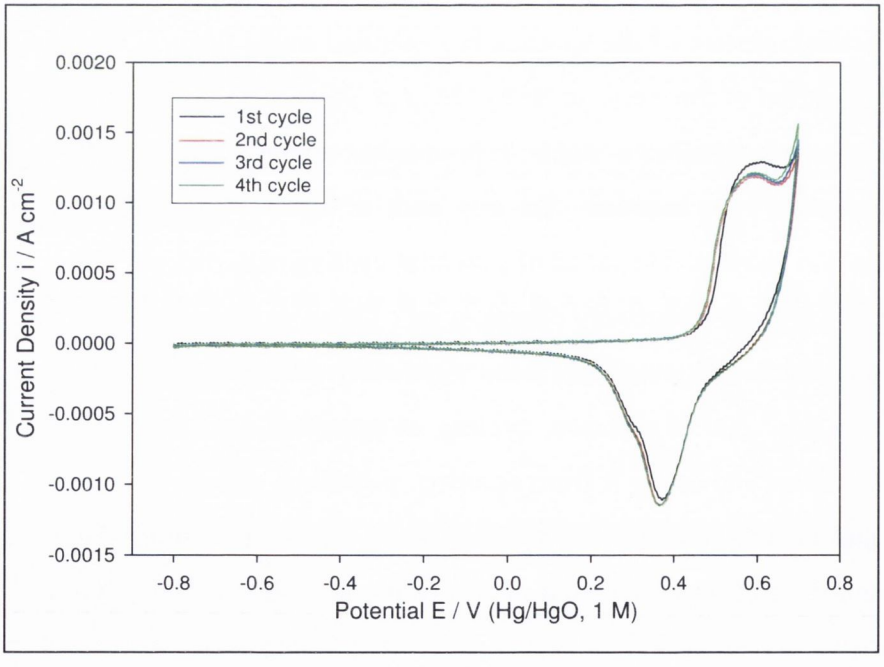


Figure 3.2.2 *The four cycles of the 5th series from Figure 3.2.1. Conditions are as outlined for that figure.*

The most general conclusion regarding the altering form of the CV profile with ageing, on going from the second series through the ninth, is that the active material is becoming increasingly anhydrous with ageing. If the simple Bode scheme (Figure

1.3.4) is admitted, this would correspond to a transition of material from the α-$Ni(OH)_2$ ↔ γ-NiOOH cycle to the β-$Ni(OH)_2$ ↔ β-NiOOH cycle, owing to the gradual dehydration of α-$Ni(OH)_2$ to form the β phase. It is worth recalling from section 1.4.1 that in cyclic voltammetry experiments, Barnard et al.[2] found, that for the β-β couple the oxidation peak potential was 0.5 V, while the reduction peak potential was 0.37 V (both vs. Hg/HgO). The corresponding values for the α-γ couple were 0.43 V for the oxidation peak and 0.34 V for the reduction peak. On this basis it would be reasonable to assume that the observed increase, with ageing, in both oxidation and reduction peak potentials in Figure 3.2.1, is indeed due to a transition of material from the α-γ cycle to the β-β cycle.

For the voltammogram of the second series in Figure 3.2.1, the onset of the oxidation current occurs at ca. 460 mV, with a broad peak present in the vicinity of 550 mV. The corresponding reduction peak potential is ~ 360 mV. For the first cycle of the ninth series it is difficult to identify a current peak owing to the onset of a significant oxygen evolution current – however it is apparent that the oxidation current profile is shifted to more anodic potentials relative to the second series. The main reduction peak for the ninth series has shifted by ca. 20 mV in the positive direction relative to the corresponding peak for the second series. It must be remembered that the cyclic voltammetry peak potentials of Barnard et al.[2] as quoted above, were determined using specifically prepared and characterised α-$Ni(OH)_2$ and β-$Ni(OH)_2$ phases, that were obtained by precipitation of the active material from nickel nitrate solutions. Comparing the CVs of Figure 3.2.1 with Barnard's data, indicates that anodic oxide films produced in the present work, initially consist of a mixture of the hydrous and anhydrous forms of nickel hydroxide/oxyhydroxide. This is bourn out by the fact that the reduction peak for the first cycle of the second series, has a value (360 mV) intermediate to those observed by Barnard et al.[2] for reduction to α-$Ni(OH)_2$ (340 mV) and reduction to β-$Ni(OH)_2$ (370 mV).

If it is accepted, as in the models of Bode et al.[3] or Sac Epee et al.[4], that nickel hydroxide and oxyhydroxide exists as four broadly distinguishable phases (i.e. α-Ni(II), β-Ni(II), γ-Ni(III or IV?) and β-Ni(III)), then, as postulated above, the shift, with ageing, in the oxidation and reduction current profiles in the anodic direction, can be associated with a progressive transition of active material from the α – γ cycle to the β – β cycle. Such an interpretation is supported by several other observations from Figure 3.2.1. Firstly, it is apparent that a shoulder appears on the negative side of

the reduction peak with ageing – compare the CV from the second series to those from the fifth and ninth. This phenomenon might be explained as follows; in the second series the reduction product probably consists largely of hydrated α-$Ni(OH)_2$ – thus only one rather broad cathodic peak is observed. With increased ageing, the reduction product will contain a progressively higher proportion of the anhydrous β-$Ni(OH)_2$. With reference again, to the work of Barnard et al.[2], it is known that in cyclic voltammetric experiments, the cathodic peak for the reduction to β-$Ni(OH)_2$ occurs at higher potentials than that for the reduction to α-$Ni(OH)_2$. In view of this, the shape of the cathodic profile for the fifth and ninth series in Figure 3.2.1, can be explained as a superposition of reduction peaks of the β – β and α – γ cycles, with the shoulder resulting from the latter.

Most usually[5, 6], the active charge capacity associated with the Ni(II)↔Ni(III) transition is characterised by integrating the cathodic voltammetric profile between its upper limit and ca. 0 V. Adopting this approach, approximate values of the charge capacity, Q, of 5.73 mC cm^{-2}, 4.91 mC cm^{-2}, and 4.37 mC cm^{-2} were calculated respectively, for the first cycles of the second, fifth and ninth series. Therefore the active charge capacity calculated for the ninth series is just ~ 76% of that recorded for the second series. This observation is also consistent with the presence of a relatively higher proportion of β-$Ni(OH)_2$ compared to α-$Ni(OH)_2$ in the ninth series, as opposed to the second series. It is a reasonable assumption that relatively ordered β-$Ni(OH)_2$ with its brucite structure (see section 1.4.1), will be less electrochemically active than the dispersed, hydrous, turbostratic α-$Ni(OH)_2$ material, which by its nature should offer a greater specific surface area to the electrolyte for reaction. This point has been alluded to by McBreen[7], in his review on nickel hydroxides.

The four cycles of the fifth series are presented in Figure 3.2.2. It is apparent from these CVs that virtually no change occurs in the voltammetric profile over the course of these four potential sweeps. Similar behaviour was noted for the four cycles of the other series. This leads to the conclusion, that for the experimental conditions employed, the ageing of the electrode in air with time, and/or effects related to the removal of oxide layers by polishing and their re-growth upon re-introduction to alkaline solution and the subsequent polarisation of the electrode, are more significant with respect to changes in voltammetric behaviour than a small number of repetitive potential sweeps. This lack of reproducibility, between series of the experiment, indicated to us, early in the course of the work, that attainment of a reproducible Ni

surface on which to conduct systematic o.e.r. studies was likely to present a significant challenge. This is especially true, considering that the voltammetric experiments described above, were conducted at less anodic potentials, and on a much shorter timescale than are required for steady-state polarisation measurements on the o.e.r. at the Ni anode.

The results of such a steady state measurement over an extended potential range on the electrode characterised above, are presented in Figure 3.2.3.

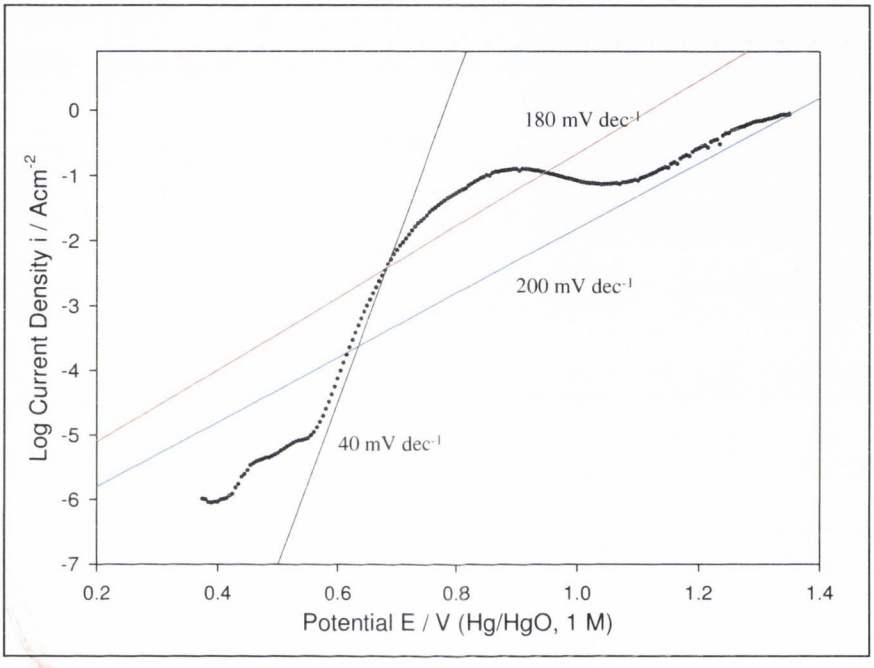


Figure 3.2.3 *IR corrected steady state polarisation curve recorded in the direction of increasing potential on a bright polycrystalline Ni electrode in 1.0 M NaOH solution at 25°C.*

Visually, this curve resembles a Tafel plot presented by Burke and Twomey[1] for a bright Ni anode in 1.0 M NaOH. The response, at the lowest current densities, in the potential region of approximately 400 – 550 mV are related to the surface electrochemistry of the Ni(II) oxidation process, as discussed above and reviewed in section 1.4.1. At potentials anodic to this, a very clearly defined straight line Tafel region with a slope of ca. 40 $mVdec^{-1}$ is observed to extend for over two decades of current density. Tafel slopes with values of approximately 40 mV dec^{-1} have been observed by Lu et al.[8] for pre-anodised Ni electrodes in 1.0 N KOH, and by Conway and Liu[9] for a pre-oxidised Ni anode (for 1 hour at 0.57 V (Hg/HgO) in 1 M NaOH) in 0.2 M NaOH. In the region of potential between approximately 750 and 850 mV a Tafel slope of the order of 180 mV dec^{-1} is apparent. This probably corresponds to a

Tafel slope of approximately 170 mV dec^{-1} reported by Lu et al.[8] for higher overpotentials. In an early work on the topic, Sato and Okamoto[10], reported the presence of a Tafel slope of ca. 100 mV dec^{-1} at higher values of current density, for the o.e.r. on Ni in alkaline media. This slope appeared at potentials positive to a region that had the characteristics of a limiting current, and was attributed by the authors to the discharge of H_2O, since its position and value was independent of pH. A straight line region is also apparent in Figure 3.2.3 beyond a broad peak between ca. 800 mV and 1 V. However, in this case the measured slope is of the order of 200 mV dec^{-1}. This upper slope region observed in anodic steady state polarisation measurements on the o.e.r. at Ni in alkaline solution, has received little attention in the literature, since most workers don't extend polarisation experiments to such high overpotentials.

As discussed in section 1.2, Tafel slope data alone, is insufficient in the elucidation of reaction mechanisms, since the predictions of kinetic analyses of different pathways can often yield the same Tafel parameters. In an attempt to clarify the situation, it has been decided in the present study, to experimentally determine reaction orders with respect to OH^- activity, a_{OH^-}, in order to provide another parameter that the kinetic analysis of a prospective mechanism must satisfy before that mechanism can be admitted as being operative. In order to accurately perform such a study, it is imperative that a reproducible catalytic surface can be achieved, so that the electrode is, in as similar a physical and chemical state as is possible, before being introduced to solutions of different OH^- activity. From a practical viewpoint, one could be confident that a given electrode is sufficiently stable to conduct reaction order studies, if the results of a steady state polarisation measurement at a given electrolyte concentration, could be satisfactorily reproduced in a number of identical experiments over a certain period of time. Given the intrinsic, progressive changes in the surface electrochemistry of the polycrystalline Ni electrode in alkaline solution, as described in relation to the data of Figure 3.2.1, it was envisaged that reproducibility could be a significant issue in attempting to obtain meaningful reaction order data for the o.e.r. in this system. Indeed, to the best of our knowledge, despite numerous literature studies on various aspects of oxygen evolution at polycrystalline Ni anodes in alkaline media, there is no reliable reaction order data available on the system. The absence of such data may be partially on account of the inherent problems with reproducibility.

The initial approach to Ni electrode pre-treatment, adopted in this work, involved mechanical polishing of the electrode, followed by its introduction to a cell containing 1.0 M NaOH, in which it was subjected to a potential cycle between –800 and 675 mV at 40 mV s^{-1}. The purpose of this voltammetric sweep was twofold – (i) to hopefully achieve a reproducible catalytic surface by oxidising and then reducing the active material following polishing and (ii) to characterise the surface electrochemistry of the electrode prior to polarisation. The results of the first and second steady state polarisation measurements on a freshly prepared Ni electrode in 3.0 M NaOH, are presented in Figure 3.2.4.

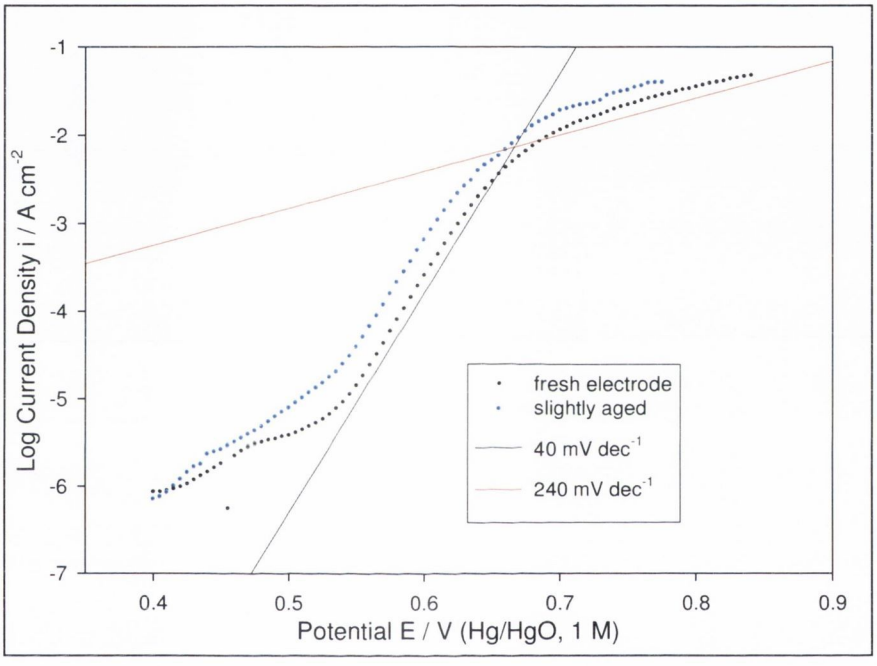


Figure 3.2.4 *IR corrected steady state polarisation curves recorded in the direction of increasing potential on precycled (see text for details) polycrystalline Ni electrodes in 3.0M NaOH solution at 25°C.*

The voltammetric profiles corresponding to the pre-treatment potential cycles of the electrodes from which the data in Figure 3.2.4 were obtained, are presented in Figure 3.2.5. It is important to understand that all the data of Figures 3.2.4 and 3.2.5 were obtained from the same electrode. For the polarisation curve denoted as "fresh electrode", this electrode was undergoing its first ever, anodic polarisation, having been previously aged by a series of cycling experiments similar to those outlined in relation to Figure 3.2.1. Before the steady state polarisation measurement, the electrode was polished, rinsed with Millipore water, placed in 1.0 M NaOH solution and the voltammogram denoted as "fresh electrode" in Figure 3.2.5 was recorded. The

electrode was then quickly transferred to a cell containing 3.0 M NaOH (the same solution as that in which the subsequent polarisation measurement was to be performed), where it was left for several minutes. Finally, the electrode was transferred to the reaction cell, and the steady state measurements were conducted according to the conditions and considerations outlined in Chapter 2.

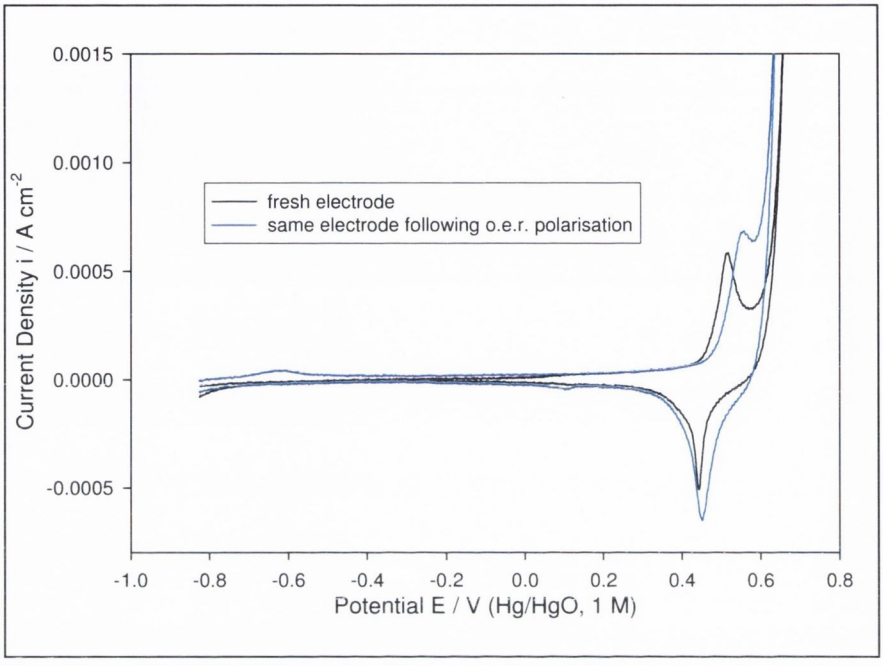


Figure 3.2.5 *Pre-treatment CVs of the electrode surfaces on which the steady state polarisation data of Figure 3.2.4 were obtained. These CVs were recorded in 1.0 M NaOH at 25°C, with a sweep rate of 40 mV s^{-1}.*

The polarisation curve denoted as "slightly aged" in Figure 3.2.4 is the result of the next steady state polarisation experiment on the same electrode. Following, the first polarisation of the previously fresh anode, the electrode potential was allowed to decay for several hours on open circuit, the electrode was then removed, polished, rinsed with Millipore water and dried. The following day, the electrode was again polished, and as before a pre-treatment CV was recorded in 1M NaOH (blue voltammogram in Figure 3.2.5). The electrode was transferred to a 3.0 M NaOH solution, using the previously described procedure, and the "slightly aged" polarisation curve was recorded.

Examining Figure 3.2.4, it is immediately apparent that the "slightly aged" electrode shows a significant enhancement of catalytic activity towards the o.e.r. in 3.0 M NaOH. As an example the recorded current density at a potential of 580 mV increases from 0.08 mA cm^{-2} for the fresh electrode to 0.22 mA cm^{-2} for the slightly aged

electrode – an almost threefold increase. On the other hand, it would appear that the oxygen evolution mechanism remains the same – evidenced by the parallel nature of the Tafel plots. As in Figure 3.2.3, a Tafel slope of ca. 40 mV dec^{-1} is observed at lower current densities. A second well-defined straight line Tafel region, is obvious at higher overpotentials in the polarisation curves of Figure 3.2.4, with a Tafel slope, *b*, of approximately 240 mV dec^{-1}.

The apparent reason behind the enhanced o.e.r. catalytic activity of the "slightly aged" Ni electrode is revealed by the cyclic voltammograms of Figure 3.2.5. Calculating the active charge capacity, it is found that for the fresh electrode Q = 1.03 mC cm^{-2}. This increases by approximately 63% to 1.68 mC cm^{-2} for the "slightly aged" electrode. Thus it would appear that the current density for the o.e.r. at a particular overpotential is proportional to the amount of active nickel oxide material. This effect was previously noted by Gennero De Chialvo et al.[6], who concluded that for nickel oxides of the same type (i.e. α-$Ni(OH)_2$ or β-$Ni(OH)_2$), this effect should be related to increasing surface roughness associated with the increasing amount of active material.

In the case of the voltammograms of Figure 3.2.5, it is clear that not only has the charge capacity of the Ni electrode increased following its first o.e.r. steady state polarisation experiment, but the potentials of both the anodic and cathodic peaks have also increased. Following the logic of the earlier discussion related to the CVs of Figure 3.2.1, it would seem reasonable to suggest that this is indicative of the presence of a higher proportion of the total material in the β – β cycle after the first steady state polarisation measurement at high anodic potentials in 3.0 M NaOH, relative to the situation before this polarisation. If it is true, as was postulated by Lu and Srinivasan[8], that β-NiOOH is the "right type of oxide" for the o.e.r. on Ni anodes, then it would be expected that the increased amount of this material would also lead to enhanced catalytic activity towards the o.e.r. It is therefore probable that the increased o.e.r. current densities of the "slightly aged" Ni electrode of Figure 3.2.4 arise from a combination of physical effects owing to increased available surface area, and electrochemical effects due to an increased concentration of the more catalytically active form of nickel oxide. What is clear, is that the pre-treatment combination of mechanical polishing and a potential cycle in 1.0 M NaOH, is ineffective in restoring the initial fresh surface of the polycrystalline Ni electrode in a reproducible manner,

following the relatively severe anodic polarisation associated with the steady state kinetic measurements.

The difficulty in reproducing the initial surface state of a Ni electrode that had never been subject to polarisation at high oxygen evolution overpotentials, following the application of such a severe potential regime, was not altogether surprising. The possibility was, however, considered, that a sufficiently reproducible electrode surface might be attained following a number of steady state polarisation measurements accompanied by the pre-treatment routine described previously. To this end the results were reviewed, of an early unsuccessful attempt to obtain reproducible steady state polarisation curves on a different polycrystalline Ni electrode in solutions of NaOH ranging from 0.5 – 5.0 M, to examine whether the results of polarisation studies became more consistent, with an increasing number of such experiments. Several of the pre-treatment voltammograms from this set of experiments are depicted in Figure 3.2.6. The corresponding subsequent steady state polarisation curves, all recorded in 1.0 M NaOH, are presented in Figure 3.2.7.

It was found that the oxygen evolution overpotential at a given current density, initially decreased with ageing of the electrode – see the three earliest scans in both Figures 3.2.6 and 3.2.7. Calculating the active charge capacities for earlier voltammograms yields; Q = ~ 3.65 mC cm^{-2} for the previously unpolarised electrode (black CV), Q = ~ 4.00 mC cm^{-2} for the electrode characterised the day after the first o.e.r. polarisation in 1.0 M NaOH (red CV), and Q = ~ 7.89 mC cm^{-2} for the surface characterised after nine polarisation experiments (green CV). It is obvious that the progressive improvement in the o.e.r. catalytic activity of the electrode over the course of the three earlier polarisation measurements in Figure 3.2.7 is related to the increased amount of active nickel oxide material, and therefore presumably increased catalytic surface area. Again this highlights the fact that mechanical polishing alone is ineffective in fully removing the anodic oxide formed on Ni in alkaline media.

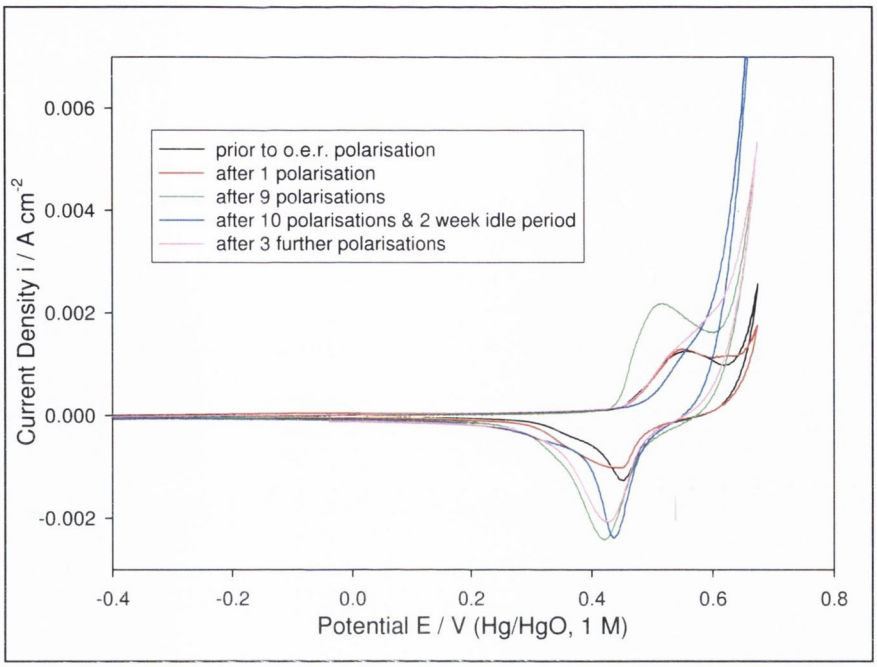


Figure 3.2.6 *Pre-treatment CVs of the electrode surfaces on which the steady state polarisation data of Figure 3.2.7 were obtained. These CVs were recorded in 1.0 M NaOH at 25°C, with a sweep rate of 40 mV s^{-1}.*

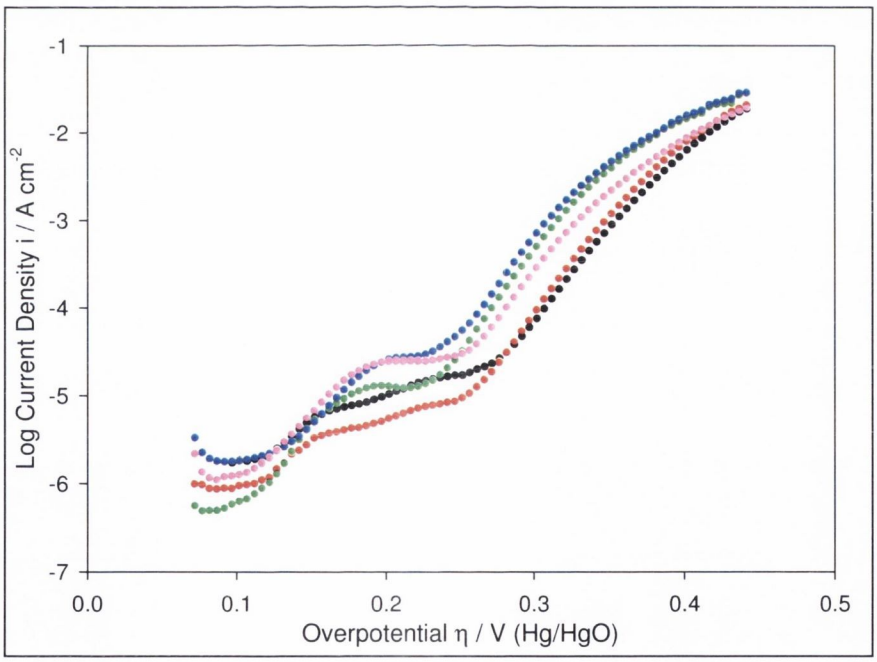


Figure 3.2.7 *IR corrected steady state polarisation curves recorded in the direction of increasing potential on precycled (see text for details) polycrystalline Ni electrodes in 1.0 M NaOH solution at 25°C. Polarisation curves were recorded subsequent to the CVs of the same colour in Figure 3.2.6.*

As is evident from Figure 3.2.6, the voltammetric profile of the active Ni surface altered dramatically after a fortnight of electrochemical inactivity, during which time it was stored in dry conditions at room temperature. The charge capacity, as calculated by the integration of the cathodic peak, was found, in this case, to be Q = ~ 6.61 mC cm^{-2} (blue CV), as compared to Q = ~ 7.89 mC cm^{-2} (green CV) for the previous pre-polarisation CV, recorded two weeks previously. However the post-idle period electrode displayed somewhat greater activity towards the o.e.r., with a current density of 0.73 mA cm^{-2} at η = 302 mV, compared to 0.51 mA cm^{-2} for the electrode characterised by the green CV in Figure 3.2.6, at the same overpotential. This observation would seem to defy the apparent existence of a proportionality between the amount of redox active oxide and the electrocatalytic activity towards the o.e.r., noted for the Ni electrode in relation to the data of Figures 3.2.4, and 3.2.5 and the earlier scans of Figures 3.2.6 and 3.2.7, as well as by other workers[6].

This apparent anomaly would appear to be related to the type of oxide that comprises the active material. It is evident that the peak potential on the cathodic profile has shifted in the positive direction by ~ 20 mV, following the period of storage at ambient conditions. The onset of significant oxidation is also shifted in the positive direction, although clearly, the concept of an anodic peak potential is rather meaningless in the case of the blue CV of Figure 3.2.6. As previously discussed in relation to Figures 3.2.1 and .2, this behaviour suggests that a greater proportion of the active material exists as the anhydrous form, following ageing in the air at room temperature for two weeks. Gradual ageing of α-$Ni(OH)_2$ to β-$Ni(OH)_2$ was envisaged by the Bode scheme[3] and is widely accepted[7]. It is certainly not surprising that dehydration of the oxide should occur when the electrode is stored for some time under dry conditions. The increased activity of this electrode towards the o.e.r., after its idle storage period, despite the smaller amount of active oxide material, again supports the conjecture of Lu and Srinivasan[8] that β-NiOOH (or the oxidation product of β-$Ni(OH)_2$ at any rate) is the optimum type of oxide for the catalysis of the o.e.r. on a Ni electrode. The absence of a transition region of potential, between the oxidation of $Ni(OH)_2$ and the onset of a significant oxygen evolution current, in the CV of the electrode aged in air, again strongly suggests that the o.e.r. is intimately linked to the oxidation of Ni(II) species to species of a higher charge state.

Following three further steady state polarisation experiments on successive days, the activity of the electrode decreased – the current density at η = 302 mV, dropped back

to 0.30 mA cm^{-2} in the case of the latest polarisation curve of the series in Figure 3.2.7. Referring to the corresponding voltammogram in Figure 3.2.8, it can be seen that this fall in catalytic activity, is related to reversion of a proportion of the oxide material to the $\alpha - \gamma$ Bode cycle, as evidenced by a shift of the reduction peak profile back in the cathodic direction. This observation is in line with the prediction of the Bode scheme[3] and some of its more recent variations[4, 11], that upon overcharge at high anodic potentials, β-Ni(III) material will be converted into the γ phase. Therefore, while aging transforms active material from the $\alpha - \gamma$ cycle to the β - β cycle via dehydration of α-$Ni(OH)_2$, overcharging of the β-Ni(III) phase returns some of the oxide to the former cycle.

Although the foregoing discussion is based upon the retrospective analysis of an unsuccessful attempt to collect reproducible reaction order data, rather than on a systematic investigation, it does nonetheless lead to several important qualitative conclusions regarding oxygen evolution at a polycrystalline Ni electrode in aqueous alkaline solution. These might be summarised as follows; (a) it is very difficult to achieve a reproducible catalytic surface for the o.e.r. on Ni by mechanical polishing alone, since this is ineffective in removing all of the anodic oxide formed on the electrode during polarisation, (b) the oxygen evolution catalytic activity of a given Ni electrode is dependent not only on the amount of redox active material but also on the nature of that material – the present work would seem to verify the literature contention[8] that the oxidation product of β-$Ni(OH)_2$ is the optimum electrocatalytic material, (c) in view of the above points, the key to achieving reproducible polarisation measurements would seem to lie in devising a more thorough pre-treatment regime, and (d) it is clear from the polarisation curves of Figures 3.2.4 and 3.2.7, that although the catalytic activity depends on the amount and composition of the active material, the mechanism of the o.e.r., at lower current densities at any rate, remains the same, as is indicated by the observation of a constant Tafel slope of ~ 40 mV dec^{-1} in all cases.

In relation to the latter point, potentially significant exceptions to this "rule" have been noted for well-aged electrodes with relatively large amounts of active material. Consider for example the steady state polarisation curves presented in Figures 3.2.8 and 3.2.9 below. The ~ 60 mV dec^{-1} Tafel slopes in these figures were recorded on successive days (3.0 M first), on a Ni anode that had been pre-treated according to the basic procedure discussed thus far.

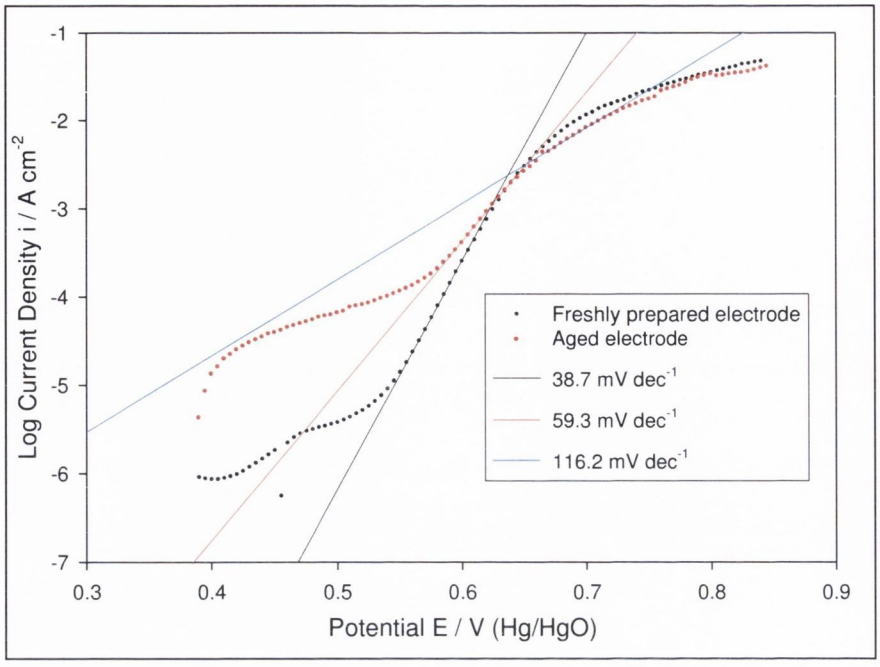


Figure 3.2.8 *IR corrected steady state polarisation curves recorded in the direction of increasing potential on precycled (see text for details) polycrystalline Ni electrodes in 3.0M NaOH solution at 25°C.*

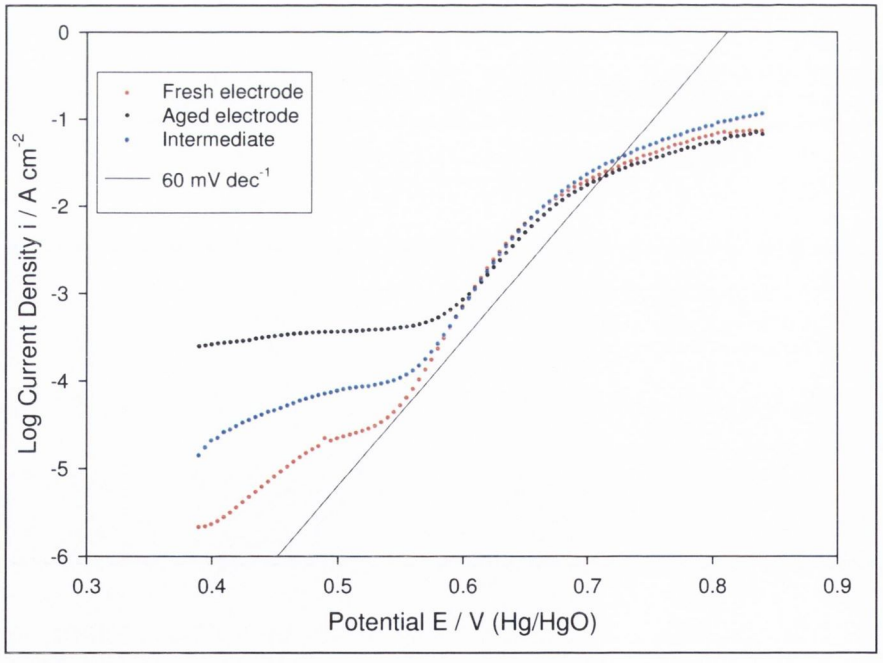


Figure 3.2.9 *IR corrected steady state polarisation curves recorded in the direction of increasing potential on pre-cycled (see text for details) polycrystalline Ni electrodes in 5.0M NaOH solution at 25°C.*

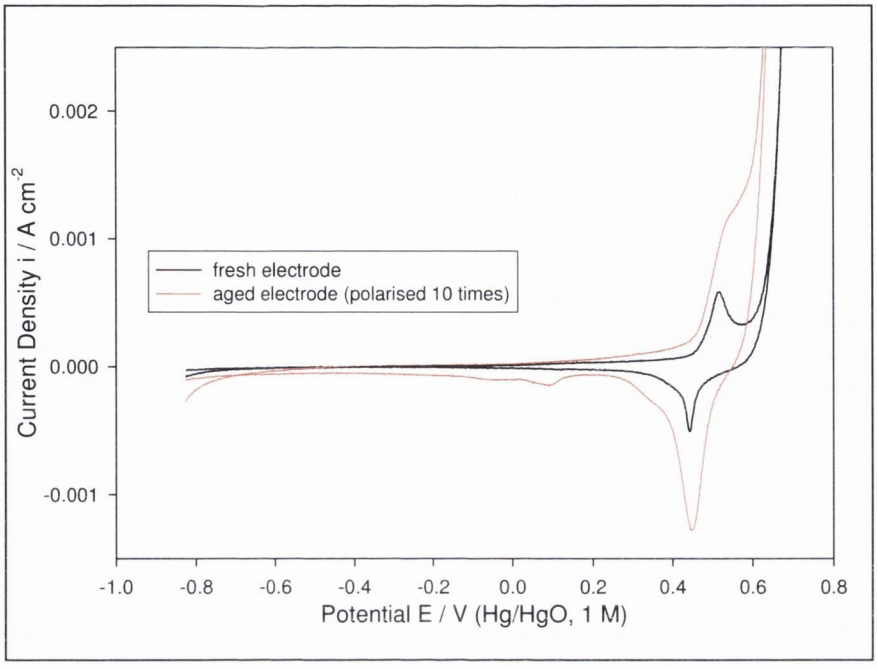


Figure 3.2.10 *Pre-treatment CV of the aged electrode surface on which the 60 mV dec^{-1} steady state polarisation curve of Figure 3.2.8 was obtained. A CV of the same electrode, when freshly prepared (fresh electrode) is included for comparison – this was the pre-treatment CV for the "freshly prepared electrode" of Figure 3.2.8. These CVs were recorded in 1.0 M NaOH at 25°C, sweep rate = 40 mV s^{-1}.*

The pre-treatment cyclic voltammogram for the "aged electrode" polarisation curve of Figure 3.2.8 is presented in Figure 3.2.10. The pre-treatment CV for the aged electrode of Figure 3.2.9, was recorded the following day, and was very similar in form, and yielded a similar active charge capacity to that of Figure 3.2.10. The integrated charge capacity calculated from the "aged electrode" CV of Figure 3.2.10 is Q = ca. 3.64 mC cm^{-2}. This electrode is the same as was characterised earlier in its life cycle by the voltammograms of Figure 3.2.5. Recall that the charge capacity of the freshly prepared electrode (also presented as the black voltammogram in Figure 3.2.10) was Q = 1.03 mC cm^{-2}, which increased to 1.68 mC cm^{-2} following one steady state polarisation in 3.0 M NaOH – see blue CV of Figure 3.2.5.

It is evident from Figures 3.2.8 and 3.2.9 that there are significant differences in the steady state polarisation behaviour of the electrode when freshly prepared and when aged with a large charge capacity. These differences would seem to be fundamentally different to the effects discussed in relation to Figures 3.2.6 and 3.2.7, where enhancements in electrode catalytic activity with ageing were largely attributed to surface area effects. In those cases the Tafel slopes remained largely unaffected by the amount of active material, however for highly charged aged electrodes, like that

characterised in Figure 3.2.10, subsequent polarisation scans (the aged curves in Figures 3.2.8 and 3.2.9) show an increase in the Tafel slope to ~ 60 mV dec^{-1} as opposed to the previously noted slopes of ~ 40 mV dec^{-1} for fresh and somewhat aged electrodes – compare the "fresh", "intermediate" and "aged" plots in Figure 3.2.9. The onset of significant oxygen evolution currents occurs at potentials of the order of 40 – 50 mV more positive in the case of the highly charged aged electrodes relative to the fresh electrodes, but the current densities at these higher onset potentials are significantly larger than those associated with the onset potentials for the fresh electrodes. Consequently these higher Tafel slopes extend over shorter regions of current density (~ 1 decade) and potential (~ 60 mV).

The 3.0 M charged, aged electrode data were more reproducible than that in 5.0 M solution, and indicates that the current densities associated with the 60 mV dec^{-1} Tafel region are greater than those recorded for the fresh electrode at the same overpotentials. In addition to this a second straight line Tafel region with a slope of ~ 116 mV dec^{-1} (approximately 2 × 2.303RT/F at 25°C) is evident at higher overpotentials for the 3.0 M experiment. In this case however the current density recorded at the aged electrode is lower than that of the fresh electrode at the same overpotential. At overpotentials beyond the ~ 120 mV dec^{-1} region, the oxygen evolution currents apparently converge for the aged and fresh electrodes, although the presence of noise in the plot for the former type makes this observation somewhat uncertain. The possible significance of the changing Tafel slope behaviour that accompanies the extreme aging of Ni anodes is discussed in relation to the kinetic mechanistic analyses of these slopes in Section 3.5.

3.2.2 Pre-reduced and Pre-oxidised Ni electrodes

As discussed previously, following early unsuccessful attempts to record meaningful, reproducible reaction order data, it was concluded that more thorough electrode pre-treatment (than merely mechanical polishing) would be required to facilitate the accomplishment of this task. To this end two separate pre-treatment regimes were devised, in the hope that their application would improve the reproducibility of the experimental data. The first of these pre-treatments involved taking a Ni electrode that had been previously subject to several polarisation studies, and therefore was not entirely fresh, polishing it and pre-reducing it at 0 V for a period of 5 minutes in 1.0

M NaOH. Following this the electrode was allowed to rest on open circuit for 10 minutes, before the recording of one cycle of a CV between –0.5 V and 0.675 V at 40 mV dec^{-1}. As before the purpose of the latter cycle was both to characterise the surface electrochemistry of the electrode, and to finish the pre-treatment procedure. A nickel electrode subjected to this pre-treatment regime will henceforth be referred to as a *pre-reduced electrode*. Following the pre-reduction, the electrode was transferred to beaker containing the same solution as that in which the subsequent steady state polarisation experiment was to be conducted. After several minutes it was then transferred to the reaction cell, and the polarisation measurement was commenced. Following the experiment, the potential of the electrode was allowed to decay on open circuit for several hours, it was then removed, polished, rinsed with Millipore water, dried and stored in dry conditions overnight. The same procedure was adopted before and during the polarisation measurement in a different NaOH solution on the following day. All of the steady sate measurements included in reaction order studies were recorded on successive days, in order to minimise possible issues arising from the ageing of the active material upon storage, as discussed previously. It was found that the pre-treatment CVs recorded following the pre-reduction procedure were satisfactorily reproducible (i.e. the calculated charge capacities agreed to within 7%,

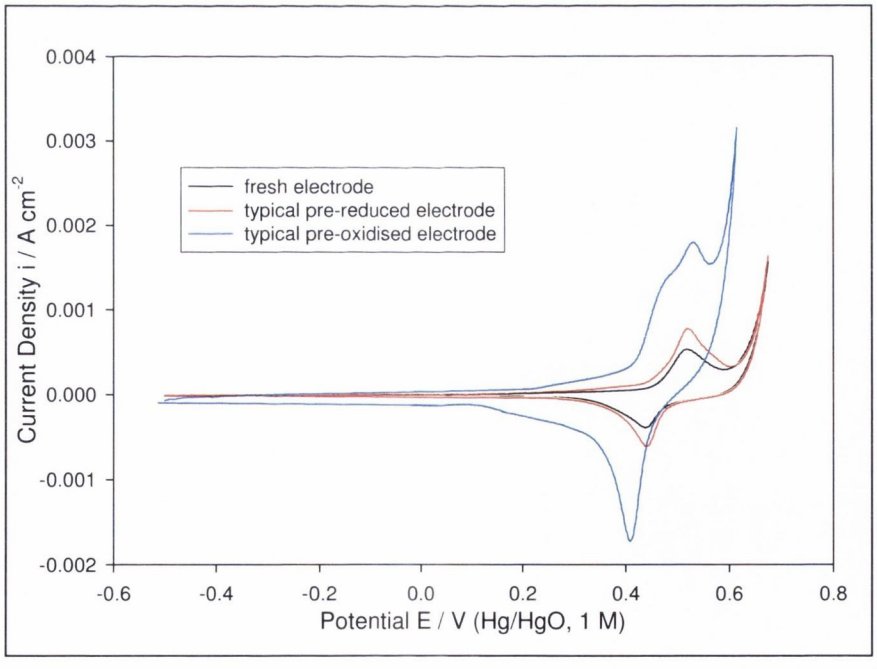


Figure 3.2.11 *Typical pre-treatment CVs of the "pre-reduced" and "pre-oxidised" Ni electrodes used in reaction order studies. Recorded in 1M NaOH at 25°C, with a sweep rate of 40 mV s^{-1}.*

while the profiles were similar in appearance) over the course of a series of 10 polarisation measurements. A typical example of such a CV for the pre-reduced electrode is presented in Figure 3.2.11.

The second form of pre-treatment followed a similar overall steps to the pre-reduction regime described above however instead of pre-reduction at 0 V for 5 minutes the following procedure was adopted. Firstly, the electrode was pre-reduced in 1.0 M NaOH at a cathodic potential of -1.2 V in the hydrogen evolution region for 1 minute. It was elected to perform this extreme reduction, since literature sources[5, 12, 13] have indicated that prior reduction at such low potentials leads to enhanced Ni(II)/ Ni(III) oxidation currents in subsequent voltammetry experiments. The electrode potential was then allowed to decay on open-circuit for 15 minutes. Following this, the electrode was pre-oxidised for 3 minutes at 465 mV (in the potential region of the Ni(II) $\rightarrow$ Ni(III) oxidation reaction) and then for a further 2 minutes at 885 mV. Electrodes that were pre-treated as described immediately above will henceforth be referred to as *pre-oxidised electrodes*. A typical pre-polarisation characterisation voltammogram for one of these pre-oxidised electrodes is depicted in Figure 3.2.11. This pre-treatment was applied to the same Ni electrode that had been used as the "pre-reduced" electrode, after the completion of the entire set of "pre-reduction" experiments.

It was hoped that the pre-oxidisation routine described above, would yield an active oxide layer that wasn't overly thick. Gennero De Chialvo et al.[6] had found that thick oxide films formed by potential cycling on Ni electrodes in 2M NaOH displayed Tafel slopes, in subsequent o.e.r. polarisation studies, that were greater (ca. 80 mV dec^{-1}) than those observed on untreated Ni anodes (ca. 46 mV dec^{-1}). In any case, the active charge capacity as calculated from the CV of the typical pre-oxidised electrode in Figure 3.2.11, Q = ~ 4.99 mC cm^{-2} is comparable with the charge capacity calculated by Gennero De Chialvo et al.[6] for their untreated Ni electrode (Q = 4.4 mC cm^{-2}) and is much smaller than the capacity associated with the higher Tafel slopes (Q = 61.5 mC cm^{-2} – 185 mC cm^{-2}). Since the aim in the present work was to obtain information regarding the kinetics of the o.e.r. at polycrystalline Ni electrodes with only thin anodic oxide layers, as opposed to the behaviour of the reaction on specifically generated thick oxyhydroxide films, it would seem, by comparison with the work of Gennero De Chialvo et al.[6], that the pre-oxidised electrodes produced, as

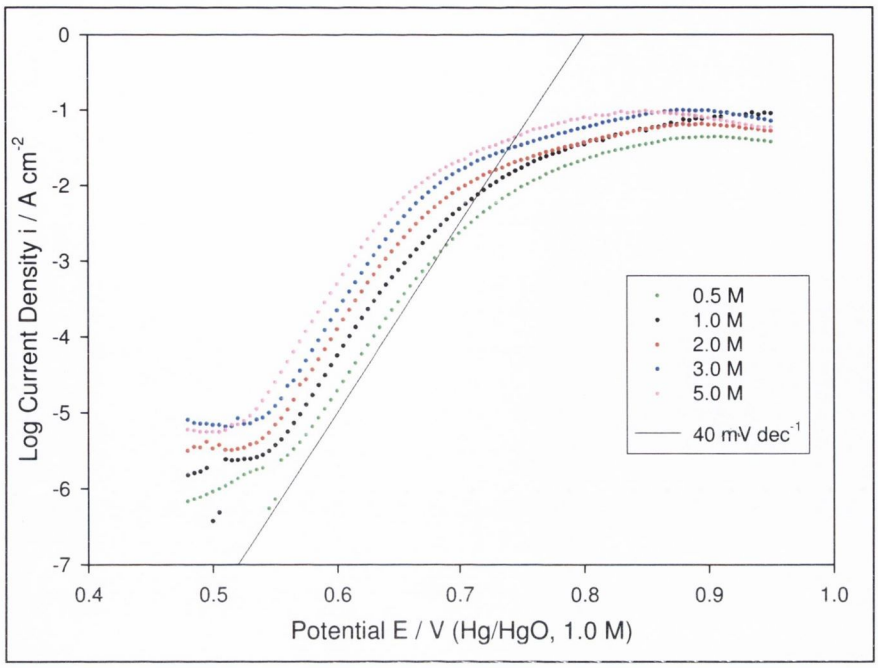


Figure 3.2.12 *IR corrected steady state polarisation curves recorded in the direction of increasing potential on a pre-reduced polycrystalline Ni electrode in NaOH solutions of various concentration at 25°C.*

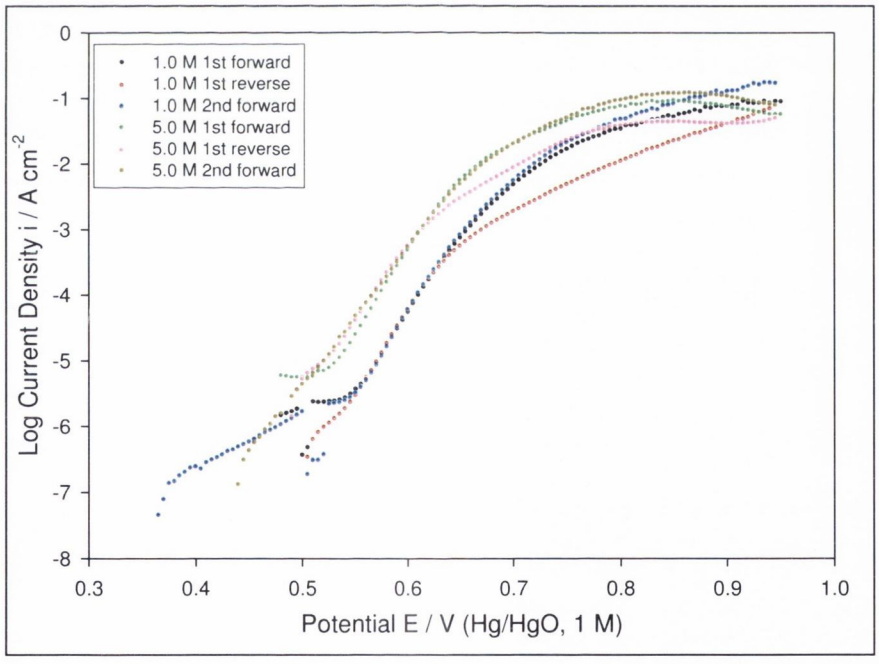


Figure 3.2.13 *IR corrected steady state polarisation curves for 1.0 and 5.0 M NaOH electrolytes, recorded continuously on a pre-reduced polycrystalline Ni electrode, initially in the direction of increasing potential (1st forward), then in the direction of decreasing potential (reverse), and finally in the direction of increasing potential for a second time (2nd forward).*

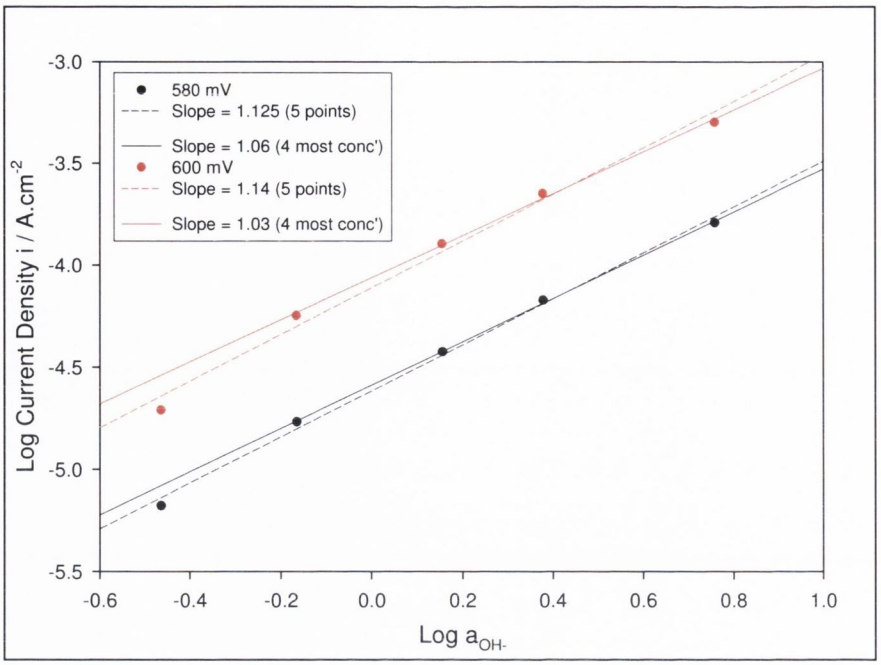


Figure 3.2.14 *Reaction order plots based upon the polarisation curves of Figure 3.2.12 for two values of potential in the 40 mV dec^{-1} Tafel slope region.*

described above, are suitable for this purpose. As a matter of interest the calculated charge capacities for the "fresh" and "typical pre-reduced" electrodes of Figure 3.2.11, were determined respectively as Q = ~1.21 mC cm^{-2}, and Q = ~1.57 mC cm^{-2}. The amount of active oxide material for the pre-oxidised electrode is therefore approximately 3.2 times that of the pre-reduced electrode in 1 M NaOH solution.

A series of IR compensated steady state polarisation curves for pre-reduced electrodes are presented in Figure 3.2.14. A Tafel slope of ~ 40 mV dec^{-1} is obvious at lower current densities across the entire studied range of NaOH solution concentrations, in agreement with the slopes observed in Figures 3.2.3 - .4, and 3.2.7 - .9 for Ni electrodes that hadn't been pre-reduced.

The issue of the appropriate direction for the recording of steady state polarisation curves was highlighted in section 2.1.1. In the present work most steady state experiments have been conducted by progressing, in the anodic direction, for several hundred millivolts, from below the potential at which significant oxygen evolution currents are noted. The direction of the potential step program is then reversed, facilitating the monitoring of the o.e.r. from potentials at which it occurs at significant steady state current density, down to the potential at which the net current becomes cathodic. The sweep direction then reverts to the direction of increasing potential. This approach enables the characterisation of the o.e.r. in both the situation where the

fractional coverage θ of reaction intermediates is expected to increase from low values towards unity (direction of increasing potential), and the opposite situation (direction of decreasing potential). Comparison of the 1st and 2nd forward scans also allows information to be obtained on the stability of the system with time. Reaction order data have generally been extracted from the first sweep in the direction of increasing potential, since the initial electrode surface condition, which has been manipulated by pre-treatment to be as similar as possible for all NaOH solutions, is likely to be progressively altered depending on OH^- concentration, as the experiment proceeds. Therefore reaction order data taken early in the course of the experiment are less likely to be affected by artefacts arising from the different rates of surface processes (such as oxide growth and possibly dissolution) occurring in hydroxide solutions of different concentration.

The bi-directional steady state polarisation curves as discussed directly above, are presented for pre-reduced Ni electrodes in both 1.0 M and 5.0 M NaOH solutions in Figure 3.2.13. The most notable feature of these curves is the severe hysterisis between the forward direction and reverse direction scans for both electrolyte concentrations at higher overpotentials. Indeed this hysterisis is also observed in the polarisation curves for the other hydroxide ion concentrations. Very few of the steady state polarisation measurements on oxygen evolution that have been reported in the literature have been conducted in both the directions of increasing and decreasing potential, and to the best of our knowledge, there has been no discussion on the phenomenon of hysterisis observed in the results of such measurements. One of the few groups of workers who have presented data recorded in both directions is Kobussen et al., who noted hysterisis at higher overpotentials in studies on the o.e.r. at both $La_{0.5}Ba_{0.5}CoO_3$[14] and polycrystalline Co[15] electrodes in alkaline media. In the former case the hysterisis was attributed to possible parasitical corrosion processes, while in the latter, the effect was noted without further comment, beyond a contention (apparently supported by the disagreement between Tafel slopes obtained by steady state polarisation and impedance methods in this potential region) that the rate-determining processes at these high overpotentials might not be "Tafel-like in appearance". Certainly it would seem logical that more credence be attributed in mechanistic analyses, to polarisation data in regions of potential, where the forward and reverse scans largely coincide, such as the 40 mV dec^{-1}, lower overpotential sectors in the plots of Figure 3.2.13.

Aside from the hysterisis, the data presented in Figure 3.2.13 warrants several further comments. Firstly, although apparent straight-line Tafel regions with slopes of ca. 120 mV dec^{-1}, are observed in the reverse sweeps, at current densities immediately above the 40 mV dec^{-1} regions, for both the 1.0 M and 5.0 M cases of Figure 3.2.13, the slopes at similar overpotentials in the reverse scans for the solutions of other concentrations, tend to vary between approximately 120 and 180 mV dec^{-1}. Hence the extraction of kinetic parameters from this region of overpotential in the reverse direction scans might be a dubious enterprise, and therefore the matter is not pursued here. Secondly, it is noteworthy, that the Tafel slope in the lower overpotential region, of the 5.0 M curve, increases from ~ 40 mV dec^{-1} on the first forward sweep to ~ 46 mV dec^{-1} on the second sweep in the same direction - an effect presumably related to the greater degree of surface oxidation that is likely to prevail at the later time of the second forward scan.

Reaction order plots with respect to OH^- activity, based upon the polarisation data of Figure 3.2.12 in the low overpotential 40 mV dec^{-1} region, are presented in Figure 3.2.14. It is obvious that the most satisfactory linearity is achieved by neglecting the data obtained from the most dilute solution (0.5 M NaOH) – if this approach is admitted then, $m_{OH^-} = 1.06$ at $E = 580$ mV and $m_{OH^-} = 1.03$ at $E = 600$ mV. In general it can be concluded that, $m_{OH^-} \approx 1$, in the 40 mV dec^{-1} Tafel slope region for the pre-reduced Ni electrode.

Steady state polarisation curves for the pre-oxidised Ni electrodes, as described above, are presented in Figure 3.2.15. Again it is clear that the data in the lower overpotential region are characterised by Tafel slopes of approximately 40 mV dec^{-1}, although it is to be admitted that in case of the 5.0 M electrolyte, the 40 mV dec^{-1} slope is only truly observed over a limited potential range from ~ 525 – 555 V, with a slope of approximately 30 mV dec^{-1}, noted at lower current densities, altering to ca. 50 mV dec^{-1} directly above to 40 mV dec^{-1} region.

Full bi-directional steady state polarisation curves for the 1.0 and 5.0 M NaOH solutions are depicted in Figures 3.2.16 and 3.2.17 respectively. Again hysterisis is evident at higher overpotentials, between the sweeps recorded in the direction of increasing potential, and those recorded in the opposite direction. Also of note is the progressive appearance over the reverse scan, and especially during the second forward scan, of an unusual "shoulder" in the lower overpotential region. This feature

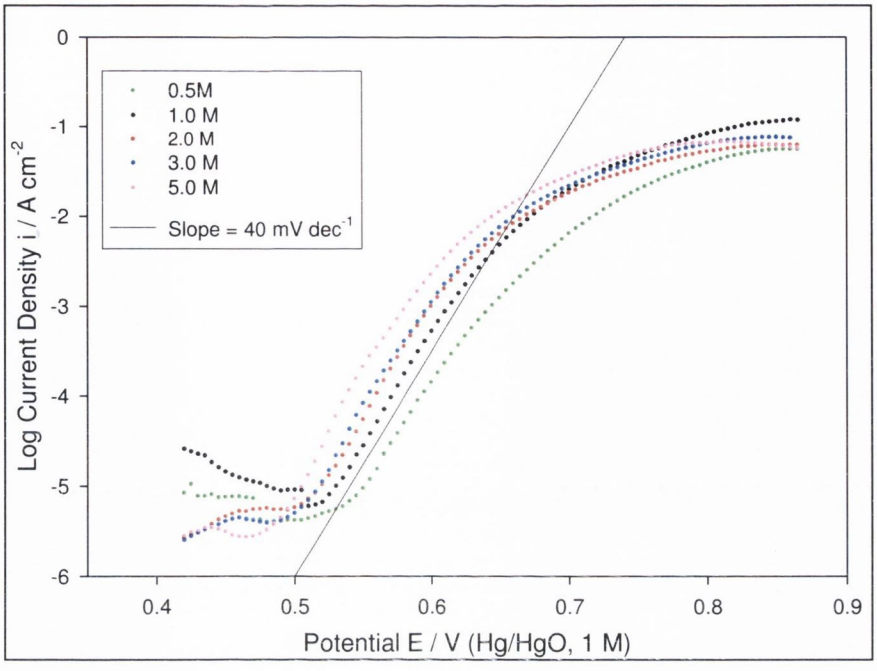


Figure 3.2.15 *IR corrected steady state polarisation curves recorded in the direction of increasing potential on a pre-oxidised polycrystalline Ni electrode in NaOH solutions of various concentration at 25°C.*

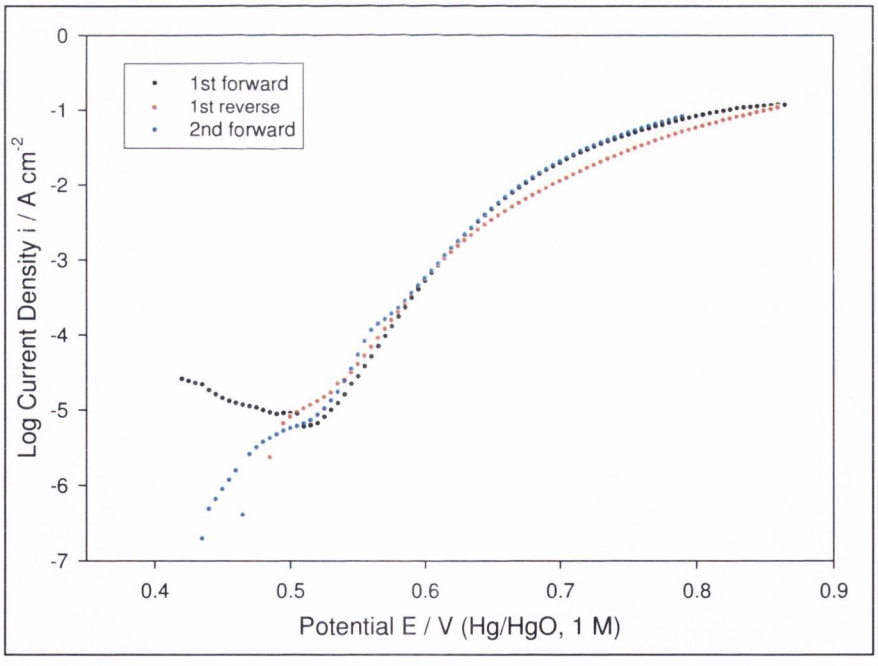


Figure 3.2.16 *Bi-directional IR corrected steady state polarisation curve recorded continuously on a pre-oxidised polycrystalline Ni electrode in 1M NaOH, initially in the direction of increasing potential, at 25°C.*

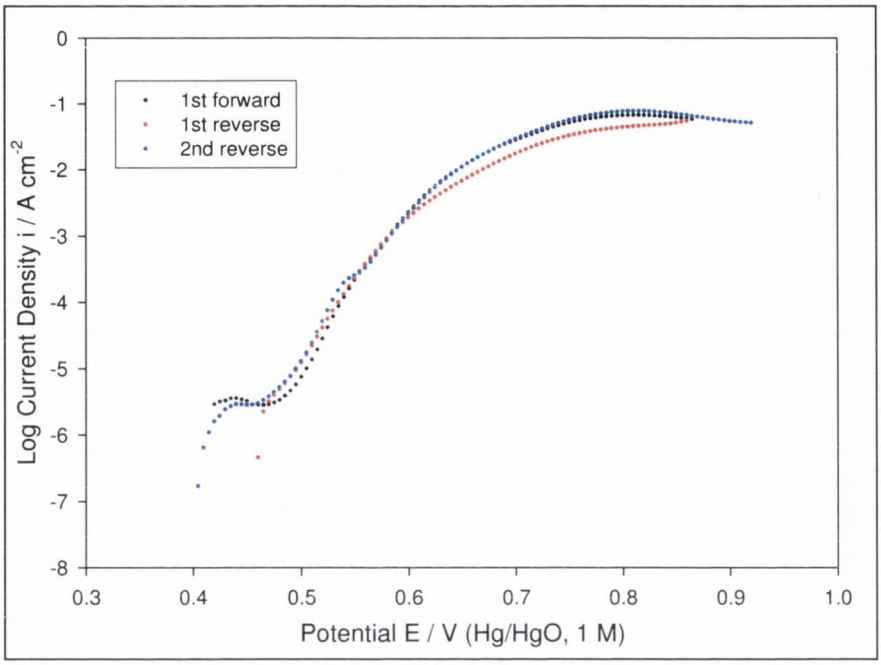


Figure 3.2.17 *Bi-directional IR corrected steady state polarisation curve recorded continuously on a pre-oxidised polycrystalline Ni electrode in 5M NaOH, initially in the direction of increasing potential, at 25°C.*

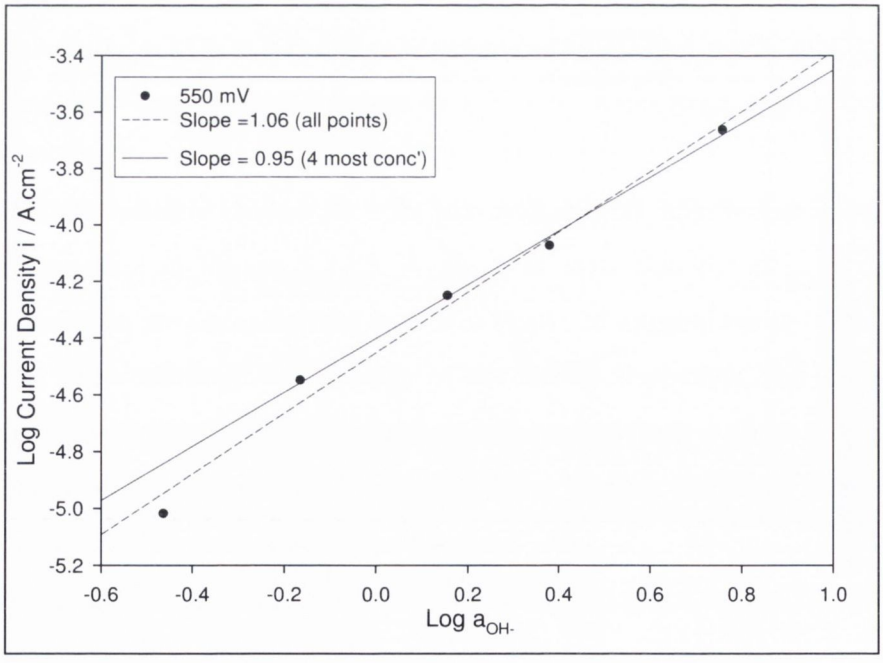


Figure 3.2.18 *Reaction order plots based upon the polarisation curves of Figure 3.2.15 at a potential of 550 mV in the 40 mV dec^{-1} Tafel slope region.*

was also noted in the reverse and second forward polarisation curves for the other concentrations of NaOH solution studied. It must be said that it is unlike anything we have encountered in the literature of oxygen evolution on various types of anode. A noteworthy point is that the second forward sweeps converge with the first sweeps in the same direction, at the upper observed limits of the constant 40 mV dec^{-1} slopes of latter sweeps. Thus for the 1.0 M polarisation curves of Figure 3.2.16, this convergence occurs at ~ 595 mV, while it occurs at ~ 560 mV for the 5.0 M curves of Figure 3.2.15 – this corresponds, as previously noted, to the upper extreme of the rather limited 40 mV dec^{-1} Tafel slope region noted in the first positive scan for the latter case.

Therefore it appears reasonable to associate the anomalous "shoulder" behaviour, with a small enhancement of the rate of the o.e.r., proceeding under the conditions that gave rise to a characteristic Tafel slope of 40 mV dec^{-1} and an associated reaction order of approximately unity (see Figure 3.2.18) during the first forward scan on the freshly pre-oxidised electrode. It would appear that further oxidation of the active surface at higher overpotentials during the first forward and reverse scans, and the subsequent desorption of the reaction intermediates as the current density was reduced to negligible values on that reverse scan, has lead to the existence of a slightly enhanced catalytic surface when adsorption of the o.e.r. intermediates re-commences on the second forward sweep. Tafel slopes of $2.303 \times 2RT/3F$ (~ 40 mV dec^{-1} at 25°C) are generally associated (see for e.g. Table 1.5.1) with low coverage Langmuir adsorption conditions. Thus it seems that the slight catalytic enhancement offered by the "further oxidised" surface prevails only under conditions of low coverage of reaction intermediates. This situation contrasts with cases (e.g. recall Figure 3.2.4) where enhancement of catalytic activity is attributed to increased surface area effects. In the latter case the entire polarisation curve (up to the attainment, at any rate, of limiting currents associated with, for example, mass transport) tends to be effectively transposed upwards on the current density scale. The observed enhancement of just one region of a polarisation curve, as depicted in Figures 3.2.16 and 3.2.17, would seem to be quite a novel electrocatalytic observation.

A reaction order plot constructed from the data of Figure 3.2.15 at 550 mV, in the ~ 40 mV dec^{-1} Tafel region is presented in Figure 3.2.18. Again, the best linearity is achieved by neglecting the data point of the lowest concentration (0.5 M) solution. In any case, regardless of whether this point is included in the reaction order plot or not,

the overall conclusion from Figure 3.2.18 is that the observed value of m_{OH^-} is, as in the case of the pre-reduced electrodes, of the order of unity.

A comparison of the first steady state polarisation curves in the direction of increasing potential in 1.0 M NaOH solutions, for the "fresh", "pre-reduced" and "pre-oxidised" electrodes, as characterised by the voltammograms of Figure 3.2.11, is presented in Figure 3.2.19.

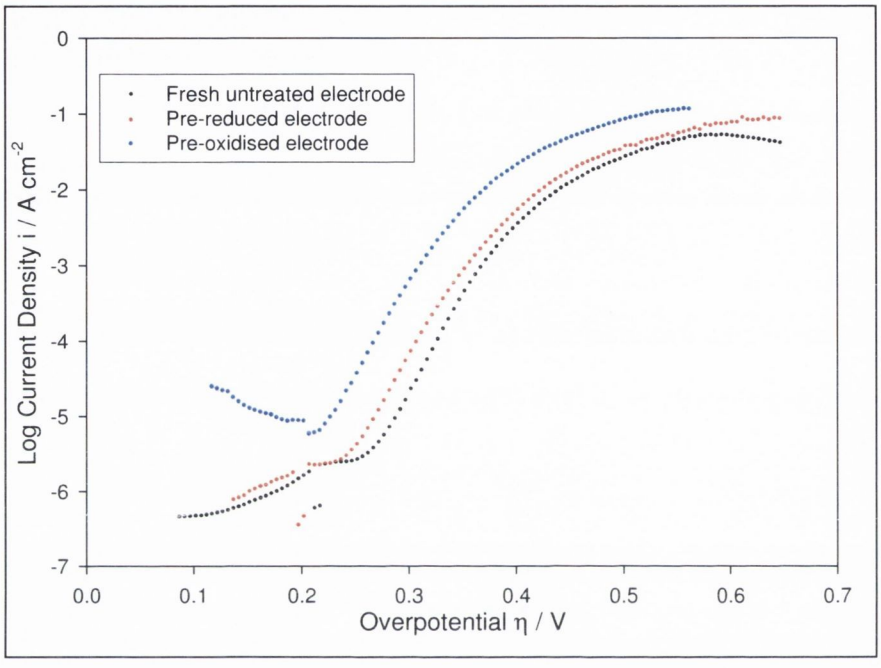


Figure 3.2.19 *Comparison of the 1st steady state polarisation plots in the forward direction in 1.0 M NaOH, for the three electrodes characterised by cyclic voltammetry in Figure 3.2.11.*

Evidently, the catalytic activity of the polycrystalline Ni anode towards the o.e.r. depends on the amount of redox active oxide material. The current density at η = 302 mV, increases from 0.0235 mA cm^{-2} for the fresh electrode, to 0.0765 mA cm^{-2} for the pre-reduced electrode, and to 0.686 mA cm^{-2} for the pre-oxidised electrode. Recall, from earlier, that the active charge capacities associated with the fresh electrode, and typical pre-reduced and pre-oxidised electrodes of Figure 3.2.11, were respectively; Q_{fresh} = ~ 1.21 mC cm^{-2}, $Q_{pre\text{-}red}$ = ~ 1.57 mC cm^{-2}, and $Q_{pre\text{-}ox}$ = ~ 4.99 mC cm^{-2}. No attempt is made here to correlate values of active charge capacity determined from cyclic voltammetry, with catalytic activity towards the o.e.r., as in the work of Gennero De Chialvo et al.[6], however their conclusion, that increased surface roughness is the main factor behind the increasing activity observed with increasing Q, would initially seem to be valid with regard to the present work – see, however section 5.5 for an alternative view.

Of greater interest here, is the fact that, despite the variation in catalytic activity with different pre-treatments, the steady state polarisation curves of Figure 3.2.19 are essentially parallel, especially in the kinetically significant straight-line Tafel slope region at lower overpotentials. This implies that the mechanism of oxygen evolution remains constant for relatively thin anodic oxide films (or equivalently relatively small values of active charge capacities) formed on polycrystalline Ni electrodes in alkaline media. Therefore, it would appear to be valid, to apply the kinetic data recorded for the pre-reduced and pre-oxidised Ni electrodes to the determination of what might be called the "intrinsic" reaction pathway for the o.e.r. on polycrystalline Ni electrodes, under limitingly small oxide film coverage – it is of course recognised that oxygen evolution occurs on oxide surfaces and that the concept of oxygen evolution on an oxide free Ni surface is impossible.

With regard to kinetic parameters, the principal result, obtained independently on Ni electrodes subjected to different pre-treatment regimes, was the observation of a Tafel slope of 40 mV dec^{-1} and an associated reaction order of approximately unity, at lower overpotentials. In the light of results for Co and Fe electrodes, that will be presented in sections 3.3 and 3.4 respectively, the observation of Tafel slopes of ~ 60 mV dec^{-1} (at lower overpotentials), and 120 mV dec^{-1} (at higher overpotentials) for a well charged, aged Ni electrode (recall Figures 3.2.8 and 3.2.9) is also noted at this point. A review of all our experimental results, conducted for the compilation of the present work, has also indicated that the presence of a well-defined Tafel slope of ca. 240 mV dec^{-1} is a common feature at higher overpotentials, in the steady state polarisation curves of relatively fresh Ni electrodes. Such Tafel slopes were noted in 3.0 M NaOH in Figure 3.2.4. A steady-state polarisation measurement on the same Ni electrode in 1.0 M NaOH, also reveals the presence of this apparent Tafel region – see Figure 3.2.20.

Finally, an experiment was devised, whereby cyclic voltammograms of the surface electrochemistry of the Ni electrode could be recorded, without an interruption, following extended polarisation at a potential associated with significant oxygen evolution. It was hoped that this measurement would yield further information about the state of the nickel electrode in the immediate aftermath of oxygen evolution, without giving the system an opportunity to relax on open circuit. The results of this experiment are presented in Figure 3.2.21. An aged Ni electrode was initially subject to two cyclic voltammetry sweeps at 40 mV s^{-1} in 1M NaOH, in order to characterise

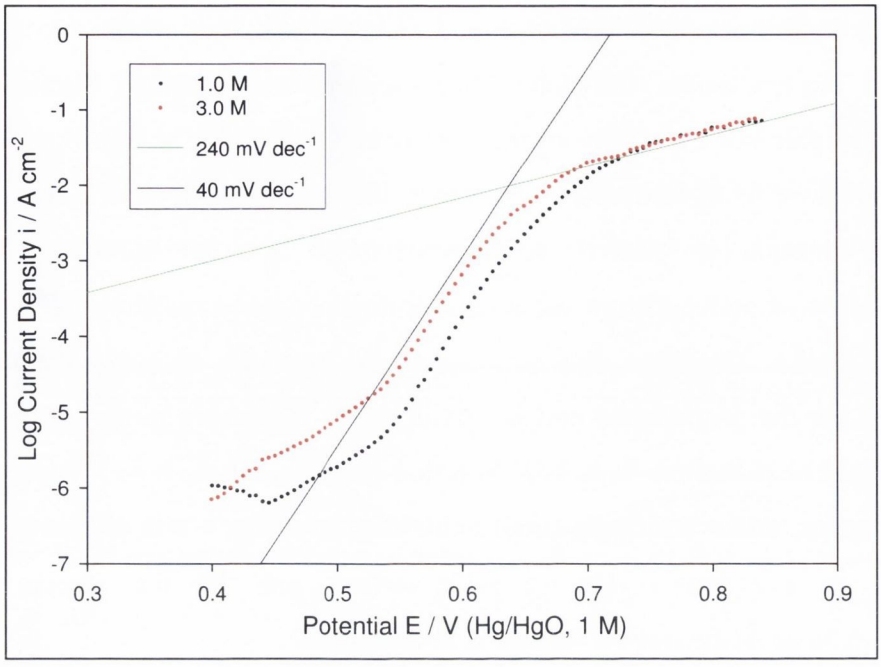


Figure 3.2.20 *IR corrected steady state polarisation curves recorded in the direction of increasing potential on a polycrystalline Ni electrode in both 1.0 M and 3.0 M NaOH solutions at 25°C. The 3.0 M scan was conducted on the electrode characterised by the blue CV of Figure 3.2.5, with the 1.0 M scan recorded on the electrode characterised by a very similar CV.*

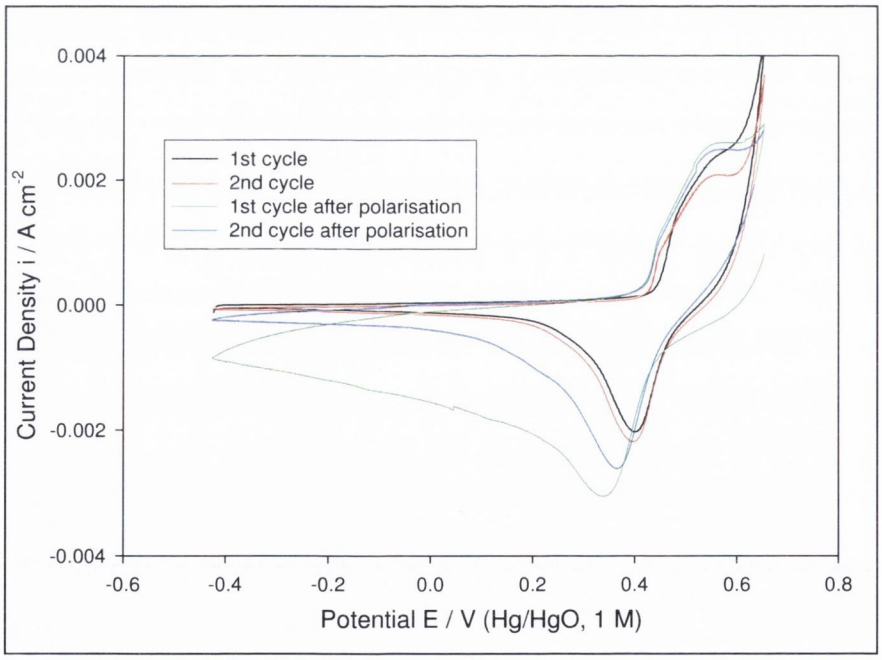


Figure 3.2.21 *Cyclic voltammograms characterising a polycrystalline Ni electrode surface, both prior to, and following potentiostatic polarisation at 655 mV for 10 hours. The system was not allowed to relax on open circuit following the polarisation – i.e. the post polarisation CVs were recorded directly after the end of the 10 hour period, commencing in the cathodic direction. All CVs were recorded at 40 mV s^{-1} in 1.0 M NaOH at 25°C.*

the surface electrochemistry before polarisation. The electrode was then removed from solution, polished, rinsed with Millipore water, and returned to the 1.0 M NaOH solution, in which it was then polarised at 655 mV for 10 hours. Following the end of this period of polarisation, two further voltammetric sweeps were recorded at $40mVs^{-1}$ as indicated in Figure 3.2.21. Overall it must be commented that the results of this experiment are rather disappointing, as they yield little further information regarding the link between the oxygen evolution reaction and the nature of the catalytic surface on which it occurs. The uncharacteristically large reduction currents observed on the first, and to a lesser extent on the second, cathodic sweep, at potentials below the Ni(III) → Ni(II) reduction peak potential, are evidently linked to the forced lowering of the potential of the highly charged Ni electrode, to these potentials, on a shorter timescale than is characteristic of this process.

Despite the distorted nature of the post polarisation CVs, one might usefully make the following observations on the data of Figure 3.2.21. The electro-reduction peak potential for the Ni(III) → Ni(II) redox transition seems to be shifted in the negative direction following the 10 hours of polarisation at 655 mV. The sharply increasing cathodic current edge (i.e. current going towards more negative values) in the potential range of 450 – 380 mV, in the less "distorted" second post polarisation cycle is coincident with the same feature in the first post polarisation cycle. This would indicate that the shift in peak potential, towards more negative values following polarisation, as noted above, is a genuine phenomenon and not an artefact. As discussed earlier in this chapter, such a negative shift in peak potential is associated with a relative transition of active oxide material from the β-β Barnard cycle to the α-γ cycle.

This hypothesis is supported by two further observations pertaining to the experiment outlined in Figure 3.2.21. Performing calculations of the active charge capacities of the second pre-polarisation CV, and the first cycle following polarisation, by integrating the oxidation charge profile of these scans between 300 mV and the upper potential at which the current becomes cathodic on the reverse scan, yields Q = ~ 7.59 mC cm^{-2} for the former case, and Q = ~ 9.36 mC cm^{-2} for the latter. It is necessary to integrate the oxidation peaks in this case, owing to the distorted reduction peaks for the post-polarisation CVs. In general this approach is less satisfactory since oxygen evolution affects the calculated charge capacities at the more anodic end of the Ni(II) → Ni (III) oxidation profile. However, for the purpose of the present qualitative

discussion integration of the oxidation peak is satisfactory. In any case, referring to the charge capacity values quoted above, it is evident that the amount of redox active oxide has increased during the course of the 10 hours of polarisation at 655 mV. Yet it is apparent from the rising edges of the o.e.r. currents at the positive extrema of the CVs of Figure 3.2.21, that, despite its lower calculated charge capacity, the second pre-polarisation CV displays a significantly greater activity towards oxygen evolution, relative to the post polarisation CV.

Further to this observation, the following points were noted regarding the behaviour of the oxygen evolution current density during the 10 hours of polarisation at 655 mV. Following the initial stepping of the potential from its open circuit value to 655 mV, it took approximately 450 s, before a sufficiently stable (to be identified with a kinetically significant) current density of 4.53 mA cm^{-2} was observed. Over the course of the 10 hours of polarisation, the recorded current density slowly decayed to ca. 0.8 mA cm^{-2}. This observation supports the conclusion from the voltammograms of Figure 3.2.21, that the nickel anode has become less catalytically active with respect to the o.e.r. following an extended polarisation at high overpotentials. Such a conclusion was also reached by Lu and Srinivasan[8] in their classic study on the effect of the oxyhydroxide film on oxygen evolution at Ni in 1N KOH, as was reviewed in section 1.5.4. These authors attributed the decrease in catalytic activity with time to the generation of Ni^{4+} ions on the surface of the oxide film, which provide "an inert site for oxygen evolution". In terms of the observations outlined above, from the voltammograms of Figure 3.2.21, and current knowledge of the redox transitions of nickel (oxy)hydroxides as reviewed in section 1.4.1, it would appear that the increasing amount of inert surface sites with polarization, arises from the conversion of β-Ni(III) material to the γ phase. Such a transition is, of course, envisaged upon overcharge of β-NiOOH by the Bode scheme[3] and its more recent variations[4, 11] – extended polarisation at potentials associated with significant o.e.r. currents are precisely the conditions at which this overcharge is likely to occur. The active material is transferred from the β-β cycle to the α-γ cycle by this overcharge, hence rationalising the negative shift in reduction peak potential, and the decreased activity towards the o.e.r. as displayed by the post-polarisation CVs of Figure 3.2.21 relative to their pre-polarisation counterparts.

3.3 Cobalt: Steady State Polarisation and Voltammetry Results

3.3.1 Bright Non-pre-treated Co electrodes

In contrast to the situation outlined for Ni anodes in section 3.2, and Fe anodes in section 3.4, it proved to be possible to record steady state polarisation curves with satisfactory reproducibility, for the o.e.r. on Co electrodes that were not subjected to any pre-treatment, beyond vigorous mechanical polishing. That is to say, where a polarisation measurement, was performed on a Co anode in a solution of a given concentration (1.0 M NaOH was usually chosen as this "reference solution"), and subsequently repeated on consecutive days (four or five days, one measurement daily) at different concentrations before re-recording in the "reference solution", no significant differences were noted in the results of the earlier and later scans in the "reference solution". Notwithstanding this, ageing effects (probably due to both continued polarisation experiments and ageing in air) are apparent on Co electrodes over longer timescales, as will be discussed below. However, it appears that of the three metals investigated in this work, polishing (as described in chapter 2) is most effective in returning the electrode surface, post polarisation, to a state similar to its pre-polarisation condition, in the case of Co.

The first steady state polarisation scans in the forward direction, for a Co electrode in NaOH solutions of various concentrations are presented in Figure 3.3.1. Beyond mechanical polishing, and rinsing in copious Millipore water, no further pre-treatment was carried out on the electrode, before recording this data. The complete bi-directional steady state polarisation scans for this Co electrode in 1.0 M and 3.0 M NaOH solutions, are depicted respectively, in Figures 3.3.2 and 3.3.3. While a relatively small degree of hysterisis between the forward and reverse direction sweeps is evident for the electrode in 1.0 M NaOH solution, a particularly extreme hysterisis effect is evident for the 5.0 M case. The amount of hysterisis between forward and reverse scan directions is evidently a function of the maximum current density achieved on the former sweep, as indicated by the data of Figure 3.3.4. In this figure, two polarisation measurements on the same Co electrode in 1.0 M NaOH are compared – the experimental conditions in each case were identical with the exception of the upper potential. For one experiment (a), this upper reversal potential was set at an overpotential of 417 mV (corresponding to a steady-state current density of 13.6mA cm^{-2}), while in the other case (b) the forward scan was allowed to continue

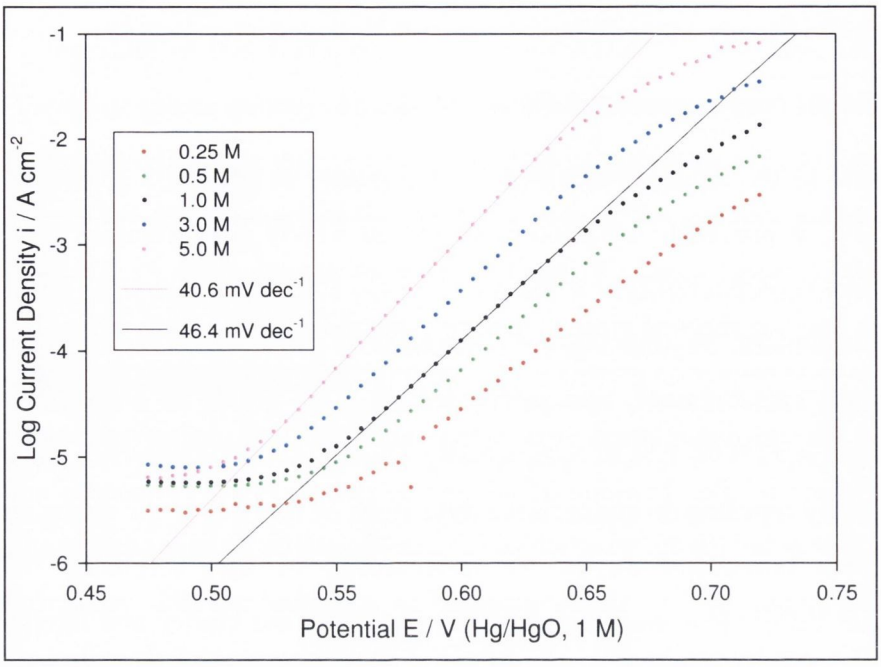


Figure 3.3.1 *IR corrected steady state polarisation curves recorded in the direction of increasing potential on a Co electrode (no electrochemical pre-treatment) in NaOH solutions of various concentration at 25°C. In this case the measurement in the most concentrated solution was performed first, with the others following in order of decreasing concentration on consecutive days.*

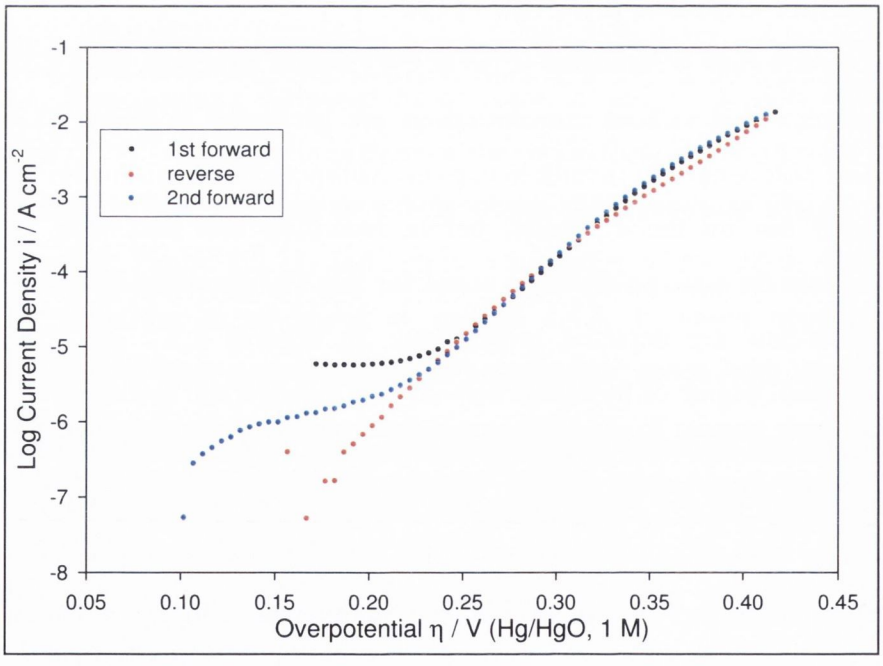


Figure 3.3.2 *Bi-directional IR corrected steady state polarisation curve recorded continuously on a Co electrode (no electrochemical pre-treatment) in 1M NaOH, initially in the direction of increasing potential, at 25°C.*

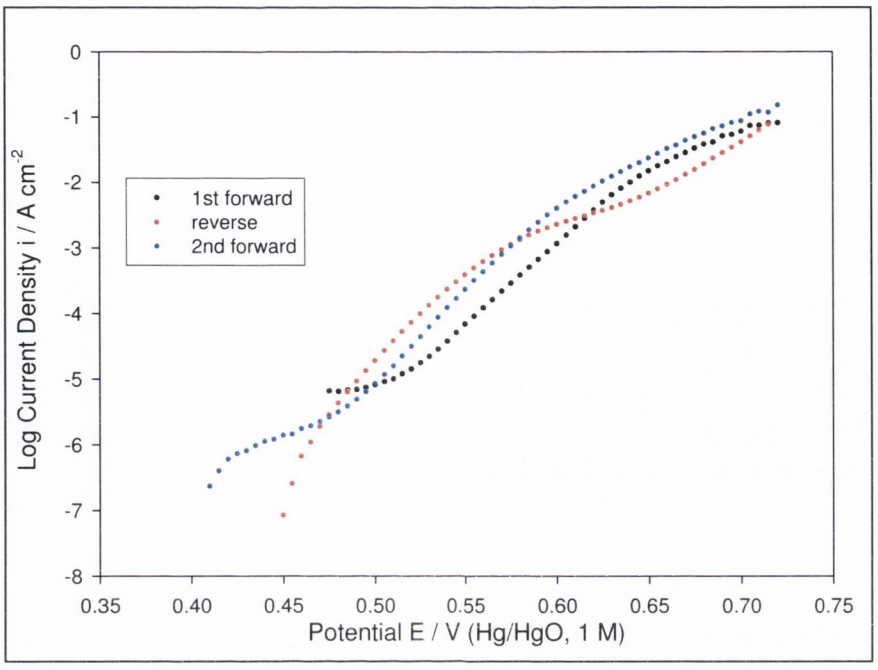


Figure 3.3.3 *Bi-directional IR corrected steady state polarisation curve recorded continuously on a Co electrode (no electrochemical pre-treatment) in 5M NaOH, initially in the direction of increasing potential, at 25°C.*

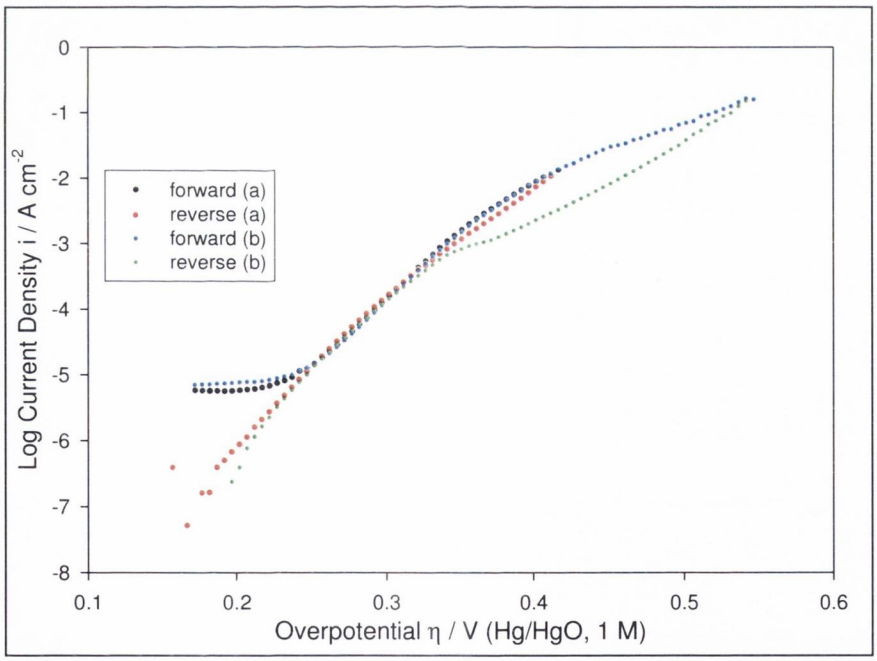


Figure 3.3.4 *Comparison of two bi-directional, IR corrected, steady state polarisation curves recorded on a Co electrodes (no electrochemical pre-treatment) in 1M NaOH, initially in the direction of increasing potential, at 25°C. The reversal overpotential for experiment (a) was 417 mV, compared to 547 mV for experiment (b). Otherwise all conditions were identical.*

130 mV further in the anodic direction to an overpotential of 547 mV (current density of 161.7 mA cm^{-2}). Clearly the hysterisis effect is much more pronounced in the experiment with the higher reversal potential. For example, in experiment (a), the current density at η = 382 mV falls by about 25 % from 4.76 mA cm^{-2} on the forward scan, to 3.61 mA cm^{-2} on the reverse scan. For the same overpotential in experiment (b), the current density decreases by ca. 70%, from 4.70 mA cm^{-2} on the forward sweep to 1.43 mA cm^{-2}. This observation would suggest that slopes derived from the reverse sweep at higher overpotentials, are not true Tafel slopes, owing to their dependence on the upper polarisation potential, and therefore cannot be admitted in kinetic analyses.

Even in the lower overpotential region, the coincidence between the forward and reverse scans is never as strong as is evident in the case of Ni – compare Figure 3.3.2 with Figure 3.2.13. The slopes for each direction are relatively similar between potentials of 560 - ~625 mV (overpotentials of 257 – 322 mV) for the 1.0 M data of Figure 3.3.2, which roughly corresponds to the potential region of the 46.4 mV dec^{-1} outlined for the forward scan in Figure 3.3.1. On closer examination it is evident that the relatively poor retracing of even the lower overpotential steady state polarisation data, upon reversal of the sweep direction, arises because the reverse scan never really exhibits true straight line behaviour. There is slight curvature in the trace, even at the potentials where the closest coincidence between the sweeps in opposite directions is observed. Very similar re-tracing behaviour has been noted by Willems et al.[15] in one of the few literature reports devoted principally to the study of oxygen evolution on polycrystalline Co electrodes in alkaline media. By contrast to this there is excellent coincidence noted between the first and second forward sweeps in Figure 3.3.2. All of this would suggest that kinetic parameters, such as Tafel slopes and reaction orders, are best extracted from the polarisation curves in the direction of increasing potential.

The hysterisis issue is even greater in the case of the 5.0 M polarisation data of Figure 3.3.3. In this case, not only is there severe hysterisis between the first forward and reverse scans at all potentials, but furthermore, the activity towards oxygen evolution is greatly enhanced in the second forward scan relative to the earlier scan in this direction. It would appear that this effect is intrinsically related to the concentration of the NaOH solution, and is not merely a result of the greater current densities achieved

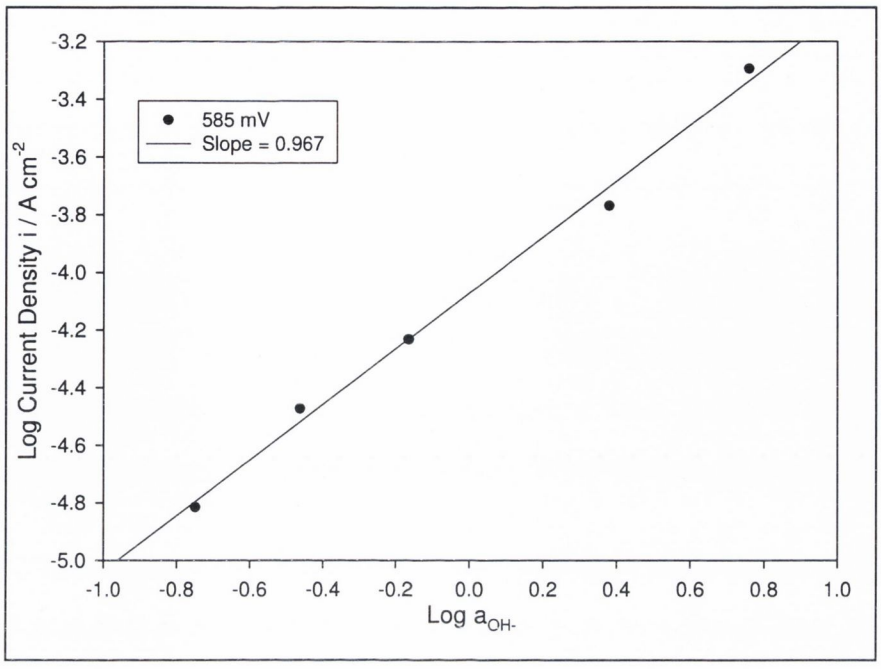


Figure 3.3.5 *Reaction order plot based upon the polarisation curves of Figure 3.3.1 at a potential of 580 mV.*

at a given overpotential in 5.0 M solution, as opposed to 1.0 M solution. While the current density of 80.9 mA cm^{-2} observed at the reversal potential of 720 mV for the 5.0 M data of Figure 3.3.3, is much larger than the value of 13.6 mA cm^{-2} associated with the same potential (η = 417 mV), for the 1.0 M data of Figure 3.3.4, experiment (a), it is less than the maximum current density of 161.7 mA cm^{-2} noted for experiment (b) presented in the same figure, and also performed in 1.0 M solution. Yet despite this, the hysterisis in the polarisation curve of Figure 3.3.4, experiment (b) is limited principally to deviation between the forward and reverse scans at higher overpotential. In contrast, there is no coincidence, at any overpotential, between the three scans of Figure 3.3.3, despite a lower current density at the reversal potential between the first forward and reverse sweeps. The logical conclusion from these observations is, that the surface of the Co electrode has fundamentally less stability with respect to polarisation at potentials of significant oxygen evolution, in 5.0 M NaOH solution relative to 1.0 M NaOH solution, even when polarisation is conducted at higher current densities in the latter solution.

Returning to the data of Figure 3.3.1, it is clear that the Tafel slope observed in the lower overpotential region, increases with decreasing OH^- activity, varying from 40.6 mV dec^{-1} in 5.0 M NaOH, through 46.4 mV dec^{-1} in 1.0 M NaOH, to 55.4 mV dec^{-1} in 0.25 M NaOH. The slope of 40.6 mV dec^{-1} observed for the 5.0 M solution, is in

excellent agreement with a slope of ~ 40 mV dec^{-1} observed by Willems et al.[15] for the o.e.r. at a polycrystalline Co electrode in 4.85 M KOH. The Tafel slope of 46.4 mV dec^{-1} noted in the present work, also agrees with a previous literature report – namely that of Scarr[16], who observed a slope of approximately 46 mV dec^{-1} for oxygen evolution on a Co anode in 1 M KOH at room temperature.

The observed variation in Tafel slope with electrolyte concentration, potentially poses a problem in extracting reaction order data from the steady state polarisation measurements of Figure 3.3.1. Conventionally, a change in Tafel slope is indicative of a change in reaction mechanism, or in rate determining step within the reaction pathway, and thus there is considerable dubiousness involved in deriving reaction order values from a data set that displays such a variation in Tafel slope with OH^- activity. Possible reasons behind this variation will be discussed further in section 3.5 – for the moment, mindful of the aforementioned reservations, a reaction order plot was nonetheless constructed from the data of Figure 3.3.1, and is presented as Figure 3.3.5. A reaction order with respect to OH^- activity, approaching unity is noted from this plot. It might be commented that, if the 0.25 M data point was neglected, the reaction order plot of Figure 3.3.5, might be more valid, because in this case the variation in slope between the various solution activities would be less than 10 mV dec^{-1}. It is obvious from Figure 3.3.5, that, if the lowest activity data point was neglected, a reaction order of the order of unity would still be recorded, although in this case the linearity of the plot would be quite poor.

The steady state polarisation data of Figure 3.3.1 were recorded in descending concentration order, with the scan in 5.0 M NaOH performed first, and the others recorded successively on consecutive days. The possibility was considered that, the increase in Tafel slope observed with decreasing OH^- activity might be due to an ageing effect associated with polarisation of the electrode at high anodic potentials. This was thought to be unlikely, owing to the fact that a 1.0 M measurement recorded before the series of scans of Figure 3.3.1, was virtually coincident with the 1.0 M trace presented in that figure, and thus also displayed a low overpotential Tafel slope of ~ 46 mV dec^{-1}. Furthermore, the almost exact agreement of the Tafel slopes for 1.0 and 5.0 M solutions recorded in the present work, with the few literature reports available, indicated the accuracy of the measurements of Figure 3.3.1. Nonetheless, it was decided to repeat, the steady state polarisation measurements on a different cobalt

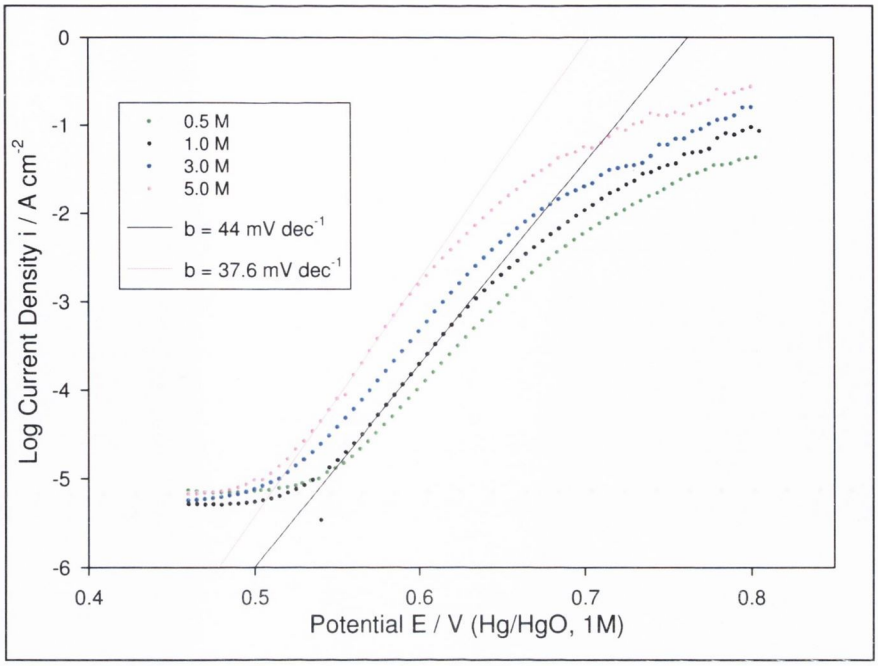


Figure 3.3.6 *IR corrected steady state polarisation curves recorded in the direction of increasing potential on a Co electrode (no electrochemical pre-treatment) in NaOH solutions of various concentration at 25°C. In contrast to the data of Figure 3.3.1 the measurement in the most dilute solution was performed first, with the others following in order of increasing concentration on consecutive days.*

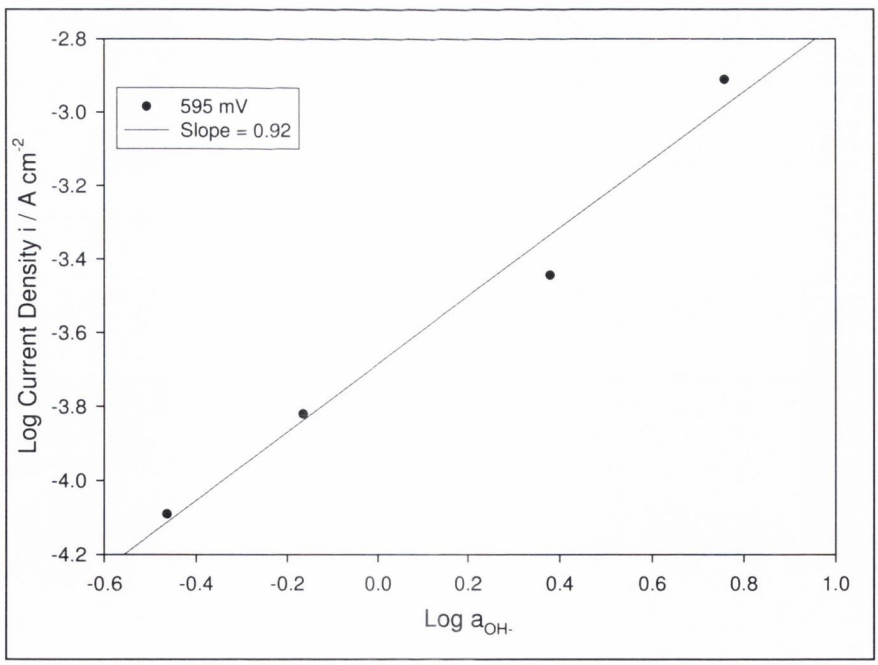
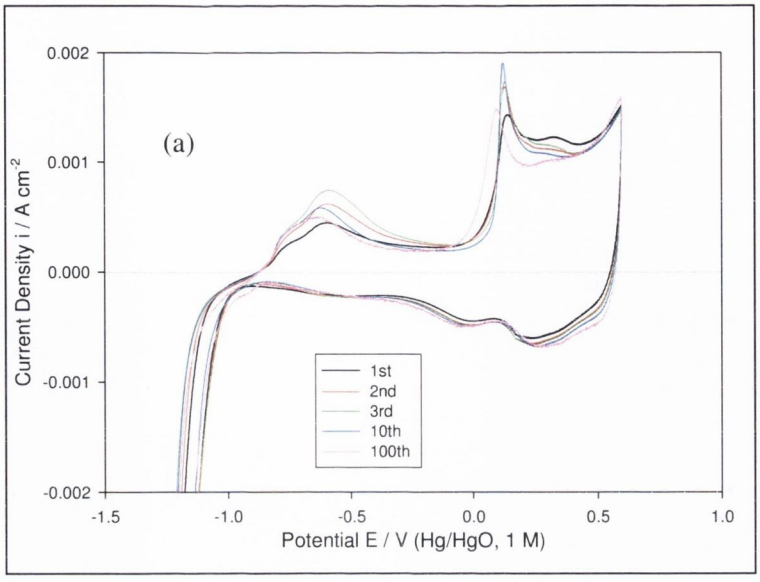


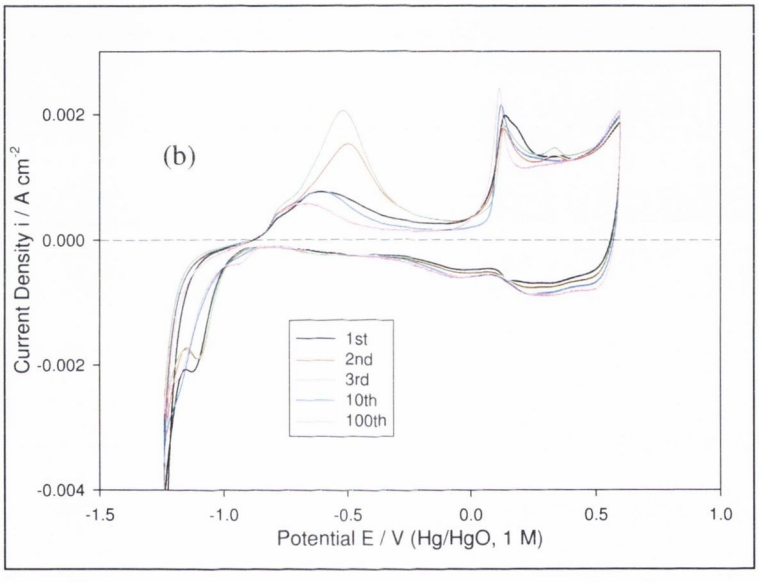
Figure 3.3.7 *Reaction order plot based upon the polarisation curves of Figure 3.3.6 at a potential of 595 mV.*

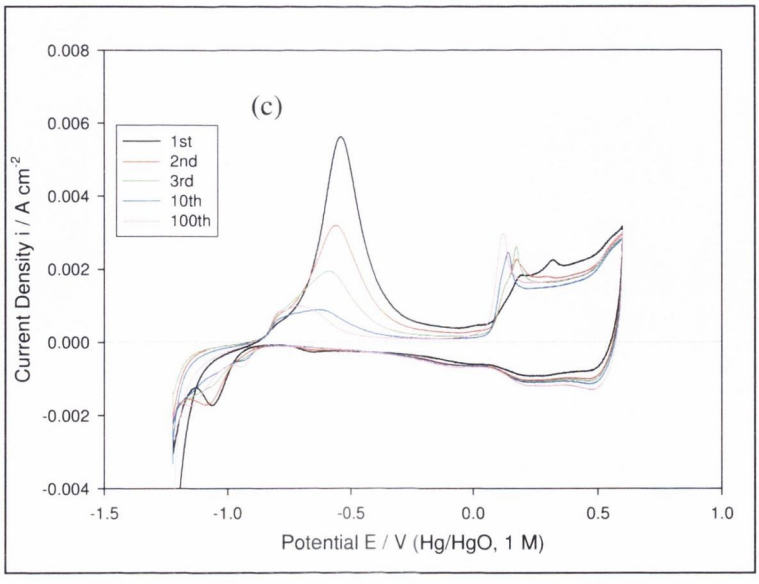
electrode, starting on this occasion with the scan in the most dilute solution. The results of these experiments are presented in Figure 3.3.6. Slightly lower Tafel slopes (ca. 2 mV dec^{-1} for each solution) were observed on this electrode, however the relative differences in slope between the data recorded in the various solutions remained constant. This confirmed that the observed variation in Tafel slope with electrolyte concentration was not due to an ageing effect. The linearity of the reaction order plot of Figure 3.3.7, based upon the polarisation measurements of the previous figure, was somewhat poor, however the overall indication was that m_{OH^-} was again of the order of unity.

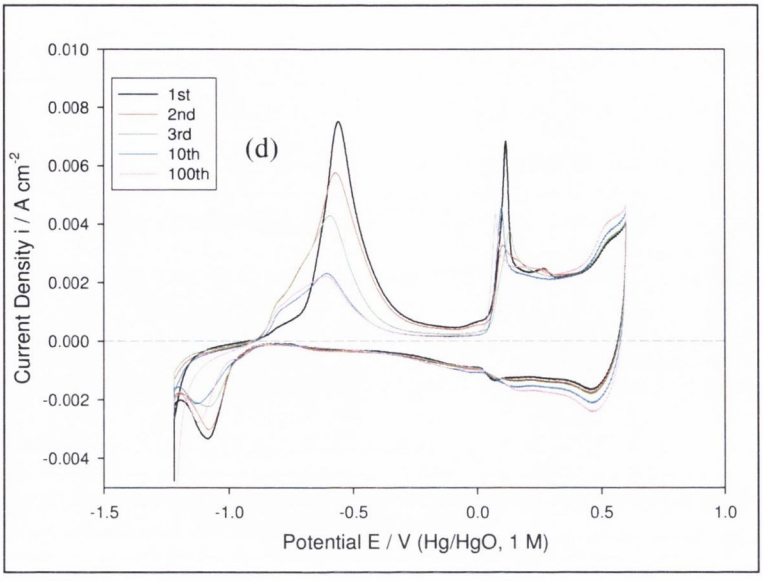
In an attempt to gain some insight into the variation of Tafel slope with OH^- activity, a series of cyclic voltammetry measurements were performed on a Co electrode, in order to characterise the surface electrochemistry at various electrolyte concentrations. For each of the chosen OH^- concentrations, a bright Co electrode was placed in the solution, and 3 successive voltammetric cycles were recorded at 40 mV s^{-1} between –1.22 and 0.6 V. A further 6 cycles were conducted between the same limits, but with a sweep rate of 300 mV s^{-1} – the 10^{th} cycle was then recorded at the analytical scan rate of 40 mV s^{-1}. Following this, the electrode was subjected to 89 cycles between the same limits as before at a scan rate of 300 mV s^{-1}. Finally the 100^{th} cycle was recorded at 40 mV s^{-1}. The 1^{st}, 2^{nd}, 3^{rd}, 10^{th}, and 100^{th} cycles recorded in the various OH^- solutions are presented in Figure 3.3.8.

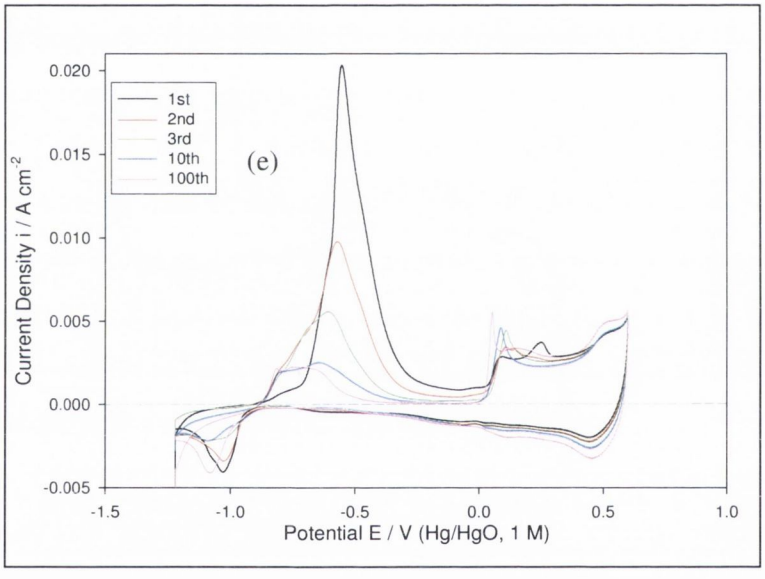
In reality these CVs do little to directly elucidate the reasons behind the variation of Tafel slope with OH^- activity. The general forms of the various voltammograms of Figure 3.3.8 agree, with the potentiodynamic behaviour of Co in concentrated alkaline solution as reviewed in section 1.4.3 – e.g. see Figure 1.4.12. From a comparative examination of the voltammetric profiles recorded in the different NaOH solutions, two possible reasons for the variation of o.e.r. Tafel slope with OH^- activity might be forwarded. Firstly, the active charge capacity associated with the oxidation of Co(II) species to Co(III), and the further surface oxidation to Co(IV) species, increases with increasing hydroxide concentration. Following the practice of several literature sources[17, 18, 19], the aforementioned charge capacities, Q, were calculated for the first cycles in the 1.0, 3.0 and 5.0 M CVs of Figure 3.3.8, by integration of the cathodic half-cycle between the limits of – 400 mV and the upper potential at which the net current density becomes negative. The calculated active charge capacities, Q, were as


(a)
Current Density i / A cm-2
Potential E / V (Hg/HgO, 1 M)
1st
2nd
3rd
10th
100th


(b)
Current Density i / A cm-2
Potential E / V (Hg/HgO, 1 M)
1st
2nd
3rd
10th
100th


(c)
Current Density i / A cm-2
Potential E / V (Hg/HgO, 1 M)
1st
2nd
3rd
10th
100th


(d)
1st
2nd
3rd
10th
100th
Current Density i / A cm-2
Potential E / V (Hg/HgO, 1 M)


(e)
1st
2nd
3rd
10th
100th
Current Density i / A cm-2
Potential E / V (Hg/HgO, 1 M)

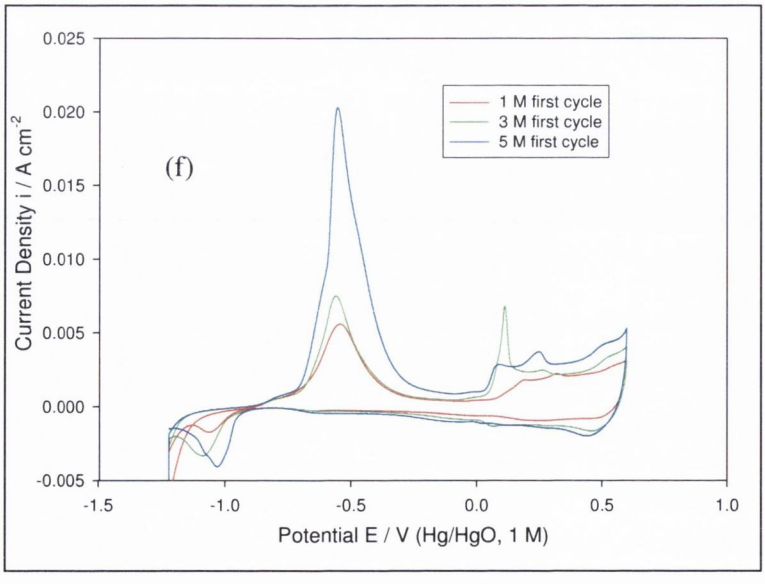

(f)
1 M first cycle
3 M first cycle
5 M first cycle
Current Density i / A cm-2
Potential E / V (Hg/HgO, 1 M)

Figure 3.3.8 *Previous two pages. Analytical CVs (cycle number as indicated in the relevant legend) recorded at 40 mV s^{-1} of an initially bright polycrystalline Co electrode in (a) 0.25 M, (b) 0.5 M, (c) 1M, (d) 3 M, and (e) 5 M solutions of NaOH. All CVs recorded between –1.22 V and 0.6 V at 25°C. The intervening cycles were performed between the same limits at 300 mV s^{-1}. In (f) a comparison is presented of the first cycles in the 1.0, 3.0 and 5.0 M electrolytes.*

as follows: 1.0 M NaOH, Q = ~ 14.6 mC cm^{-2}, 3.0 M NaOH, Q = ~ 24.0 mC cm^{-2}, 5.0 M, Q = ~ 27.4 mC cm^{-2}. Thus one possible reason for the decreasing Tafel slopes observed with increasing NaOH concentration in Figures 3.3.1 and 3.3.6, is that the amounts of redox active oxyhydroxide material formed (or electrochemically accessible at any rate) upon polarisation of an initially bright Co electrode, increases with increasing OH^- activity. In the case of the anodic oxide films formed on Ni electrodes in alkaline media, as discussed in section 3.2, it was noted (e.g. see Figures 3.2.4 or 3.2.7) that an increase in the active charge capacity of an oxide surface, was associated with an increase in observed o.e.r. current density at a given overpotential, for electrodes in solutions of the same OH^- concentration, however the Tafel slopes remained essentially invariant. This effect was attributed to increasing surface roughness accompanying higher calculated values of Q. Thus while surface area effects might lead to an increase in catalytic activity as measured by current density, they are less likely to cause a change in reaction mechanism, as indicated by Tafel slope.

This assertion is apparently backed up by data provided by Gennero De Chialvo et al.[19]. These authors found that although the o.e.r. catalytic activities in 1 M NaOH solution, of hydrous cobalt oxide films (generated by potential cycling of a polycrystalline Co electrode), were enhanced in a linear manner with their calculated active charge capacities (over a range from Q = 36.2 mC cm^{-2} to Q = 237.3 mC cm^{-2}), the observed Tafel slopes remained constant at ~ 50 mV dec^{-1}. The observed increases in oxygen evolution current densities at given values of η, with increasing oxide charge, were again explained by the authors in terms of a concurrent increase in the roughness factor of the oxide-solution interface. In view of this, it would appear that the decreasing Tafel slope, observed, with increasing OH^- activity (at least in the concentration range of 1.0 – 5.0 M) in the present work, is related to a change in more fundamental catalytic properties of the oxide film with increasing hydroxide concentration, than merely physical, surface area effects.

A second possible reason for the variation in Tafel slope with OH^- concentration is suggested by examining the changes in the voltammetric profiles of Figure 3.3.8 with repetitive cycling, especially in the potential region from –0.7 to –0.3 V. Recall, from the review of Co surface electrochemistry presented in section 1.4.3, that the potentiodynamic profile in this potential region is generally attributed to a combination of the oxidation of metallic cobalt to Co(II) species such as $Co(OH)_2$ (equation 1.4.24) or CoO (equation 1.4.25), and of a dissolution process involving the formation of the soluble Co(II) species $CoO{\cdot}OH^-$ (equation 1.4.26).

Comparing the voltammograms of Co in 1 M NaOH recorded in the present work (Figure 3.3.8 (c)) with those recorded by Gomez Meier et al.[20] (albeit at a faster scan rate of 300 mV s^{-1}) in 1 M KOH (see Figure 1.4.12), it is clear that there is very good agreement between these two sets of results. In each case a broad symmetrical anodic peak, with a peak potential of ca. –550 mV, is noted in the first few voltammetric cycles. The magnitude of this peak diminishes rapidly from cycle to cycle over the first number of cycles. As discussed in section 1.4.3, this behaviour is believed to be due to the dissolution process mentioned above, which is very significant in the initial formation of the inner region of the passivating oxide film via a dissolution/precipitation mechanism, during the early voltammetric cycles. By of the 10^{th} cycle of Figure 3.3.8 (c) the developing oxide film has apparently become stable with respect to the dissolution reaction, and the redox peak in this potential region, at this stage is principally related to the oxidation of Co to Co(II) species, probably at the metal-oxide interface. In summary, it might be commented that, for the bright Co electrode in 1 M NaOH (Figure 3.3.8 (c)), a dissolution / precipitation mechanism is important in the initial formation of the passivating oxide, with solid state electrochemical processes becoming more significant later in the development of the oxide film.

Now, examine the series of voltammograms for the same, initially bright Co electrode, in 0.25 M and 0.5 M NaOH solutions – Figure 3.3.8 (a) and (b), respectively. It is immediately apparent that the behaviour over the course of the first few voltammetric cycles is fundamentally different in these lower concentration cases as compared with the 1.0 M situation. For both the 0.25 M and 0.5 M experiments, the magnitude of the anodic peak in the vicinity of –0.5 to –0.7 V, actually increases over these early cycles, in marked contrast to the behaviour that prevails in the 1.0 M case. The data of Figure 3.3.8 (a) and (b) strongly suggests that dissolution / precipitation is

largely unimportant in the initial formation of the passive oxide film, during the first voltammetric cycles of a bright Co electrode in either 0.25 or 0.5 M NaOH. For the 0.5 M NaOH solution, the progressive increase in magnitude of the voltammetric peak, and the shift of its peak potential in the positive direction to ca. –500 mV, over the course of the second and third cycles suggests some dissolution activity, however even on this third cycle it is visibly obvious that the ratio of the magnitude of this peak compared with the more stabilised profile of the 10^{th} cycle, is much smaller than the ratio between the 1^{st} and 10^{th} cycle profiles in this potential region for the 1.0 M solution. The general profile of the 0.5 M NaOH CV of Figure 3.3.8 (b), and its evolution with repetitive cycling, are in good agreement with voltammetric data for the exact same system (polycrystalline Co electrode in 0.5 M NaOH) presented by Liu et al.[18], albeit that the scans of the latter work, were conducted at a lower sweep rate of 20 mV s^{-1}.

The voltammetric behaviour of the Co electrode in 3.0 M NaOH (Figure 3.3.8 (d)) in the potential region between –0.9 and –0.4 V, is largely similar to that described above for the same electrode in 1.0 M NaOH. Again a large symmetric anodic peak, centred at ca. –550 mV, associated with the dissolution / precipitation process discussed previously, is observed on the first cycle, with its magnitude decreasing markedly over the next two voltammetric sweeps. A stable anodic voltammetric profile is established in this region of potential by the 10^{th} cycle, with little difference in this section of the voltammogram between the latter cycle and the 100^{th} cycle. The stabilised profile seemingly consists of the superimposition of two anodic peaks, one centred at ~ -0.8 V, with the other displaying its peak in the region of –0.6 V. The persistent appearance of two peaks in this potential region, even up to the 100^{th} cycle, may suggest that some degree of dissolution is still significant at this relatively advanced stage in the formation of the oxide film in 3.0 M NaOH. The peak centred at ca. –0.6 V, seems to be "the evolution" of the initial large dissolution / precipitation peak centred at ~ -0.55 V, while the more negative peak is presumably related to a solid state electrochemical oxidation of Co to Co(II) species in the vicinity of the metal/oxide interface. It is noteworthy that by the 100^{th} cycle in 1.0 M NaOH, the voltammetric profile, in this potential region has more or less resolved into one broad peak centred around 150 mV negative to the peak potential of the 1^{st} cycle dissolution peak. Thus it would seem that while some soluble species formation continues in 3 M NaOH up to the 100^{th} cycle, this process has largely ceased in 1.0 M NaOH by that

stage. Figure 3.3.8 (f) shows that the initial, first cycle dissolution / precipitation peak has a somewhat larger magnitude for the 3.0 M solution in comparison with the 1.0 M electrolyte. Again this suggests a greater degree of soluble species formation, on increasing the OH^- concentration from 1 M to 3 M.

While, figure 3.3.8 (f), shows the aforementioned increase in dissolution / precipitation peak magnitude for the first voltammetric cycle in 3.0 M solution relative to 1.0 M NaOH, undeniably the most striking feature of this figure, is the huge increase in the dissolution current on increasing the electrolyte concentration from 3.0 to 5.0 M. To date, estimations have been avoided of the charge transferred during the anodic processes in this potential region for the various NaOH solutions, due to the overlap of the peaks associated with solid state redox transitions and the dissolution / precipitation process. However for the voltammograms of Figure 3.3.8 (f), it has been elected to integrate the profiles between –0.7 and –0.1 V, in order to obtain an approximate estimate of the relative extent of dissolution during the initial stages of passive film formation in the three electrolyte solutions. The following charge densities were calculated; Q_{1M} = 32.2 mC cm^{-2}, Q_{3M} = 37.7 mC cm^{-2}, Q_{5M} = 92.7 mC cm^{-2}. This rough estimate indicates that the charge involved in the dissolution / precipitation process on the first voltammetric cycle is ~ 17% greater in 3.0 M NaOH relative to 1 M NaOH. However it almost trebles, if the voltammogram of the 5.0 M solution is compared with that of the 1.0 M solution.

In summary then, the voltammograms of Figure 3.3.8, reveal that dissolution becomes increasingly important with rising OH^- activity, in the early stages of passive film formation on initially bright Co electrodes in aqueous alkaline solution. For the lower NaOH concentrations investigated (i.e. 0.25 and 0.5 M), a solid state oxidation process predominates in the potential region of the Co → Co(II) redox transition during the first voltammetric cycle at 40 mV s^{-1}. A change-over point in the initial voltammetric behaviour in this same potential region, occurs at NaOH concentrations between 0.5 and 1.0 M. The first cycle in the latter solution displays a large symmetrical peak centred at ~ -0.55 V characteristic of the formation and precipitation of soluble Co(II) species – CoO_2H^- has been suggested by Burke et al.[17], while Šimpraga[21] proposed $Co(H_2O)_x^{2+}$ as the possible identity of the soluble entity. The significance of the dissolution process continues to increase with increasing OH^- concentration above 1 M – for the case of 5 M electrolyte solution, the dissolution/precipitation currents on the first few voltammetric cycles completely

overwhelm the currents due to the solid-state processes in the region from –0.7 to –0.4 V.

The observations summarised in the previous paragraph corroborate the results of the rotating ring disc electrode (RRDE) and scanning electrochemical microscopy (SECM) study of Erts et al.[22], which was reviewed in section 1.4.3. Recall, that these workers detected no soluble Co^{2+} species by either the RRDE, or more sensitive SECM methods in the potential range of the Co → Co(II) oxidation process, for 0.1 M NaOH. In contrast both methods detected Co^{2+} ions in 1.0 M NaOH solution, over the same region of potential. A much larger dissolution current was noted by SECM than by the classical RRDE method – it was envisaged that this was due to rapid precipitation of the soluble Co^{2+} ions, so that much of the soluble species couldn't escape to the bulk solution and register a ring current. In view of the results of Figure 3.3.8, combined with the conclusions of Erts et al.[22], it seems that the initial passivation of bright Co electrodes in NaOH solution of concentrations of 1M or greater, occurs via the rapid precipitation of soluble Co^{2+} species back onto the metallic substrate. The relative importance of this dissolution / precipitation process, compared to the solid-state electrochemical oxidation of metallic Co to species such as $Co(OH)_2$ or CoO, increases with increasing OH^- activity.

At this point it is important to recall the "sandwich" model of the passive film formed on Co in alkaline solution – a viewpoint that has been adopted by several workers in this area[20, 21, 23, 24]. This model envisages that the Co(II) oxide formed at potentials below ca. –0.2 V, exists as a layer, sandwiched between the Co metal, and the thicker outer hydrous oxide, which consists mainly of Co(III) species. One of the common justifications cited for this model, is that while the surface charge capacities associated with the Co(III)/Co(IV) oxide formation and reduction, increase with repetitive cycling, the charge capacities associated with the Co(II) oxide remain essentially constant (after the first few voltammetric cycles in any case). This behaviour is apparent at all concentrations in Figure 3.3.8. Therefore it would seem likely that the Co(II) oxide exists in a region adjacent to the metal surface. At the lower end of the cathodic cycles it is reduced back to metallic Co, which is in turn re-oxidised to CoO or $Co(OH)_2$ at potentials between approximately –0.9 and –0.2 V on the subsequent anodic sweep.

In the steady state polarisation measurements of Figures 3.3.1 – 3.3.4 and 3.3.6, polished, initially bright Co electrodes were placed in the various NaOH solutions

utilised. In general, instantaneous open circuit potentials between –0.7 and –0.8 (Hg/HgO, 1 M NaOH) were observed, although these potentials were not left to stabilise and thus were not systematically recorded. According to the thermodynamic data of Göhr[25], the standard potentials for the oxidation of metallic Co to $Co(OH)_2$ and CoO according to equations (1.4.24) and (1.4.25) are respectively, ~ -0.82V and ~ -0.8V. Thus, it would seem that there is a spontaneous formation of a Co(II) oxide film on a bright Co electrode, upon its introduction to concentrated alkaline solution, analogous to the situation that prevails for Ni electrodes under the same conditions. To conduct the polarisation measurements, the electrode potential was stepped from its open circuit value to 450 mV (Hg/HgO, 1M NaOH), and the potential step program (see chapter 2) was applied in the direction of increasing potential, upon stabilisation of the current at this potential. Presumably, upon, and subsequent to, the stepping of the electrode potential to 450 mV, passivation of Co surface must occur, in a manner somewhat similar to that, revealed by the first anodic sweep of a voltammetry experiment in the same solution. If this is true, then the nature (as well as the thickness) of the passive oxide layer formed immediately before, and during the o.e.r. steady state polarisation measurements, would be expected to vary to a certain extent with the OH^- activity of the electrolyte solution. Since the voltammetry experiments of Figure 3.3.8, reveal fundamental differences in the initial passivation (Co → Co(II) oxidation) of Co electrodes at different NaOH concentrations, it might be expected that (at least) the inner regions (sandwich model) of the passive oxides formed in these different electrolyte solutions would have somewhat different properties. In section 3.5, it will be proposed that different electrical properties of the oxide films formed on Co in OH^- solutions of different concentration, might explain the variation in o.e.r. Tafel slopes measured in these solutions.

While it is possible that a variation, with OH^- concentration, in the nature of the passive oxide films formed on bright Co electrodes, may contribute to the differences in Tafel slopes observed at different NaOH electrolyte concentrations, it can be shown with more certainty that ageing leads to changes in the o.e.r. Tafel slope for the same Co electrode in the same NaOH solution, at different stages in its life-cycle. To consider these effects, steady state polarisation curves are presented in Figure 3.3.9, for a given Co electrode in 3.0 M NaOH. When used initially, a Tafel slope of 43.5 $mV\ dec^{-1}$, extending over the course of ca. 2 decades of current density is evident. This behaviour is consistent with the data of Figure 3.3.1, where the 3.0 M Tafel slope

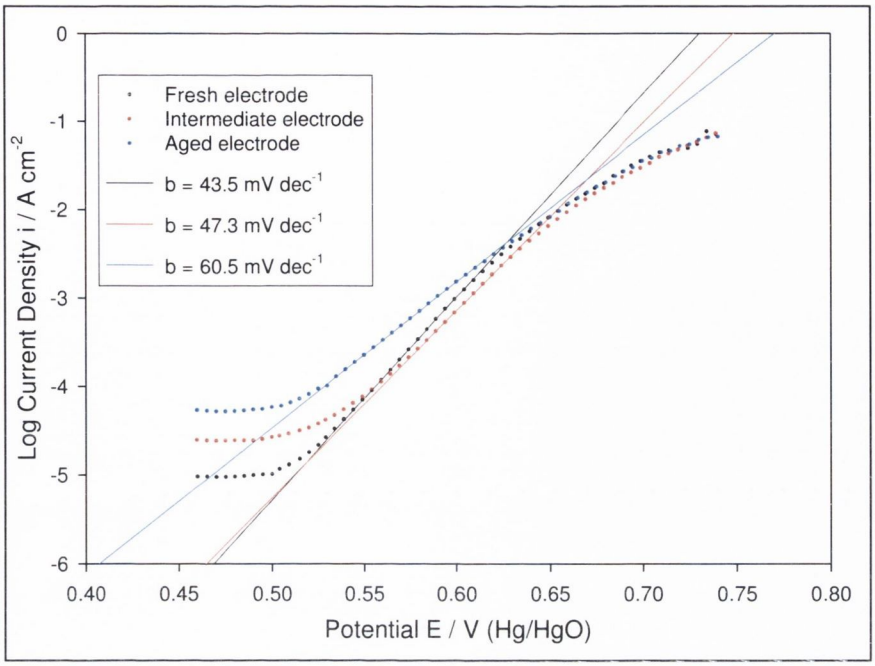


Figure 3.3.9 *IR corrected steady state polarisation curves recorded in the direction of increasing potential on the same Co electrode, aged to different degrees, in 3.0 M NaOH solution at 25°C.*

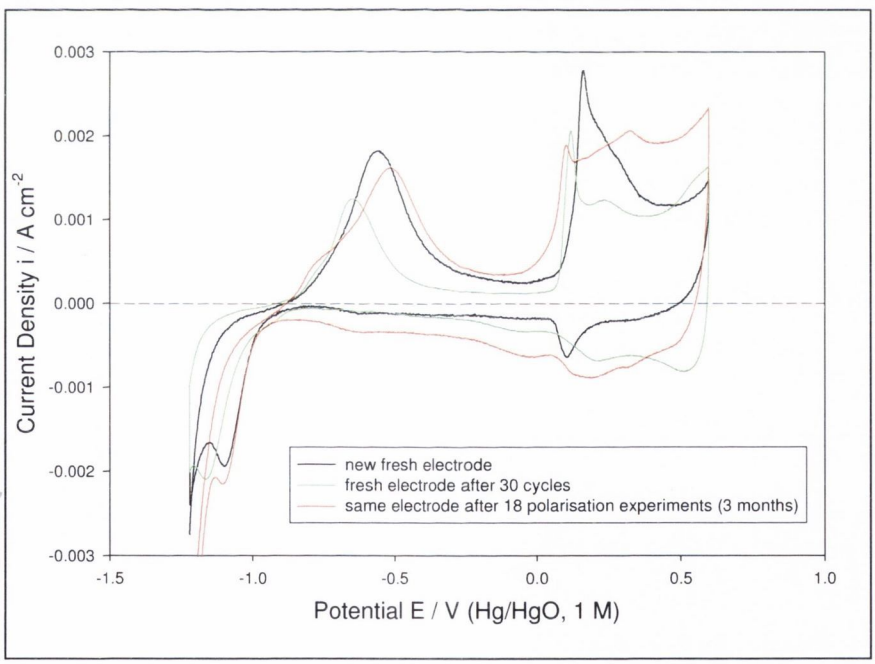


Figure 3.3.10 *Cyclic voltammograms, characterising the surface electrochemistry of the initially bright Co anodes, on which the "fresh" and "intermediate" steady state polarisation curves of Figure 3.3.9 were recorded. The 30th voltammetric sweep of a multi-cycling experiment on the "fresh" electrode is also included for comparison. All the above CVs were recorded in 1.0 M NaOH between –1.22 and 0.6 V, with a scan rate of 40 mV s^{-1} at 25°C.*

has a value intermediate to the 40.6 mV dec^{-1}, and 46.4 mV dec^{-1} values recorded respectively for the 5.0 and 1.0 M NaOH solutions. A cyclic voltammogram, recorded in 1.0 M NaOH, in order to characterise this fresh bright electrode is presented in Figure 3.3.10. The "intermediate" polarisation curve of Figure 3.3.9 was recorded on the same electrode, three months later, after it had been used in 18 polarisation experiments in NaOH solutions of various concentrations between 0.5 and 5.0 M. It is evident that the Tafel slope recorded for the "intermediate" electrode, has increased by ca. 4 mV dec^{-1}, relative to that recorded for the fresh electrode. This increase in slope causes a slight reduction in oxygen evolution current density relative to the fresh electrode, over the range of the potential corresponding to the straight line Tafel region – although the polarisation curves apparently converge at higher current densities. A CV, which characterises this "intermediate" behaviour Co electrode is also presented in Figure 3.3.10.

Following all polarisation experiments performed on the electrode, it was polished, rinsed and dried (in soft tissue paper). Unlike Ni, which retains its bright metallic finish throughout the course of oxygen evolution polarisation measurements, a dark brown coloured oxide film forms on Co, when polarised at high anodic potentials in alkaline solution. This film was readily removed by polishing, so that the "fresh" and "intermediate" Co electrodes of Figures 3.3.9 and 3.3.10 were visually similar, with bright "mirror" finishes. Thus, while the "intermediate" electrode could accurately be described as being "bright", it is clear from comparison of its characteristic CV in Figure 3.3.10, with that of the fresh electrode, that there are significant differences in the electrochemistry of their surfaces. In view of the data of Figures 3.3.9 and 3.3.10, it can be concluded, that while, bright polycrystalline Co is more stable with respect to ageing effects than bright Ni (consider for example that it was possible to record reproducible Co steady state polarisation curves over a series of 5 – 10 experiments, which wasn't achievable with Ni), ageing does become significant after a larger number of experiments (>10).

Calculation of the reversibly available redox charge capacities for the "fresh" and "intermediate" electrodes, by integration of the cathodic profiles, down to a potential of – 400 mV, yields the following; Q_{fresh} = ~ 4.5 mC cm^{-2}, Q_{inter} = ~13.7 mC cm^{-2}. Therefore, even though its active charge capacity is only of the order of 1/3 of that of the "intermediate" electrode, the "fresh" electrode actually displays a slightly superior activity towards the o.e.r. in the straight line Tafel region (Figure 3.3.9). At first

glance, this seems to contradict the previously mentioned observation of Gennero De Chialvo et al.[19] that the activity of the o.e.r. increases approximately linearly with active charge capacity, for cobalt oxide films grown by repetitive voltammetric cycling on Co electrodes in alkaline solution. However, this effect (which is intuitively what one might expect, on the basis of increased surface roughness associated with larger charge capacities) was noted for freshly prepared films, which were presumably, very similar in chemical composition, differing only in thickness and available surface area. In the case of the "intermediate" electrode of the present work it would seem, that, although its calculated charge capacity is greater than that of the "fresh" electrode, its oxide film is intrinsically less catalytically active towards the o.e.r. than that of the latter electrode.

That, there are significant differences in the composition of the anodic oxides films on the "fresh" and "intermediate" Co electrodes, is apparent from a comparison of their respective CVs in Figure 3.3.10. It would appear that the first voltammetric cycle on the more aged "intermediate" electrode, represents in essence, the further growth of a residual passive film, which has not been completely removed by mechanical polishing. At potentials above ca. –100 mV, both in the anodic and cathodic profiles, the voltammogram of the first cycle on the "intermediate" electrode bears a much closer similarity to the profile of the 30^{th} cycle of the developing hydrous oxide on the "fresh" electrode, rather than to that of the initial cycle on the same electrode. Furthermore, on the basis of the earlier discussion related to the evolution with cycling of the CVs of Figure 3.3.8, it would seem that, the presence of a very obvious shoulder on the cathodic side of the voltammetric profile in the Co → Co(II) potential region of the CV of the "intermediate" electrode, is indicative of the fact that this profile represents a superposition of the expected dissolution current with a significant steady state oxidation current. By contrast, the symmetrical nature of the anodic peak centred at ca. –550 mV in the first voltammetric cycle on the "fresh" electrode, would indicate that the dissolution/precipitation process has a greater relative importance in this case. In summary it would seem, that while the first cycle on the "fresh" electrode represents the initial stages of the passivation of a metallic Co surface, the corresponding cycle on the "intermediate" electrode reveals that the basis of a passivating oxide already exists on this more aged electrode surface. If this viewpoint is accepted, then the o.e.r. proceeds on an entirely new oxide film in the case of the "fresh" electrode, but on the surface of the "development of an existing passivating

film" in the case of the "intermediate" electrode. Thus, the observed differences in oxygen evolution behaviour (Figure 3.3.9) are not surprising.

With further ageing (> 30 polarisation experiments) a substantially different steady state polarisation plot was noted for the o.e.r. on the Co electrode (see "aged" electrode curve in Figure 3.3.9), relative to those recorded for the "fresh" and "intermediate" electrodes as described above. The slope in the straight line Tafel region increased further to ca. 60 mV dec^{-1}, however, in contrast to the "intermediate" electrode, the o.e.r. current density was increased relative to the "fresh" electrode over this range of potential. At a potential of 530 mV, which approximately corresponds to the lower limit of the straight line Tafel regions for both of these electrodes, the current density observed for the "aged" electrode (0.103 mA cm^{-2}) is roughly four times that recorded for the "fresh" electrode (0.027 mA cm^{-2}). Owing to their different Tafel slopes, the o.e.r. current densities for these two electrodes become practically co-incident at the upper potential end of the straight-line Tafel region.

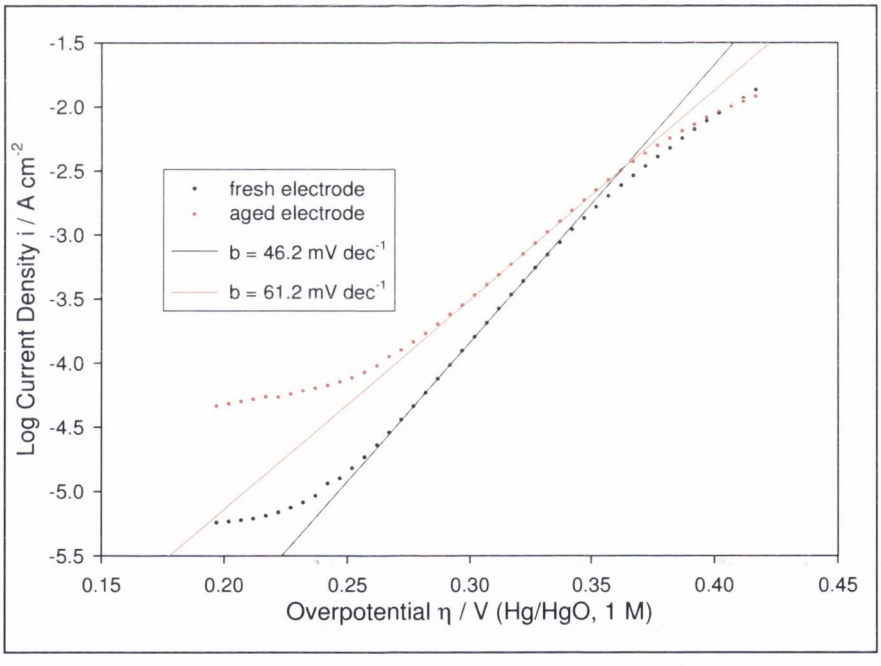


Figure 3.3.11 *IR corrected steady state polarisation curves recorded in the direction of increasing potential on the same Co electrode, aged to different degrees, in 1.0 M NaOH solution at 25°C.*

Similar behaviour with respect to increasing o.e.r. Tafel slopes accompanying electrode ageing are also apparent for steady state polarisation curves recorded in 1.0 M NaOH – see Figure 3.3.11. CVs which characterise the surface electrochemistry, of the initially bright electrodes on which the polarisation data of Figure 3.3.11 were collected, are presented in Figure 3.3.12.

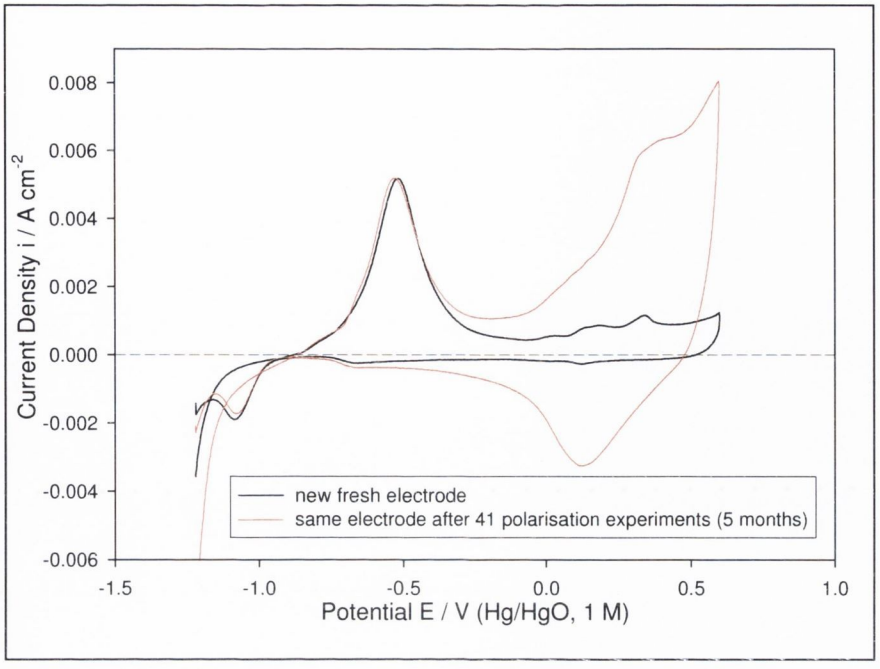


Figure 3.3.12 *Cyclic voltammograms, characterising the surface electrochemistry of the initially bright Co anodes, on which the "fresh" and "aged" steady state polarisation curves of Figure 3.3.11 were recorded. The above CVs were recorded in 1.0 M NaOH between –1.22 and 0.6 V, with a scan rate of 40 mV s^{-1} at 25°C.*

The characteristic CV of the (different) highly aged electrode, on which the ~ 60 mV dec^{-1} Tafel slope of Figure 3.3.9 (3.0 M) was recorded, was similar in profile to that of the aged electrode (red trace) depicted in Figure 3.3.12. While the anodic profiles in Figure 3.3.12 are remarkably similar in the Co/Co(II) potential region below –0.2 V, there is clearly a huge difference in the charge capacities associated with the Co(III) and Co(IV) potential regions. Calculation of the reversibly accessible redox charge capacity for this potential range in the usual manner yields; Q_{fresh} = ~ 3.47 mC cm^{-2}, compared to Q_{aged} = ~ 32.0 mC cm^{-2}. Recall from section 3.2, Figures 3.2.8 – 3.2.10, that similar ca. 60 mV dec^{-1} Tafel slopes were observed in 3.0 and 5.0 M NaOH solutions for aged bright Ni electrodes with high charge capacities. As was generally true with Ni electrodes that hadn't been subjected to pre-oxidation or pre-reduction potential regimes, reproducibility issues rendered impossible, the gathering of reaction order data for the o.e.r. on such electrodes. However in the case of Co, it did prove possible to reproducibly record steady state polarisation curves such as the

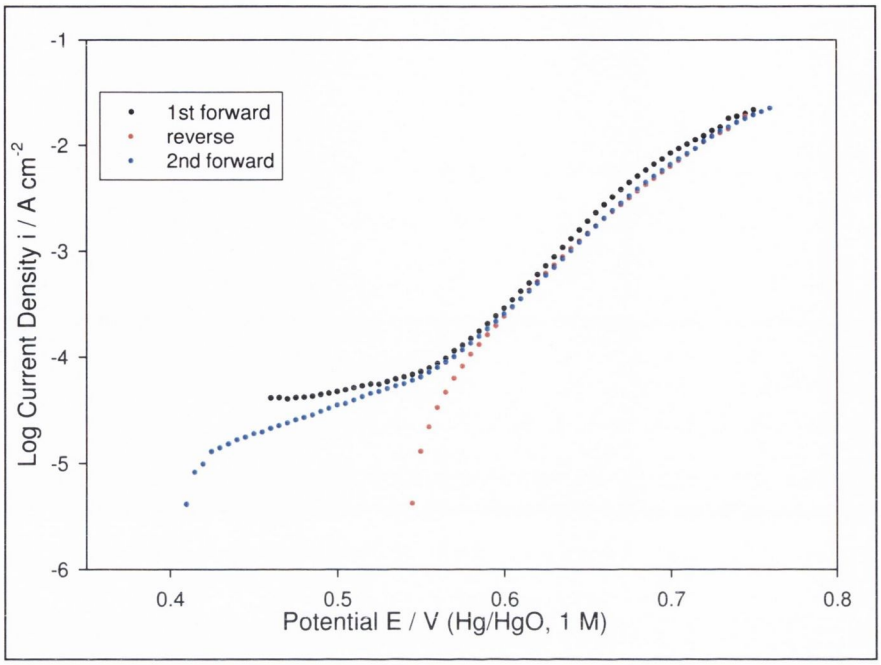


Figure 3.3.13 *Bi-directional IR corrected steady state polarisation curve recorded continuously on an aged Co electrode (no electrochemical pre-treatment – characteristic CV similar to aged CV of Fig 3.3.12) in 1M NaOH, initially in the direction of increasing potential, at 25°C.*

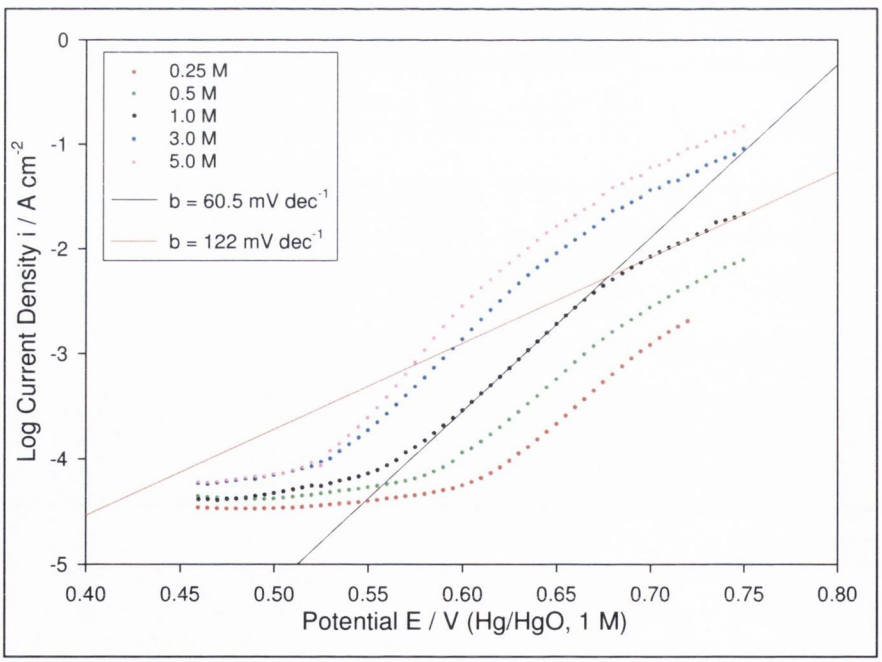


Figure 3.3.14 *IR corrected steady state polarisation curves recorded in the direction of increasing potential on an aged Co electrode (no electrochemical pre-treatment) in NaOH solutions of various concentration at 25°C. The 1.0 M curve of this figure corresponds to the first forward sweep depicted in Figure 3.3.13.*

60 mV dec^{-1} plots of Figures 3.3.9 and 3.3.11, at least over the course of a small number (< 10) of experiments. A full bi-directional steady state polarisation curve recorded in 1.0 M NaOH solution, on the aged electrode characterised in the red CV of Figure 3.3.12 is presented in Figure 3.3.14. Two straight-line Tafel regions are suggested upon examination of this curve – a well-resolved region at lower overpotentials with a Tafel slope of ca. 60 mV dec^{-1}, and a somewhat less well defined (though nevertheless apparent) region at higher overpotentials with a slope of ca. 120 mV dec^{-1}. These Tafel slopes are clearly marked on the 1 M trace of Figure 3.3.14, which is in fact just the first forward sweep of Figure 3.3.14. Similar steady state polarisation measurements were performed on this aged electrode in NaOH solutions of various concentrations (0.25 M – 5.0 M), and the first forward sweeps of these experiments are presented in Figure 3.3.14. Just like the polarisation curves presented in Figures 3.3.1 and 3.3.6, for "fresh" bright polycrystalline Co electrodes, it is obvious that the values of the Tafel slopes in the lower overpotential region, decrease somewhat with increasing OH^- activity.

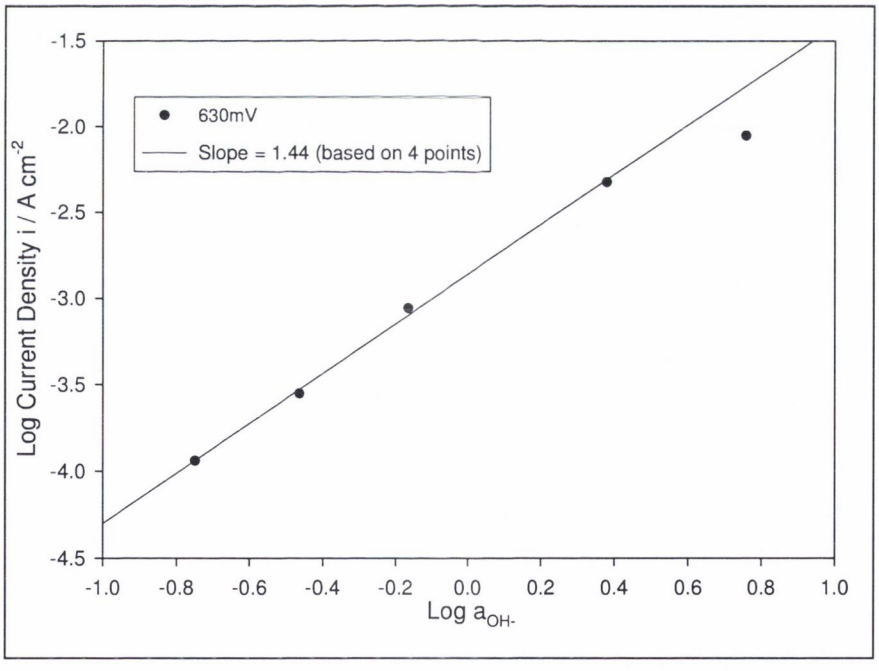


Figure 3.3.15 *Reaction order plot based upon the polarisation curves of Figure 3.3.14 at a potential of 630 mV in the lower Tafel slope region.*

As before this variation in Tafel slope with electrolyte concentration, poses questions regarding the validity of extracting reaction order information from such data sets. A further problem with the construction of reaction order plots from the polarisation curves of Figure 3.3.14, arises from the limited potential window over which the ca.

60 mV dec^{-1} Tafel behaviour prevails. Thus at the potentials (600 – 630 mV) at which the straight line Tafel behaviour becomes prevalent for the lower concentration solutions (0.25 – 1.0 M), the polarisation plot for the 5.0 M solution has already gone beyond its lower slope region. Despite these issues the reaction order plots of Figure 3.3.15 for the lower Tafel slope region, and Figure 3.3.16 for the higher straight-line region were constructed.

For the lower overpotential region, a plot constructed from the polarisation data at a potential of 630 mV was found to yield the most satisfactory degree of linearity. The data point for the 5.0 M NaOH solution is excluded from the slope calculation in Figure 3.3.16, because the polarisation plot for this concentration has moved into the transition region between the lower and upper slopes. Making such a compromise was necessary in order to obtain a (hopefully) meaningful reaction order value.

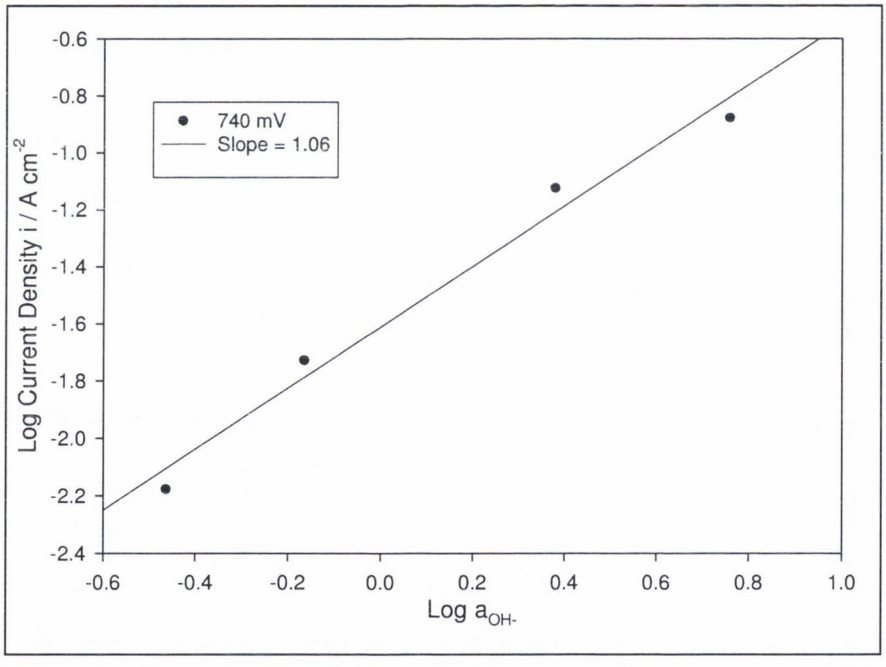


Figure 3.3.16 *Reaction order plot based upon the polarisation curves of Figure 3.3.14 at a potential of 740 mV in the upper Tafel slope region.*

Figure 3.3.16, is a typical representation of a reaction order plot, based upon the polarisation curves, at a potential in the ca. 120 mV dec^{-1} Tafel slope region. Regardless of the exact potential on which reaction order plots were constructed for this region, the linearity, as in Figure 3.3.16, was not great. Overall, while there are several sources of dubiousness in this reaction order study, the best obtainable results suggest a reaction order approaching a non-integral value of 3/2 for the lower Tafel

region, while a reaction order of approximately unity is associated with the upper Tafel region.

3.3.2 Pre-reduced and Pre-oxidised Co electrodes

As previously mentioned, the variation in Tafel slope with OH^- activity presents possible difficulties in the interpretation of reaction order data, derived not only from Figure 3.3.14 for the aged Co electrode, but also from Figures 3.3.1 and 3.3.6 for fresh Co electrodes. In view of this, it was elected to subject Co electrodes to electrochemical pre-treatment regimes, to investigate whether o.e.r. Tafel slopes, consistent over a range of concentrations, might be obtained from steady state polarisation measurements on such electrodes.

The first of these pre-treatments to be considered, involved a 5 minute pre-reduction of a polished bright Co electrode at –1.15 V in 1 M NaOH. Referring to any of the 1.0 M cyclic voltammograms of Figures 3.3.8, 3.3.10, or 3.3.12, it can be seen that this potential is associated with the reduction of Co(II) oxide species and is just anodic to the potentials associated with significant hydrogen evolution. Following the cathodic reduction the electrode potential was left to relax on open circuit for several minutes, before the electrode was subjected to one voltammetric cycle between the limits of –1.22 and 0.6 V at a rate of 40 mV s^{-1}. It was hoped that this cycle following the pre-reduction, would commence the passivation process on the Co surface, therefore helping to reduce the impact of the steady state polarisation test solution on the initial passivation of this surface, a factor which we have proposed to be of possible importance in causing the variation of o.e.r. Tafel slope with the concentration of the test solution. Following the pre-treatment in 1.0 M NaOH, the electrode was transferred to the relevant test solution, using the same procedure outlined in section 3.2, for the transfer of Ni electrodes after pre-treatment.

The first steady state polarisation scans in the direction of increasing potential for a pre-reduced Co electrode, in various NaOH test solutions, are presented in Figure 3.3.17. The full bi-directional polarisation plot for the pre-reduced electrode is presented in Figure 3.3.18. Again it can be seen that the is very significant hysterisis between the forward and reverse sweeps, with their slopes only appreciably coinciding at the lowest (η < 275 mV) and highest (600 < η < 650 mV) overpotentials considered. At first glance the hysterisis in Figure 3.3.18 appears to be more severe than that of Figure 3.3.4 for non-pre-treated Co electrodes, however this

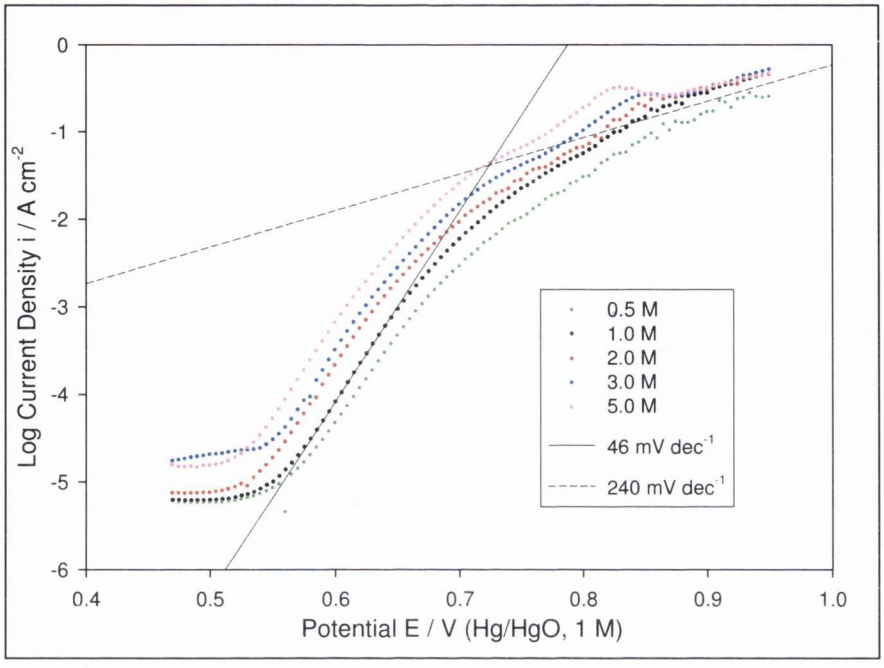


Figure 3.3.17 *IR corrected steady state polarisation curves recorded in the direction of increasing potential on a pre-reduced Co electrode (see text for further details) in NaOH solutions of various concentration at 25°C.*

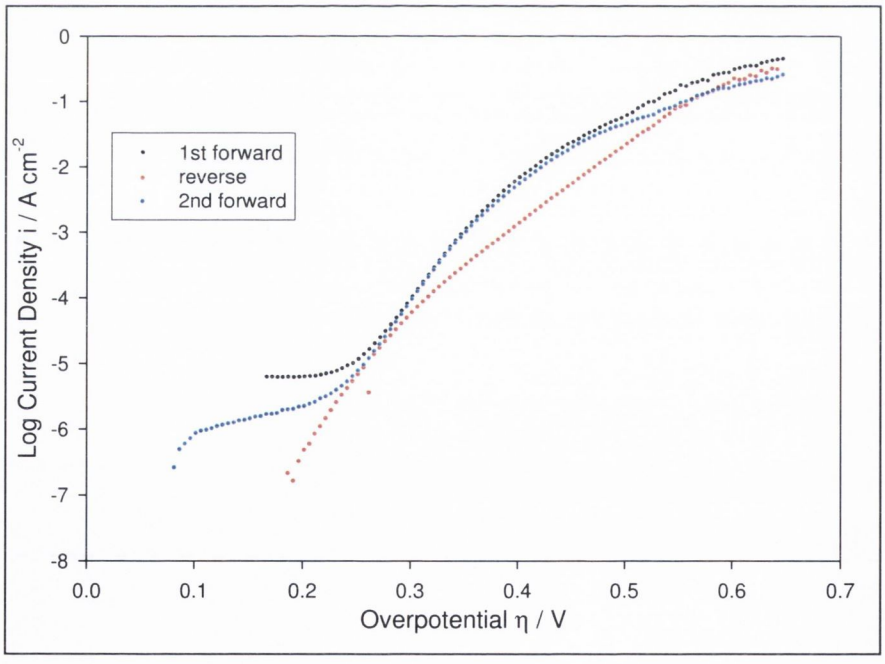


Figure 3.3.18 *Bi-directional IR corrected steady state polarisation curve recorded continuously on a pre-reduced Co electrode in 1M NaOH, initially in the direction of increasing potential, at 25°C.*

most likely arises, because the reversal potential (η = 647 mV) of the scan of Figure 3.3.18 is a full 100 mV greater than the higher reversal potential of Figure 3.3.4, and

thus higher steady state current densities are achieved in the scans for the pre-reduced electrode. Despite the hysterisis upon reversal of the scan direction, it is also noteworthy that there is excellent coincidence between the 1st and 2nd forward sweeps in the low overpotential straight line Tafel slope region.

Examining Figure 3.3.17, it is evident that the initial straight-line sections of the polarisation curves for NaOH concentrations ≥ 1.0 M, are essentially parallel, with a Tafel slope of ca. 46 mV dec^{-1}. In the case of the data recorded in the 0.5 M solution, the Tafel slope in this region is slightly greater – ca. 49 mV dec^{-1}. The good agreement in Tafel slope values recorded for the various NaOH solutions, means that reaction order parameters derived from the data of Figure 3.3.17, should be free from the reservations surrounding such parameters obtained from the data sets of Figures 3.3.1 and 3.3.6. The observation of an essentially concentration invariant Tafel slope for the pre-reduced electrode, lends further weight to our conjecture regarding the importance of the influence of the initial stages of passive oxide formation on the observed Tafel slope for a bright Co electrode. It is noteworthy that the Tafel slopes

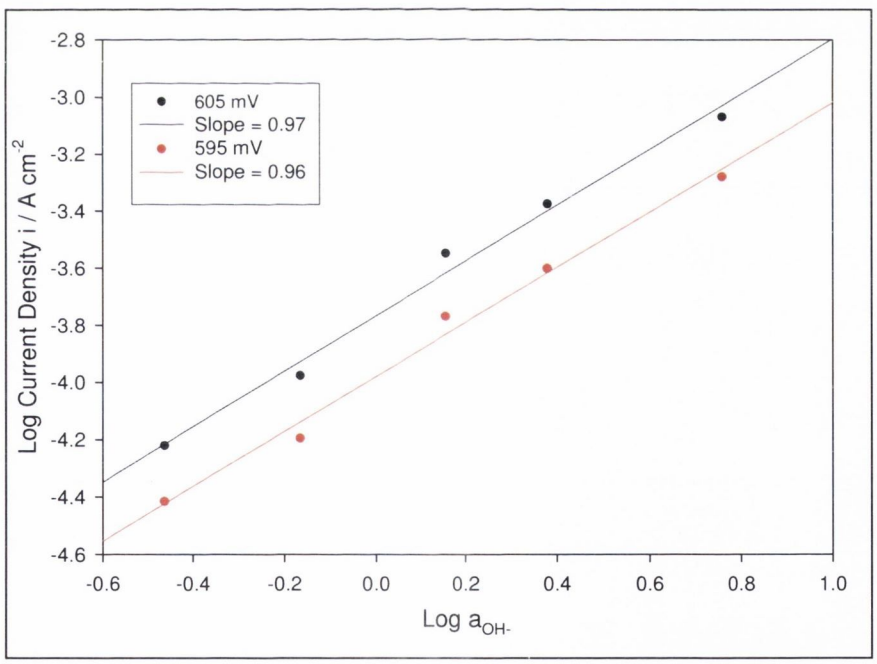


Figure 3.3.19 *Reaction order plot based upon the polarisation curves of Figure 3.3.17 at potentials of 595 and 605 mV in the ca. 46 mV dec^{-1} Tafel slope potential region.*

measured in the four most concentrated solutions, adopt the value (46 mV dec^{-1}) previously noted (Figures 3.3.1 and 3.3.6) for un-pre-treated Co electrodes in 1.0 M NaOH, the very solution in which the initial passivation of the "pre-reduced"

electrodes took place, during a voltammetric sweep following on their reduction at –1.15 V for 5 minutes in the same solution.

Reaction order plots, constructed from the polarisation curves of Figure 3.3.17 at two values of potential within the ca. 46 mV dec^{-1} straight-line region, are presented in Figure 3.3.19. Good co-incidence was noted between the initial and second sweeps in the positive direction for the 1.0 M polarisation data of Figure 3.3.18 – in fact this is true for the polarisation curves of the pre-reduced electrode at all NaOH concentrations. This is mentioned here, because reaction order plots derived from the second forward scan in the 46 mV dec^{-1} Tafel slope potential region, actually display somewhat more satisfactory linearity than those of Figure 3.3.19. An example of one such plot, based on the second forward sweep, current density values at 585 mV, is depicted in Figure 3.3.20. In any case, whether one considers the slopes of Figure 3.3.19 or Figure 3.3.20, their overall conclusion must be, that, the value of the reaction order with respect to OH^- activity is of the order of unity, just as was suspected on the basis of the polarisation results on the un-pre-treated Co electrodes – see Figures 3.3.5 and 3.3.7.

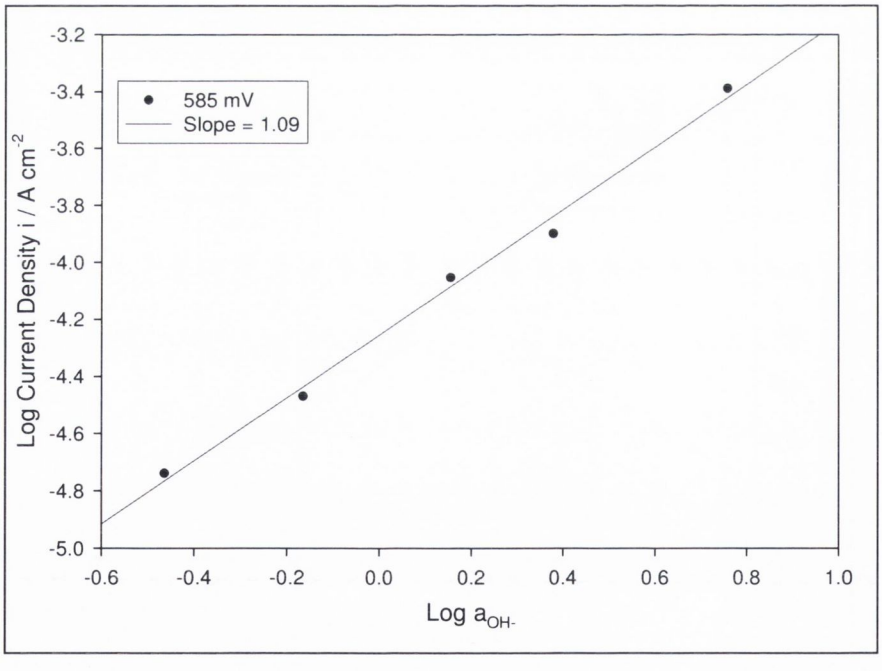


Figure 3.3.20 *Reaction order plot based on the corresponding "second forward" steady state polarisation sweeps to the "first forward" sweeps of Figure 3.3.17.*

A second type of pre-treatment regime utilised, involved the pre-reduction of a polished Co electrode, again for 5 minutes at –1.15 V, but this time in 5.0 M NaOH. Instead of following this pre-reduction with a potential cycle as for the so-called "pre-

reduced" electrodes of Figure 3.3.17, the electrode surface was then pre-oxidised (still in 5.0 M NaOH) by polarising at a potential of 750 mV for a 3 minute period. Electrodes pre-treated in this manner will be referred to as "pre-oxidised" electrodes in the following discussion. Following the pre-oxidation, the electrode was transferred to the appropriate test solution using the method originally described for pre-treated Ni electrodes in section 3.2.

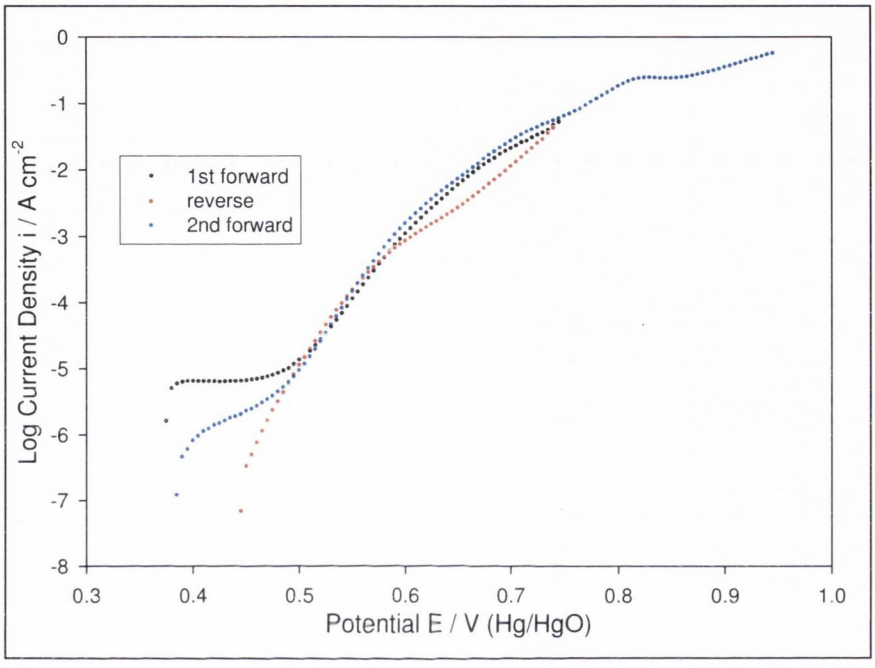


Figure 3.3.21 *Bi-directional IR corrected steady state polarisation curve recorded continuously on a pre-oxidised Co electrode in 5 M NaOH, initially in the direction of increasing potential, at 25°C.*

A full bi-directional oxygen evolution steady state polarisation curve for one of these pre-oxidised electrodes in 5.0 M NaOH solution, is presented in Figure 3.3.21. As usual for such polarisation experiments hysterisis is noted between the forward and reverse scans. The catalytic activity towards the o.e.r is enhanced slightly on the second forward sweep relative to the initial sweep in this direction, however the general shape of the trace remains the same, so as usual the initial scan will be used in the reaction order determination. This slight enhancement in current density is probably due to an increase in active surface area, arising from the extended polarisation of the catalytic oxide. Figure 3.3.22 is a comparative plot of the first forward polarisation sweeps on pre-oxidised electrodes in various NaOH solutions.

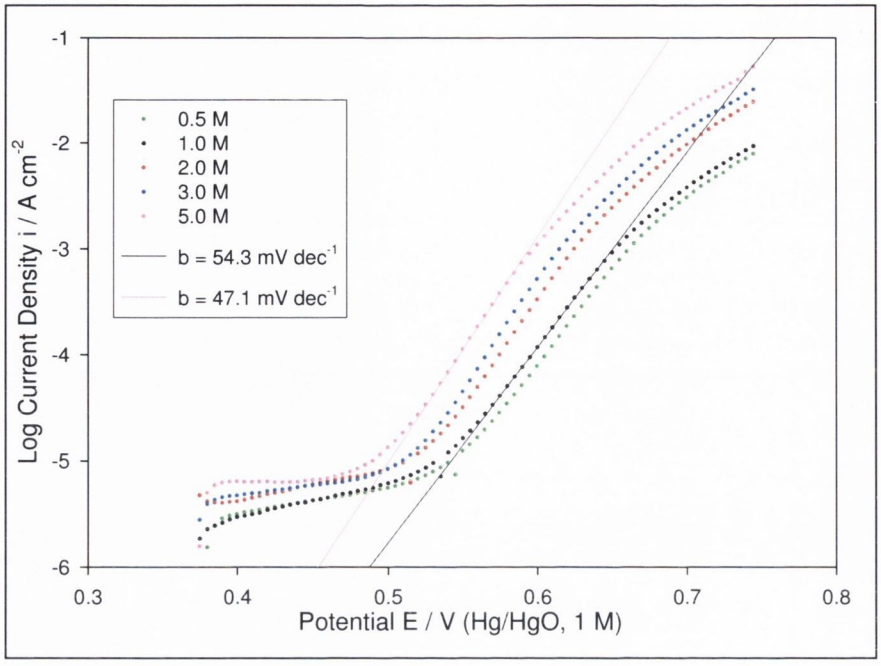


Figure 3.3.22 *IR corrected steady state polarisation curves recorded in the direction of increasing potential on a pre-oxidised Co electrode (see text for further details) in NaOH solutions of various concentration at 25°C.*

Examining Figure 3.3.22, the pre-oxidation regime appears to have had the effect of increasing the Tafel slope at all OH^- concentrations by ca. 7 mV dec^{-1}, relative to those observed for fresh non-pre-treated electrodes (see Figure 3.3.1). Thus, unlike the previously considered pre-reduction regime, the pre-oxidation is unable to produce a catalytic oxide that displays the same Tafel slope in polarisation measurements, across a range of OH^- activities. It will be shown in section 3.5, that, while a theoretical basis can be provided for Tafel slopes of ca. 46 – 47 mV dec^{-1} (~ 2.303 × 4/5 RT/F at 25°C), it is difficult to rationalise a slope of ca. 54 mV dec^{-1}, as has been observed for the pre-oxidised Co electrode in 1.0 M NaOH. Interestingly, in one of the few published steady state polarisation studies on the o.e.r. at polycrystalline Co electrodes in alkaline media, Burke et al.[17] noted a Tafel slope of ~ 52 mV dec^{-1}in 6.0 M NaOH at 30°C, for an initially bright Co electrode, on which a thick hydrous oxide was grown by potential cycling in the same solution. These workers also admitted that such a Tafel slope was difficult to reconcile theoretically, with any possible kinetic reaction mechanism, and made the tentative suggestion that rate control in this case might be due to a combination of steps within a given pathway.

Reaction order plots (Figure 3.3.23) were constructed, based on the polarisation curves of Figure 3.3.22. The same possible reservations are attached to the interpretation of reaction order data extracted from the plots of Figure 3.3.23, as were highlighted earlier in the case of bright non-pre-treated Co anodes, owing to the variation in Tafel slope with OH^- activity that is evident in Figure 3.3.22. It is evident

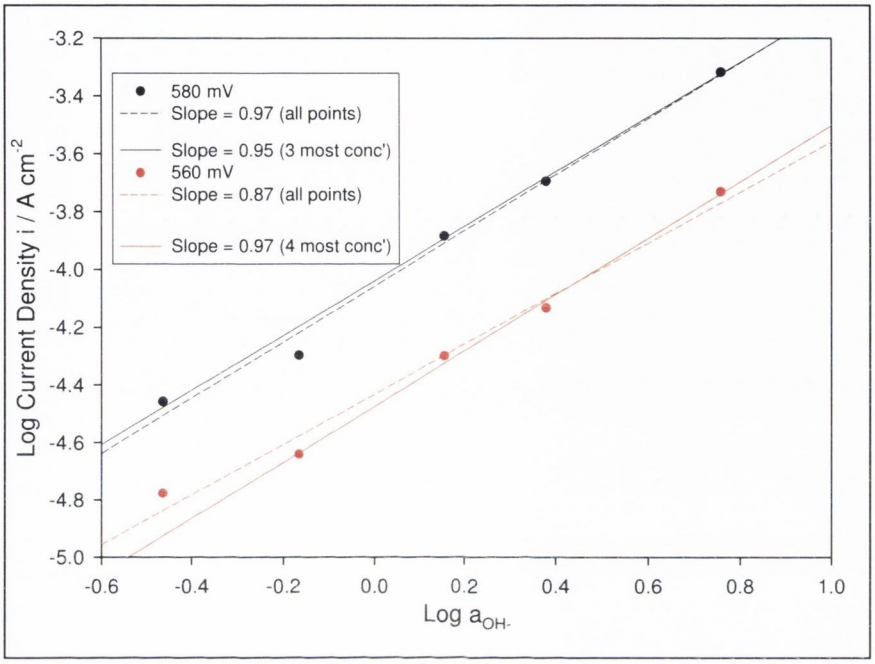


Figure 3.3.23 *Reaction order plots based upon the polarisation curves of Figure 3.3.22 at potentials of 560 and 580 mV.*

that this variation, affects the linearity of the data presented in Figure 3.3.23. Owing to the large disparity between the slopes obtained in the most concentrated (5.0 M) and most dilute (0.5 M) electrolyte solutions, it was necessary to neglect the data points related to the latter, in order to achieve a satisfactory degree of linearity. Following this approach, it would seem that the polarisation measurements on the pre-oxidised Co electrodes are again indicative of a reaction order of approximately unity. A comparison of steady state polarisation curves recorded in 5.0 M NaOH, for the same Co electrode, subjected to the various pre-treatments (or lack thereof) outlined previously, is presented in Figure 3.3.24. It is apparent, that at lower overpotentials, the non-pre-treated, and pre-oxidised electrodes, display similar activities towards the

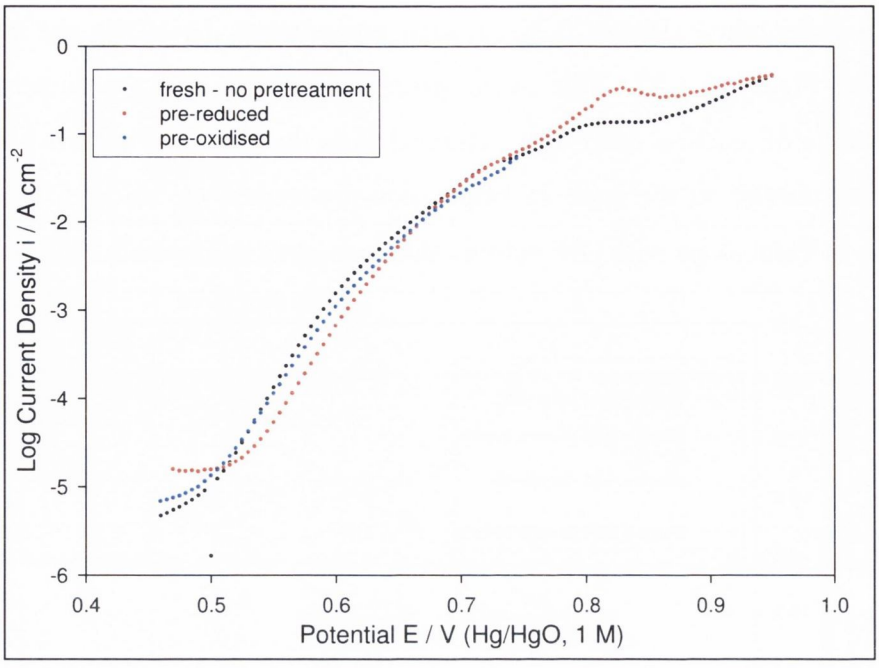


Figure 3.3.24 *Comparison of the 1st steady state polarisation plots in the forward direction in 5.0 M NaOH, for the same polycrystalline Co electrode, subjected to the various pre-treatment regimes described previously in the text.*

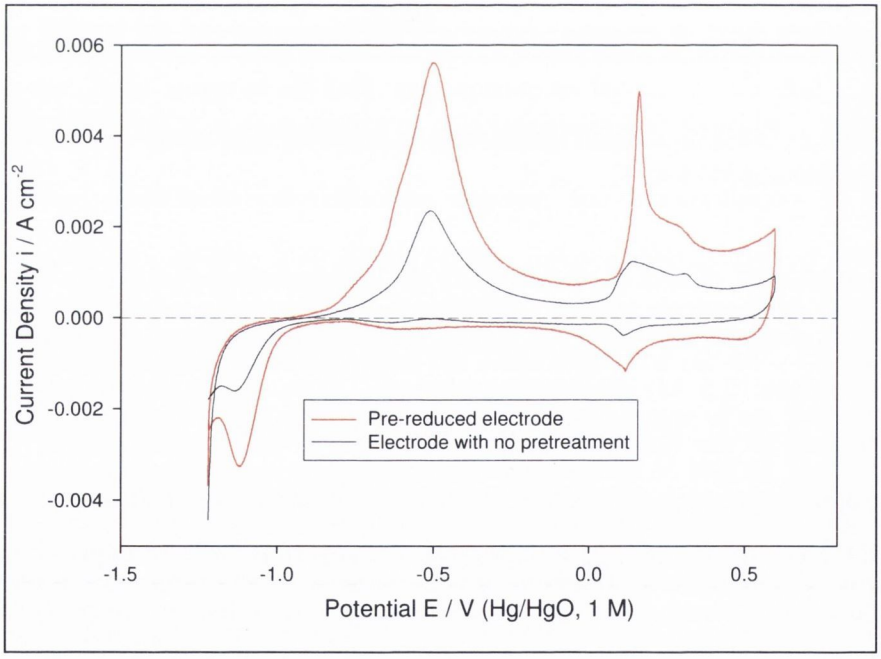


Figure 3.3.25 *CVs, recorded in 1.0 M NaOH, characterising the surface electrochemistry of the electrodes on which the "fresh" and "pre-reduced" polarisation curves of Figure 3.3.24 were recorded. The scan rate was 40 mV s^{-1}.*

o.e.r. The current density recorded at the pre-oxidised electrode becomes steadily less than that at the fresh electrode with increasing potential, owing to the higher Tafel slope (ca. 47 mV dec^{-1}) characteristic of the former electrode relative to the latter (ca. 40 mV dec^{-1}). Of the three types of electrode considered, the pre-reduced electrode displays the lowest catalytic activity towards oxygen evolution at low overpotential. A current density of 0.234 mA cm^{-2} was recorded at a potential of 560 mV for the non-pre-treated electrode, whereas the corresponding value for the pre-reduced electrode at this potential was 62% smaller (0.0905 mA cm^{-2}). While the kinetics of oxygen evolution were characterised by similar slopes of ~ 40 mV dec^{-1}, for the fresh and pre-reduced electrodes in the lower overpotential region, this slope persisted to higher current densities in the latter case, with the result that polarisation curves converge at potentials in the vicinity of 700 mV. At higher potentials, in the vicinity of the peak-like feature above ca. 760 mV, the current density recorded at the pre-reduced electrode is greater than that observed at the fresh electrode. Finally, the fresh and pre-reduced curves converge again, at the highest potentials (→ 950 mV) considered.

Characterisation of "fresh" and "pre-reduced" electrode surfaces, similar to those on which the directly aforementioned polarisation curves were recorded, had previously been attempted by cyclic voltammetry in 1.0 M NaOH. The resulting voltammograms are compared in Figure 3.3.25. Evaluation of the active charge capacities by the usual method yields; Q_{fresh} = ~3.1 mC cm^{-2}, while $Q_{pre\text{-}red}$ = ~10.1 mC cm^{-2}. However, as discussed above, despite its smaller calculated active charge capacity, the "fresh" electrode displays superior catalytic activity towards the o.e.r., relative to the "pre-reduced" electrode, at potentials between ~ 520 and 680 mV in 5.0 M NaOH (Figure 3.3.25). As with the "fresh" and "intermediate aged" electrodes of Figures 3.3.9 and 3.3.10, this indicates that, for a comparison of Co anodes in alkaline solution, superior redox activity towards the Co(II)/Co(III) → Co(IV) transition, is not necessarily indicative of similarly superior electrocatalytic activity towards the o.e.r. at higher anodic potentials.

In view of the conclusions of Gennero De Chialvo et al., that o.e.r. catalytic activity is directly proportional to the active charge capacities related to the Ni(II)/Ni(III) transition[6], or the Co(II)/Co(III) transition[19] for the respective metallic electrodes, provided that the *same type* (i.e. similarly prepared) *of oxide* is compared, it seems likely that the properties of the oxide surface produced by the pre-reduction regime are somewhat different to those found for the fresh electrode. That this is the case is

also suggested by the CVs of Figure 3.3.25. Although the profiles for the non-pre-treated, and pre-reduced electrodes are generally similar, except that the charge capacities associated with the various redox processes are much larger for the latter electrode, there is a noteworthy difference in the forms of the anodic scans above ca. 100 mV. For the pre-reduced electrode a narrow sharp peak centred at ~ 160 mV is evident, with a reasonably well-defined shoulder apparent at higher potentials (200 – 350 mV). The tall, narrow peak is indicative of a sharp Co(II)/Co(III) oxide phase transition, presumably producing a well defined relatively crystalline material. Such a sharp transition is absent from the voltammogram of the non-pre-treated electrode, being replaced by a broader less well defined peak, with evidence of an anodic shoulder at ca. 300 mV. Although, as pointed out by Burke et al.[17], extraction of detailed information relating to the Co(II)/Co(III) transition from voltammetry is difficult, owing to the large background currents in this potential region, it would seem reasonable to suggest that the oxide formed on the non-pre-treated electrode is of a more dispersed, less well structurally defined nature, than that formed following pre-reduction of the electrode at –1.15 V in 1 M NaOH. Thus, while the former electrode, may display a lower active charge capacity than the pre-reduced anode, its more defective oxide seems to offer a superior catalytic surface for the o.e.r. (at lower overpotentials in any case).

So far, no comment has been passed on the peak-like feature or "hump", observed at higher overpotentials in steady-state polarisation curves recorded in the direction of increasing potential, for all of the Co electrodes (various pre-treatments) utilised in the present work. This feature is evident in Figure 3.3.24, at potentials between approximately 750 and 850 mV for the "fresh" and "pre-reduced" electrodes in 5.0 M NaOH, and is also apparent in the same potential range on the second forward sweep for a "pre-oxidised" electrode in the same solution in Figure 3.3.21. This feature hasn't been discussed in any of the (scarce) detailed steady state polarisation studies on the o.e.r. at Co that have been identified in the literature[15, 17, 19], since the workers involved did not extend their measurements to the high overpotentials applied in the present work. The polarisation "hump" may be due to mass transport limitation on the kinetics of the o.e.r. at lower overpotentials, although this remains speculation in the absence of working electrode rotation. Alternatively, it may be due to some parasitical corrosion process (c.f. reference 14), which is also related to the hysterisis observed between the current responses on the forward and reverse steady-state polarisation

sweeps for Co electrodes. In any case, steady state measurements alone are inadequate to elucidate the origins of this "hump".

The final results to be discussed in the present section are related to experiments, in which cyclic voltammograms were recorded, initially in the cathodic direction, on Co electrodes that had just undergone an extended polarisation in the significant oxygen evolution region, without breaking the circuit between the polarisation and the potentiodynamic measurements. Recall that similar experiments were described for Ni in section 3.2, the results of which were presented in Figure 3.2.21. In the case of Co, a bright electrode was polished, placed in 1.0 M NaOH, and without further pre-treatment, two voltammetric cycles were recorded continuously, initially in the cathodic direction, between the limits of 780 mV and – 300 mV at a scan rate of 40 mV s^{-1}. The electrode potential was then allowed to relax on open circuit, before the electrode was removed from solution and polished in the usual manner. Following this the electrode was replaced in 1.0 M NaOH, and polarised at 780 mV for 10 hours.

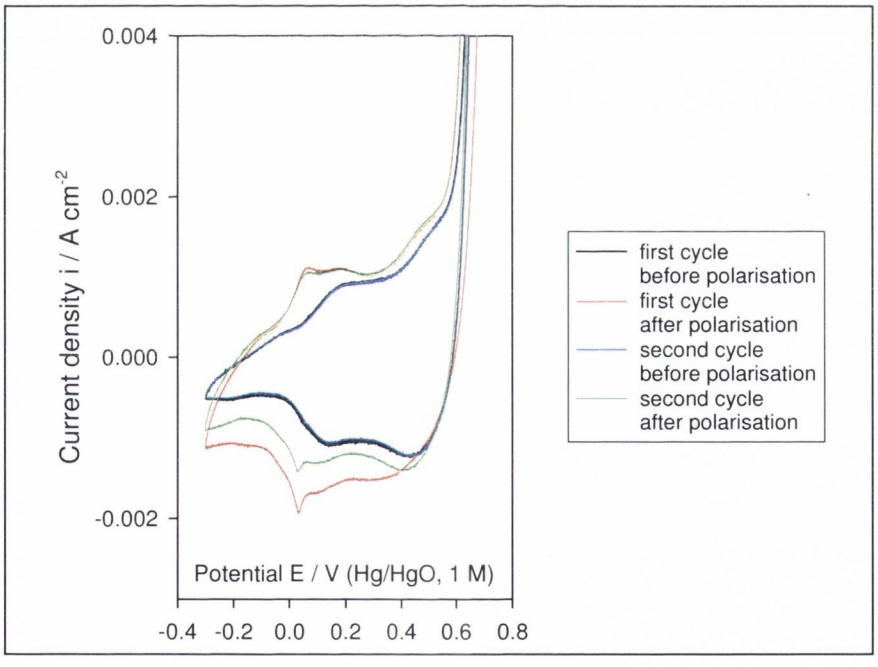


Figure 3.3.26 *Cyclic voltammograms characterising a polycrystalline Co electrode surface, both prior to, and following potentiostatic polarisation at 780 mV for 10 hours. The system was not allowed to relax on open circuit following the polarisation – i.e. the post polarisation CVs were recorded directly after the end of the 10 hour period, commencing in the cathodic direction. All CVs were recorded at 40 mV s^{-1} in 1.0 M NaOH at 25°C.*

Directly after this 10hour polarisation, two further cyclic voltammograms were recorded, with the same control parameters as before. The voltammograms recorded

on the freshly polished, and extensively polarised electrodes are compared in Figure 3.3.26. A relatively long time (ca. 1450 s) was required for the establishment of a steady state current, following the large initial potential step from the open circuit potential (ca. –0.75 V) to the anodic polarisation potential (0.78 V). The steady state current observed after 1450 s was 1.50 mA cm^{-2}. In contrast to the > 80% reduction in o.e.r. steady state current recorded over the course of a 10 hour polarisation at 655 mV for a Ni electrode, as described in section 3.2, there was only a small reduction in the steady state current for Co to 1.46 mA cm^{-2} after 10 hours of polarisation. These results are, of course, not directly comparable since the polarisations were conducted at widely different oxygen overpotentials, however they are noted here in the context of a full description of the respective experiments.

Examining Figure 3.3.26, it is evident that there are significant differences between the voltammograms recorded on the bright and post polarisation electrodes. It is probably most appropriate to compare the more stabilised second post polarisation scan to the bright electrode profiles. Essentially, it would appear that the differences between this second post polarisation scan and the bright electrode scans arise, due to the presence of an addition sharp cathodic peak at ~ 40 mV in the former. A corresponding anodic peak is evident at ~ 60 mV on the subsequent anodic half-cycle. Although, there is an enhanced active charge capacity associated with the second post polarisation scan, it is quite evident that the broad cathodic peaks centred at ~ 420 mV and ~100 mV are related to corresponding peaks in the profiles of the bright electrode. Similarly it seems, for the second post polarisation CV, that the anodic peak centred at ~ 180 mV, and that at potentials immediately preceding significant o.e.r. currents, have analogues in the "bright" electrodes scans.

As with the assignment of any voltammetric peaks in the Co(II)→Co(III) region of potential, the large background currents and the variety of different possible Co(III) products[17], renders identification, with a specific redox process, of the additional sharp peaks in the post polarisation CV, as somewhat arbitrary. If it is true, as would be intuitively expected, that redox transitions of materials with a well defined stoichiometry, are manifested in voltammetry as sharper peaks than those associated with the redox transitions of less stoichiometric materials, then the appearance of addition sharp peaks in the post polarisation profiles of Figure 3.3.26, would indicate the presence of a more stoichiometric oxide in the surface region following the 10 hours of polarisation. This is readily understandable in terms of the dehydration

during oxygen evolution, of the surface layers of a somewhat hydrous oxide formed initially on polycrystalline Co, at potentials below those associated with significant o.e.r. currents.

3.4 Iron: Steady State Polarisation and Voltammetry Results

3.4.1 Bright Non-pre-treated Fe Electrodes

As with the Ni and Co electrodes discussed in the previous sections, cyclic voltammetry was employed to characterise the surface electrochemistry of polycrystalline Fe electrodes, before their use as oxygen evolution anodes. Upon repetitive cycling of a bright Fe electrode in 1.0 M NaOH, many of the characteristic electrochemical features of this system, as previously described by earlier workers (see section 1.4.2), were observed. The results of this experiment are outlined in Figure 3.4.1. The first, second and third voltammetric cycles of Figure 3.4.1 were recorded continuously at a scan rate of 40 mV s^{-1} between limits of –1.3 and 0.75 V, on an initially bright Fe electrode. The next six cycles (not shown) were conducted at a more rapid sweep rate of 300 mV s^{-1} between these same limits, before the recording of the 10^{th} cycle at 40 mV s^{-1}. A relatively thick hydrous oxide film was then produced, as previously described by Burke and Lyons[26], using repetitive potential cycling for 89 cycles between the limits mentioned above. Finally, an analytical scan (100^{th} cycle) was recorded at 40 mV s^{-1}. The hydrous oxide layer formed by the procedure described above was visually evident from its golden-brownish colour, as compared with the initial "mirror bright" appearance of the electrode. It is apparent that the general profiles of the voltammograms of Figure 3.4.1 are in agreement with those depicted in Figure 1.4.8, although owing to the magnitude of the peaks of the 100^{th} cycle, the fine structure of the traces of the earlier cycles is not particularly evident. This fine structure is much clearer in the profiles of Figure 3.4.2, and will be discussed shortly.

With regard to Figure 3.4.1, it is noted that the voltammetric profile of the initially bright Fe electrode changes, with repetitive cycling, exactly as was described by Burke and Lyons[26]. That is to say (adopting for the moment, the same peak naming scheme as these authors – see Figure 1.4.8(a)), that only peak A3, associated with the Fe(II)/Fe(III) transition in a hydrous oxide phase (recall for example reactions (1.4.14) or (1.4.15)), and its complementary cathodic peak C2 become enhanced on

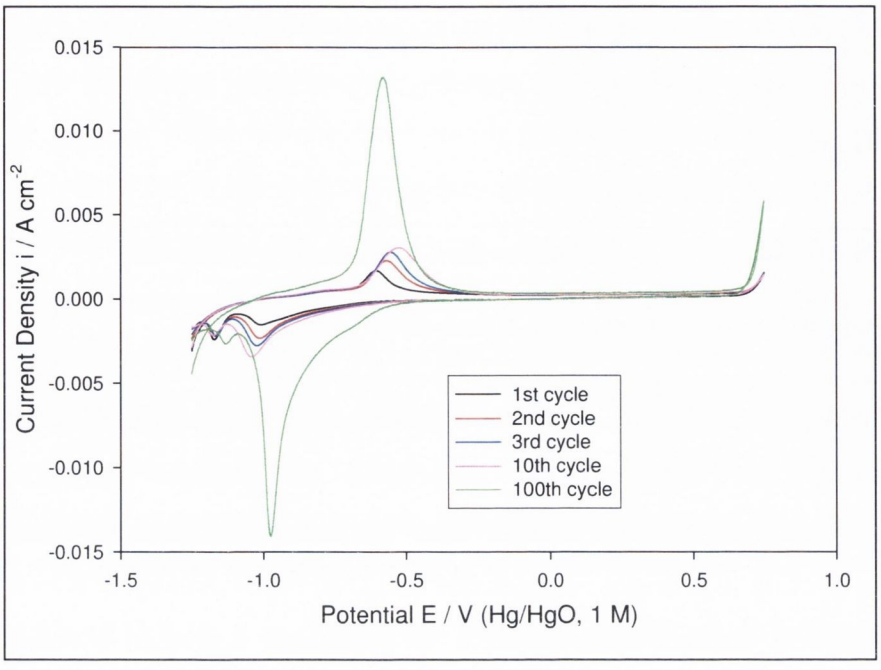


Figure 3.4.1 *Analytical CVs (cycle number as indicated in the legend) recorded at 40 mV s^{-1}, of an initially bright polycrystalline Fe electrode in 1M NaOH. All CVs recorded between –1.3 and 0.75 V at 25°C. The intervening cycles were performed between the same limits at 300 mV s^{-1}.*

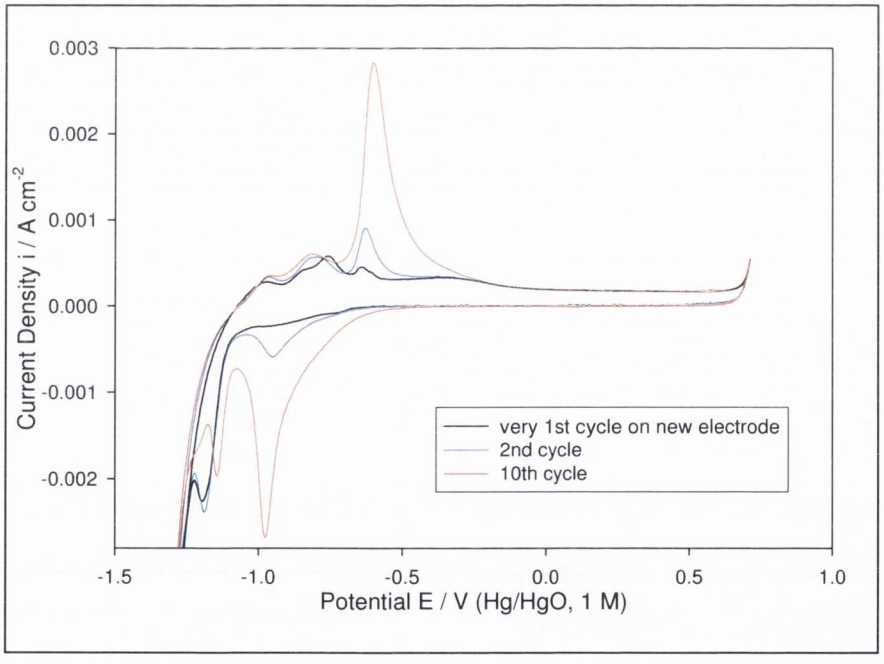


Figure 3.4.2 *First series of voltammograms performed on a freshly prepared polycrystalline Fe electrode in 1.0 M NaOH at 25°C. Reproduced above are the profiles of the 1^{st}, 2^{nd} and 10^{th} sweeps. These scans and the 3^{rd} – 9^{th} sweeps were recorded continuously at a rate of 40 mV s^{-1}, between limits of –1.42 and 0.68 V.*

repetitive potential cycling. It is obvious from the voltammetric profiles of Figure 3.4.1, that the activity of the electrode surface towards the o.e.r. becomes enhanced with repetitive cycling – the rising edge of significant oxygen evolution current clearly becomes significant at lower potentials in the trace of the 100^{th} cycle relative to those of the earlier cycles. Therefore it can be concluded that the relatively thick hydrous oxide film formed as described above, is a superior o.e.r. electrocatalyst compared to the oxide formed initially on a bright Fe electrode, when its potential is swept towards high anodic values. Of course, as discussed in Chapter 2, cyclic voltammetry at scan rates such as those employed here, is not an appropriate experimental method for the characterisation of the kinetics of oxygen evolution, and so the conclusion of the previous sentence is made on a qualitative rather than quantitative basis. Indeed no effort has been devoted, in the present work, to a more comprehensive study of the o.e.r. on thick hydrous oxide films formed by repetive potentiodynamic cycling of Fe in alkaline media, since this subject has previously been probed by Lyons and Burke[27, 28].

The observation in Figure 3.4.1 of enhanced catalytic activity towards oxygen evolution on specifically prepared hydrous iron oxyhydroxide films, relative to initially bright iron substrates, corroborates results reported by the latter authors [27, 28]. As was briefly mentioned in section 1.5.4, steady state polarisation measurements conducted by these workers, indicated an approximate ten-fold enhancement in o.e.r. current density at an oxygen overpotential of 421 mV (converted from R.H.E scale used in refs 27, 28) for a multi-cycled Fe electrode in 1 M NaOH, relative to a non-cycled Fe anode in the same electrolyte solution. Significantly however, the same Tafel slope behaviour was observed in both cases (a slope of ~ 60 mV dec^{-1} at lower overpotentials, rising to ~ 120 mV dec^{-1} with increasing potential), indicating a common o.e.r. pathway. The authors proposed a modified Krasil'shchikov mechanism (reproduced in chapter 1 as equations (1.5.23 I-IV)), however their analysis was based solely on Tafel slope parameters. Further experimental testing of this hypothesis, was the original motivation for oxygen evolution studies, early in the course of the laboratory work on which the present thesis is based. Since Lyons and Burke found that the pathway for oxygen evolution is apparently the same on both, initially bright and cycled Fe electrodes, it was decided, from the point of view of mechanistic determination, to concentrate on the former electrode type, and so, as mentioned above, no steady state measurements were conduced on pre-cycled electrodes in the

present work. In principal, if the reaction mechanisms are the same on both types of Fe electrode, the mechanistic data obtained from multi-cycled electrodes should lead to the same overall conclusions, as that recorded from initially bright electrodes. However we choose to work with bright electrodes, since we were interested in determining the "intrinsic" mechanism (recall the comments made on this concept in relation to the o.e.r. on Ni in section 3.2) of oxygen evolution on polycrystalline Fe anodes, if indeed such a concept is actually meaningful. In any case, it will be shown that experimental observation of dual ~ 60/120 mV dec^{-1} Tafel slope behaviour for the o.e.r. on a "bright" Fe electrode, is not a trivial matter.

Having reviewed the literature on the electrochemistry of the iron electrode in alkaline media, Amaral et al.[29] commented that, in cyclic voltammetry experiments "three or four anodic and one or two cathodic peaks are normally identified". Indeed in the literature review on the same system in section 1.4.2 of the present work, it was noted (Figure 1.4.3) that there were significant differences in the voltammetric profiles recorded by different workers for bright Fe electrodes in 1.0 M NaOH at 25°C. Thus it seems, that it would be fair to comment, that a reasonable amount of irreproducibility exists in the literature, between voltammetric measurements on Fe electrodes in alkaline solution, provided by different workers. While much of this disparity probably arises owing to differing experimental conditions (i.e. upper and lower voltammetric limits, scan rates, pre-treatments, electrolyte concentration) utilised by different workers, the data of Figure 3.4.2 exposes another, more fundamental factor, that will lead to irreproducibility in such voltammetric measurements.

The scan denoted as the "very first cycle on new electrode" is just that – it was recorded on a freshly prepared iron foil electrode (see section 2.2.2), which had been exposed to alkaline solution for the first time, immediately before the experiment was conducted. This profile represents what is probably the closest possible approximation (under normal ambient laboratory conditions) to the CV of an initially "truly bright" Fe electrode in alkaline solution. In this context "truly bright" refers to an electrode free from any residual anodic oxide that is resistant to removal by normal polishing procedures. The effects of such residual oxides on the ageing of Ni and Co electrodes were considered in the previous two sections.

The above claim regarding the initially "truly bright" electrode is based upon the fact that the upper cathodic peak (denoted C2 in the scheme of Burke and Lyons[26] – see

Figure 1.4.3 (a)) is virtually absent in the first cycle of Figure 3.4.2. In addition the corresponding anodic peak (A3 in scheme of Burke and Lyons), which appears at potentials between ca. –625 and –650 mV in Figure 3.4.2, has a very small charge associated with it on the first cycle. It is this pair of peaks that increase in magnitude with repetitive cycling, as is apparent from the profiles of the second and tenth cycles. As was discussed in section 1.4.2 and referred to again earlier in the present section, Burke and Lyons[26] have provided very strong arguments, based on observed peak potential shifts with electrolyte pH, to show that this peak pair corresponds to the formation and reduction of a complex, hydrous, outer, Fe(III) oxyhydroxide based, passivating film. In view of this, the first cycle of Figure 3.4.2, obviously represents the very earliest stage of the passivation of a bright Fe electrode, where the formation of the aforementioned hydrous outer oxide is barely significant. The importance of this process has obviously increased by the second cycle, with significant enhancements in the magnitudes of the anodic peak centred at ~ -625 mV and the corresponding cathodic peak centred at ~ -950 mV. Five anodic peaks are apparent in the profile of the first cycle, with the peak centred at ~ -750 mV and the "shoulder" at ~ -850 mV apparently evolving into one peak centred at ~ -800 mV on the second and subsequent cycles. The second cycle therefore displays four anodic peaks and is very similar in profile to that recorded by Burke and Lyons[26] for a bright Fe electrode in 1.0 M NaOH at 40 mV s^{-1} and reproduced in the present work as Figure 1.4.3 (a).

A further significant observation is that, upon removing the electrode from solution, polishing to a bright finish, and replacing in 1.0 M NaOH, it was impossible to record a voltammetric profile similar to the first cycle of Figure 3.4.2. Instead the profile was more reminiscent of the second cycle of Figure 3.4.2 (or equivalently the CV of Figure 1.4.3 (a) due to Burke and Lyons[26]), with A3 and C2 peaks of significant magnitude. This behaviour is apparent in the first cycle of Figure 3.4.1, which was recorded on a slightly aged Fe electrode, polished to a bright finish (for a clearer view of this type of first cycle see Figure 3.4.22). Indeed, the only way to recapture a bright Fe electrode voltammogram, similar to the first cycle of Figure 3.4.2, was to completely destroy the electrode surface by thorough sanding with rough grit paper, followed by re-preparation of the electrode.

The behaviour described above, suggests that upon the initial passivation of a Fe electrode in alkaline solution, a strongly bound thin compact oxide layer is formed that is resistant to subsequent removal by mechanical polishing. When the apparently

bright electrode is again subjected to potential cycling following such polishing, the passivation process effectively resumes from the second cycle of Figure 3.4.2. It may be that the residual oxide that remains after polishing, provides a "structural template" that facilitates the formation of the outer passive film (see duplex layer model – Figure 1.4.9) more readily than on a bare metal surface (in as much as an Fe surface will ever be free of some native oxide formed in air or during polishing).

While, the foregoing discussion is of more direct relevance to the theory of the passivation of iron in concentrated alkaline solution, than it is to oxygen evolution on Fe anodes, it does point to the fact that electrode ageing is again likely to have a significant influence on the latter process. It will be shown presently, that this is indeed the case, with electrode ageing making it virtually impossible to obtain reproducible steady state polarisation data for non-pre-treated "bright" Fe electrodes.

A typical bi-directional polarisation curve for the o.e.r. on such a "bright" Fe electrode in 1 M NaOH is presented in Figure 3.4.3. This particular curve was recorded initially in the direction of decreasing potential, following the establishment of a steady state current at the upper overpotential, η, of 647 mV. A very significant hysterisis is apparent between the polarisation sweeps in opposite directions, over the entire examined range of significant values of oxygen evolution current density (i.e. $10^{-6} \leq i \leq \sim 10^{-1}$ A cm^{-2}). This contrasts with the hysterisis observed in polarisation curves for oxygen evolution at Ni and Co electrodes, where the sweeps in opposite directions, although displaying hysterisis at higher current densities, were largely co-incident at lower current densities. At η = 347 mV, a current density of i = 47.9 μA cm^{-2} was observed for the reverse direction sweep of Figure 3.4.3.

At the same overpotential in the subsequent forward direction scan this value had decreased by ca. 78% to i = 10.2 μA cm^{-2}. This enhancement of oxygen evolution catalytic activity on reverse direction sweeps relative to those in the forward direction, turns out to be a general phenomenon for Fe electrodes, and is independent of the order in which the scans in opposing directions are recorded – see Figure 3.4.7. For the present, it is noted that the Tafel slopes in the lower overpotential region (approximately 300 mV $\leq \eta \leq$ 420 mV) are approximately equal with values of 36 - 37 mV dec^{-1}.

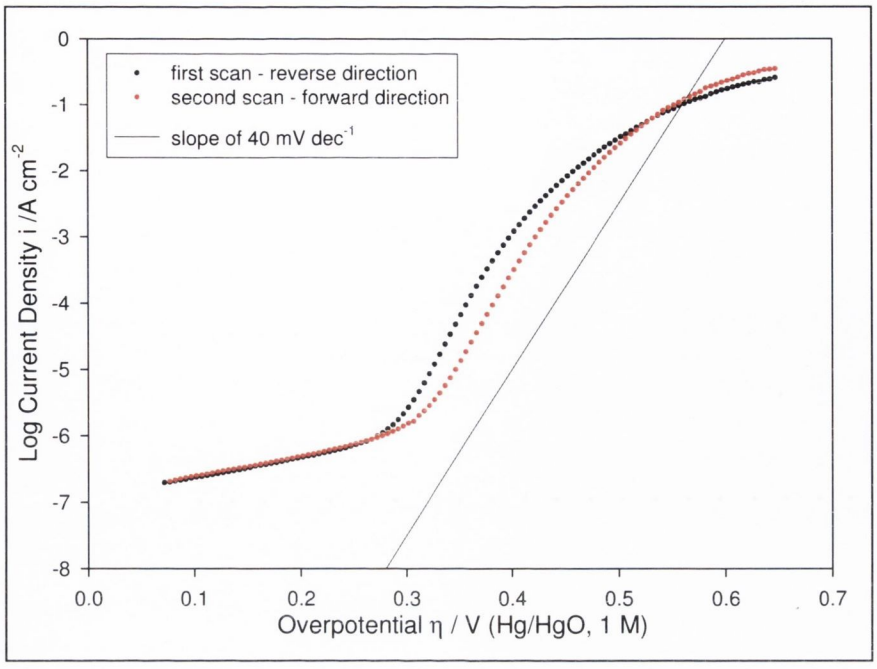


Figure 3.4.3 *Bi-directional IR corrected steady state polarisation curve recorded continuously on a bright Fe electrode in 1M NaOH, initially in the direction of decreasing potential, at 25°C.*

An attempt was made to determine the reaction order, m_{OH^-}, associated with this Tafel region, by recording oxygen evolution steady state polarisation curves for a bright Fe electrode in various NaOH solutions, with concentrations ranging from 0.5 – 5.0 M. The "bright" electrode was prepared by polishing of the surface in the usual manner, with no further pre-treatment. The first of the series of steady state polarisation curves was recorded in 0.5 M NaOH, with the other measurements performed in order of increasing OH^- concentration, on successive days (one experiment per day). These polarisation curves are presented in Figure 3.3.4. For the purpose of comparison the reverse direction polarisation curve (1.0 M) of Figure 3.4.3 is included. This was recorded immediately prior (i.e. the day before) to the commencement of the concentration studies as described above. The lack of co-incidence between the two 1.0 M traces of Figure 3.4.4 is the first of several difficulties, which one might note in relation to the results of that figure, from the point of view of extracting meaningful values of the reaction order parameter. Owing, presumably to some electrode ageing process, the o.e.r. activity of the "bright" electrode has decreased significantly in the "black" polarisation curve relative to the "red" polarisation curve of Figure 3.4.4, even though the latter was recorded just two days before the former. In the intervening period the 0.5 M polarisation curve was recorded, and the electrode was polished to a mirror bright finish, before and after each measurement.

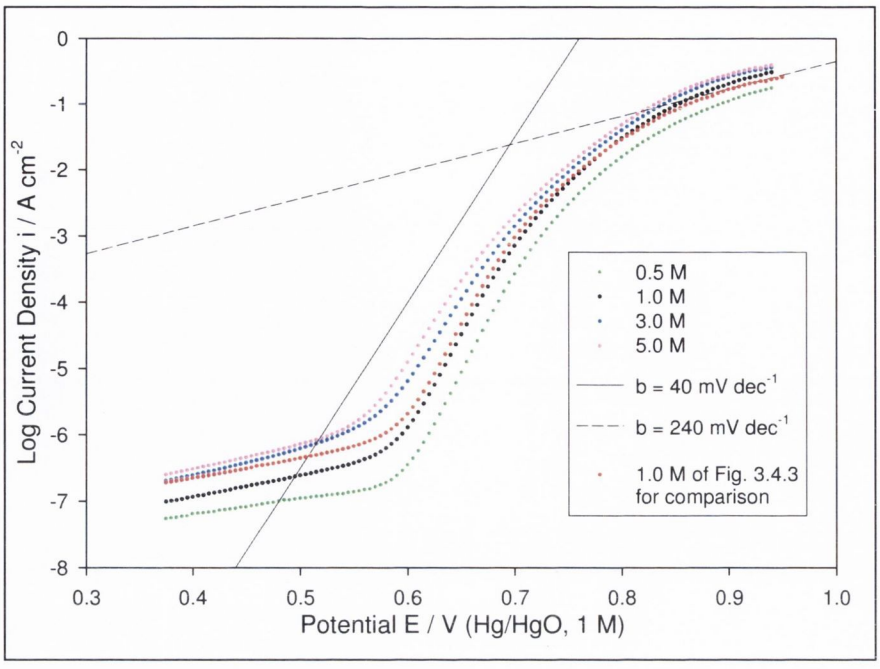


Figure 3.4.4 *IR corrected steady state polarisation curves recorded in the direction of decreasing potential on an initially "bright" Fe electrode (no electrochemical pre-treatment) in NaOH solutions of various concentrations at 25°C.*

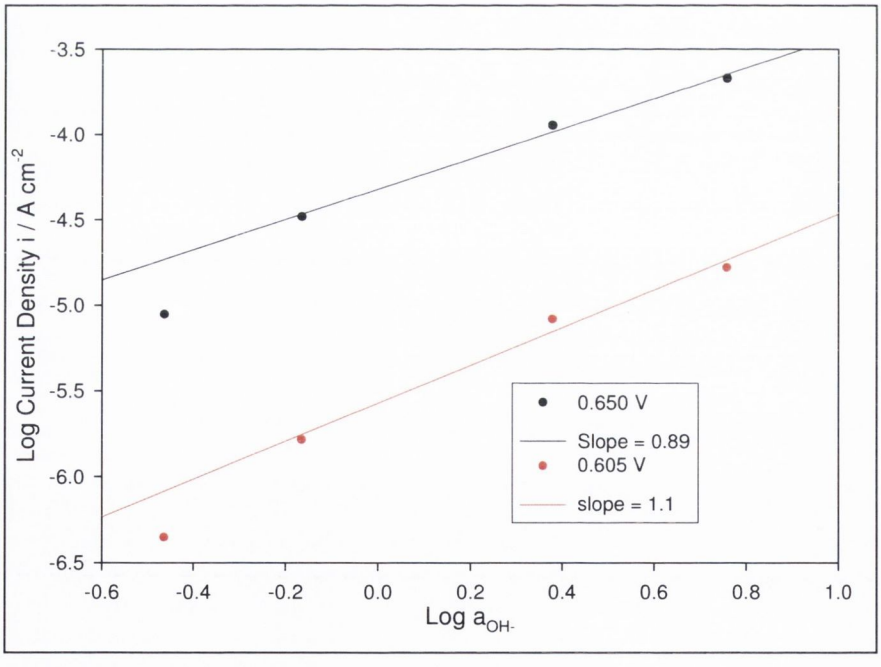


Figure 3.4.5 *Attempts to extract reaction order parameters from the steady state polarisation curves of Figure 3.4.4, at potentials of 605 and 650 mV.*

A decrease in electrode activity was also noted when the steady state polarisation experiment was repeated in 0.5 M NaOH, after the completion of the experiments detailed in Figure 3.4.4, although, just as with the 1.0 M curves of that figure, it was observed that the Tafel slope remained essentially constant. It would therefore appear, that it is extremely difficult to record reproducible oxygen evolution polarisation data for bright Fe anodes, probably due to electrode ageing effects related to the inability of polishing alone, to completely remove the oxide formed during anodisation. Recall that similar problems were encountered with bright Ni electrodes in section 3.2, while in contrast, the polarisation behaviour of bright Co electrodes (section 3.3) displayed satisfactory reproducibility, over the course of a small number (< 10) experiments.

A further difficulty, with respect to the extraction of reaction order parameters from the data of Figure 3.4.4, is that the value of the Tafel slope in the lower overpotential region apparently increases with increasing OH^- activity. The slope over this range of potential has a value of b = ~ 36 mV dec^{-1} for the 1.0 M electrolyte, increasing to *b* = ~ 42 mV dec^{-1} for the 5.0 M solution. The possibility was considered that, this observed increase in Tafel slope with increasing OH^- activity was an artefact arising from electrode ageing (remember that the 5.0 M data was the last to be recorded), however this notion would seem to be dispelled by the results presented in Figure 3.4.6. These steady state polarisation plots were recorded on a "bright" Fe electrode (somewhat more aged than that used for the experiments of Figure 3.4.4), in order of decreasing electrolyte concentration. Although the Tafel slopes are slightly different to those noted in Figure 3.4.4, the same conclusion is suggested – i.e. the Tafel slope increases by approximately 6 – 7mV dec^{-1} upon increasing the NaOH solution concentration from 1 M to 5 M. Thus it would appear that the increase in slope with OH^- concentration is a genuine feature of the o.e.r. at initially "bright" Fe electrodes. Note that the polarisation curves of Figure 3.4.6 were recorded with a initial forward direction sweep, in contrast to those of Figure 3.4.4 – hence while the recorded current density values depend on the sweep direction (Figure 3.4.3), the Tafel slope behaviour is independent of this direction. This gradual increase in Tafel slope with increasing OH^- concentration, is in direct contrast with the situation observed for bright Co electrodes in Figures 3.3.1 and 3.3.6, where the Tafel slope *decreased* by ca. 6 - 7 mV dec^{-1} on increasing the NaOH electrolyte concentration from 1.0 – 5.0 M. Issues regarding the relevance of reaction order parameters derived from polarisation

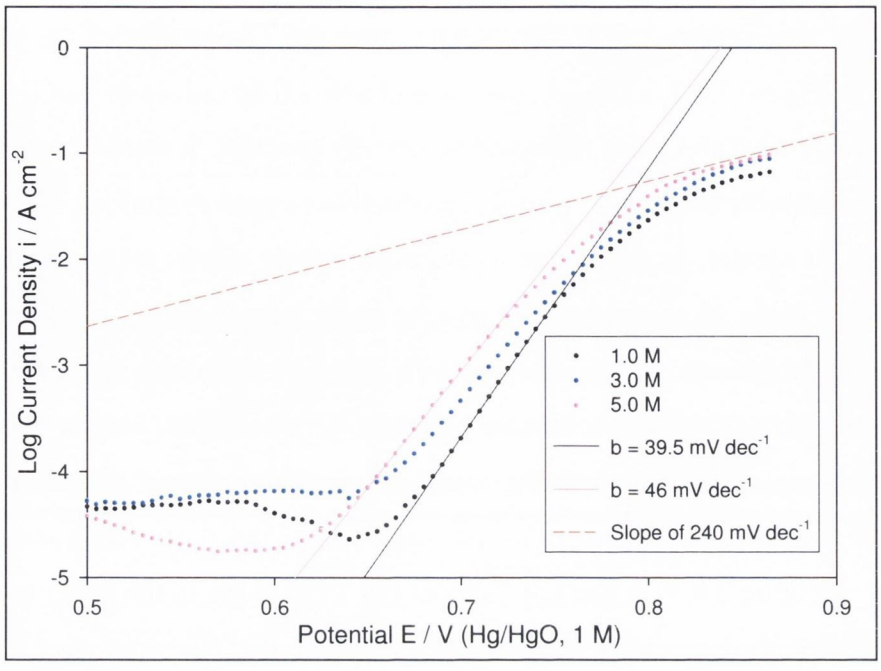


Figure 3.4.6 *IR corrected steady state polarisation curves recorded in the direction of increasing potential on an initially "bright" Fe electrode (no electrochemical pre-treatment) in NaOH solutions of various concentrations at 25°C.*

curves that exhibit a change in Tafel slope with changing OH^- activity, were discussed in section 3.3 with regard to the Co data cited in the previous sentence, and the potential reservations raised there are equally applicable to the present discussion. Nonetheless an attempt was made to glean a value for m_{OH^-} from the polarisation curves of Figure 3.4.4 – see Figure 3.4.5. Owing to the relative differences in Tafel slope recorded for the different OH^- concentrations, the value of $\left(\partial \log i / \partial \log a_{OH^-}\right)_E$ depends on the exact value of potential, E, within the straight line Tafel region at which this slope is evaluated. In the event, plots of log$i$ against loga_{OH^-} were constructed in Figure 3.4.5, for the lower (605 mV) and upper (650 mV) limits of the straight-line region observed for the 5 M case (note the straight line Tafel region is significantly longer for the 1.0 M solution). As was the case in the reaction order plot of Figure 3.2.14 for pre-reduced Ni anodes, it is necessary to neglect the data points of the most dilute (0.5 M) NaOH solution in order to achieve satisfactory linearity in the plots of Figure 3.4.5. Adopting such an approach, the plots indicate that a reaction order (if this is indeed truly meaningful) in the range of ~0.89≤ m_{OH^-}≤ ~1.1 is associated with the lower overpotential straight-line Tafel region.

3.4.2 Pre-reduced and Aged Fe Electrodes

Recall from section 3.3, that application of a pre-reduction regime to Co electrodes, yielded reproducible steady state polarisation curves, with practically constant, low overpotential, Tafel slopes of ca. 46 mV dec^{-1} over a range of OH^- activities, thus allowing the derivation of more reliable reaction order data, relative to the situation that prevailed for non-pre-treated electrodes. With this in mind, it was decided to adopt a similar approach for bright Fe electrodes, in the hope of obtaining reproducible o.e.r. polarisation data, that would form the basis of a more reliable determination of the reaction order associated with the straight line Tafel slope region. The pre-reduction regime for the Fe electrode consisted of an initial polishing step, followed by polarisation of the electrode at a potential of –1.1 V for a period of 5 minutes in 1.0 M NaOH. As can be appreciated from Figures 3.4.1 and 3.4.2, this potential lies at the lower end of the range of potentials associated with the reduction of the outer Fe(III) based passive film, while being too positive for significant hydrogen evolution to occur. The pre-treatment was completed by one potentiodynamic cycle between the limits of –1.175 and 0.625 V in the same 1.0 M NaOH solution at a scan rate of 40 mV s^{-1}. Following pre-treatment, the electrode was transferred to the relevant test solution, using the method outlined originally for Ni electrodes in section 3.2.

A bi-directional oxygen evolution steady state polarisation curve, recorded in 1.0 M NaOH for a "bright" Fe electrode that had been subjected to the pre-reduction procedure outlined above, is presented in Figure 3.4.7. While the traces recorded in the forward direction are effectively coincident along the length of the straight-line Tafel region, displaying a slope of ~ 40 mV dec^{-1}, it is apparent, just as in Figure 3.4.3, that there is significant hysterisis between the curves recorded in opposite directions. Again the reverse direction scan displays a greater activity towards the o.e.r. relative to the first forward scan, over a range of overpotentials from ca. 335 mV to ca. 500 mV. A comparison of the current density values for the first forward and reverse sweeps at η = 347 mV (as in the analysis of the non-pre-treated electrode data of Figure 3.4.3) shows that i = 40.4 μA cm^{-2} for the latter and i = 10.3 μA cm^{-2} for the former. Thus, while the recorded current density at η = 347 mV on the reverse sweep is somewhat smaller for the pre-reduced Fe electrode compared to the "bright" electrode of Figure 3.4.3 (47.9 μA cm^{-2}), the values of i at this overpotential on the

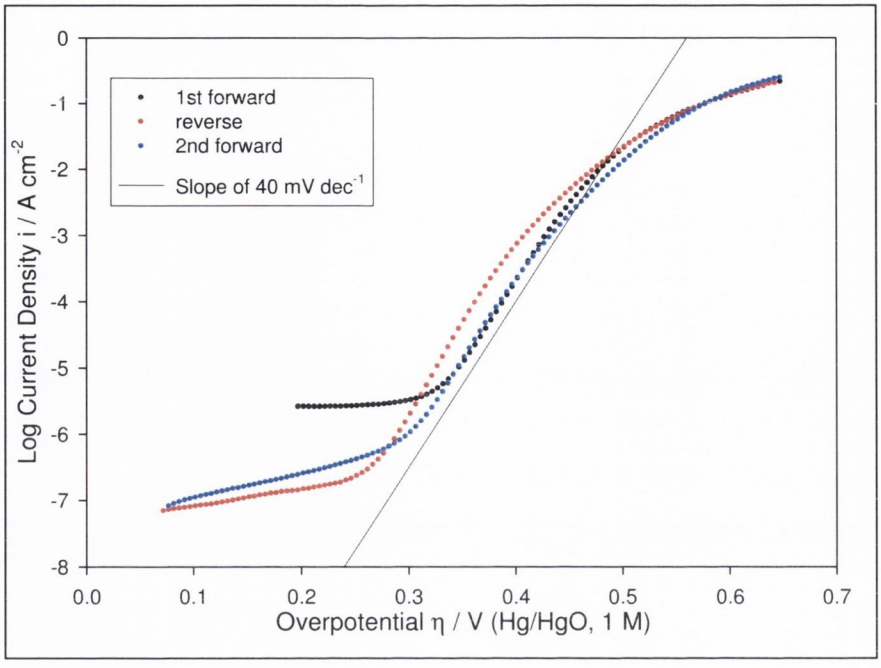


Figure 3.4.7 *Bi-directional IR corrected steady state polarisation curve recorded continuously on a pre-reduced Fe electrode in 1M NaOH, initially in the direction of increasing potential, at 25°C.*

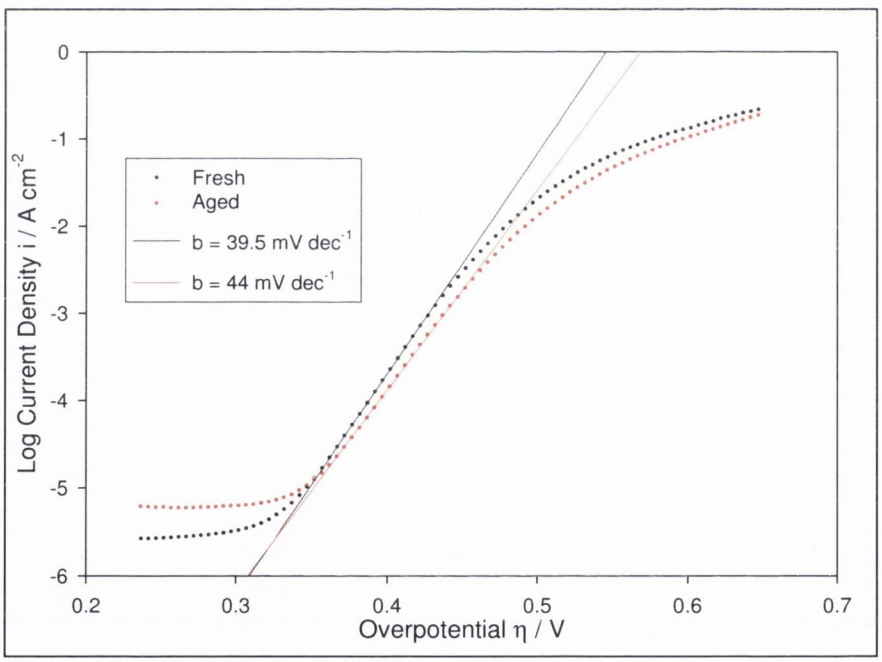


Figure 3.4.8 *IR corrected steady state polarisation curves, recorded in the direction of increasing potential in 1M NaOH, at 25°C, on a pre-reduced Fe electrode at different times in its life-cycle. The "Fresh" electrode had previously been used in 4 polarisation measurements, while the "Aged" electrode had been used in 15 previous polarisation experiments.*

respective forward sweeps are remarkably similar for both types of electrode (i = 10.3 μA cm^{-2} for pre-reduced, i = 10.2 μA cm^{-2} for non-pre-treated). The slope of the straight line Tafel region on the reverse sweep of Figure 3.4.7 is slightly less (~ 36 mV dec^{-1}) than that observed for the forward sweeps.

While it was possible to record reproducible o.e.r. steady state polarisation curves similar to that of Figure 3.4.7 for the first three or four polarisation experiments (each conducted following the application of the pre-reduction procedure), on a freshly prepared Fe electrode, it was noted that subsequent to the fifth such experiment the values of the Tafel slope began to increase by several mV dec^{-1}. After approximately 10 polarisation measurements the Tafel slope behaviour had stabilised sufficiently to allow a reliable series of polarisation curves at different OH^- concentrations to be recorded. A comparison of the forward direction steady state polarisation curves in 1.0 M NaOH, recorded early in the life cycle of a pre-reduced electrode (4^{th} polarisation measurement), and at the stage by which the Tafel slope behaviour had stabilised (16^{th} polarisation measurement), is presented in Figure 3.4.8. While a Tafel slope of 39.5 mV dec^{-1} was recorded when the electrode was relatively "fresh" as in Figure 3.4.7, this value increased by ca. 5 mV upon ageing of the electrode. Thus, while the electrode was subjected, before each polarisation measurement, to the pre-reduction regime outlined above, and was polished thoroughly subsequent to each experiment, it appears that an ageing process was still able to influence its electrocatalytic properties towards the o.e.r. The affects of this ageing process on the polarisation curves recorded in NaOH solutions other than 1 M are presented in Figure 3.4.9.

An examination of the CVs recorded as the final step of the pre-reduction procedure casts some light on possible reasons for the observed increase in Tafel slope with electrode ageing – see Figure 3.4.10. This figure shows the development of the CV profile of a Fe electrode from its initial characterisation after preparation (Fresh electrode), to the stage at which it has become well aged, after 20 steady state polarisation experiments in NaOH solutions of various concentrations, over a period of 39 days. The polarisation curve of Figure 3.4.8 displaying a Tafel slope of 39.5 mV dec^{-1} was recorded on the electrode characterised by the "After 4 scans" profile of Figure 3.4.10. The lower slope polarisation traces for 0.5 M and 5.0 M NaOH presented in Figure 3.4.9, were recorded on pre-reduced electrodes with similar voltammetric profiles.

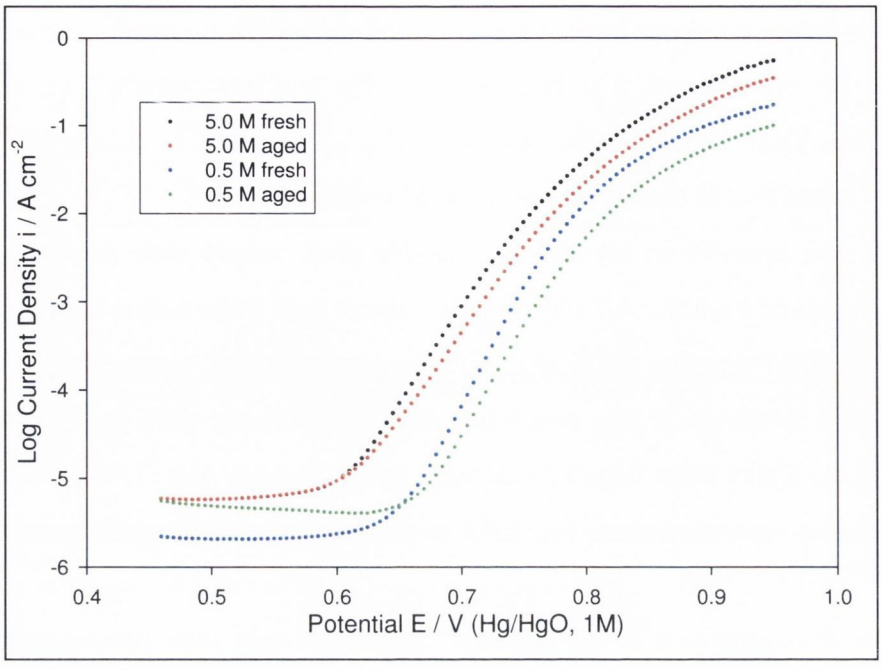


Figure 3.4.9 *IR corrected steady state polarisation curves, recorded in the direction of increasing potential at 25°C, on a pre-reduced Fe electrode, in both 0.5 and 5.0 M NaOH solutions. The "fresh" scans show the initial polarisation behaviour for such an electrode, whereas the "aged" scans are typical of the stabilised behaviour achieved after some electrochemical ageing (ca. 10 polarisation experiments) of the electrode.*

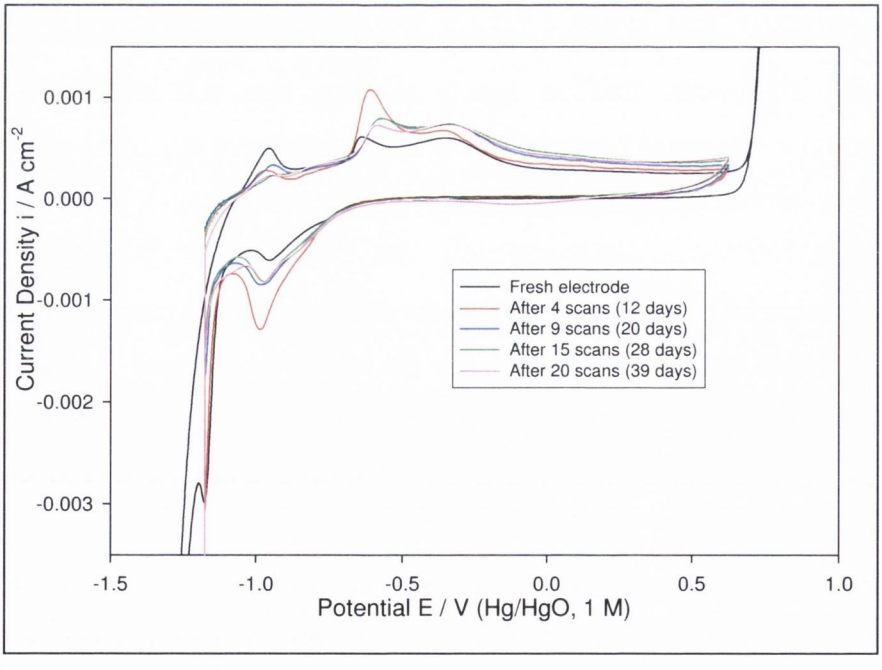


Figure 3.4.10 *CVs (1M NaOH, scan rate = 40 mV s^{-1}) characterising the changing surface electrochemistry of a pre-reduced Fe electrode, with electrochemical ageing. All voltammograms, except that of the fresh electrode, were recorded immediately following pre-reduction of the electrode at –1.1 V for 5 minutes in the same 1M NaOH solution.*

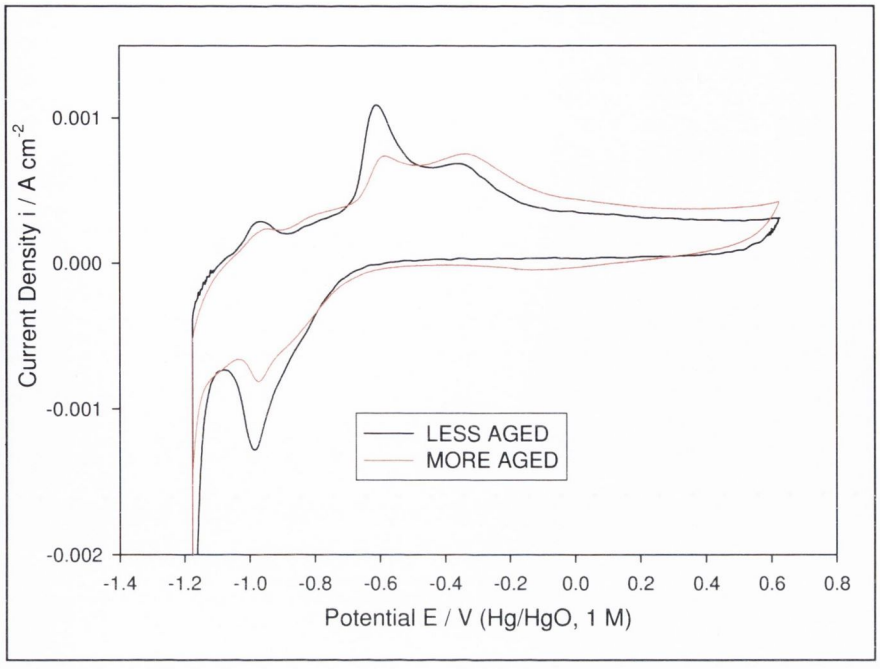


Figure 3.4.11 *Comparison of the voltammetric profiles following 4 polarisation experiments (Less Aged) and after 20 such experiments (More Aged) from Figure 3.4.11. These two CVs are reproduced in this figure for clarity of comparison.*

It can be appreciated that the profiles of the CVs of Figure 3.4.10, become largely similar from that recorded after 9 scans onward. This stabilisation of the CV after pre-reduction, corresponded to the stabilisation of the Tafel slopes observed in the steady state polarisation measurements which followed, to values of the order of 5 – 7 mV dec^{-1} greater than those observed in the initial experiments on the pre-reduced electrode. Accordingly, the other polarisation curve of Figure 3.4.8 displaying a Tafel slope of 44 mV dec^{-1} was recorded on the electrode characterised by the "After 15 scans" profile of Figure 3.4.10. Further ageing of the electrode didn't bring about any significant change in Tafel slope – a polarisation curve recorded in 1.0 M NaOH for the o.e.r. on the electrode characterised by the "After 20 scans" CV of Figure 3.4.10 exhibited a Tafel slope of ca. 45 mV dec^{-1}. This latter CV profile (typical of the stabilised aged pre-reduced Fe electrode) is presented in Figure 3.4.11, for clarity of comparison, alongside the early pre-reduced CV profile of the electrode on which a Tafel slope of 39.5 mV dec^{-1} was recorded.

The anodic peak centred at ca. –600 mV and the corresponding cathodic peak centred at ca. –970 mV are significantly more prominent in the voltammogram of the "Less Aged" electrode in Figure 3.4.11, relative to the profile of the "More Aged" electrode. This peak pair correspond to the A3/C2 peaks in the scheme of Burke and Lyons[26]

(see Figure 1.4.8), and again it is recalled that these authors attributed these peaks to the formation and reduction of an outer, dispersed, hydrous, Fe(III) based oxyhydroxide layer.

In contrast the anodic feature centred at ca. 340 mV has a significantly larger associated charge in the "More Aged" profile compared to the voltammogram of the fresher electrode. In the literature review of section 1.4.2 it was seen that Burke and Lyons[26] attributed this particular anodic peak (A4) to the oxidation of Fe(II) species in the inner amorphous region of the passive film, close to the metal/film interface. These authors envisaged, that in contrast to the hydrous Fe(III) species formed in the process giving rise to peak A3, the oxidation process of peak A4 produces anhydrous phases of species such as Fe_2O_3, Fe_3O_4 or FeOOH, located in the inner region of the oxide film. Thus, it would seem to be a reasonable to conclude that the latter type process has a greater overall influence in the surface chemistry of the "More Aged" electrode relative to the "Less Aged" anode. If this is true, then it might be commented that an increasing influence of the inner compact anhydrous region on the overall properties of the anodic oxide film, has associated with it, an increase in the lower overpotential o.e.r. Tafel slope of ca. 5 – 7 mV dec^{-1} (from ~ 39 to ~ 45 mV dec^{-1} for 1.0 M NaOH).

The "More Aged" profile apparently displays a broad shallow cathodic peak centred between 0 and -200 mV, which is obviously absent from the voltammogram of the "Less Aged" electrode. Indeed the cathodic half-cycle of the latter CV is featureless with virtually zero current density over a range of potential from ~ 400 mV to ~ -600 mV. The possible significance of the aforementioned cathodic feature in the "More Aged" CV will be discussed later.

Aged pre-reduced Fe electrodes characterised by voltammograms similar in profile to the "More Aged" CV of Figure 3.4.11, facilitated the measurement of reasonably reproducible oxygen evolution steady state polarisation curves over a range of NaOH concentrations from 1.0 – 5.0 M. Typical first forward direction scans recorded on such pre-reduced electrodes are presented in Figure 3.4.12. Reaction order plot were constructed, based upon the current densities of Figure 3.4.12 in the ca. 44 – 45 mV dec^{-1} lower overpotential straight-line Tafel region. Typical of these plots is that presented in Figure 3.4.13. The linearity of this reaction order plot is not altogether satisfactory, possibly owing to the fact that the Tafel slopes for the 2.0 and 3.0 M

NaOH solutions are slightly larger (~ 47 mV dec^{-1}) than those of the 1.0 and 5.0 M solutions (~ 44 mV dec^{-1}). In fact superior linearity was observed when reaction order

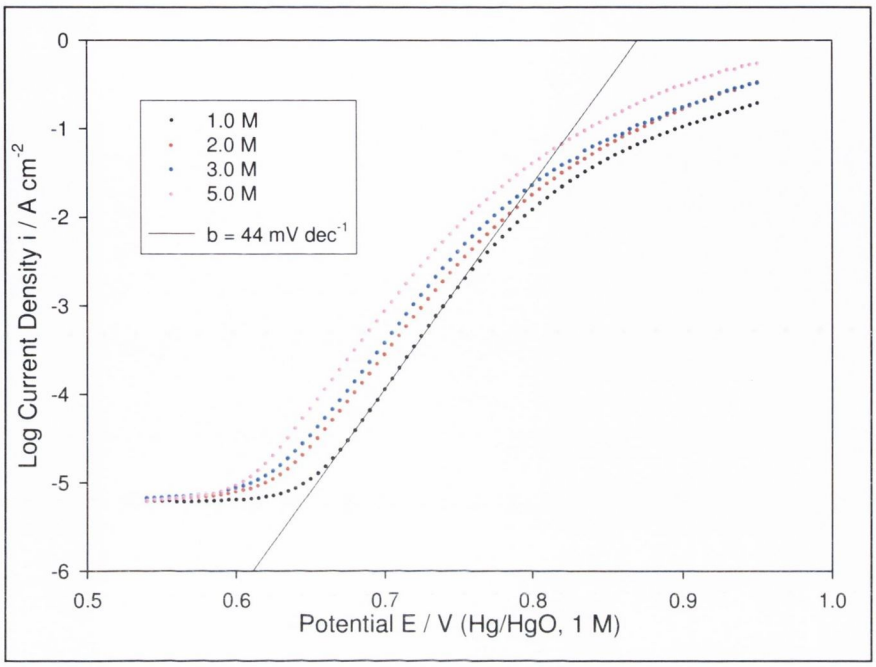


Figure 3.4.12 *IR corrected steady state polarisation curves recorded in the direction of increasing potential on a pre-reduced polycrystalline Fe electrode in NaOH solutions of various concentrations at 25°C.*

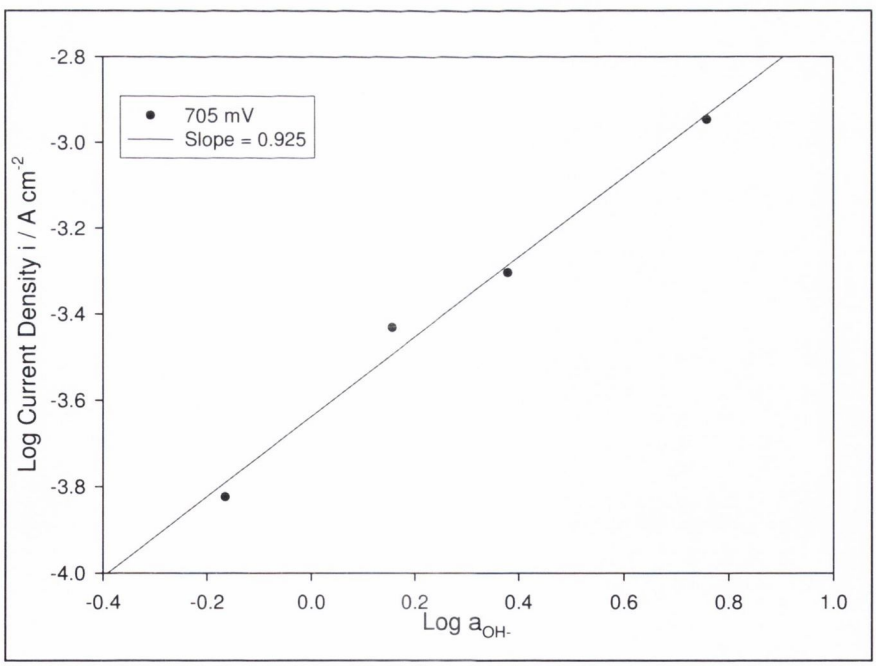


Figure 3.4.13 *Reaction order plot based on the steady state polarisation data of Figure 3.4.12, at a potential of 705 mV.*

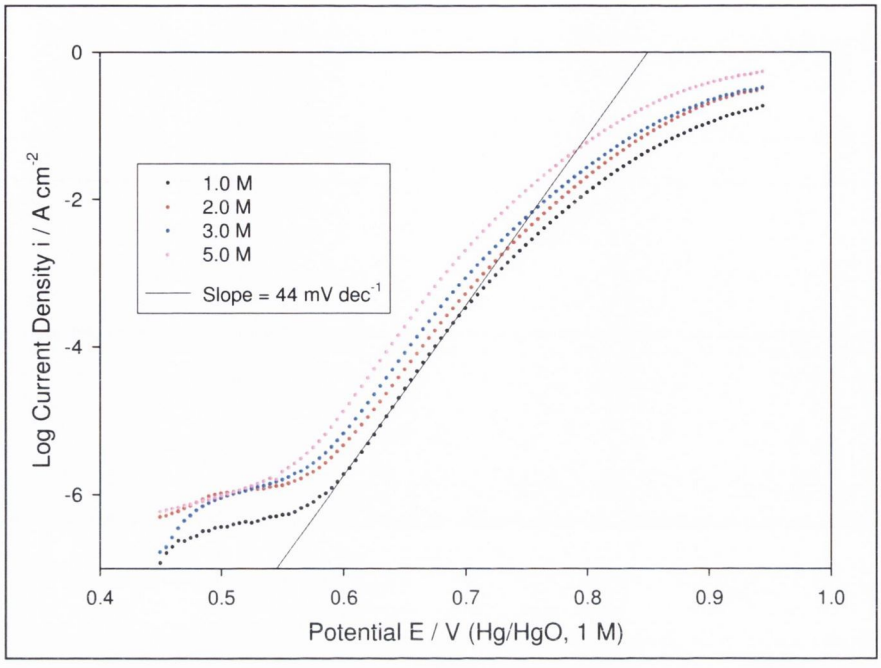


Figure 3.4.14 *IR corrected steady state polarisation curves recorded in the direction of decreasing potential on a pre-reduced polycrystalline Fe electrode in NaOH solutions of various concentrations at 25°C.*

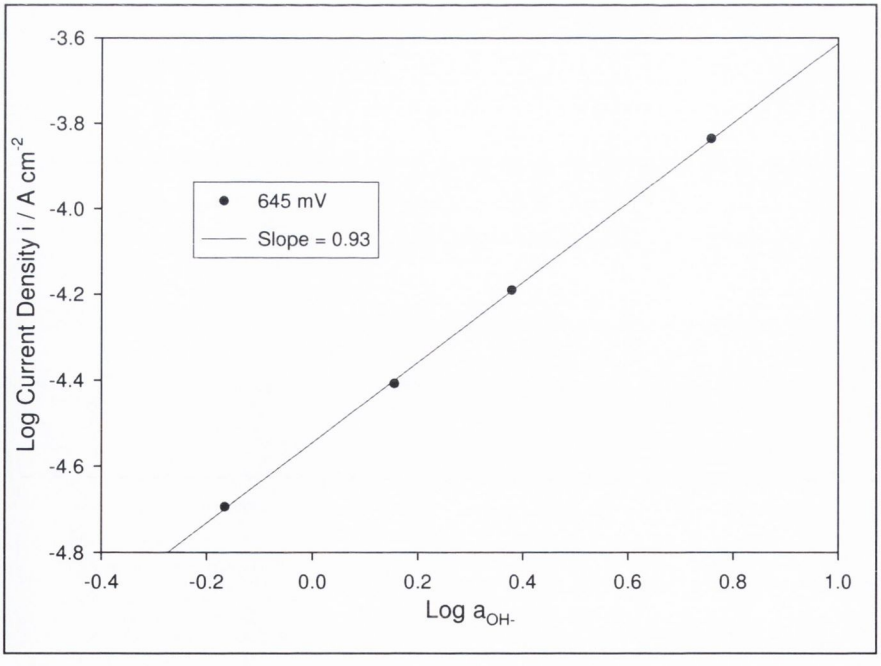


Figure 3.4.15 *Reaction order plot constructed from the steady state polarisation data of Figure 3.4.14, at a potential of 645 mV.*

plots were constructed from the reverse direction polarisation sweeps that followed directly upon the forward scans of Figure 3.4.12. These polarisation curves, recorded in the direction of decreasing potential are presented in Figure 3.4.14. As with the bi-directional polarisation curve recorded in 1.0 M NaOH, for a "fresh" pre-reduced electrode and presented in Figure 3.4.7, the slope of the lower overpotential straight-line region is somewhat lower (41 mV dec^{-1}, compared with 44 mV dec^{-1}) on the reverse direction sweep, relative to that recorded in the forward direction. A typical reaction order plot constructed from the data of Figure 3.4.14 at a potential of 645 mV in the straight-line Tafel region is presented in Figure 3.4.15.

Considering the polarisation curves of Figures 3.4.12 and 3.4.14 for the pre-reduced Fe electrode and the associated reaction order plots (Figures 3.4.13 and 3.4.15), in conjunction with the corresponding (albeit not particularly reproducible) data recorded for the non-pre-treated "bright" Fe electrode (see Figures 3.4.4 and 3.4.5), it can be concluded that the o.e.r. at bright Fe electrodes is characterised in the lower overpotential region by a Tafel slope lying in the range of 38 – 47 mV dec^{-1} (depending on how aged the electrode is), and an associated reaction order m_{OH^-} that tends towards unity. The mechanistic implications of these experimental parameters will be discussed in section 3.5.

Recall that earlier in the present section it was commented, that the initial motivation behind the pursuit of oxygen evolution studies in the present body of work, was related to the further investigation of dual Tafel slope behaviour (~60 mV dec^{-1} at lower η and ~120 mV dec^{-1} at higher values of η) observed in o.e.r. steady state polarisation studies on bright and multi-cycled Fe anodes by Lyons and Burke[28]. As discussed in the previous paragraph, our results outlined so far for "bright" Fe electrodes, don't suggest a Tafel slope of 60 mV dec^{-1} in the lower overpotential region of significant oxygen evolution current density. Therefore, the results of the present work, are apparently at odds with those obtained by Lyons and Burke[28]. However steady state polarisation measurements have been performed as part of the present project that collaborate, and expand on, the aforementioned results of Lyons and Burke[28]. The key factor here seems to be the previous history of the Fe anode.

The initial oxygen evolution measurements on Fe, carried out as part of the present work, were performed on a polycrystalline Fe electrode, which had previously been used in extensive voltammetric studies in alkaline media[30]. The CVs recorded during those studies were initially similar to those presented in Figures 3.4.1 and 3.4.2.,

although with ageing of the electrode the profile became more similar to that of the "More Aged" electrode of Figure 3.4.11. Lack of reproducibility hindered initial attempts at o.e.r. steady state polarisation studies on this aged electrode, as part of the present project. In an attempt to circumvent these problems a severe pre-treatment regime was devised, consisting of pre-reduction of the electrode at a potential of –1.3 V for 15 minutes in 1.0 M NaOH, followed by one voltammetric cycle between the limits of –1.175 and 0.625 V in the same solution at a scan rate of 40 mV s^{-1}.

It was observed that reproducible, oxygen evolution steady state polarisation curves could be obtained for such a pre-treated electrode, which displayed the same dual Tafel slope behaviour as that described by Lyons and Burke[28]. Such a polarisation curve is presented in Figure 3.4.16 – this measurement was conducted in 1.0 M NaOH, the same electrolyte as used by Lyons and Burke. In contrast to the bi-directional polarisation studies already detailed for a non-pre-treated Fe electrode (see Figure 3.4.3) and a pre-reduced Fe electrode (Figure 3.4.7), it can be seen that the first forward and reverse sweeps of Figure 3.4.16 are largely coincident. The range of current densities over which linear steady state polarisation data could be recorded is significantly limited compared to the other types of Fe electrodes considered previously, with a lower limit of somewhat less than 10^{-4} A cm^{-2} apparent from Figure 3.4.16, compared to values < 10^{-6} A cm^{-2} observed for both the non-pre-treated (Figure 3.4.3) and pre-reduced (Figure 3.4.7) Fe electrodes in the same concentration solution. The lower current density limit of the ca. 60 mV dec^{-1}, straight-line region observed on the first forward sweep is higher still at just under 10^{-3} A cm^{-2}. Accordingly, this Tafel region extends only for approximately one decade of current density, or over a potential range of just 60-70 mV. Lyons and Burke[28] observed the ca. 60 mV dec^{-1} Tafel region over a much greater range of current densities (approximately 10^{-5} – 10^{-2} A cm^{-2}), significantly however, the transition from this region to the upper (ca. 120 mV dec^{-1}) Tafel region, occurs at similar values of current density (ca. 10^{-2} A cm^{-2}) in their published polarisation curve, and in the curves of the present work. This indicates that the first forward sweep of the polarisation curve of Figure 3.4.16 characterises the same type of oxygen evolution behaviour, as was originally investigated by Lyons and Burke[28].

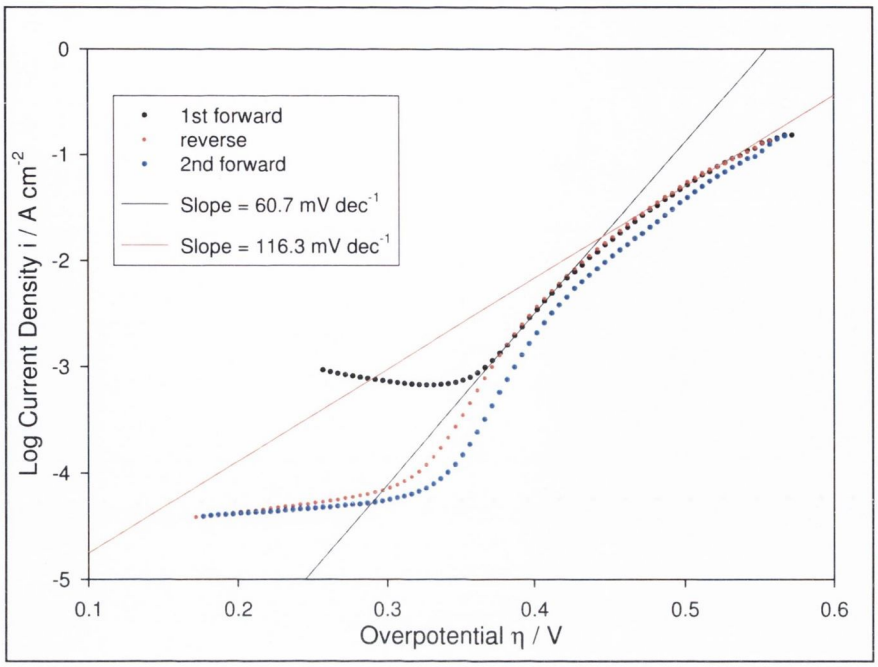


Figure 3.4.16 *Bi-directional IR corrected steady state polarisation curve recorded continuously on a pre-reduced aged Fe electrode (see characteristic CV in Figure 3.4.17) in 1M NaOH, initially in the direction of increasing potential, at 25°C.*

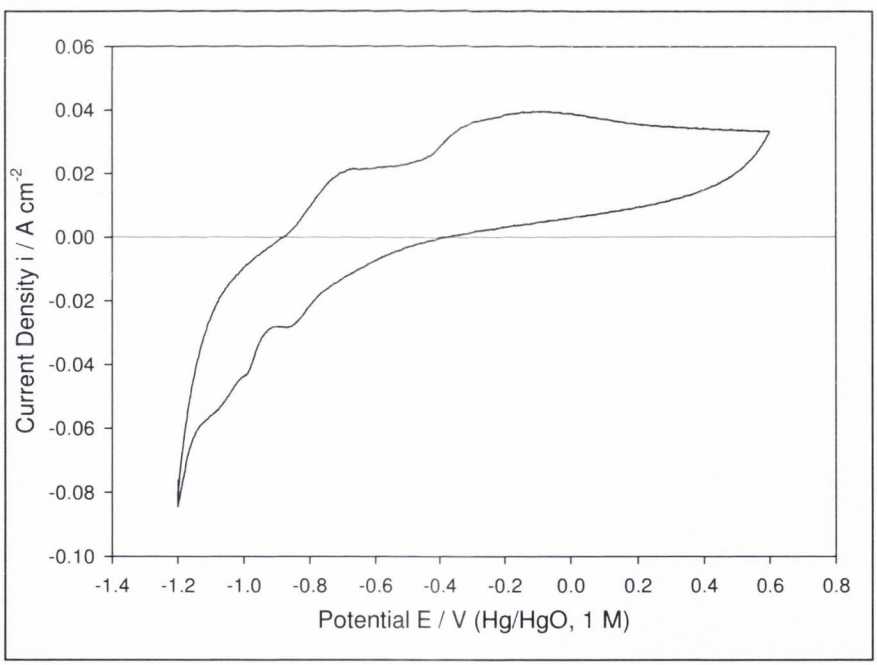


Figure 3.4.17 *Typical CV characteristic of the type of Fe electrode surface on which dual slope polarisation curves similar to that of Figure 3.4.16, were recorded. This voltammogram was measured at a scan rate of 40 mV s^{-1} in 1 M NaOH at 25°C.*

The distorted form of the characteristic CV (see Figure 3.4.17) of the electrode surface, on which the polarisation data of Figure 3.4.16 was recorded, with its large background charge at potentials immediately below those associated with significant rates of oxygen evolution, is reminiscent of the CV of the "highly charged" aged Co electrode presented in Figure 3.3.12. Recall that o.e.r. steady state polarisation measurements on this type of Co electrode also yielded curves displaying dual slope (~60 mV dec^{-1} changing to ~ 120 mV dec^{-1} at higher values of η) Tafel behaviour – Figures 3.3.11 and 3.3.14. The ~60 mV dec^{-1} Tafel region could only be accessed over ca 1.5 decades of current density from ~ 10^{-4} A cm^{-2} upwards in a manner similar to the polarisation curve of Figure 3.4.16. The large background currents associated with the surface electrochemistry of these aged Co and Fe electrodes, makes it impossible to follow the kinetics of oxygen evolution from lower current densities (< 10^{-6} A cm^{-2}) as is feasible with relatively "fresh" electrodes, instead polarisation measurements effectively "break" into the o.e.r. log$i$ – E characteristic at a point near the upper end of the ca. 60mV dec^{-1} Tafel region. This appears to be a "double-edged sword" situation, with the highly charged condition of the surface leading to a different type of o.e.r. behaviour than was observed on less aged electrodes, but at the same time rendering the characterisation of this behaviour by polarisation experiments difficult, owing to the limited range of oxygen evolution current densities accessible to such measurements.

It is interesting to note that Lyons and Burke[28] did not observe the ~ 38 – 47 mV dec^{-1} Tafel slope behaviour as outlined earlier in this section, when they conducted steady state polarisation measurements on a bright un-cycled electrode – recall that they noted the dual slope ~60/120 mV dec^{-1} behaviour for both "bright" and multi-cycled electrodes, albeit that the o.e.r. catalytic activity was much enhanced at the latter type of anode. A more complete overview of this body of work by Lyons and Burke[26-28] reveals that the primary focus of their studies, was on the electrochemistry of hydrous oxides formed by the multi-cycling of Fe electrodes in alkaline media – their observations on oxygen evolution were therefore, effectively a side study. If they used the same electrodes in their o.e.r. measurements[28], as in the main body of their work[26, 27], it is likely that these electrodes were somewhat aged by voltammetric cycling, similar to the electrode on which the ~60/120 mV dec^{-1} Tafel slope behaviour was recorded in the present study. This would certainly explain why these workers didn't

observe the ca. 40 mV dec^{-1} Tafel slope behaviour characteristic of freshly prepared bright iron electrodes – see Figure 3.4.3. As noted earlier in this section, conventional mechanical polishing methods (as were also employed by Lyons and Burke[28]) do not restore the surface of a Fe electrode to the "bright" condition of its initial preparation, since it seems that a (presumably relatively thin) residual oxide layer remains, resistant to removal by polishing.

The distorted form of the CV of Figure 3.4.17 probably arises from the extremes of polarisation to which this Fe electrode was subjected. Recall that during the pre-reduction procedure, the electrode was polarised for 15 minutes at –1.3 V in 1.0 M NaOH. This potential is associated with significant hydrogen evolution. Following the pre-reduction, the electrode is then polarised at the other end of the range of the solvent stability, during o.e.r. steady state polarisation measurements. In view of this it is hardly surprising that the voltammetric profile of an electrode, which has been subjected, several times, to such harsh polarisation conditions (even if it was thoroughly polished after each experiment), should differ from that of an electrode, which has been exposed only to milder polarisation.

It is interesting to note that the voltammetric limits for the optimisation of the charge capacity associated with hydrous multi-cycled oxide films grown on Fe electrodes in 1.0 M NaOH, were determined by Burke and Lyons[26] to be ca –1.43 V (cathodic) and 0.32 V (anodic – both of these values have been converted from the R.H.E. scale originally used in ref. 26 to the Hg/HgO scale). Indeed, the hydrous oxide films for which the dual slope ~60/120 mV dec^{-1} Tafel behaviour was noted were produced[27, 28] by potential cycling between these limits for 30 cycles in 1.0 M NaOH at a rate of 350 mV s^{-1}. Hence, these electrodes, just like the Fe electrode on which similar Tafel behaviour was noted in the present work, were subject to polarisation at extreme cathodic values of potential, prior to their use in oxygen evolution steady state polarisation experiments. This is significant in light of another experimental observation of Burke and Lyons[26, 27], namely that the rate of hydrous oxide growth on Fe electrodes with repetitive cycling, depends markedly on the lower limit of the potential sweep – as mentioned above, the optimum lower limit was found to lie within the region of significant hydrogen evolution. The authors proposed, that at such low cathodic potentials, partial reduction of the inner compact anhydrous oxide region occurs, with rearrangement of oxy-cation species at the metal surface, leaving the compact film in a somewhat disrupted state. When such a partially reduced oxide

material, is re-oxidised at higher potentials, the inner compact layer is restored, however its outer regions will form a more hydrous, dispersed, metastable oxide, as was graphically depicted in Figure 1.4.9. Based on the experiences of the present work and the results and structural theories of Burke and Lyons[26 - 28], it seems reasonable to conclude that dual slope ~60/120 mV dec^{-1} o.e.r. Tafel behaviour, is associated with *rather highly charged, hydrous, disorganised,* oxide films. The distorted voltammetric profile of the Co electrode (Figure 3.3.12) for which similar oxygen evolution steady state polarisation behaviour was noted, is also indicative of such a surface oxide film.

As previously mentioned, the mechanistic analysis conducted by Lyons and Burke[28] on this ~60/120 mV dec^{-1} o.e.r. Tafel behaviour, was somewhat limited by the fact that the authors, had the sole experimental criterion of the Tafel slope against which to test the validity of their proposed modified Krasil'shchikov pathway. The experimental investigation of the kinetics of oxygen evolution associated with the aforementioned Tafel slope behaviour was taken a step further in the present study, by recording o.e.r. steady state polarisation curves for the electrode characterised in Figure 3.4.17 in NaOH solutions of various concentrations. These polarisation curves are presented in Figure 3.4.18. Reaction order plots were constructed based upon the data of Figure 3.4.18 at various potentials associated with both the ~60 mV dec^{-1} and the ~120 mV dec^{-1} straight-line Tafel regions. A typical plot for a value of potential in each of these regions is presented in Figure 3.4.19. As with the reaction order plot for the ca. 60 mV dec^{-1} Tafel region observed on aged Co electrodes (Figures 3.3.14 and 3.3.15), the limited potential window over which this slope appears causes difficulties in the construction of associated reaction order plots. The plot for this Tafel region in Figure 3.4.19 is based upon only the polarisation data for the upper three OH^- concentrations utilised, since, as is obvious from Figure 3.4.18, the characteristic for the 3.0 M solution has already passed through this ~60 mV dec^{-1} region at the potential for which a significant o.e.r. current appears for the 0.25 M solution.

The plots of Figure 3.4.19 indicate that a reaction order approaching 3/2 is associated with the lower Tafel slope region, while the upper Tafel region is has a characteristic reaction order tending towards a limiting value of unity. Hence, there is excellent agreement between the experimental kinetic parameters measured for the o.e.r. on extremely aged Co and Fe electrodes. An appropriate reaction pathway that accounts for these kinetic parameters will be proposed in section 3.5.

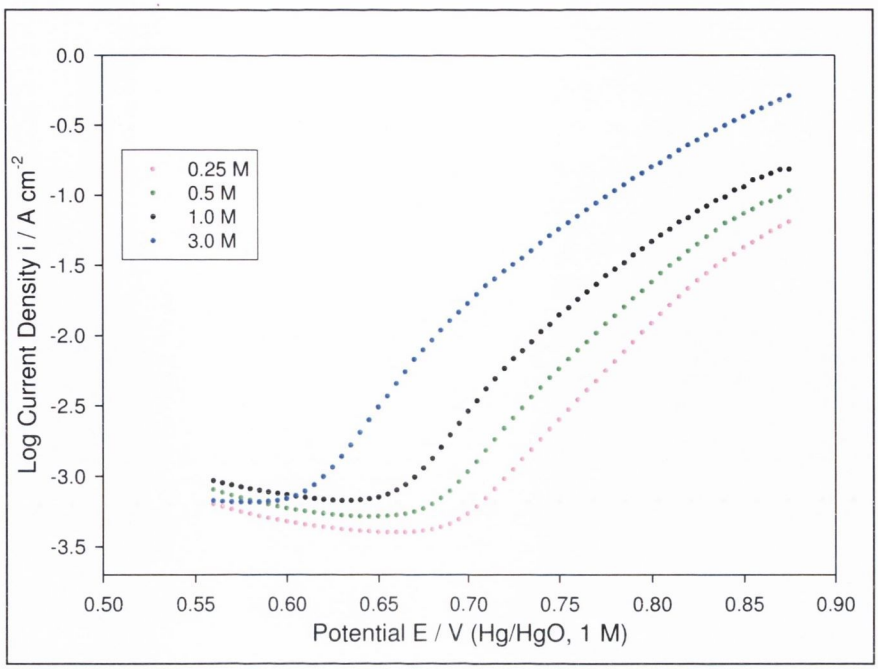


Figure 3.4.18 *IR corrected steady state polarisation curves recorded in the direction of increasing potential on an aged, pre-reduced Fe electrode (similar to that characterised in Figure 3.4.17) in NaOH solutions of various concentration at 25°C.*

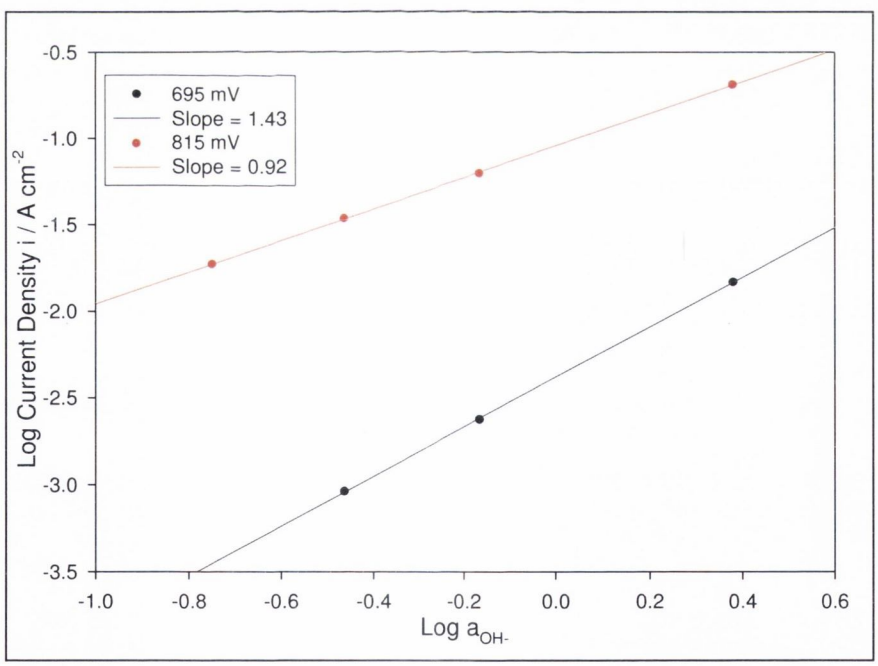


Figure 3.4.19 *Reaction order plots constructed from the polarisation data of Figure 3.4.18 at potentials of 695 mV and 815 mV.*

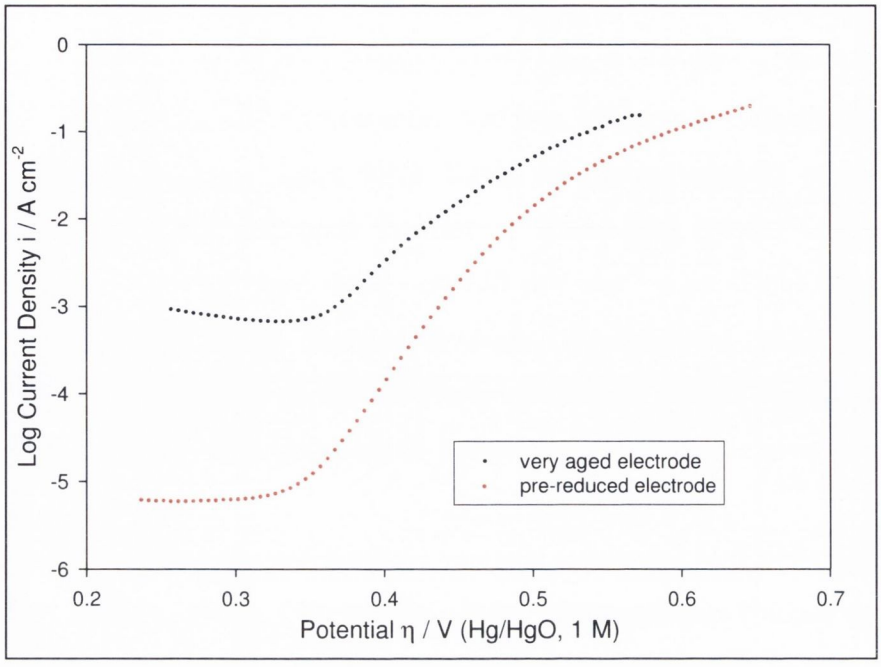


Figure 3.4.20 *Comparison of IR corrected, oxygen evolution steady state polarisation curves (1M NaOH), recorded in the direction of increasing potential for, the very aged, "60/120 mV dec^{-1} Tafel slope Fe electrode" (CV profile Figure 3.4.17), and a less aged pre-reduced, "bright" Fe electrode (CV profile Figure 3.4.11, red trace).*

A comparison of the 1.0 M polarisation curve of Figure 3.4.18 for the extremely aged Fe electrode (with its characteristic Tafel slopes of ~ 60 and 120 mV dec^{-1}), with the 1.0 M polarisation curve of Figure 3.4.12 for a pre-reduced, bright Fe electrode (characteristic Tafel slope of ca. 44 mV dec^{-1}), is presented in Figure 3.4.20. This comparison suggests that there is a much-enhanced catalytic activity towards oxygen evolution for the extremely aged "60/120 mV dec^{-1} Tafel slope Fe electrode" relative to the less aged pre-reduced electrode, across the range of potentials examined. We are however, somewhat cautious about making comparisons of the catalytic activities of these two types of electrode surfaces based on the data of Figure 3.4.20, since these surfaces were achieved on two different iron electrodes. Perhaps, a more accurate comparison of the relative catalytic activities associated with the two types of Fe electrode oxygen evolution polarisation behaviour (i.e. the ~ 60/120 mV dec^{-1} Tafel slope behaviour vs. the ~ 38-47 mV dec^{-1} Tafel slope behaviour) encountered in this study, can be taken from Figure 3.4.21. Both of the polarisation curves presented in Figure 3.4.21 were recorded on the same electrode in 1.0 M NaOH. The "less aged" trace is the result of the third polarisation experiment on a newly prepared Fe electrode. The electrode was polished before the measurement but was not subject to

any electrochemical pre-treatment. The "well aged" curve was recorded on the same electrode following its use in 22 polarisation experiments over the course of three months. Again polishing was the only pre-treatment applied to the electrode before the polarisation measurement depicted in Figure 3.4.21.

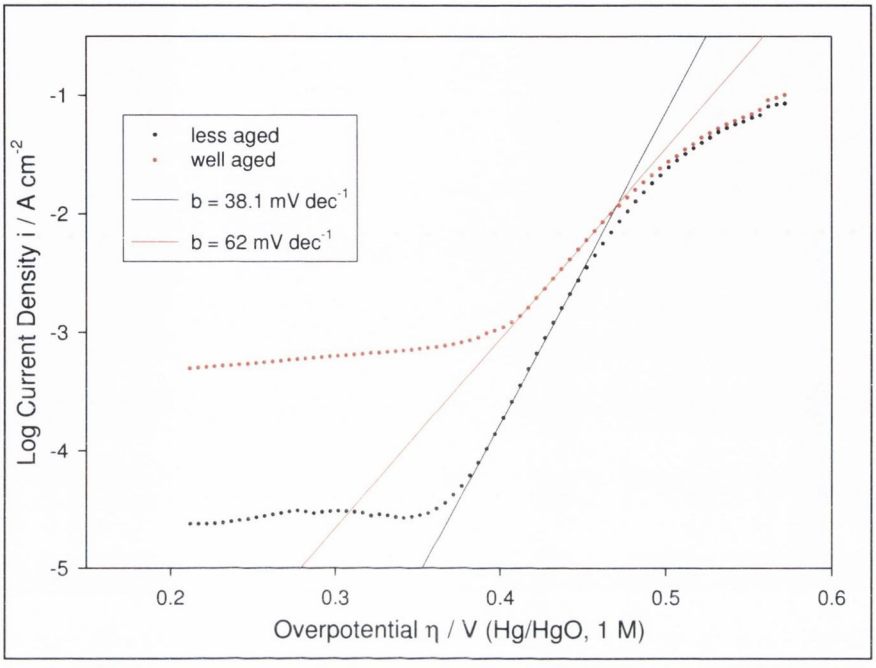


Figure 3.4.21 *Comparison of the IR corrected, oxygen evolution steady state polarisation curves (1M NaOH), recorded in the direction of increasing potential for the same polycrystalline Fe electrode at two points in its life cycle. The "less aged" curve is the result of the 3rd polarisation experiment on the electrode subsequent to its preparation. The "well aged" curve was recorded after 22 further polarisation experiments, over the course of three months. In each case the electrode was polished to a bright finish, but no electrochemical pre-treatment was used.*

Comparing the current densities at η = 412 mV (the lower limit of the ca. 60 mV dec^{-1} Tafel region in the well aged curve) shows an almost four-fold increase in the rate of oxygen evolution at the "well aged" electrode (i = 1.41 mA cm^{-2}), in comparison to the "less aged" electrode (i = 0.36 mA cm^{-2}). The two polarisation curves become increasingly convergent with increasing overpotential. It is noteworthy that there is a strong similarity between the polarisation behaviour displayed for fresh and well aged Fe electrodes in Figure 3.4.21, and that displayed for fresh and well aged Co electrodes in Figure 3.3.11.

In the literature review on the oxygen evolution reaction (sections 1.5.3 and 1.5.4), it was noted that several workers in the field, emphasised the intimate link between surface redox transitions and the o.e.r. For example, Tseung and Jasem[31] proposed

that oxygen evolution could only occur at a metal oxide surface at or above the potential of a given lower oxide/higher oxide redox transition. Rasiyah and Tseung[32, 33] later proposed a pathway for the o.e.r. on $NiCo_2O_4$ electrodes in alkaline solution, that emphasised the importance of the valance state of the surface Co and Ni ions – see equation (1.5.24). This idea was taken up by Willems, Kobussen and co-workers[15] in their proposed reaction mechanism (see equation (1.5.24)) for the o.e.r. on Co electrodes in KOH solution. The importance of the oxidation of surface Ru^{4+} ions to a higher oxidation state in the course of the o.e.r. at RuO_2 electrodes in alkaline solution was emphasised by O'Grady et al.[34] – see Table 1.5.1, mechanism (IV). Burke and Twomey[1] showed that the voltammetric peak potentials for the Ni(II)/Ni(III) transition for a cycled Ni electrode, and the potentials for the onset of oxygen gas evolution at a variety of nickel oxide surfaces, had the same relative dependence on solution pH, over a broad range of pH. In view of this they concluded that "the oxygen evolution process at electrocatalytically active oxide electrodes may be regarded as a side-reaction arising basically from the decomposition of an anodically generated, unstable oxide entity". The few examples cited above, demonstrate that the concept of a close inter-relationship between particular surface redox transitions and oxygen evolution is widely accepted in the literature.

The "particular surface redox transitions" that precede oxygen evolution at Ni and Co electrodes in alkaline solution are evident from cyclic voltammetry experiments. Examining the voltammograms of various Ni electrode surfaces presented in Figures 3.2.1, 3.2.5, 3.2.6, 3.2.10 and 3.2.11, it is readily apparent that the rising current edge associated with oxygen evolution occurs at potentials immediately anodic to the Ni(II) → Ni(III) oxidation peak (although it is worth bearing in mind the complexity of this redox transition as discussed in section 1.4.1 – in particular, that the average oxidation state associated with the γ oxidation product phase can be as high as 3.67 – see Bode scheme of Figure 1.4.3). In the voltammetric profiles of some types of Ni electrode surface (probably those where the β- $Ni(OH)_2$ → β- NiOOH cycle predominates, e.g. see the "after 10 polarisations" scan of Figure 3.2.6), the Ni(II) → Ni(III) oxidation current effectively continues directly into the rising edge of the oxygen evolution current, with no clear transition point between the two processes. The latter observation would seem to support the viewpoint of Burke and Twomey[1] as quoted in the previous paragraph, in relation to oxygen evolution at nickel oxide anodes in any case. Indeed, the anodic currents due to the surface oxidation processes are often

captured at the lower overpotential end of steady state polarisation curves for the o.e.r. at Ni electrodes – e.g. see Figure 3.2.3.

In the literature review of the surface electrochemistry of Co in section 1.4.3, it was seen that there is general consensus, that the broad anodic peak at potentials above ca. 450 mV (see Figures 3.3.8, 3.3.10, 3.3.25, and 3.3.26) is related to the oxidation of surface Co(III) species to Co(IV) species – recall equation (1.4.31). In the voltammograms of Figure 3.3.26 it can clearly be seen, that the rising edge of the oxygen evolution current is effectively superimposed on this peak at potentials anodic to ca. 500 mV.

It would therefore appear, that if the viewpoint of Tseung and Jasem[31] were to be adopted, oxygen evolution commences at potentials just above those associated with the onset of the Ni(II)→ Ni(III) redox transition in the case of Ni anodes, or the onset of the Co(III) → Co(IV) transition, for Co electrodes. This raises the question as to which redox transition is associated with the onset of oxygen evolution in the case of Fe electrodes in alkaline solution? Referring to the voltammograms of Figure 3.4.2, which characterise the surface electrochemistry of an initially bright, newly prepared polycrystalline Fe electrode, over the potential range of the aqueous solvent stability for 10 cycles, it would appear that the anodic redox transition, closet in potential to oxygen evolution, is that related to the broad shoulder extending from ~ -500 to 100 mV (first two cycles) – a full 750 mV (approximately) below the appearance of the rising edge of the oxygen evolution current. A similar situation is evident for the pre-reduced Fe electrodes characterised by voltammetry in Figure 3.4.10 (although these CVs were not recorded up to sufficiently high anodic potentials to actually see the rising edge of the o.e.r. current density).

Recall from section 1.4.2 that the aforementioned anodic shoulder is related to the oxidation of Fe(II) species (or magnetite Fe_3O_4) to Fe(III) species. At potentials between the upper limit of this anodic feature and the appearance of the oxygen evolution current, the Fe voltammogram (Figure 3.4.2) is characterised by an apparently featureless region of constant background current density, extending over the course of approximately 750 mV. On the basis of in–situ Raman spectroscopy and electrochemical impedance measurements, Joiret et al.[35] proposed that gradual and progressive oxidation of Fe_3O_4 to such Fe(III) species as γ-Fe_2O_3 and/or its hydrated form γ-FeOOH occurs at potentials anodic to the Fe(II)→ Fe(III) shoulder – see section 1.4.2. Furthermore, EQCM studies performed by these workers indicated a

gradual expulsion of solvent water molecules from the oxide film over the course of the featureless constant current density region. In view of these observations one must ask whether the o.e.r. at iron oxide surfaces is somehow different from that occurring at nickel, cobalt and other oxide (e.g. RuO_2[34, 36]) surfaces, in that it occurs at potentials far removed from any apparent oxide redox transitions, or if indeed the association between oxygen evolution and such redox transitions as noted for the latter types of oxide are merely coincidental?

On the basis of several experimental observations made during the course of the present project, we believe that we can shed some light on this question. The following results did not arise from a systematic experimental effort to answer the question posed at the end of the last paragraph. Instead they are somewhat random, if potentially useful observations, that arose from cyclic voltammetry scans, which were conducted to characterise various Fe electrode surfaces.

Some such voltammograms are presented in Figure 3.4.22. These scans were recorded on a relatively un-aged Fe electrode, following polishing, on three different occasions. The striking feature of the voltammograms of Figure 3.4.22 is the additional pair of voltammetric peaks – an anodic peak located at potentials between ca. 300 and 600 mV, and a complementary cathodic peak between approximately 100 and –150 mV. The blue profile was the latest of the three to be recorded, and it is obvious that the magnitude of both peaks have increased with electrode ageing. It is evident (especially for the blue trace) that the rising current associated with oxygen evolution becomes significant at potentials just above the aforementioned anodic peak.

On one occasion, following the observation of the CV recorded on the bright electrode, a further nine voltammetric cycles were performed, also at 40 mV s^{-1}. The profiles of the first and tenth cycles are compared in Figure 3.4.23. While the magnitudes of the anodic peak centred at ~ -600 mV, and its complementary cathodic peak centred just below –1 V, increase, as is always noted on multi-cycling of an Fe electrode in 1.0 M NaOH (see Figures 3.4.1 and 3.4.2), the charge associated with the upper pair of peaks remains largely constant. This suggests that the redox process giving rise to this unusual peak pair, is occurring in the inner region of the passive film.

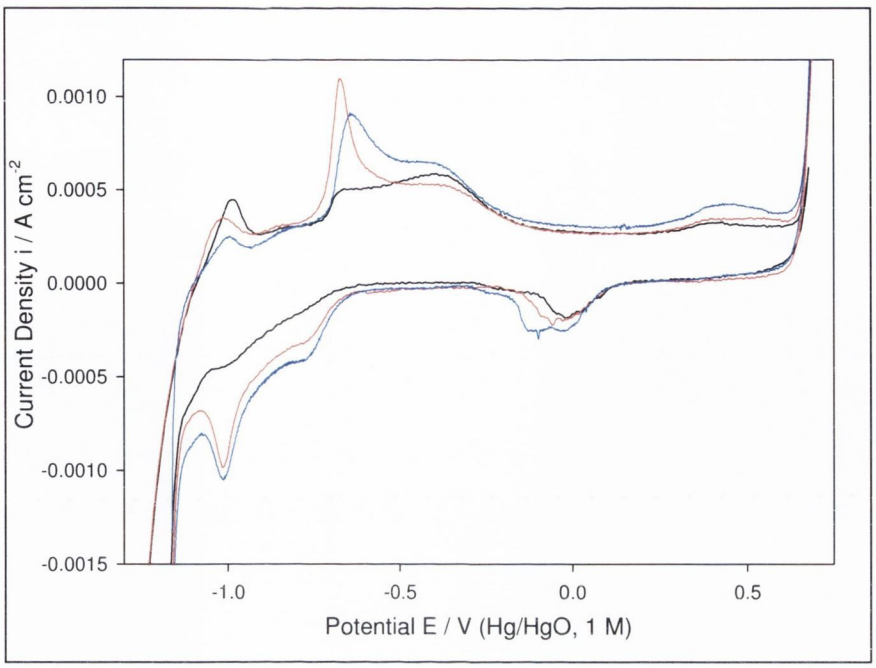


Figure 3.4.22 *CVs recorded on different occasions for a relatively un-aged, bright polycrystalline iron electrode in 1M NaOH at 25°C. The scan rate was 40 mV s^{-1}.*

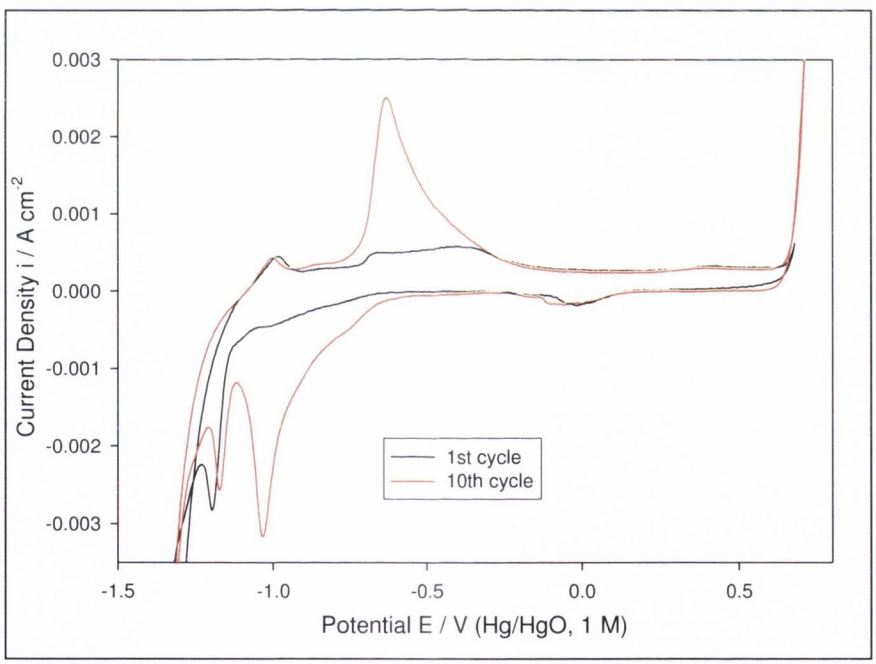


Figure 3.4.23 *The "1st cycle" is the black voltammogram of the previous figure. Nine further cycles were performed continuously on the same electrode, again at a scan rate of 40 mV s^{-1}. The "10th cycle" is the final one of these.*

Following the original observation of the aforementioned peak pair, the possibility was considered, that these unusual features arose due to the presence of some contaminant, either on the electrode surface or in the electrolyte solution. The

electrode was vigorously polished and rinsed before the next measurement, and a fresh NaOH solution prepared, however, as is evident from Figure 3.4.22, the unusual features remained, indicating their authenticity.

The next issue that must be considered, is the identity of the redox couple giving rise to the unusual peak pairs of Figures 3.4.22 and 3.4.23. The observation of a pair of redox peaks at potentials similar to those associated with the unidentified features of the aforementioned figures, is not entirely unprecedented. As was discussed in section 1.4.2, Joiret et al.[35] have observed similar features in a voltammogram performed on an iron film electrodeposited on a gold EQCM electrode – see Figure 1.4.11. The same workers claim to have observed similar peaks in voltammetric studies on a mild steel specimen in alkaline solution. By referencing the Pourbaix diagram for iron[37] they have attributed their observed peak pair to a Fe^{3+}/Fe^{6+} redox transition. Referring to a recent revision[38] of Pourbaix's original potential-pH diagram for the iron-water system, the predicted thermodynamic corrosion product at 25°C for potentials above ca. 0.75 V (vs. S.H.E. – i.e. ca. 650 mV on the (Hg/HgO, 1M OH^-) scale) at pH 14, is soluble FeO_4^{2-}. For immediately lower potentials at the high pH end of the revised diagram, the predicted products involve iron in the +3 oxidation state.

A potential modulated reflectance (PMR) spectroscopy study[39], on the passive films formed on Fe electrodes in solutions of various pH from 1 to 14, across the entire potential range of aqueous solvent stability, casts some further light on the chemical nature of these films at various potentials. The workers involved compared their spectroscopic data to previously measured UV-visible spectra of as many oxy-iron compounds as was possible, and made their peak designations on this basis. In 1.0 M NaOH, as the potential was increased from ~ 0.075 to 0.575 V (converted from the R.H.E. scale used in the original publication) the PMR data indicated the progressive conversion of α-FeOOH to α-Fe_2O_3, and likewise of γ-FeOOH to γ-Fe_2O_3 – both processes occurring due to de-hydration of the film. Significantly, in the present context, as the potential of significant oxygen evolution was approached, the PMR peak for α-Fe_2O_3 disappeared being replaced by a maximum at wavelengths, for which it previously had been noted, that soluble FeO_4^{2-} ferrate species displayed an adsorption band. On this basis, the authors concluded that α-Fe_2O_3 was oxidised to FeO_4^{2-} in this region of applied potential.

In view of the thermodynamic considerations and experimental results outlined above, and owing to the similarity in the potentials associated with unidentified peak pair of

Figures 3.4.22 and the aforementioned peaks observed by Joiret et al.[35], it seems that a tentative designation of the former to a Fe^{3+}/Fe^{6+} redox transition is also in order. In light of these observations it would appear that the "missing" lower oxide/higher oxide transition associated with oxygen evolution at iron oxide surfaces might well be the surface oxidation of Fe(III) species to Fe(VI) species. While the observations of Figures 3.2.22 and 3.2.23 might fall short of being unambiguous direct proof for the role of ferrate species in oxygen evolution at Fe electrodes in high pH solutions, they certainly seem to strengthen the case.

Of course the question arises as to why the peaks attributed here to a Fe^{3+}/Fe^{6+} redox transition, are not always observed in voltammograms characterising Fe electrode surfaces. The reason for this is presently unclear. The electrode for which the CVs of Figures 3.2.22 and 3.2.23 were recorded, was prepared in the same manner, and from the same iron foil as the other Fe electrodes utilised in the present work – see section 2.2.2. It can only be speculated, that some aspect of the surface preparation of the electrode, has lead to the formation of sites (possibly in microscopic cracks or pores) that catalyse the Fe(III)→Fe(VI) oxidation process in the inner region of the passive film. In the more general case, voltammetric peaks for the Fe(III)↔Fe(VI) redox transition are not observed, probably because the process is restricted to the immediate surface of the oxide layer, where it is facilitated by exposure to the alkaline electrolyte solution. Furthermore, since the oxidation process involves the formation of an unstable product at the electrode surface, as opposed to a transition between two reasonably well-defined solid phases, it is likely that it may occur over a relatively wide range of potentials, with an appreciable surface concentration of the ferrate entity, arising only at the potential corresponding to the appearance of a substantial oxygen evolution current.

Finally in this regard, it is worth re-visiting the "More Aged", pre-reduced electrode voltametric profile of Figure 3.4.11. When previously discussing this CV, a broad shallow cathodic peak centred between 0 and -200 mV was noted, but no further comment was made at that stage. Close examination of the anodic half cycle, shows that the current density begins to rise slowly from ~ 450 mV upwards – a potential well below the appearance of the sharp rising current edge associated with the o.e.r. – see Figure 3.4.10 for comparison. One might tentatively suggest that the aforementioned voltammetric features are indicative of a surface Fe(III)↔Fe(VI) redox transition, while conceding that they certainly don't constitute definitive proof.

3.5 Further Discussion

From the point of view of mechanistic determination, the experimentally derived kinetic parameters outlined in sections 3.2 – 3.4 indicate four principal phenomena that must be explained. These are as follows; (a) the observation for Ni electrodes of lower overpotential Tafel slopes of ~ 38 – 40 mV dec^{-1}, with associated reaction order values of approximately unity, (b) the reason for the variation of the lower overpotential Tafel slopes from ca. 40 mV dec^{-1} to ca. 46 mV dec^{-1} with OH^- concentration and degree of ageing, as was noted for Co and Fe electrodes, (c) the observation of a reaction order of approximately unity associated with the aforementioned ca. 46 mV dec^{-1} Tafel slope behaviour, (d) the observation of dual slope Tafel behaviour (~ 60 mV dec^{-1} with reaction order of ~ 3/2 at lower values of η, ~ 120 mV dec^{-1} with reaction order of approximately unity at higher values of η) for extremely aged Fe and Co electrodes. These four points will now be discussed in turn with the aim of providing a full mechanistic basis for the observed experimental behaviour of sections 3.2 – 3.4.

3.5.1 Mechanistic Pathway for Oxygen Evolution at Ni Electrodes

In the situations where it was possible to record reliable, reproducible steady state polarisation curves for the o.e.r. on Ni electrodes at various NaOH solution concentrations, the kinetics of the reaction at lower overpotentials were characterised by Tafel slopes of ~ 2.303×2RT/3F (= 39.4 mV dec^{-1} at 25°C) and a reaction order of approximately unity. To recap, this behaviour was observed in the following situations:

- Pre-reduced bright Ni electrodes – Figures 3.2.12 and 3.2.14
- Pre-oxidised Ni electrodes – Figures 3.2.15 and 3.2.18

Lower overpotential Tafel slopes of ~2.303×4RT/5F (= 47.3 mV dec^{-1} at 25°C) which were commonly observed for the o.e.r. at Co and Fe electrodes, were rarely observed for Ni. The one exception was for the bright pre-reduced Ni electrode where the Tafel slope observed to increase from ~ 40 to 46 mV dec^{-1} between first steady state polarisation sweep in the positive direction in 5.0 M NaOH, and the second sweep in the same direction – Figure 3.2.13. In view of this, the task of mechanistic

determination for the o.e.r. on Ni electrodes in aqueous alkaline media is essentially reduced to a matter of identifying an appropriate pathway with a particular rate determining step, the kinetic analysis of which will predict $b = d\eta/d\log i = 2.303\times2RT/3F$, and $m_{OH^-} = \left(\partial \log i/\partial \log a_{OH^-}\right)_\eta = 1$.

A low Tafel slope of 2.303×2RT/3F is indicative of a rate-determining step subsequent to the initial electron transfer step, which is characterised by a Tafel slope of 2.303×2RT/F (under Langmuir adsorption conditions - c.f. Table 1.5.1), and involves the primary discharge of an OH^- ion at a catalytically active surface site S. If it is assumed that the fractional coverage of the reaction intermediate θ follows the low coverage Langmuir adsorption isotherm at lower overpotentials (i.e. $\theta\rightarrow0$), a reaction order of 1 implies that only one mole of OH^- ions has been adsorbed per mole of active sites S, during the r.d.s. or any steps preceding it. Considering earlier mechanistic analyses of the oxygen evolution reaction, it appears that the only general schemes that suitably account for the experimental kinetic parameters under consideration in the present section, are those due to O'Grady and Yeager[34] or a development of the same mechanism by Burke and co-workers[40, 41]. With reference to Table 1.5.1 section 1.5.4, it can be seen that while the Krasil'shchikov pathway (that most commonly proposed for the o.e.r. on metal oxide electrodes) can account for a Tafel slope of 2.303×2RT/3F, if the third step is considered rate controlling under Langmuir adsorption conditions with $\theta\rightarrow0$, it cannot account for an associated reaction order of unity, instead giving rise to a prediction of 2 for this parameter.

The pathway of O'Grady and Yeager, included in Table 1.5.1 as mechanism (IV), was discussed in section 1.5.4. As presented in Table 1.5.1, the suggestion is, that a complex species M^zOH is formed by the initial discharge of an OH^- ion at a metal ion site M^z – this electron is transferred directly to the external circuit, with the oxidation state of the metal ion M remaining unchanged. In the second step the metal ion is oxidised from M^z to M^{z+1} with transfer of a further electron, without discharge of a second OH^- ion. In the case of Burke's publications[40, 41], the first two steps of the pathway can be generally represented as,

$$(M(Z))^{p-} + OH^- \leftrightarrows (M(Z+1)OH)^{p-} + e^- \qquad (3.5.1, I)$$

$$(M(Z+1)OH)^{p-} \leftrightarrows (M(Z+1)OH)^{(p-1)-} + e^- \ , \qquad (3.5.2, II)$$

where, $(M(Z))^{p-}$ represents a complex hydrous oxide catalytic site ($[RhO_m(OH)_n \cdot zH_2O]^{p-}$ in the case of ref. 41, where p=2m+n-4 for the case of Rh(IV), or $(-O-)_2RuO^{-}(OH)_3$ for ref. 40) with a central metal ion in the Z oxidation state – p is a positive integer. It is noteworthy, that in contrast to O'Grady and Yeager's pathway as presented in Table 1.5.1, oxidation of the central metal ion occurs in the initial discharge step of scheme (3.5.1), with the second electron transfer occurring due to a one electron discharge of the overall charge on the complex surface species.

The key difference between the pathways of O'Grady and Yeager, or Burke et al. and other proposed mechanisms for the o.e.r. (see for example the literature review of section 1.5.4 and Table 1.5.1) is that the former type of mechanism envisages that oxygen evolution involves a cyclical surface redox transition, whereas other schemes effectively see the electrode as merely an electron sink, that catalyses the o.e.r. by stabilising the reaction intermediates through electro-sorption. The logic of the O'Grady and Yeager, or Burke et al. mechanisms is that oxygen evolution occurs to effectively "quench" an unstable higher oxide entity. The concept of the involvement of a cyclical formation/decomposition of higher oxides in the o.e.r. was considered as early as 1909 by Foerster[42] but was largely ignored until the aforementioned work of O'Grady and Yeager[34] in the 1970s. In addition to O'Grady and Yeager[34] and Burke et al.[40, 41], the role of unstable higher oxides in the o.e.r. has also been proposed by Tseung et al. for $NiCoO_4$[43, 44] and Li-doped Co_3O_4[45] electrodes, and by Willems and Kobussen[15] for polycrystalline Co electrodes in alkaline solutions. Although the involvement of unstable high valance states of transition metal ions in oxygen evolution is far from universally accepted, it is difficult to rationalise the kinetic data obtained for Ni electrodes in the present study without admitting the aforementioned concept. In view of this, the following pathways, based upon the concepts of Burke et al.[40, 41], are now outlined for the oxygen evolution reaction on Ni electrodes in aqueous alkaline solution.

Recall from the discussion of section 1.4.1 regarding the complex electrochemistry of the oxidation of Ni(II) species to higher oxidation states that the highest stable whole-number oxidation state is Ni(III). In any case this is the valance state associated with β-NiOOH, which has previously been described[8] as the "right type of oxide" for the o.e.r. In consideration of this we believe, that one view of a feasible pathway for the o.e.r. on Ni is as follows:

$$Ni(III)OOH + OH^- \leftrightarrows Ni(IV)O(OH)_2 + e^- \quad (3.5.2, I)$$

$$Ni(IV)O(OH)_2 \leftrightarrows [Ni(IV)O(OH)_2]^+ + e^- \quad (3.5.2, II)$$

$$[Ni(IV)O(OH)_2]^{1+} + 2OH^- \leftrightarrows [Ni(III)O]^{1+} + O_2 + 2H_2O + 2e^- \quad (3.5.2, III)$$

$$[Ni(III)O]^{1+} + OH^- \leftrightarrows Ni(III)OOH \quad (3.5.2, IV)$$

Owing to central importance of the oxidation state of the metal ion, it has been decided to explicitly highlight this value in parenthesis in mechanism (3.5.2) and those that follow. For mechanism (3.5.2), the unstable higher oxide that precipitates oxygen evolution (or, looking at the situation from a different angle, the o.e.r. reaction intermediate) is envisaged as being the $Ni(IV)O(OH)_2$ species.

As has previously been discussed in the literature reviews on Ni, Fe and Co electrodes (sections 1.4.1-1.4.3), the nature of the surface electrochemistry of hydrous passive oxide films on various transition metal oxides (including Ni[1,5], Fe[26, 27], Co[17], Ir[46], Rh[47] and Au[48] - overall reviews given in refs. 49, 50) has been widely investigated by the research group of Burke. A common theme observed for hydrous oxides formed in aqueous solution, across this range of metals, is their amphoteric nature. That is to say, that these oxides act as bases (adsorbing protons or OH^- ions and thus acquiring positive charge) at low pH, and conversely act as acids (adsorbing OH^- ions or donating protons and thus becoming negatively charged) at high pH. The fundamentals of the acid/base chemistry of metal oxides in aqueous solution were discussed in section 1.1.3 (e.g. - see Figure 1.1.7), whereas the concept of super-Nernstian shifts (an experimental indicator of amphoteric oxide behaviour) was treated in section 1.4.1. It is in view of the acidic nature of the hydrous oxide formed on Rh in alkaline solution, that O'Sullivan and Burke[41] envisaged that the highly charged metal ion coordinates excess hydroxide ions, and that therefore the active site for oxygen evolution can be considered as being the $[RhO_m(OH)_n \cdot zH_2O]^{p-}$ surface complex, mentioned previously.

Although Burke and co-workers made their observations regarding amphoterism, for thick hydrous oxide films formed by repetitive potential cycling, it was seen in sections 1.4.1 – 1.4.3, that even on the first voltammetric cycle, the outer regions of the passive films formed on Ni, Co and Fe electrodes at higher anodic potentials, are likely to be somewhat hydrated and dispersed. This should certainly be true for the surface layer, in which the species catalytically active towards oxygen evolution reside. By analogy with Rh[41], and with reference to the generally accepted model of a

complex non-stoichiometric higher Ni oxide as discussed in section 1.4.1, we suggest that the Ni(III) ions on the oxide surface at oxygen evolution potentials could reasonably be considered to be present in the form of charged complex species, that might be represented as $[Ni(III)O_m(OH)_n]^{p-}$, where p=2m+n-3. Charge neutrality is provided by associated counter-ions in the outer Helmholtz layer. Taking these considerations into account, an essentially equivalent version of pathway (3.5.2) can be written, which envisages the catalytic metal ion as being complexed in an anionic surface species:

$$[Ni(III)O_m(OH)_n]^{p-} + OH^- \leftrightarrows [Ni(IV)O_m(OH)_{n+1}]^{p-} + e^- \qquad (3.5.3, I)$$

$$[Ni(IV)O_m(OH)_{n+1}]^{p-} \leftrightarrows [Ni(IV)O_m(OH)_{n+1}]^{(p-1)-} + e^- \qquad (3.5.3, II)$$

$$[Ni(IV)O_m(OH)_{n+1}]^{(p-1)-} + 2OH^- \leftrightarrows [Ni(III)O_m(OH)_{n-1}]^{(p-1)-} + O_2 + 2H_2O + e^- \qquad (3.5.3, III)$$

$$[Ni(III)O_m(OH)_{n-1}]^{(p-1)-} + OH^- \leftrightarrows [Ni(III)O_m(OH)_n]^{p-} + e^- \qquad (3.5.3, IV)$$

Indeed such a representation might be more correct than that presented in (3.5.2), since it would avoid the formation of the positively charged $[Ni(IV)O(OH)_2]^+$ species – an entity, the existence of which runs contrary to the negatively charged surface expected for a potentially amphoteric oxide in alkaline solution. The more simplistic representation of scheme (3.5.2) is left in place, since it illustrates the fundamental nature of the reaction very clearly and follows the traditional notion of β-NiOOH being the active material for oxygen evolution[8]. In any case, if (as is most likely) m = 1, the $[Ni(III)O_m(OH)_n]^{p-}$ species is merely a NiOOH surface group that has coordinated extra hydroxide ions, owing to the acidic nature of the hydrous oxide.

A formal kinetic analysis is now conducted on the basis of the quasi-equilibrium principle and other concepts introduced in sections 1.2.1 – 1.2.3. It will be shown that if the *second step* in mechanisms (3.5.2) or (3.5.3) is considered to be rate-determining, and if low coverage ($\theta \rightarrow 0$) Langmuir adsorption of the Ni(IV) reaction intermediate (formed in the respective first steps) is admitted, then the experimental kinetic parameters can be satisfactorily rationalised.

Recall, that an elementary multi-step kinetic analysis was conducted for the so-called Bockris Electrochemical Oxide mechanism (equation (1.2.37) or Pathway II in Table 1.5.1) in sections 1.2.2 – 1.2.4, under various conditions of fractional intermediate coverage. In the derivation of the form of the Electrochemical Langmuir Adsorption

Isotherm in section 1.2.2, the rates of reaction for step (1.2.37, I) in both the forward (v_1 with units of mol $cm^{-2}s^{-1}$), and reverse (v_{-1}) directions, were written in equations (1.2.38) and (1.2.39) respectively. From a formal kinetic point of view, the initial discharge step of pathway (1.2.37) (i.e. $M + OH^- \leftrightarrows MOH + e^-$) is identical to the first step of schemes (3.5.2) or (3.5.4), since the exact oxidation state of the surface metal ion is irrelevant (explicitly at least) in the kinetic analysis. Thus the rate equations for the forward and reverse of steps (3.5.2, I) or (3.5.3, I) are identical to equations (1.2.38) and (1.2.39) respectively, and can be rewritten here as,

$$v_1 = k_1'^0 a_{OH} (1-\theta) \exp(\beta\eta F / RT) \quad , \tag{3.5.4}$$

$$v_{-1} = k_{-1}'^0 \theta \exp(-(1-\beta)\eta F / RT) \quad , \tag{3.5.5}$$

where, θ is the fractional coverage of the electrode surface by the adsorbed species formed in these steps (which was given the general representation $(M(Z+1)OH)^{p-}$ in equation (3.5.1, I) , while a_{OH} is the activity of OH^- in the electrolyte solution. The terms $k_1'^0$ and $k_{-1}'^0$ are standard electrochemical rate constants, which were introduced in equations (1.2.14) and (1.2.15) of section 1.2.1. The other symbols in equations (3.5.4) and (3.5.5) also retain the significance originally attributed to them in section 1.2.1.

Recall, that under the hypothesis of pseudo-equilibrium (section 1.2.3), a step or number of steps preceding the RDS can effectively be considered to be in equilibrium if their rate is much greater than that of the RDS. The condition for a step j to be in pseudo-equilibrium is that $i_j \approx 0$. This in turn implies that the forward v_j and reverse v_{-j} rates are approximately equal; $v_j \approx v_{-j}$. Applying this pseudo-equilibrium principle to the first step of pathways (3.5.2) or (3.5.3) involves equating the rate equations (3.5.4) and (3.5.5), from which operation, the following expression for θ can be extracted,

$$\theta = \frac{K a_{OH} e^{\eta F / RT}}{1 + K a_{OH} e^{\eta F / RT}} \quad , \tag{3.5.6}$$

where, $K = k_1'^0 / k_{-1}'^0 = \exp(-\Delta G'^0/RT)$. The $Kc_{OH}e^{\eta F/RT}$ term can be written as $a_{OH}\exp\left[\left(-\Delta G'^0 + \eta F\right)/RT\right]$. At lower values of η, the $\Delta G'^0$ term will dominate the exponent, which will therefore be a significant negative quantity, and thus, in this overpotential range $Kc_{OH}e^{\eta F/RT} << 1$ and equation (3.5.6) reduces to:

$$\theta = Ka_{OH}\exp(\eta F/RT) \tag{3.5.7}$$

Since $\theta = Ka_{OH}e^{\eta F/RT} << 1$, it is clear that at low overpotentials, the Langmuir isotherm is operative in its low coverage mode. The general expression for the rate equation of the second step of schemes (3.5.2) or (3.5.3) is written as:

$$v_{II} = k_{II}'^0\theta\exp(\beta\eta F/RT) \tag{3.5.8}$$

Since, this second step is rate determining, v_{II} will also be the rate of the overall process. Substituting equation (3.5.7) into equation (3.5.8) yields:

$$v_{II} = Kk_{II}'^0 a_{OH}\exp((1+\beta)\eta F/RT) \tag{3.5.9}$$

The rate of transfer of two electrons is limited by the velocity of the rds – therefore the overall current density for oxygen evolution can be written as:

$$i = 2Fv_{II} = 2FKk_{II}'^0 a_{OH}\exp((1+\beta)\eta F/RT) \tag{3.5.10}$$

Taking natural logarithms of equation (3.5.10) yields:

$$\ln i = \ln 2FKk_{II}'^0 + \ln a_{OH} + (1+\beta)\eta F/RT \tag{3.5.11}$$

Assuming, as is the standard practice in such derivations, that β = ½, leads to values for the Tafel slope, b, and the reaction order with respect to OH^- ion concentration, m_{OH^-}, of:

$$b = \left(\frac{\partial \eta}{\partial \log i} \right)_{a_{OH}} = 2.303 \frac{2RT}{3F} \qquad (3.5.12)$$

$$m_{OH-} = \left(\frac{\partial \ln i}{\partial \ln a_{OH}} \right)_{\eta} = 1 \qquad (3.5.13)$$

Hence, it is apparent that the mechanistic pathways outlined in schemes (3.5.2) or (3.5.3), can predict the experimental parameters of b = ~ 40 mV dec^{-1}, and m_{OH^-} = ~ 1. Experimentally measured anodic Tafel slopes can only yield information on oxygen evolution, regarding steps up to, and including the RDS. Thus, as with all o.e.r. mechanisms based on finding agreement between experimental kinetic parameters, and the theoretical values for the same parameters, the proposed steps subsequent to the rds are purely speculative, and other schemes that yield one mole of O_2 as the final product, with regeneration of the original catalytic site may be equally as valid.

It was previously mentioned that, after O'Grady and Yeager[34], a pathway could be written for oxygen evolution, that differs from the mechanism of Burke et al.[40, 41] (which has been adopted in the present work), in the details of the steps subsequent to the RDS. Thus, retaining the concept of a negatively charged hydroxylated surface complex as being the active site towards oxygen evolution, the following mechanism of the type postulated by O'Grady and Yeager[34] can be written;

$$[Ni^{III}O_m(OH)_n]^{p-} + OH^- \leftrightarrows [Ni^{IV}O_m(OH)_{n+1}]^{p-} + e^- \qquad (3.5.14, I)$$

$$[Ni^{IV}O_m(OH)_{n+1}]^{p-} \leftrightarrows [Ni^{IV}O_m(OH)_{n+1}]^{(p-1)-} + e^- \qquad (3.5.14, II)$$

$$\begin{array}{lllll} [Ni^{IV}O_m(OH)_{n+1}]^{(p-1)-} & OH^- & [Ni^{III}O_m(OH)_n\text{-}O\text{-}H\text{--}OH]^{p-} & [Ni^{III}O_m(OH)_n]^{p-} & O \quad HOH \\ + \quad \rightarrow & & | \quad \rightarrow & & + \; \| \; + \\ [Ni^{IV}O_m(OH)_{n+1}]^{(p-1)-} & OH^- & [Ni^{III}O_m(OH)_n\text{-}O\text{-}H\text{--}OH]^{p-} & [Ni^{III}O_m(OH)_n]^{p-} & O \quad HOH \end{array} \qquad (3.5.14, III)$$

While it is obvious that the kinetic analysis of a pathway such as (3.5.14), with a rate limiting second step, would be identical to that presented in equations (3.5.4) to (3.5.13), it is intuitively rather difficult to understand how step (3.5.14, III), which requires the interaction of two surface species could proceed at any appreciable rate under low coverage Langmuir conditions. The steps proposed by Burke et al.[40, 41]

subsequent to the RDS, would seem to be more realistic, and this is a major factor in our adoption of the type of pathway envisaged by these workers, in preference to the scheme of O'Grady and Yeager. It is worth noting that a stoichiometric number of v = 2 is associated with a rate-determining second step in scheme (3.5.14), as opposed to a value of v = 1 for a rate-limiting second step in schemes (3.5.2) or (3.5.3). If the stoichiometric number could be accurately experimentally determined, it would be possible to confidently admit one of these types of mechanistic pathway, while dismissing the other. However, as was discussed in section 1.5.1, it is widely believed that the principle of microscopic reversibility cannot be applied to the oxygen electrode, and consequently experimentally determined values of the stoichiometric number are unreliable.

3.5.2 The Variation of the Tafel Slope From ca. 40 to 46 mV dec^{-1} and an Appropriate Mechanism.

In section 3.5.1, mechanistic pathways were proposed for the oxygen evolution reaction on Ni electrodes, subjected to various types of pre-treatment, on which the kinetics of the reaction were characterised by a Tafel slope of ~ 2.303×2RT/3F and an associated reaction order of approximately unity. However, for some situations with Co and Fe electrodes, the Tafel slope was closer to 2.303×4RT/5F. The latter experimental observation prevailed in the following cases:

1. Pre-reduced bright Ni electrode – Tafel slope observed to increase from ~ 40 to 46 mV dec^{-1} between first steady state polarisation sweep in the positive direction in 5.0 M NaOH, and the second sweep in the same direction – Figure 3.2.13. This was the only observation of a slope of ca. 2.303×4RT/5F for any type of Ni electrode.
2. Non-pre-treated bright Co electrodes – Tafel slope observed to decrease from ~ 2.303×4RT/5F to ~ 2.303×2RT/3F over a range of NaOH solution concentrations from 1.0 M to 5.0 M – Figures 3.3.1, 3.3.5 – 3.3.7
3. Non-pre-treated Co electrode – Tafel slopes recorded in 3.0 M NaOH observed to increase from ca. 43.5 mV dec^{-1} when "fresh" to ca. 47.5 mV dec^{-1} when aged to an "intermediate" degree – Figure 3.3.9.

4. Pre-reduced bright Co electrodes – Tafel slope of ~ 2.303×4RT/5F with an associated reaction order of ca. 1 observed for all concentrations of NaOH solutions – Figures 3.3.17, 3.3.19, 3.3.20.
5. Pre-oxidised Co electrodes – Tafel slopes observed to decrease from ~ 54 to 47 mV dec^{-1} over a range of NaOH solution concentrations from 1.0 M to 5.0 M – Figure 3.3.22.
6. Non-pre-treated bright Fe electrodes – Tafel slopes observed to increase from ~2.303×2RT/3F to ~2.303×4RT/5F over a range of NaOH solution concentrations from 1.0 M to 5.0 M – Figures 3.4.4 – 3.4.6. This trend is directly opposite to that observed for Co electrodes in points 2 and 5.
7. Pre-reduced bright Fe electrode – Tafel slope measured in 1.0 M NaOH observed to increase from 39.5 mV dec^{-1} when the electrode was fresh, to 44 mV dec^{-1} when the electrode was more electrochemically aged – Figure 3.4.8. Similar behaviour noted for polarisation curves recorded in 0.5 and 5.0 M NaOH solutions – Figure 3.4.9.
8. Pre-reduced bright Fe electrodes – Tafel slope of ~2.303×4RT/5F with an associated reaction order of ca. 1 observed for all concentrations of NaOH solutions – Figures 3.4.12 -3.3.15.

Owing to the reservations mentioned in sections 3.3 and 3.4, regarding the reliability of reaction order data derived from plots of log$i$ vs. loga_{OH^-}, which were constructed from steady state polarisation curves where the Tafel slope was observed to vary somewhat with a_{OH^-}, it has been decided not to admit m_{OH^-} parameters determined under such circumstances to our analysis. Therefore, only the reaction order data mentioned in point 4 above, will be considered reliable in the case of Co, while the data cited in point 8 is the only case recorded for Fe electrodes, where b didn't appreciably vary with a_{OH^-}. For both of the aforementioned sets of results an OH^- concentration invariant Tafel slope of ~2.303×4RT/5F was observed, with an associated reaction order of approximately unity. Hence, we seek an oxygen evolution pathway, the mechanistic analysis of which predicts the aforementioned values of these kinetic parameters. Furthermore it is necessary to explain the increase in Tafel slope from ~2.303×2RT/3F to ~2.303×4RT/5F with increasing OH^- concentration, as was noted in point 6 above, for non-pre-treated Fe electrodes. The directly opposite effect was noted in the case of Co (see points 3 and 5 above) and this must also be

discussed. In addition to this an increase in Tafel slope, again from ~2.303×2RT/3F to ~2.303×4RT/5F, was noted upon ageing for non-pre-treated bright Co electrodes (point 3) and for pre-reduced bright Fe electrodes (point 7).

It is also noteworthy, that Tafel slopes of both ~2.303×2RT/3F and ~2.303×4RT/5F are commonly reported in the literature for the o.e.r. at Ni electrodes in alkaline solution. Amongst the workers who, as in the present work, have observed a slope of ~2.303×2RT/3F are Lu and Srinivasan[8], Conway and Liu[9], and Bocca et al.[51] (for sandblasted Ni). Slopes of ~2.303×4RT/5F have been noted by Scarr[52], Sato and Okamoto[53], Bronoel and Reby[54], and Gennero De Chialvo et al.[6]. Publications on the o.e.r. at Co are not nearly as numerous as for Ni, however, Willems et al.[15] noted a Tafel slope of ~2.303×2RT/3F, whereas Scarr[52] observed slopes of ~2.303×4RT/5F. The latter author[52] also reported a Tafel slope of ~ 2.303×4RT/5F for a bright Fe electrode in 1 M KOH solution. It is therefore clear that Tafel slopes of ~2.303×2RT/3F and ~2.303×4RT/5F are commonly observed in polarisation measurements on the o.e.r. at first row transition metal electrodes in alkaline solution.

We now propose that the observation of Tafel slopes of ~2.303×4RT/5F arises from some *dual barrier effect*. Recall from section 1.5.4 that a *dual barrier model* envisages that only a fraction of the total potential difference across the metal/solution interface has a direct effect on the kinetics of the o.e.r. Reviewing the literature, uncovered several such models, which are potentially applicable in the present case. Our preferred model is that due to MacDonald and Conway[56], which we now apply to our experimental results. Subsequent to that, we will make some comments on other dual barrier models, and discuss why they are less likely to be applicable in the present case.

The model of MacDonald and Conway[56] was developed to rationalise lower oxygen evolution Tafel slopes of ~ 2.303×4RT/5F observed by the authors for gold electrodes in acid and alkaline solutions, and an upper slope of ~ 2.303×4RT/F noted only for the alkaline media. The model envisages that only a fraction of the total potential difference, E, between the metallic electrode and the solution is effective in charge transfer at the electrode/solution interface with the remainder of the potential drop occurring across an electronically conductive barrier oxide layer, through which the charge passed during the course of the o.e.r. must migrate. This type of model was first proposed by Meyer[57] to explain very high Tafel slopes observed for cathodic

processes occurring at zirconium electrodes covered by a barrier layer of ZrO_2, and was adapted by MacDonald and Conway for the anodic oxygen evolution reaction. Applying the dual barrier model, MacDonald and Conway[56] envisaged that the total applied potential, E, could be expressed as $E = V_f + V_s$, where V_s is the potential affecting the normal electrochemical charge transfer barrier at the electrode/solution interface, while V_f is the potential affecting the charge migration process across the barrier oxide. Meyer[57] had pointed out that when interfacial electrochemical charge transfer process (oxygen evolution in the present case) is occurring at a steady state, the rate controlling step of that process must be in equilibrium with the charge transfer process through the film. Neither Meyer[57] nor MacDonald and Conway[56] speculated as to the detailed nature of the barrier film charge migration processes, since, as will be shown in the formal analysis, this point is in principle, unimportant with regard to the kinetics of oxygen evolution. Following Meyer, it was assumed by MacDonald and Conway that the rate of the field dependent migration of the charge carriers (magnitude of charge = ze) could be described by the Mott-Cabrera model[58] i.e. –

$$i \propto \exp(ze\delta\Phi / RT) \tag{3.5.14}$$

where, i, is the current through the film, δ is the half jump distance of the charge carriers, and Φ is the magnitude of the electric field. Rewriting equation (3.5.14) in terms of the potential V_f, yields,

$$i_f \propto \exp(ze\delta V_f / DRT) = \exp(ze\beta_f V_f / RT) \tag{3.5.15}$$

where, D is the thickness of the barrier film, and β_f (= δ/D) is the symmetry factor for the field assisted migration of the charge carriers in the film. In order to obtain an analytical expression for the overall steady state electron transfer rate, v, Meyer wrote rate equations for the two individual charge transfer processes. In the case of the interfacial electrochemical charge transfer reaction, the rate equation takes the standard form, that was discussed in sections 1.2.1 – 1.2.3, i.e.

$$v_s = k_s'^{0} \pi_i \left(a_{is}^{mi,s}\right) \exp(\beta_s V_s F / RT) \tag{3.5.16}$$

where, $\pi_i\left(a_{i,s}^{mi,s}\right)$ is the product of the activities of the reactants raised to the appropriate power m_i, and β_s, is the symmetry factor for the reaction. For mathematical convenience the rate equation (equation (3.5.15)) for the field assisted charge migration through the oxide film was presented as:

$$\nu_f = k_f'^0 \pi_j\left(a_{jf}^{mj,f}\right)\exp\left(\beta_f V_f F / RT\right) \tag{3.5.17}$$

Regarding equation (3.5.17), Meyer[57] commented that it should be regarded purely as a formal equation giving the rate of charge transport through an oxide film of constant thickness as a function of the activities $\left(a_{j,f}^{mj,f}\right)$ and the potential V_f. The activities in equation (3.5.17) depend on the nature of the oxide charge migration process and may be thought of, in terms of the effective concentration of the barrier oxide film charge carriers – again it will be shown below that the exact details of the film charge transfer process, are largely irrelevant in the formal kinetic analysis of the interfacial charge transfer reaction. Equating equations (3.5.16) and (3.5.17), and eliminating the V_f and V_s terms by recalling that the overall applied potential, E, is equal to the sum of these two potential terms, yields, after some rather laborious algebra, the following overall rate equation,

$$\nu = K_t\left[\pi_i\left(a_{is}^{mi.s}\right)^{\frac{\beta_f}{\beta_f+\beta_s}}\right]\left[\pi_j\left(a_{jf}^{mj,f}\right)^{\frac{\beta_s}{\beta_s+\beta_f}}\right]\exp\left(\beta_t EF / RT\right), \tag{3.5.18}$$

where,

$$\beta_t = \frac{\beta_f \beta_s}{\beta_f + \beta_s} \tag{3.5.19}$$

and,

$$K_t = k_f'^{0\frac{\beta_s}{\beta_s+\beta_f}} \times k_s'^{0\frac{\beta_f}{\beta_f+\beta_s}} \tag{3.5.20}$$

The term β_t as defined in equation (3.5.19) is an overall symmetry factor taking account of the two charge transfer barriers.

We now examine whether the type of reaction mechanism proposed for the o.e.r. at Ni electrodes in the previous section (schemes (3.5.2) or (3.5.3)), can account for the kinetic parameters (b = ~ 2.303×4RT/5F and $m_{OH^-} \approx 1$) observed for Co and Fe electrodes under the dual barrier model. The second step is again considered to be rate limiting. The rate equations for the first step in the forward and reverse direction are analogous to equations (3.5.4) and (3.5.5), except that the single barrier symmetry factor β is replaced by the more complex β_t symmetry factor defined in equation (3.5.19). Applying the pseudo-equilibrium principle and solving for the fractional coverage θ of the adsorbed intermediates, yields an identical expression to equation (3.5.6). If we assume low coverage Langmuir adsorption this expression for θ reduces, as before, to equation (3.5.7). In this situation the rate equation for the interfacial charge transfer reaction (expressed now in terms of its current density, i_s, cf. equation 3.5.16) becomes:

$$i_s = 2Fk'^{0}_{II}\theta\exp(\beta_s V_s F/RT) = 2Fk'^{0}_{II}K\exp(EF/RT)a_{OH}\exp(\beta_s V_s F/RT) \tag{3.5.21}$$

The expression for the overall current density is therefore,

$$i = 2FK_T(a_{OH})^{\frac{\beta_f}{\beta_f+\beta_s}}\exp((1+\beta_t)EF/RT) \tag{3.5.22}$$

where, $K_T = K.K_t.\left[\pi_{jf}\left(a_{jf}^{mj,f}\right)^{\frac{\beta_s}{\beta_s+\beta_f}}\right]$.

Making, the standard assumption that $\beta_f = \beta_s = ½$ for a single electron transfer step, and inserting these values into equation (3.5.19), gives $\beta_t = ¼$. Inserting this value for the overall symmetry factor into equation (3.5.22) yields:

$$i = 2FK_T(a_{OH})^{\frac{1}{2}}\exp(5EF/4RT) \tag{3.5.23}$$

Taking natural logarithms of equation (3.5.23) achieves:

$$\ln i = \ln 2FK_T + \ln\left(a_{OH}^{1/2}\right) + 5EF/4RT \tag{3.5.24}$$

The predicted values for the Tafel slope, b, and the reaction order with respect to OH^- ion concentration, m_{OH}, are thus:

$$b = \left(\frac{\partial E}{\partial \log i}\right)_{a_{OH}} = 2.303\frac{4RT}{5F} \tag{3.5.25}$$

$$m_{OH} = \left(\frac{\partial \ln i}{\partial \ln a_{OH}}\right)_E = 1/2 \tag{3.5.26}$$

It is clear that while, application of the dual barrier model to the oxygen evolution pathway of schemes (3.5.2) and (3.5.3) (with the second step as RDS and $\theta \rightarrow 0$), leads to the prediction of the experimentally observed Tafel slope for pre-reduced Co and Fe electrodes, it cannot account for the observed reaction order of approximately unity. Referring to equation (3.5.18), it is obvious that the *apparent reaction order* with respect to the activity a_s of a particular reactant species in the electrochemical charge transfer reaction, as measured by $\left(\partial \log i/\partial \log a_s\right)$ is given by the expression:

$$\left(\frac{\partial \log i}{\partial \log a_s}\right)_E = \frac{m_s\beta_f}{\beta_f + \beta_s} \tag{3.5.27}$$

That is to say, that in cases where a potential dependent, field assisted charge migration process occurs in series with the interfacial charge transfer reaction, the experimentally measured $\left(\partial \log i/\partial \log a_s\right)_E$ quantity is actually a fraction, $\beta_f/\beta_f+\beta_s$, of the true reaction order m_s for the latter reaction. If it is again assumed that $\beta_f = \beta_s = ½$, then the quantity $\beta_f/\beta_f+\beta_s = ½$. This explains why the kinetic analysis of schemes (3.5.2) or (3.5.3) under the dual barrier model yielded a value of $\left(\partial \log i/\partial \log a_s\right)_E = ½$ in equation (3.5.26), rather than the correct order of unity for the interfacial oxygen evolution reaction, as was derived in equation (3.5.13). The reaction order given by (3.5.27) is a reaction order for the overall charge transfer process (interfacial

electrochemical reaction and field assisted charge transfer across the barrier oxide), with respect to the activity of one of the reactants in the interfacial electrochemical reaction.

From the point of view of our experimental data, if we admit the applicability of the dual barrier model (assuming again that $\beta_f = \beta_s = ½$ and thus, $\beta_f / \beta_f + \beta_s = ½$), the observation of an experimental apparent reaction of $\left(\partial \log i / \partial \log a_s\right)_E = 1$, in association with a lower overpotential Tafel slope of ~2.303×4RT/5F, implies that the analysis of an appropriate pathway for the o.e.r. on Co and Fe electrodes must predict a Tafel slope of ~ 2.303×2RT/3F and a reaction order of *two* when the oxygen evolution reaction is considered in isolation from the oxide film charge transfer process. Such a combination of b and m_{OH} values cannot arise from the analysis of the O'Grady[34] – Burke[40, 41] type of mechanism that we predicted for the o.e.r. at Ni electrodes in section 3.5.1, schemes (3.5.2) or (3.5.3). Thus, on the basis of the foregoing analysis, it must be concluded that the o.e.r. in alkaline solution proceeds via a different pathway in the cases of Co and Fe electrodes, as compared to the Ni electrode.

It is tentatively suggested at this stage that an appropriate mechanism for oxygen evolution on Co and Fe electrodes in alkaline media, is a pathway of the Bockris Electrochemical Oxide type, i.e.,

$$M + OH^- \leftrightarrows MOH + e^- \qquad (3.5.28, I)$$

$$MOH + OH^- \leftrightarrows MO + H_2O + e^- \qquad (3.5.28, II)$$

$$MO + MO \leftrightarrows 2M + O_2 \qquad (3.5.28, III)$$

where, M, is an electrocatalytically active surface site. In fact this mechanism has already been presented as reaction (1.2.37), and has been used as the "standard mechanism" for the discussion of multi-step electrode kinetics in section 1.2.3, in the discussion of adsorption isotherms and pseudo-capacitance in sections 1.2.2 and 1.2.4. Thus, it has already been shown in the sample kinetic analysis of section 1.2.3, equations (1.2.84) – (1.2.89), that if step (3.5.28, II) is taken as the RDS and low coverage Langmuir adsorption of MOH ($\theta_{MOH} \rightarrow 0$) prevails, then the predicted values for the Tafel slope and reaction order are respectively, b = 2.303×2RT/3F and m_{OH^-} = 2.

Subjecting pathway (3.5.28) to kinetic analysis under the dual barrier model, it is clear that the rate equations for step (3.5.28, I) in the forward and reverse directions will be identical to equations (3.5.4) and (3.5.5) respectively, except that β is now replaced by β_t. As before, if the pseudo-equilibrium principle is applied to step (3.5.28, I), and it is assumed that low coverage Langmuir adsorption conditions apply, the expression for the fractional coverage θ_{MOH} reduces to that of equation (3.5.7). The rate equation for the o.e.r., as affected by the potential drop, V_s, across the barrier for interfacial electrochemical charge transfer is thus,

$$i_s = 2Fk_{II}'^{0} K \exp(EF/RT) a_{OH}^2 \exp(\beta_s V_s F/RT) \tag{3.5.29}$$

leading, to the following expression for the overall current, through the two barriers,

$$i = 2FK_T (a_{OH})^{\frac{2\beta_f}{\beta_f+\beta_s}} \exp((1+\beta_t)EF/RT) \tag{3.5.30}$$

where, K_T, has the same significance as in equation (3.5.22). If $\beta_f = \beta_s = ½$ is inserted into equation (3.5.30), and logarithms are taken of each side, it can readily be shown that:

$$b = \left(\frac{\partial E}{\partial \log i}\right)_{a_{OH}} = 2.303\frac{4RT}{5F} \tag{3.5.31}$$

$$m_{OH} = \left(\frac{\partial \log i}{\partial \log a_{OH}}\right)_E = 1 \tag{3.5.32}$$

These theoretical values for b and m_{OH}- are in good agreement with the experimental values for the same parameters, observed in steady state polarisation measurements on pre-reduced Co and Fe electrodes – see, respectively, points 4 and 8 at the beginning of the present section. Thus, it can be seen that the Bockris Electrochemical Oxide type of o.e.r. pathway can suitably account for the experimental behaviour observed for these pre-reduced Co and Fe electrodes.

We emphasise that the mechanism, as presented in (3.5.28) is not the final version of the pathway that we wish to propose for oxygen evolution at Co and Fe electrodes. At

this point in the discussion, no speculation will be made as to the nature, or oxidation states, of the active sites, M, on polycrystalline Co and Fe surfaces. Furthermore, we have previously expressed reservations (with regard to step (3.5.14, III) in the previous section) about the concept of a chemical recombination step such as (3.5.28, III) proceeding at a sufficient rate, such as not to be rate-limiting, where $\theta \rightarrow 0$. Our definitive view of a feasible mechanism for the o.e.r. at Co and Fe anodes, is reserved for the next section, where the dual slope (~ 60/120 mV dec^{-1}) polarisation behaviour observed for well aged electrodes is discussed. The pathway of scheme (3.5.28) is merely used to illustrate the point that a mechanism involving the electrochemical discharge of one equivalent of OH^- ions in each of the first two steps, is appropriate in the rationalisation of the most reliable experimental data collected for relatively "fresh" Co and Fe electrodes. In addition, a perusal of the summary of expected values for kinetic parameters presented in Table 1.5.1, indicates that under the dual barrier model, both the Krasil'shchikov path with step 3 as the RDS under low coverage Langmuir adsorption conditions, or Kobussen's path with a rate determining second step under similar adsorption conditions, could give rise to the experimental values of b = 2.303×4RT/5F and m_{OH^-} = ~1. The reason behind our preference for the Bockris Electrochemical Oxide type of pathway will also be discussed in the next section.

Some further evidence for the applicability of the dual barrier model in the rationalisation of the o.e.r. steady state polarisation behaviour of Co and Fe electrodes, can be obtained by considering the situation at higher overpotentials. In this case, the $Ka_{OH}e^{EF/RT}$ term in equation (3.5.6) becomes >> 1, and therefore θ_{MOH} approaches unity. In the limit of $\theta_{MOH} \rightarrow 1$, equation (3.5.29) reduces to,

$$i_s = 2Fk_{II}'^{0}\theta_{MOH}a_{OH}\exp(\beta_s V_s F/RT) = 2Fk_{II}'^{0}a_{OH}\exp(\beta_s V_s F/RT) \qquad (3.5.33)$$

and, thus the overall current becomes,

$$i = 2FK_T(a_{OH})^{\frac{\beta_f}{\beta_f+\beta_s}}\exp(\beta_t EF/RT) \qquad (3.5.34)$$

where, on this occasion $K_T = K_t.\left[\pi_{jf}\left(a_{jf}^{mj,f}\right)^{\frac{\beta_s}{\beta_s+\beta_f}}\right]$.

If, as usual it is assumed that $\beta_f = \beta_s = ½$, and logarithms are taken of each side of equation (3.5.34), it follows that:

$$b = \left(\frac{\partial E}{\partial \log i}\right)_{a_{OH}} = 2.303\frac{4RT}{F} \tag{3.5.35}$$

$$m_{OH} = \left(\frac{\partial \log i}{\partial \log a_{OH}}\right)_E = 1/2 \tag{3.5.36}$$

No systematic attempt was made to determine Tafel slopes and associated reaction orders at higher overpotentials, since, as was discussed in section (3.2) – (3.4), it was difficult to determine these parameters in a reproducible manner, even at lower values of η. Indeed, many of the steady state polarisation curves presented earlier in this chapter do not display well-defined linear regions at high anodic overpotentials. Notwithstanding this, upon reviewing the aforementioned polarisation curves in the preparation of this text, it was noted that apparent upper linear Tafel regions with b = ~2.303×4RT/F (= ~236 mV dec^{-1} at 25°C) were present in certain situations. Such upper Tafel slope regions are indicated in Figure 3.3.17 for pre-reduced bright Co electrodes, and in Figures 3.4.4 and 3.4.6 for Fe electrodes.

In the case of the mechanism proposed for oxygen evolution at Ni electrodes (schemes (3.4.2) and (3.4.3)), a analysis similar to that of equations (3.4.33) –(3.4.36), indicates that for this pathway, with $\theta \rightarrow 1$, under the dual barrier model, the expected values of the Tafel slope and reaction order are b = 2.303×4RT/F and m_{OH^-} = 0. We mention this, because higher overpotential Tafel slopes of ~2.303×4RT/F are clearly evident in some of the polarisation curves recorded for the o.e.r. on Ni electrodes – see Figures 3.2.4 and 3.2.20. Combining this observation with that of point 1 at the start of this section, and with the fact that several literature sources[6, 52-55] have reported lower overpotential Tafel slopes of b= ~2.303×4RT/5F, it would appear that, under certain circumstances, dual potential barriers to charge transfer can also be a feature of the o.e.r. at Ni electrodes in alkaline media. The fact that upper slopes of ~2.303×4RT/F (characteristic of the dual barrier model) are noted in Figures 3.2.4 and

3.2.20, at potentials higher than those where slopes of ~2.303×2RT/3F (characteristic of only the normal single barrier to interfacial electron transfer) are observed, is indicative of the fact that dual barrier behaviour may be associated with oxide film ageing, possibly related to the increasing dehydration of the film with increasing anodic potential. Possible physical origins of the oxide film charge transfer barrier are discussed below.

The next issue meriting discussion is the increase in Tafel slope from ~2.303×2RT/3F to ~2.303×4RT/5F with electrochemical ageing, observed for Co and Fe electrodes (points 3 and 7 at the start of the section), and the variation of the Tafel slope between these two values with changing OH^- concentration, also noted for these electrodes (albeit that the trend is directly opposite for Co as compared with Fe – see points 2, 5 and 6 from the start of the section). We believe that these phenomena can be explained, if the oxide film charge transfer barrier, is identified with the inner compact anhydrous region of the anodic oxide films formed on Co and Fe electrodes, or with the interface between this inner region, and the outer more disperse and hydrated region of these films. The dual layer, or sandwich type structure envisaged for the passive films on Ni, Fe and Co electrodes was discussed in the literature review of sections 1.4.1 – 1.4.3. In the dual layer passive oxide model due to Burke and co-workers[59, 60], depicted schematically in Figure 1.4.9, it is envisaged that the majority of the potential drop across the oxide film occurs at the compact layer/dispersed layer interface. It has been pointed out[27] that under conventional steady state anodisation conditions the inner compact layer is likely to be of limited thickness since the activation energy for atom or ion migration is generally quite large. This is due to the fact that in this amorphous, anhydrous inner layer, the ions are held in a rigid manner, in a network of polar covalent bonds that drastically reduce ion transport through this region of the oxide, in turn inhibiting its expansion. In contrast, the model envisages that the outer more dispersed region of the oxide has a similar morphology to redox polymers with the transfer of electrons along the "polymer" chains via a process of self exchange between neighbouring oxy metal groups. In terms of this dual layer model, it would certainly seem that the inner anhydrous oxide region fits the profile of the barrier oxide envisaged by Meyer[57], and MacDonald and Conway[56].

While the discussion of the previous paragraph is all very well from a modelistic point of view, clearly some experimental evidence is required to support the concept of the

identification of the inner compact oxide region with a barrier to charge transfer in series with the standard interfacial electron transfer barrier. We believe that we can provide such evidence.

We deal firstly with the case of Fe electrodes, and the observation that for pre-reduced electrodes, the oxygen evolution Tafel slope increases from ~2.303×2RT/3F to ~2.303×4RT/5F with electrochemical ageing – see point 7 at the start of this section. The relevant steady state polarisation curves for this discussion are Figures 3.4.7 – 3.4.9, while voltammetric profiles characterising the surface electrochemistry of these bright pre-reduced Fe electrodes at various stages in their life-cycle are presented in Figures 3.4.10 and 3.4.11. Without wishing to repeat the discussion of these results, presented in section 3.4, it is worth recalling the comparative CVs of Figure 3.4.11. The "less aged" profile is typical of a pre-treatment scan, subsequent to which a Tafel slope of ~2.303×2RT/3F was recorded in a polarisation measurement in 1.0 M NaOH solution. The "more aged" profile is characteristic of an electrode on which a Tafel slope of ~2.303×4RT/5F was recorded in all NaOH solutions – it was from polarisation experiments on electrodes like this that the reliable reaction order data of m_{OH^-} = ~1 was derived – see Figures 3.4.12 – 3.4.15. Owing to the increased magnitude of the anodic feature centred at ca. 340 mV in the "More Aged" profile compared to the voltammogram of the fresher electrode, it was concluded in our discussion that the inner compact oxide region had a larger relative influence on the surface electrochemistry of the former type of electrode (with its associated o.e.r. Tafel slope of ~2.303×4RT/5F), than the latter (associated Tafel slope of ~2.303×2RT/3F). On this basis, it seems reasonable to connect the rise in o.e.r. Tafel slope with electrode ageing, to a simultaneous increase in the influence of the compact anhydrous oxide on the overall electrochemical properties of the electrode surface.

What of the variation in oxygen evolution Tafel slope from ~2.303×2RT/3F in 1.0 M NaOH to ~2.303×4RT/5F in 5.0 M NaOH, observed for fresh non-pre-treated bright Fe electrodes (see Figures 3.4.4 – 3.4.6)? A gradual ageing effect is clearly an unsatisfactory explanation for this behaviour. Instead, in an attempt to rationalise the aforementioned experimental observation, we refer to a set of experiments performed by Burke and Lyons[26, 27] regarding the influence of OH^- concentration on the extent of growth of hydrous oxide films (expressed in terms of redox charge capacity), formed by repetitive potential cycling of an Fe electrode in solutions of NaOH of

various concentrations. In the case of layers grown for a shorter activation time (5 minutes) a maximum charge capacity was observed at $[OH^-]$ = 1.0 M. However for layers grown for 20 minutes the maximum charge capacity was noted for $[OH^-]$ = 0.1 M, with a sharp decrease in charge capacity with increasing hydroxide ion activity.

The authors postulated that the behaviour noted for longer times was due to a suppression of hydroxide dissociation with increased OH^- ion activity, causing an inhibition of crystallisation of the hydrous outer layer. This in turn leads to the formation of a more amorphous film structure that is more effective in excluding water from the inner region of the film, thereby inhibiting the growth of the dispersed outer hydrous layer. The net effect of this is that the inner compact layer will have an increasing influence on the overall surface electrochemistry of an Fe electrode with increasing OH^- concentration. Thus the explanation for the increase in Tafel slope for fresh bright Fe electrodes with increasing NaOH solution concentration, may be effectively equivalent to that forwarded for the similar Tafel slope increase that accompanies electrode ageing. It is recognised however, that drawing direct parallels between the growth of oxide films by repetitive potential cycling, and their growth during slow potential stepping experiments associated with recording of steady state polarisation curves, may not be an entirely valid exercise.

As previously mentioned, a directly opposite dependence of o.e.r. Tafel slope on $[OH^-]$ was noted for non-pre-treated Co anodes – i.e. b decreases from ~2.303×4RT/5F to ~2.303×2RT/3F upon increasing the NaOH solution concentration from 1.0 M to 5.0 M. In this case it seems that the dual barrier effect is operative at lower OH^- ion concentrations ($[OH^-] \leq 1$ M), but not at higher solution concentrations. Again, we believe that this behaviour can be satisfactorily explained, if the oxide charge transport barrier is associated with the inner compact region of the passive film.

The variation in the initial passivation process of Co electrodes (i.e. the formation of a Co(II) based inner compact oxide phase) with OH^- ion concentration as revealed by the voltammograms of Figure 3.3.8, was discussed in great detail in section 3.3. In the closing comment of that discussion, it was remarked that since the aforementioned voltamograms "reveal fundamental differences in the initial passivation (Co → Co(II) oxidation) of Co electrodes at different NaOH concentrations, it might be expected that (at least) the inner regions (sandwich model) of the passive oxides formed in these different electrolyte solutions would have somewhat different properties".

Without wishing to repeat the exact details of the arguments presented in section 3.3, it was concluded that at the lowest NaOH concentration studied (0.25 M), the initial passivation of the electrode occurs essentially via a solid state Co→ Co(II) oxidation process, similar to the initial passivation of Fe via the formation of an anhydrous compact Fe(II) based oxide. With increasing concentration, especially for $[OH^-] > 1$ M, a rapid dissolution/precipitation mechanism becomes progressively more important in the formation of the initial Co(II) oxyhydroxide film.

At higher potentials (regardless of the OH^- concentration, over the range considered) the outer regions of the initially formed Co(II) based oxide film (CoO or $Co(OH)_2$) will be further oxidised to Co(III) species to form what is generally accepted (see the literature review of section 1.4.3) to be a more hydrated and dispersed outer oxide phase. The properties of the inner passive layer formed at lower OH^- concentrations should be similar to those envisaged in the model of Burke and co-workers[59, 60] discussed above for Fe; i.e. – an anhydrous, compact, amorphous phase, with the ions tightly bound in a network of polar covalent bonds. It is this type of oxide that we have proposed to form a significant barrier to charge transfer, and thus it is not surprising that the dual barrier model appears to be applicable to the kinetics of the o.e.r. at bright Co electrodes in solutions where $[OH^-] \leq 1$ M. On the other hand, the oxide film formed by a rapid dissolution/precipitation reaction, is lightly to be a somewhat crystalline phase albeit with a high defect concentration, owing to the rapid rate of re-precipitation, as envisaged by Erts et al.[22]. Such a phase, would be expected to be characterised, by significantly higher electronic conductivity and ionic mobility, than the inner oxide region formed at lower $[OH^-]$, and thus present a much lower potential barrier to charge migration. The aforementioned considerations provide a satisfactory explanation for the appearance of dual barrier, Tafel slope behaviour in the 1.0 M steady state polarisation curves of Figures 3.3.1 and 3.3.6, while such behaviour is absent from the data recorded in 5.0 M NaOH solutions.

The data of Figure 3.3.9, which shows that the Tafel slope for a non-pre-treated bright Co electrode, increases from ~ 43 mV dec^{-1} to ~ 47.3 mV dec^{-1}, with electrode ageing, is in agreement with similar trends noted for Fe electrodes (Figures 3.4.8 and 3.4.9) as were discussed above. The ineffectiveness of mechanical polishing in removing the entire oxide film formed during anodic polarisation, obviously leads to the gradual build-up over time of a residual barrier type passive oxide layer, adjacent to the metallic surface. Therefore, electrodes, which were initially free from dual barrier

effects with respect to the o.e.r. in a solution of a particular OH^- concentration, display such effects in polarisation measurements in the same solution, when they become somewhat aged (after repeated usage and polishing).

In the case of the polarisation data recorded on pre-reduced bright Co electrodes (Figure 3.3.17), for which a reproducible Tafel slope of ~2.303×4RT/5F (with an associated reaction order of approximately unity) was noted over a range of OH^- concentrations, the applicability of the dual barrier model at all concentrations can be attributed to the pre-reduction regime. Recall from section 3.3, that these electrodes were polished, before being pre-reduced at –1.15 V in 1 M NaOH for five minutes. Polarisation at such a low cathodic potential (just above the onset of a significant hydrogen evolution current) should be effective in rupturing the polar covalent bonds between metal cations and oxyanions, and therefore weakening, if not completely reducing any residual compact oxide structures (resistant to removal by polishing) remaining from previous experiments. Subsequent to the pre-reduction, the electrodes were subjected to one voltammetric cycle between the limits of –1.22 and 0.6 V at a rate of 40 mV s^{-1} in the same 1.0 M NaOH. This meant that the initial re-passivation of the electrode, following pre-reduction took place under identical conditions. Therefore the nature of the innermost compact oxide, adjacent to the metal surface, could be expected to be relatively independent of the concentration of the test solution in which the electrode was to be polarised. This interpretation would seem to be bourn out by the fact that the pre-reduced electrodes displayed the Tafel slope of 2.303×4RT/5F, characteristic of polarisation experiments in 1.0 M NaOH (see above), at all electrolyte concentrations (Figure 3.3.17). By pre-treating the electrodes in 1.0 M NaOH, a barrier type inner compact oxide was formed prior to each polarisation measurement, thus removing the variable that caused a change in Tafel slope with OH^- concentration, and allowing an accurate determination of the reaction order m_{OH^-} (see Figure 3.3.19), subject to the correct required under the dual barrier model.

Further justification of our identification of the oxide charge migration barrier, with the inner compact region of the passive film formed on certain transition metals, can be found by looking beyond our own work. For example, O'Sullivan and Burke[41] prepared thick hydrous oxide films on Rh electrodes in 1.0 M NaOH, by repetitive potential cycling at a rapid rate of 6 V s^{-1} between the limits of 0 and 1.50 V (vs. R.H.E.) for the duration of 3600 cycles. Oxygen evolution steady state polarisation measurements conducted directly on this pre-cycled electrode, indicated a lower Tafel

slope of ca. 48 mV dec^{-1}. In a separate experiment, these workers, subjected an electrode, pre-cycled exactly as before, to a further 255 potential cycles at a much slower rate of 195 mV s^{-1} between extended limits of 0 – 1.9 V, before conduction the steady state polarisation measurement. On this occasion a Tafel slope of ca. 40 mV dec^{-1} was observed. This might be explained by the fact, that during the excursions to cathodic potentials on the slower sweeps (195 mV s^{-1}), sufficient time was available to effect a significant reduction of the inner region of the oxide film, effectively removing the barrier layer that might well have been the source of the higher Tafel slope observed in the other experiment.

From the foregoing analysis and discussion, the dual barrier model of Meyer[57], and MacDonald and Conway[56], although apparently long forgotten in the field of oxygen evolution electrochemistry, would seem to be a satisfactory theory in the rationalisation of Tafel slopes, such as 2.303×4RT/5F or 2.303×4RT/F, that cannot be accounted for by conventional analyses of the standard schemes proposed for the o.e.r. in the literature. Our contribution to the model is the identification of the film charge migration barrier with the inner compact anhydrous region of the anodic oxide, at least for metals on which the duplex layer model of Burke and co-workers[59, 60] or similar models are applicable.

As previously mentioned, there are alternative dual barrier type models, outlined in the literature, that might also be suitable candidates for the rationalisation of some of the experimental kinetic parameters obtained in the present work. One such model is the development by Scarr[52] for the o.e.r., of a dual barrier model originally proposed by Gnanamuthu and Petrocelli[61] to explain Tafel slopes observed in steady state polarisation measurements on the oxygen reduction reaction at Pt, Pd and Au electrodes, in aqueous solutions at various values of pH. This model was discussed in detail in section 1.5.4 (see scheme 1.5.26, equation (1.5.27) and the adjacent text) and it is not proposed to repeat the treatment here. Instead, we recall equation (1.5.27),

$$b = \frac{\nu}{\Sigma_i Z_i f_i + (1-\alpha) Z_r f_r} \cdot \rho \qquad (1.5.27)$$

and apply it to our proposed reaction mechanism for the o.e.r on bright Ni electrodes (scheme 3.5.2 or 3.5.3) with the second step considered to be rate limiting, as in the kinetic analysis of equations (3.5.4) – (3.5.13). For this particular case the

stoichiometric number v is 1. The Z_i parameter also has a value of 1, since only one electron is transferred prior to the RDS. This electron transfer in the first step occurs from a species in solution (OH^-) across the entire interface, to the metallic electrode, and thus $f_i = 1$. One electron is also transferred during the RDS, and so $Z_r = 1$. This particular electron is transferred from the adsorbed complex surface species (envisaged to be located at the inner Helmholtz plane I.H.P.) to the electrode. Hence, under Scarr's model, it is considered that only half of the total potential across the complex interface is effective in this electron transfer, and so $f_r = ½$. The cathodic transfer coefficient is assigned the value of $\alpha = ½$. Recalling from section 1.5.4 that ρ = 2.303RT/F, and inserting the above values into equation (1.5.27) predicts a Tafel slope, b, of 2.303×4RT/5F. Therefore the mathematical prediction of the Gnanamuthu, Petrocelli – Scarr dual barrier model, when applied to a pathway such as that envisaged for the o.e.r. at Ni in schemes (3.5.2) and (3.5.3), is in accord with the Tafel slopes of ~ 2.303×4RT/5F observed in some of the polarisation measurements of the present study.

Now, applying this model to the pathway (3.5.28 – second step rate determining) proposed for oxygen evolution at bright Co and Fe electrodes, the various parameters take the following values: $v = 2$, $Z_i = 1$, $f_i = 1$, $Z_r = 1$, and $f_r = 1$(in contrast to schemes (3.5.2) and (3.5.3), the electron in (3.5.28, II) is transferred from solution to the external circuit). Inserting these values into equation (1.5.27) yields b = 2.303×4RT/3F – clearly not in accord with our experimental data. Variations of pathway (3.5.28) can be envisaged where the stoichiometric number would have a value of $v = 1$, however in this case the predicted value of b would be 2.303×2RT/3F, which is the same as the value yielded by a kinetic analysis in the absence of admitting a dual barrier model.

Clearly, when applied to some mechanisms, the kinetic analysis of which predict a Tafel slope of 2.303×2RT/3F under normal circumstances, the Gnanamuthu, Petrocelli – Scarr dual barrier model can yield a prediction of b = 2.303×4RT/5F. In fact, it can be shown that if the second step of the Krasil'shchikov mechanism (as presented in Table 1.5.1) is taken as rate determining under this dual barrier model, a Tafel slope of 2.303×4RT/5F is also predicted (for this case with low coverage Langmuir adsorption of MOH, a value of b = 2.303×RT/F is produced by the conventional analysis). There is however an obvious flaw with regard to the interpretation of our experimental data in terms of the aforementioned dual barrier

model. With regard to the experimental data mentioned in points 1, 3 and 7 at the beginning of the section, the Tafel slope in these cases increases from ~ 2.303×2RT/3F to ~ 2.303×4RT/5F with ageing of the same electrode. It is very difficult to see how the assumptions of Scarr's model would apply to a somewhat aged electrode, and not apply to the same electrode in the same electrolyte solution when that electrode was "fresher". Furthermore it is difficult to understand how the model would apply in 1.0 M NaOH at a Co electrode, but not at the same electrode in 5.0 M solution, and then display the exact opposite behaviour with respect to OH^- concentration for Fe electrodes. In view of these difficulties the basis of the Gnanamuthu, Petrocelli – Scarr dual barrier model must be dismissed as a possible reason for the observation of Tafel slopes of ~ 2.303×4RT/5F.

The model of MacDonald and Conway[56] is not the only dual barrier theory that accounts for the possible impact of anodic oxide films on the measured kinetic parameters of the o.e.r. at a metallic electrode. In fact, the most developed theory with regard to the effect of oxide films on the rate of oxygen evolution, is that developed by Schultze and Vetter[62] for Pt electrodes in H_2SO_4, and latter expanded by Damjanovic, Birss and co-workers[63 - 65]. There has already been some discussion of the dual barrier model due to the latter authors, with regard to the mechanism of the o.e.r. at Pt electrodes in alkaline solution in the literature review of section 1.5.4 (see pathway (1.5.20) and the adjacent text). The development of this model commenced in the 1970s, with work conducted by Damjanovic et al.[66, 67] on the o.e.r. on the surface of thin anodic films (grown either by potentiostatic or galvanostatic pre-polarisation) in acidic solutions.

The first of these publications[66] involved measuring the effect of anodic film thickness, measured by in-situ ellipsometry, on the rate of the o.e.r. in 0.1 N H_2SO_4. Among the important results of this study were (a) that the film thickness increased with the logarithm of the pre-polarisation current density and (b) the electrode potential recorded in galvanostatic steady state polarisation experiments increased with increasing film thickness (films investigated were no more than 15 Å thick), indicating that the rate of the o.e.r. dropped as film thickness was increased. The subsequent publication[67] employed potentiostatic rather than galvanostatic techniques, and the experiments were conducted in 1N H_2SO_4. The following behaviour was noted (a) the longer the pre-polarisation time at a given anodic potential (5, 10 or 40 minutes), the lower the subsequent activity towards the o.e.r. as revealed by steady

state polarisation measurements, (b) the higher the potential of the pre-polarisation for a given period of time, the lower the activity of the electrode and (c) the catalytic activity of a pre-reduced electrode towards oxygen evolution decreased with the length of time of polarisation at a given overpotential. The authors rationalised these results in terms of the oxide film acting as a barrier to charge transfer in series with the double-layer barrier, and proposed[66, 67] the following expression for the oxygen evolution steady state current density i, across an anodic film of thickness d, at an applied potential V,

$$i = A\exp\left(\frac{-\xi d}{2}\right)\exp\left(\frac{FV}{2RT}\right) \tag{3.5.38}$$

where, A and ξ are constants. Clearly equation (3.5.38) implies that the rate of oxygen evolution decreases exponentially with increasing barrier oxide layer thickness.

In view of the aforementioned work and subsequent[64] results on the dependence of oxygen evolution rates on pH in acidic solutions, Damjanovic, Birss and Boudreaux published[65] a detailed account of their model of electron transfer through anodic oxide films during the o.e.r. at Pt electrodes in acidic solutions. In this dual barrier model, the potential drop across the outer barrier (the outer Helmholtz layer) and the inner barrier (a composite of the oxide film and the inner Helmholtz layer) must be considered separately. As, with their model for the o.e.r. at Pt in alkaline solutions reviewed in section 1.5.4, this model envisaged that only the Galvani potential difference across the inner barrier, $\Delta\phi_{ib}$, controls the rate of the o.e.r., and so, as the electrode potential increases only $\Delta\phi_{ib}$ increases, with the Galvani potential difference across the outer barrier, $\Delta\phi_{ob}$, remaining constant at a given solution pH. Therefore the authors defined what they called the "operative potential difference" E - E_0 (where E is the potential of the electrode with respect to a pH independent reference electrode, and E_0 is the potential at the I.H.P. vs. the same reference electrode), which determines the rate of the o.e.r., as follows,

$$E - E_0 = \Delta E_{ib} = \Delta\phi_{ib} = \phi_M - \phi_{IHP} \tag{3.5.39}$$

where, M represents the metal of the electrode (below the barrier oxide layer). The model envisages that electrons *tunnel* from water molecules located at the I.H.P. through an *insulating* anodic Pt oxide film (10 - 15Å thick) to the underlying metallic electrode. Such a model was originally forwarded by Schultze and Vetter[62], who were in turn, basing their ideas, on earlier concepts of quantum electrochemistry developed by Gurney[68] and Gerischer[69].

Schultze and Vetter[62] also observed an exponential decrease in oxygen evolution current density, for oxide layers formed on Pt electrodes, in 1N H_2SO_4. These workers coulometrically estimated the oxide films in question to be between 4 and 8 Å in thickness. They pointed out that if an electron in an adsorbed water molecule occupies an energy level E_{ad} greater than the Fermi level of the metallic electrode, an electron transfer can take place. However no electron states of the same energy exist in an insulating oxide, and therefore the electron transfer must occur by "direct elastic tunnelling to the unoccupied states in the metal".

With reference to the earlier work of Schultze and Vetter[62], Damjanovic, Birss and Boudreaux[65] produced the following equation for the electron tunnelling current, as a function of the applied potential E (or more correctly $E - E_0$ at constant pH - see equation 3.5.39):

$$i(E)=\nu\kappa\frac{kT}{h}e_0\int_{\varepsilon}N(\varepsilon)S(\varepsilon)[1-f(\varepsilon)]W(\varepsilon,D)\,d\varepsilon \qquad (3.5.40)$$

In equation (3.5.40), κ is the transmission coefficient, υ, as usual, is the stoichiometric number, $N(\varepsilon)$ is the distribution function of electron energy levels , ε, for the water molecules at the I.H.P., $S(\varepsilon)$ is the density of electron states in the metal, $f(\varepsilon)$ is the Fermi function for electron states in the metal, $W(\varepsilon,D)$ is the probability that an electron with energy ε will tunnel across a potential energy barrier of thickness D, while the other symbol retain their usual significance in quantum chemistry.

The authors analysed the effect of changing potential on the various terms in equation (3.5.40) and concluded that at a constant film thickness D, the distribution function of the donor energy levels $N(\varepsilon)$ "is the dominant factor in determining the rate of the o.e.r. with E". Thus the Tafel slopes of ca. 120 mV dec^{-1} observed for Pt electrodes covered by thin oxide films (the thickness D of which didn't vary during the course of the polarisation measurements) in acidic solution[64, 65, 66], and at higher overpotentials

in alkaline solution[70, 71] can be explained as follows; as the applied potential increases by 120 mV, the energy at the Fermi level of the metal with respect to the vacuum decreases by 120 meV, and for the adsorbed water molecules, the number of electrons in energy levels above the Fermi level increases tenfold.

It is notable that the only term in equation (3.5.40) with a dependence on the insulating film thickness D, is the tunnelling probability term, $W(\varepsilon,D)$. Damjanovic et al.[65] analysed this function using the WKB-Gamov approximation, and found that for electrons in the donor water molecules with energies $\Delta\varepsilon$ above or below the Fermi level of the metal electrode E_F, it takes the following form,

$$W(\Delta\varepsilon, D) = \exp\left\{\left[-4\pi(2m_e)^{1/2}/h\right]\cdot\int_0^d [V(x)-\Delta\varepsilon]^{1/2}dx\right\} \qquad (3.5.41)$$

where, $V(x)$ is the magnitude of the potential energy barrier (also measured with respect to E_F), as experienced by a tunnelling electron at a distance x from the metal/oxide interface, and m_e is the relativistic electron mass. The barrier height $V(x)$ is not known and therefore is approximated by the authors as,

$$V(x) = V_{x=0} + \frac{e\Delta\phi_{ib}}{D}x \qquad (3.5.42)$$

where, $V_{x=0}$, is the potential energy barrier height at $x = 0$. Following this analysis, it is clear that the $W(\varepsilon,D)$ term decreases with increasing film thickness D, thus explaining the fall in o.e.r. current density with increasing oxide film thickness. Since, as previously outlined, $\Delta\phi_{ib}$ increases with potential, $V(x)$ also increases with potential, implying that $W(\varepsilon,D)$ decreases, as the applied potential is raised. However the authors point out that since the oxygen evolution current density rises, as the potential is increased, the $N(\varepsilon)$ term must show a significantly stronger dependence on electrode potential than $W(\varepsilon,D)$ does. Indeed they estimate from their ellipsometric and steady state polarisation data on the o.e.r. at a thin oxide film (d = 10 Å) on Pt in acidic solution[63, 66], that while the o.e.r. activity increases by 6 orders of magnitude with a 720 mV increase in applied potential, the $W(\varepsilon,D)$ term in equation (3.5.40) only decreases by a factor of 3. On the basis of the opposing effects of $N(\varepsilon)$ and $W(\varepsilon,D)$ on the current density with increasing potential, the authors estimate that the Tafel slope

should display, a small increase from 120 – 129 mV dec^{-1}. Their analysis further shows, that the correction to the Tafel slope should increase with increasing insulating film thickness, i.e. for films with $D > 10$ Å, not only should the o.e.r. current density drop relative to the 10 Å case that they analysed, but the Tafel slope should increase further from 129 mV dec^{-1}. In fact, while the former effect was observed in their experiments[66, 67], they note that no significant deviation from a Tafel slope of 120 mV dec^{-1} was noted for any of the oxide films over the thickness range investigated, of 10 Å$\leq D \leq$15 Å. On this basis, the authors concluded, that over the range of film thickness examined, it is the distribution function of the donor energy levels $N(\varepsilon)$ that effectively controls the Tafel slope.

While the model described above, provides a relatively sophisticated description of the effect of insulating films on the o.e.r., it cannot make an analytical prediction on the magnitude of the expected increase in Tafel slope (due to $W(\varepsilon,D)$) from the ideal value dictated by $N(\varepsilon)$. This arises from the fact that the detailed form of the function $V(x)$ is not known. The prediction by Damjanovic et al.[65] of a 9 mV dec^{-1} increase in Tafel slope for a 10 Å oxide film, utilised the concept of an average barrier height V_{AV}, the magnitude of which was derived from empirical considerations.

As regards the applicability of the dual barrier model of Damjanovic et al.[65] to the present results on the o.e.r. at Ni, Co and Fe electrodes, one must consider the nature and thickness of the oxide films on these electrodes in alkaline solution, at potentials associated with significant oxygen evolution. A spectroscopic ellipsometric study[72] on a polycrystalline Ni electrode in 1.0 M NaOH at 0.5 V (vs. Hg/HgO, 1 M – this potential is just below the onset of significant oxygen evolution – cf. the data presented in section 3.2) recorded following a potential sweep from –0.9 V, revealed an oxide film of a total thickness of 92 Å. Lu and Srinivasan[8] found that the lower overpotential oxygen evolution steady state polarisation behaviour of a Ni electrode in 1 N KOH, didn't vary much (Tafel slope of ca. 40 mV dec^{-1} observed) for ellipsometrically determined values of oxide film thickness between ~230 and ~1400 Å. The activity decreased somewhat with increasing passive oxide thickness but the authors concluded that, "the chemical nature of the top few layers of the film plays a more important role than the film thickness in the electrocatalysis of the oxygen evolution reaction on nickel".

In the case of Co in 0.1 M NaOH, Foelske and Strehblow[73] used XPS sputter depth profile analysis to measure the thickness of the passive film formed at various

potentials. The oxide film formed by potentiostatic polarisation for 5 minutes at 700 mV (vs. S.H.E.), was found to have a thickness of ca. 60 Å. Strehblow, on this occasion working with Haupt[74], performed similar XPS based, depth profile analysis on the passive oxide layer formed on Fe electrodes in 1 M NaOH. Passive films were again grown by potentiosatic polarisation for 5 minutes at a range of potentials. At ca. 500 mV (vs. Hg/HgO, 1M NaOH, converted from S.H.E. scale used in the original work) the film was determined to be ~ 45 Å thick, increasing to ~ 52 Å for a film grown at ca. 700 mV. In an ellipsometry study on a polycrystalline Fe electrode in 0.05 M NaOH, Huang and Ord[75] found that the inner passive film had a thickness of 38 Å at oxygen evolution on the first galvanostatic cycle, with the outer film increasing its thickness by over 100 Å on each subsequent cycle.

The aforementioned oxide thickness data for Ni, Co and Fe electrodes in alkaline media, indicates that the anodic films present on the surfaces of these metals at oxygen evolution potentials, are significantly thicker than the films of 10 – 15 Å on which Damjanovic et al.[63-67] made experimental observations leading to the development of their aforementioned dual barrier model[65]. In view of the sharp decrease in tunneling current density expected with increasing film thickness (see equations 3.5.40 – 3.5.42) it is significantly less likely that electron tunneling would occur across the thicker films formed on first row transition metal electrodes, relative to those formed on Pt. Of course, in an analogous manner to our association of the charge migration barrier in the Meyer type model with the inner compact oxide region, it is possible that this same region could be the "insulating oxide" through which electrons must tunnel in the Damjanovic model. There is however, significant evidence[75, 76], that the inner compact type of oxide, as envisaged under the duplex layer model[59, 60], acts as a barrier for field limiting ionic transport under anodic conditions, just as envisaged by MacDonald and Conway[56] in their development of Meyer's model. In view of the conclusions of Šimpraga and Conway, that, even at low temperatures (down to -90°C), the initial oxide growth on Ni[77], Co[21] and Fe[78] electrodes in alkaline solution occurs via a nucleation and growth mechanism, as opposed to the sub-monolayer deposition of 2-D arrays of adsorbed OH or O species that characterises the initial oxidation of Pt surfaces, it is likely that the inner passive film on the former electrodes will differ substantially to the phase oxide that forms on Pt, with respect to both structure and electronic conductivity.

In view of the foregoing discussion, it would seem that the Meyer-MacDonald and Conway type dual barrier model, which accounts very well, in a classical manner, for Tafel slopes of ~ 2.303×4RT/5F and ~ 2.303×4RT/F, provides a more suitable rationalisation of these anomalous slopes in the present case, than does the tunnelling model of Damjanovic et al. Nevertheless, the latter model cannot be entirely ruled out, although experimental studies of its applicability to the o.e.r. at first row transition metals, would require the ability and instrumentation to grow, and quantify the thickness of, anodic oxide films on these metals in a reproducible manner.

3.5.3 The Dual Tafel Slope Polarisation Behaviour of Extremely Aged Electrodes

Having rationalised in terms of appropriate mechanisms, the ~ 2.303×2RT/3F Tafel slopes observed for bright Ni electrodes (see section 3.5.1), and the ~ 2.303×4RT/5F Tafel slopes observed for bright Co and Fe electrodes (see section 3.5.2), the one remaining task is to provide an explanation for the observation of Tafel slopes of ~ 2.303×RT/F (59.2 mV dec^{-1} at 25°C) at lower overpotentials, and ~ 2.303×2RT/F (118.3 mV dec^{-1} at 25°C) at higher overpotentials, in steady state polarisation measurements on what we have dubbed "extremely aged" Co and Fe electrodes. To recap, the latter type of Tafel slope behaviour was noted in the following cases:

1. Aged bright Co electrode – surface electrochemistry characterised by voltammetry in Figure 3.3.12. Tafel slope of b = ~ 2.303×RT/F, with m_{OH^-} = ~3/2 noted at lower η, b = ~ 2.303×2RT/F, with m_{OH^-} = ~1 observed at higher η – Figures 3.3.13 – 3.3.16.
2. Aged bright Fe electrode – surface electrochemistry characterised by voltammetry in Figure 3.4.17. Tafel slope of b = ~ 2.303×RT/F, with m_{OH^-} = ~3/2 noted at lower η, b = ~ 2.303×2RT/F, with m_{OH^-} = ~1 observed at higher η – Figures 3.4.16, 3.4.18, 3.4.19.
3. Tafel slopes of ~ 2.303×RT/F were also noted for aged bright Ni electrodes (as characterised by voltammetry in Figure 3.2.10) in 3.0 M and 5.0 M NaOH solutions – see Figures 3.2.8 and 3.2.9 respectively. This type of polarisation behaviour didn't prove to be sufficiently reproducible to determine reaction order values.

As noted in section 3.4 during the discussion of the data referenced in point 2 above, similar oxygen evolution steady state polarisation behaviour was noted by Lyons and Burke[27, 28] for both multi-cycled and bright Fe electrodes in 1.0 M NaOH. Recall, from the literature review of section 1.5.4, that these workers proposed the following modified Krasil'shchikov pathway to explain the observed Tafel slopes,

$$S + OH^- \leftrightarrows SOH + e^- \qquad (3.5.43, I)$$

$$SOH + OH^- \leftrightarrows SO^- + H_2O \qquad (3.5.43, II)$$

$$SO^- + OH^- \leftrightarrows SO_2H^- + e^- \qquad (3.5.43, III)$$

$$SO_2H^- + OH^- \leftrightarrows S + O_2 + H_2O + 2e^- \qquad (3.5.43, IV)$$

where, S denotes an oxyiron electrocatalytic species on the oxide surface. In the formal kinetic analysis[27, 28] of this reaction pathway, under the assumption of Langmuir adsorption conditions, the rate equations for the first step (forward and reverse directions) and the second step (in the forward direction) can be written as follows,

$$v_I = k_I'^0 a_{OH} a_S \exp(\beta\eta F / RT) \quad , \qquad (3.5.44)$$

$$v_{-I} = k_{-I}'^0 a_{SOH} \exp(-(1-\beta)\eta F / RT) \qquad (3.5.45)$$

$$v_{II} = k_{II} a_{SOH} a_{OH} \qquad (3.5.46)$$

where, k_{II}, is a standard chemical rate constant (note the absence of the ′ superscript, which, as was noted in section 1.2.1, is reserved for electrochemical rate constants). Assuming that the overall rate is determined by the second, chemical, step of scheme (3.5.43), we can write,

$$v = v_{II} = v_I - v_{-I} \qquad (3.5.47)$$

Substituting for v_I, v_{-I} and v_{II} from equations (3.5.44) – (3.5.46), into equation (3.5.47), and solving for a_{SOH}, the steady state activity of the surface intermediate species, yields:

$$a_{SOH} = \frac{k_I'^0 a_{OH} a_S \exp(\beta\eta F / RT)}{k_{-I}'^0 \exp(-(1-\beta)\eta F / RT) + k_{II} a_{OH}} \tag{3.5.48}$$

The overall current density is then given by,

$$i = nFv_{II} = \frac{nFk_I'^0 k_{II} a_{OH}^2 a_S \exp(\beta\eta F / RT)}{k_{-I}'^0 \exp(-(1-\beta)\eta F / RT) + k_{II} a_{OH}} \tag{3.5.49}$$

where we have substituted for a_{SOH} from equation (3.5.48) into equation (3.5.46). If step (3.5.42, II) is rate determining at steady state, it follows that $v_{-I} >> v_{II}$. In turn this implies that, $k_{-I}'^0 \exp(-(1-\beta)\eta F / RT) >> k_{II} a_{OH}$, and thus equation (3.5.49) reduces to:

$$i = nFk_{II}\left\{\frac{k_I'^0}{k_{-I}'^0}\right\} a_{OH}^2 a_S \exp(\eta F / RT) \tag{3.5.50}$$

A logarithmic analysis of equation (3.5.50) yields:

$$b = \left(\frac{\partial\eta}{\partial \log i}\right)_{a_{OH}} = 2.303\frac{RT}{F} \tag{3.5.51}$$

$$m_{OH} = \left(\frac{\partial \ln i}{\partial \ln a_{OH}}\right)_{\eta} = 2 \tag{3.5.52}$$

On the other hand, if the initial discharge step is considered to be rate determining, $k_{II} a_{OH} >> k_{-I}'^0 \exp(-(1-\beta)\eta F / RT)$, a reversal of the above situation, and in this case equation (3.5.49) becomes,

$$i = nFk_1'^{0} a_{OH} a_S \exp(\beta\eta F / RT) \tag{3.5.53}$$

Following the normal practice of inserting β = ½ for a single electron transfer step, and then taking logarithms of both sides of (3.5.53) leads to the following values of the Tafel slope b, and the reaction order m_{OH^-},

$$b = \left(\frac{\partial \eta}{\partial \log i} \right)_{a_{OH}} = 2.303 \frac{2RT}{F} \tag{3.5.54}$$

$$m_{OH} = \left(\frac{\partial \ln i}{\partial \ln a_{OH}} \right)_{\eta} = 1 \tag{3.5.55}$$

Thus, Lyons and Burke[27, 28] rationalised their experimental results in terms of scheme (3.5.43), with the second step rate limiting at lower overpotentials leading to the observation of a Tafel slope of ~ 2.303×RT/F, and with rate control switching to the initial discharge step at higher values of η, corresponding to the appearance of a Tafel slope of ~ 2.303×2RT/F. These workers conducted all their steady state polarisation measurements in 1.0 M NaOH, and thus were not in a position to confirm the predictions of the above kinetic analysis with respect to the reaction order m_{OH^-}. In section 3.4, it was argued that the polarisation behaviour referenced in point 2 above, is characteristic of the oxygen evolution reaction proceeding with the same mechanism as it did in the experiments of Lyons and Burke[27, 28]. If, as is likely, this is the case, a problem arises with the suitability of pathway (3.5.43), in the rationalisation of the experimental kinetic parameters. Thus, while the kinetic analysis of scheme (3.5.43) is in good agreement with our experimental parameters (b = ~ 2.303×2RT/F, m_{OH^-} = ~ 1) at higher overpotentials, it predicts a reaction order of m_{OH^-} = 2 for the 2.303×RT/F lower overpotential Tafel region, whereas our experiments suggest that m_{OH^-} = ~3/2. In view of this, an alternative o.e.r. pathway must be identified, the analysis of which, predicts values for the four kinetic parameters (b and m_{OH^-} at both lower and higher η) which are in agreement with the experimental values.

Referring to the comparisons of the polarisation curves of relatively fresh Co electrodes with those of the aged Co electrodes presented in Figure 3.3.9 for 3.0 M

NaOH, and Figure 3.3.11 for 1.0 M NaOH, it would appear that while the current density for the o.e.r. is greater at lower overpotentials for the aged electrode, the curves converge at higher potentials. In addition to this, the range of current densities at which the enhanced current, ca. 60 mV dec^{-1} Tafel slope region is observed is limited in comparison with that at which the lower values of b (ca. 43 – 47 mV dec^{-1}) are noted for the fresher electrodes. The latter steady state polarisation behaviour was rationalised in terms of the Bockris Electrochemical oxide path (3.5.28), with the second step as the RDS, under low coverage Langmuir adsorption of MOH. In view of the enhanced current density observed for the aged electrodes (with their ca. 60 mV dec^{-1} Tafel slopes) at potentials corresponding to the upper current end of the 43 – 47 mV dec^{-1} Tafel region for the fresher electrodes, it would seem to be a reasonable proposal to envisage that the same pathway applies for both types of electrode, but with a higher value of θ_{MOH} on the aged electrode surface at lower overpotentials. That is to say, that for some reason associated with the changed surface electrochemistry of the aged electrode relative to the fresh electrode (see Figure 3.3.12), the Temkin adsorption isotherm applies to the o.e.r. at the former type of electrode, over the upper end of the potential window at which the low coverage Langmuir isotherm applies to the same reaction at the latter electrode type. The convergence of the polarisation curves for both types of electrode at higher overpotentials, is indicative of a common reaction mechanism, proceeding under high coverage ($\theta_{MOH} \rightarrow 1$) Langmuir adsorption conditions. Similar behaviour to that described above for Co, is evident in the comparison of the o.e.r. polarisation curves for relatively fresh, and extremely aged Fe electrodes in Figure 3.4.21.

On the basis of the discussion of the previous paragraph, it seems that a suitable reaction pathway, in the rationalisation of the b = ~ 2.303×RT/F (with m_{OH^-} = ~3/2) Tafel slope behaviour noted at lower η for aged Co and Fe electrodes, might be a Bockris electrochemical oxide type scheme (3.5.28), with the second discharge step rate limiting under Temkin adsorption ($0.2 < \theta < 0.8$) conditions. However, the kinetic analysis for this very situation has already been performed, as an example derivation in section 1.2.3 (equations (1.2.95) – (1.2.99)), and yielded a prediction of b = 2.303 $2RT/F$, and m_{OH} = 1, the exact same prediction that prevails, for the same pathway with the same RDS, under the Langmuir isotherm with $\theta \rightarrow 1$. Thus it would appear that our speculation of the previous paragraph has been without foundation. Re-

examining the derivation of equations (1.2.95) – (1.2.99), however, offers another possibility.

As before the rate equations for the first step in both the forward and reverse directions are,

$$v_I = k_I'^0 a_{OH}(1-\theta_{MOH})\exp(\beta\eta F/RT)\exp(-\gamma r_{MOH}\theta/RT) \quad , \tag{3.5.56}$$

$$v_{-I} = k_{-I}'^0 \theta_{MOH}\exp(-(1-\beta)\eta F/RT)\exp((1-\gamma)r_{MOH}\theta)/RT) \tag{3.5.57}$$

where, γ is (recall section 1.2.2.) a symmetry factor, $0 < \gamma < 1$, and $\gamma = 1-\beta$. It is also worth recalling from sections 1.2.2 – 1.2.4, that r_{MOH} (the Temkin interaction parameter) is the rate of change of the free energy of adsorption of MOH with the total fractional coverage. In equations (1.2.97) and (1.2.98) it was shown that the rate equation for the rate determining, second discharge step, can be written as:

$$v_{II} = k_{II}'^0 a_{OH}\theta_{MOH}\exp(\eta F/2RT)\exp\{(r_{MOH}\theta - \tfrac{1}{2}r_{MOH}\theta - \tfrac{1}{2}r_{MO}\theta)/RT\} \tag{3.5.58}$$

In the original analysis of section 1.2.3, it was assumed that the value of r for the MO intermediate species formed in rate determining second step, would be similar to the value of the same parameter for the MOH intermediate formed in the first step (i.e. formally $r_{MO} = r_{MOH} = r$), since in both cases, adsorption was achieved by bonding of oxygen atoms to the substrate M. The analysis was further pursued on this basis. However, if a physical situation could be envisaged, whereby the rate of change of the free energy of adsorption, r_{II}, of the intermediate species formed in the second step, is negligible in comparison to r_{MOH}, then the kinetic analysis would take a different course. Assuming that such a situation prevails ($r_{MOH} >> r_{II}$), equation (1.2.97) would reduce to,

$$v_{II} = k_{II}'^0 a_{OH}\theta_{MOH}\exp(\beta\eta F/RT)\exp\{(1-\gamma)r_{MOH}\theta)/RT\} \tag{3.5.59}$$

With the second step rate determining, it can be assumed that the initial discharge step is at pseudo-equilibrium. Equating equations (3.5.56) and (3.5.57), in an attempt to obtain an expression for θ_{MOH}, yields:

$$\left\{\frac{\theta_{MOH}}{1-\theta_{MOH}}\right\}\exp\left[\frac{r_{MOH}\theta}{RT}\right]=\frac{k_I^{'0}}{k_{-I}^{'0}}a_{OH}\exp\left[\frac{F\eta}{RT}\right]=Ka_{OH}\exp\left[\frac{F\eta}{RT}\right] \tag{3.5.60}$$

Following Conway and Gileadi[79], it is assumed, that for intermediate values of θ_{MOH}, the linear pre-exponential term in θ_{MOH} can be assumed to approach unity, thus yielding the following simplification of equation (3.5.60):

$$\exp\left[\frac{r_{MOH}\theta}{RT}\right]=Ka_{OH}\exp\left[\frac{F\eta}{RT}\right] \tag{3.5.61}$$

Taking natural logarithms of equation (3.5.61) and rearranging, achieves:

$$r_{MOH}\theta = RT\ln(Ka_{OH})+F\eta \tag{3.5.62}$$

Substituting into the rate equation (3.5.59), yields an expression for the overall rate of oxygen evolution –

$$v = k_{II}^{'0}a_{OH}\theta_{MOH}\exp(\beta\eta F/RT)\exp\left\{(1-\gamma)\ln(Ka_{OH})+\frac{(1-\gamma)\eta F}{RT}\right\} \tag{3.5.63}$$

This expression can be further tidied up as follows:

$$v = k_{II}^{'0}a_{OH}\theta_{MOH}\exp(\beta\eta F/RT)\exp\left\{\ln(Ka_{OH})^{1-\gamma}+\frac{(1-\gamma)\eta F}{RT}\right\}$$

$$v = k_{II}^{'0}a_{OH}\theta_{MOH}(Ka_{OH})^{1-\gamma}\exp\left\{\frac{(1-\gamma+\beta)\eta F}{RT}\right\}$$

Multiplying by $2nFA$ and completing the tidying yields the following expression for the overall current density i:

$$i = 2nFAk_{II}'^{0}\theta_{MOH}K^{1-\gamma}a_{OH}^{2-\gamma}\exp\left\{\frac{(1-\gamma+\beta)\eta F}{RT}\right\} \tag{3.5.64}$$

Performing a logarithmic analysis on equation (3.5.64) achieves:

$$b = \left(\frac{\partial\eta}{\partial\log i}\right)_{a_{OH}} = 2.303\frac{RT}{(1-\gamma+\beta)F} \tag{3.5.65}$$

$$m_{OH} = \left(\frac{\partial\ln i}{\partial\ln a_{OH}}\right)_{\eta} = 2-\gamma \tag{3.5.66}$$

If it is assumed that the symmetry factors β and γ adopt the standard value of ½ for a single electron transfer process, then b = 2.303×RT/F and m_{OH^-} = 3/2. These values are in very agreement, with those obtained experimentally for aged Co and Fe electrodes at lower oxygen evolution overpotentials.

While this is all very well in theory, it is based upon the assumption that the rate of change of the free energy of adsorption, r_{II}, of the intermediate species formed in the second step, is negligible in comparison to r_{MOH}. Clearly such a situation doesn't prevail in the classical Bockris Electrochemical Oxide path (equation 3.5.28), where the production of the MO intermediate species in step (3.5.28, II) involves the formation of a second M-O bond – in this situation r_{MOH} and r_{II} would be expected to be very similar. The most feasible suggestion that has been forwarded for a physically reasonable situation where $r_{MOH} >> r_{II}$, is due to Bockris and Otagawa[80, 81], as was reviewed in section 1.5.4, scheme(1.5.28) and the adjacent text. These authors envisaged the formation of a *physisorbed* hydrogen peroxide intermediate species in an electrochemical step, subsequent to the initial discharge step. This situation is presented in Figure 3.5.1, which is a schematic of the first two steps of oxygen evolution at a perovskite electrode surface in aqueous alkaline solution, as visualised by Bockris and Otagawa. It is interesting to note from this schematic, that they postulate that the electron transfer steps may be accompanied by a series of proton transfers in the hydration spheres of the OH^- ions that are about to be discharged at the electrode surface.

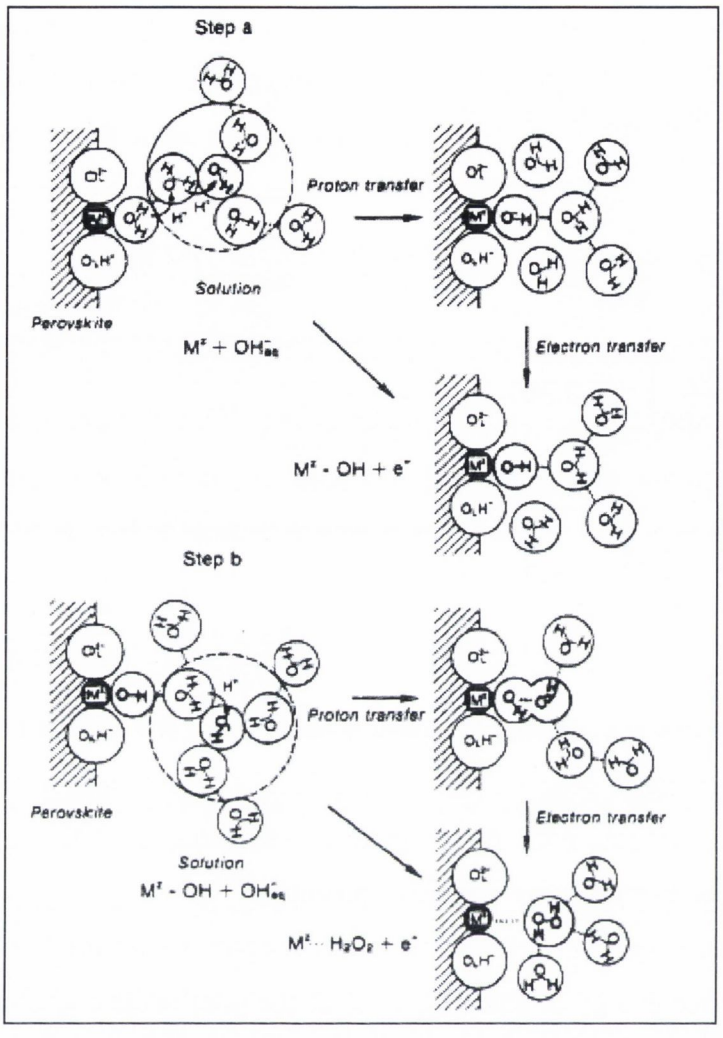


Figure 3.5.1 *Schematic representation of the initial OH^- discharge step (Step A) and the formation of a physisorbed peroxide intermediate (Step B) as originally envisaged by Bockris and Otagawa for the o.e.r. at perovskite type oxide surfaces in aqueous alkaline solution. Reproduced from ref. 80.*

On the basis of the foregoing discussion, the experimental kinetic parameters observed at lower overpotentials in oxygen evolution steady state polarisation measurements on aged Co and Fe electrodes (i.e. b = ~2.303×RT/F and m_{OH^-} = ~3/2) can be accounted for, by a mechanism of the following form,

$$S + OH^- \leftrightarrows S\text{-}OH + e^- \qquad (3.5.67, I)$$

$$S\text{-}OH + OH^- \leftrightarrows S\text{-} \text{-}H_2O_2 + e^- \qquad (3.5.67, II)$$

$$S\text{-} \text{-}H_2O_2 + OH^- \leftrightarrows S\text{-} \text{-}HO_2^- + H_2O \qquad (3.5.67, III)$$

$$S\text{-} \text{-}H_2O_2 + S\text{-} \text{-}HO_2^- \leftrightarrows O_2 + H_2O + OH^- \qquad (3.5.67, IV)$$

where, as before, S is a catalytically active surface site (the nature of which will be discussed later), and S- -H_2O_2 represents physisorbed hydrogen peroxide. Note that the kinetic analysis of this pathway with step (3.5.67, II) as the RDS, under low coverage Langmuir adsorption conditions, is formally identical to that of the Bockris Electrochemical oxide path (scheme 3.5.28). As shown in section 1.2.3, equations (1.2.84) – (1.2.89), this means that such an analysis yields predicted values of b = 2.303×2RT/3F and m_{OH^-} = 2, for the Tafel slope and the reaction order respectively at lower overpotentials. In section 3.5.2 it was shown (equations (3.5.29) – (3.5.32)) that, if the Meyer dual barrier model is admitted, such a mechanism leads to experimentally measured values for the aforementioned kinetic parameters of b = 2.303×4RT/5F and m_{OH^-} = 1. Thus, the physisorbed peroxide mechanism of scheme (3.5.67) can suitably account for the experimental kinetic parameters measured for oxygen evolution on both fresh (section 3.5.2) and aged (current section) Co and Fe electrodes in alkaline solution. Therefore it is our view, that the change in lower overpotential Tafel slope from b = 2.303×2RT/3F or 2.303×4RT/5F (depending on whether a barrier oxide layer exists) for fresh electrodes to b = 2.303×RT/F for extremely aged electrodes, is not due to a change in reaction mechanism, but due to an increased concentration of intermediate species at the surface of the aged electrodes, relative to the fresh electrodes. Possible reasons for this will be explored shortly.

Account must still be made for the kinetic parameters observed for the aged Co and Fe electrodes at higher overpotentials (i.e. b = ~ 2.303×2RT/F, with m_{OH^-} = ~1). The analysis (equations (3.5.44 – 3.5.55) of the modified Krasil'shchikov pathway (scheme 3.5.43) originally proposed to explain the o.e.r. steady state polarisation behaviour at Fe electrodes by Lyons and Burke[27, 28], indicated that such values of b and m_{OH^-} are consistent with rate control by the initial OH^- discharge step, where θs_{OH} → 1. That conclusion is equally valid with respect to the physisorbed peroxide mechanism of scheme (3.5.67), although it would require a change in the RDS from the second step (which is envisaged to be rate limiting under both low coverage Langmuir, and Temkin adsorption conditions) to the first step. On the other hand, it was shown in sections 1.2.2 – 1.2.3, equations (1.2.38) – (1.2.40) and (1.2.90) – (1.2.93), that a kinetic analysis of the Bockris Electrochemical oxide type mechanism (3.5.28) with the second step rate limiting, under high coverage Langmuir adsorption conditions, also predicts b = 2.303×2RT/F, and m_{OH^-} = 1. Again, this analysis is

formally identical to an analysis of the physisorbed peroxide mechanism of scheme (3.5.67), with (3.5.67, II) as the RDS and $\theta_{SOH} \rightarrow 1$. On balance this would seem to be a more satisfactory rationalisation of the kinetic parameters observed for the aged Co and Fe electrodes at higher oxygen evolution overpotentials. In conclusion, it can be commented that the physisorbed peroxide mechanism of equation (3.5.67), with its second step rate limiting, can account for all of the various oxygen evolution Tafel slopes observed for "bright" Co and Fe electrodes. The different slopes are not indicative of different reaction pathways and/or rate determining steps, but rather of changing fractional coverage, θ_{SOH}, of the reaction intermediate S-OH formed in the initial discharge step. The various experimentally observed kinetic parameters, and the adsorption conditions for which they arise are summarised in Table 3.5.1 below.

Experimental Tafel slope	**Experimental Reaction order, m_{OH^-}**	**Adsorption Conditions**
~2.303×2RT/3F	Not reproducible	Langmuir, $\theta_{SOH} \rightarrow 0$
~2.303×4RT/5F	~1 (apparent)	Langmuir, $\theta_{SOH} \rightarrow 0$, Meyer dual barrier applies
~2.303×RT/F	~3/2	Temkin, $0.2 \leq \theta_{SOH} \leq 0.8$, $r_{SOH} >> r_{S\text{-}\text{-}H2O2}$
~2.303×2RT/F	~1	Langmuir, $\theta_{SOH} \rightarrow 1$

Table 3.5.1 *Observed experimental Tafel slopes and reaction orders for Co and Fe electrodes, and the intermediate species adsorption conditions under which each set of parameters can be rationalised by admitting the physisorbed peroxide mechanism of scheme (3.5.67) as operative, with its second step as the RDS.*

The next question that arises is as to the nature of catalytically active surface site S, envisaged in pathway (3.5.67). In the original version of this reaction scheme, S, was represented by Bockris and Otagawa[80, 81] as M^z , where M is a transition metal ion at the surface of a thermally prepared perovskite electrode surface. The perovskite material had the general formula $La_{1-x}A'_xMO_3$ (A' = Sr, K, Ca, Ce, Th, M = Cr, Mn, Fe, Co, Ni), and the authors envisaged that the active site for oxygen evolution was a surface transition metal ion, probably in the +3 oxidation state – i.e. in Figure 3.5.1, z = 3+. The desorption of the M^z- -H_2O_2 species was considered to be rate determining,

with the authors justifying this assertion by using molecular orbital considerations to show that while the M^z-OH bond strength increases in the order Ni < Co < Fe < Mn < Cr, the activity of the $La_{1-x}A'_xMO_3$ electrodes towards the o.e.r. increases in the directly opposite direction.

Recall, from the literature review of section 1.4.3 and the voltammetric results of the present work (section 3.3), that it is widely accepted, that the highest stable valance state of Co, at anodic potentials immediately below the onset of significant oxygen evolution, is the Co(IV) oxidation state. Gennero De Chialvo et al.[19] have proposed that at the surface of the outer hydrous region of the passive layer formed anodically on Co electrodes in NaOH solution, the Co(IV) species is more likely to have a structure similar to a cobaltite IV (CoO_3Na_2) rather than discrete CoO_2 structures. For Fe electrodes in concentrated alkaline solution, it was proposed in section 3.4, that the highest relatively stable oxidation state at high anodic potentials is the Fe(VI) state. Indeed, in one of the few publications dedicated to the o.e.r. at polycrystalline Fe electrodes in alkaline media, Lyons and Burke[28] hypothesised that electrocatalytic surface oxyiron species might well be a ferrate FeO_4^{2-} entity.

On the other hand, the formation of the highly charged Co(IV) or Fe(VI) species is most likely to occur on a non-stoichiometric, defective and quite hydrated oxide surface, as has been proposed for the formation of Ni(IV) ions – see the literature review of section 1.4.1. Furthermore, in view of the amphoteric nature of hydrated anodic oxide surfaces (this point was discussed in detail in sections 1.4.1 and 3.5.1), hydroxylation of these surfaces, possibly by a mechanism similar to that envisaged by Bockris and Otagawa for perovskite surfaces in Figure 3.5.1, is also likely. In view of this, one might feel justified, after O'Sullivan and Burke[41], in representing the active surface sites S of scheme (3.5.67) as $[Co(IV)O_m(OH)_n]^{p-}$ where p=2m+n-4, or $[Fe(VI)O_m(OH)_n]^{p-}$, where p=2m+n-6, as was also proposed for Ni in section 3.5.1. Indeed the case of iron, it is difficult to see how the o.e.r. could proceed at Fe(VI) sites without envisaging the formation of such an anionic surface complex, since FeO_4^{2-} ions are soluble in aqueous alkaline solution[38, 82, 83], and thus are not the most likely candidate for a surface catalytic site. However Fe(VI) ions may be stabilised at the oxide surface if they form negatively charged complex species by coordinating excess hydroxide ions, as proposed above. There may be objections regarding the direct translation of the concept of anionic surface complexes from thick hydrous oxide films formed by repetitive potential cycling, for which it was originally

developed[41, 48], to the surface of the anodic films of the present work. In this regard it is worth recalling the results of Lyons and Burke[28] for oxygen evolution on both bright, and multi-cycled Fe electrodes in 1.0 M NaOH, as were reviewed in both sections 1.5.4 and 3.4. Although the multi-cycled cycled electrode displayed superior catalytic activity, effectively identical Tafel slopes were noted for both types of anode. This indicates that the mechanism, and therefore the nature of the catalytic sites is the same for both types of Fe electrode, albeit that the cycled electrode possesses a greater concentration of these sites per unit geometric surface area.

A representation of a variation of the physisorbed hydrogen peroxide pathway (scheme (3.5.67)) in terms of the negatively charged Fe(VI) surface complex would be as follows:

$$[Fe(VI)O_m(OH)_n]^{p-} + OH^- \leftrightarrows [Fe(VI)O_m(OH)_{n+1}]^{p-} + e^- \quad (3.5.68, I)$$

$$[Fe(VI)O_m(OH)_{n+1}]^{p-} + OH^- \leftrightarrows [Fe(VI)O_m(OH)_n\text{-} \text{-}H_2O_2]^{p-} + e^- \quad (3.5.68, II)$$

$$[Fe(VI)O_m(OH)_n\text{-} \text{-}H_2O_2]^{p-} + OH^- \leftrightarrows [Fe(VI)O_m(OH)_n\text{-} \text{-}HO_2]^{p-} + H_2O + e^- \quad (3.5.68, III)$$

$$[Fe(VI)O_m(OH)_n\text{-} \text{-}HO_2]^{p-} + OH^- \leftrightarrows [Fe(VI)O_m(OH)_n]^{p-} + O_2 + H_2O + e^- \quad (3.5.68, IV)$$

Clearly, an equivalent pathway can be written for the $[Co(IV)O_m(OH)_n]^{p-}$ catalytically active surface site. We have chosen to alter the original pathway of Bockris and Otagawa[80, 81] (reaction 3.5.67) in the steps following the RDS (3.5.68, II), for the same reason that we expressed a preference for pathway (3.5.3) for the o.e.r. on Ni, as opposed to pathway (3.5.14), namely, that it is difficult to intuitively envisage how the chemical recombination reaction in step (3.5.67, IV) could proceed sufficiently rapidly, under low coverage Langmuir adsorption conditions, such as not to render it rate determining.

The question arises as to why the concentration of the adsorbed intermediate $[MO_m(OH)_{n+1}]^{p-}$, is greater at low oxygen evolution overpotentials, on the aged Co and Fe electrodes relative to the fresher electrodes of the same metals? In other words why does the Temkin adsorption isotherm apply at these potentials for the extremely aged electrodes, while the Langmuir isotherm with $\theta \rightarrow 0$ characterises the adsorption of the reaction intermediate on the fresher electrodes? On the basis of the typical voltammetric profiles of these electrodes (Figure 3.3.12 for Co and Figure 3.4.17 for

Fe), with their unusually large background charges at potentials below the onset of significant oxygen evolution, we can only speculate that a rather hydrous oxide phase forms on these electrode surfaces at anodic potentials. This probably arises as a cumulative result of a continuous cycle, over their long periods of service, of mechanical polishing (which we have shown to be not completely effective in the removal of oxide phases) and subsequent re-passivation of surfaces containing some residual oxide material. It may also be related to the long term ageing of a thin residual oxide phase, adjacent to the metal, which is particularly resistant to removal by polishing.

Whatever about this speculation, it does seem certain that the surfaces of the extremely aged electrodes contain a relatively larger concentration of the highly charged metal ions (Co^{4+} or Fe^{6+}) at lower oxygen evolution overpotentials, relative to the fresher electrodes. Therefore at these overpotentials the aged electrode surfaces are possessed of a higher density of acidic proton donating groups, which facilitate the adsorption of hydroxide ions. However, the rate of the increase in concentration of these surface acidic groups is greater for the fresher electrodes, with the result that the oxygen evolution current densities for the fresher and aged anodes, become convergent at higher overpotentials where $\theta \rightarrow 1$. This convergence (see Figures 3.3.9, 3.3.11 and 3.4.21) indicates that the total available active surface area for oxygen evolution is largely unaffected by the ageing of the electrodes.

A further point that requires clarification, is the reason as to why, the polarisation behaviour of the extremely aged Co and Fe electrodes is apparently unaffected by a barrier oxide layer, an issue which becomes increasingly significant for fresher electrodes of these metals with electrochemical ageing. The lack of a dual barrier effect in the case of the extremely aged Fe electrodes, is probably attributable to the fact that these electrodes were subjected to a severe pre-reduction regime (polarisation at –1.3 V for 15 minutes in 1.0 M NaOH – see section 3.4 for more details) prior to the recording of each oxygen evolution steady state polarisation curve. Such a pre-treatment is likely to reduce, or at least weaken the structure, of the residual compact oxide layer, the progressive development of which, the increasing prevalence of the dual barrier effect, with the ageing of fresh Fe electrodes was attributed.

The extremely aged Co electrodes were not subjected to a systematic pre-reduction regime prior to the recording of o.e.r. polarisation data, however before the series of measurements presented in Figure 3.3.14, the electrode had undergone several multi-

cycling experiments in 5.0 M NaOH (-1.22 – 0.6 V at 40 mV s^{-1} for 100 cycles followed by vigorous polishing), in order to see if a voltammetric profile similar to that of a fresh electrode could be regained, by oxidising the surface and then removing the oxide by polishing – it couldn't. However, since these experiments were conducted at an OH^- ion concentration, at which the initial passivation of the electrode occurs largely by a dissolution/precipitation mechanism, it is expected that the inner oxide so formed would not be effective as a barrier layer. Therefore the residual oxide that leads to the unusual voltammetric profile of the aged electrode (see Figure 3.3.12), and to the enhanced o.e.r. catalytic activity of this electrode relative to a fresh anode at lower overpotentials, would not be expected to have the structural properties of a barrier type oxide, as were discussed in section 3.5.2.

An experimental result that hasn't been discussed so far is the observation of Tafel slopes of ~2.303×RT/F for the o.e.r. at aged bright Ni electrodes (as characterised by voltammetry in Figure 3.2.10) in 3.0 M (Figure 3.2.8) and 5.0 M (Figure 3.2.9) NaOH solutions. Unfortunately, it proved impossible to conduct reproducible concentration studies to characterise this polarisation behaviour, and therefore caution must be exercised in interpreting these results. However, in view of our analysis of the Tafel slopes of ~ 2.303×RT/F, observed for oxygen evolution on similarly aged Co and Fe electrodes, it would seem that the aforementioned behaviour is indicative of the o.e.r. proceeding on the aged Ni surface, under Temkin adsorption conditions.

Referring to the mechanistic pathway (scheme 3.5.3) proposed for the o.e.r. at Ni electrodes in section 3.5.1, and denoted the rate of change of the free energy of adsorption of the intermediate species, $[Ni(IV)O_m(OH)_{n+1}]^{p-}$, formed in (3.5.3, I) as r_I, and same parameter for the intermediate, $[Ni(IV)O_m(OH)_{n+1}]^{(p-1)-}$, formed in (3.5.3, II) as r_{II}, it is apparent, that just as for the physisorbed peroxide mechanism of scheme (3.5.67) it can be assumed that $r_I >> r_{II}$. This arises, since the formation of the $[Ni(IV)O_m(OH)_{n+1}]^{(p-1)-}$ entity in the rate determining step, doesn't involve the formation of a Ni-O bond, unlike the formation of the $[Ni(IV)O_m(OH)_{n+1}]^{p-}$ species in the primary discharge step. This means that under a Temkin analysis of pathway (3.5.3), with the second step as rate determining, the rate equation for this second step will be given by,

$$\nu_{II} = k_{II}'^{0}\theta \exp(\beta\eta F / RT)\exp\{(1-\gamma)r_I\theta) / RT\} \qquad (3.5.69)$$

where, θ, is the fractional coverage of $[Ni(IV)O_m(OH)_{n+1}]^{p-}$. Equation (3.5.69) differs from the rate equation (3.5.59) for the second step of the physisorbed peroxide mechanism under similar Temkin adsorption conditions, by only a factor of a_{OH}. Therefore the remainder of the kinetic analysis of pathway (3.5.3), under Temkin adsorption conditions, is directly analogous to that presented in equations (3.5.59) – (3.5.66), with the exception of the aforementioned a_{OH} factor. If such an analysis was conducted, it is clear that it would yield, b = 2.303×RT/F and m_{OH^-} = ½. Thus, the observed Tafel slope of ca. 60 mV dec^{-1} for the aged Ni electrode in 3.0 and 5.0 M NaOH solutions, can be rationalised in terms of our previously proposed Ni o.e.r. pathway (scheme 3.5.3) proceeding under conditions of Temkin adsorption. Unfortunately the lack of an experimentally derived value for m_{OH^-}, doesn't permit the further verification of, or alternatively the rejection of, this proposal.

3.5.4 Concluding Remarks on the Mechanism of Oxygen Evolution on Ni, Co and Fe Electrodes in Alkaline Solution, as Revealed by Steady State Polarisation Measurements

On the basis of the oxygen evolution steady state polarisation measurements outlined and discussed in this chapter, we conclude, that while the reaction proceeds via a common pathway on bright polycrystalline Co and Fe electrodes, the mechanism is somewhat different for bright polycrystalline Ni electrodes. An appropriate mechanism for the o.e.r. at Ni electrode surfaces is presented in section 3.5.1, scheme (3.5.3). The most suitable oxygen evolution reaction pathway for Co and Fe electrodes is scheme (3.5.68), section 3.5.3. These conclusions mirror those of Bockris and Otagawa[80, 81] who studied the o.e.r. on perovskite electrodes in alkaline solution, and found that whereas a common mechanism applied for cobaltates and ferrites, the details of the pathway for nickelates were somewhat different.

The mechanism proposed for Ni, and that proposed for Co and Fe in the present work, do bear some similarities to each other. In both cases, the rate-determining step is envisaged to be an electron transfer step, immediately subsequent to the primary discharge process. However the differences arise in the role of the central metal cation

of the catalytically active surface group. In the case of Ni, the oxygen evolution process involves the oxidation of a Ni^{3+} cation to a Ni^{4+} cation, and the subsequent decomposition of the unstable product so formed. The metal cations of the complexes formed on the hydrated oxide surfaces of Co and Fe electrodes, play a more "passive" role, facilitating the coordination of an OH group in the primary discharge step without actually being oxidised to a higher valance state. Thus, while Ni ions are actually oxidised in the oxygen evolution process, the Co and Fe electrodes, effectively act as electron sinks, facilitating the transfer of electrons from OH^- ions to the external circuit, but with no oxidation of metal cations.

The above conclusions are based on the fact that it is very difficult to rationalise the kinetic parameters obtained for the o.e.r. on Ni electrodes, without admitting the concept of the cyclical formation and decomposition of a higher oxide, while at the same time, we cannot envisage a pathway for Co and Fe electrodes, that can both account for the experimental parameters and involve the participation of a higher oxide entity. Whereas the concept of oxygen evolution as a "side reaction" to facilitate the decomposition of unstable higher oxide species formed at extreme anodic potentials in aqueous solution is appealing, we are forced to conclude that this idea is not generally true.

Bockris and Otagawa[80, 81] proposed the pathway presented as scheme (3.5.67), as the operative mechanism for the o.e.r. on cobaltate and ferrite electrodes in alkaline solution. These workers obtained the same values for the Tafel slope and associated reaction order for nickelate electrodes at lower oxygen evolution overpotentials, as were observed for bright polycrystalline Ni electrodes in the present study – i.e. b = ~2.303×2RT/3F and m_{OH^-} = ~1. As was discussed in section 3.5.1, these values for b and m_{OH^-} can only be reasonably rationalised in terms of a rate determining second electron transfer step that doesn't involve the discharge of an OH^- ion from solution, subsequent to the primary discharge step. To maintain consistency with the pathway (3.5.67) that they proposed for cobaltates and ferrites, Bockris and Otagawa[80] devised a variation of this mechanism, where the OH^- ion required to form the physisorbed peroxide species in the second step, is provided from an oxygen vacancy on the surface of the oxide lattice. This surface OH^- ion is envisaged to be formed, when an oxide surface O^{2-} ion accepts a proton from H_2O according to the process depicted below,

$$\begin{matrix} Ni + H_2O \leftrightarrows Ni—OH^- \\ | \qquad\qquad | \\ O^{2-} \qquad\quad OH^- \end{matrix} \qquad (3.5.70)$$

and, is replenished in the last step of the proposed o.e.r. pathway. This proposal dispenses with the need for one of the electrons lost to the external circuit in the first two steps of the mechanism, to be provided by the oxidation of a Ni^{3+} ion to Ni^{4+}.

The participation of oxygen atoms from the oxide surface in the o.e.r. is a rather controversial subject. An oft cited study on the o.e.r. at an oxidised Pt electrode surface, performed by Rozental' and Vesolovskii[86], in which ^{18}O labelling techniques were used in combination with mass spectrometry, indicated that some of the evolved oxygen originated from the oxide lattice. The same conclusion was drawn from a similar experiment conducted on Li-NiO[87]. On the basis of the findings of Rozental' and Vesolovskii[86], a mechanism based upon the involvement of oxygen atoms from the surface oxide film of pre-anodised Pt electrodes, in the o.e.r. at such electrodes in acidic solution was forwarded by Damjanovic and Jovanovic[67]. However a more recent ^{18}O labelling study by Willsau et al.[88] found that the gaseous oxygen evolved in both acidic and alkaline solutions from pre-oxidised Pt anodes contained no appreciable amount of O originating from the oxide film, and thus casts doubt on the original findings of Rozental' and Vesolovskii[86]. Although Bockris and Otagawa[80, 81] didn't have any direct evidence, of the ^{18}O labelling experiment variety, for the participation of lattice oxygen atoms in the o.e.r. at nickelate electrodes, they cite a thermogravimetry study by Nakamura et al[89] which studied the chemical stability of perovskites $LaBO_3$ (B= V, Cr, Mn, Fe, Co, Ni) at 1000^0C in an environment in which the partial pressure of O_2 could be varied. Of all these perovskite phases, the nickelate phase displayed the lowest stability, indicating lattice oxygen atoms were most easily removed from this material. This observation could explain why the lattice oxygen mechanism might be operative at nickelate surfaces, but not at ferrite or cobaltate electrodes.

In view of the absence of experimental evidence for the direct participation of lattice oxygen atoms in the o.e.r. at Ni (or indeed nickelate) electrode surfaces, we must conclude that the more likely pathway for the reaction is that involving the cyclical formation and decomposition of surface Ni^{4+} ions - entities, the existence of which is very well authenticated in the literature (see section 1.4.1). Nevertheless, a reaction

pathway analogous to that proposed by Bockris and Otagawa[80, 81] for nickelates, cannot be entirely dismissed.

Chapter 3 References

1 Burke, L.D., Twomey, T.A.M., *J. Electroanal. Chem.,* **1984**, *167*, 285.

2 Barnard, R., Randell, C.F., Tye, F.L., *J. Appl. Electrochem.*, **1980**, *10*, 109.

3 Bode, H., Dehmelt, K., Witte, J., *Electrochimica. Acta.,* **1966**, *11*, 1079.

4 Sac-Epee, N., Palacin, M.R., Delahaye-Vidal, A., Chabre, Y., Tarascon, J-M., *J. Electrochem. Soc.*, **1998**, *145*, 1434.

5 Burke, L.D., Twomey, T.A.M., *J. Electroanal. Chem.,* **1984**, *162*, 101.

6 Gennero De Chialvo, M.R., Chialvo, A.C., *Electrochimica. Acta.,* **1988**, *33*, 825.

7 McBreen, J., in "Handbook of Battery Materials", Besenhard, J.O., Ed., Wiley-VCH, Weinheim, 1999.

8 Lu, P.W.T., Srinivasan, S., *J. Electrochem. Soc.*, **1978**, *125*, 1416.

9 Conway, B.E., Liu, T., *J. Chem. Soc., Faraday Trans, 1,* **1987**, *83*, 1063.

10 Sato, N., Okamoto, G., *Electrochimica. Acta.,* **1965**, *10*, 495.

11 Srinivasan, V., Cornilsen, B.C., Weidner, J.W., *J. Solid State Electrochem.*, **2005**, *9*, 61.

12 Seghiouer, A., Chevalet, J., Barhoun, A., Lantelme, F., *J. Electroanal. Chem.,* **1998**, *442*, 113.

13 Wolf, J.F., Yeh, L-S. R., Damjanovic, A., *Electrochimica. Acta.,* **1981**, *26*, 409.

14 Kobussen, A.G.C., Mesters, C.M.A.M., *J. Electroanal. Chem.,* **1980**, *115*, 131.

15 Willems, H., Kobussen, A.G.C., De Wit, J.H.W., and Broers, G.H.J., *J. Electroanal. Chem.*, **1984**, *170*, 227.

16 Scarr, R.F., *J. Electrochem .Soc.,* **1969**, *116*, 1526.

17 Burke, L.D., Lyons, M.E.G., Murphy, O.J., *J. Electroanal. Chem.*, **1982**, *132*, 247.

18 Liu, T.-C., Pell, W.G., Conway, B.E., *Electrochimica. Acta.,* **1999**, *44*, 2829.

19 Gennero De Chialvo, M.R., Chialvo, A.C., *Electrochimica. Acta.,* **1990**, *35*, 437.

20 Gomez Meier, H., Vilche, J.R., Arvia, A.J., *J. Electroanal. Chem.*, **1982**, *138*, 367.

21 Šimpraga, R.P., *J. Electroanal. Chem.*, **1993**, *355*, 79.

22 Erts, D., Ahlberg, E., Asbjörnsson, J., Olin, H., Prikulis, J., *J. Appl. Phys.,* **1998**, *A 66*, S477.

23 Gomez Meier, H., Vilche, J.R., Arvia, A.J., *J. Electroanal. Chem.*, **1982**, *134*, 251.

24 Foelske, A., Strehblow, H.-H., *Surf. Interf. Anal.*, **2002**, *34*, 125.

25 Göhr, H., *Electrochimica. Acta.,* **1966**, *11*, 827.

26 Burke, L.D., Lyons, M.E.G., *J. Electroanal. Chem.*, **1986**, *198*, 347.

27 Lyons, M.E.G., Ph.D. Thesis, University College, Cork, 1983.

28 Lyons, M.E.G., Burke, L.D., *J. Electroanal. Chem.*, **1984**, *170*, 377.

29 Amaral, S.T., Martini, E.M.A., Muller, I.L, *Corros. Sci.,* **2001**, *43*, 853.

30 Brandon, M.P., Final Year Undergraduate Project, Trinity College, Dublin, 2003.

31 Tseung, A.C.C., Jasem, S., *Electrochimica. Acta.,* **1977**, *22*, 31.

32 Rasiyah, P., Tseung, A.C.C., Hibbert, D.D., *J. Electrochem. Soc.*, **1982**, *129*, 1724.

33 Rasiyah, P., Tseung, A.C.C., *J. Electrochem. Soc.*, **1983**, *130*, 2384.

34 O'Grady, W., Iwakura, C., Huang, J., Yeager, E., in "Proceedings of the Symposium on Electrocatalysis", Breiter, M.W., ed., The Electrochemical Society Inc., Pennington, NJ, 1974, p286.

35 Joiret, S., Keddam, M., Novoa, X.R., Perez, M.C., Rangel, C., Takenouti, H., *Cement & Concrete Composites*, **2002**, *24*, 7.

36 O'Sullivan, E.J.M., Burke, L.D., *J. Electrochem. Soc.*, **1990**, *137*, 466.

37 Pourbaix, M., "Atlas of Electrochemical Equilibrium in Aqueous Solutions", Pergamon Press, London, 1965.

38 Beverskog, B., Puigdomenech, I., *Corros. Sci.,* **1996**, *38*, 2121.

39 Larramona, G., Gutierrez, C., *J. Electrochem. Soc.*, **1989**, *136*, 2171.

40 Lyons, M.E.G., Burke, L.D., *J. Chem. Soc., Faraday Trans. 1*, **1987**, *83*, 299.

41 O'Sullivan, E.J.M., Burke, L.D., *J. Electrochem. Soc.*, **1990**, *137*, 466.

42 Foerster, F., *Z. Phys. Chem.*, **1909**, *69*, 236.

43 Rasiyah, P., Tseung, A.C.C., Hibbert, D.D., *J. Electrochem. Soc.*, **1982**, *129*, 1724.

44 Rasiyah, P., Tseung, A.C.C., *J. Electrochem. Soc.*, **1983**, *130*, 2384.

45 Rasiyah, P., Tseung, A.C.C., *J. Electrochem. Soc.*, **1983**, *130*, 365.

46 Burke, L.D., Whelan, D.P., *J. Electroanal. Chem.,* **1984**, *162*, 121.

47 Burke, L.D., Lyons, M.E.G., O'Sullivan, E.J.M., Whelan, D.P., *J. Electroanal. Chem.,* **1981**, *122*, 403.

48 Burke, L.D., Lyons, M.E.G., Whelan, D.P., *J. Electroanal. Chem.,* **1982**, *139*, 131.

49 Burke, L.D., Scannell, R.A., *Platinum Metals Rev.*, **1984**, *28*, 56.

50 Burke, L.D., Lyons, M.E.G., in "Modern Aspects of Electrochemistry, Vol. 18", White, R.E., Bockris, J.O'M., Conway, B.E., Ed., Plenum Press, New York, 1986, p169.

51 Bocca, C., Barbucci, A., Cerisola, G., *Int. J. Hydrogen Energy*, **1997**, *23*, 247.

52 Scarr, R.F., *J. Electrochem .Soc.,* **1969**, *116*, 1526.

53 Sato, N., Okamoto, G., *Electrochimica. Acta.,* **1965**, *10*, 495.

54 Bronoel, G., Reby, J., *Electrochimica. Acta.,* **1980**, 25, 973.

55 Davidson, C.R., Kissel, G., Srinivasan, S., *J. Electroanal. Chem.*, **1982**, *132*, 129.

56 MacDonald, J.J., Conway, B.E., *Proc. R. Soc. London, Ser. A*, **1962**, *269*, 419.

57 Meyer, R.E, *J. Electrochem. Soc.*, **1960**, *107*, 847.

58 Cabrera, N., Mott, N.F., *Repts. Prog. Phys.,* **1948-49**, *12*, 163.

59 Burke, L.D., O'Sullivan, E.J.M., *J. Electroanal. Chem.*, **1981**, *117*, 155.

60 Burke, L.D., Casey, M.I., Cunnane, V.J., Murphy, O.J., Twomey, T.A.M., *J. Electroanal. Chem.*, **1985**, *189*, 353.

61 Gnanamuthu, D.S., Petrocelli, J.V., *J. Electrochem. Soc.*, **1967**, *114*, 1036.

62 Schultze, J.W., Vetter, K.J., *Electrochimica. Acta.,* **1973**, *18*, 889.

63 Birss, V.I., Damjanovic, A., *J. Electrochem. Soc.*, **1983**, *130*, 1688.

64 Birss, V.I., Damjanovic, A., *J. Electrochem. Soc.*, **1983**, *130*, 1694.

65 Damjanovic, A., Birss, V.I., Boudreaux, D.S. *J. Electrochem. Soc.*, **1991**, *138*, 2549.

66 Damjanovic, A., Ward, A.T., O'Jea, M. *J. Electrochem. Soc.*, **1974**, *121*, 1186.

67 Damjanovic, A., Jovanovic, B. *J. Electrochem. Soc.*, **1976**, *123*, 374.

68 Gurney, R.W., *Proc. R. Soc. London, Ser. A*, **1931**, *134*, 137.

69 Gerischer, H., *Z. Phys. Chem. NF*, **1960**, *26*, 223.

70 Birss, V.I., Damjanovic, A., *J. Electrochem. Soc.*, **1987**, *134*, 113.

71 Birss, V.I., Damjanovic, A., Hudson, P.G., *J. Electrochem. Soc.*, **1986**, *133*, 1621.

72 de Souza, L.M.M., Kong, F.P., McLarnon, F.R., Muller, R.H., *Electrochimica. Acta.*, **1997**, *42*, 1253.

73 Foelske, A., Strehblow, H.-H., *Surf. Interf. Anal.*, **2002**, *34*, 125.

74 Haupt, S., Strehblow, H.-H., *Langmuir*, **1987**, *3*, 873.

75 Huang, Z.Q., Ord, J.L., *J. Electrochem. Soc.*, **1985**, *132*, 24.

76 Ho, F.C., Ord, J.L., *J. Electrochem. Soc.*, **1972**, *119*, 139.

77 Šimpraga, R., Conway, B.E., *J. Electroanal. Chem.*, **1990**, *280*, 341.

78 Šimpraga, R., Conway, B.E., *J. Electroanal. Chem.*, **1991**, *313*, 161.

79 Conway, B.E., Gileadi, E., *Trans. Faraday Soc.*, **1962**, *58*, 2493.

80 Bockris, J.O'M., Otagawa,T., *J. Phys. Chem.*, **1983**, *87*, 2960.

81 Bockris, J.O'M., Otagawa,T., *J. Electrochem. Soc.*, **1984**, *131*, 290.

82 Bouzek, K., Rousar, I., *J. Appl. Electrochem.*, **1993**, *23*, 13.

83 Bouzek, K., Rousar, I., *J. Appl. Electrochem.*, **1996**, *26*, 919.

84 Buckley, D.N., Burke, L.D., *J.C.S. Faraday I*, **1976**, *72*, 2431.

85 Miles, M.H., Huang, Y.H., Srinivasan, S., *J. Electrochem. Soc.*, **1978**, *125*, 1931.

86 Rozental', K.I., Vesolovskii, V.F., *Doklady Akad. Nauk, SSSR*, **1956**, *111*, 637.

87 Lee, C., Riga, A., Yeager, E., in "Mass Transport Phenomena in Ceramics", Cooper, A.R., Heuer, A.H., Ed., Plenum Press, New York, 1975, p 489.

88 Willsau, J., Wolter, O., Heitbaum, J., *J. Electroanal. Chem.*, **1985**, *195*, 299.

89 Nakamura, T., Petzow, G., Gauckler, L.J., *Mater. Res. Bull.*, **1979**, *14*, 649.

CHAPTER 4

ELECTROCHEMICAL IMPEDANCE SPECTROSCOPY STUDIES

4.1 Introduction

This chapter deals with the results of electrochemical impedance spectroscopy (EIS) studies on polycrystalline Ni, Co and Fe electrodes in 1.0 M NaOH solutions in the potential range associated with significant oxygen evolution current densities. The background theory for this technique has been presented in chapter 2, sections 2.1.4 – 2.1.8.

4.2 EIS Studies of Oxygen Evolution on Fe Electrodes

4.2.1 Experimental Results and Discussion of an Appropriate Equivalent Circuit

It has been elected to start the treatment of the EIS data by considering the results obtained for various Fe electrodes, since, of the three metals examined, these anodes display the most general impedance behaviour with respect to oxygen evolution. It will, for example, be shown that the equivalent circuit models most likely to be applicable to the o.e.r. at Ni and Co electrodes, are special cases of that suggested by the impedance measurements on the reaction at the Fe substrate.

Bode plots recorded at various potentials for a pre-reduced 'extremely' aged Fe electrode in 1.0 M NaOH are presented in Figure 4.2.1. This is the type of electrode that was characterised by voltammetry in Figure 3.4.17. The relevant o.e.r. steady state polarisation curves were presented in Figures 3.4.16 and 3.4.18. In the discussions of this chapter it is always useful to acquire a sense of the position within the o.e.r. potential range, of a potential at which a given EIS spectrum has been recorded, by consulting the relevant polarisation curve. These impedance data were recorded continuously, starting at the lowest potential (0.68 V) and proceeding in the direction of increasingly potential. Each measurement lasted for approximately five and a half minutes. For the present, we concentrate only on the raw impedance data points - the circles in Figure 4.2.1 and the plots that follow. As indicated in the captions to these figures, the continuous lines represent the results of fitting the raw data to appropriate equivalent circuit models. It has been decided to present the data firstly, and then to address the issue of appropriate equivalent circuits.

Although difficult to visualise from the $|Z|$ plot, it is evident from the phase angle plot, that there are (at least) three RC time constants involved in the impedance

response (at potentials between 0.68 and 0.72 V in any case). This behaviour is particularly pronounced for the spectra recorded at potentials of 0.7 and 0.72 V.

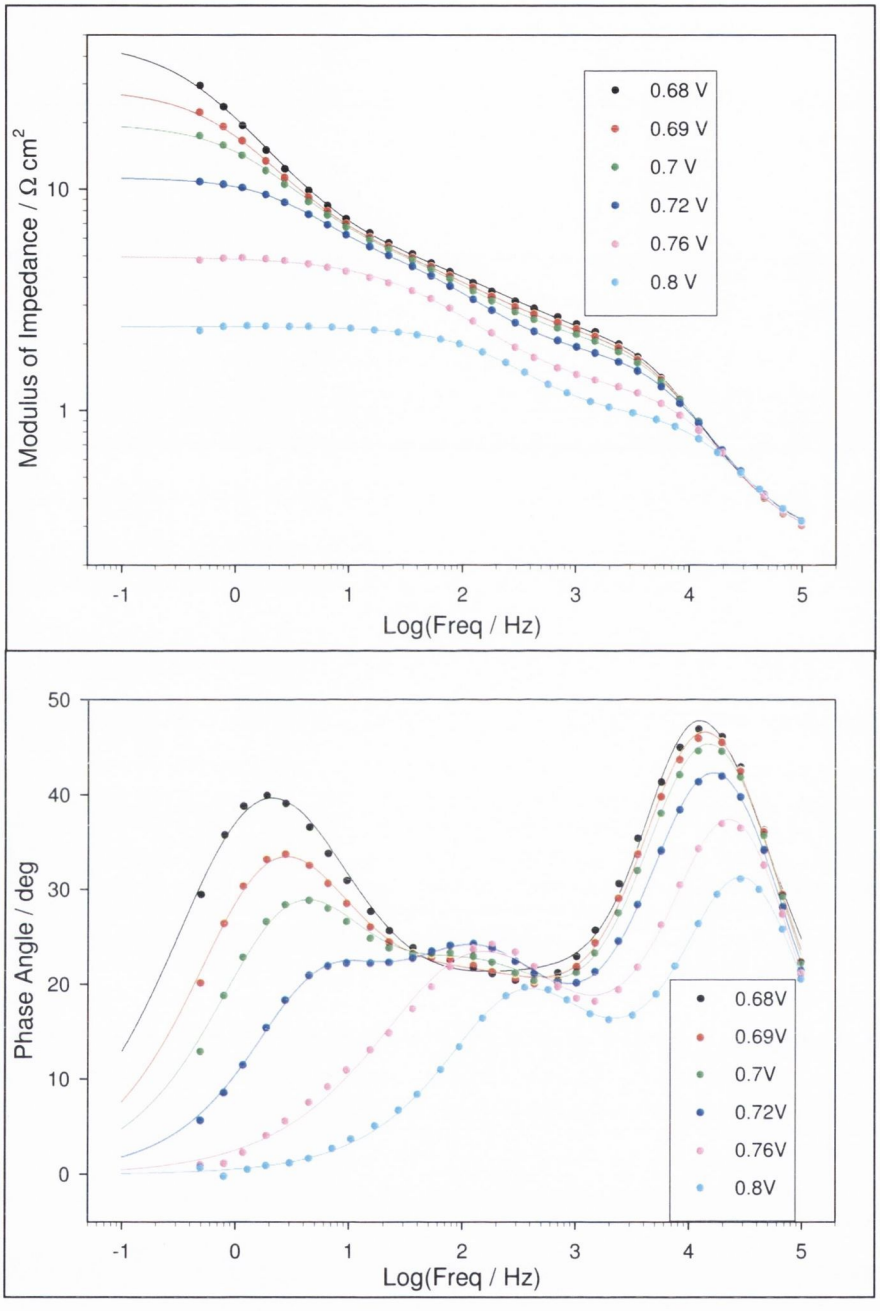


Figure 4.2.1 *Bode plots recorded at various potentials within the region of significant oxygen evolution current density for a pre-reduced aged polycrystalline Fe electrode in 1.0 M NaOH at 25°C. The raw data is represented by the dots. The continuous lines are the results of CNLS fits to Circuit 4 (0.76 and 0.8 V) or Circuit 3 (all the others) – see later.*

The presence of the three RC time constants is also evident in the Nyquist representation of this impedance data – see Figure 4.2.2.

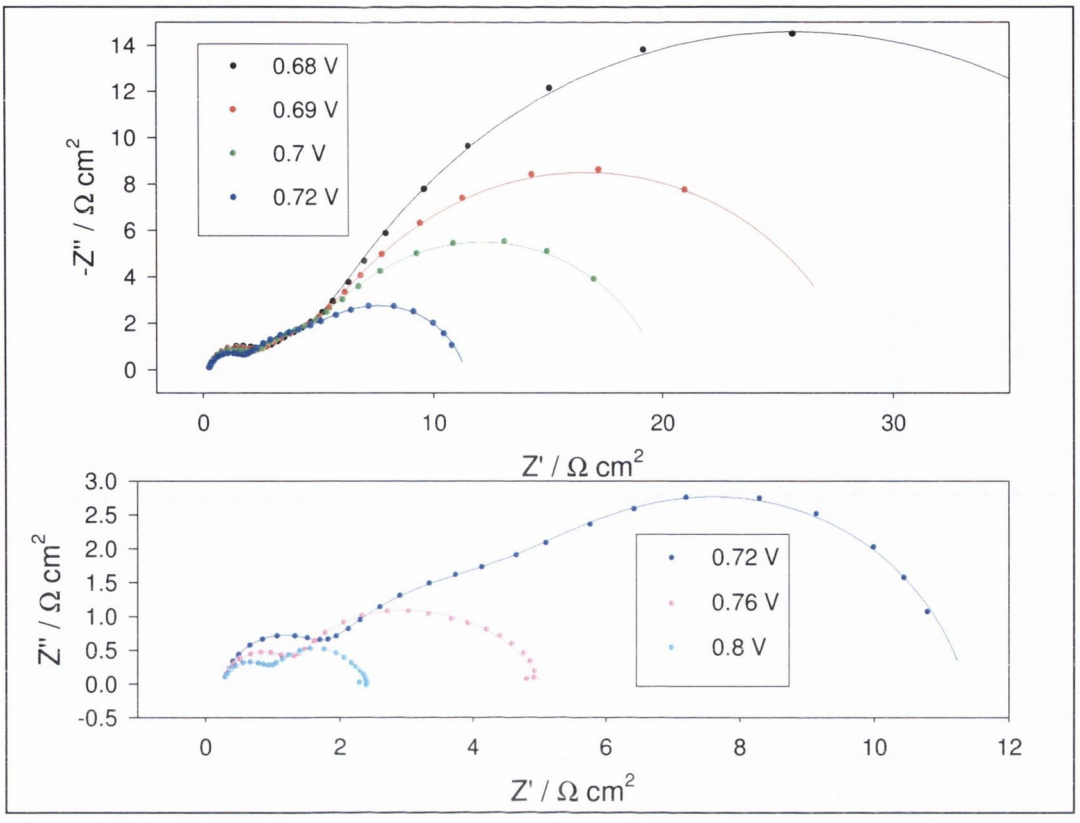


Figure 4.2.2 *Nyquist representations of the impedance data presented for a pre-reduced aged Fe electrode in Fig 4.2.1. As before the raw data is represented by the dots. The continuous lines are the results of CNLS fits to Circuit 4 (0.76 and 0.8 V) or Circuit 3 (all the others) – see later.*

EIS data for a so-called "fresh" non-pre-treated Fe electrode in 1.0 M NaOH is presented in Bode form in Figure 4.2.3. The appropriate reference steady state polarisation plot for this data is the 1.0 M trace of Figure 3.4.6. Inspection of the log | Z | plot suggests the presence of only two RC time constants for this data set. However, the phase angle vs. log frequency plot is more effective in discriminating between the various relaxation processes, and careful examination of this graph in the region below 10^3 Hz, again suggests the presence of three RC time constants for at least the spectra recorded at 0.68 and 0.7 V. If the impedance response below ca. 10^3 Hz is indeed characterised by two relaxation processes, there is significantly more overlap in the frequency domains of these processes for this fresh electrode compared to the pre-reduced aged electrode of Figures 4.2.1 and 4.2.2. This observation is supported by the Argand plane representation of the data of Figure 4.2.3 in Figures 4.2.4 and 4.2.5. In the Nyquist representations of the impedance data for the aged iron

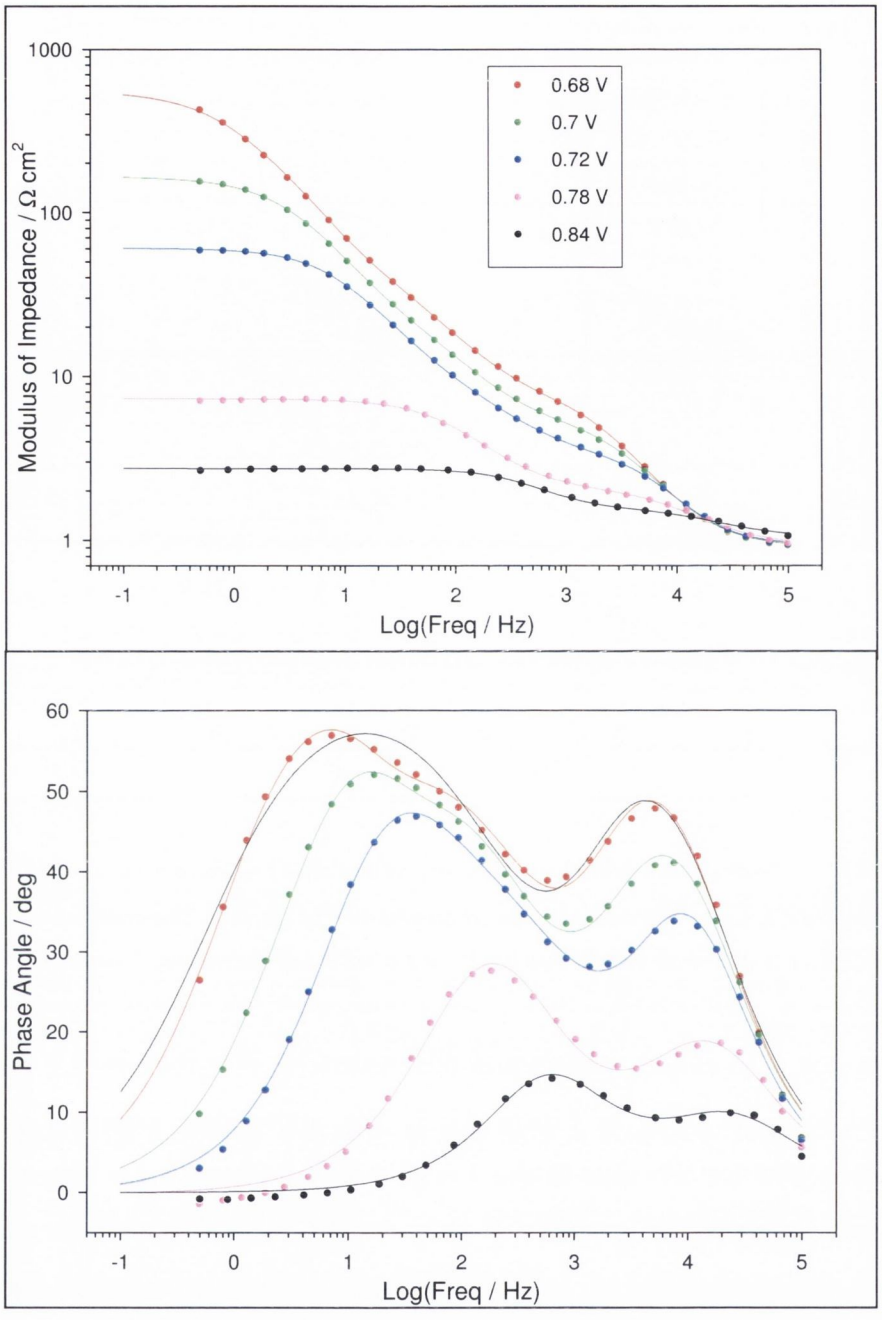


Figure 4.2.3 *Bode plots recorded at various potentials within the region of significant oxygen evolution current density for a non-pre-treated fresh bright polycrystalline Fe electrode in 1.0 M NaOH at 25°C. The raw data is represented by the dots. The continuous lines are the results of CNLS fits to Circuit 4 (0.78, 0.84 V and black line fitted to 0.68V phase angle plot) or Circuit 3 (all the others) – see later.*

electrode, the arcs corresponding to each of the three RC time constants can be readily visualised – see especially the larger-scale trace for 0.72 V in the lower part of Figure 4.2.2. In contrast to this, only one pseudo-semi-circular arc is apparent at first glance

in the complex plane representation of the impedance data for the fresh electrode at potentials of 0.68, 0.7 and 0.72 V –see Figure 4.2.4. That there are at least two distinct

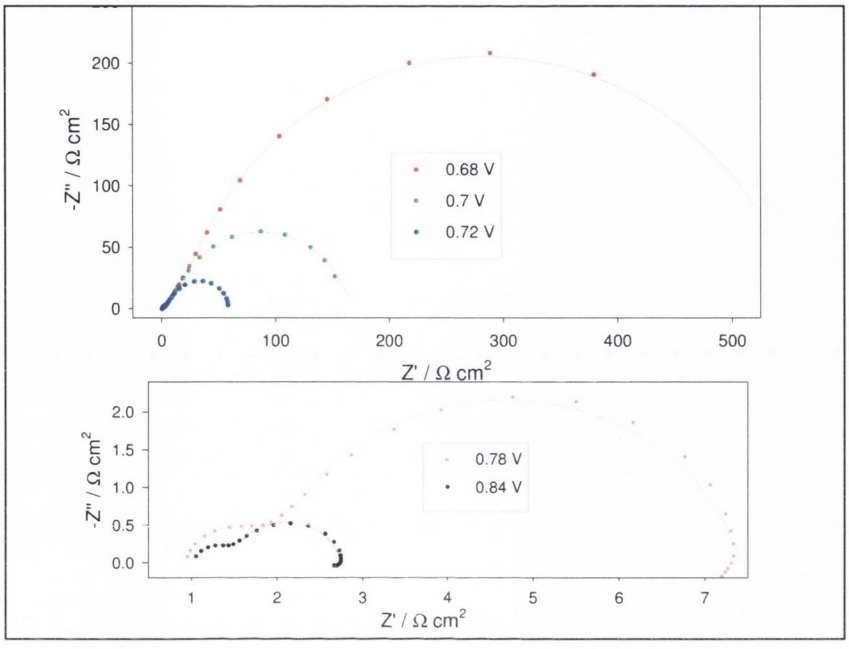


Figure 4.2.4 *Nyquist representations of the impedance data presented for a fresh Fe electrode in Fig 4.2.3. As before the raw data is represented by the dots. The continuous lines are the results of CNLS fits to Circuit 4 (0.78 and 0.84 V) or Circuit 3 (all the others) – see later.*

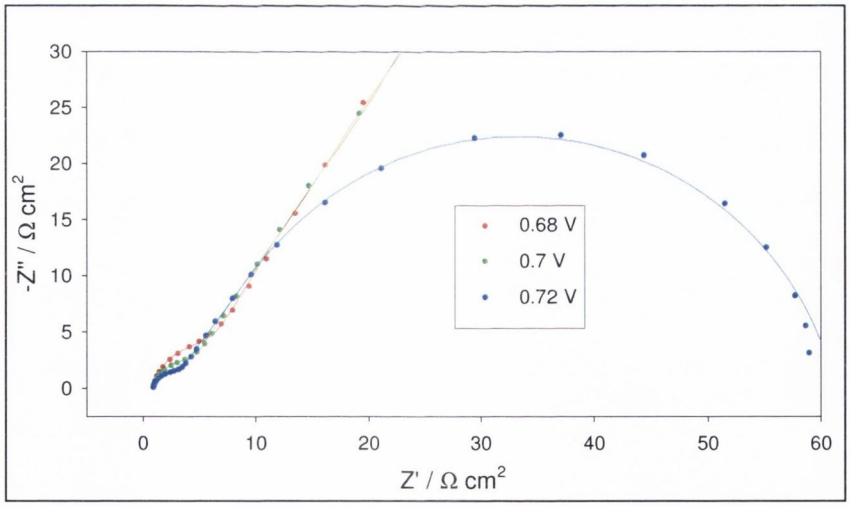


Figure 4.2.5 *Smaller scale representation of the Nyquist diagram of the upper part of Fig 4.2.4. At this resolution the existence of an arc due to the relaxation process occurring at frequencies above 10^3 Hz is obvious.*

RC time constants manifested at all potentials investigated, is apparent from Figure 4.2.5, where the high frequency response of the upper graph of Figure 4.2.4 is examined at a higher resolution. In fact it will be shown later, that for example, at 0.68 V, the CNLS fitting of the impedance data to an equivalent circuit with two RC loops is considerably less satisfactory than fitting to a circuit with three such loops.

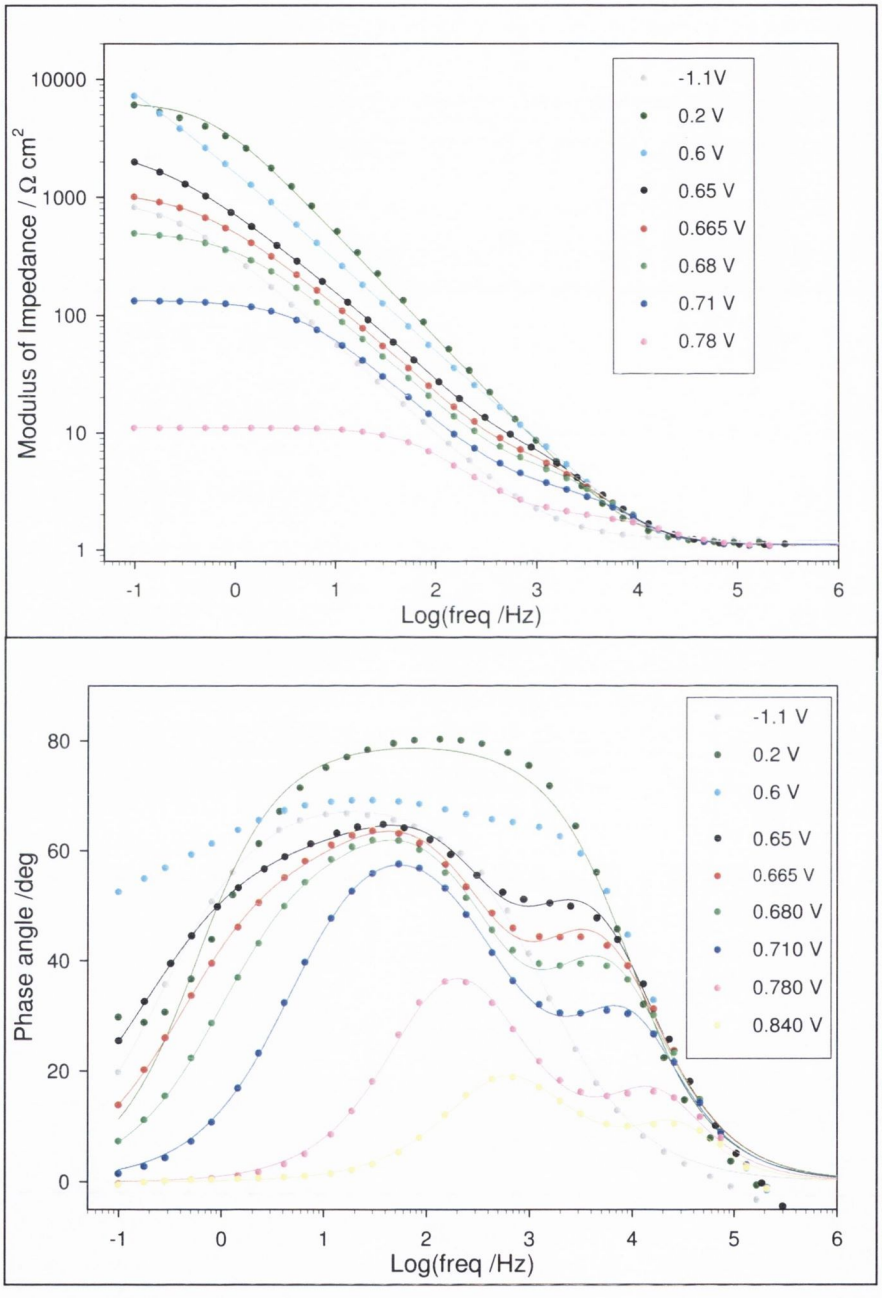


Figure 4.2.6 *Bode plots recorded at various potentials within the region of significant oxygen evolution current density for a pre-reduced polycrystalline Fe electrode in 1.0 M NaOH at 25°C. The raw data is represented by the dots. The data for 0.84 V is not included in the log $|Z|$ vs. log frequency plot for clarity of presentation. The continuous lines are the results of CNLS fits to Circuit 4 (0.78 and 0.84 V) or Circuit 3 (all the others) – see later.*

The third "type" of Fe electrode considered in chapter 3 was a relatively fresh pre-reduced bright anode – see the 1.0 M polarisation curve of Figure 3.4.12. Impedance spectra were also recorded for such an electrode, not just at potentials in the oxygen evolution region, but also at –1.1 V in the so-called "double-layer" region (see for example the CV for this type of Fe electrode in Figure 3.4.11), and at some intermediate potential values. The results of these experiments are presented in Bode

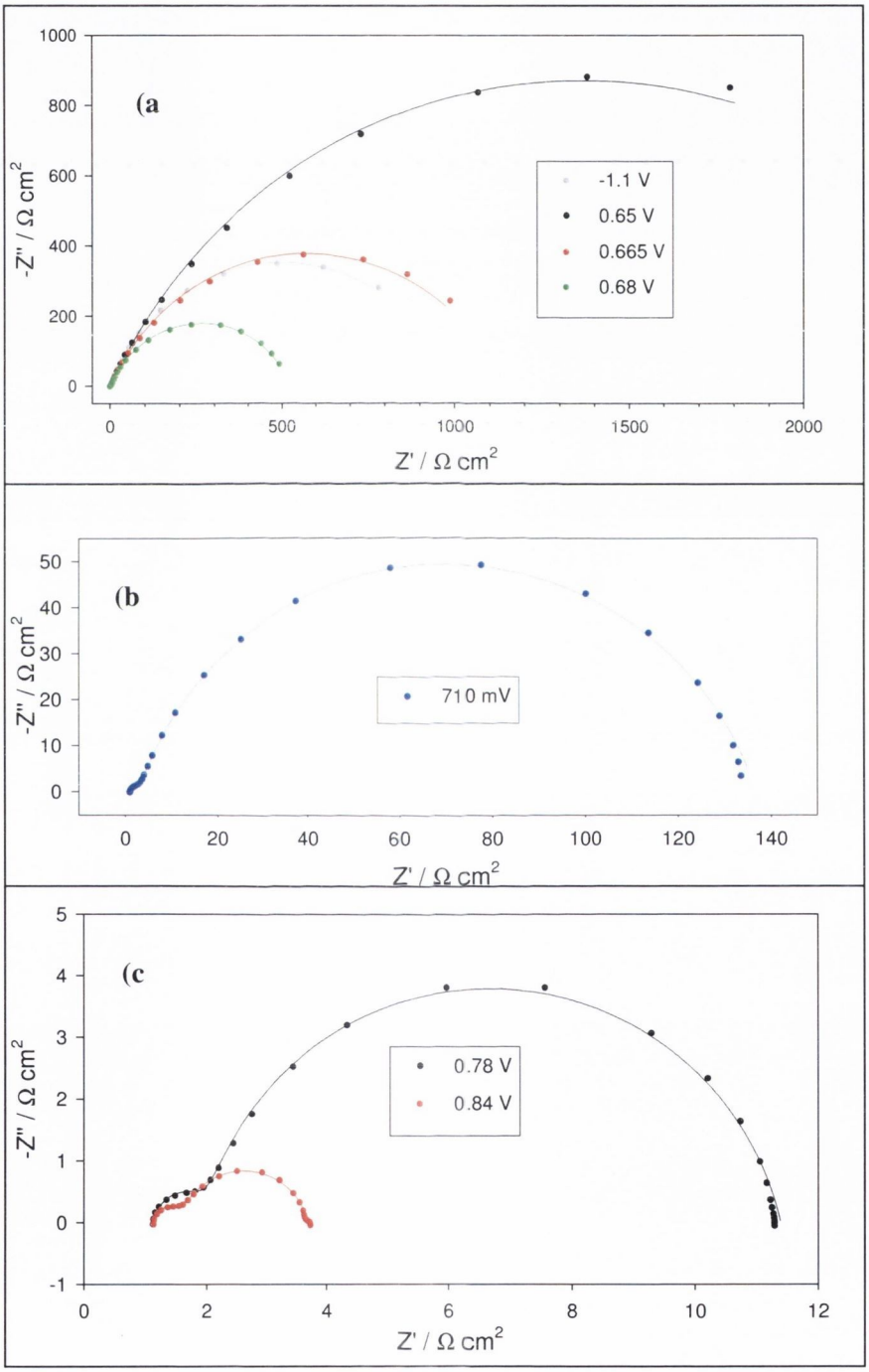


Figure 4.2.7 *Nyquist representations of the impedance data presented for a pre-reduced Fe electrode in Fig 4.2.1. As before the raw data is represented by the dots. The continuous lines are the results of CNLS fits to Circuit 4 (0.78 and 0.84 V) or Circuit 3 (all the others) – see later.*

format in Figure 4.2.6. The $\log|Z|$ vs. log frequency plot of Figure 4.2.6 is suggestive of just two RC time constants – however the rather irregular shape of the phase angle characteristics for the spectra recorded at 0.65, 0.665 and 0.68 V for frequencies below 10^3 Hz, indicates the possible superposition of two relaxation processes for these longer time scales. Consulting the Nyquist representations of the same data in Figure 4.2.7 does little to settle the question, with only one pseudo-semi-circular region apparent at lower overpotentials – see graph (a). As with the fresh Fe electrode, a second semi-circular region corresponding to the impedance response at frequencies above 10^3 Hz becomes increasingly obvious due to the reducing scale of the Nyquist plots at higher potentials – Figure 4.2.7 (b) and (c).

Having presented the results of the EIS studies on the various Fe electrodes in 1.0 M NaOH we turn our attention to the task of extracting useful information from this data regarding the nature of the o.e.r. on these electrode surfaces. The concept of fitting raw EIS data to equivalent circuit models was discussed in section 2.1.7. Following the discussion of that section, it is necessary to identify a physically reasonable equivalent circuit model, if the fitting parameters are to have any significance. It is emphasised at this stage that we fully recognise the fact that the successful fitting of an EIS data set to a particular equivalent circuit model is not sufficient grounds for the unambiguous admission of that model as being truly representative of the physical situation. Nevertheless, as pointed out by Cahan and Chen[1] a careful and informed analysis of the variation of the impedance response with dc potential can lead to the identification of equivalent circuit models, that should at the very least be useful in aiding our understanding of a particular system. We are also aware of the analysis by Harrington and Conway[2] regarding the significance of equivalent circuit models in relation to the ac impedance of faradaic reactions involving electrosorbed intermediates – indeed this work will be cited in the forthcoming discussion.

The various equivalent circuit models that will be considered in the present work are illustrated in Figure 4.2.8. It is noteworthy that instead of ideal capacitors all these circuits contain constant phase elements, CPEs, the concept of which were discussed in some detail in section 2.1.7. To achieve satisfactory fitting to the experimental data it was found to be necessary to admit these elements. The simplest equivalent circuit model, Circuit 1, consists merely of an RC loop in series with the uncompensated solution resistance R_Ω. Such a circuit was used by Willems, Kobussen and co-workers[3] in the analysis of impedance data recorded at various oxygen evolution

overpotentials, for a polycrystalline Co electrode in 6M KOH. These workers observed just one pseudo-semi-circular feature in the complex plane representation of their data – it will be shown later, that the impedance response of a Co electrode in this region of potential, as recorded in the present work in 1.0 M NaOH demands a more detailed equivalent circuit model.

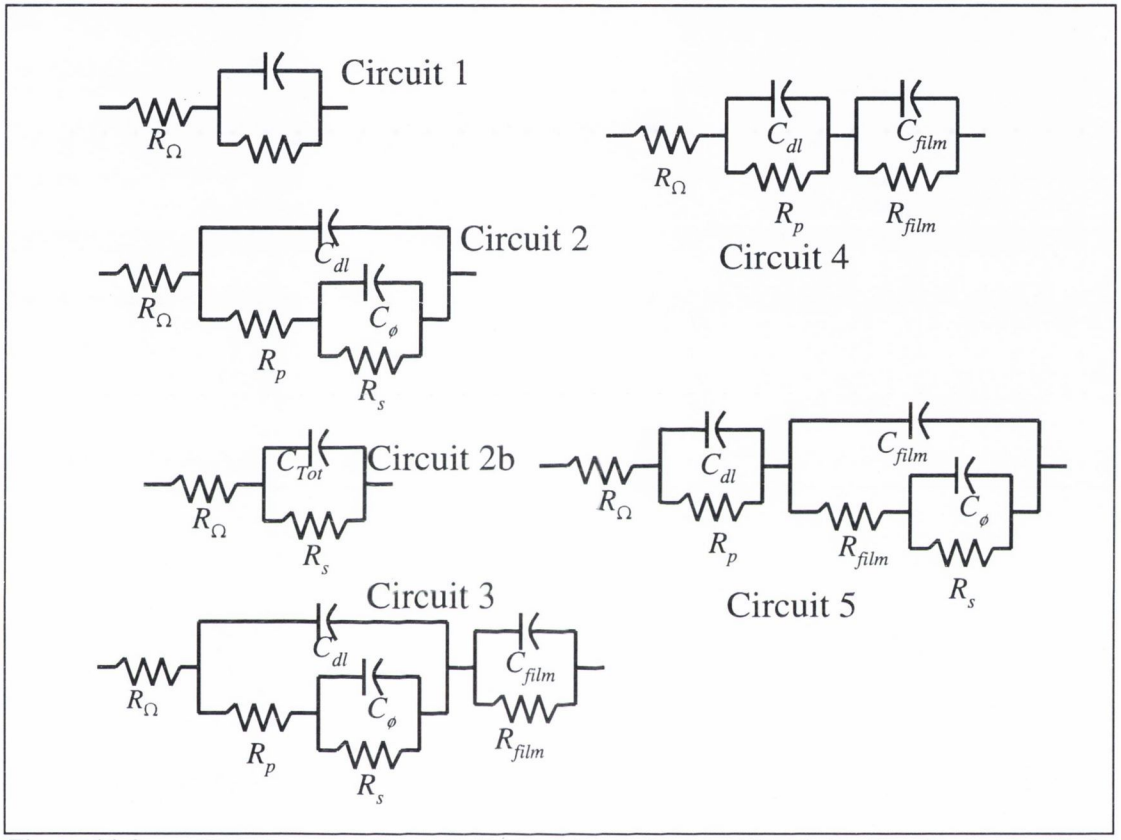


Figure 4.2.8 *Various equivalent circuit models to be considered in the discussion of the impedance response of Fe, Ni and Co electrodes in 1.0M NaOH at various potentials in the region of significant o.e.r. current densities.*

This simple model was also applied, perhaps rather dubiously, by Cappadonia et al.[4] to the analysis of EIS data recorded for a Ni electrode in 8.2 M KOH, across a large range of potentials from –0.8 to 1.0 V (vs. Hg/HgO). As previously noted our impedance data for Fe is characterised (for the lower potentials examined in any case) by at least two relaxation processes, and thus it is an obvious conclusion that Circuit 1 is too simple to be utilised in the analysis of these results.

The presence of two pseudo-semi-circular regions in the Nyquist plots for the o.e.r. at the polycrystalline Fe surface is reminiscent of the impedance results obtained for the h.e.r. at both Pt [5, 6] and the amorphous alloy G14 ($Fe_{60}Co_{20}Si_{10}B_{10}$)[7] in alkaline

solutions as well as the chlorine evolution reaction on freshly reduced Pt in 0.9 M NaCl + 0.1 M HCl[8]. Therefore one might be tempted to treat our Fe o.e.r. data in a similar manner to the analyses of these systems by admitting Circuit 2, and interpreting the high frequency semicircle as being due to the relaxation of the interfacial double layer capacitance, with the lower frequency arc arising from the relaxation of the pseudocapacitance associated with adsorbed reaction intermediate species. Circuit 2 is of course the so-called Armstrong-Henderson equivalent circuit which was discussed in section 2.1.7 as a model example for the fitting of impedance data to an equivalent circuit model. Referring to Figure 2.1.7, it is clear that there are some similarities between the phase angle vs. log frequency plot for the Armstrong-Henderson circuit constructed from ideal resistors and capacitors presented therein, and the equivalent plots for our real impedance data presented in Figures 4.2.1, 4.2.3 and 4.2.6. However in the case of Figure 2.1.7 the relaxation time τ (τ = RC) of each of the RC loops have been deliberately chosen to be widely separated (2.7×10^{-5} s for the outer loop compared with 6.75×10^{-2} s for the inner). In addition to this it is easy to differentiate between the resistive and capacitive regions in the $\log|Z|$ vs. log frequency plot of Figure 2.1.7, since the capacitive elements are ideal, do not display dispersion with frequency, and hence are manifested as diagonal regions with slopes of –1. The greater complexity of the real Bode plots presented for Fe (and indeed Ni and Co) in the present work, arises from the frequency dispersion of the capacitive processes (necessitating the utilisation of CPEs in the equivalent circuit models) and from the fact that the time constants for the various relaxation processes are not well separated and indeed in some cases are very similar.

Indeed Circuit 2 has been used in the analysis of oxygen evolution for several different systems, including Pt in 1.0 M NaOH[9], Co oxide electrodeposited on Ni and Pt disk electrodes in 1.0 M NaOH[10], and Co and Ni mixed oxides on a Ni substrate also in 1M NaOH[11]. In reference 10, Castro et al. point out that where $R_p << R_s$, only one apparent semi-circle will appear in the complex plane impedance representation and Circuit 2 will reduce to Circuit 2b, where $C_{Tot} = C_{dl} + C_{\phi}$. Of course Circuit 2b is identical to Circuit 1, however there is a more definite significance attached to the elements of the former, arising as it does as a limiting case of the Armstrong-Henderson circuit.

Following this analysis it would seem that Circuit 2 is a strong candidate for the modelling of the Fe impedance data. However we have opted against this course for

several reasons. Firstly, as discussed previously, there is considerable evidence for the presence of a third relaxation process, especially in the case of the pre-reduced aged anode (Figures 4.2.1 and 4.2.2) but also for the other Fe electrodes at lower oxygen evolution overpotentials. Secondly, the most rapid relaxation process occurs at frequencies in the vicinity of 10^4 Hz (see the maxima in the phase angle plots of Figures 4.2.1, 4.2.3 and 4.2.6). It will be seen in sections 4.3 and 4.4, that for Co and Ni electrodes respectively, no relaxation process is detected on such a short timescale. If, following the Armstrong-Henderson model, the process with the shortest RC time constant was to be attributed to the relaxation of the double layer capacitance, it is difficult to understand why this process should occur much more rapidly in the case of Fe, than Co or Ni. Thus it would seem to be unlikely that the fastest relaxation process is associated with the double-layer capacitance.

Consulting the literature, reveals that while Castro et al.[10] observed just one pseudo-semi-circle in the Nyquist representation of the results of their aforementioned impedance study on the o.e.r. at Co oxide electrodeposited on Ni and Pt disk electrodes, they noted an additional capacitive contribution in the high frequency range for the same oxide deposited on an Fe substrate. Kessler et al.[7] used EIS to study the o.e.r. at the amorphous alloys G14 ($Fe_{60}Co_{20}Si_{10}B_{10}$) and G16 ($Co_{50}Ni_{25}Si_{15}B_{10}$) in 1.0 M KOH. In the case of the predominantly iron alloy (G14) two capacitive semi-circles were noted in the complex plane presentation of the results. For the G16 electrode the higher frequency feature was apparently absent. In both of the aforementioned cases the authors attributed the high frequency RC loop to the dielectric properties of the anodic oxide layer. Thus it would seem, on the basis of the data presented in the present work in addition to the observations of Castro et al.[10] and Kessler et al[7], that impedance measurements on Fe (or Fe based) anodes are sensitive to an oxide film capacitance at higher frequencies, that is not detected for Co, Ni or Pt electrodes. This behaviour is not restricted to just Fe – for example similar high frequency impedance features have been noted by Conway and Lu[12] in an impedance study on the o.e.r. at Co_3O_4 deposited on a Ti substrate, and by Da Silva et al.[13] for Ti-supported (Ru + Ti + Ce)O_2 electrodes. Thus it would appear that EIS measurements are also sensitive to the capacitance of the anodic oxide film formed on Ti. Da Silva et al.[13] have proposed that the highly resistive TiO_2 anodic oxide film (TiO_2 interlayer) that forms between the metallic Ti support and the conductive oxide material during electrode preparation, acts as a dielectric material, thus giving rise to

the high frequency capacitive response. In view of the dual layer model proposed for the anodic oxide on Fe electrodes (see the literature review of section 1.4.2), and by analogy with the aforementioned concept of Da Silva et al., an appealing if speculative idea would be to associate the inner compact layer with the dielectric medium, sandwiched between the metal, and the more conductive outer dispersed region of the oxide.

Owing to the large variation of the lower frequency capacitive contributions with potential (this is particularly evident from the Nyquist plots of Figures 4.2.2, 4.2.4, 4.2.5 and 4.2.7) it is reasonable to assume that these must be related to the faradaic reaction of oxygen evolution. However, the relaxation of the double layer is a process common to ac impedance measurements of any electrode/solution interface – we are therefore drawn to the conclusion that this relaxation process must occur with a characteristic time constant intermediate to that associated with the film capacitance and that associated with the pseudo-capacitance of the electrosorbed faradaic reaction intermediates. It would appear that the time constants related to the double layer capacitance and the pseudo-capacitance are quite similar (especially in the cases of the fresh Fe electrode and the relatively fresh pre-reduced Fe electrode) leading to the apparent 'bundling together' of these processes in the experimental impedance responses – this certainly explains the rather unsymmetrical forms of the phase angle vs. log frequency plots at frequencies below ca. 10^3 Hz for lower oxygen evolution overpotentials – see Figures 4.2.3 and 4.2.6. In the case of the extremely aged pre-reduced Fe electrode there is greater resolution of the two longer relaxation processes – for example in the case of the Nyquist representation of the data recorded at 0.72 V (see Figure 4.2.2) the respective contributions with increasing frequency (right to left) of the pseudo-capacitance, double layer capacitance and film capacitance semicircles to the overall form of the diagram, can be readily appreciated.

Having satisfied ourselves regarding the general nature of the elements required to construct a meaningful equivalent circuit model, the next question that arises is as to the nature of the connection scheme. A general discussion on this problem was provided by Cahan and Chen[1] and the concepts treated therein should be of use in the present work. These authors produced a schematic of the Bode plot that would arise for the oxygen evolution reaction occurring atop an oxide film in the idealised case where the capacitive processes behave as ideal capacitors (i.e. no frequency dispersion) and the characteristic time constants for the various relaxation processes

differ significantly – this is reproduced as Figure 4.2.9 with only the notation being altered from the original work.

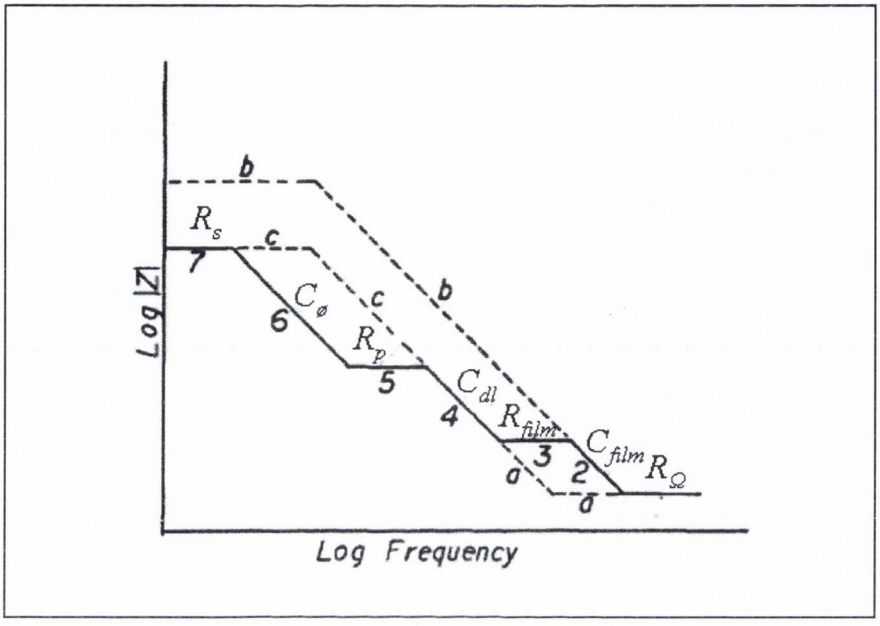


Figure 4.2.9 *Ideal schematic log|Z| vs. log frequency plot for the o.e.r. on an oxide covered electrode. See text for further details. Adapted from ref. 1.*

Such a Bode plot might be modelled by either Circuit 3 or Circuit 5 from Figure 4.2.8. The most appropriate choice of these two for the impedance data of the present work will be outlined later – however to facilitate this it is necessary to admit to the discussion a few further concepts from the analysis of Cahan and Chen[1]. These authors commented that C_ϕ is normally >> C_{dl}, and that for an oxide film thicker than a few angstroms with any reasonable value of dielectric constant, $C_{film} < C_{dl}$. The unbroken trace in Figure 4.2.9, then represents the situation where $R_\Omega << R_{film} << R_p$. In the case where $R_{film} << R_\Omega$, line segment 3 moves down until segment 2 disappears. Therefore R_{film} and C_{film} are no longer experimentally accessible, as in curve a. This is an example of a general phenomenon highlighted by Cahan and Chen, whereby the removal of a series resistive and/or capacitive element from an appropriate equivalent circuit model (Circuit 3 in this case), causes the plot (or part of the plot) of Figure 4.2.9 to move downward and to the left. The converse will clearly be true for the interposition of any resistive or capacitive element in series with the network.

On the other hand at potentials where C_ϕ is no longer significant, the continuous curve will move to the position outlined by the broken line c as a limiting value. This is equivalent to removing the R_sC_ϕ loop from Circuit 3, in which case it reduces to

Circuit 4 (Figure 4.2.8). So the removal of a parallel resistive and/or capacitive element has the effect of translating the curve (or a part thereof) upward and to the right. Again the converse is true if a new parallel addition is made to the equivalent circuit.

Examining the form of the Bode plots that they obtained for the passive film on iron in borate buffer solution (pH 8.4) at various potentials corresponding to significant oxygen evolution, Cahan and Chen[1] concluded that their experimental results were best explained by curve b of Figure 4.2.9 – i.e. where $R_{film} >> R_s$. At a potential of 1.1 V (vs. R.H.E.), which is below that associated the onset of significant oxygen evolution currents, the Bode representation of their data (frequency range of $10^{-1} \rightarrow 10^{4}$ Hz) was characterised by a diagonal line with no resistive plateau at the low frequency end. In other publications[14, 15] the same authors had shown that the passive film in this region of potential was an insulator with a resistivity of ~ 10^{15} Ω cm. They thus proposed that the aforementioned Bode plot at this potential arose due to situation characterised by curve b of Figure 4.2.9, with no low frequency resistive shelf being observed, since in this case R_{film} is so high that its characteristic time constant would be detected on a longer time scale than that of the experiment – i.e. at frequencies below 10^{-1} Hz.

As the potential was increased into the range associated with significant oxygen evolution current densities, Cahan and Chen[1], noted that the experimental log $|Z|$ vs. log frequency curve moved downwards, a situation that they interpreted in terms of Circuit 5 (Figure 4.2.8), as being due to a new RC circuit (the R_sC_ϕ loop) appearing in parallel with the $R_{film}C_{film}$ loop. At a potential of 1.5 V the authors observed the appearance of a low frequency resistive plateau – they postulated that this was largely due to R_{film} (it is of course due to the sum of all the resistive components but will be largely determined by R_{film} in the case where this is significantly larger than any of the other elements) on the basis that, at this potential the value of the film resistance is ca. 10^{5} Ω, and therefore is just resolvable by an impedance measurement at 10^{-1} Hz. With further increase of the applied potential the low frequency resistance was observed to decrease in such a manner that would yield an effective "Tafel slope" of 50 – 60 mV dec^{-1} (see equation (2.1.44), section 2.1.7).

While the foregoing discussion may, at first glance, seem to be rather unremarkable, its implications led Cahan and Chen to arguably the most controversial assertion ever contained in a publication on the o.e.r. – namely that, for the particular system under

study, the "Tafel slope" as measured, either directly by the steady state polarisation method, or extracted from EIS measurements, was due, not to the kinetics of the o.e.r. but to the increasing conductivity of the passive film over a range of potentials anodic to ~ 1.5 V (hence the use of inverted commas with the last two instances of Tafel slope). The authors explained this phenomenon in terms of what they called the "chemi-conductor" model, the principles of which were outlined in a separate publication[16].

The "chemi-conductor" model postulates that the passive film formed on iron in borate buffer solution (pH 8.4) consists of an insulating film "with a composition like, although not necessarily precisely FeOOH"[16]. The ingress of protons from solution allows the existence of an exponential distribution of Fe^{2+} ions outward from the metal surface into the oxide film, with charge neutrality at the metal/oxide interface being maintained. Furthermore, the model envisages, that with increasing potential a small proportion of the Fe^{3+} species at the outer surface of the oxide will be further oxidised to Fe^{4+}. Again an exponential concentration gradient of Fe^{4+} will extend back into the passive film. At a sufficiently high anodic potential the penetration of Fe^{4+} species back into the film will be deep enough to enable an overlap of the Fe^{2+} and Fe^{4+}-rich regions, and thus dc conduction can occur (by e.g. an electron hoping mechanism owing to the non-stoichiometry) along with oxygen evolution. As mentioned above, if the chemi-conductor model is admitted, the appropriate equivalent circuit model in the potential region where the film conductivity becomes appreciable is Circuit 5. The observed downward movement with increasing potential[1] of the $\log|Z|$ vs. log frequency curve, is then due to the R_sC_ϕ loop (characteristic of the adsorption behaviour of the o.e.r. intermediate species) coming in parallel to the $R_{film}C_{film}$ loop as R_{film} decreases. The overall dc current density at a given overpotential will then be governed by the resistivity of the oxide film, implying that the actual kinetics of the o.e.r. may actually be much faster than those characterised by the apparent "Tafel slope". Cahan and Chen[1] conducted further EIS studies on an Au electrode in 1 N $HClO_4$ solution in the potential region of oxygen evolution, and also reached the conclusion for this system that a poorly conducting oxide film masked the true o.e.r. kinetics. On the basis of their two sample systems they made the following rather bold statement[16] that "the previous literature which measures the apparent kinetics of oxygen evolution, may simply have been measuring the dc resistivity of the film rather than the kinetics".

Although the foregoing assertion of Cahan and Chen lays down the gauntlet for future workers in the field to prove that experiments purporting to measure the kinetics of the o.e.r., do actually characterise those kinetics, this is a challenge that few workers seem to have taken up. From our point of view, this question has become inseparable from the issue of choosing the appropriate equivalent circuit model for our EIS data. The indications are, that the suitable equivalent circuit should contain a $R_{film}C_{film}$ loop, a R_sC_ϕ loop and a R_pC_{dl} loop. The problem then reduces to the following – can we adopt Circuit 3 or are we forced to admit Circuit 5, thereby rendering the steady state polarisation data and the discussion of chapter 3 effectively worthless? This question can only be resolved by applying an analysis similar to that performed by Cahan and Chen to our EIS data.

Perhaps the best starting point for such an analysis lies with the Bode representation of the impedance data recorded for the relatively fresh pre-reduced Fe electrode (see Figure 4.2.6), since in this case EIS measurements have also been conducted at several potential values away from those associated with significant oxygen evolution. As mentioned previously the impedance response at –1.1 V is characteristic of the behaviour of the electrode in its so-called "double-layer" region. This data was recorded immediately subsequent to the pre-treatment procedure for this type of electrode, as outlined in section 3.4.2. Comparing the log | Z | vs. log frequency curve for the "double-layer" region with that for the data recorded at 0.6 V allows several inferences to be made. Referring to the CVs of Figure 3.4.11 and the 1.0 M NaOH steady state polarisation curve of Figure 3.4.12, it is clear that 0.6 V is slightly below the potential at which significant o.e.r. currents arise, and is not apparently associated with any other faradaic process (although it is worth recalling that we postulated in relation to the data of Figure 3.2.22 that there may be some production of surface ferrate species in this region of potential). The log | Z | vs. log frequency curve for 0.6 V is translated upward and to the right relative to the corresponding plot for –1.1 V. According to Cahan and Chen[1] this is indicative of the addition of a series capacitive and/or resistive element to the equivalent circuit model applicable in the double layer region. Assuming that the impedance response in the double layer region can be modelled in terms of a R_pC_{dl} loop in series with the solution resistance R_Ω, the "upward" translation of the log | Z | vs. log frequency curve for 0.6 V, is readily understood by the serial addition of a $R_{film}C_{film}$ loop arising from the development of the passive film over the range of potentials between –1.1 V and 0.6 V. This series

addition of a $R_{film}C_{film}$ loop to the ubiquitous R_pC_{dl} loop is of course consistent with either Circuit 3 or Circuit 5. The appearance of the additional film capacitance at frequencies approaching 10^4 Hz for the spectrum recorded at 0.6 V is very obvious from the phase angle plot – such a feature is completely absent from this plot for the measurement performed at –1.1 V. The film capacitance is thus manifested in the log | Z | vs. log frequency curve as the final part of the steeply descending curve at frequencies immediately below the high frequency R_Ω shelf, just as envisaged by Figure 4.2.9.

As the frequency is increased, the entire the log | Z | vs. log frequency curve at 0.6 V appears to descend diagonally into this C_{film} region, without arrest or inflection. This may be suggestive of the type of behaviour leading to curve b of Figure 4.2.9 – that is, at 0.6 V the impedance response is possibly indicative of a highly resistive film. Indeed it is noteworthy that the overall (low frequency) specific resistance at 0.2 V is lower than at 0.6 V, being just resolved with a value of ca. 6 KΩ cm^2 by the impedance measurement at 0.1 Hz. Referring to the CVs of Figure 3.4.11, it can be seen that 0.2 V corresponds to the extreme anodic end of the voltammetric feature related to the oxidation of the Fe^{2+} species of the inner region of the passive film, to Fe^{3+} species. However, despite the apparent similarity between the log | Z | vs. log frequency curve for 0.6 V and those obtained by Cahan and Chen, one must be cautious about concluding that the former is the impedance response of a highly resistive film.

Looking at the highly asymmetrical form of the phase angle plot, it is apparent that this is the superposition of the contributions of at least two, and probably three relaxation processes. It is therefore most likely that the high overall resistance is due principally to a large faradaic resistance rather than the situation depicted in curve b of Figure 4.2.9. The various components of the Bode plot are not clearly resolved (as in the unbroken curve of Figure 4.2.9) owing to insufficient separation of time constants, leading to an experimental curve that resembles those of Cahan and Chen. Having said that, it is also true that the uppermost phase angle vs. log frequency maximum shifts towards higher frequencies with increasing potential. As will be discussed presently, the film capacitance remains largely constant with potential, so this implies that the film resistance decreases as the overpotential is increased. Therefore it is true that the film resistance does indeed drop between 0.6 and 0.65 V – what isn't clear is whether it drops from such a high value as cannot be resolved at or

above 0.1 Hz (i.e. as with curve b figure 4.2.9), or from a much lower value that isn't experimentally accessible owing to the overlap of relaxation processes.

There is an obvious change in the form of the log | Z | vs. log frequency curve as the potential is raised to the values associated with the ca. 44 mV dec^{-1} Tafel slope of Figure 3.4.12. The capacitive response of the film at frequencies $\rightarrow 10^4$ Hz remains essentially constant, however an inflection appears in the curves at frequencies immediately below this range. This arrest region covers frequencies from approximately 10^3 Hz up to those at which the film capacitance becomes manifest. As the potential is increased, this shelf region becomes more obvious as it moves downward – simultaneous to this the phase angle maximum corresponding to the relaxation of the film capacitance is shifted towards higher frequencies. The later observation is consistent with a decrease in R_{film} with potential since, as previously noted C_{film} remains largely constant. It is therefore appropriate to associate R_{film} with the aforementioned downward moving shelf region, since this behaviour is also indicative of a decreasing resistive component. Thus we reach the important conclusion, that for this Fe electrode in 1.0 M NaOH, the low frequency impedance response at potentials corresponding to the straight-line Tafel region of the o.e.r. steady state polarisation curve, is *not* dictated primarily by the resistivity of anodic oxide film. Therefore we can be confident that the Tafel slope extracted from this impedance data via equation (2.1.44), or indeed as measured by dc steady state polarisation methods, is in fact characteristic of the kinetics of the oxygen evolution reaction. Furthermore, the above discussion implies that the most appropriate equivalent circuit model for this system is that of Circuit 3, Figure 4.2.8. Such an equivalent circuit model has been proposed for the o.e.r. in alkaline solution on cobalt oxides deposited on Fe disk electrodes by Castro et al.[10], and also for oxygen evolution on an IrO_2-Ta_2O_5 mixed electrode in 0.5 M H_2SO_4 solution[17].

One might question why the log | Z | vs. log frequency curves of Figure 4.2.6 do not display distinct diagonal regions corresponding to the impedance response of the double layer capacitance and the adsorption pseudo-capacitance, or a horizontal (or at least low slope) region corresponding to the resistive elements R_s, as envisaged schematically in Figure 4.2.9. As discussed briefly above, the primary reason for this is due to the poor separation of the time constants related to the relaxation of the double layer and the coverage of the o.e.r. intermediate species. Furthermore, one must be careful regarding the significance of the results of the CNLS fitting to an

equivalent circuit, of impedance data characteristic of two relaxation processes, having poorly separated time constants, as was discussed by Macdonald et al.[18]. DaSilva et al.[13] caution about the danger of "apparent" results arising from fitting routines where the ratio of the characteristic time constants of two physicochemical processes sensed by EIS is less than 100. Bearing these comments in mind, CNLS fitting (as described in section 2.1.7) of the impedance data of Figures 4.2.6 and 4.2.7 to Circuit 3 (Figure 4.2.8) was performed. The optimum fit parameters are listed in Table 4.2.1.

E V	R_{film} Ω cm^2	C_{film} μF cm^{-2}	α	R_s Ω cm^2	C_ϕ μF cm^{-2}	α	R_p Ω cm^2	C_{dl} μF cm^{-2}	α	R_Ω Ω cm^2
0.65	4.288	28.128	0.907	2719.8	8.233	0.605	208.620	42.544	0.871	1.11
0.665	3.829	24.194	0.906	923.04	17.139	0.664	238.320	53.667	0.860	1.11
0.68	3.042	22.311	0.915	338.58	29.983	0.800	182.340	64.056	0.850	1.11
0.71	1.894	20.006	0.940	72.99	48.450	0.813	59.130	86.556	0.847	1.11
0.78	0.718	15.495	1.031	3.814	250.28	1.011	5.598	142.28	0.884	1.16

Table 4.2.1 *Optimum fit parameters for the CNLS fitting of the data of Figures 4.2.6 and 4.2.7 (relatively fresh pre-reduced Fe electrode) to Circuit 3.*

Immediately, it is apparent that there is a difficulty with the fitting results for the EIS data recorded at 0.78 V. The value of a CPE exponent α should be less than, or equal to unity. For the case of the best fit parameters for both C_{film} and C_ϕ the exponent has taken on values in excess of unity. As discussed in section 2.1.7, the physical meaning of α is dubious enough for $\alpha < 1$ – a CPE with a value of α greater than unity is a meaningless concept. Examining the phase angle vs. log frequency plot for 0.78 V, it is clear that the profile at frequencies below 10^3 Hz is considerably more symmetrical than at lower potentials. On this basis it would appear that the lower frequency impedance response at 0.78 V is largely due to just one relaxation process. An attempt to fit impedance data characteristic of two RC time constants to Circuit 3, with its three RC loops may be the reason for the anomalous fitting parameters. It is to be expected[9, 19, 20] that the adsorption pseudo-capacitance should tend towards zero at overpotentials beyond those corresponding to the lower Tafel region as the fractional coverage θ of the adsorbed intermediate species tends to unity. It is possible that the ac pseudo-capacitive response has moved outside its potential window at 0.78 V and

therefore Circuit 3 should reduce to Circuit 4 (Figure 4.2.8). This should certainly be true for the impedance response at 0.84 V. Some comments will be made on the significance of adsorption pseudo-capacitance as detected by ac impedance methods later.

On the basis of the foregoing discussion the EIS data recorded at 0.78 V and 0.84 V (Figures 4.2.6 and 4.2.7) were fitted to Circuit 4. The best-fit values of the equivalent circuit elements are listed in Table 4.2.2.

E V	R_{film} Ω cm^2	C_{film} μF cm^{-2}	α	R_p Ω cm^2	C_{dl} μF cm^{-2}	α	R_Ω Ω cm^2
0.78	0.777	17.88	0.987	9.459	159.66	0.8590	1.149
0.84	0.494	14.172	0.977	2.158	165.28	0.8450	1.178

Table 4.2.2 *Optimum fit parameters for the CNLS fitting of the data of Figures 4.2.6 and 4.2.7 recorded at higher potentials (relatively fresh pre-reduced Fe electrode) to Circuit 4.*

The theoretical transfer functions derived from the CNLS fitting are presented as the continuous lines in Figures 4.2.6 and 4.2.7. A comparison of the simulated phase angle vs. log frequency plots arising from the fitting of the impedance response at 0.65 V to both Circuit 3 and Circuit 4 is presented in Figure 4.2.10. Although it is recognised that increasing the number of fitting variables will improve the "goodness" of a particular CNLS fit, the scenarios presented in Figure 4.2.10 are least indicative of the validity of our earlier assumption that at potentials corresponding to the lower Tafel slope region, the impedance response of the pre-reduced Fe electrode is characteristic of three relaxation processes.

An interesting aspect of the fitting parameters listed in Tables 4.2.1 and 4.2.2 is the fact that the double layer capacitance increases with potential. It is also noteworthy that the modelled film capacitance is a more "pure" capacitive element than the simulated double-layer capacitance, in that the α exponent for the former is closer to the ideal value of unity for a capacitor displaying no frequency dispersion. This is probably not surprising given the description of the film capacitance provided above, following the model of Da Silva et al.[13]. According to this model the film capacitance is effectively a solid-state capacitance (directly analogous to a conventional hardware capacitor) as opposed to an electrochemical interfacial capacitance like the double

layer capacitance. As was discussed in section 2.1.7 the frequency dispersion that necessitates the use of a CPE in an equivalent circuit in place of an ideal capacitor is

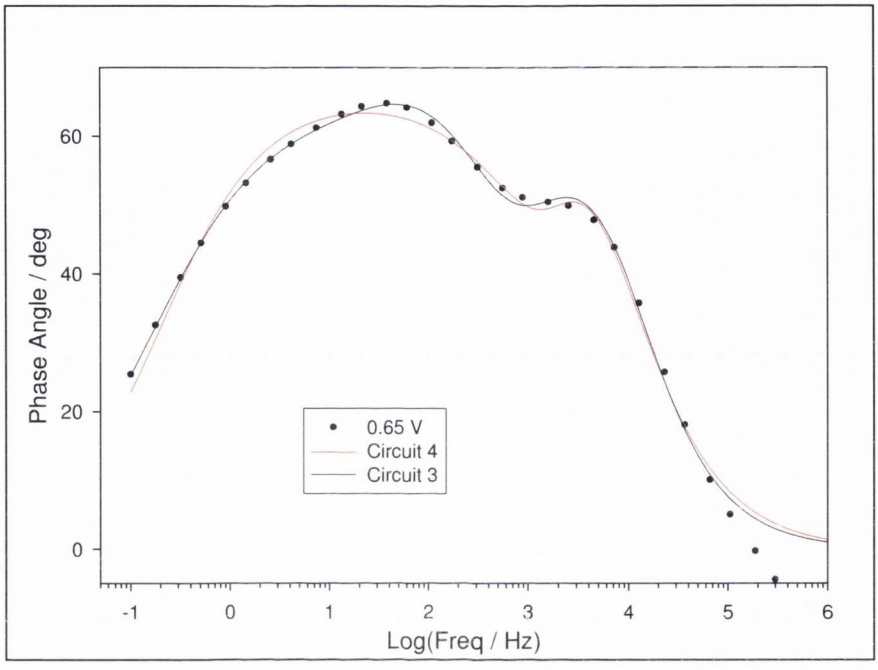


Figure 4.2.10 *Comparison of the phase angle vs. log frequency plots for the CNLS fitting to Circuits 3 and 4 (Fig.4.2.8), of the impedance response for the relatively fresh pre-reduced Fe electrode in 1.0 M NaOH at 0.65 V. The raw data is presented as dots, and the simulated fitting functions as continuous lines.*

generally associated with surface roughness and inhomogeneities. It is usually assumed, albeit without any particularly rigorous physically basis, that the lower the value of α, the greater the surface roughness.

Returning to the increase in the fitted value of C_{dl} with rising potential, calculation of the effective double layer capacitances $C_{dl\ eff}$ by the method suggested by Jovic[21] (see section 2.1.7 – a worked example of this method will be provided later for a Co electrode) indicates that this increases from 23.12 μF cm^{-2} for E = 0.65 V to 62.31 μF cm^{-2} at E = 0.78 V, although there is a decrease back to 48.29 μF cm^{-2} for E = 0.84 V. Recall from the discussion of real surface area estimation techniques in section 2.1.10 that (rather speculatively) values of 40 μF cm^{-2} [22] or 60 μF cm^{-2} [23] have been suggested for the double-layer capacitance of a smooth oxide covered electrode. On this basis to value of 23.12 μF cm^{-2} for E = 0.65 V would seem to be too small to be physically reasonable. Furthermore an increase of the double layer capacitance in the oxygen evolution region is difficult to rationalise – indeed if anything its value would

be expected to drop at higher overpotentials (an effect probably associated with the copious evolution of oxygen bubbles that is noted for Ni and Co electrodes and will be discussed in more detail later in this chapter) as is actually observed between 0.78 V and 0.84 V. The apparent increase in C_{dl} with applied potential between E = 0.65 V and E = 0.78 V may well be an artefact of fitting impedance data with poorly separated time-constants, the potential pitfalls of which were highlighted by Macdonald et al.[18] and DaSilva et al.[13]. This effect may also be manifested in the fitting values obtained for C_ϕ at 0.65 and 0.665 V – see Table 4.2.1. The low α values obtained in this situation render the C_ϕ fitting parameters effectively physically meaningless, although as indicated by the scenarios presented in Figure 4.2.10, it is necessary to admit a R_sC_ϕ loop in parallel with the R_pC_{dl} loop in the equivalent circuit model to achieve a satisfactory fit of the experimental data. We have observed, that by starting the CNLS fitting procedure for E = 0.65 V with somewhat different seed values for R_p, C_{dl}, R_s and C_ϕ, the process will converge to a similarly good fit to that demonstrated by the black trace of Figure 4.2.10, but with significantly (albeit not dramatically i.e. not involving changes in orders of magnitude) different fitting parameters to those listed in Table 4.2.1. This again demonstrates the caution with which one must approach fitted parameters obtained from a situation where there is considerable overlap in the characteristic time scales of two relaxation processes.

At first glance the fitted C_ϕ parameter may seem to provide a route towards the construction of an experimental adsorption pseudo-capacitance vs. overpotential plot, and thus to make inferences regarding the nature of the adsorption isotherm required to account for the variation of the reaction intermediate coverage with potential – recall section 1.2.2. There are however problems with such an approach and these are of a more fundamental nature than those associated with the difficulties related to the CNLS fitting of experimental data where two time constants are poorly separated. Indeed, as will be discussed below, there are very good reasons why the general concept of the adsorption pseudo-capacitance has been denoted by different notation at various points in the present work. The discussion that follows has been informed by a theoretical treatment, due to Harrington and Conway[2], of the significance of various experimental parameters that may be obtained from EIS measurements on faradaic reactions involving electrosorbed intermediates (and in particular the h.e.r.).

These authors point out that the quantity, most commonly referred to in the literature as "the pseudo-capacitance", is that discussed in section 1.2.2 and denoted in the present work as C_{ps}. They contend that this quantity, defined as,

$$C_{ps} = q_1 \frac{d\theta_{SS}}{d\eta_{SS}}, \tag{4.2.1}$$

(where the various symbols retain the significance attributed to them in section 1.2.2, except that we now emphasise that these are the steady state values of these parameters), should more properly be called the *steady-state pseudo-capacitance.*

The pseudo-capacitive parameter that can be obtained from the impedance response of a electrode at a given frequency ω is a complex, frequency dependent quantity denoted by Harrington and Conway as $\tilde{C}_{ac}$ which measures how the sinusoidal variation of charge stored by the adsorbed intermediate depends on the sinusoidal changes of the potential. It is only at zero frequency (i.e. in the steady state) that the change in this adsorbate charge is in phase with the sinusoidal change in applied potential and that $\left|\tilde{C}_{ac}\right| = C_{ps}$.

The other pseudo-capacitive quantity that has appeared in the present work (chapter 2 and the present chapter) is C_{ϕ}, which we understand to be the value of a capacitor (or in reality a CPE) which in parallel with the resistance, R_s, in an equivalent circuit model, correctly models the relaxation of the charge associated with the adsorbed intermediate. Harrington and Conway show that C_{ϕ} will only be identical to C_{ps} in the special case where the net rate of consumption/production of electrons is equal respectively to the net rate of production/desorption of the adsorbed species. A real example where this condition is satisfied is in the underpotential deposition (u.p.d) of hydrogen or other species. In this case it can be shown[2] that the R_s element of the Armstrong-Henderson equivalent circuit (i.e. that which is generally used to model the adsorption of a single species – see Circuit 2, Figure 4.2.8) is infinite and thus this equivalent circuit reduces to the simple Randles circuit depicted in Figure 2.1.5(b) (left hand side).

Harrington and Conway[2] explain the more general disparity between C_{ϕ} and C_{ps} as arising from the fact that it is only in the upd processes that the faradaic charge passed is all stored as adsorbate. For faradaic reactions such as the h.e.r. (recall equations

(1.3.8) – (1.3.10), section 1.3.2) in which the adorbed species is merely an intermediate that is consumed in steps (or a step) subsequent to its adsorption, these steps effectively facilitate charge leakage (in the language of capacitors) and break the equality between the charge passed and stored and thus the equality between C_{ϕ} and C_{ps}. Clearly the situation becomes more complex for electrode reactions, including possibly the o.e.r., involving significant coverages of more than one intermediate species (although recall from chapter 3 that the pseudo-equilibrium analysis of our steady sate polarisation data, indicated that for the systems studied, only the OH_{ads} formed in the first step of the relevant pathway had a significant coverage). The general conclusion from the foregoing discussion is that values of C_{ϕ}, as obtained from the CNLS fitting of EIS data to equivalent circuit models, do not have a simple relationship to the steady state pseudocapacitance C_{ps}. It is therefore not in order to attempt to draw conclusion regarding the nature of the appropriate adsorption isotherm by monitoring the variation in C_{ϕ} with overpotential.

The significance of the resistive elements R_p and R_s of the Armstrong-Henderson equivalent circuit were also discussed by Harrington and Conway[2]. The authors comment that a common interpretation was that R_p is the charge transfer resistance of the electrosorption step, while R_s is the charge transfer of the electrodesorption process. However, on the basis of their analysis they reject such a simplistic rationalisation and show that the aforementioned resistive elements "are each properties of two or more steps in the reaction". Following the analyses of Harrington and Conway[2], it would appear that the usefulness of the CNLS fitting parameters are restricted to the following applications – (a) the estimation of values of the roughness factor, as discussed in section 2.1.10 and (b) the derivation of Tafel slopes via equation (2.1.44) for potentials where the lower frequency limit doesn't permit the continuation of the complex plane representation of the data to the intersection with the Z' axis that yields the value of $R_s + R_p + R_{film} + R_{\Omega}$ (cf. Figure 2.1.6).

So far much of the discussion has focussed on the impedance data of Figures 4.2.6 and 4.2.7 for the relatively fresh pre-reduced electrode. Examination of the impedance responses of the two other Fe electrodes (the extremely aged pre-reduced electrode (Figures 4.2.1 and 4.2.2) and the fresh non-pre-treated electrode (Figures 4.2.3 – 4.2.5)) shows that most of the commentary passed on data of Figures 4.2.6 and 4.2.7 is also valid for these data sets. In particular, well-defined C_{film} and R_{film} regions are obvious at the upper frequency ends of the $\log|Z|$ vs. log frequency Bode plots of

Figures 4.2.1 and 4.2.3, implying that low frequency resistive response in each case are characteristic of the kinetics of the o.e.r., and not of the resistance of a poorly conducting film as envisaged by Cahan and Chen[1]. Indeed for the case of impedance data recorded at E = 0.72 V for the extremely aged electrode (Figure 4.2.1) it could be argued that distinct regions are apparent in the Bode plot corresponding to each of those highlighted in the ideal schematic plot of Figure 4.2.9. As with the relatively fresh pre-reduced electrode, the impedance responses for the other two Fe electrodes at lower oxygen evolution overpotentials were fitted to Circuit 3. Again the phase angle vs. log frequency plots of Figure 4.2.1 and 4.2.3 suggest that Circuit 4 is the more appropriate equivalent circuit model for the data recorded at higher overpotentials. The optimum fit parameters for the extremely aged Fe electrode, and the fresh non-pre-treated Fe electrode are presented in Tables 4.2.3 and 4.2.4 respectively.

(a)

E V	R_{film} Ω cm^2	C_{film} μF cm^{-2}	α	R_s Ω cm^2	C_ϕ mF cm^{-2}	α	R_p Ω cm^2	C_{dl} μF cm^{-2}	α	R_Ω Ω cm^2
0.68	1.924	23.74	0.897	39.917	1.263	0.799	5.040	262.03	0.690	0.254
0.69	1.774	23.328	0.904	21.292	1.821	0.841	5.504	265.08	0.671	0.254
0.7	1.562	22.694	0.918	13.162	1.789	0.823	5.237	246.24	0.667	0.258
0.72	1.407	22.105	0.904	5.531	2.383	0.823	4.255	309.11	0.742	0.270

(b)

E V	R_{film} Ω cm^2	C_{film} μF cm^{-2}	α	R_p Ω cm^2	C_{dl} μF cm^{-2}	α	R_Ω Ω cm^2
0.76	0.861	20.973	0.937	3.902	302.94	0.666	0.263
0.8	0.652	20.532	0.912	1.489	387.04	0.777	0.267
0.84	0.453	18.749	0.927	0.713	365.25	0.810	0.297

Table 4.2.3 *Optimum fit parameters for the CNLS fitting of the data of Figures 4.2.1 and 4.2.2 (extremely aged, pre-reduced Fe electrode) to (a) Circuit 3 for lower potentials, and (b) Circuit 4 for higher potentials.*

(a)

E V	R_{film} Ω cm^2	C_{film} μF cm^{-2}	α	R_s Ω cm^2	C_ϕ μF cm^{-2}	α	R_p Ω cm^2	C_{dl} μF cm^{-2}	α	R_Ω Ω cm^2
0.68	4.441	19.65	0.944	446.760	85.22	0.973	110.250	59.28	0.779	0.912
0.7	3.424	18.26	0.917	110.394	135.83	0.982	52.254	85.44	0.808	0.912
0.72	2.246	17.11	0.926	40.644	128.78	0.916	17.464	104.1	0.837	0.939

(b)

E V	R_{film} Ω cm^2	C_{film} μF cm^{-2}	α	R_p Ω cm^2	C_{dl} μF cm^{-2}	α	R_Ω Ω cm^2
0.78	1.069	20.878	0.854	5.396	245.33	0.859	0.948
0.84	0.494	26.383	0.843	1.202	284.72	0.900	1.046

Table 4.2.4 *Optimum fit parameters for the CNLS fitting of the data of Figures 4.2.3 - 4.2.25 (fresh, non-pre-treated Fe electrode) to (a) Circuit 3 for lower potentials, and (b) Circuit 4 for higher potentials.*

Of note are the very low α exponent parameters obtained for the C_{dl} element in the CNLS fitting of the data for the extremely aged Fe electrode to the equivalent circuit models – Table 4.2.3. Recall that this is the electrode characterised by the distorted voltammetric profile of Figure 3.4.17. In section 3.5.3 it was speculated that the extremely aged Fe and Co electrodes encountered in the present study have particularly inhomogeneous surfaces, and relative to fresher electrodes, are possessed of a higher density of acidic proton donating groups, which facilitate the adsorption of hydroxide ions. The double-layer capacitance arising at the interface between such a surface and an electrolyte is much less likely to be satisfactorily modelled by a conventional parallel plate capacitor than that arising at, say, a Hg/solution interface, and hence the physically uncertain fitting parameters of Table 4.2.3 are not surprising in this case.

A further illustration of the authenticity of our assertion, that the impedance responses at frequencies below ~ 10^3 Hz for Fe electrodes at lower oxygen evolution overpotentials are characteristic of two relaxation processes, is facilitated by comparing the results of fitting the data recorded at 0.68 V for the fresh non-pre-treated Fe electrode (Figures 4.2.3 – 4.2.5) to both Circuits 3 and 4. The unsatisfactory nature of the fit of the two RC loop Circuit 4 to this data at lower frequencies is obvious from the phase angle vs. log frequency plot of Figure 4.2.3 –

see caption for more details. From a graphical point of view this is even more clearly illustrated by the Nyquist representation presented in Figure 4.2.11.

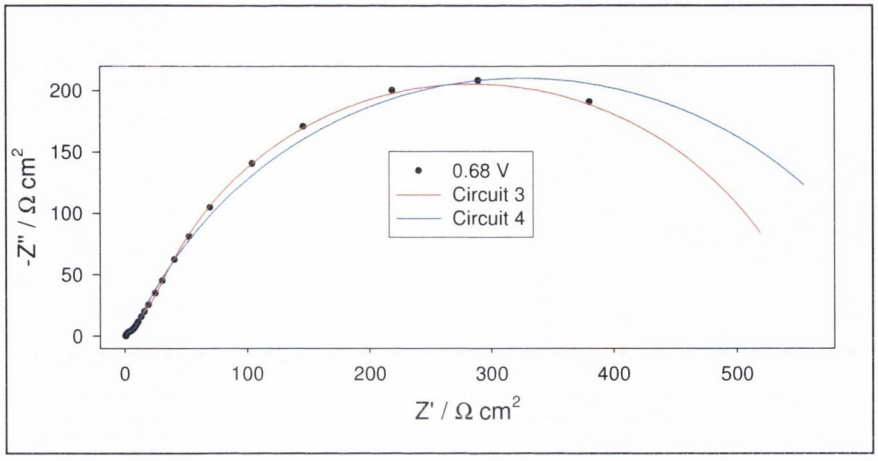


Figure 4.2.11 *Graphical illustration of the need to admit the 3 RC loop Circuit 3 in preference to the 2 RC loop Circuit 4 to achieve satisfactory modelling of the impedance response for the fresh non-pre-treated Fe electrode in 1.0 M NaOH at 0.68 V. The raw data is presented as dots, and the simulated fitting functions as continuous lines.*

4.2.2 Derivation of Tafel slopes from the Impedance Data for the Fe Electrodes

Recall from section 2.1.7 that it should be possible to extract the value of the oxygen evolution Tafel slope, b, from the value of the total faradaic resistance. The relevant expression is equation (2.1.44) (reproduced below):

$$\log\left(\frac{1}{R_{far}}\right) = \frac{\eta}{b} + \log\left(\frac{2.303 i_0}{b}\right) \qquad (2.1.44)$$

As noted previously this equation predicts that the slope of a plot of log ($1/R_{far}$) against η is equal to the inverse of the Tafel slope. In preparing the plots presented below, the value of R_{far} was extracted directly from the low frequency intercept with the Z' axis of the Nyquist representation of the relevant impedance data where this was feasible (i.e. in cases where R_{far} was sufficiently high to be completely resolved at the low frequency limit of measurement, as for example with the data recorded at E = 0.78 V for the relatively fresh pre-reduced Fe electrode and presented in Figure 4.2.7(c)). Otherwise the value of R_{far} was calculated by the addition of the relevant fit

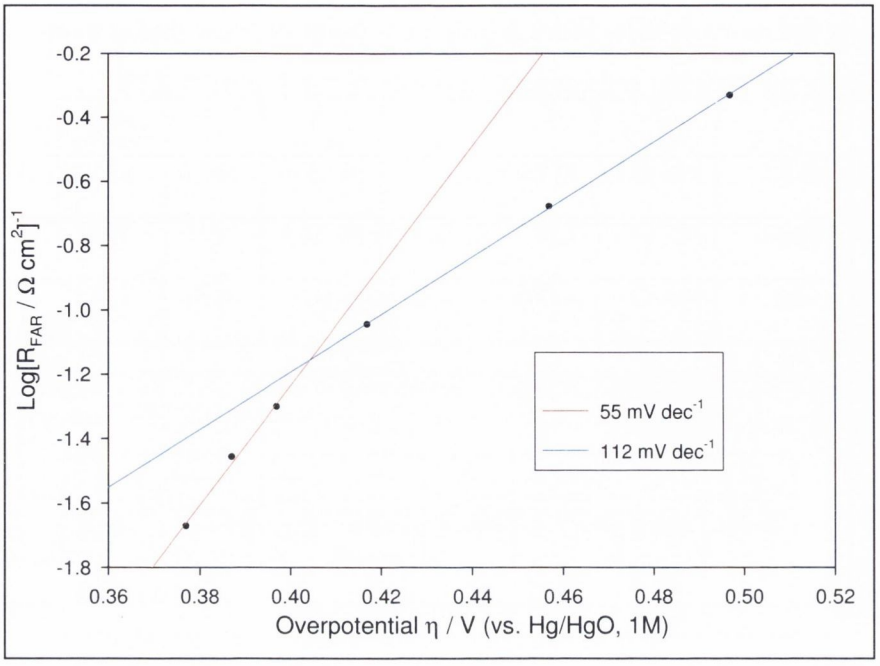


Figure 4.2.12 *Log $(R_{far})^{-1}$ vs. overpotential, η, plot constructed from the impedance data of Fig. 4.2.1 for the extremely aged, pre-reduced Fe electrode in 1.0 M NaOH at 25°C. This Tafel plot should be compared to that of the first forward scan of Fig. 3.4.16, which was obtained from steady state polarisation measurements on the same system.*

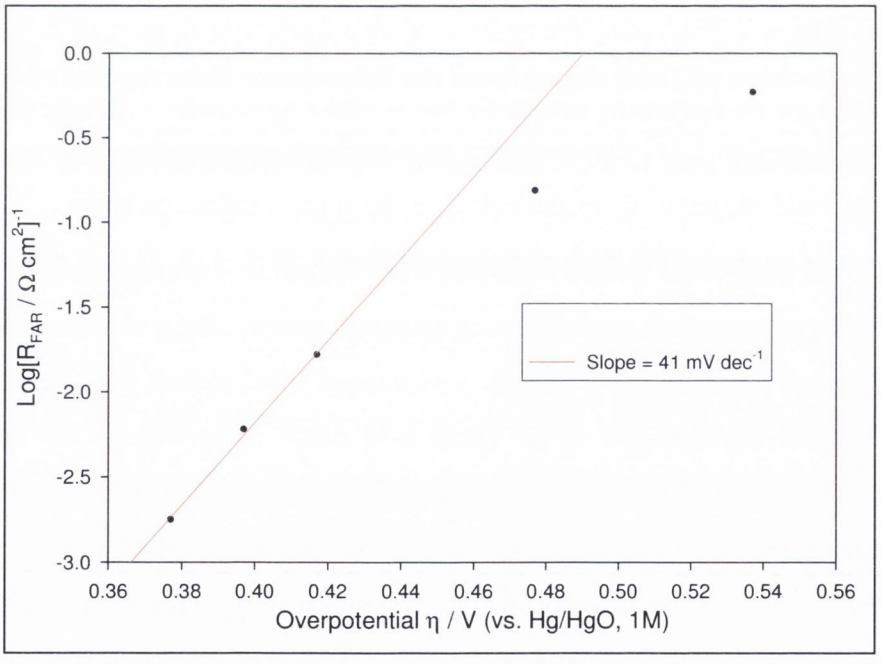


Figure 4.2.13 *Log $(R_{far})^{-1}$ vs. overpotential, η, plot constructed from the impedance data of Fig. 4.2.3 for the fresh non-pre-treated Fe electrode in 1.0 M NaOH at 25°C. This Tafel plot should be compared to that of the 1.0 M scan of Fig. 3.4.6, which was obtained from steady state polarisation measurements on the same system.*

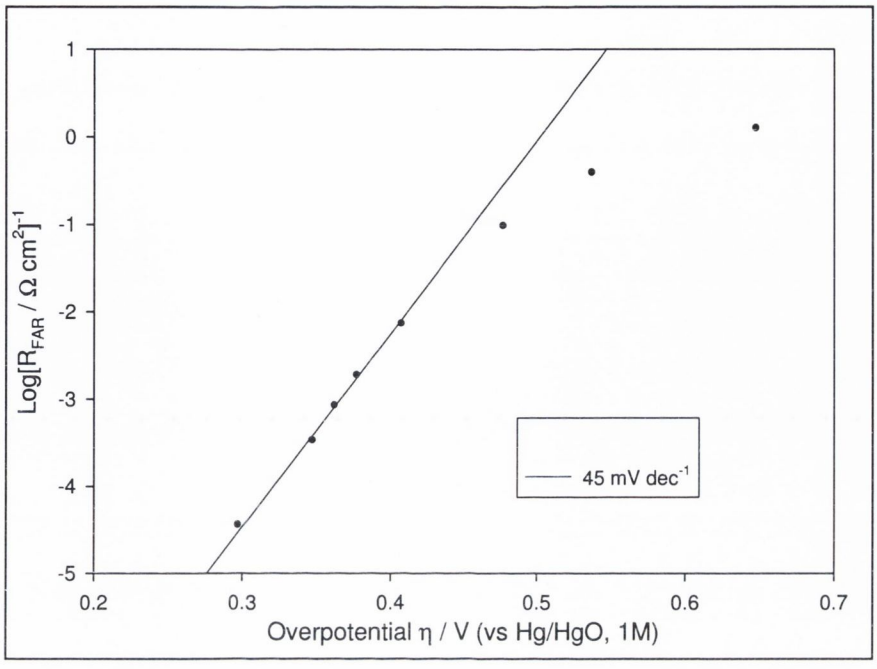


Figure 4.2.14 *Log $(R_{far})^{-1}$ vs. overpotential, η, plot constructed from the impedance data of Fig. 4.2.6 for the relatively fresh pre-reduced Fe electrode in 1.0 M NaOH at 25°C. This Tafel plot should be compared to that of the more aged scan of Fig. 3.4.8, which was obtained from steady state polarisation measurements on the same system.*

parameters listed in Tables 4.2.1 – 4.2.4. For the case of data fitted to Circuit 3, R_{far} is given by $R_{far} = R_s + R_p + R_{film}$ – obviously the R_s term drops out of the sum for data fitted to Circuit 4. Plots of log $(R_{far})^{-1}$ vs. overpotential, η, for the three "types" of Fe electrode studied, are presented in Figures 4.2.12 – 4.2.14 – further details are given in the captions. It is evident that there is excellent agreement between the Tafel slopes obtained from the impedance data, b_{EIS}, and those obtained by the steady state polarisation method, b_{SS}, in the case of the fresh non-pre-treated Fe electrode (Fig. 4.2.13, b_{SS} = 39.5 mV dec^{-1}, b_{EIS} = 41 mV dec^{-1}) and the relatively fresh pre-reduced Fe electrode (Fig. 4.2.14, b_{SS} = 44 mV dec^{-1}, b_{EIS} = 45 mV dec^{-1}). There is also reasonable agreement between the Tafel slopes obtained by the two methods for the extremely aged Fe electrode (Fig. 4.2.12), with values of b_{SS} = ~61 mV dec^{-1}, b_{EIS} = 55 mV dec^{-1} for the lower overpotential region, and b_{SS} = 116 mV dec^{-1}, b_{EIS} = 112 mV dec^{-1} for higher overpotentials.

The observed agreement between the Tafel slopes obtained via the two methods suggests that the measured slopes do indeed characterise the oxygen evolution reaction in the steady-state. The fact that the ac impedance technique also

distinguishes between the Tafel slopes of ~ 2.303×2RT/3F characteristic of the fresh non-pre-treated Fe anode, and of ~2.303×4RT/5F characteristic of the somewhat aged pre-reduced electrode, indicates the authenticity of existence of different types of kinetic behaviour for these two systems, as was postulated and discussed in the previous chapter.

4.3 EIS Studies of Oxygen Evolution on Co Electrodes

Impedance data recorded for a pre-reduced Co electrode in 1.0 M NaOH at various potentials are presented in Bode format in Figure 4.3.1. These data were recorded for the type of electrode characterised by the red voltammetric profile of Figure 3.3.25. The o.e.r. steady state polarisation curves relevant to this electrode are those of Figures 3.3.17 and 3.3.18. As with the impedance measurements on the Fe electrodes outlined in the previous section, all EIS data reported here were recorded continuously in the direction of increasing potential. With regard to the results presented in Figure 4.3.1, the spectra recorded between frequencies of 0.1 Hz and 150 KHz required between 15 and 16 minutes for acquisition, while those recorded down to 0.04 Hz took approximately a half an hour for completion. The data of Figure 4.3.1 are presented in the Nyquist representation in Figure 4.3.2.

Recall from section 3.3.2 that o.e.r steady state polarisation measurements were also performed on pre-oxidised Co electrodes – see Figure 3.2.22. The impedance responses of such an electrode in 1.0 M NaOH at various potentials associated with oxygen evolution, are presented in Figure 4.3.3.

It would appear from the phase angle vs. log frequency plots of Figures 4.3.1 and 4.3.3, and from the higher resolution Nyquist plot of Figure 4.3.2, that the impedance response of both of these "types" of Co electrode is characteristic of just two relaxation processes. In the analysis of the Fe impedance data in section 4.2.1, it was proposed that the relaxation process with the shortest characteristic time constant was associated with resistance and capacitance of the anodic oxide film. These electrical properties dominated the impedance response at frequencies approximately in the

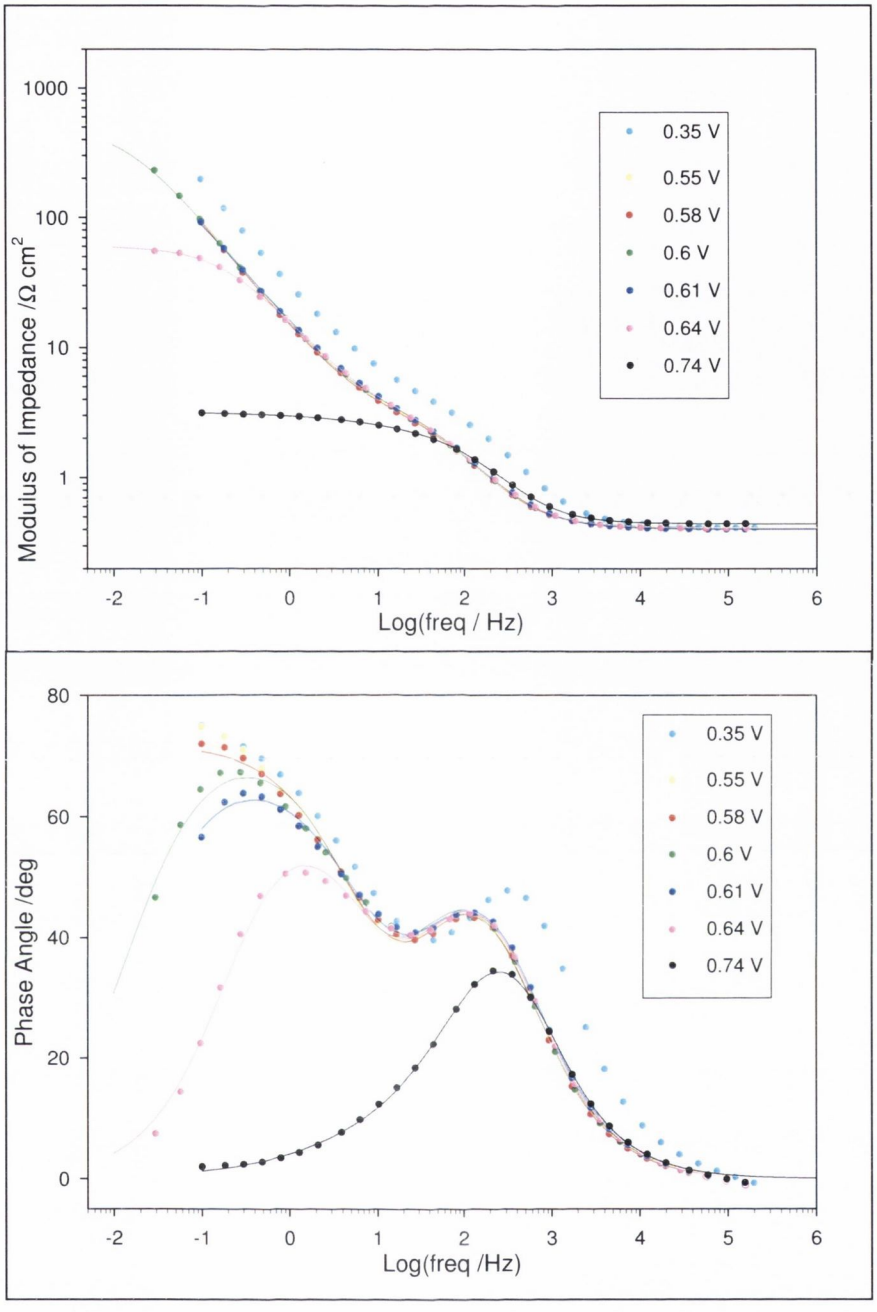


Figure 4.3.1 *Bode plots recorded at various potentials for a pre-reduced polycrystalline Co electrode in 1.0 M NaOH at 25°C. The raw data is represented by the dots. The continuous lines are the results of CNLS fits to Circuit 2 – see later.*

range of 5 – 50 KHz. The higher frequency maxima in the phase angle vs. log frequency plots of Figures 4.3.1 and 4.3.3 appear at lower frequencies than these – between 10^2 and 10^3 Hz. This is in fact the same frequency range that we associated with the impedance response of the double layer capacitance for the Fe electrodes. It would therefore appear that the shorter time constant relaxation process is associated

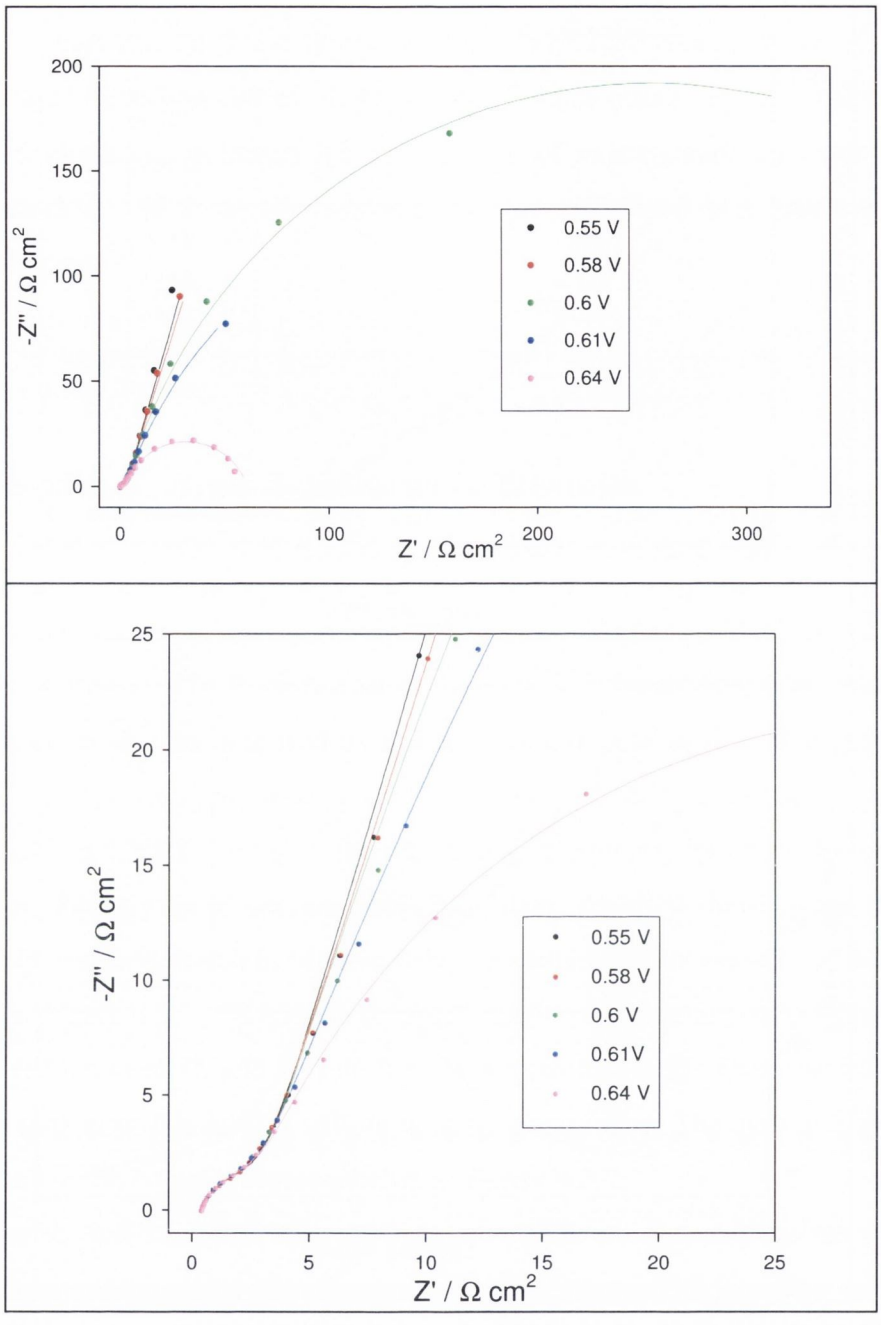


Figure 4.3.2 *Nyquist representation of the impedance data presented in Fig.4.3.1. The raw data is represented by the dots. The continuous lines are the results of CNLS fits to Circuit 2 – see later. The lower plot is a reproduction of the higher plot at a higher resolution with the purpose of showing the high frequency data more clearly.*

not with the electrical properties of the anodic oxide film, but rather with the double-layer capacitance. The potential variation of the impedance response in this frequency range conforms to the expectations for the double layer capacitance. Consider the log | Z | vs. log frequency curves of Figure 4.3.1. The relatively steep region of these

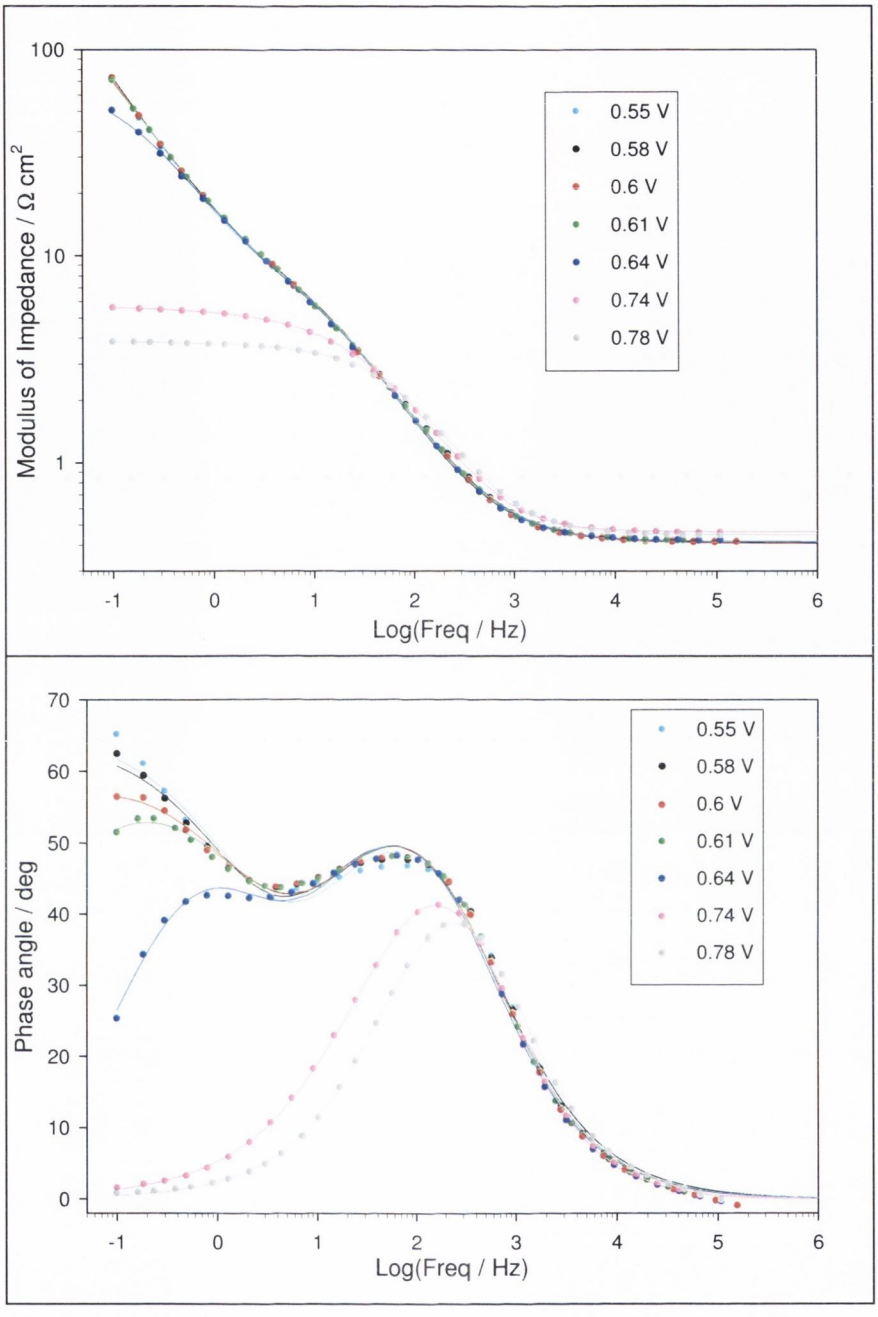


Figure 4.3.3 *Bode plots recorded at various potentials within the region of significant oxygen evolution current density for a pre-oxidised polycrystalline Co electrode in 1.0 M NaOH at 25°C. The raw data is represented by the dots. The continuous lines are the results of CNLS fits to Circuit 1 – see later.*

plots between approximately 10^2 and 10^3 Hz are dominated by the capacitive reactance that we've proposed to be associated with the interfacial double layer. The decrease in $|Z|$ between 0.35 V and the potentials from 0.55 V upwards that are associated with significant oxygen evolution current densities can be rationalised in terms of an increase in the double layer capacitance (recall that $C_{dl} \propto 1/|Z|$) associated

with either increasing surface roughness as the passive film is further oxidised, or a change in the nature of the double layer due to OH^- adsorption at high anodic potentials (c.f. ref. 24), or indeed to a combination of these factors. For the lower oxygen evolution current densities associated with the potentials between 0.55 and 0.64 V, $|Z|$ remains essentially constant over this range of frequencies – however for the higher o.e.r. current density associated with E = 0.74 V, the capacitance decreases, as evidenced by an increase in $|Z|$. Of further note, is the increase in the solution resistance (flat region of the plot above ~10^4 Hz) that accompanies this decrease in capacitance. This capacitance decrease in the frequency range of ca. 10^2 - 10^3 Hz is even more pronounced in the log $|Z|$ vs. log frequency plots at E = 0.74 and 0.78 V for the pre-oxidised Co electrode – see Figure 4.3.3. Again in this case, the aforementioned drop in capacitance is clearly accompanied by an increase in the solution resistance value.

The decrease in capacitance in the frequency range between 10^2 and 10^3 Hz at higher oxygen evolution current densities for the impedance data of Figures 4.3.1 and 4.3.3, is most readily understood, if this capacitive contribution is indeed attributed to the double layer capacitance. Vigorous oxygen bubble formation is obvious at higher o.e.r. overpotentials, and this is likely to lead to a drop in the value of the double layer capacitance due to a decrease in the effective electrode surface area. This may occur due to the exclusion of some of the "inner" surface area associated with pores and fissures in oxide surface, as these regions become occupied by gaseous oxygen bubbles[25]. In addition the geometric surface area might be somewhat diminished by the momentary adhesion of gas bubbles to the oxide surface – an effect that would lead to a time-averaged decrease in surface area over the course of the periods of imposition of the perturbation signal at a given frequency. The latter effect would also explain the increase in the uncompensated solution resistance at higher o.e.r. current densities[26]. The increase in this resistance can be attributed to a time-averaged decrease in the effective area for interfacial charge transfer and/or to an increase in the resistivity of the electrolyte solution in the immediate vicinity of the electrode owing to the high concentration of oxygen bubbles. Overall, the characteristic frequencies of this capacitive contribution and the variation of its magnitude with potential are strongly indicative of the double layer capacitance as opposed to an oxide film capacitance.

Having attributed the shorter RC time constant to the R_pC_{dl} impedance response it seems likely that the longer time-scale relaxation process is that associated with the adsorption of the o.e.r. intermediate species. As with the low frequency EIS behaviour for Fe electrodes, this slower relaxation process for Co anodes is manifested in the impedance response at potentials corresponding to the lower Tafel slope regions of the appropriate steady state polarisation curves recorded for the same systems. The lower Tafel regions are those likely to be associated with the most rapid change in intermediate coverage with applied potential, and hence it is reasonable to expect a significant pseudo-capacitive response in EIS measurements conducted at these overpotentials (bearing in mind, of course, that the relation between the pseudo-capacitance as sensed by EIS and the conventional steady state pseudo-capacitance $C_{ps,}$ is rather complicated, as discussed in section 4.2.1). Therefore, Circuit 2 of Figure 4.2.8 seems to be an appropriate equivalent circuit to model the impedance response of the pre-reduced and pre-oxidised Co electrodes at potentials associated with significant oxygen evolution.

It is noteworthy that the characteristic time constant, τ, of the slower relaxation process, is significantly longer for the Co electrodes than for the Fe electrodes discussed in sections 4.2.1 – 4.2.2. So slow is the process at lower oxygen evolution overpotentials, that at the lower frequency limit of the data presented in Figures 4.3.1 and 4.3.3, the capacitive response is only partially characterised and the resistive response is effectively not characterised at all. Only at higher overpotentials (0.64 V) is satisfactory characterisation of this resistive response approached on the timescale of the experiments outlined in Figures 4.3.1 and 4.3.3. This is of course the reason why the lower frequency pseudo-semi-circles are only partially developed in the Nyquist plots of Figure 4.3.2 for the lower o.e.r. potentials. This extremely slow relaxation process will be discussed in further detail later.

Implicit in the foregoing discussion on the origins of the longer and shorter time constants, is the fact that the regions of the Bode plots of Figures 4.3.1 and 4.3.3, which are dominated separately by the impedance responses of the R_Ω, C_{dl}, R_p, C_ϕ and R_s elements, are clearly deconvoluted – c.f. Figure 4.2.9. This again, clearly implies, that for dc steady state polarisation measurements, the kinetics of the o.e.r. are not masked by the variation of the resistivity of a poorly conducting oxide film as was proposed by Cahan and Chen[1] for Fe in borate buffer solution (pH 8.4). For the Co electrodes studied here, it would seem that the situation illustrated by line segment a

of Figure 4.2.9 prevails – i.e. $R_{film} << R_{\Omega}$, and the impedance response of the $R_{film}C_{film}$ loop occurs on a shorter timescale than can be resolved by our experiments. We do however note that the extremely large time constant of the lower frequency impedance response, does lead to issues regarding the kinetic significance of the dc polarisation experiments carried out on the o.e.r. at these electrodes in 1.0 M NaOH – see later.

Following the foregoing discussion, the EIS data for both Co electrodes were fitted to Circuit 2, Figure 4.2.8. The optimum fitting parameters are listed in Tables 4.3.1 and 4.3.2 for the pre-reduced and pre-oxidised electrodes respectively.

E V	R_s Ω cm^2	R_s Error %	C_ϕ mF cm^{-2}	α	R_p Ω cm^2	C_{dl} μF cm^{-2}	α	R_Ω Ω cm^2
0.55	------		2.484	0.820	3.955	749.94	0.825	0.412
0.58	------		2.209	0.804	3.735	746.50	0.825	0.413
0.6	503.60	21.96	2.515	0.835	4.411	729.89	0.807	0.414
0.61	407.15	24.83	1.775	0.784	3.911	695.83	0.820	0.405
0.64	56.58	3.21	2.059	0.807	4.012	699.65	0.819	0.411
0.74	1.05	2.58	1.631	0.521	1.701	596.51	0.851	0.441

Table 4.3.1 *Optimum fit parameters for the CNLS fitting of the data of Figures 4.3.1 and 4.3.2 (pre-reduced Co electrode) to Circuit 2.*

E *V*	R_s Ω cm^2	R_s Error %	C_ϕ mF cm^{-2}	α	R_p Ω cm^2	C_{dl} μF cm^{-2}	α	R_Ω Ω cm^2
0.55	------		1.353	0.727	10.191	577.1	0.748	0.412
0.58	------		1.268	0.721	11.212	590.15	0.748	0.410
0.6	1388.27	47.79	0.953	0.683	9.629	612.11	0.764	0.412
0.61	409.04	24.7	1.029	0.696	9.752	607.02	0.761	0.416
0.64	60.63	9.47	1.505	0.750	10.075	641.71	0.787	0.421
0.74	3.96	1.01	0.189	0.503	1.356	521.07	0.875	0.469
0.78	2.02	1.65	0.196	0.542	1.400	451.05	0.860	0.451

Table 4.3.2 *Optimum fit parameters for the CNLS fitting of the data of Figure 4.3.3 (pre-oxidised Co electrode) to Circuit 2.*

It is immediately noticeable that a column has been included in Tables 4.3.1 and 4.3.2 for the % error in the fitted value for R_s, and that indeed for the data recorded at 0.55 and 0.58 V no optimum fit parameters have been listed. In fact the Thales SIM fitting program outputs an estimate of the error in the fitted value for each circuit element, based upon the difference between the experimental and calculated impedances at the frequency at which a given element has its maximum significance in determining the overall measured impedance. For a visually satisfactory fit (with respect to both phase angle and $|Z|$) these error estimates are generally small (< 3%), and for this reason as well as for clarity of presentation it has been decided not to include these values in the tables of CNLS fit parameters presented in the present work. However owing to the issues regarding the extremely high R_sC_ϕ time constants and the fact that at the associated lower o.e.r. overpotentials the R_s contribution to $|Z|$ is not clearly resolved even at the lowest experimental frequencies, it has been elected to include %error estimates for R_s in this case. For both Co electrodes the R_s parameter is completely meaningless at 0.55 and 0.58 V. As the potential is increased, the % error in the calculated value of R_s drops as the contribution of this resistive component to the measured impedance begins to become resolved at the lowest measurement frequencies. Notwithstanding this, the errors associated with the fitted R_s parameters are too large to allow a meaningful Tafel slope analysis to be conducted on the basis of these parameters, as was performed for Fe in section 4.2.2. The largest error in an R_s parameter used in the calculation of R_{far} for the Fe electrodes was 3.1%.

While the impedance responses of Figures 4.3.1 – 4.3.2 may not be useful for the evaluation of o.e.r. Tafel slopes, they do demonstrate greater separation in time constants between the R_pC_{dl} and R_sC_ϕ relaxation processes than were displayed by the EIS spectra recorded for Fe (section 4.2.1). Therefore the fitting parameters for C_{dl} should be more accurate for Co than Fe. The method of Jovic[21], for obtaining an effective value of the double layer capacitance, $C_{dl\ eff}$, from fitted CPE ($C_{\alpha=1}$, α) and R_p parameters, was discussed in section 2.1.7. A example of the use of this method to extract the effective double layer capacitance at E = 0.64 V, for the pre-reduced Co electrode in 1.0 M NaOH, from the fitting parameters listed in Table 4.3.1 is now provided.

The relevant fitting parameters are $C_{\alpha=1}$ = 699.65 μF cm^{-2}, α = 0.819 and R_p = 4.012 Ω cm^2. We have created a Microsoft Excel® spreadsheet, that, taking the three parameters listed above as inputs, calculates the value of |Z″|, according to equation

(2.1.40), over the range of measurement frequencies, and outputs the results as a plot of -|Z''| vs. log frequency. The result of using this spreadsheet with the above parameters is presented in Figure 4.3.4.

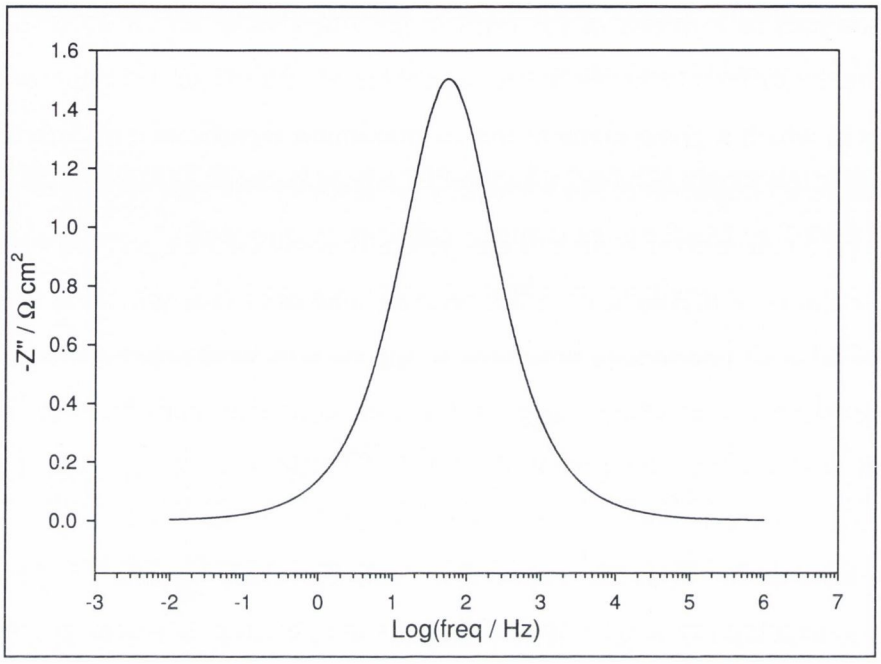


Figure 4.3.4 *Plot of -|Z''| vs. log frequency calculated according to equation (2.1.40) for the fitting parameters* C_{dl}, α, and R_p *obtained for the pre-reduced Co electrode at 0.74 V and listed in Table 4.3.1.*

Recall that the expression for calculating $C_{dl\ eff}$, presented in section 2.1.7 as equation (2.1.39), is as follows:

$$C_{dl\,eff} = C_{\alpha=1}\left(\omega''_{\max}\right)^{\alpha-1} \qquad (2.1.39)$$

The value of ω''_{max} required for this equation, is extracted from the value of the frequency f ($\omega''= 2\pi f$), for which the -|Z''| vs. log f relation plotted in Figure 4.3.4 is maximised. It transpires that the aforementioned function displays its maximum at f = 57 Hz, therefore ω''_{max} = 358.1 Hz. Inserting this value into equation (2.1.39), along with the values of $C_{\alpha=1}$ (699.65 μF cm^{-2}) and α (0.819) obtained from the CNLS fitting of the impedance data to Circuit 2, yields a value of $C_{dl\ eff}$ = 241.04 μF cm^{-2}. All of the values of $C_{dl\ eff}$ used in the estimation of the relevant roughness factors for the various electrodes presented in Chapter 5 have been calculated from CNLS fitting parameters, using the procedure outlined above.

Referring to Tables 4.3.1 and 4.3.2, it is apparent from the very low values obtained for the CPE α parameters, for both the pre-reduced (α = 0.521) and pre-oxidised (α = 0.503) Co electrodes at E = 0.74 V, that the contribution of the adsorption pseudo-capacitance has become largely insignificant at this potential. It is visually apparent that this is the case by examining the phase angle vs. log frequency plots of Figures 4.3.1 and 4.3.3. Thus it is clear, for polycrystalline Co electrodes, that at higher oxygen evolution overpotentials, anodic to the lower straight line Tafel slope region revealed in steady state polarisation measurements, the appropriate equivalent circuit model will progressively reduce from Circuit 2 to Circuit 1. In view of this, the data recorded for the pre-oxidised Co electrode at potentials between 0.74 - 0.86 V, were fitted to Circuit 1 – the optimum fit parameters are listed in Table 4.3.3.

E V	R Ω cm^2	C μF cm^{-2}	α	R_Ω Ω cm^2
0.74	5.039	515.66	0.756	0.455
0.78	3.352	465.05	0.790	0.445
0.86	0.5718	492.42	0.857	0.440

Table 4.3.3 *Optimum fit parameters for the CNLS fitting to Circuit 1 of the impedance response of the pre-oxidised Co electrode at three higher oxygen evolution overpotentials.*

The fact that the α parameter remains higher for C_{dl} when fitted to Circuit 2 than Circuit 1 for E = 0.74 and 0.78 V indicates that the former circuit still provides a more realistic model of the system at these overpotentials. In contrast, at E = 0.86 V, the α parameter of 0.857 (which is comparable to the highest values of this parameter obtained at lower overpotentials with Circuit 2) suggests that the single RC loop in series with R_Ω, constitutes a good equivalent circuit model of the system at this, the highest overpotential at which impedance data with an acceptably high signal to noise ratio could be recorded.

As was noted above, the fact that the total faradaic resistance, R_{far}, is not satisfactorily resolved on the timescale of the impedance measurements of Figures 4.3.1 – 4.3.3 for potentials below 0.64 V, prevents the performance of a Tafel slope analysis based on this data, as was conducted for the Fe electrodes in section 4.2.2. To provide an idea of the timescale required for the resolution of R_{far}, two extended EIS measurements

(10^{-3} - 2 $\times 10^{5}$ Hz) were performed on a Co electrode in 1.0 M NaOH at potentials of 0.575 and 0.625 V – see Figure 4.3.5.

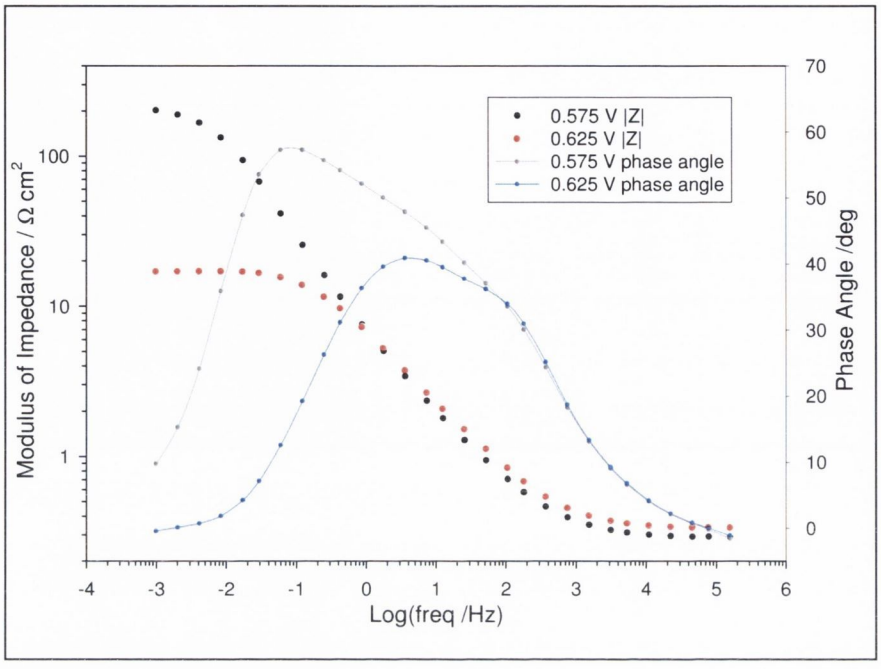


Figure 4.3.5 *Bode representation of EIS data recorded for a Co electrode in 1.0 M NaOH at potentials of 0.575 and 0.625 V over an extended frequency range (10^{-3} - 2×10^{5} Hz). A continuous line has been drawn through the phase angle data to assist in its visual distinction from the |Z| data.*

It is evident from Figure 4.3.5, that even at a frequency of 10^{-3} Hz, the total faradaic resistance is not completely resolved for E = 0.575 V (towards the bottom of the lower straight line Tafel region). The time required for the acquisition of data of satisfactory quality over this large frequency range is significant. While one single measurement period at 10^{-3} Hz is obviously 1000 s, it is necessary to repeat this measurement over a number of periods to facilitate the integration of the impedance response as was discussed in section 2.1.6. (equations (2.1.31) – (2.1.34)). In practice 30 measurement periods were used for frequencies above 66 Hz and 9 periods for lower frequencies in the acquisition of the data of Figure 4.3.5, requiring a total measurement time of ~ 15 hours for each spectrum. This renders inapplicable for such extensive frequency ranges, the method of continuous impedance measurement at a range of potentials (polarisation bias changed from selected overpotential to the next selected overpotential in the direction of increasing potential) without interruption of polarisation, as was used in the acquisition of the data of Figures 4.3.1 – 4.3.3. Obtaining 'full' impedance spectra (i.e. down to the frequencies required for the satisfactory characterisation of the total faradaic resistance) of satisfactory quality at

several values of η associated with the lower Tafel slope region, would clearly require several days of continuous polarisation using our FRA based EIS equipment. Further oxide growth and ageing of the oxide film are likely[27, 28] to have significant effects on the impedance response over such an extended timescale, thus casting doubt over the kinetic authenticity of Tafel slopes derived by the continuous FRA measurement of wide frequency range impedance spectra at different overpotentials. Overall, it would appear that FRA based impedance spectroscopy is not the most useful method for obtaining a kinetically significant Tafel slope value in the case of the o.e.r. on Co in 1.0 M NaOH, since long experimental timescales are required for the satisfactory resolution of R_{far}, however anodic polarisation of the electrode over such time scales is likely to change the nature of the reactive surface, placing doubt over the kinetic significance of the measured value of R_{far}.

4.4 EIS Studies of Oxygen Evolution on Ni Electrodes

Presented in Figure 4.4.1 in Bode plot form, are the impedance responses, at various overpotentials, of a pre-reduced Ni electrode in 1.0 M NaOH. This is the "type" of Ni electrode that was characterised by the red voltammogram of Figure 3.2.11. An o.e.r. steady state polarisation curve for this electrode is presented in Figure 3.3.12.

On initial inspection this data seems to conform to the situation of curve b of Figure 4.2.9, as was envisaged for the o.e.r. at Fe electrodes in borate buffer solution (pH 8.4) by Cahan and Chen[1] – see section 4.2.1 for a full discussion of this concept. Recapping briefly, these authors proposed that log|Z| vs. log frequency plots of EIS data recorded at potentials associated with significant oxygen evolution, which apparently display only one region of constant negative slope between two flat shelf regions at the high and low frequency extremes, are indicative of a situation where the true kinetics of the o.e.r. are masked by the impedance response of the resistance of a poorly conducting oxide film. Under the "chemi-conductor" model[1,16] it was envisaged that the magnitude of the film resistance giving rise to the low frequency log|Z| shelf would decrease with increasing potential giving rise to an apparent straight line Tafel region in dc steady state polarisation measurements. It must be admitted that the aforementioned log|Z| vs. log frequency curve shape and potential dependence would seem to provide a good description of the experimental impedance responses presented in Figure 4.4.1. Furthermore the phase angle vs. log frequency

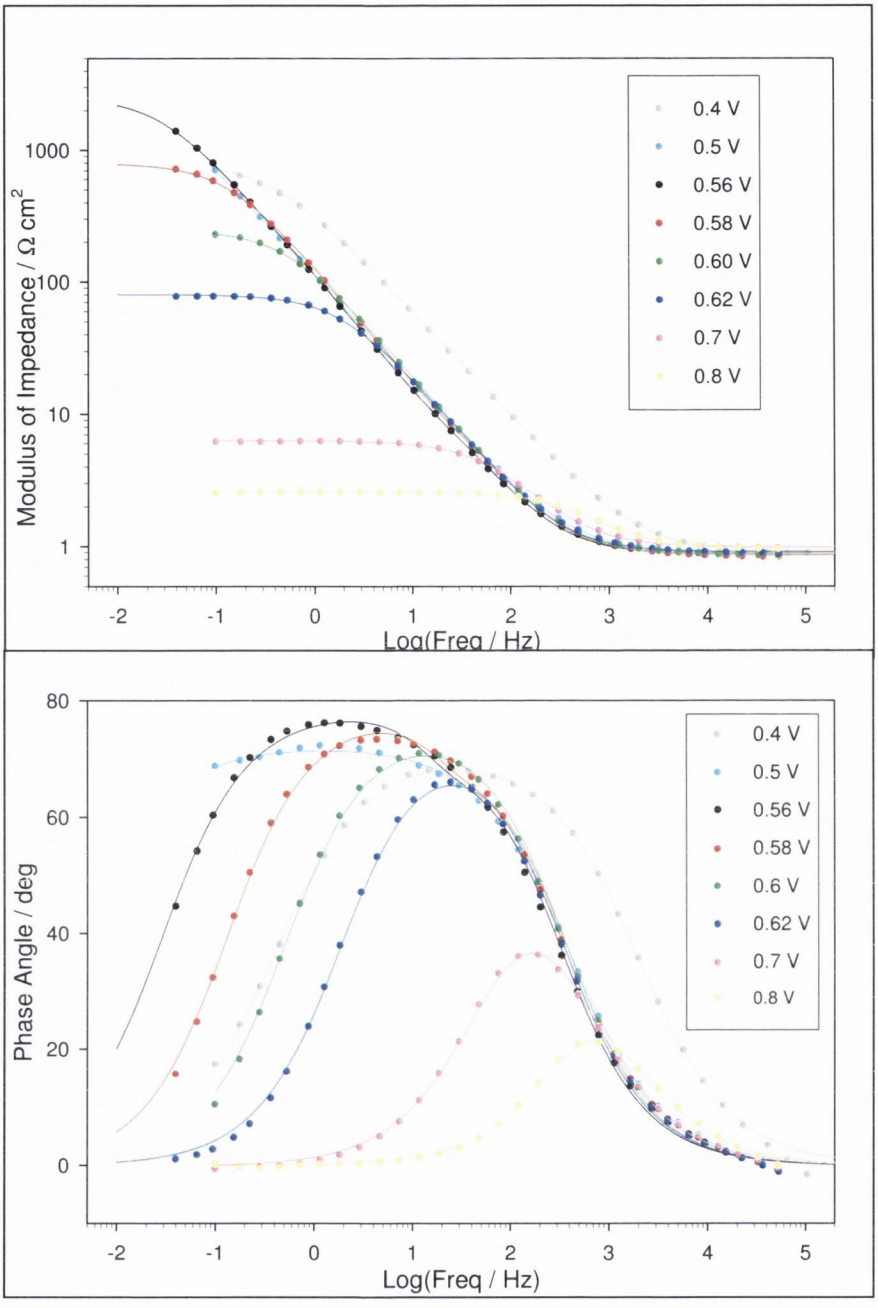


Figure 4.4.1 *Bode plots recorded at various potentials within the region of significant oxygen evolution current density for a pre-reduced Ni electrode in 1.0 M NaOH at 25°C. The raw data is represented by the dots. The continuous lines are the results of CNLS fits to Circuit 1 (0.7, 0.8 V) or Circuit 2 (all the others) – see later.*

plot is apparently characterised by just one maximum, which would suggest that the EIS measurements are sensitive to only one relaxation process – possibly related to the oxide film resistance and capacitance if one was to adopt the viewpoint of Cahan and Chen[1]. It is however noteworthy that this maximum is quite broad at the onset

potential of significant o.e.r. current density (0.56 V), but becomes narrower and more symmetrical as the overpotential is increased.

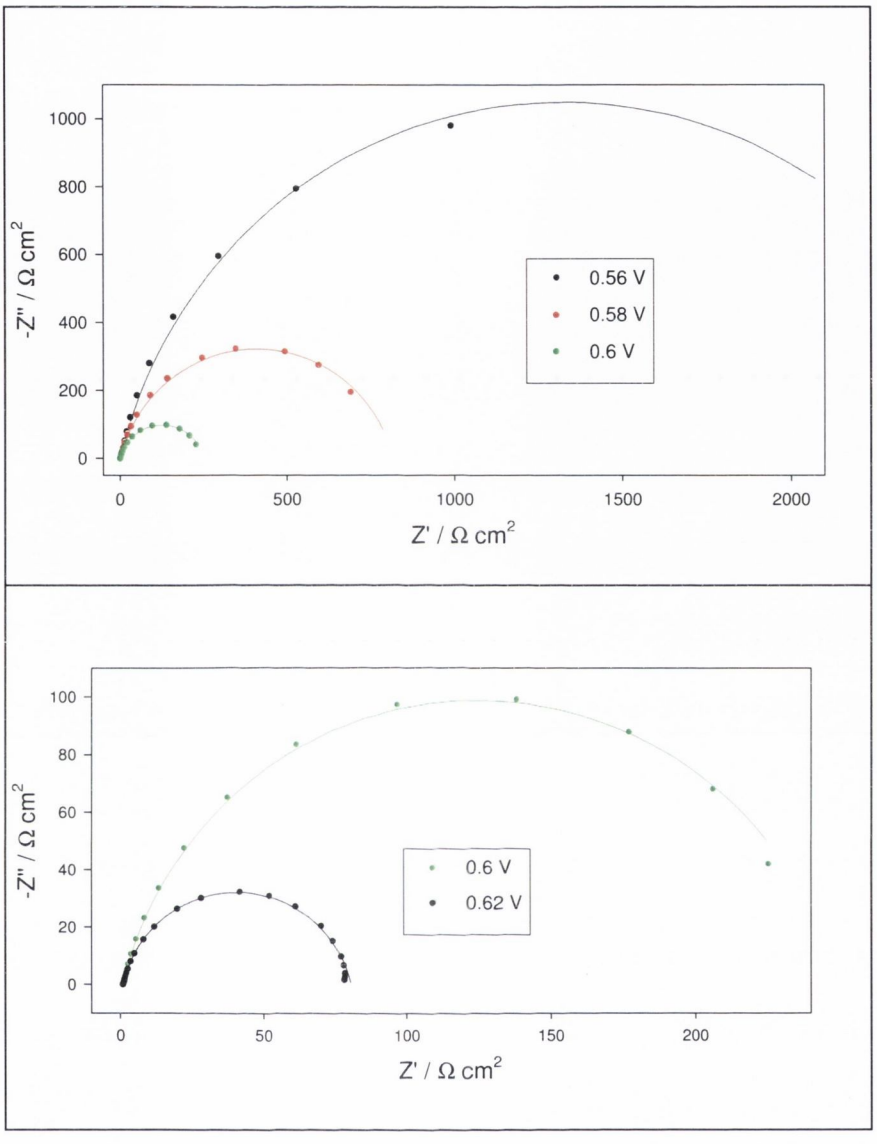


Figure 4.4.2 *Nyquist representations of the impedance data presented for a pre-reduced Ni electrode in Fig 4.4.1. As before the raw data is represented by the dots. The continuous lines are the results of CNLS fits to Circuit 2– see later.*

The apparent characterisation of just one relaxation process by the impedance response of the pre-reduced Ni electrode between lower frequency limits of 0.1 or 0.04 Hz and an upper limit of 10^5 Hz, is further emphasised by fact that the Nyquist representation of the data consists of a single pseudo-semi-circle over a range of measurement potentials – see Figure 4.4.2.

Bode plot representations of EIS data recorded for a pre-oxidised Ni electrode in 1.0 M NaOH, are presented in Figure 4.4.3. A voltammetric characterisation of this

electrode can be seen in Figure 3.2.11 (blue CV). The relevant o.e.r steady state polarisation curves for pre-oxidised Ni electrodes can be found in Figures 3.2.15 - .16.

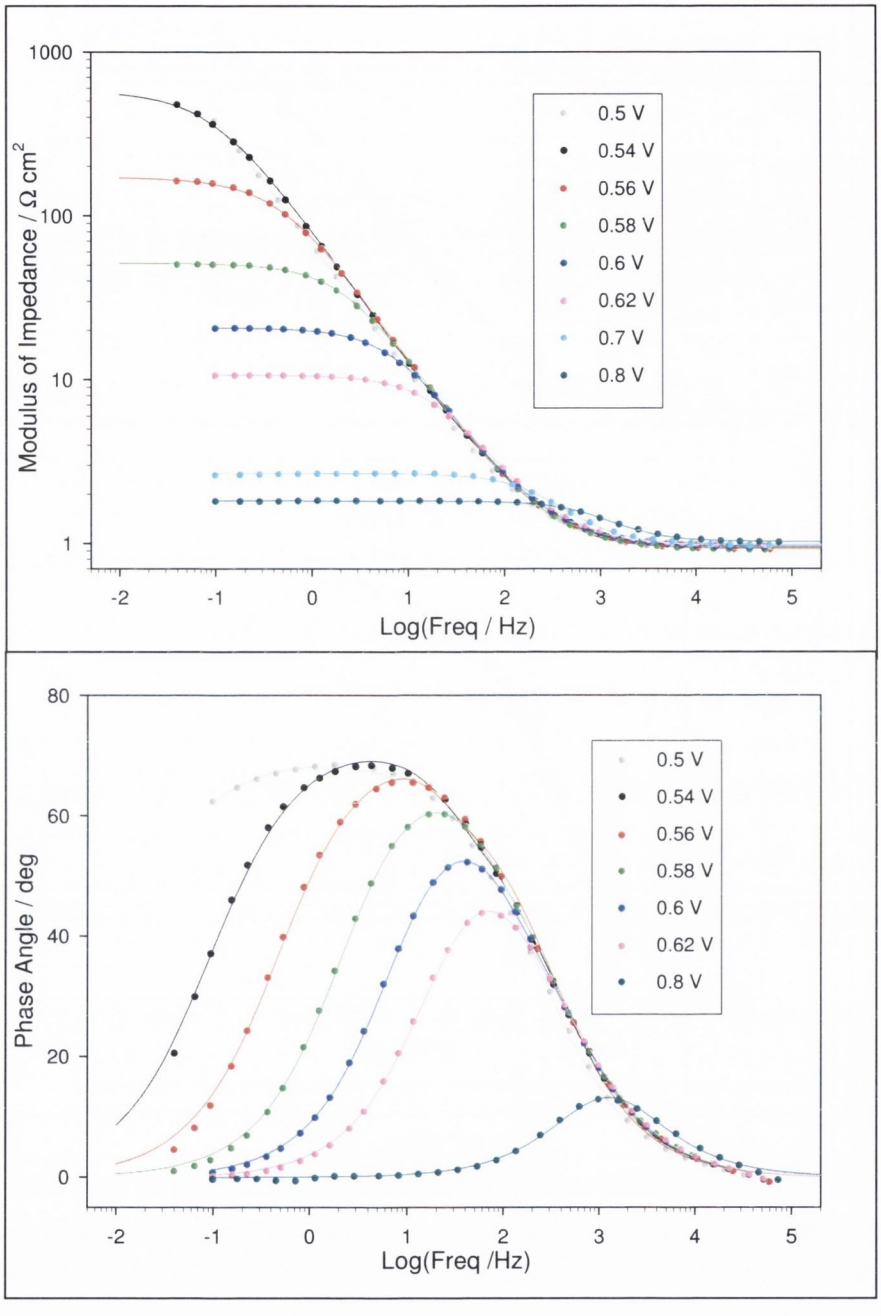


Figure 4.4.3 *Bode plots recorded at various potentials within the region of significant oxygen evolution current density for a pre-oxidised Ni electrode in 1.0 M NaOH at 25°C. The raw data is represented by the dots. The continuous lines are the results of CNLS fits to Circuit 1 (0.8 V) or Circuit 2 (all the others) – see later.*

Complex plane representations of the some of the EIS data of Figure 4.4.3 are presented in Figure 4.4.4.

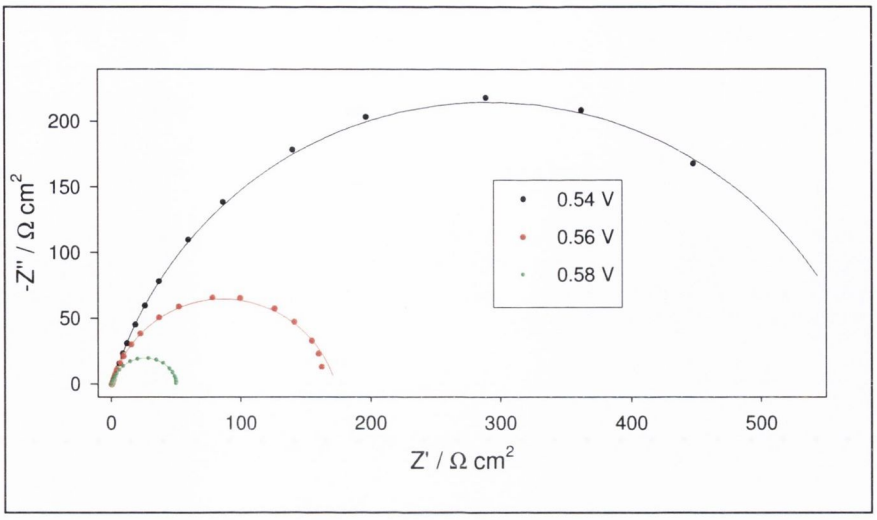


Figure 4.4.4 *Nyquist representations of the impedance data presented for a pre-oxidised Ni electrode in Fig 4.4.3. As before the raw data is represented by the dots. The continuous lines are the results of CNLS fits to Circuit 2– see later.*

It is apparent that the foregoing comments on the EIS data for the pre-reduced Ni electrode apply equally to the impedance responses of the pre-oxidised Ni electrode in the same overpotential range. Does this mean that apparent Tafel slopes for the o.e.r. at Ni electrodes in alkaline solution, derived either from steady state polarisation measurements or from EIS spectra, are actually characteristic of the increasing conductivity of the anodic oxide film with increasing applied potential (as proposed by Cahan and Chen[1]) and not of the kinetics of oxygen evolution? While this would contrast with the conclusions of sections 4.2.1 and 4.3, that the impedance responses of Fe and Co electrodes at lower frequencies (< 10^2 Hz) are representative of the kinetics of the o.e.r., it does seem that the EIS spectra for the Ni electrodes conform to the behaviour expected for the situation where the "chemi-conductor" model of Cahan and Chen prevails.

There is however evidence that the latter conclusion regarding Ni is incorrect. Consider the Bode plots of Figure 4.4.5. These impedance responses were obtained as part of our initial studies on the o.e.r. at bright non-pre-treated Ni electrodes in 1.0 M NaOH. Recall from section 3.2.1 that although it proved impossible to obtain reproducible o.e.r. steady state polarisation curves from such electrodes with respect to the current density at a given overpotential, the curves (e.g. see Figures 3.2.3 and 3.2.7) always displayed lower straight-line Tafel regions with slopes very close to

2.303×2RT/3F – i.e. the same Tafel slopes that were obtained for the pre-reduced and pre-oxidised Ni electrodes under consideration at present. Thus it is reasonable to assume that the Tafel slope for such bright non-pre-treated Ni electrodes characterises

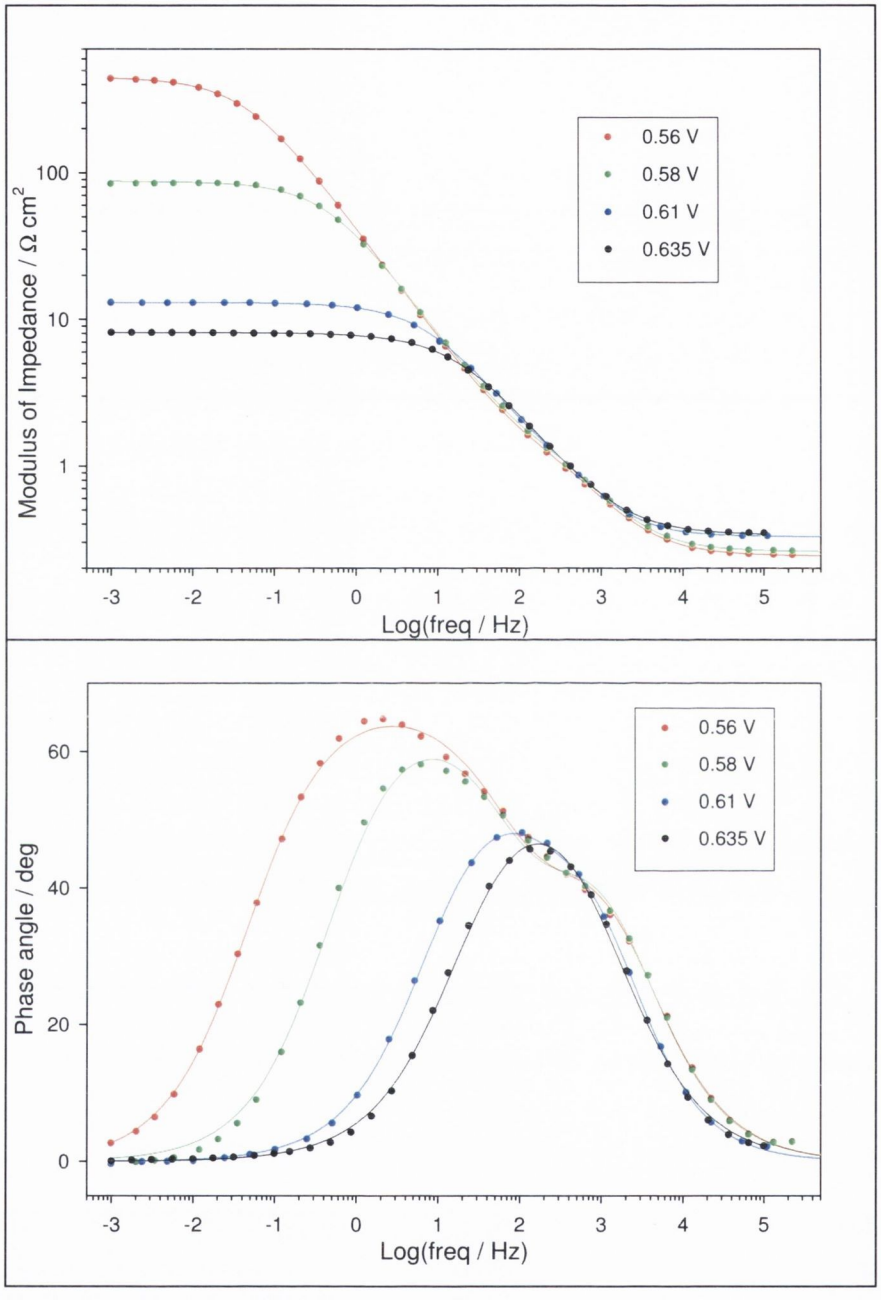


Figure 4.4.5 *Bode plots recorded at various potentials within the region of significant oxygen evolution current density for a bright non-pre-treated Ni electrode in 1.0 M NaOH at 25°C. The raw data is represented by the dots. The continuous lines are the results of CNLS fits to Circuit 1 (0.635 V) or Circuit 2 (all the others) – see later.*

the same physicochemical process as the Tafel slopes for the pre-reduced and pre-oxidised Ni electrodes, be that the kinetics of the oxygen evolution reaction or the

variation of conductivity of the passive oxide film. It is readily apparent from the phase angle vs. log frequency plot that the impedance responses of Figure 4.4.5 at E = 0.56 and 0.58 V are characteristic of two relaxation processes. The phase angle maximum for the more rapid of these processes at all potentials, occurs at frequencies between 10^2 and 10^3 Hz – this is precisely the frequency range of the phase angle maxima for the double layer relaxation in the case of Fe (section 4.2.1) and Co electrodes (section 4.3). Furthermore the behaviour of the longer timescale relaxation process with increasing oxygen evolution overpotential, is reminiscent of that of the R_sC_ϕ behaviour observed for the Fe and Co electrodes – i.e. this process contributes significantly to the overall impedance response in the potential range immediately anodic to the appearance of significant oxygen evolution current densities, however its overall influence diminishes with increasing overpotential, as both $R_s \rightarrow 0$ and $C_\phi \rightarrow 0$.

With careful examination of the log|Z| vs. log frequency plots of Figure 4.4.5 for E = 0.56 and 0.58 V, regions of the spectrum corresponding to R_Ω, C_{dl}, R_p, C_ϕ and R_s can be distinguished, as envisaged by curve a of Figure 4.2.9. Thus for the high frequency shelf above 10^4 Hz, the impedance response is due to R_Ω, the steeply sloped region between ca. 300 and 1000 Hz is characteristic of C_{dl}, while over the course of the slight arrest in slope between ca. 100 and 300 Hz the polarisation resistance R_p dominates. At frequencies below 100 Hz the slope of the log|Z| vs. log frequency plot becomes steeper again as the impedance response becomes dominated by C_ϕ, and finally the low frequency shelf is dominated by R_s. The fact that all these distinct regions of the spectra can be isolated implies that EIS is sensitive to the kinetics of the o.e.r. for this non-pre-treated Ni electrode and doesn't merely monitor the resistive and dielectric properties of the surface oxide layer. Indeed the passive film resistance is obviously too small (i.e. $R_{film} << R_\Omega$) to be captured by impedance methods, as was envisaged by curve a of the ideal impedance response sketched in Figure 4.2.9. The foregoing discussion indicates that Circuit 2 of Figure 4.2.8 is an appropriate equivalent circuit model for the non-pre-treated Ni anode at lower potentials associated with significant oxygen evolution – as the overpotential is increased Circuit 2 will reduce to Circuit 1. The values of the optimum fitting parameters for the CNLS fitting of the data of Figure 4.4.5 to Circuits 2 and 1 are listed in Tables 4.4.1 (a) and (b) respectively.

(a)

E V	R_s Ω cm^2	C_ϕ μF cm^{-2}	α	R_p Ω cm^2	C_{dl} μF cm^{-2}	α	R_Ω Ω cm^2
0.56	452.57	398.64	0.762	2.102	308.15	0.760	0.246
0.58	85.71	431.67	0.777	2.187	293.71	0.775	0.261
0.61	11.05	254.52	0.702	1.801	329.24	0.826	0.332

(b)

E V	R Ω cm^2	C μF cm^{-2}	α	R_Ω Ω cm^2
0.61	13.00	377.55	0.711	0.321
0.635	7.82	372.41	0.732	0.336

Table 4.4.1 *Optimum fit parameters for the CNLS fitting of the data of Figure 4.4.5 (non-pre-treated Ni electrode) to (a) Circuit 2 for lower potentials, and (b) Circuit 1 for higher potentials.*

What then of the significance of the impedance data for the pre-reduced (Figures 4.4.1 and 4.4.2) and pre-oxidised (Figures 4.4.3 and 4.4.4) Ni electrodes? It would be an unlikely coincidence that (as established above) the kinetics of the o.e.r. would give rise to a Tafel slope of 2.303×2RT/3F in steady state polarisation measurements for a non-pre-treated Ni electrode in 1.0 M NaOH, while the increasing conductivity of a poorly conducting oxide film would give rise to an identical value of Tafel slope for the other Ni electrodes (i.e. pre-reduced and pre-oxidised) in the same electrolyte solution. Therefore it is likely, contrary to initial impressions, that the impedance spectra, recorded at lower oxygen evolution potentials for the pre-reduced and pre-oxidised Ni electrodes, actually consist of the superposition of the impedance responses of two relaxation processes.

That this is the case might also be surmised by careful consideration of the phase angle vs. log frequency plots of Figures 4.4.1 and 4.4.3. For example, referring to the former of these plots, it can be appreciated that the broad maxima observed for lower oxygen evolution overpotentials, are gradually resolved into a well-defined symmetrical bell-shaped function in the spectrum recorded at 0.7 V. Significantly the maximum at this potential lies between 10^2 - 10^3 Hz, which, by analogy with our analyses of the EIS spectra for the Fe, Co and non-pre-treated Ni electrodes, is strongly indicative of the impedance response of the relaxation of the interfacial

double layer. Note also that the log|Z| vs. log frequency plot for this potential exhibits a shift upward and to the left relative to the traces for lower overpotentials. This is the exact same type of behaviour as that noted for Co electrodes in Figures 4.3.1 and 4.3.3. Recall that this was explained in terms of a decrease in the double layer capacitance with increasing oxygen evolution current density, arising from the blockage of a fraction of the electrode surface by bubbles of oxygen.

Thus there is ample evidence that the impedance response at 0.7 V is largely attributable to the double layer relaxation process. Our experience with the analyses of the impedance responses of the Fe and Co electrodes would suggest that the broader maxima, at lower oxygen evolution overpotentials, in the phase angle vs. log frequency plots of Figure 4.4.1, must arise as the result of a superposition of the responses of the double-layer relaxation process and a relaxation process with a longer time constant – i.e. the relaxation of the coverage of the reaction intermediate species. Similar conclusions to those discussed in the previous and present paragraph are also clearly applicable to the data of Figure 4.4.3 for the pre-oxidised Ni electrode. It isn't possible to distinguish discrete regions of the log|Z| vs. log frequency plots of Figures 4.4.1 and 4.4.3, where the overall measured impedance is dominated respectively, with increasing frequency, by the contributions of R_s, C_ϕ, R_p, C_{dl} and R_Ω as in the ideal situation portrayed by curve a in Figure 4.2.9. This arises, not because the true kinetics of the o.e.r. are masked by the properties of the anodic oxide film, but rather due to the fact that the R_sC_ϕ and R_pC_{dl} time constants occupy similar characteristic time scales.

In view of the foregoing discussions, the raw impedance data for the pre-reduced and pre-oxidised Ni electrodes were fitted to Circuits 2 (for lower potentials) and/or 1(for higher potentials) of Figure 4.2.8. The best-fit values of the equivalent circuit elements are listed in Table 4.4.2 for the pre-reduced Ni electrode and Table 4.4.3 for the pre-oxidised Ni electrode. The fact is, that owing to the similarity of the R_sC_ϕ and R_pC_{dl} time constants for lower oxygen evolution potentials, the experimental data recorded at these potentials, fits quite well to Circuit 1 as well as Circuit 2. Nonetheless, the quality of the fits to Circuit 2 are slightly superior, as can be appreciated by comparing the phase angle vs. log frequency plots of Figure 4.4.3 with those presented in Figure 4.4.6. Both figures contain the same raw data, obtained for the pre-oxidised Ni electrode. The continuous lines in Figure 4.4.3 are the optimum transfer functions that arise from the CNLS fitting of this raw data to Circuit 2 (with

(a)

E V	R_s Ω cm^2	C_ϕ μF cm^{-2}	α	R_p Ω cm^2	C_{dl} μF cm^{-2}	α	R_Ω Ω cm^2
0.56	2464.00	82.94	0.919	26.416	467.69	0.860	0.879
0.58	780.00	81.25	0.906	18.256	414.88	0.867	0.874
0.60	234.40	67.31	0.947	11.029	387.37	0.860	0.877
0.62	75.30	82.56	0.895	4.272	377.19	0.864	0.905
0.70	4.88	74.94	0.819	0.503	267.38	0.845	0.993

(b)

E V	R Ω cm^2	C μF cm^{-2}	α	R_Ω Ω cm^2
0.58	815.040	440.12	0.856	0.881
0.60	247.840	421.00	0.858	0.888
0.62	80.080	427.63	0.857	0.919
0.70	5.392	324.50	0.834	1.000
0.80	1.618	204.50	0.854	0.976

Table 4.4.2 *Optimum fit parameters for the CNLS fitting of the data of Figure 4.4.1 (pre-reduced Ni electrode) to (a) Circuit 2 for lower potentials, and (b) Circuit 1 for higher potentials.*

(a)

E V	R_s Ω cm^2	C_ϕ μF cm^{-2}	α	R_p Ω cm^2	C_{dl} μF cm^{-2}	α	R_Ω Ω cm^2
0.54	562.24	144.19	0.974	18.912	444.37	0.802	0.957
0.56	158.94	168.68	0.982	12.949	433.06	0.815	0.944
0.58	42.51	197.44	0.981	8.366	438.62	0.827	0.928
0.60	16.67	214.31	0.892	3.306	391.81	0.852	0.962
0.62	8.01	211.25	0.842	1.862	346.50	0.874	0.986

(b)

E V	R Ω cm^2	C μF cm^{-2}	α	R_Ω Ω cm^2
0.54	593.92	486.06	0.801	0.973
0.56	174.88	480.56	0.813	0.960
0.58	51.584	488.56	0.821	0.943
0.60	20.368	455.63	0.821	0.975
0.62	10.003	412.75	0.821	0.993
0.70	1.722	325.75	0.860	0.985
0.80	0.805	214.75	0.863	1.029

Table 4.4.3 *Optimum fit parameters for the CNLS fitting of the data of Figure 4.4.3 (pre-oxidised Ni electrode) to (a) Circuit 2 for lower potentials, and (b) Circuit 1.*

the exception of the data recorded at 0.8 V), while in Figure 4.4.6 these lines plot the transfer functions yielded by fitting the data to Circuit 1. It is visually evident, for the impedance responses recorded between 0.54 and 0.62 V, that, while Circuit 1 can provide reasonable modelling of the frequency dependence of the phase angle, the quality of the fitting is improved by admitting Circuit 2. This visual impression is

supported by the error estimates of the Thales SIM fitting program. As an example, for the fitting of the data recorded at E = 0.54 V, the program returns a mean error of 0.2 deg with a maximum error of 3.5 deg for Circuit 1, in comparison to a mean error of 0.1 deg and a maximum error of 2.2 deg for Circuit 2. While it is true that increasing the number of fitting parameters can improve the quality of a CNLS fit, the comparison of Figures 4.4.3 and 4.4.6 indicates, that contrary to initial appearances the raw data is indeed characteristic of two relaxation processes. It is noteworthy that

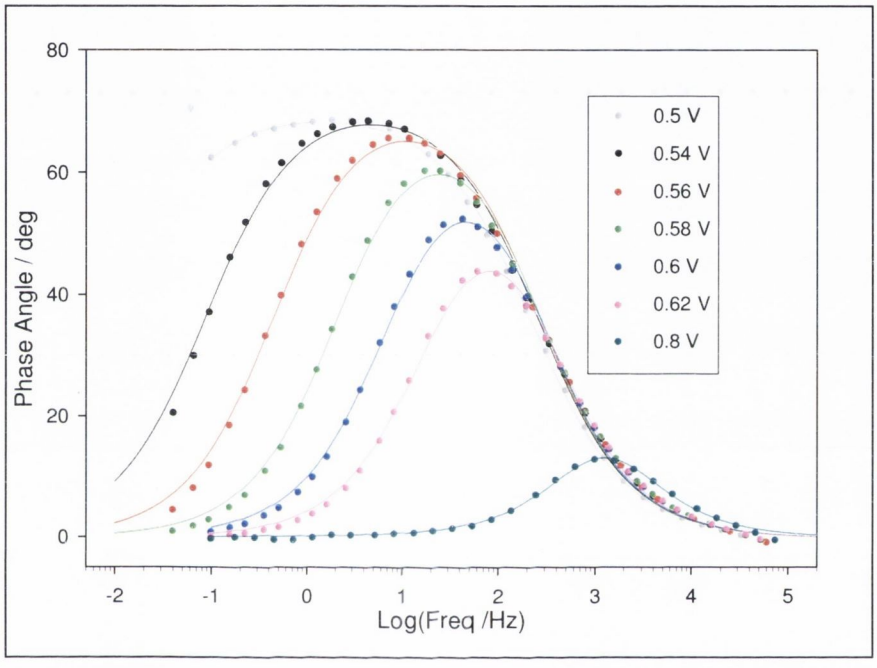


Figure 4.4.6 *Optimum transfer functions (continuous lines) for the CNLS fitting to Circuit 1, of the raw phase angle vs. log frequency data (dots) recorded for a pre-oxidised Ni electrode in 1.0 M NaOH. This raw data was previously presented in Figure 4.4.3.*

analogously to our EIS spectra for the pre-reduced and pre-oxidised Ni anodes, Conway and Liu[9] obtained impedance data for the o.e.r. on a Pt electrode in 1.0 M NaOH, that when presented in Nyquist plot form, also consisted of just one apparent pseudo-semi-circle. This behaviour prevailed at potentials between 1.54 – 1.90 V (vs. R.H.E.), which were associated, in steady state polarisation measurements on the same system, with a lower Tafel slope region with b = ~ 46 mV dec^{-1}. These workers also obtained satisfactory fitting of their experimental data to an equivalent circuit model directly analogous to our Circuit 2, with the same significance attributed to the various elements. Interestingly, they obtained best-fit values for the C_ϕ element of the order of hundreds of μF cm^{-2}, in agreement with order of magnitude obtained for the

same element in the present work for Fe and Ni electrodes at lower oxygen evolution potentials in the same electrolyte solution.

The question arises as to why it was readily possible to visually identify the presence of two distinct relaxation processes giving rise to the total impedance response in the case of the phase angle vs. log frequency plots for the non-pre-treated Ni electrode (Figure 4.4.5) but not for the pre-reduced (Figure 4.4.1) or pre-oxidised (Figure 4.4.3) Ni electrodes? Similarly for the impedance studies on Fe electrodes (section 4.2.1), one might question why there is greater separation of the R_sC_ϕ and R_pC_{dl} time constants in the case of the extremely aged pre-reduced Fe electrode (Figure 4.2.1) as opposed to the fresh non-pre-treated Fe electrode (Figure 4.2.3) or the less aged pre-reduced Fe electrode (Figure 4.2.6)? A clue to the origin of the aforementioned observations may be obtained by examining the respective CNLS fitting parameters.

Comparing the parameters of Table 4.4.1 (a) for the fitting of the non-pre-treated Ni electrode EIS data to Circuit 2, with those of Tables 4.4.2 (a) and Table 4.4.3 (a) for the respective fitting of the impedance responses of the pre-reduced and pre-oxidised Ni electrodes to the same equivalent circuit model, it is obvious that over approximately the same ranges of potential, the listed values of the CPE α parameters are smaller for both the C_ϕ and C_{dl} elements in Table 4.4.1 relative to the latter two tables. As was discussed in section 2.1.7, the double layer capacitance frequency dispersion (requiring the admission of CPEs as opposed to ideal capacitors in equivalent circuit models) often observed in EIS measurements on real electrochemical systems, is believed to arise from electrode surface inhomogeneities and surface roughness effects (the smaller the value of α, the less ideally homogeneous the surface), although the exact physical means by which the surface inhomogeniety gives rise to the frequency dispersion is ill understood. The physical significance of the α parameter related to the adsorption pseudo-capacitance is even less certain, however since smaller C_ϕ α values accompany smaller C_{dl} α values for Table 4.4.1 (a) relative to Tables 4.4.2 (a) and 4.4.3(a), it might be a reasonable inference that the C_ϕ α value is also somewhat related to electrode surface inhomogenieties. In short, what we are tentatively proposing is that the degree of temporal separation of the R_sC_ϕ and R_pC_{dl} time constants, is related to the relative amount of surface inhomogeniety – the less uniform the electrode surface, the greater the separation of the aforementioned time-constants.

The latter proposal would also seem to be bourn out for the various Fe electrodes considered in section 4.2.1. Comparing the parameters listed in Table 4.2.1 (relatively fresh pre-reduced Fe electrode), Table 4.2.3 (a) (extremely aged pre-reduced Fe electrode) and Table 4.2.4 (a) (fresh non-pre-treated Fe electrode), it is clear that the electrode displaying the greatest surface inhomogeniety (if it is accepted that the C_{dl} α value is characteristic of this) is the extremely aged, pre-reduced Fe electrode (Table 4.2.3.). It is also true, that of the three "types" of Fe electrodes studied, this extremely aged electrode is the one that displays the greatest separation of the R_sC_ϕ and R_pC_{dl} time constants in EIS experiments – compare the spectra of Figure 4.2.1 with those of Figures 4.2.3 and Figure 4.2.6. In light of the discussion of the history and electrocatalytic properties of this extremely aged electrode in section 3.4.2 and its unusual characteristic CV (Figure 3.4.17), it is not surprising that it displays a greater degree of surface inhomogeneity than the other Fe electrodes.

As mentioned above, the physical reason for the correlation between double-layer capacitance frequency dispersion and surface roughness is unclear and remains a source of controversy in the literature[29]. Since C_ϕ is a measurable quantity (related to the rate of change of the surface concentration of the reaction intermediate species with potential - see section 4.2.1) with the dimensions of capacitance, as opposed to a capacitance in the conventional sense, it is perhaps even more difficult in this case, to propose a firm physical basis for frequency dispersion related to surface non-uniformities. Therefore our proposal, that the separation of the R_sC_ϕ and R_pC_{dl} time constants is related in someway to the degree of surface inhomogeneity, is based on observation and not on a developed physical theory. Nonetheless, it will be shown in chapter 5, that Co, the electrode metal, which displays, of the three studied here, the greatest separation of the R_sC_ϕ and R_pC_{dl} time constants in EIS measurements, is also the metal with the greatest associated apparent roughness factor.

To conclude the discussion on the EIS measurements performed on Ni electrodes, we compare the Tafel slopes, b_{EIS}, obtained from these experiments by means of equation (2.1.44) with those, b_{SS}, measured by steady state polarisation methods. The same procedure was used in preparing the plots of log $(1/R_{far})$ against η for the Ni electrodes, as was used for the Fe impedance data in section 4.2.2. That is to say, that where possible, R_{far}, was taken directly from the raw experimental data - otherwise its value was calculated by the addition of the relevant R_s and R_p fitting parameters. The plots of log $(1/R_{far})$ against η for the pre-reduced and pre-oxidised Ni electrodes are

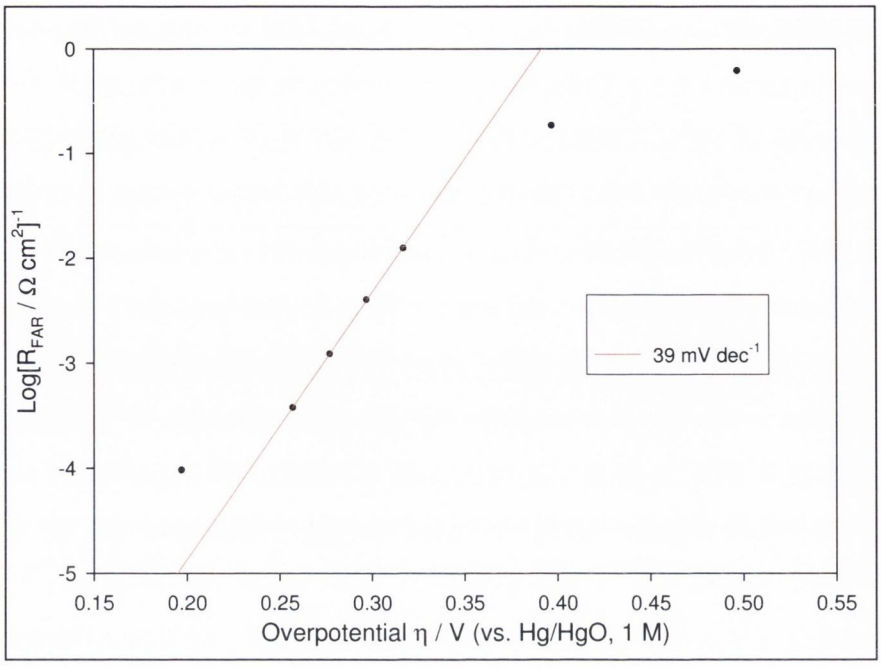


Figure 4.4.7 *Log $(R_{far})^{-1}$ vs. overpotential, η, plot constructed from the impedance data of Fig. 4.4.1 for a pre-reduced Ni electrode in 1.0 M NaOH at 25°C. This Tafel plot should be compared to the 1.0 M scan of Fig. 3.2.12, which was obtained from steady state polarisation measurements on the same system.*

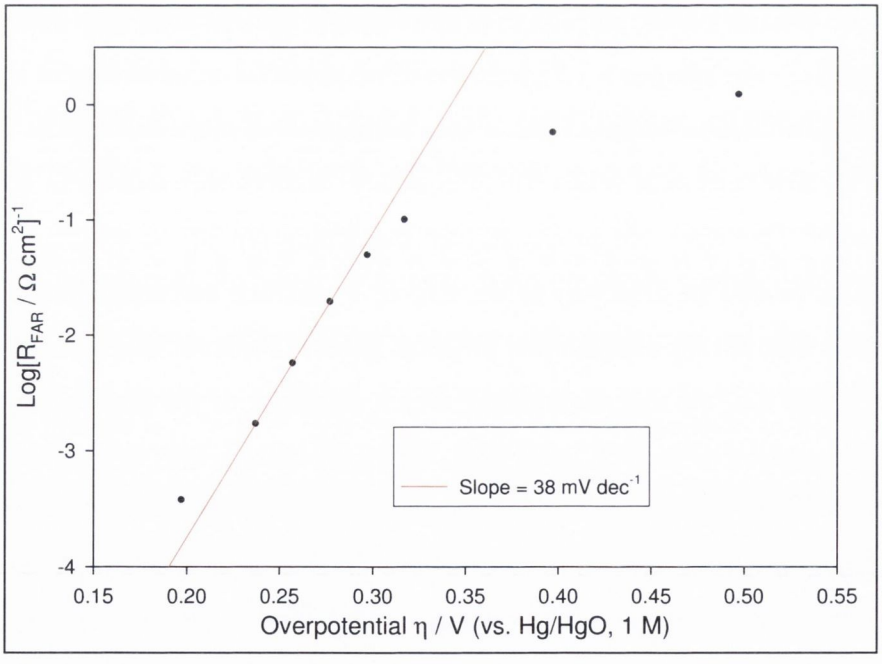


Figure 4.4.8 *Log $(R_{far})^{-1}$ vs. overpotential, η, plot constructed from the impedance data of Fig. 4.4.3 for a pre-oxidised Ni electrode in 1.0 M NaOH at 25°C. This Tafel plot should be compared to the 1st forward scan of Fig. 3.2.16, which was obtained from steady state polarisation measurements on the same system.*

presented in Figures 4.4.7 and 4.4.8 respectively.

It is clear that there is excellent agreement between the values of b_{EIS} and b_{SS}. For the pre-reduced Ni electrode in 1.0 M NaOH, the impedance method yields b_{EIS} = 39 mV dec^{-1}, while the steady state polarisation measurements yield b_{SS} = 40 mV dec^{-1}. In the case of the pre-oxidised Ni electrode in 1.0 M NaOH the experimental values are b_{EIS} = 38 mV dec^{-1} and b_{SS} = 40 mV dec^{-1}. As was remarked in section 4.2.2 for the Fe electrodes, the agreement in the values of the Tafel slopes obtained independently by dc and ac techniques, points to the genuine kinetic significance of the consensus values.

Chapter 4 References

1 Cahan, B.D., Chen, C.T., *J. Electrochem. Soc.*, **1982**, *129*, 700.

2 Harrington, D.A., Conway, B.E., *Electrochimica Acta.*, **1987**, *32*, 1703.

3 Willems, H., Kobussen, A.G.C., De Wit, J.H.W., and Broers, G.H.J., *J. Electroanal. Chem.*, **1984**, *170*, 227.

4 Cappadonia, M., Divisek, J., von der Heyden, T., Stimming, U., *Electrochimica Acta.*, **1994**, *39*, 1559.

5 Bai, L., Harrington, D.A., Conway, B.E., *Electrochimica Acta.*, **1987**, *32*, 1713.

6 Bai, L., Gao, L., Conway, B.E., *J. Chem. Soc., Faraday Trans.*, **1993**, *89(2)*, 235.

7 Kessler, T., Vilche, J.R., Ebert, M., Jüttner, K., Lorenz, W.J., *Chem. Eng. Technol.*, **1991**, *14*, 263.

8 Conway, B.E., Ping, G., *J. Chem. Soc., Faraday Trans.*, **1990**, *86*, 923.

9 Conway, B.E., Liu, T.-C., *Langmuir*, **1990**, *6*, 268.

10 Castro, E.B., Gervasi, C.A., Vilche, J.R., *J. Appl. Electrochem.*, **1998**, *28*, 835.

11 Wu, G., Li, N., Zhou, D-R., Mitsuo, K., Xu, B-Q., *J. Solid State Chem.*, **2004**, *177*, 3682

12 Conway, B.E., Liu, T.-C., *Ber. Bunsenges. Phys. Chem.*, **1987**, *91*, 461.

13 Da Silva, L.M., Fernandes, K.C., Faria, L.A., Boodts, J.F.C., *Electrochimica Acta.*, **2004**, *49*, 4893.

14 Cahan, B.D., Chen, C.T., *J. Electrochem. Soc.*, **1982**, *129*, 17.

15 Cahan, B.D., Chen, C.T., *J. Electrochem. Soc.*, **1982**, *129*, 474.

16 Cahan, B.D., Chen, C.T., *J. Electrochem. Soc.*, **1982**, *129*, 921.

17 Hu, J-M., Zhang, J-Q., Cao, C-N, *Int. J. Hydrogen Energy.*, **2004**, *29*, 791.

18 Macdonald, J.R., Schoonman, J., Lehnen, A.P., *J. Electroanal. Chem.*, **1982**, *131*, 77.

19 Conway, B.E., Gileadi, E., *Trans. Faraday Soc.*, **1962**, *58*, 2493.

20 Conway, B.E., Liu, T.-C., *J. Chem. Soc., Faraday Trans. 1,* **1987**, *83*, 1063.

21 Jovic, V.D., Gamry Instruments, Application Note, "Determination of the correct value of C_{dl} from the impedance results fitted by the commercially available software", Gamry Instruments, 2003.

22 Ho, J.C.K., Piron, D.L., *J. Appl. Electrochem.*, **1996**, *26*, 515.

23 Bockris, J.O'M., Otagawa,T., *J. Electrochem. Soc.*, **1984**, *131*, 290.

24 Bockris, J.O'M., Otagawa,T., *J. Phys. Chem.*, **1983**, *87*, 2960.

25 Da Silva, L.M., Alves, V.A., Da Silva, M.A.P., Trasatti, S., Boodts, J.F.C., *Electrochimica Acta.*, **1997**, *42*, 271.

26 Conway, B.E., Bai, L., *J. Chem. Soc., Faraday Trans. 1,* **1985**, *81*, 1841.

27 Gennero De Chialvo, M.R., Chialvo, A.C., *Electrochimica Acta*, **1990**, *35*, 437.

28 Willems, H., Kobussen, A.G.C., Vinke, I.C., De Wit, J.H.W., and Broers, G.H.J., *J. Electroanal. Chem.*, **1985**, *194*, 287.

29 Conway, B.E., in "Impedance Spectroscopy – Theory, Experiment, and Applications", 2nd Edition, Barsoukov, E., Macdonald, J.R., Ed., J. Wiley & Sons, 2005, section 4.5.

CHAPTER 5

ACTIVE SURFACE AREAS AND COMPARISON OF CATALYTIC PERFORMANCE

5.1 Introduction

The present chapter is devoted to the estimation of the roughness factors associated with some of the Ni, Co and Fe electrodes, using the discharge current transient method discussed in sections 2.1.9 and 2.2.11. The roughness factors determined by that technique are compared, in sections 5.2 – 5.4, with those yielded by the double-layer capacitance ratio approach. The normalisation of steady state current densities to the estimated truly active surface areas, facilitates, in sections 5.5 and 5.6, a more meaningful comparison of the activities of the various electrodes towards the o.e.r.

5.2 Roughness Factors for the Ni Electrodes

Recall from section 2.1.9 that the *roughness factor*, f_r, is defined as the real surface area per unit geometric surface area – i.e. $f_r = A/A_g$, where A is the real surface area and A_g is the geometric surface area. In that section, there was a discussion of an in-situ method, proposed initially by Ho and Piron[1], for the estimation of appropriate roughness factors for oxide electrodes under conditions of significant oxygen evolution current densities. It was decided to attempt similar measurements in the present work – the practical aspects of this were outlined in section 2.2.11.

Several discharge current vs. time transients, recorded using the apparatus of Figure 2.2.2, for a fresh, bright, non-pre-treated Ni electrode in 1.0 M NaOH, are presented in Figure 5.2.1. Transients were recorded for a range of applied current densities, i_{appl}, the particular values of which corresponded to the steady state current densities at given potentials as observed in oxygen evolution steady state polarisation measurements on the same system. All experiments were conducted initially in the direction of increasing applied current density for values of i_{appl} derived from the first forward sweep of the steady state polarisation curve. Upon achieving the maximum value of i_{appl}, the experiment was continued in the direction of decreasing current density with the i_{appl} values now determined with reference to the reverse direction steady state polarisation trace. As was observed by Ho and Piron[1], cathodic currents were recorded upon the discharge of the electrode, the initial magnitudes of which were much larger than the corresponding i_{appl} magnitude.

The total charge, Q_{dec}, passed in the course of the decay process was evaluated by determining the area under the i-t transients, between $t = 0$, and the time at which the

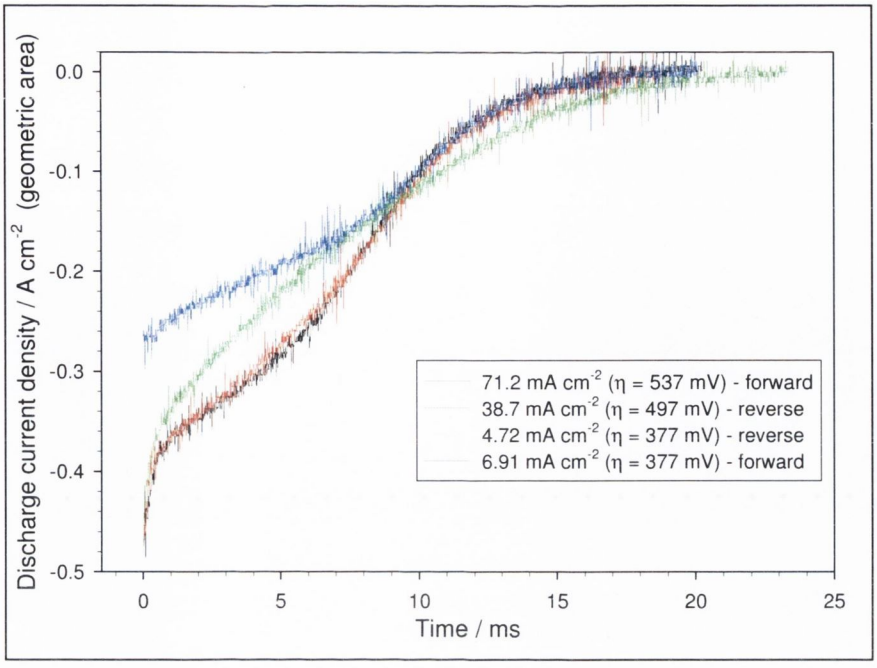


Figure 5.2.1 *Raw current decay transients for a fresh, bright, non-pre-treated polycrystalline Ni electrode in 1.0 M NaOH solution at 25°C. The values of the relevant prior anodic charging current densities are indicated in the legend.*

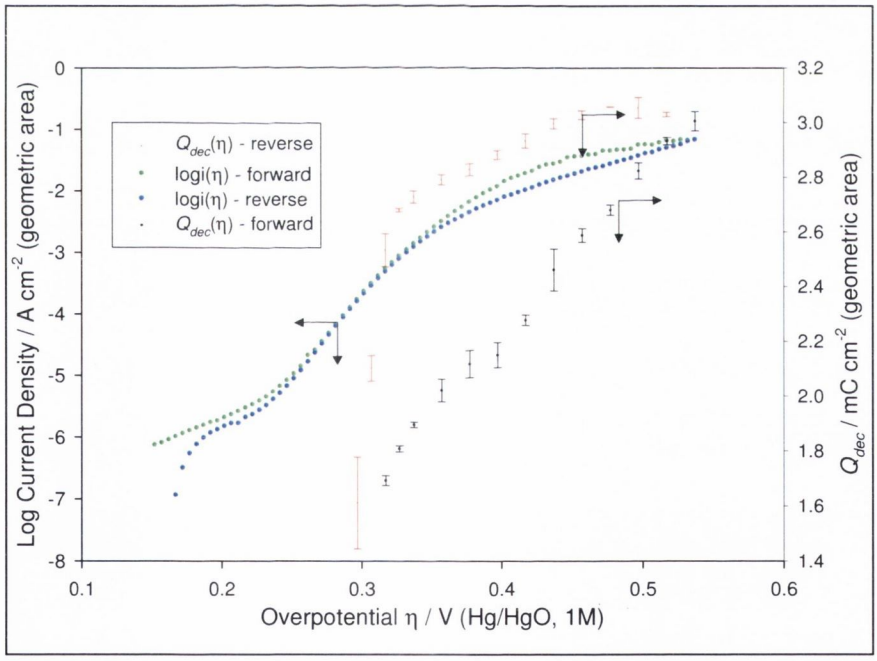


Figure 5.2.2 *Total charge, Q_{dec}, passed during the discharge of a fresh non-pre-treated Ni electrode in 1.0 M NaOH at 25°C vs. oxygen evolution overpotential η. Also included are the o.e.r. steady state polarisation curves recorded in both the directions of increasing (forward) and decreasing (reverse) potential for the same system.*

decay current became zero. It is evident from Figure 5.2.1 that the raw transients, as recorded by the digital storage oscilloscope, are rather noisy. As was mentioned in section 2.2.11, the measurement at each applied current density value was repeated four times on consecutive days in order to estimate the experimental error.

Recall from the discussion of section 2.1.9, that Ho and Piron[1] envisaged a rather different oxygen evolution pathway for their anodes in aqueous alkaline solution (see equations (2.1.65, I and II)), than that proposed in the present work for Ni (scheme (3.5.2) or equivalently (3.5.3)). The question arises as to whether the desorption of the o.e.r. intermediate species can still be postulated to occur with a 2 electron transfer, upon the termination of galvanostatic polarisation (as envisaged by Ho and Piron – reverse of step (2.1.65, I)) for the o.e.r. pathway of schemes (3.5.2) and (3.5.3)? If we consider our proposed o.e.r. mechanism for Ni in the form of scheme (3.5.2), it is clear from the kinetic mechanistic analysis of section 3.5.1, that the only intermediate species envisaged to occur with a significant fractional coverage, θ, is the $Ni(IV)O(OH)_2$ formed in step (3.5.2, I). When the anodic charging current i_{appl} is interrupted the discharge of the electrode can occur via the following overall reaction, which we propose to give rise to the transients recorded on the oscilloscope:

$$Ni(IV)O(OH)_2 + H_2O + 2e^- \rightarrow Ni(II)(OH)_2 + 2OH^- \qquad (5.2.1)$$

Indeed reaction (5.2.1) is probably a more realistic representation of the discharge of a Ni electrode than the reverse of reaction (2.1.65, I) proposed by Ho and Piron[1], since, as was discussed in section 1.4.1 the reversible potential of the Ni(II)↔Ni(III) redox transition is anodic to the oxygen electrode reversible potential. Overall, it can be concluded that our proposed reaction pathway for oxygen evolution at a Ni electrode in aqueous alkaline solution is consistent with a 2 electron current decay process, when the applied polarisation sustaining the o.e.r. proceeding at a steady state current density is broken. Thus, if we, like Ho and Piron[1] after Fedorova and Frumkin[2], adopt the benchmark value of 420 μC cm^{-2} for a two electron overpotential deposition O adsorption process, then the roughness factors for the Ni electrodes employed in the present study can also be estimated using the following expression:

$$f_r = \frac{Q_{dec}(plateau)}{420\mu C\,cm^{-2}} \qquad (5.2.2)$$

The overall results of the current decay experiments for the fresh, non-pre-treated Ni electrode in 1.0 M NaOH, are presented in Figure 5.2.2. The $Q_{dec}(\eta)$ data points in Figure 5.2.2 represent the mean value of Q_{dec} calculated from the four transients recorded for each value of i_{appl}, while the vertical error bars span ± one standard deviation from this mean. For ease of interpretation the $Q_{dec}(\eta)$ data is plotted on a common η axis with the o.e.r. steady state polarisation curve for the same system, from which the values of i_{appl} were extracted.

As expected there is a close relationship between the o.e.r. steady state polarisation curve and the $Q_{dec}(\eta)$ plot presented in Figure 5.2.2. It wasn't possible to perform a meaningful evaluation of Q_{dec} (in either direction) for values of i_{appl} corresponding to $\eta < \sim 0.31$ V, since the small magnitude of the transient decay currents lead to a high signal to noise ratio. This is of course the potential region associated with the low slope ($b \sim 2.303 \times 2RT/3F$) Tafel region, and the observation of the last sentence is consistent with our postulation (section 3.5.1) of low coverage Langmuir adsorption ($\theta \rightarrow 0$) of $Ni(IV)O(OH)_2$ over this potential range.

What is less easy to explain is the hysterisis observed in Figure 5.2.2 between the $Q_{dec}(\eta)$ data recorded in the direction of increasing i_{appl} and those recorded in the direction of decreasing i_{appl}. This phenomenon is almost certainly related to the hysterisis in the corresponding o.e.r. steady state polarisation curve. As was discussed in chapter 3 there does not exist in the literature, to the best of our knowledge, a satisfactory explanation for the hysterisis that we, and others, have observed in o.e.r. steady state polarisation curves. An attempt was made by Kobussen et al.[3] to rationalise the hysterisis observed in polarisation curves recorded for oxygen evolution at $La_{0.5}Ba_{0.5}CoO_3$ electrodes in 3M KOH. Like us, these workers observed that the activity of their electrodes for a given potential, was lower on a sweep in the direction of decreasing potential, that on a prior sweep in the opposite direction. They proposed that anodisation of the electrodes at higher oxygen evolution overpotentials (i.e. at potentials above those associated with the lower straight line Tafel region) leads to further passivation and a loss of activity for oxygen evolution. However some of the details of their model are in possible conflict with the o.e.r. mechanisms that we have proposed for Ni (scheme (3.5.3)), Co and Fe (scheme (3.5.68)) electrodes in chapter 3. In particular they postulated that the decline in oxygen evolution activity was related to the formation of inert Co(IV) sites on the electrode surface at higher overpotentials, with Co(III) sites being those catalytically active towards the o.e.r. By

constrast the reaction pathway proposed for oxygen evolution on Co anodes in the present work envisages that Co(IV) sites are actually the catalytically active reaction centres.

Whatever the reason, it is apparent from the steady state polarisation curves of Figure 5.2.2 that for $\eta > \sim 0.34$ V, the electrode surface displays superior catalytic activity towards the o.e.r. on the initial forward sweep, than on the reverse sweep (which was recorded continuously following the attainment of the maximum potential in the forward direction). The $Q_{dec}(\eta)$ behaviour is the direct opposite to the $\log i(\eta)$ behaviour in that, for a given overpotential η, the associated value of Q_{dec} is larger for the decreasing direction of i_{appl} than for the increasing direction. For example consider the case at $\eta = 0.517$ V. Consulting the polarisation curve in the forward direction reveals that the steady state current density i at this potential is 67.6 $mAcm^{-2}$ (geometric surface area). Using this as a value for i_{appl} in the transient decay measurements in the direction of increasing i_{appl}, yielded a value of $Q_{dec} = 2932 \pm 2$ $\mu C\ cm^{-2}$. For the polarisation curve in the direction of decreasing potential a steady state current of 51.9 $mA\ cm^{-2}$ was observed at $\eta = 0.517$ V. A total charge of $Q_{dec} = 3035 \pm 1$ $\mu C\ cm^{-2}$ was passed during the discharge of the Ni electrode following polarisation at the latter current density as part of the transient decay measurements in the direction of decreasing i_{appl}. Therefore despite a lower anodic polarisation current density i_{appl}, a larger Q_{dec} was recorded for the Ni electrode in the direction of decreasing i_{appl}.

This behaviour can be understood as follows. Owing to the lower catalytic activity of the electrode (as indicated by the complementary steady state polarisation curve) following the reversal of the direction of the change in i_{appl} from positive to negative, it is to be expected that the steady state coverage of $Ni(IV)O(OH)_2$ will be higher for the same value of η on the negative sweep relative to the previous positive sweep. This arises because the decrease in catalytic activity is indicative of a drop in the velocity of the RDS – i.e. step (3.5.2, II), in which $Ni(IV)O(OH)_2$, the only intermediate species with a significant fractional coverage, is consumed. A higher surface concentration of $Ni(IV)O(OH)_2$ is allowed to accumulate in the steady state, when the rate of the RDS diminishes. This in turn explains the observation of larger values of Q_{dec} associated with a given overpotential, when the transient decay experiment is performed in the direction of decreasing i_{appl}, relative to the other direction.

Also implicit in this explanation is the expectation that the "plateau" in the $Q_{dec}(\eta)$ plot (where the fractional coverage of the reaction intermediate is assumed to approach unity, thus yielding information on the real surface area through the associated value of Q_{dec}) should occur at lower overpotentials for the Q_{dec} data obtained in the direction of decreasing i_{appl}. Referring to Figure 5.2.2, this prediction seems to be bourn out. The values of Q_{dec} recorded in the reverse direction are approximately constant (i.e. lie in the range from approximately 3.0 – 3.1 mC cm^{-2}) over a range of η from 0.517 – 0.437 V – this would appear to be the $\theta \approx 1$ plateau region as was observed by Ho and Piron[1] for their electrodeposited Ni, Co and $Ni_{20}Co_{80}$ electrodes. The magnitude of Q_{dec} decreases gradually with decreasing overpotential for $\eta < 0.437$ V, before dropping dramatically for $\eta \leq 0.317$ V - i.e. in the lower Tafel slope region of potential, where it was envisaged in section 3.5.1 that $\theta \rightarrow 0$.

By contrast the values of Q_{dec} recorded in the direction of increasing i_{appl} increase in an almost linear manner with η, over the entire investigated range of overpotential. There is no apparent plateau region in the forward direction Q_{dec} vs. η plot, although the Q_{dec} value associated with the highest overpotential, $\eta = 0.537$ V, is of a similar magnitude to the aforementioned "Q_{dec} plateau" in the reverse direction plot. Thus it would appear that a steady state fractional coverage of the $Ni(IV)O(OH)_2$ species of almost unity prevails at this overpotential for the transient decay measurements performed in the forward direction. Although the rate of consumption of $Ni(IV)O(OH)_2$ via the rate determining step (3.5.2., II), is greater at $\eta = 0.537$ V on the forward sweep ($i = 71.2$ mAcm^{-2}), than at $\eta = 0.437$ V on the reverse sweep ($i =$ 15.6 mA cm^{-2}) it seems that a fractional coverage of this species tending towards unity arises in both of these situations. The greater rate of reaction in the former case would tend to diminish the steady state intermediate fractional coverage relative to the latter case - this effect is however offset by the more rapid rate of adsorption of OH^- from solution (via step (3.5.1, I)) at the higher positive overpotential. Note that we are not saying anything here about why the electrode is less active towards the o.e.r. on the reverse steady state polarisation "sweep", relative to a prior forward "sweep" – we are merely commenting on the effect that this is likely to have on the relative surface concentrations of the intermediate species at a given overpotential in the opposite scan directions. Finally, we note that issues related to hysterisis in Q_{dec} vs. η plots were not discussed by Ho and Piron[1, 4] in their pioneering papers on the transient decay method

of roughness factor determination, since these workers report only on $Q_{dec}(\eta)$ data recorded in the direction of decreasing i_{appl}.

With regard to the problem of real surface area estimation from the experimental $Q_{dec}(\eta)$ data, the discussions of the foregoing two pages would imply that a meaningful value of Q_{dec}(plateau) (see equation (5.2.2)) can be most satisfactorily extracted from the reverse direction Q_{dec} vs. η plot for $0.517 \geq \eta \geq 0.457$ V. Taking the mean of the Q_{dec} values over this range of overpotentials yields 3.047 mC cm^{-2}. A reasonable estimate of the experimental error is the difference between this mean value and that value of Q_{dec}, covered by the error bars of the data points for $0.517 \geq \eta \geq 0.457$ V, which is furthest from the mean – performing such an analysis yields an estimate for Q_{dec}(plateau) of 3.05 ± 0.05 mC cm^{-2}. Inserting this value into equation (5.2.2) yields an estimate for the roughness factor for the fresh non-pre-treated Ni electrode of f_r = 7.3 ± 0.1. The quoted error is of course, merely the experimental error – in reality the true error is likely to be much larger owing to the questionable nature of some of the assumptions on which the technique is based. For example, as pointed out by Ho and Piron[1], the theoretical value of 420 μC cm^{-2} for a two electron O adsorption process is merely chosen as "universal accepted reference" value, and the degree of its significance has not been independently experimentally verified for the electrodes of the present study (if such verification is indeed possible).

The transient decay roughness factor determination method was also applied to the pre-reduced "type" of Ni electrode introduced in section 3.2.2. Bi-directional steady state polarisation and Q_{dec} vs. η plots for such an electrode are presented in Figure 5.2.3. This steady state polarisation curve has previously been presented in Figure 3.2.13 and was discussed in section 3.2.2. Although there are less experimental $Q_{dec}(\eta)$ points in Figure 5.2.3 than in Figure 5.2.2, it is immediately apparent that the Q_{dec} vs. η plot for the pre-reduced Ni electrode has a similar shape to the corresponding plot for the non-pre-treated Ni electrode in the same electrolyte solution – therefore the commentary passed above on the latter plot is equally valid with regard to the former (pre-reduced electrode) plot. Taking the mean Q_{dec} value for the data recorded in the direction of decreasing i_{appl} for $0.617 \geq \eta \geq 0.547$ V and estimating the experimental error, as was described above for the non-pre-treated Ni electrode, yields a value of Q_{dec}(plateau) = 2.64 ± 0.09 mC cm^{-2}. This in turn leads to a roughness factor estimate of f_r = 6.3 ± 0.2 for the active surface area for the o.e.r. at the pre-reduced Ni electrode in 1.0 M NaOH at 25°C.

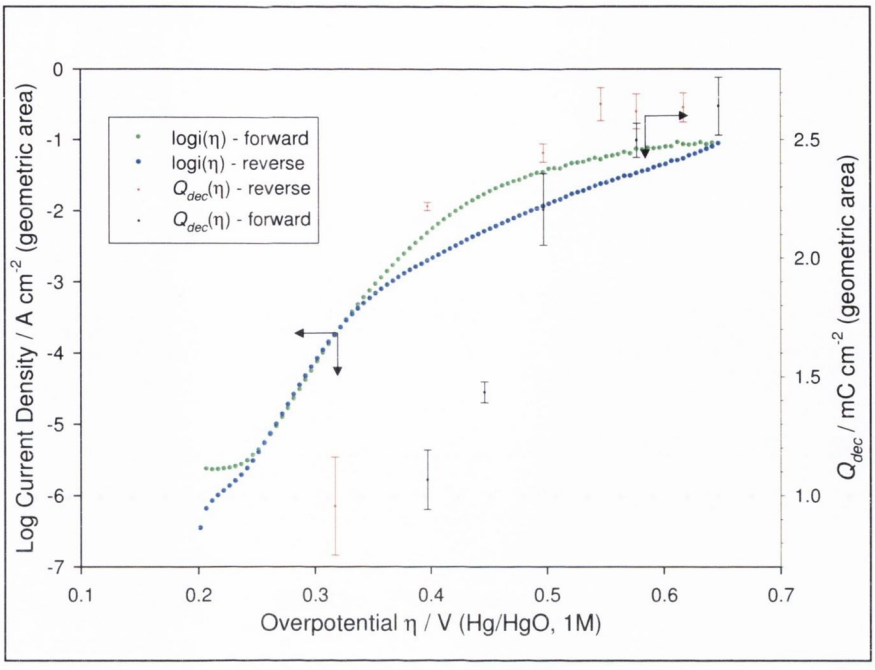


Figure 5.2.3 *Total charge, Q_{dec}, passed during the discharge of a pre-reduced Ni electrode in 1.0 M NaOH at 25°C vs. oxygen evolution overpotential η. Also included are the o.e.r. steady state polarisation curves recorded in both the directions of increasing (forward) and decreasing (reverse) potential for the same system.*

Recall from section 4.4, that EIS measurements were also conducted on this pre-reduced Ni electrode in 1.0 M NaOH solution, at overpotentials associated with significant o.e.r. current densities. CNLS fitting of the raw impedance data to Equivalent Circuit Models 1 and 2 was performed, and the best-fit values for the various circuit elements were listed in Table 4.4.2. A method proposed by Jovic[5] for the determination of an effective value of the double layer capacitance, $C_{dl\ eff}$, from fitted CPE ($C_{\alpha=1}$, α) and R_p parameters, was discussed in section 2.1.7, with a worked example provided in section 4.3. Applying the method of Jovic to the fitting parameters of Table 4.4.2, values of $C_{dl\ eff}$ were calculated for the various values of η at which impedance spectra were recorded. The principles (and indeed shortcomings) of estimating roughness factors from experimental values of the double layer capacitance for a given electrode were discussed in section 2.1.10. To maintain consistency with Ho and Piron[1], it has been decided in the present work to adopt the value of 40 μF cm^{-2} as the 'benchmark' double-layer capacitance for a smooth oxide covered electrode – as mentioned in section 2.1.10 this value was originally due to Frumkin[6]. The values of $C_{dl\ eff}$ for the pre-reduced Ni electrode, calculated from the optimum fit parameters of Table 4.4.2, are listed in Table 5.2.1, along with the

estimated values of the roughness factor which arise from the division of these $C_{dl\ eff}$ values by 40 μF cm^{-2}. For EIS data that was fitted to both Circuits 1 and 2, the value of $C_{dl\ eff}$ was calculated for the model that yielded the highest value of the α parameter, which in each case was Circuit 2.

E V	η V	R_p Ω cm^2	C_{dl} μF cm^{-2}	α	$C_{dl.\ eff}$ μF cm^{-2}	f_r	Circuit Model
0.56	0.257	26.416	467.69	0.860	252.50	6.3	2
0.58	0.277	18.256	414.88	0.867	216.73	5.4	2
0.60	0.297	11.029	387.37	0.860	180.65	4.5	2
0.62	0.317	4.272	377.19	0.864	157.25	3.9	2
0.70	0.397	0.503	267.38	0.845	66.85	1.7	2
0.80	0.497	1.618	204.50	0.854	63.22	1.6	1

Table 5.2.1 *Calculated values for the effective double layer capacitance, $C_{dl.\ eff}$, of a pre-reduced Ni electrode in 1.0 M NaOH at various overpotentials η, based upon the optimised C_{dl}, α and R_p parameters of Table 4.4.2. Also included are the associated estimates of the electrode roughness factor, f_r.*

It is apparent from Table 5.2.1, that the values of $C_{dl\ eff}$ and consequently the estimates of f_r decrease steadily with increasing oxygen evolution overpotential. This phenomenon has already been discussed for Co and Ni electrodes in sections 4.3 and 4.4 respectively, and is believed to be related to a time-averaged blockage of an increasing fraction of the surface area by oxygen bubbles, as the overpotential is raised. In view of this it would seem, that the most appropriate value of $C_{dl\ eff}$ for the estimation of f_r, is that derived from the EIS data recorded at η = 0.257 V i.e. just above the onset potential for significant o.e.r. current densities. This leads to an estimation of a roughness factor of f_r = 6.3 by the double layer capacitance ratio method. Clearly this is in excellent agreement with the roughness factor of f_r = 6.3 ± 0.2, determined by the transient decay method for the same electrode in the same electrolyte solution. Indeed this level of agreement between these two methods of roughness factor estimation is somewhat surprising, considering their relative crudeness as experimental approaches.

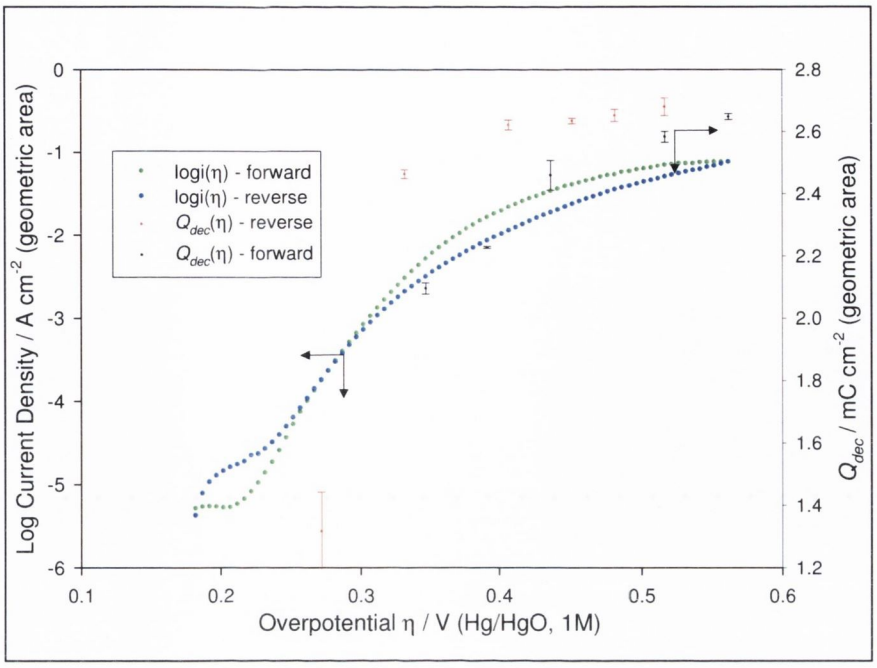


Figure 5.2.4 *Total charge, Q_{dec}, passed during the discharge of a pre-oxidised Ni electrode in 1.0 M NaOH at 25°C vs. oxygen evolution overpotential η. Also included are the o.e.r. steady state polarisation curves recorded in both the directions of increasing (forward) and decreasing (reverse) potential for the same system.*

E V	η V	R_p Ω cm^2	C_{dl} μF cm^{-2}	α	$C_{dl,\,eff}$ μF cm^{-2}	f_r	Circuit Model
0.54	0.237	18.912	444.37	0.802	172.39	4.3	2
0.56	0.257	12.949	433.06	0.815	166.40	4.2	2
0.58	0.277	8.366	438.62	0.827	166.50	4.2	2
0.60	0.297	3.306	391.81	0.852	146.43	3.7	2
0.62	0.317	1.862	346.50	0.874	137.29	3.4	2
0.70	0.397	1.722	325.75	0.860	114.29	2.9	1
0.80	0.497	0.805	214.75	0.863	65.54	1.6	1

Table 5.2.2 *Calculated values for the effective double layer capacitance, $C_{dl,\,eff}$, of a pre-oxidised Ni electrode in 1.0 M NaOH at various overpotentials η, based upon the optimised C_{dl}, α and R_p parameters of Table 4.4.3. Also included are the associated estimates of the electrode roughness factor, f_r.*

Bi-directional o.e.r. steady state polarisation and Q_{dec} vs. η curves for a pre-oxidised Ni electrode (as introduced in section 3.2.2) in 1.0 M NaOH are presented in Figure

5.2.4. This steady state polarisation curve was previously presented in Figure 3.2.16 and was discussed in the adjacent text. Taking the value of Q_{dec} at η = 0.517 V as Q_{dec}(plateau) yields Q_{dec}(plateau) = 2.68 ± 0.03 mC cm^{-2}, which in turn leads to a value of f_r = 6.4 ± 0.1 for the roughness factor as determined by the transient decay method.

Referring to Table 5.2.2, it is apparent that the double layer capacitance ratio method yields significantly lower estimates for the roughness factor. Again, considering the values of $C_{dl\ eff}$ calculated from the CNLS fitting parameters for EIS data recorded at overpotentials corresponding to lower o.e.r. current densities (i.e. $0.237 \leq \eta \leq 0.277$), it can be seen that f_r is estimated to be 4.2 – 4.3. Since the pre-oxidised anode was the same polycrystalline Ni electrode, that had earlier in its service life been used as the pre-reduced Ni electrode with its estimated roughness factor of approximately 6.3 (as determined by both the transient decay and double layer capacitance methods - see above), it is likely that the value of f_r = 6.4 ± 0.1, as yielded by the transient decay method, is the more accurate estimate for the roughness factor of this pre-oxidised electrode. This would imply that the relatively mild pre-reduction and pre-oxidation regimes for the Ni electrode outlined in section 3.2.2, have little effect on the electrode roughness factor.

The lower roughness factor estimate of 4.2 – 4.3 yielded by the double layer capacitance ratio method may arise due to the relatively low values (0.802 – 0.827) of the CPE α parameters for C_{dl} at the lower o.e.r. overpotentials ($0.237 \leq \eta \leq 0.277$) in Table 5.2.2 from which the f_r estimate is derived. As was discussed in chapter 4, the lower the α parameter, the less identifiable the raw impedance data with the classical concept of a capacitance. Contrast the situation that arises for the CNLS fitting of the impedance data for the pre-oxidised Ni electrode to that which prevails for the pre-reduced Ni electrode (Table 5.2.1). In the latter case the α parameter for the EIS data recorded at η = 0.257 has a value of 0.86 implying that the impedance response in this case is more genuinely characteristic of a conventional double layer capacitance as compared to the impedance response for the pre-oxidised Ni electrode at this overpotential (α = 0.815). The roughness factor of 6.3 estimated from the value of $C_{dl\ eff}$ determined by the method of Jovic in the case of the 0.86 α parameter was in excellent agreement with that estimated from the transient decay method (pre-reduced electrode) – by comparison the value of f_r arising from the CNLS fitting parameters

with lower α values (pre-oxidised electrode) did not agree so well with the roughness factor estimated for this electrode by the alternative method.

5.3 Roughness Factors for the Co Electrodes

Typical discharge current decay transients are presented in Figure 5.3.1, for a pre-reduced Co electrode in 1.0 M NaOH solution, following the interruption of the prior anodic charging current densities indicated in the legend. This "type" of Co electrode was introduced and discussed in section 3.3.2.

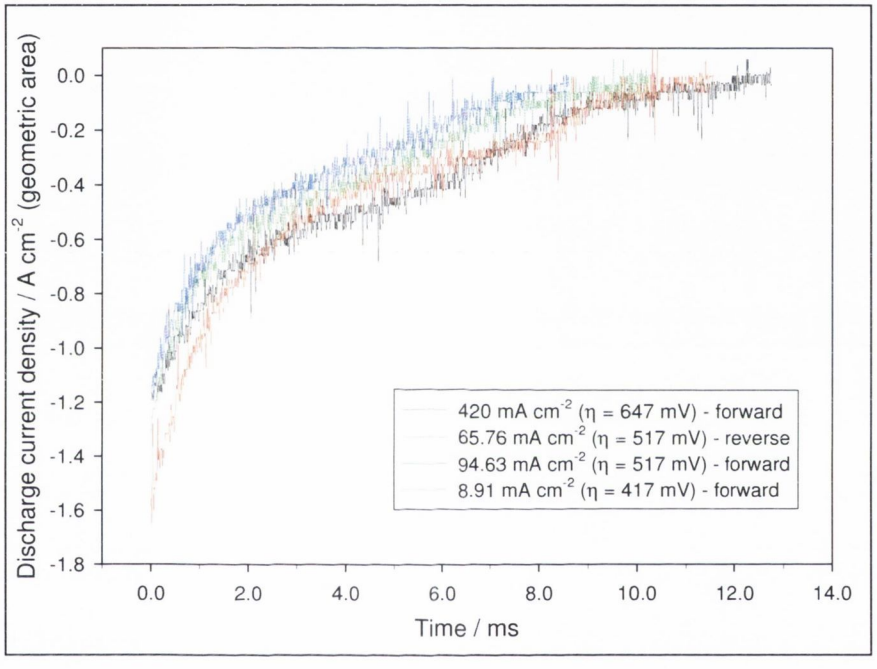


Figure 5.3.1 *Raw current decay transients for a pre-reduced polycrystalline Co electrode in 1.0 M NaOH solution at 25°C. The values of the relevant prior anodic charging current densities are indicated in the legend.*

As discussed previously for the Ni electrodes, it is important that we identify a reaction by which the Co electrode can discharge, which is consistent with the o.e.r. pathway that was postulated for Co in reaction scheme (3.5.68) of section 3.5.3. According to the kinetic mechanistic analysis of this reaction scheme, the only intermediate species that will achieve a significant fractional coverage of the active surface (tending towards unity at very high oxygen evolution overpotentials) is the $[Co(IV)O_m(OH)_{n+1}]^{p-}$ entity produced in step (3.5.68, I) and consumed in the rate determining step (3.5.68, II). The charged Co electrodes used in the transient decay

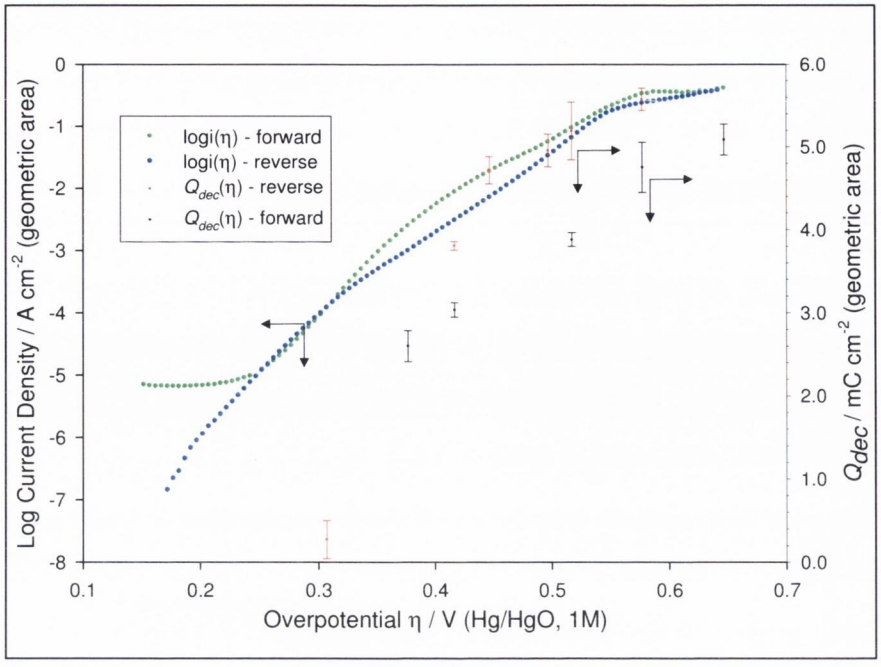


Figure 5.3.2 *Total charge, Q_{dec}, passed during the discharge of a pre-reduced Co electrode in 1.0 M NaOH at 25°C vs. oxygen evolution overpotential η. Also included are the o.e.r. steady state polarisation curves recorded in both the directions of increasing (forward) and decreasing (reverse) potential for the same system.*

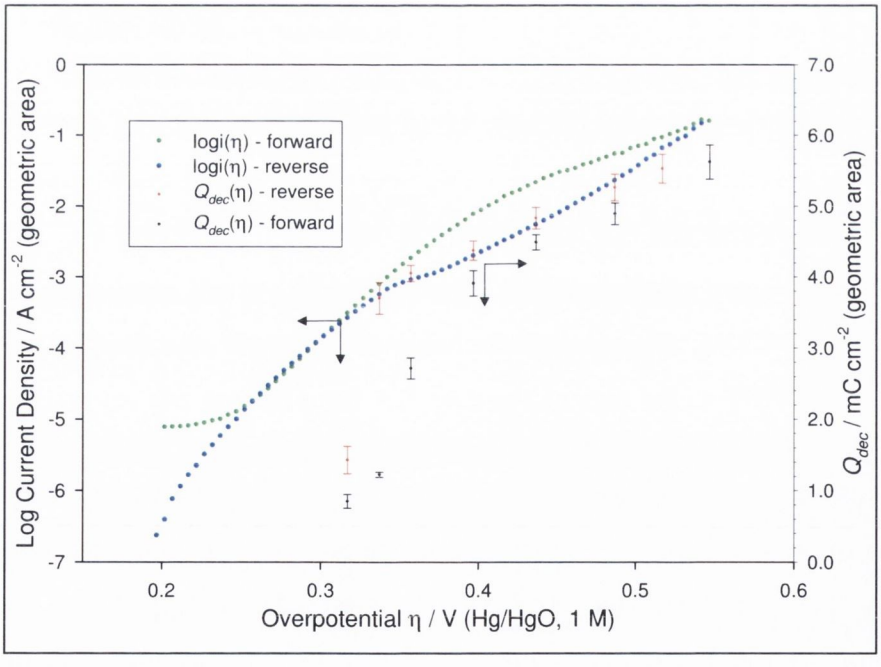


Figure 5.3.3 *Total charge, Q_{dec}, passed during the discharge of a non-pre-treated Co electrode in 1.0 M NaOH at 25°C vs. oxygen evolution overpotential η. Also included are the o.e.r. steady state polarisation curves recorded in both the directions of increasing (forward) and decreasing (reverse) potential for the same system.*

experiments, might then be envisaged to discharge via the following overall reaction, following the termination of the anodic galvanostatic polarisation –

$$[Co(IV)O_m(OH)_{n+1}]^{p-} + H_2O + 2e^- \rightarrow [Co(III)O_{m-1}(OH)_{n+1}]^{p-} + 2OH^- \qquad (5.3.1)$$

Reaction (5.3.1) provides a feasible pathway for the desorption of the o.e.r. intermediate species via a $2e^-$ discharge process, that is also consistent with the mechanism postulated in section 3.5.3 for oxygen evolution at Co electrodes in aqueous alkaline solution. It also implies that equation (3.2.2) can be used for roughness factor estimation for Co electrodes, just as with Ni electrodes.

Note that in reaction (5.3.1), the desorption of the o.e.r. intermediate results in the reduction of the Co ions of the anodic oxide to the +3 cobalt oxidation state. This contrasts with the situation envisaged to occur for the discharge of the Ni electrodes in reaction (5.2.1), where the desorption of the o.e.r. intermediate is postulated to occur with simultaneous reduction of the Ni ions of the oxide surface from the +4 to the +2 oxidation state. As commented previously, this occurs because the reversible potential of the Ni(II)↔Ni(III) redox transition (see section 1.4.1 for more details) is anodic to the oxygen electrode reversible potential (0.303 V vs. Hg/HgO, 1 M OH^-). Referring to the Co cyclic voltammograms of Figures 3.3.8 (c) and 3.3.10, each conducted at a scan rate of 40 mV s^{-1} in 1.0 M NaOH, or indeed to that of Figure 1.4.12 recorded at 300 mV dec^{-1} in 1.0 M KOH, it is obvious that the voltammetric features generally attributed (see the literature review of section 1.4.3) to the oxidation of Co^{2+} to Co^{3+} species have their onset potentials in the range of 0 – 0.1 V (vs. Hg/HgO, 1 M OH^-) – i.e. significantly cathodic to the oxygen electrode reversible potential. This observation suggests that discharge of the surface Co ions of the anodic oxide film should continue to the Co(III) oxidation state , following the interruption of a steady state polarising current corresponding to a significant rate of the oxygen evolution reaction. This viewpoint is also supported by thermodynamic data[7] which indicates that the oxidation of Co(II) species should begin in the region of –0.4 V (vs. Hg/HgO, 1 M KOH), with Co_3O_4 being the initial oxidation product. It should also be commented that hydroxylation of the oxide surface to form negatively charged complex surface species is less likely at the potential of the discharged electrode, than in the range of potentials associated with significant rates of oxygen evolution. In this case, the charge p on the species formed on the right hand side of equation (5.3.1)

would be equal to zero. In section 3.5.3, p for the complex Co anionic surface species was defined as p=2m+n-4. Setting p = 0 and m = 2 implies that n = 0, and in this case $[Co(III)O_{m-1}(OH)_{n+1}]^{p-}$ reduces to CoOOH which is often proposed to one of the most likely forms for the Co(III) species of the passive film formed on Co in alkaline solution – recall section 1.4.3.

Bi-directional o.e.r. steady state polarisation and Q_{dec} vs. η curves for the pre-reduced Co electrode in 1.0 M NaOH are presented in Figure 5.3.2, while Figure 5.3.3 contains similar plots for a bright, non-pre-treated Co electrode in the same electrolyte. These Q_{dec} vs. η curves display the same general trends as the corresponding plots for Ni electrodes, with larger values of Q_{dec}, for a given overpotential, being noted in the direction of decreasing i_{appl} relative to that of increasing i_{appl}. An explanation for this was discussed earlier in this section in relation to the experimental $Q_{dec}(\eta)$ and $\log i(\eta)$ data for the Ni electrodes, and the same principles are also applicable to the corresponding Co electrode data.

The presence of a 'plateau' region in the reverse direction Q_{dec} vs. η curves is not as obvious for the Co data of Figures 5.3.2 and 5.3.3, as was the case for the Ni data of Figures 5.2.2 – 5.2.4. This may be related to the presence of the unexplained peak or "hump" feature that arises at higher oxygen evolution overpotentials in Co steady state polarisation curves – recall section 3.3.2. Such a feature is apparent at higher values of η, in both directions, for the polarisation curve of Figure 5.3.2. That said, within the limits of experimental error, $Q_{dec}(\eta)$ in the reverse direction seems to be "levelling out" at overpotentials above 0.447 V – it has therefore been decided to use, as Q_{dec}(plateau), the mean of the Q_{dec} values recorded at the two uppermost potentials of measurement (η = 0.517 V and 0.577 V) in this direction. Adopting this approach yields Q_{dec}(plateau) = 5.4 ± 0.3 mC cm^{-2}, which in turn leads to an estimated roughness factor of f_r = 12.9 ± 0.7 for the pre-reduced Co electrode.

In the case of the bright non-pre-treated Co electrode of Figure 5.3.3, the steady state polarisation measurements (which are of course the source of the i_{appl} polarisation current density values for the transient decay experiments) were not continued as far as the overpotentials associated with the "hump" region, being terminated at η = 0.547 V, which is just below the onset potential of the "hump". In the lack of a clearly discernable "plateau" region in the Q_{dec} vs. η plot of Figure 5.3.3, it has been elected to use the value of Q_{dec} at η = 0.517 V in the reverse direction for the determination of f_r using equation (5.2.2). Although this may lead to an underestimation of f_r, we

speculated that the Q_{dec} vs. η plot for the pre-reduced Co electrode was "levelling off" at this overpotential, and considering the similarity in the shapes of the steady state polarisation curves for these two Co electrodes, it is probably a fair assumption that there would not be a dramatic increase in Q_{dec} at overpotentials anodic to η = 0.517 V for the non-pre-treated electrode. Following the aforementioned course of action leads to the determination of a roughness factor of 13.1 ± 0.5 for the non-pre-treated Co electrode, based on the use of $Q_{dec}(\eta = 0.517\ V) = 5.5 \pm 0.2$ mC cm^{-2} as the Q_{dec}(plateau) value in equation (5.2.2). It should be remarked that although similar roughness factors have been estimated by the transient decay technique for the pre-reduced and non-pre-treated Co electrodes, these were two distinct Co electrodes, unlike the case discussed for the pre-reduced and pre-oxidised Ni electrodes in section 5.2, where it was found that different (mild) pre-treatment of the same Ni electrode had little effect on the value of f_r.

Recall from section 4.3, that EIS measurements were performed on the pre-reduced Co electrode in 1.0 M NaOH, at overpotentials associated with significant rates of oxygen evolution – see Figures 4.3.1 and 4.3.2. It should therefore be possible to make an estimate of the electrode roughness factor using the double layer capacitance ratio method. The aforementioned EIS data was fitted to Circuit 2 and the optimum values of the various equivalent circuit models were listed in Table 4.3.1. Taking from this table, the values of $C_{\alpha=1}$ and α for the CPE representative of the double layer capacitance and the associated value of R_p for each overpotential, values of $C_{dl\ eff}$ have been calculated and are listed in Table 5.3.1.

E V	η V	R_p Ω cm^2	C_{dl} μF cm^{-2}	α	$C_{dl,\ eff}$ μF cm^{-2}	f_r	Circuit Model
0.55	0.247	3.955	749.94	0.825	270.51	6.8	2
0.58	0.277	3.735	746.50	0.825	266.73	6.7	2
0.6	0.297	4.411	729.89	0.807	241.55	6.0	2
0.61	0.307	3.911	695.83	0.820	240.67	6.0	2
0.64	0.337	4.012	699.65	0.819	241.04	6.0	2
0.74	0.437	1.701	596.51	0.851	213.55	5.3	2

Table 5.3.1 *Calculated values for the effective double layer capacitance, $C_{dl,\ eff}$, of a pre-reduced Co electrode in 1.0 M NaOH at various overpotentials η, based upon the optimised C_{dl}, α and R_p parameters of Table 4.3.1. Also included are the associated estimates of the electrode roughness factor, f_r.*

As was discussed for the values of $C_{dl\ eff}(\eta)$ for the Ni electrodes in section 5.2, the most appropriate of these data for the estimation of the electrode roughness factor is that calculated for the overpotential associated with the onset of a significant oxygen evolution rate. In view of this the most suitable value of $C_{dl\ eff}$, is that pertaining to the overpotential of 0.247 V – i.e. $C_{dl\ eff} = 270.51\ \mu F\ cm^{-2}$. Using as before, 40 $\mu F\ cm^{-2}$ as the reference value of the double-layer capacitance for a smooth oxide covered electrode, an electrode roughness factor of $f_r = 6.8$ is calculated for the pre-reduced Co electrode – see Table 5.3.1. This value of f_r is of course significantly smaller than that estimated for the same electrode by the transient decay method – i.e. $f_r = 12.9 \pm 0.7$. As discussed for the pre-oxidised Ni electrode in section 5.2, the smaller f_r estimate yielded by the double layer capacitance ratio method based upon the calculated value of $C_{dl\ eff}$ (relative to the transient decay method), may be related to the relatively low value of the CPE α parameter ($\alpha = 0.825$ in the present case). In view of this, the higher roughness factor as determined by the overpotential deposited O desorption method, might be considered to be a more satisfactory estimate of the true roughness factor.

5.4 Roughness Factors for the Fe Electrodes

Examples are presented in Figure 5.4.1, of discharge current decay transients, for a pre-reduced fresh Fe electrode in 1.0 M NaOH, following the interruption of prior anodic charging currents. While it was postulated that the current decay transients for the desorption of the active o.e.r. intermediate species from Ni and Co electrodes, were characteristic of a two electron discharge, the situation is likely to be somewhat different for Fe anodes. Referring to the cyclic voltammograms recorded for polycrystalline Fe electrodes in 1.0 M NaOH solution as part of the present work (e.g. Figures 3.4.2 and 3.4.10) or indeed those due to other workers (see Figure 1.4.8), it is obvious that the peaks associated with the Fe(II)↔Fe(III) transition occur at potentials significantly cathodic to the oxygen electrode reversible potential of 0.303 V (vs. Hg/HgO, 1 M OH^-). Burke and Lyons[8] showed that the peak potential for the A3 anodic feature (see Figure 1.4.8 (a)), which they associated with the oxidation of the Fe ions of the outer region of the passive film from the +2 to +3 oxidation state, increased steadily from ~ -0.6 to ~ -0.4 V (converted here to the Hg/HgO, 1M OH^- scale from the R.H.E. scale of the original publication) over a range of voltammetric

scan rates from 1 mV s^{-1} to 400 mV s^{-1}. The foregoing observations indicate strongly that desorption of the o.e.r. intermediate species from an iron electrode in 1.0 M NaOH solution (upon the interruption of a galvanostatic polarising current density associated with the o.e.r. proceeding at a significant rate in the steady state), will involve the discharge of the active oxide surface Fe sites to the +3 oxidation state, from a higher valance state. Recall from section 3.5.3, that we have postulated that this higher state is the Fe(VI) state which is stabilised at the oxide surface (at high anodic potentials in concentrated alkaline solution) by existing in the form of an anionic hydroxylated surface complex represented as $[Fe(VI)O_m(OH)_n]^{p-}$, where p=2m+n-6.

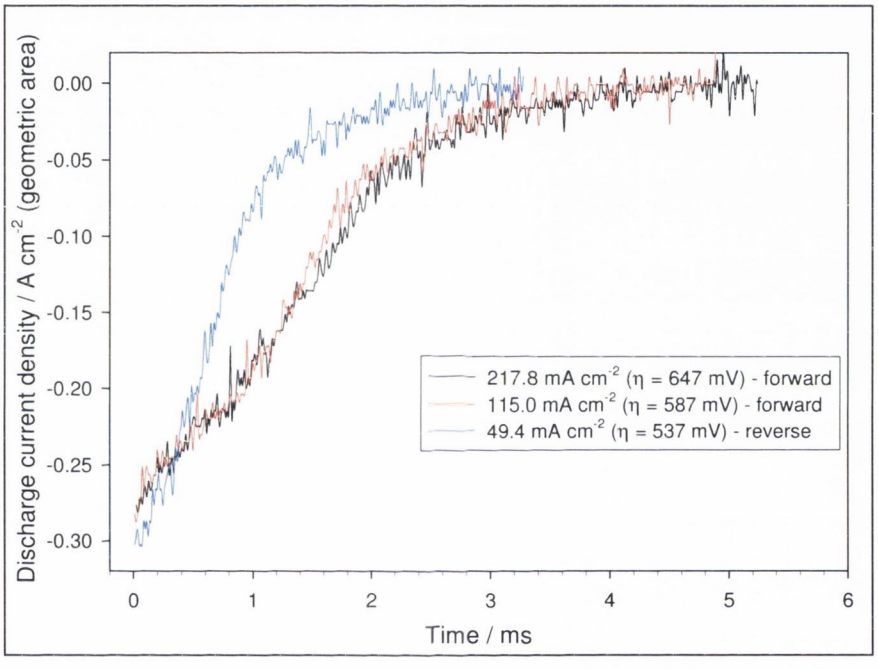


Figure 5.4.1 *Raw current decay transients for a pre-reduced fresh polycrystalline Fe electrode in 1.0 M NaOH solution at 25°C. The values of the relevant prior anodic charging current densities are indicated in the legend.*

According to the pathway proposed for the o.e.r. at the iron oxide surface in scheme (3.5.68), the only intermediate species that will achieve a significant fractional coverage of the active surface is the $[Fe(VI)O_m(OH)_{n+1}]^{p-}$ entity formed in step (3.5.68, I) and consumed in the rate-limiting step (3.5.68, II). Following the termination of the galvanostatic polarisation, the desorption of this intermediate might be envisaged to occur via the following overall reaction:

$$[Fe(VI)O_m(OH)_{n+1}]^{p-} + H_2O + 4e^- \rightarrow [Fe(III)O_{m-1}(OH)_{n-1}]^{p-} + 4OH^- \qquad (5.4.1)$$

Equation (5.4.1) predicts that the discharge current transients, recorded for the desorption of the o.e.r. intermediate species from an anodic oxide covered Fe electrode in aqueous alkaline solution, are due to a four electron discharge process. This implies that the "benchmark" value of 420 μC cm^{-2} used in equation (5.2.2) for the estimation of roughness factors for Ni and Co electrodes must be doubled for the case of Fe electrodes. A further noteworthy point is that the discharged Fe(III) surface ion which exists at a lower potential than the o.e.r. intermediate, is less likely to coordinate OH^- ions from solution and form an anionic complex relative to an Fe(VI) entity at a higher anodic potential. A similar comment was passed on the discharged Co(III) species formed in reaction (5.3.1). In the case of the product of reaction (5.4.1), setting p = 0 and m = 2, implies that n = 2, thereby identifying this product as FeOOH which is commonly proposed to be Fe(III) oxide species of the passive film formed on iron electrodes in aqueous alkaline solution – see the literature review of section 1.4.2.

Bi-directional o.e.r. steady state polarisation and Q_{dec} vs. η plots for a fresh, bright, non-pre-treated Fe electrode in 1.0 M NaOH are presented in Figure 5.4.2. It is apparent that the degree of hysterisis between the $Q_{dec}(\eta)$ data in the directions of increasing and decreasing i_{appl} is much smaller for this Fe electrode than was the case for the Ni and Co electrodes of sections 5.2 and 5.3 respectively. This observation accompanies the fact that there is little or no hysterisis in the steady state polarisation curves at $\eta \geq$ ~0.55 V, indicating the correctness of our discussion in section 5.2 regarding the origin of the $Q_{dec}(\eta)$ hysterisis for Ni (and by extension Co) electrodes. The $Q_{dec}(\eta)$ data does not present a higher overpotential "plateau" region as obvious as that observed for Ni electrodes – it is nonetheless apparent that there is a "levelling off" in the Q_{dec} vs. η plots at the highest investigated overpotentials (i.e. η = 0.642 and 0.682 V). On this basis it has been elected to use the value of $Q_{dec}(\eta = 0.682\ V) = 440 \pm 20$ μC cm^{-2} as the Q_{dec}(plateau) value in equation (5.4.2), which is a modification of equation (5.2.2) to account for the 4 electron decay involved in the desorption of the o.e.r. intermediate species from anodic oxide covered Fe electrodes:

$$f_r = \frac{Q_{dec}(plateau)}{840\mu C\,cm^{-2}} \qquad (5.4.2)$$

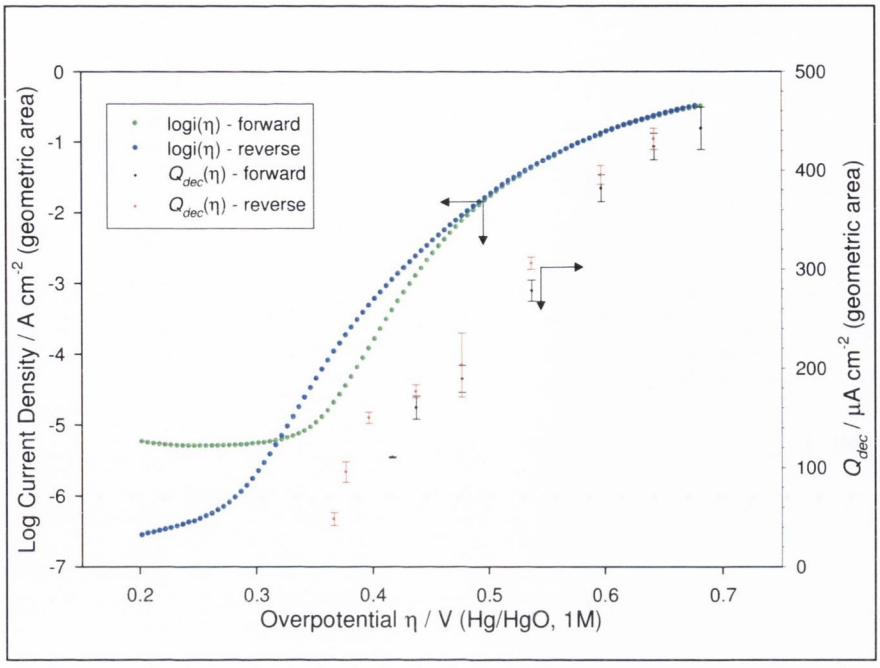


Figure 5.4.2 *Total charge, Q_{dec}, passed during the discharge of a fresh non-pre-treated Fe electrode in 1.0 M NaOH at 25°C vs. oxygen evolution overpotential η. Also included are the o.e.r. steady state polarisation curves recorded in both the directions of increasing (forward) and decreasing (reverse) potential for the same system.*

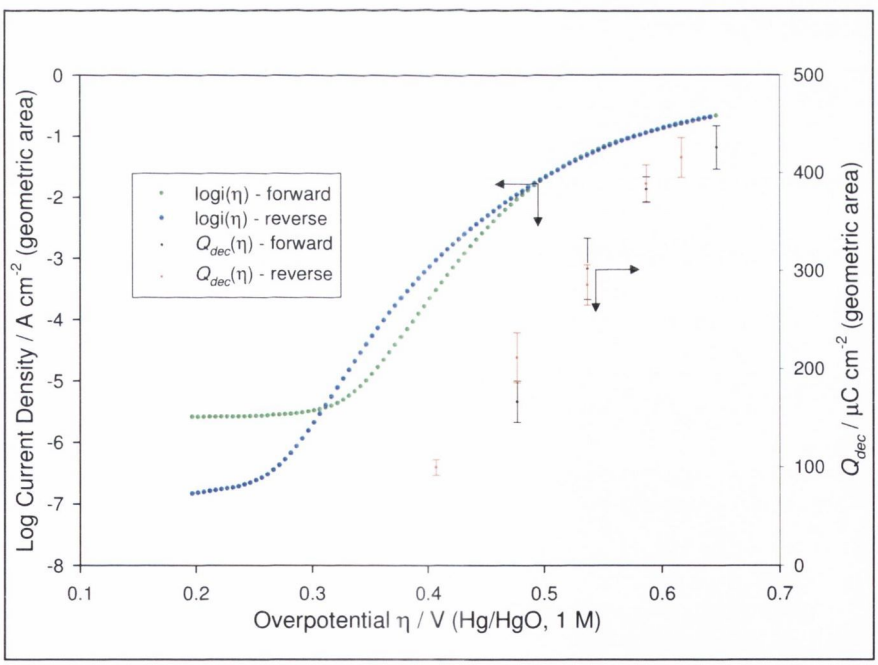


Figure 5.4.3 *Total charge, Q_{dec}, passed during the discharge of a fresh pre-reduced Fe electrode in 1.0 M NaOH at 25°C vs. oxygen evolution overpotential η. Also included are the o.e.r. steady state polarisation curves recorded in both the directions of increasing (forward) and decreasing (reverse) potential for the same system.*

Inserting the aforementioned value of Q_{dec}(plateau) into equation (5.4.2), yields a value for f_r of 0.52 ± 0.02.

It is obvious that the steady state polarisation and Q_{dec} vs. η plots of Figure 5.4.3 for a fresh pre-reduced Fe electrode in 1.0 M NaOH, are similar in form to those of Figure 5.4.2 for the non-pre-treated Fe anode. This pre-reduced Fe electrode was characterised voltammetrically by a profile similar to that of the "Less Aged" trace of Figure 3.4.11, while the steady state polarisation curve has previously been presented as the "Fresh" data of Figure 3.4.8. It was for this electrode that the raw decay current transients of Figure 3.4.1 were recorded. Using the value of $Q_{dec}(\eta = 0.647\ V) = 430 \pm 20\ \mu C\ cm^{-2}$ as the Q_{dec}(plateau) value in equation (5.4.2), yields a value for the roughness factor of $f_r = 0.51 \pm 0.02$, which is very similar to that estimated above for the fresh non –pre-treated Fe electrode.

These sub-unity roughness factors imply of course, that only a fraction of the geometric surface area (and thus an even smaller fraction of the real oxide surface area, since this is likely to be, at least, somewhat greater than the geometric area) is catalytically active towards the o.e.r for these anodic oxide covered Fe electrodes in 1.0 M NaOH. This conclusion is not altogether surprising, given the model that we have proposed in section 3.5.3 for the catalytically active sites on the surface of the passive iron oxyhydroxide film. As mentioned at the start of the present section in connection with equation (5.4.1), we have proposed that the somewhat acidic nature of the iron oxide film in solutions of high pH, allows for the stabilisation of Fe(VI) metal centres as part of anionic surface complex species (represented as $[Fe(VI)O_m(OH)_n]^{p-}$) at high anodic potentials. However since it is known[9-11] that soluble Fe(VI) ions (probably in the form of FeO_4^{2-}) are formed at Fe electrode surfaces in aqueous alkaline solution at high anodic potentials, it is likely that only a fraction of the surface Fe(VI) species will be stabilised by coordinating extra OH^- ions, and thus only this fraction of surface sites are available for the catalysis of oxygen evolution, leading to the observed fractional values of f_r.

Compare this to the situation that prevails at the oxide surface on Co electrodes, for which we have proposed the same o.e.r. pathway (scheme 3.5.68) as that operative at the passive oxide surface on Fe. There is widespread acceptance (see the literature review of section 1.4.3) that the anodic voltammetric peak at potentials from ca. 0.4 V (vs. Hg/HgO) upwards (see Figure 3.3.26) from which the rising edge of the o.e.r. current develops at yet higher potentials, is due to the formation of Co^{4+} ions in the

surface region of the oxide film. We have chosen, in the present work, to represent these species in form of hydroxylated anionic surface complexes, $[Co(IV)O_m(OH)_n]^{p-}$, the central Co^{4+} ion of which, we envisage to be the active centre for oxygen evolution. The fact that the formation of these species gives rise to a voltammetric peak at potentials below the rising edge of the oxygen evolution current, indicates that it is appropriate to think in terms of a relatively stable surface phase of Co(IV) species, that can achieve a significant fractional coverage of the electrode *real* surface area. This can lead to roughness factors well in excess of unity, for the catalytically active area relative to the geometric area, as is apparently the case for the Co anodes utilised in the present work – see section 5.3. On the other-hand an anodic voltammetric peak is generally not observed for the formation of the $[Fe(VI)O_m(OH)_n]^{p-}$ species (although see section 3.4.2 , Figures 3.4.22 – 3.4.23 and the related discussion), implying that these species are rather unstable surface entities and that it is inappropriate to think in terms of the existence of a complete surface layer of an Fe(VI) based oxide.

The experimental observation, that only a fraction of the electrode surface area is active, with respect to the electrosorption of the o.e.r. intermediate species, is reminiscent of the situation known to prevail for the h.e.r. at Pt[12, 13] and Ni[14] electrode surfaces. For these systems, it was deduced that the adsorption of overpotential deposited H atoms occurred only on some active fraction of the total number of metallic surface atoms. It should be noted however, that this does not render inapplicable the postulation of high coverages of intermediate species ($\theta \rightarrow 1$) in kinetic mechanistic analyses, i.e. limitingly low or high (Langmuir isotherm) or indeed intermediate (Temkin isotherm) fractional coverages with respect to the total available number of *active* sites, can still be envisaged[14].

Recall from section 3.4.2 the extremely aged, pre-reduced "type" of Fe electrode as characterised by the cyclic voltammogram of Figure 3.4.17. In explaining the different values of Tafel slope and OH^- reaction order observed for this electrode, relative to fresh non-pre-treated and fresher pre-reduced Fe anodes, it was speculated in section 3.5.3, that the oxide surface at the extremely aged electrode was rougher than that at the other Fe electrodes, and that this facilitated the existence of a relatively larger concentration of the $[Fe(VI)O_m(OH)_n]^{p-}$ species. This is turn was proposed as the reason for the applicability of the Temkin adsorption isotherm to the extremely aged electrode, over a range of overpotentials, at which intermediate

adsorption at the fresher electrodes was envisaged to follow the low coverage Langmuir adsorption isotherm. If this scenario is indeed accurate, then it would be expected that the extremely aged Fe electrode should have a larger associated roughness factor, as estimated by the current decay transient method. To this end the latter method was applied to the extremely aged pre-reduced Fe electrode and the relevant bi-directional steady state polarisation and Q_{dec} vs. η plots are presented in Figure 5.4.4.

Rather unusually, there is significant hysterisis in the Q_{dec} vs. η plot despite the fact that there is little hysterisis in the steady state polarisation plot. Within the range of

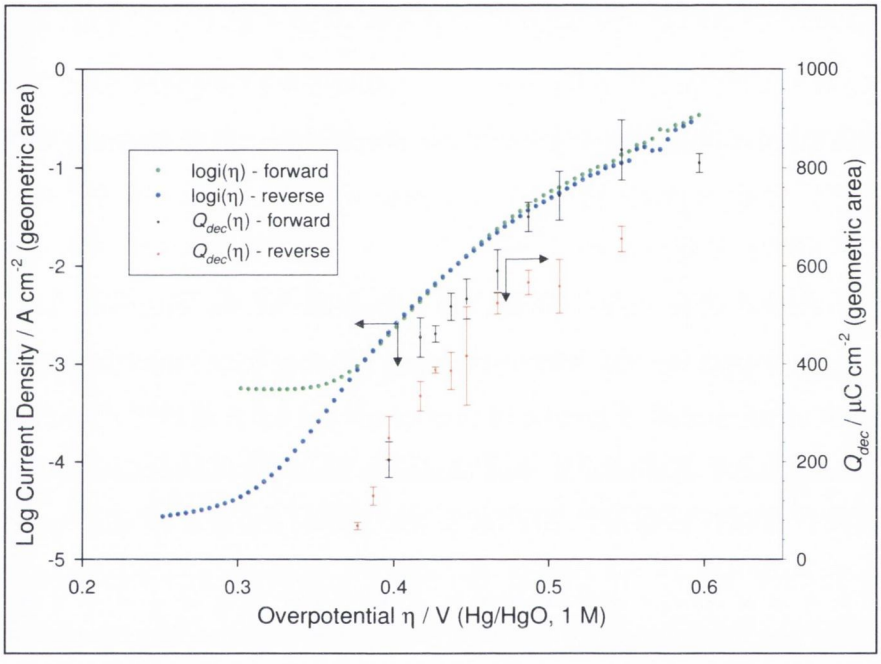


Figure 5.4.4 *Total charge, Q_{dec}, passed during the discharge of an extremely aged pre-reduced Fe electrode in 1.0 M NaOH at 25°C vs. oxygen evolution overpotential η. Also included are the o.e.r. steady state polarisation curves recorded in both the directions of increasing (forward) and decreasing (reverse) potential for the same system.*

the depicted error bars, a "plateau" region is suggested in the Q_{dec} vs. η plot for the direction of increasing i_{appl} at the two highest values of η investigated. Taking the mean of these two values of $Q_{dec}(\eta)$ yields Q_{dec}(plateau) = 820 ± 70 μC cm^{-2}, which leads to a roughness factor of f_r = 0.98 ± 0.8, when inserted in equation (5.4.2). This value of f_r is therefore, as expected, significantly greater (approximately twice as

large) than those estimated for the fresh non-pre-treated and pre-reduced fresh Fe electrodes.

Owing to our speculation above, that the fractional coverage of the catalytically active Fe(VI) entity, with respect to the truly available (that area wettable by the electrolyte solution perhaps?) surface area, is likely to be significantly less than unity, strong agreement is not expected between the values of f_r estimated by the transient current decay, and double layer capacitance ratio methods. In any case, it is worth recalling from chapter 4, that the impedance response of the double layer capacitance for the Fe electrodes, does not conform to the readily explainable trends observed for the Ni and Co electrodes – i.e. it doesn't display the steady decrease in double layer capacitance

(a)

E V	η V	R_p Ω cm^2	C_{dl} μF cm^{-2}	α	$C_{dl,\,eff}$ μF cm^{-2}	f_r	Circuit Model
0.65	0.347	208.620	42.544	0.871	23.12	0.58	3
0.665	0.362	238.320	53.667	0.860	29.30	0.73	3
0.68	0.377	182.340	64.056	0.850	32.90	0.82	3
0.71	0.407	59.130	86.556	0.847	38.64	0.97	3
0.78	0.477	5.598	142.28	0.884	62.31	1.56	3
0.84	0.537	2.158	165.28	0.845	48.29	1.21	4

(b)

E V	η V	R_p Ω cm^2	C_{dl} μF cm^{-2}	α	$C_{dl,\,eff}$ μF cm^{-2}	f_r	Circuit Model
0.72	0.417	4.255	309.11	0.742	55.82	1.40	3
0.8	0.497	1.489	387.04	0.777	73.36	1.83	4
0.84	0.537	0.713	365.25	0.810	76.13	1.90	4

(c)

E V	η V	R_p Ω cm^2	C_{dl} μF cm^{-2}	α	$C_{dl,\,eff}$ μF cm^{-2}	f_r	Circuit Model
0.68	0.377	110.250	59.28	0.779	19.57	0.49	3
0.7	0.397	52.254	85.44	0.808	30.17	0.75	3
0.72	0.417	17.464	104.1	0.837	37.16	0.93	3
0.78	0.477	5.396	245.33	0.859	96.39	2.41	4
0.84	0.537	1.202	284.72	0.900	128.60	3.22	4

Table 5.4.1 *Calculated values for the effective double layer capacitance, $C_{dl,\,eff}$, of (a) a relatively fresh pre-reduced Fe electrode, (b) an extremely aged pre-reduced Fe electrode and (c) a fresh non-pre-treated Fe electrode, all in 1.0 M NaOH at various overpotentials η, based upon optimised C_{dl}, α and R_p parameters obtained by the CNLS fitting of EIS data – see section 4.2.1. Also included are the associated estimates of the electrode roughness factor, f_r. Note that $C_{dl,\,eff}$ is calculated only for three overpotentials in the case of the extremely aged electrode – this arises since the values of α obtained at other overpotentials were so small as the render the concept of a capacitance meaningless in these cases – see Table 4.2.3.*

with increasing η, attributed to the time-averaged blockage of a fraction of the electrode surface by oxygen bubbles, an effect that becomes more significant with increasing oxygen evolution current densities. Notwithstanding these reservations and for the sake of completeness, the values of $C_{dl\ eff}$ and the associated roughness factors as calculated based on the CNLS fitting parameters of Tables 4.2.1 – 4.2.2 (relatively fresh pre-reduced Fe electrode), Table 4.2.3 (extremely aged pre-reduced Fe electrode) and Table 4.2.4 (fresh non-pre-treated Fe electrode), are listed in Table 5.4.1.

It is clear that the general trend displayed in Table 5.4.1 is that of an increase in $C_{dl\ eff}$ with increasing η – i.e. the directly opposite trend to that observed for Ni and Co electrodes. Of potential importance in explaining this phenomenon, is the fact, as is evident from a perusal of Tables 4.2.1 – 4.2.4 (section 4.2), that the resistance, R_{film}, of the anodic passive film on each of the three "types" of Fe electrode examined, decreases with increasing overpotential. The apparent increase in electrode surface area in conjunction with the decrease in R_{film} as the oxygen evolution overpotential is raised, points to a possible "opening" of the outer hydrous region of the passive film. Significantly Burke and Lyons[8] noted that cyclic voltammogram recorded in 1.0 M NaOH (between the onset potentials of significant H_2 and O_2 evolution currents) following prolonged anodisation in the same solution, at oxygen evolution overpotentials, of an iron electrode initially covered by a thick hydrous oxide layer (formed by the repetitive cycling technique), was similar to that of a freshly polished Fe electrode rather than a multi-cycled electrode. These authors concluded that the lengthy anodic treatment of the electrode had the effect of damaging and eventually removing the pre-grown passive oxide layer, probably due to soluble ferrate formation.

In the light of the observations of Burke and Lyons, it might be suggested that the apparent increase in f_r and accompanying decrease in R_{film} with increasing η, could be related to the degradation of the anodic oxide film, as its constituent Fe ions are lost to the electrolyte solution by the formation of soluble ferrates. Of course the resulting increase in the double layer capacitance with increasing overpotential, as measured by EIS, should be somewhat offset by the oxygen bubble effect (which as mentioned above prevails at Ni and Co electrode surfaces) which becomes more significant with increasing o.e.r. current density (and hence with increasing η). The logical conclusion from this discussion is that, the variation in the magnitude of $C_{dl\ eff}$ with η for Fe

electrodes is due to a number of factors. In view of this, it is difficult to identify a value of η for which the associated $C_{dl\ eff}$ value could be confidently considered to have a meaningful relation to the true surface area, as was the case for $C_{dl\ eff}$ associated with overpotentials at the onset of significant o.e.r. current densities in the case of the Ni and Co electrodes. Perhaps the most significant point that can be taken from the values of f_r listed in Table 5.4.1, is that these roughness factors estimated by the double layer capacitance ratio method are smaller than those derived by the same approach for the Ni and Co electrodes. This is also the case for the values of f_r estimated by the desorption current transient method for the Fe electrodes relative to the Ni and Co electrodes. Therefore it can be concluded with some degree of confidence that a lower active area to geometric area ratio is one of the factors behind the apparently inferior o.e.r. catalytic performance of the Fe anodic oxide relative to the oxide films on Co and Ni electrodes. This latter point will be discussed further in the next section.

5.5 Comparison of Active Surface Area Normalised O.E.R. Catalytic Activities

The roughness factors, estimated by the discharge current transient method, for the various electrodes subjected to charge/discharge experiments, are summarised in Table 5.5.1.

Electrode	f_r
Ni non-pre-treated	7.3 ± 0.1
Ni pre-reduced †	6.3 ± 0.2
Ni pre-oxidised †	6.4 ± 0.1
Co non-pre-treated	13.1 ± 0.5
Co pre-reduced	12.9 ± 0.7
Fe non-pre-treated	0.52 ± 0.02
Fe pre-reduced (fresh)	0.51 ± 0.02
Fe pre-reduced (v. aged)	0.98 ± 0.08

Table 5.5.1 *Summary of the roughness factors, f_r, determined for various Ni, Co and Fe electrodes in 1.0 M NaOH solution, using the discharge current transient technique. † indicates the same electrode subjected to different pre-treatment regimes. Error estimates are experimental errors – true errors are likely to be larger, owing to the questionable value of the reference charge associated with the desorption of a monolayer of reaction intermediate species.*

The steady state polarisation curves, recorded in the direction of increasing potential, and presented in Figures 5.2.2 – 5.2.4 for non-pre-treated, pre-reduced and pre-

oxidised Ni electrodes respectively, are re-plotted in Figure 5.5.1 with the log current density values normalised according to the roughness factors of Table 5.5.1. At this point the reader might like to reacquaint him/herself with the exact details of the pre-treatment regimes, which were discussed in detail in section 3.2.2. The o.e.r. catalytic activities, based on *geometric surface areas*, of a non-pre-treated Ni electrode, a pre-reduced Ni electrode and a pre-oxidised Ni electrode were compared (in 1.0 M NaOH solution) in Figure 3.2.19. Figure 5.5.1 is effectively a re-evaluation of this comparison, based, in this case, on the current density values calculated in terms of the estimated, real, catalytically active surface areas. It should be mentioned that no charge/discharge experiments were conducted on the non-pre-treated electrode for which the steady state polarisation curve of Figure 3.2.19 was recorded - therefore the normalised "non-pre-treated" plot of Figure 5.5.1 was obtained for a different freshly prepared Ni electrode.

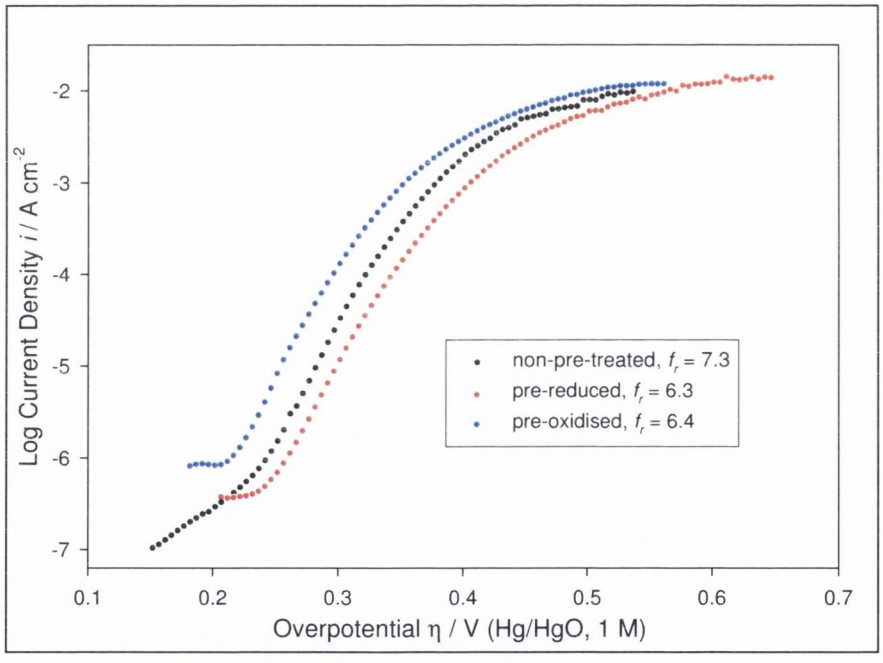


Figure 5.5.1 *IR corrected steady state polarisation curves recorded in 1.0 M NaOH solution at 25°C, for Ni electrodes, subjected to different pre-treatment regimes. The values of log i(η) are normalised to the estimated truly active surface areas, based on the stated roughness factors.*

Since very similar roughness factors were estimated in section 5.2 for the pre-reduced and pre-oxidised Ni electrodes, the catalytic superiority of the latter towards the o.e.r that was evident in Figure 3.2.19 is also obvious in Figure 5.5.1. The o.e.r. steady state current density for the pre-oxidised Ni electrode at the arbitrary overpotential of

0.302 V is i = 1.34 (± 0.02) × 10^{-4} A cm^{-2}. This is over ten times greater than that (i = 1.21 (± 0.04) × 10^{-5} A cm^{-2}) observed at the same overpotential for the pre-reduced Ni electrode. An intermediate value of i = 3.34 (± 0.05) × 10^{-5} A cm^{-2} is observed for the non-pre-treated Ni electrode of Figure 5.5.1, at η = 0.302 V.

The pre-reduced and pre-oxidised Ni electrodes were characterised by cyclic voltammetry in Figure 3.2.11. A much larger value of the active charge capacity, Q, associated with the Ni(II)↔Ni(III) transition was noted for the pre-oxidised electrode (Q = ~ 4.99 mC cm^{-2}) compared with the pre-reduced electrode (Q = ~ 1.57 mC cm^{-2}). On this basis it was speculated in section 3.2.2 (see text immediately subsequent to Figure 3.2.19), after the ideas of Gennero De Chialvo et al.[15], that the superior catalytic activity of the pre-oxidised electrode, was principally due to its possessing a larger real surface area relative to the pre-reduced electrode. However this view is contradicted by the experimental results of section 5.2, in which the estimated values of f_r were found to be very similar for the pre-reduced and pre-oxidised Ni electrode – see Table 5.5.1.

The Q_{dec} vs. η plots of Figures 5.2.3 (pre-reduced) and 5.2.4 (pre-oxidised) point to similar values of Q_{dec}(plateau), which in turn leads to similar estimates for f_r. The key difference is that the onset potential for the $Q_{dec}(\eta)$ "plateau" occurs in the region of η ≈ 0.4 V for the pre-oxidised electrode, as compared to η ≈ 0.55 V for the pre-reduced electrode. This suggests that while the surface area available for the o.e.r. is similar for both electrodes, the pre-oxidation regime produces an oxide surface with a higher concentration of the most catalytically active form of the nickel oxyhydroxide (β-NiOOH if the concepts of Lu and Srinivasan[16] are adopted) towards oxygen evolution. Therefore at lower values of η, discharge of OH^- ions from solution to form the o.e.r. intermediate species (envisaged to be $[Ni(IV)O_m(OH)_{n+1}]^{p-}$ according to step (3.5.3, I) of the reaction pathway that we have proposed for oxygen evolution at Ni anodes in section 3.5.1) occurs at a relatively larger concentration of surface Ni^{3+} ions for the pre-oxidised electrode relative to the pre-reduced electrode. From Figure 5.5.1, it would appear that once the applied overpotential reaches η ≈ 0.5 V for the pre-oxidised electrode, all Ni oxide surface sites with the potential to catalyse oxygen gas evolution are active with respect to reaction (3.5.3, I), and thus a limiting current density is observed in the log i vs. η plot.

Owing to the less active nature of the oxide surface produced by the pre-reduction regime, a higher applied potential is necessary to achieve the same o.e.r current

density at this "type" of Ni electrode relative to the pre-oxidised electrode. Across the lower overpotential region of Figure 5.5.1, associated with parallel log i vs. η plots (b = ~ 2.303×2RT/3F) for the three Ni electrodes, it is obvious that an applied potential, greater in magnitude by ~ 40 mV, is required to achieve the same rate of reaction at the pre-reduced electrode as at the pre-oxidised electrode. Since we have estimated similar values of f_r for both electrodes, this difference in overpotential might be envisaged to reflect the extra energy required to make the o.e.r proceed with the same rate, at a surface with a lower concentration of the "right type of oxide" (i.e. β-NiOOH after reference 16) for the catalysis of the reaction. The extra energy is required to achieve reaction at the less optimal catalytic sites, possibly identifiable with the γ-Ni phase of the Bode scheme – recall Figure 1.4.3. Under this description, given two Ni electrodes with different "levels" of activity towards the o.e.r, the difference in applied potential required to achieve the same rate of reaction (normalised to account for real surface area) at the two electrodes, will be governed by the relative proportions of the less and more active Ni(III) sites at each electrode surface.

In terms of the real surface area normalised data of Figure 5.5.1, the pre-oxidised electrode might be considered to be that with the largest relative concentration of "more active" Ni sites. The pre-oxidation routine obviously has the effect of increasing the surface concentration of these sites relative to the non-pre-treated Ni electrode. In contrast the pre-reduction treatment has the effect of decreasing the relative proportion of these "more active" sites by comparison with the non-pre-treated electrode.

The forward direction steady state polarisation curves of Figures 5.3.2 and 5.2.3 for pre-reduced and non-pre-treated Co electrodes respectively, are re-plotted in Figure 5.5.2 with the log i values normalised according to the roughness factors of Table 5.5.1. The non-pre-treated electrode exhibits a somewhat greater catalytic activity towards oxygen evolution over the approximate range of $0.26V \leq \eta \leq 0.5V$. Steady state current densities of $i = 1.15\ (\pm\ 0.04) \times 10^{-5}$ A cm^{-2} and $i = 7.4\ (\pm\ 0.4) \times 10^{-6}$A cm^{-2} are observed at $\eta = 0.302$ V for the non-pre-treated and pre-reduced Co electrodes respectively. A possible explanation for this difference in catalytic activity, related to the relative thickness of the inner regions of the passive oxide layers on the two Co electrodes, is explored below.

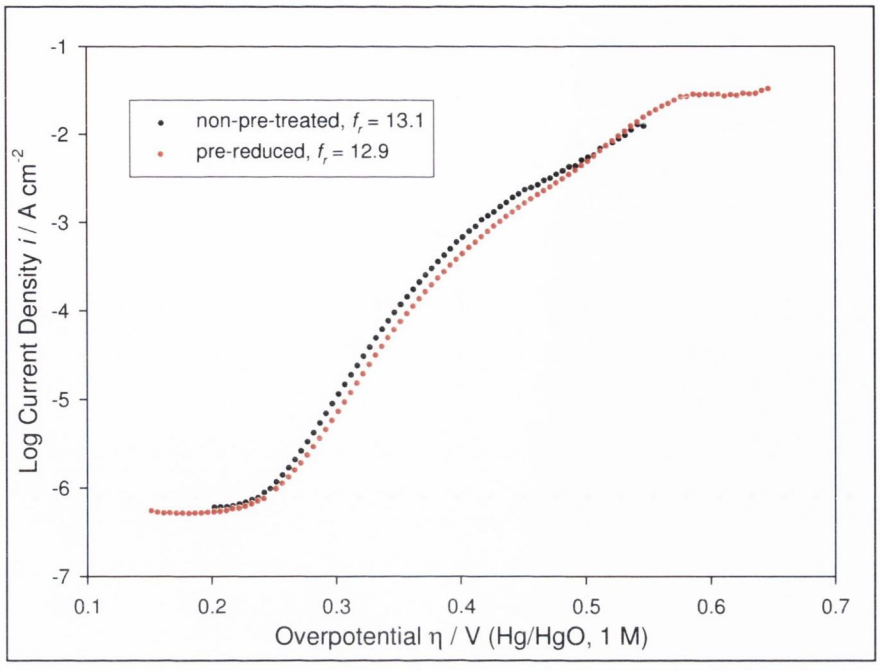


Figure 5.5.2 *IR corrected steady state polarisation curves recorded in 1.0 M NaOH solution at 25°C, for Co electrodes, subjected to different pre-treatment regimes. The values of log i(η) are normalised to the estimated truly active surface areas, based on the stated roughness factors.*

It is noteworthy that the lower overpotential Tafel slope exhibited by the pre-reduced electrode (b = 47.5 mV dec^{-1}) is somewhat greater than that measured for the non-pre-treated electrode (b = 46.0 mV dec^{-1}). Extrapolation of these lower overpotential straight line Tafel regions to η = 0 V (i.e. the oxygen electrode reversible potential), yields values for i_0, that coincide within the limits of experimental error - i_0 = 3.3 (± 0.2) × 10^{-12} A cm^{-2} for the pre-reduced electrode, i_0 = 3.3 (± 0.1) × 10^{-12} A cm^{-2} for the non-pre-treated electrode. This implies that the difference in catalytic activity, referred to above, between the two electrodes, is related the small difference in their associated lower overpotential Tafel slopes. In section 3.5.2, the observation of experimental Tafel slopes with values between ~ 45 – 48 mV dec^{-1} for the o.e.r. at Fe and Co electrodes at 25° C, was explained in terms of a development of a dual barrier model originally proposed by Meyer[17] and MacDonald and Conway[18]. Recapping briefly, this model proposes that only a fraction of the total potential difference, E, between the metallic electrode and the solution is available to the o.e.r. at the electrode/solution interface. The remainder of the potential drop appears across an electronically conductive barrier oxide layer, through which the electrons required for the o.e.r. must migrate. From experimental observation, we have postulated that the

aforementioned barrier layer is associated with the inner compact region of the passive oxide films that form on Fe and Co electrodes in alkaline solution.

Recall from the mathematical analysis of the aforementioned dual barrier model, that the symmetry factor, β_t, for the overall process is given by the following expression (originally presented as equation (3.5.19)),

$$\beta_t = \frac{\beta_f \beta_s}{\beta_f + \beta_s} \quad , \tag{3.5.1}$$

where, β_f, β_s, are the symmetry factors for the charge migration process through the barrier oxide layer, and the electron transfer process at the oxide/solution interface respectively. It was shown in section 3.5.2 (see equations 3.5.21 - .25) that under the dual barrier model, the kinetic analysis of a proposed o.e.r. reaction mechanism that otherwise (i.e. with no dual barrier model admitted) yields a Tafel slope prediction of b = 2.303×2RT/3F, instead predicts that b = 2.303×4RT/5F, if both charge transfer barriers are considered to be symmetrical , i.e. - $\beta_f = \beta_s = ½$. The numerical value of the theoretical Tafel slope, b = 2.303×4RT/5F, is 47.3 mV dec^{-1} at 25°C, which is slightly different to the experimental values that we have observed for both the non-pre-reduced Co electrode (46.0 mV dec^{-1}) and the pre-reduced Co electrode (47.5 mV dec^{-1}). According to equation (3.5.22) these deviations from the theoretical value arise due to the fact that $\beta_t \neq ¼$, which is expected (through equation (3.5.1)) if $\beta_f = \beta_s = ½$. As was discussed in sections 1.2.1 and 1.2.3 it is standard practice in kinetic mechanistic analyses of proposed o.e.r. pathways, to adopt a value of $\beta_s = ½$. If we follow this convention here, the deviation in the experimental Tafel slope values at 25° C from 47.3 mV dec^{-1} can be explained in terms of values of β_f that differ from ½. Consider the experimental value of b = 46.0 mV dec^{-1} = 2.303×0.778 RT/F obtained for the non-pre-treated Co electrode. In this case, 0.778 is the reciprocal of the value of the (1 + β_t) term in the exponent of equation (3.5.22), which implies that 0.778^{-1} = 1.285 = 1 + β_t, and therefore β_t = 0.285. Substituting this value of β_t into equation (3.5.1), setting $\beta_s = ½$, rearranging and solving for β_f, yields β_f = 0.665. Performing a similar analysis for the experimental value of b = 47.5 mV dec^{-1} observed for the pre-reduced Co electrode, leads to the calculation of a value of β_f = 0.482.

The next question that arises is, as to the physical significance of these values of β_f? Recall from section 3.5.2 that the field dependent migration of the charge carriers through the barrier oxide layer was described in terms of the Mott-Cabrera[19] model. Comparing equations (3.5.14) and (3.5.15) it is clear that $\beta_f = \delta/D$, where D is the thickness of the barrier film and δ is the half jump distance of the charge carriers. This implies that the symmetry factor β_f is inversely proportional to the thickness of the barrier oxide layer, which we have associated with the inner compact region of the passive oxide film. Following this logic, the pre-reduction routine that has been utilised with some Co electrodes in the present work (see section 3.3.2 for precise details) produces an inner passive layer of such thickness D, that it acts as almost an ideal symmetrical barrier for charge migration ($\beta_f = 0.482$ compared with the ideal value of 0.5). In the case of the non-pre-treated Co electrode, the inner compact region of the passive layer has not developed to a sufficient thickness to provide a symmetrical energy barrier. The value of $\beta_f = 0.665$ calculated for this situation, implies that approximately 2/3 of the energy associated with the potential drop across the barrier layer is available to the charge migration process, as compared to only ½ in the case of the (almost) symmetrical energy barrier that prevails in the case of the pre-reduced electrode. This in turn leads to a greater rate of the overall twin barrier process at a given overpotential, for the non-pre-treated electrode compared to the pre-reduced electrode.

The expression for the overall electrode current density, i, under the dual barrier model was given by equation (3.5.22), which can clearly be re-written as,

$$i = i_0 \exp((1+\beta_t)\eta F / RT) \quad , \tag{5.5.2}$$

where $i_0 = 2FK_T(a_{OH})^{\frac{\beta_f}{\beta_f+\beta_s}}$ is the exchange current density. As mentioned above, very similar experimental i_0 values have been noted for the non-pre-treated and pre-reduced Co electrodes, which implies that the different activities displayed by these electrodes towards the o.e.r. at $\eta > \sim 0.26$ V, arise principally due to the exponential term in Figure 5.5.2. The larger value of β_t that prevails for the non-pre-treated electrode relative to the pre-reduced electrode (owing to the larger value of β_f associated with the former electrode), leads to the prediction, as is observed experimentally in Figure 5.5.2, that, over the range of overpotentials at which

equation (5.5.2) is applicable, a greater faradaic current density will be observed at the former electrode compared to the latter. In addition the relative magnitude of the current density at the non-pre-treated electrode in comparison to the pre-reduced electrode, is expected to increase with increasing η over the potential range of the lower straight-line Tafel region, an effect that is also obvious from Figure 5.5.2. As discussed above, these observations can be explained in terms of the formation of a thicker barrier oxide at the pre-reduced Co electrode (owing to its pre-treatment regime), compared with the non-pre-treated Co anode.

The forward direction steady state polarisation curves for various Fe electrodes, originally presented in Figures 5.4.2 – 5.4.4, are re-plotted in Figure 5.5.3 with the values of log$i(\eta)$ normalised according to the roughness factors of Table 5.5.1.

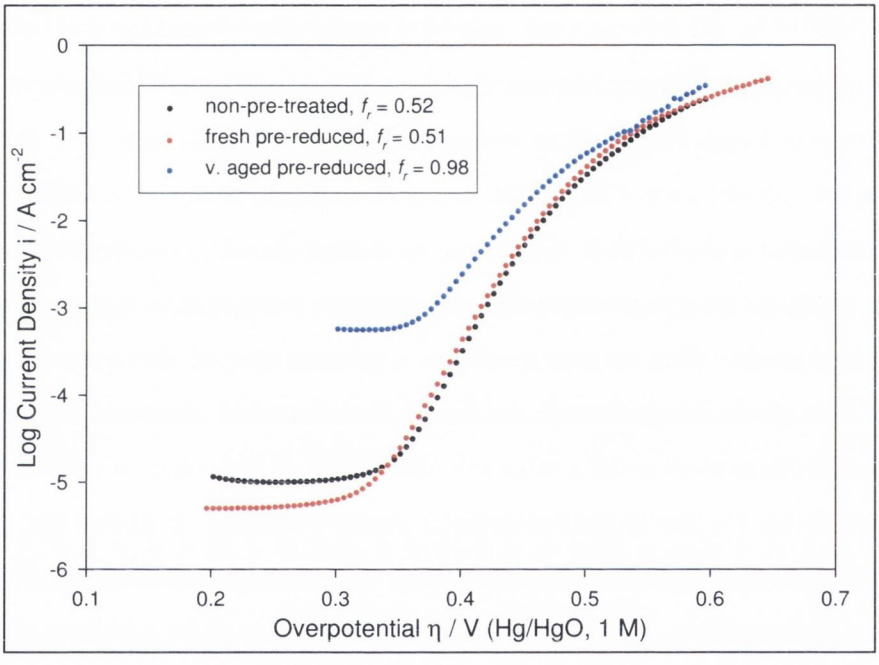


Figure 5.5.3 *IR corrected steady state polarisation curves recorded in 1.0 M NaOH solution at 25°C, for Fe electrodes, subjected to different pre-treatment regimes. The values of log i(η) are normalised to the estimated truly active surface areas, based on the stated roughness factors.*

For the Ni and Co real surface area normalised, steady state polarisation curves of Figures 5.5.1 and 5.5.2 respectively, the steady state current density at each electrode for η = 0.302 V, was used to compare its o.e.r. catalytic activity to that of other electrodes of the same metal, which had undergone different pre-treatment routines. Clearly the polarisation curves of Figure 5.5.3 for the various Fe electrodes, do not present a straight-line Tafel region at η = 0.302 V – therefore it was opted to compare

the current density values at η = 0.402 V. Current densities of $i = 4.5(\pm 0.2)\times10^{-4}$ A cm^{-2} and $i = 5.0\ (\pm 0.2) \times 10^{-4}$A cm^{-2} are observed at this overpotential for the fresh, pre-reduced Fe electrode and the non-pre-treated Fe electrode respectively. The extremely aged pre-reduced electrode displays significantly greater catalytic activity at the same overpotential, with a steady state current density of $i = 2.5(\pm 0.2)\times10^{-3}$ A cm^{-2} being recorded.

It is apparent that there is little difference between the fresh non-pre-treated and fresh pre-reduced Fe electrodes with regard to oxygen evolution catalytic activity. This would suggest that, in contrast to Ni, there is no "right type of oxide" or "less optimum type of oxide" in the catalysis of the o.e.r. by iron oxyhydroxide species, the relative proportions of which can be changed by the specific nature of a pre-treatment routine. Recall however from section 3.4.1, that steady state polarisation measurements on non-pre-treated Fe electrodes, were not sufficiently reproducible to permit the reliable experimental determination of kinetic parameters such as the Tafel slope and associated OH^- reaction order. The catalytic activity varied with ageing, an observation that was attributed to oxide film effects. As discussed in section 3.4.2, this problem was somewhat circumvented by using an electrode pre-reduction routine, although even then, ageing was significant with fresh pre-reduced electrodes displaying a Tafel slope of $b = \sim 2.303\times2RT/3F$ compared with $b = \sim 2.303\times4RT/5F$ – see Figure 3.4.8. In light of the recapping of the last few sentences, it should be pointed out that the similar catalytic activities noted for the pre-reduced and non-pre-treated Fe electrodes in Figure 5.5.3, refer to *non-aged electrodes*, as is evidenced by the fact that both steady state polarisation curves exhibit Tafel slopes of $b = \sim 2.303\times2RT/3F$ (as opposed to $\sim 2.303\times4RT/5F$) for $0.35 \leq \eta \leq 0.45$ V.

The real surface area adjusted polarisation behaviour of the extremely aged Fe electrode, relative to the fresher Fe electrodes serves to confirm the hypothesis of section 3.5.3. Recall that it was envisaged in the discussion of that section, that the o.e.r. proceeds with a common mechanism (i.e. scheme 3.5.68) at both the extremely aged and fresher electrodes. The superior catalytic performance and greater Tafel slope ($b = \sim 2.303\times RT/F$ compared to $b = \sim 2.303\times2RT/3F$) that characterise the extremely aged Fe electrode, relative to the fresher electrodes at lower oxygen evolution overpotentials, was proposed to arise as a consequence of Temkin intermediate species adsorption conditions ($0.2 < \theta < 0.8$) prevailing at these overpotentials for the former type of electrode, in comparison with the low coverage

Langmuir adsorption ($\theta \rightarrow 0$) conditions envisaged over the same potential range for the less aged anodes. At higher overpotentials, the polarisation curves for the extremely aged and fresher electrodes are expected to converge, with the same o.e.r. mechanism proceeding under high coverage ($\theta \rightarrow 1$) Langmuir adsorption conditions at both "types" of electrode. This is quite evidently true for the data presented in Figure 5.5.3 for $\eta \geq \sim 0.5$ V.

5.6 Relative Activities of the Anodic Oxides Formed on Ni, Co and Fe Electrodes Towards the O.E.R. in Alkaline Solution

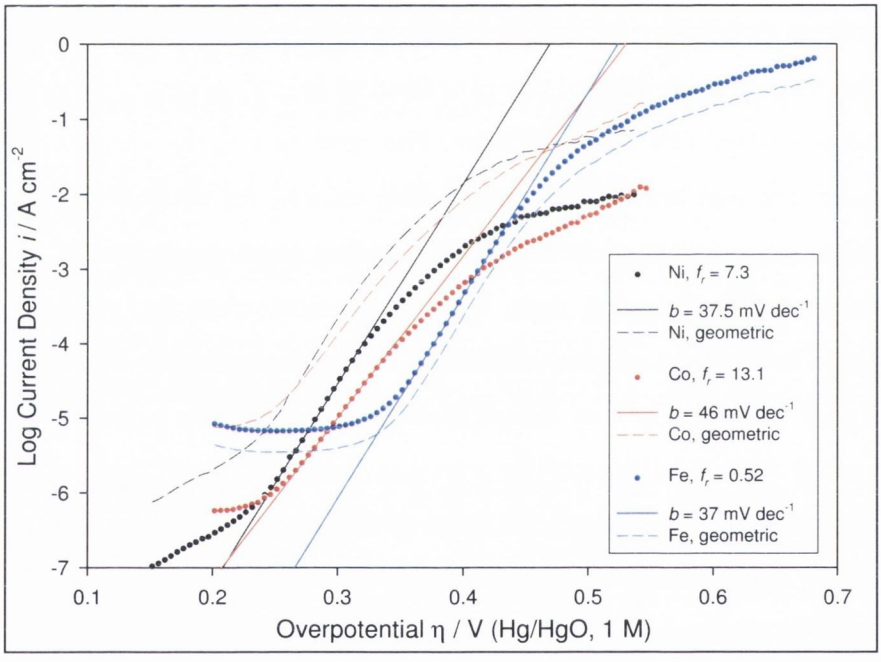


Figure 5.6.1 *Comparison of IR corrected steady state polarisation curves recorded in 1.0 M NaOH solution at 25°C, for fresh non-pre-treated Ni, Co and Fe electrodes. For the dotted plots the values of log i(η) are normalised to the estimated truly active surface areas, based on the stated roughness factors. The dashed lines represent the same polarisation curves, where the values of log i(η) are based on the geometric electrode surface areas.*

Electrode	f_r	Tafel slope b (mV dec^{-1})	i_0 (A cm^{-2})	$i(\eta = 0.302$ V) (A cm^{-2})
Ni	7.3 ± 0.1	37.5	2.75 (±0.04) ×10^{-13}	3.34 (± 0.05) × 10^{-5}
Co	13.1 ± 0.5	46.0	3.2 (±0.1) ×10^{-12}	1.15 (± 0.04) × 10^{-5}
Fe	0.52 ± 0.02	37.0	6.1 (±0.2) ×10^{-15}	9.5 (±0.4) ×10^{-7} †

Table 5.6.1 *Comparison, based on the data of Figure 5.6.1, of various parameters related to the o.e.r. catalytic activity of fresh non-pre-treated Ni, Co and Fe electrodes in 1.0 M NaOH at 25°C. The quoted current densities are based on the estimated true active surface areas for the o.e.r. for each electrode. † - Estimated by the extrapolation of the lower overpotential Tafel slope line.*

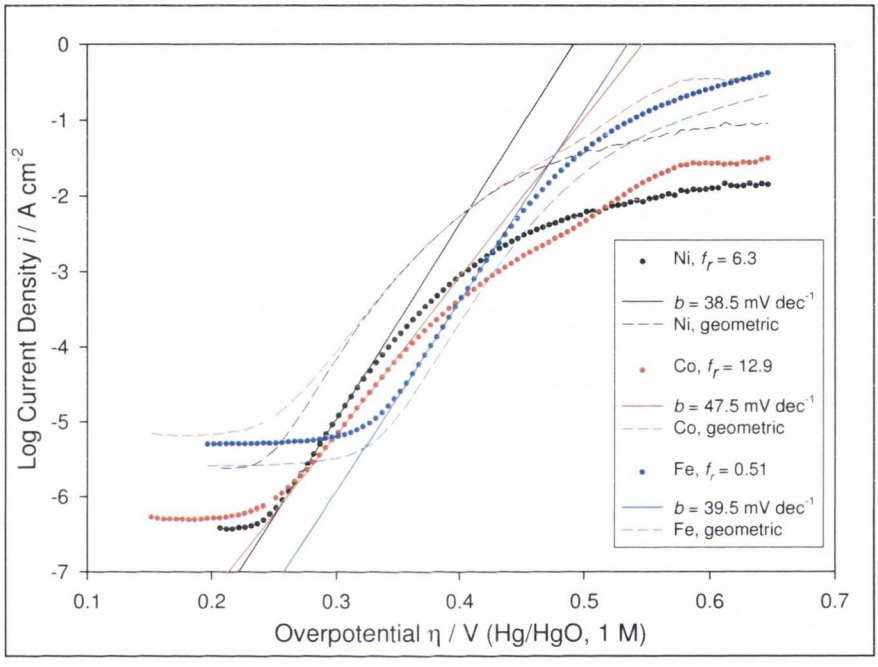


Figure 5.6.2 *Comparison of IR corrected steady state polarisation curves recorded in 1.0 M NaOH solution at 25°C, for pre-reduced Ni, Co and Fe electrodes. For the dotted plots the values of log i(η) are normalised to the estimated truly active surface areas, based on the stated roughness factors. The dashed lines represent the same polarisation curves, where the values of log i(η) are based on the geometric electrode surface areas.*

Electrode	f_r	Tafel slope b (mV dec^{-1})	i_0 (A cm^{-2})	$i(\eta = 0.302$ V) (A cm^{-2})
Ni	6.3 ± 0.2	38.5	1.78 (±0.07) ×10^{-13}	1.21 (± 0.04) × 10^{-5}
Co	12.9 ± 0.7	47.5	3.3 (±0.2) ×10^{-12}	7.4 (± 0.4) × 10^{-6}
Fe	0.51 ± 0.02	39.5	2.9 (±0.2) ×10^{-14}	1.3 (± 0.1) × 10^{-6} †

Table 5.6.2 *Comparison, based on the data of Figure 5.6.2, of various parameters related to the o.e.r. catalytic activity of pre-reduced Ni, Co and Fe electrodes in 1.0 M NaOH at 25°C. The quoted current densities are based on the estimated true active surface areas for the o.e.r. for each electrode. † - Estimated by the extrapolation of the lower overpotential Tafel slope line.*

Oxygen evolution steady state polarisation curves, with the electrode current density normalised to the active surface area through the indicated roughness factors, are plotted on the same graphs for fresh non-pre-treated (Figure 5.6.1) and pre-reduced (Figure 5.6.2) Ni, Co and Fe electrodes in 1.0 M NaOH at 25°C. These figures facilitate the comparison of the activities of anodic oxide covered polycrystalline electrodes of the three metals towards the o.e.r. in aqueous alkaline solution over a wide range of overpotential. Also depicted in the aforementioned figures are the same polarisation curves, where the values of $\log i(\eta)$ are referred to the geometric surface area. Some parameters, relevant to the comparison of the o.e.r. catalytic efficiencies of the various electrodes are listed in Tables 5.6.1 and 5.6.2, for the non-pre-treated and pre-reduced electrodes respectively.

In the review of general concepts of electrocatalysis, presented in section 1.3.1, it was commented that the electrocatalytic activities of different electrode materials towards a given reaction are normally compared in terms of the experimentally observed values of the exchange current density i_0. However, as was pointed out by Conway et al.[20], the value of the Tafel slope, b, is as important as i_0 in characterising electrocatalysis. Consider, for example, the parameters presented for the non-pre-treated Ni and Co anodes in Table 5.6.1. From the quoted steady state current density values, it is obvious that, at an overpotential of η = 0.302 V (which lies within the lower straight line Tafel regions in the polarisation curves for both anodes), it is the Ni electrode that displays the superior catalytic activity – yet it is the Co electrode that has the higher i_0 value. This arises due to the larger value of b in the case of the Co anode. This leads to the general conclusion, that where different electrodes present significantly different Tafel slopes for a given reaction, a comparison of the exchange current densities is not a useful exercise[21, 22], if one is interested in the relative catalytic abilities of the electrodes at practically useful rates of reaction. The foregoing statement is particularly true for kinetically, highly irreversible reactions such as the o.e.r.

An alternative approach, and that utilised in the present work, is to compare the values, for different electrodes, of the real steady current densities observed for the same reaction at a given overpotential. It has been elected to conduct such comparisons at an overpotential of η = 0.302 V. This overpotential was selected because it facilitates ready comparison of the real current densities observed at Ni, Co and Fe electrodes in the present work, with those observed by Bockris and Otagawa[20]

for nickelate, cobaltate and ferrite electrodes at η = 0.3 V. The latter authors[20] have described the low overpotential section of the Tafel region as being "the practically important region for comparison".

Miles et al.[22] used a thermal decomposition method to electro-deposit layers of the oxides of various metals from solutions of the appropriate metal chloride onto titanium wires. These wires were then sealed into Teflon tubing to make electrodes, and their catalytic activities towards the o.e.r. were compared by recording steady state polarisation curves in 30wt% KOH solutions (~ 5.35 M) at 80°C. Different Tafel slopes were noted for different metal oxides – of interest in the present work is that slopes of 0.071 ± 0.011, 0.126 ± 0.004 and 0.191 ± 0.002 V dec^{-1} were noted for the nickel-, cobalt-, and iron-oxide electrodes respectively. The authors sought to circumvent the problems of catalytic activity comparison associated with different values of b, by comparing values of what they called the Tafel parameter, a, where $a = -b\log i_0$. Under this definition it is clear that a represents the experimental overpotential at a steady state current density of 1 A cm^{-2}. Comparing the experimental values of a, the following activity series with respect to catalysis of the o.e.r. was reported - Ru >Ir~Pt~Rh~Pd~Ni~Os>>Co>>Fe. It must however be commented that all current densities in the work of Miles et al. were referred to geometric surface areas and not to estimated real active surface areas.

As an aside, it is of interest to note that of all the metal oxide electrodes they prepared, Miles et al., found it most difficult to obtain reproducible polarisation data for the nickel oxide anode. This may well be related to changes in the relative proportions of the "right type of oxide" (β-NiOOH according to Lu et al.[16]) and the less catalytically active type (the γ phase) with electrochemical ageing. Similar issues have been encountered with the Ni electrodes in the present work, and were discussed in sections 3.2.1 and 5.5.

As was discussed in the literature review of section 1.5.3, Scarr[23] conducted, what was, until the present work (to the best of our knowledge), the only comparative study on the catalytic performance of polycrystalline Ni, Co and Fe electrodes towards the o.e.r. in alkaline solution. This worker observed oxygen evolution Tafel slopes of b = ~ 2.303×4RT/5F for each of the three metals in 1M KOH, thereby rendering meaningful a comparison of catalytic activities based on the relative values of the exchange current densities. In agreement with the trend reported by Miles et al.[22], values of $i_0 = 2 \times 10^{-10}$ A cm^{-2}, $i_0 = 8 \times 10^{-11}$ A cm^{-2} and $i_0 = 2 \times 10^{-13}$ A cm^{-2} were

observed by Scarr[23] for the Ni, Co and Fe anodes respectively. In common with the work of Miles et al., Scarr's catalytic comparison suffers the weakness of the reported exchange current densities being based on geometric, rather than real electrode surface areas.

Examination of Figures 5.6.1 and 5.6.2, and the associated Tables 5.6.1 and 5.6.2, reveals that, for $\eta \leq 0.4$ V (i.e. the range of overpotentials associated with the entire length of the lower *b* straight line regions for the Ni and Co electrodes, and most of the length of this region for the Fe electrodes), the real surface area normalised steady state polarisation curves of the present work are indicative of the same o.e.r. catalytic activity series as observed by Miles et al.[22] and Scarr[23] – i.e. Ni > Co > Fe. The data presented in these figures also indicates that the degree of inferiority of the catalytic activity of the Fe electrodes, relative to the Co and Ni electrodes, is overstated by steady state polarisation curves based on geometric surface areas, at least in the case of the polycrystalline metallic electrodes utilised here. This arises of course, due to the fact that roughness factors of less than unity have been estimated, via the desorption current transient method, for the Fe electrodes, in comparison with factors significantly larger than unity yielded by the same technique for the Ni and Co electrodes. Indeed in the case of the pre-reduced electrodes (Figure 5.6.2), at overpotentials in the approximate range of $0.25 \text{ V} \leq \eta \leq 0.32$ V, the steady state polarisation curves normalised to the geometric surface area, indicate that the Co electrode is catalytically superior to the Ni electrode. However, normalisation of these data to the respective values of the active surface area, reveals that the aforementioned apparent conclusion is actually incorrect.

Bockris and Otagawa[21] have reported the following values of o.e.r. steady state current densities, for various perovskite electrodes in 1.0 M NaOH (25°C) at η = 0.3V: $i = 1.3 \times 10^{-5}$ A cm^{-2} for a nickelate electrode ($f_r = 5.6 \times 10^3$) , $i = 1.4 \times 10^{-6}$ - 1.0×10^{-5} A cm^{-2} for various cobaltate anodes (f_r values of the order of $10^2 - 10^3$), i = 5.0×10^{-7} A cm^{-2} ($f_r = 6.0 \times 10^2$) for a $La_{0.7}Sr_{0.3}FeO_3$ ferrite electrode, and $i = 8.1 \times 10^{-7}$ A cm^{-2} ($f_r = 3.3 \times 10^3$) for a for a $La_{0.5}Sr_{0.5}FeO_3$ ferrite electrode. The quoted roughness factor values were estimated using the double layer capacitance ratio approach in conjunction with cyclic voltammetry measurements, as was described in section 2.1.9. Comparing the values of $i_{(\eta = 0.3V)}$ obtained by Bockris and Otagawa[21] for their perovskite electrodes with the values of $i_{(\eta = 0.303V)}$ observed in the present work and listed in Tables 5.6.1 and 5.6.2, it is apparent that there is agreement to

within an order of magnitude between the values quoted for our polycrystalline metal electrodes and the perovskite electrodes of the former authors, based on the same metal oxide - i.e. $i_{(\eta = 0.3V)}$ for the nickelate electrode of ref. 21 is in reasonable agreement with $i_{(\eta = 0.303V)}$ for our polycrystalline Ni electrodes and so on. This order of magnitude agreement prevails despite the fact that the roughness factors of the perovskite electrodes are 2 – 3 orders of magnitude greater than the roughness factors of our anodic oxide covered metallic electrodes. It might therefore be suggested that the o.e.r. occurs at *essentially the same type of active site* on an anodic oxide covered metallic electrode surface, as on the corresponding perovskite electrode surface.

We have already suggested in section 3.5.4, that the o.e.r. at the cobaltate and ferrite electrodes of Bockris and Otagawa[21, 24] proceeds via the same reaction mechanism (scheme (3.5.68)), as at the oxide covered Co and Fe electrodes of the present work. Furthermore it was commented in the same section, that the pathway proposed in the current work for oxygen evolution at Ni electrodes (i.e. scheme (3.5.3)), can successfully account for the experimental kinetic parameters noted by Bockris and Otagawa[24] for their nickelate electrode, or alternatively their "oxide vacancy" scheme (see equation (3.5.70)) could potentially be operative at our anodic oxide covered Ni electrodes. In his review on the o.e.r., Kinoshita[25] commented that electrodes consisting of specifically pre-synthesised metal oxides (like the peroskite electrodes of Bockris and Otagawa[21, 24]) generally display superior catalytic properties towards the reaction, compared to (anodic oxide covered) metallic electrodes. However, most literature reports on the o.e.r. do not attempt to normalise observed steady state current densities to estimated real surface areas With this latter point in mind, and considering the conclusions of the previous paragraph, it might be suggested, that the apparently superior o.e.r. performance of synthesised metal oxide electrodes, relative to the oxide formed anodically on polycrystalline electrodes of the same metal, arises principally due to the larger available active specific surface areas of the former type of anode, and not due to any intrinsically superior electrocatalytic properties of the synthesised oxides.

Ho and Piron[1] also noted superior o.e.r. catalytic activity for their electrodeposited Ni electrode in 5.0 M KOH, relative to their electrodeposited Co electrode. Active surface area (determined by the same method utilised in the present work) normalised current densities of 4.2×10^{-3} and 6.6×10^{-4} A cm^{-2} were observed at $\eta = 0.4$ V for the Ni and Co electrodes respectively. Interestingly, these workers found that their Ni

anodes exhibited a lower roughness factor than their Co anodes, just as was observed in the present work. However, while they estimated a similar value of f_r (7 ± 1) for their electrodeposited Ni electrode to those determined here for anodic oxide covered Ni electrodes, their electrodeposited Co electrode was characterised by a much larger roughness factor (f_r = 91 ± 7) than was suggested experimentally for our oxide covered Co electrodes.

The concept of a volcano plot was discussed in section 1.3.1, while volcano plots devised for the h.e.r. and the o.r.r. were reproduced in Figures 1.3.2 and 1.3.3 respectively. Attempts to draw correlations between electrode physicochemical properties and o.e.r. catalytic activity is complicated by the fact that it is the metal oxide and not metal that catalyses oxygen evolution. Perhaps the most complete attempt to provide an interpretation of o.e.r. catalytic performance in terms of physicochemical parameters was provided by Bockris and Otagawa[21] in their study of the reaction at perovskite electrodes. For perovskites based on the first row transition metal M (general formula AMO_3, where A is a lanthanide), they found that there was an inverse linear relationship between the estimated M(III)-OH bond strength and $i_{(\eta = 0.3V)}$ – i.e. while the estimated bond strength increases in the order Ni < Co < Fe < Mn < Cr, the o.e.r. catalytic activity follows the reverse of this series. They rationalised this in terms of a rate determining step involving the desorption of the OH_{ads} species adsorbed in the initial discharge step – obviously the weaker the M-OH bond the greater the rate of desorption at a given overpotential. Bockris and Otagawa devised molecular orbital diagrams for the bonding of an OH entity to a $M(III)O_5$ species (which they proposed as a valid model for a transition metal site in the {001} plane of the perovskite unit cell) and concluded that the M-OH bond strength had an inverse dependence on the number of d electrons occupying antibonding orbitals (4 for Ni(III)-OH, 3 for Co(III)-OH etc).

While at first glance, the aforementioned concepts of Bockris and Otagawa would appear to be in accord with our experimental observation of an o.e.r. activity series of Ni > Co > Fe at overpotentials associated with a (deduced) rate determining OH desorption step (for Co and Fe at least), some caution is in order. The relationship between M-OH bond strength and o.e.r. catalytic activity, and the molecular orbital analysis referred to above, apply specifically to first row transition metal ions in the +3 oxidation state. In contrast, the rate determining step (step (3.5.3, II)) of the pathway that we have proposed for the o.e.r. at Ni doesn't involve the desorption of

an OH species, while for the RDS (step (3.5.68, II) envisaged in the present work for the o.e.r at oxide covered Co and Fe surfaces the bonds of interest would be Co(IV)-OH and Fe(VI)-OH respectively. Nevertheless it must be admitted that if the oxygen vacancy pathway of Bockris and Otagawa[24] (see section 3.5.4) was admitted for the o.e.r. at a passive oxide covered Ni surface, then the correlation envisaged by the same authors between the number of d electrons in antibonding orbitals and o.e.r. catalytic activity would also hold for the electrodes of the present work, based on rate determining steps involving the breaking of Ni(III)-OH (4 antibonding electrons), Co(IV)-OH (2 antibonding electrons) and Fe(IV)-OH (1 antibonding electon) bonds. This conclusion assumes that the molecular orbital electron configurations for the Co(IV)-OH and Fe(IV)-OH bonds are the same as those proposed by Bockris and Otagawa[21] (see Figures 14 and 20 in this reference) for Fe(III)-OH and V(III)-OH respectively.

Whether such compliance with the proposed volcano type relation of Bockris and Otagawa is sufficient grounds for the admission of their "oxygen vacancy" pathway for the o.e.r. at passive oxide covered Ni electrodes, in preference to the pathway forwarded in the present work (reaction (3.3.5)), is questionable, given the lack of consensus in the literature regarding the possible role of oxide surface oxygen atoms in the gas evolution reaction – recall section 3.5.4. Finally it should be commented that the fact, as discussed above, that we have observed similar (real surface area normalised) o.e.r. catalytic activities at passive oxide covered Co (catalytic site envisaged to be in the Co(IV) valance state) and Fe (catalytic site envisaged to be in the Fe(VI) valance state) electrodes, as those observed by Bockris and Otagawa[21] at their cobaltate and ferrite electrodes, may cast some doubt on the conviction of these authors (based on rather little experimental evidence) that M(III) sites are the o.e.r. active centres at the surface of electrodes of all perovskites. If this assumption regarding the valance state of the catalytic ions at perovskite surfaces is not true, then the correlation of o.e.r. activity with the number of antibonding d-electrons becomes more complicated than that presented in reference 21 (although it might well still be applicable).

Chapter 5 References

1 Ho, J.C.K., Piron, D.L., *J. Appl. Electrochem.*, **1996**, *26*, 515.

2 Fedorova, A.I., Frumkin, A.N., *J. Phys. Chem. USSR*, **1953,** *27*, 247.

3 Kobussen, A.G.C., Willems, H., Broers, G.H.J., *J. Electroanal. Chem.,* **1982**, *142*, 85.

4 Ho, J.C.K., Piron, D.L., *J. Electrochem. Soc.*, **1995**, *142*, 1144.

5 Jovic, V.D., Gamry Instruments, Application Note, "Determination of the correct value of C_{dl} from the impedance results fitted by the commercially available software", Gamry Instruments, 2003.

6 Frumkin, A. N., *J. Res. Inst. Catalysis* (Hokkaido Univ.), **1967**, *15*, 61.

7 Behl, W.K., Toni, J.E., *J. Electroanal. Chem.*, **197I**, *31*, 63.

8 Burke, L.D., Lyons, M.E.G., *J. Electroanal. Chem.*, **1986**, *198*, 347.

9 Beverskog, B., Puigdomenech, I., *Corros. Sci.,* **1996**, *38*, 2121.

10 Bouzek, K., Rousar, I., *J. Appl. Electrochem.*, **1993**, *23*, 13.

11 Bouzek, K., Rousar, I., *J. Appl. Electrochem.*, **1996**, *26*, 919.

12 Frumkin, A. N., Dolin, P., Ershler, B.V., *Acta Physiochim., U.R.S.S.*, **1940**, *13*, 747 & 802.

13 Bai, L., Harrington, D.A., Conway, B.E., *Electrochimica. Acta.,* **1987**, *32*, 1713.

14 Krstajic, N., Popovic, M., Grgur, B., Vojnovic, M., Sepa, D., *J. Electroanal. Chem.,* **2001**, *512*, 16.

15 Gennero De Chialvo, M.R., Chialvo, A.C., *Electrochimica. Acta.,* **1988**, *33*, 825.

16 Lu, P.W.T., Srinivasan, S., *J. Electrochem. Soc.*, **1978**, *125*, 1416.

17 Meyer, R.E, *J. Electrochem. Soc.*, **1960**, *107*, 847.

18 MacDonald, J.J., Conway, B.E., *Proc. R. Soc. London, Ser. A*, **1962**, *269*, 419.

19 Cabrera, N., Mott, N.F., *Repts. Prog. Phys.,* **1948-49**, *12*, 163.

20 Conway, B.E., Bai, L., Satter, M.A., *Int. J. Hydrogen Energy*, **1987**, *12*, 607.

21 Bockris, J.O'M., Otagawa,T., *J. Electrochem. Soc.*, **1984**, *131*, 290.

22 Miles, M.H., Huang, Y.H., Srinivasan, S., *J. Electrochem. Soc.*, **1978**, *125*, 1931.

23 Scarr, R.F., *J. Electrochem .Soc.,* **1969**, *116*, 1526.

24 Bockris, J.O'M., Otagawa,T., *J. Phys. Chem.*, **1983**, *87*, 2960.

25 Kinoshita, K., "Electrochemical Oxygen Technology", Wiley-Interscience, New York, 1992, chapter 2.

CHAPTER 6

CONCLUSIONS AND FUTURE WORK

6.1 Summary of Conclusions

The "backbone" of the present work is to be found in the steady state polarisation measurements presented in Chapter 3. The aim of these measurements was to obtain experimental values for the o.e.r. Tafel slope, b, and the OH^- ion reaction order, m_{OH^-}, for polycrystalline Ni, Co and Fe electrodes in aqueous alkaline solution, with a view to performing classical kinetic mechanistic analyses, in order to identify the operative oxygen evolution pathway for each of these anodes.

Obtaining sufficiently reproducible steady state polarisation curves for bright non-pre-treated electrodes proved very difficult except in the case of Co. However, even for this metal, problems arose when trying to extract the m_{OH^-} parameter from the polarisation data recorded in solutions of different OH^- concentration. The difficulties arose from the fact that the lower overpotential Tafel slope varied from ~ 2.303×4RT/5F to ~ 2.303×2RT/3F over a range of NaOH solution concentrations from 1.0 M to 5.0 M (e.g. Figure 3.3.1). In the case of Ni, on the basis of voltammetric characterisation of electrodes, the aforementioned irreproducibility was attributed to changing relative proportions of the "right type of oxide" (β-NiOOH)[1], and the less active form of oxyhydroxide (γ-Ni phase) for oxygen evolution. The changing composition of the active surface was due to both electrochemical and temporal ageing.

In order to circumvent the aforementioned reproducibility issues, electrochemical pre-treatment routines were devised for the various electrodes, the details of which are outlined in sections 3.2.2, 3.3.2 and 3.4.2 for the Ni, Co and Fe anodes respectively. Tafel slopes of ~ 2.303×2RT/3F and an associated reaction order, m_{OH^-}, of approximately unity were observed for Ni electrodes subjected to relatively mild pre-reduction or alternatively mild pre-oxidation regimes (Figures 3.2.12 – 3.2.18). Pre-reduction of Co electrodes lead to the observation of Tafel slopes of ~2.303×4RT/5F for a range of NaOH solution concentrations (0.5 – 5.0 M), and the deduction of m_{OH^-} = ~ 1 for this system (Figures 3.3.17 – 3.3.19).

In the case of Fe, even pre-reduction of the electrode initially failed to achieve reproducibility in subsequent steady state polarisation measurements. With repeated polarisation, and application of the pre-reduction routine before each experiment, reproducible Tafel slopes of ~2.303×4RT/5F with an associated m_{OH^-} value of the order of unity, were eventually achieved (Figures 3.4.12 – 3.4.15). This was in

contrast to values of b = ~ 2.303×2RT/3F observed in 1.0 M NaOH following pre-reduction of a newly prepared Fe electrode (Figure 3.4.7). The contrast between the o.e.r. steady state polarisation curves recorded for pre-reduced, new, and somewhat aged Fe electrodes (Figures 3.4.8 and 3.4.9), was, on the basis of voltammetric characterisation of both "types" of electrode (Figures 3.4.10 and 3.4.11), attributed to ageing of the anodic oxide film. It was concluded (and this is also true to a certain extent for the Ni and Co electrodes) that a residual amount of the oxide film is significantly resistant to removal by mechanical polishing and the pre-reduction routine that was utilised. Upon ageing, the presence of this residual film leads to the formation of a passive oxide, the properties of which are more dependent on the inner compact region, than is the case for the anodic oxide formed on less aged Fe electrodes (Figure 3.4.11).

The influence of the extent of electrode ageing (through the composition and/or structure of the passive oxide) on the catalytic properties of Co and Fe electrodes towards the o.e.r., is also illustrated by the observation of quite different steady state polarisation behaviour for, what we have called "extremely aged" electrodes of these metals, relative to fresher substrates. The extremely aged Co and Fe electrodes exhibit Tafel slopes of b = ~ 2.303×RT/F at lower η with associated, non-integral reaction orders of ~ 3/2, while at higher overpotentials b is observed to increase to ~ 2.303×2RT/F with m_{OH^-} = ~ 1 (Figures 3.3.14 – 3.3.16, and 3.4.16 – 3.4.19). Overall, the observed dependence of oxygen evolution steady state polarisation data on the nature (or lack) of electrode pre-treatment and the extent of electrode ageing, points to the likely reason for much of the disparity observed in literature values of parameters such as b and i_0 for the o.e.r. at Ni, Co and Fe electrodes in aqueous alkaline solution.

The relatively low values of b outlined above, are indicative of a rate determining desorption step at some point in the o.e.r. mechanistic pathway subsequent to the initial OH^- discharge step. As discussed in section 3.5.1, the experimental kinetic mechanistic parameters observed for the Ni electrodes are strongly indicative of a pathway involving the adsorption of just one mole of OH^- ions per mole of active sites, during the RDS or any steps preceding it. On this basis, we have proposed scheme (3.5.3) as a suitable candidate for the o.e.r. at the passive oxide covered Ni electrode surface in alkaline solution. This type of mechanism was originally developed by Burke and co workers[2, 3], and envisages that the catalytic metal ion

exists as part of a hydroxylated surface complex species. With reference to CVs, such as those presented in Figures 3.2.6 or 3.2.21, it is clear that the rising edge of the oxygen evolution current becomes significant at potentials anodic to those associated with the Ni(II)↔Ni(III) transition. Therefore we believe that an appropriate representation of the complex catalytically active surface site is $[Ni(III)O_m(OH)_n]^{p-}$, where p=2m+n-3. Such anionic surface complexes can exist due to the somewhat acidic nature of metal oxides in alkaline solution, with charge neutrality provided by counter-ions in the outer Helmholtz layer. The initial discharge of an OH^- ion (step (3.5.3, I)) occurs with oxidation of the Ni^{3+} ion of the surface catalytic species to the Ni(IV) state. This Ni ion is reduced back to the Ni(III) state, with the simultaneous evolution of a mole of gaseous O_2 in step (3.5.3, III). The $[Ni(III)O_m(OH)_n]^{p-}$ active site is re-generated in the final step of the pathway, and so the cyclic process can begin again.

In an attempt to rationalise the Tafel slopes of ~2.303×4RT/5F observed for pre-reduced Co and Fe electrodes, consideration was given, in section 3.5.2, to three different "dual-barrier" models that have been proposed in the literature. Of these, the model due to Meyer[4], and MacDonald and Conway[5] was considered to be the most appropriate to the systems under study. This model envisages that only a fraction of the total potential difference between the metallic electrode and the solution is effective in charge transfer at the electrode/solution interface with the remainder of the potential drop occurring across an electronically conductive barrier oxide layer, through which the electrons required for the o.e.r. must migrate. Assuming that both the barriers for charge migration across the oxide layer and for the electron transfer reaction at the oxide surface are symmetrical, it was shown in section 3.5.2, that an o.e.r. pathway with a specific RDS, which normally gives rise to a prediction of b = 2.303×2RT/3F, will instead be characterised by a Tafel slope of 2.303×4RT/5F under the dual barrier model.

At first glance, it therefore appears that a pathway analogous to scheme (3.5.3) can also be admitted for the o.e.r. at anodic oxide covered Co and Fe electrodes. However, it was shown, according to equation (3.5.27), that, under the dual barrier model, the experimentally observed reaction orders of ~ 1 for both the Co and Fe electrodes are actually indicative of theoretical m_{OH^-} values of 2 for the surface electron transfer reaction. Therefore experimental parameters of b = 2.303×4RT/5F and m_{OH^-} = 1 for the dual barrier process, correspond to theoretical parameters of b = 2.303×2RT/3F

and $m_{OH^-} = 2$ for the surface oxygen evolution reaction. The o.e.r. pathway of scheme (3.5.68) gives rise to the latter set of kinetic parameters, where the second step is considered to be rate limiting under low coverage ($\theta \rightarrow 0$), Langmuir intermediate adsorption conditions. We have opted for the peroxide type mechanism of scheme (3.5.68) in preference to other previously proposed o.e.r. pathways (e.g. the Krasil'shchikov mechanism) because the former (peroxide) type of mechanism can also explain the kinetic parameters observed experimentally for the "extremely aged" Co and Fe electrodes.

The values of $b = \sim 2.303 \times RT/F$ and $m_{OH^-} = \sim 3/2$ associated with the o.e.r. at these aged electrodes at lower overpotentials, can potentially arise from a kinetic mechanistic analysis of scheme (3.5.68), where it is considered that the M-OH intermediate species formed in the initial discharge step (here M is representative of the surface active site) achieve an intermediate fractional coverage of the active sites ($0.2 < \theta_{MOH} < 0.8$), rendering the Temkin adsorption isotherm applicable. If a physical situation arises where the Temkin parameter, r_{II}, of the intermediate species formed in the second step of an envisaged o.e.r. pathway, is negligible in comparison to r_{MOH}, the Temkin parameter for the intermediate formed in the initial step, then the formal kinetic analysis yields $b = 2.303 \times RT/F$ and $m_{OH^-} = 3/2$, as observed experimentally. The formation of the *physisorbed* hydrogen peroxide intermediate species in step (3.5.68, II) provides just such a physical situation[6], which is rather difficult to envisage arising otherwise. The experimental values of $b = \sim 2.303 \times 2RT/F$ and $m_{OH^-} = \sim 1$, observed at higher overpotentials for the extremely aged electrodes, can also be rationalised by scheme (3.5.68) with the same rate determining step as before. The changes in Tafel slope and reaction order are envisaged to occur due to the fact that $\theta_{MOH} \rightarrow 1$ at higher values of η.

Returning momentarily to the dual barrier model discussed above, we have made the development in the present work, of associating the barrier oxide layer, with the inner compact anhydrous regions of the passive oxide films formed on Co and Fe electrodes. For Co this deduction is based on the comparison of the voltammetric profiles (Figure 3.3.8) of a non-pre-treated Co electrode at lower OH^- concentrations (0.25, 0.5 and 1.0 M) for which o.e.r Tafel slopes of $\sim 2.303 \times 4RT/5F$ were observed, and at $[OH^-] = 5.0$ M, for which $b = \sim 2.303 \times 4RT/5F$. The argument is outlined in section 3.5.2, and is related to our observation, that the initial passivation of Co electrodes in the lower concentration OH^- solutions, occurs principally via a solid

state electrochemical mechanism, whereas for [OH^-] > 1.0 M a rapid dissolution/precipitation mechanism prevails. In the case of Fe, the deduction is made, principally on the basis of the comparative CVs of Figure 3.4.11 for a fresh pre-reduced Fe electrode (associated o.e.r. Tafel slope = ~ 2.303×2RT/3F) and the same electrode, again pre-reduced, but now more aged (associated o.e.r. Tafel slope = ~ 2.303×4RT/5F).

Comparing the CVs recorded to characterise the Co electrodes of the present work (e.g. Figure 3.3.26), with those presented and discussed in the literature, we have proposed that the active complex species for oxygen evolution at passive oxide covered Co anodes should be represented as $[Co(IV)O_m(OH)_n]^{p-}$ (p=2m+n-4) - i.e. the central Co ion is in the +4 oxidation state. Normally, CV profiles of Fe electrodes in aqueous alkaline solution are essentially featureless for both the anodic and cathodic half cycles, over a potential window extending ~ 0.75 V below the rising edge of the o.e.r. current – e.g. Figures 3.4.2 and 3.4.10. Since the onset of significant rates of oxygen evolution occurs at potentials just anodic to those associated with the Ni(II)→Ni(III) voltammetric peak for Ni electrodes, and the Co(III)→Co(IV) voltammetric feature for Co electrodes, it would seem likely, as envisaged by earlier authors, that the o.e.r. is related to the formation of higher metal valance states. The question then arises as to the identity of the redox transition that precedes the onset of oxygen evolution at Fe electrodes. On the basis of some unusual voltammetric profiles recorded for a particular Fe electrode (Figures 3.4.22 and 3.4.23) and with reference to thermodynamic considerations, we have proposed that a surface Fe(III)→Fe(VI) oxidation, produces the active sites (which can thus be represented as $[Fe(VI)O_m(OH)_n]^{p-}$ (p=2m+n-6)) for the o.e.r. at oxide covered Fe electrodes. It is worth noting that a significant difference between scheme (3.5.3) proposed for the o.e.r. at Ni, and scheme (3.5.68) for the reaction at Fe and Co electrodes, is that the former pathway envisages the oxidation of the active Ni(III) metal centre, whereas in the case of the latter mechanism the electrode surface is not further oxidised, and acts essentially as an electron sink.

As was discussed in chapter 4, electrochemical impedance spectroscopy (EIS) provides a means to obtain additional and complementary information on the o.e.r, to that accessible by traditional dc measurements. One of the most significant conclusions arising from our EIS work, is that the Tafel slope, measured for our systems, either by steady state polarisation or derived from EIS measurements, is truly

characteristic of the kinetics of the o.e.r., and does not arise due to the increasing conductivity at high anodic potentials, of a previously, essentially insulating oxide film. It was necessary to test the authenticity of the measured Tafel slopes with respect to their characterisation of the kinetics of the o.e.r., in light of the concepts of Cahan and Chen[7], who proposed (rather convincingly) that the apparent o.e.r. Tafel slopes recorded for Fe electrodes in borate buffer solution (pH 8.4) and for Au electrodes in 1 N $HClO_4$, were actually characteristic of the changing conductivity with potential, of the passive oxide films formed on these electrodes (chemi-conductor model).

For all the Fe electrodes (fresh non-pre-treated, relatively fresh pre-reduced and extremely aged pre-reduced anodes) studied by ac impedance, three relaxation processes were identified. The most rapid of these, with characteristic frequencies in the vicinity of 10^4 Hz was attributed to the resistivity (R_{film}) and dielectric properties (C_{film}) of the anodic oxide film. For all the electrodes, Ni, Co and Fe, the impedance response at the lower frequency end of the relevant spectra, was attributed to the relaxation of the coverage of electrosorbed Faradaic reaction intermediates (R_sC_ϕ), whilst the response at intermediate frequencies (approximately10^2 -10^3 Hz) was attributed to the relaxation of the double layer capacitance (R_pC_{dl}). Only the latter two relaxation processes were detected by the EIS measurements on the Ni and Co electrodes. Evidently the oxide film resistance and/or capacitance is so small for these electrodes, that the $R_{film}C_{film}$ time constant is characteristic of a shorter time-scale than can be resolved by ac impedance spectroscopy.

In the case of the Fe electrodes, with the exception of the extremely aged pre-reduced electrode (Figures 4.2.1 and 4.2.2), the time constants related to the double layer capacitance and the pseudo-capacitance are quite similar and it is therefore difficult to decouple the contributions of these separate processes. For this reason the Nyquist representations of the impedance data for the non-pre-treated (Figures 4.2.4 and 4.2.5) and fresh pre-reduced (Figure4.2.7) Fe electrodes, apparently consist of two psuedo-semi-circular regions – the upper frequency arc is related to the properties of the passive film, the lower frequency response is actually the superposition of the responses of the R_pC_{dl} and R_sC_ϕ relaxation processes. A similar 'bundling together' of the R_pC_{dl} and R_sC_ϕ time constants occurs for the Ni electrodes, with the result that the complex plane representations of their EIS responses, seem to consist of only one psuedo-semi-circular region (Figure 4.4.4).

There is clearer temporal resolution of the R_pC_{dl} and R_sC_ϕ relaxation processes for the Co electrodes, as is evident from the Nyquist plots of Figure 4.3.2. By contrast with the complex plane representations of the Fe EIS data, the high frequency arcs of Figure 4.3.2 are due to the relaxation of the double layer capacitance, while the lower frequency arcs are related to the relaxation of the adsorption pseudo-capacitance.

Using a complex non-linear least squares (CNLS) fitting program, the raw EIS data was fitted to appropriate equivalent circuit models (Circuit 2 of Figure 4.2.8 for the Ni and Co data and Circuit 3 (Figure 4.2.8) for the Fe data) and the optimum fit values of the various elements have been tabulated. Where possible (see section 4.2.2), values of the total Faradaic resistance, R_{far}, ($R_{far} = R_s + R_p + R_{film}$), were extracted directly from the raw impedance data, otherwise they were evaluated from the optimum fitting parameters, and values for the o.e.r. Tafel slope were calculated from plots of log $(R_{far})^{-1}$ vs. η, according to equation (2.1.44). Very good agreement was found between the Tafel slopes obtained in this manner, and those measured directly by the dc steady state polarisation technique, for the various Ni and Fe electrodes investigated. Such a Tafel slope analysis could not be performed for the Co electrodes, because R_{far} was not satisfactorily resolved (at the low frequency end of the EIS spectra) for practical experimental time-scales – see section 4.3.

In order to obtain meaningful comparisons between the catalytic activities of the Ni, Co and Fe electrodes towards the o.e.r. (and indeed between electrodes of the same metal subjected to different pre-treatments), it is necessary to estimate electrode roughness factors, f_r, thus permitting normalisation of the current density observed at a given overpotential to the catalytically active surface area. As was discussed in section 2.1.9, most of the techniques usually applied to the determination of real surface area are not applicable to anodic oxide covered base metal electrodes, and those that are involve the admission of some potentially dubious assumptions. Notwithstanding this, a method of roughness factor estimation was adopted, based on the evaluation of the total charge, Q_{dec}, passed during the desorption of the o.e.r. intermediate species following the interruption of the reaction proceeding in the steady state. The technique involved the evaluation of Q_{dec}, by the integration of experimental electrode cathodic discharge current vs. time transients. We rationalised the origin of the experimental cathodic currents in terms of a 2 electron per active site discharge for the Ni and Co electrodes (see reactions (5.2.1) and (5.3.1) respectively),

and a 4 electron per active site discharge current for the Fe electrodes (reaction (5.4.1)).

The roughness factors determined by the current decay transient method for various Ni, Co and Fe electrodes are summarised in Table 5.5.1. The sub-unity f_r values estimated for the fresh Fe electodes indicates that only a fraction of the wettable electrode surface area is active towards the o.e.r. for these electrodes. This is consistent with our view, that the active sites for oxygen evolution at oxide covered Fe electrodes are surface Fe(VI) centred anionic complex species. A relatively low coverage of such entities is expected because most of the Fe^{6+} ions produced at the electrode surface at high anodic potentials, are expected to dissolve as FeO_4^{2-} ferrate species.

Normalising the o.e.r. steady state polarisation curves recorded in 1.0 M NaOH according to the roughness factors of Table 5.5.1, leads to the activity series, Ni > Co > Fe at overpotentials corresponding to the lower straight line Tafel regions. Such a trend is also displayed if the Faradaic currents are normalised to the geometric surface area, however, relative to the Ni electrode, this approach leads to an underestimation of the performance of the Fe electrode, and an overestimation of the activity of the Co anode. Application of the pre-reduction and pre-oxidation routines to a Ni electrode in 1.0 M NaOH was observed to produce surfaces with very similar roughness factors – however the pre-oxidised electrode displayed significantly enhanced o.e.r. performance relative to the pre-reduced anode – see Figure 5.5.1. A non-pre-treated Ni electrode exhibited an intermediate catalytic activity. This behaviour was explained in terms of the pre-oxidation producing a surface with a relatively higher density of the active nickel oxyhydroxide species (β-NiOOH) in comparison to the non-pre-treated surface. By contrast, it would seem that the pre-reduction of the Ni electrode leads to a surface with a higher proportion of the less active form of the oxyhydroxide (γ phase) relative to the non-pre-treated anode.

6.2 Future Work

As commented by Gottesfeld and Srinivasan[8]; " the "science" of the o.e.r. is a "science" of the oxides and their properties". With this in mind, it is our belief, that for a given electrode, traditional electrochemical techniques cannot yield much further information on the oxygen evolution reaction, and the nature of the catalytically

active surface, than that of the type presented in the present work for passive oxide covered polycrystalline Ni, Co and Fe electrodes. In order to move the "science" of the o.e.r. to the next level, there is a need to combine electrochemical approaches with techniques of surface science.

As we have seen in the present work, the thickness, conductivity and structure of the anodic oxide film, as well as the chemical nature of the surface species, are all important factors in determining the o.e.r. electrocatalytic performance of a given electrode at a particular overpotential. There are few accounts in the literature, of the influence of oxide film thickness (accurately measured by in-situ techniques such as ellipsometry or XPS sputter depth profile analysis) on o.e.r. catalytic activity. Using in-situ ellipsometry, Lu and Srinivasan[1] found that the chemical nature of the surface of the anodic oxide formed on Ni in 1 N KOH was more significant than the film thickness in determining o.e.r. catalytic performance. By contrast, the quantum mechanical tunnelling dual barrier model proposed by Damjanovic and co workers (see section 3.5.2 and references contained therein) for the o.e.r. at pre-anodised Pt electrodes envisages a strong dependence of catalytic activity on oxide layer thickness. In situ ellipsometric measurements by these workers[9] corroborated their theory (albeit only for very thin oxide films < 15 Å). The two examples cited above, reach contradictory conclusions (which may very well arise from the fundamental differences in the nature of the anodic films formed on Pt and Ni), but they do at least point to the need for more investigation of the effect of oxide layer thickness on o.e.r. catalytic activity. Computational developments, which allow the fitting of the optical data obtained in ellipsometric measurements to elaborate physical models of oxide film structure (e.g. see reference 10), mean that in-situ spectroscopic ellipsometry, potentially offers a route to the accurate characterisation of oxide film thickness, structure, composition, conductivity and surface roughness.

Other non-electrochemical techniques that could possibly help to elucidate the influence of the physical and/or chemical properties of oxide electrodes on their catalytic activities towards the o.e.r., include XPS (as demonstrated for example by the work of Strehblow and co-workers on the passive oxide films formed on Co and Fe electrodes[11, 12]) and spectroscopic techniques such as potential modulated reflectance (see, for example, reference 13) and in-situ Raman spectroscopy (both unenhanced and surface enhanced)[14]. The major drawback of XPS, or indeed other potentially useful ex-situ surface science techniques such as scanning electron

microscopy (SEM), energy dispersive X-ray analysis (EDX) and Auger electron spectroscopy (AES), is that these methods require the removal of an electrode from solution and its transferral to a high vacuum or ultra high vacuum chamber. This effectively limits the use of these techniques in electrode characterisation, to research groups that specialise in combining electrochemical and surface science measurements. A number of research groups have invested great effort in developing elaborate transfer systems which move working electrodes from electrochemical cells directly to vacuum chambers without exposure to air. Some of these systems are the subject of a topical review by Reniers[15], who points out that the transfer of an electrode through air from a liquid environment to a vacuum chamber may induce an uncontrolled post-oxidation or adsorption process, that would distort the result of the ex-situ characterisation. The application to electrochemical systems of the in-situ techniques referred to above (e.g. ellipsometry, Raman spectroscopy) also requires specialist experimental set-ups, and thus these types of analysis are also largely restricted to research groups that specialise in such work. Furthermore, it is obvious that combining surface science techniques with electrochemical methods requires the coming together of workers with expertise in these different disciplines.

Chapter 6 References

1 Lu, P.W.T., Srinivasan, S., *J. Electrochem. Soc.*, **1978**, *125*, 1416.

2 Lyons, M.E.G., Burke, L.D., *J. Chem. Soc., Faraday Trans. 1*, **1987**, *83*, 299.

3 O'Sullivan, E.J.M., Burke, L.D., *J. Electrochem. Soc.*, **1990**, *137*, 466.

4 Meyer, R.E, *J. Electrochem. Soc.*, **1960**, *107*, 847.

5 MacDonald, J.J., Conway, B.E., *Proc. R. Soc. London, Ser. A*, **1962**, *269*, 419.

6 Bockris, J.O'M., Otagawa,T., *J. Phys. Chem.*, **1983**, *87*, 2960.

7 Cahan, B.D., Chen, C.T., *J. Electrochem. Soc.*, **1982**, *129*, 700.

8 Gottesfeld, S., Srinivasan, S., *J. Electroanal. Chem.*, **1978**, *86*, 89.

9 Damjanovic, A., Ward, A.T., O'Jea, M. *J. Electrochem. Soc.*, **1974**, *121*, 1186.

10 de Souza, L.M.M., Kong, F.P., McLarnon, F.R., Muller, R.H., *Electrochimica. Acta.*, **1997**, *42*, 1253.

11 Foelske, A., Strehblow, H.-H., *Surf. Interf. Anal.*, **2002**, *34*, 125.

12 Haupt, S., Strehblow, H.-H., *Langmuir*, **1987**, *3*, 873.

13 Larramona, G., Gutierrez, C., *J. Electrochem. Soc.*, **1989**, *136*, 2171.

14 Kostecki, R., McLarnon, F., *J. Electrochem. Soc.*, **1997**, *144*, 485.

15 Reniers, F., *J. Phys. D: Appl. Phys.*, **2002**, *35*, R169.